De la dynamique de la lithosphère

Laurent Husson

▶ **To cite this version:**

Laurent Husson. De la dynamique de la lithosphère. Sciences de la Terre. Universite Rennes 1, 2010. tel-01138112

HAL Id: tel-01138112

https://hal-insu.archives-ouvertes.fr/tel-01138112

Submitted on 1 Apr 2015

HAL is a multi-disciplinary open access archive for the deposit and dissemination of scientific research documents, whether they are published or not. The documents may come from teaching and research institutions in France or abroad, or from public or private research centers.

L'archive ouverte pluridisciplinaire **HAL**, est destinée au dépôt et à la diffusion de documents scientifiques de niveau recherche, publiés ou non, émanant des établissements d'enseignement et de recherche français ou étrangers, des laboratoires publics ou privés.

UNIVERSITÉ RENNES 1

De la dynamique de la lithosphère

par

Laurent Husson

Mémoire d'habilitation à diriger les recherches

Jury :

Rapporteurs

Claude Jaupart, Directeur de Recherche, IPGP

Carolina Lithgow-Bertelloni, Reader, University College London

Patrice Rey, Professeur, Université de Sydney

Examinateurs

Philippe Davy, Directeur de Recherche, CNRS

Claudio Faccenna, Professeur, Università Roma 3

Trond Torsvik, Professeur, Université de Oslo

soutenu le 8 janvier 2010 à Rennes

Géosciences Rennes, Université Rennes 1, 263, av du général Leclerc, 35042 RENNES cedex, 02 23 23 60 75, http://www.geosciences.univ-rennes1.fr

Laurent Husson

Expérience Professionelle

2006-	**Chargé de Recherche 1ère classe**, *CNRS*
2004-2006	**Chercheur postdoctorant**, *MIT*
2002-2004	**Chercheur postdoctorant**, *Collège de France*
2002	**Ingénieur consultant**, *Beicip-Franlab*
2001-2002	**Chercheur postdoctorant**, VIE, *IRD*

Formation

1998-2001	**Doctorat en Sciences de la Terre**, *ENS-Lyon* Dynamique et regime thermique des chaines de montagnes dir. Yanick Ricard & Isabelle Moretti
1997-1998	**DEA "Dynamique de la Lithosphere"** *Universite Joseph Fourier, Grenoble*

Projets de recherche financés

2006-2007 "Reliefs" INSU/CNRS
Couplages entre circulation mantellique, érosion et topographie : exemple de la Patagonie méridionale (J. Martinod)

2006-2007 "3F" INSU/CNRS
Circulations de fluides et localisation de la déformation dans un décrochement lithosphérique : le Cisaillement Sud Armoricain
(P. Boulvais)

2007-2008 "Reliefs" INSU/CNRS
Quantification des altitudes de la chaîne hercynienne ouest -européenne
(P. Boulvais)

2007-2008 "Reliefs" INSU/CNRS
Couplages entre circulation mantellique, érosion et topographie : exemple de la Patagonie méridionale (J. Martinod)

2007-2008 "Reliefs" INSU/CNRS
Continents inondés à l Archéen : contrôles internes ou externes ?
(N. Coltice)

2007-2008 "SEDIT" INSU/CNRS
Dynamiques des subductions (L. Husson)

2008-2009 INSU/CNRS
Géodynamique des variations du niveau marin relatif (L. Husson)

2008-2009 "Reliefs" INSU/CNRS
Continents inondés à l' Archéen : contrôles internes ou externes ?
(N. Coltice)

2009-2010 Univ. Rennes-1
Géodynamique du niveau marin (L. Husson)

Encadrements et pédagogie

2006-2009 **Thèse de Doctorat**, Christelle Loiselet, 50% (co-direction Jean Braun)
Dynamique de la subduction, Univ. Rennes 1

2008-2011 **Thèse de Doctorat**, Emilie Ostanciaux, 50% (co-direction Cécile Robin)
Dynamique des variations du niveau marin : observations, Univ. Rennes 1

2009-2012 **Thèse de Doctorat**, Fatima Messar, 50% (co-direction Gaël Choblet)
Dynamique des variations du niveau marin : modélisation, Univ. Rennes 1

2009-2012 **Thèse de Doctorat**, Mélanie Gérault, 30% (co-direction Thorsten Becker)
Impact des collisions sur la géodynamique globale, Univ. South California

---

2007 **M2 ST**, Paul Planton, 30%
Etude de la déformation horizontale à travers la topographie : exemple de la faille Apline, Nouvelle Zélande, Univ. Rennes 1

2008 **M2 ST**, Mélanie Gérault, 50%
Influence des chaînes de montagnes sur le mouvement des plaques tectoniques, Univ. Rennes 1

2009 **M1 ST**, Thomas Chevalier, 50%
Modélisation analogique d'une collision à contrainte constante, Univ. Rennes 1

2007 **L3 Matériaux**, Steven Le Cléach, 100%
Modélisation analogique en géologie, Univ. Rennes 1 / Univ. Rome 3

2009 **L2 ST**, Cécile Prigent, 50%
Modélisation analogique d'une collision à contrainte constante, Univ. Rennes 1

2008 Jury d'attribution des bourses de thèses MNR, Univ. Rennes 1

2008-2009 Rapporteur M2 ST, M2 H3, Univ. Rennes 1

2009 Jury M2 Planétologie et Géodynamique, Univ Nantes

2006-2009 **Enseignement**, L3, M1, M2, Univ. Rennes 1, Univ Nantes

Publications

Articles en Préparation

♣ Husson, L., Conrad, C.P., *Impact of the Hapagea surpercontinental aggregation on American Cordilleras and the seafloor age distribution*, en préparation.

♣ Kreemer, C., Husson, L., *On the correlation between the intraplate stress field and absolute plate motions* , en préparation.

♣ Pedoja, K., Regard, V., Husson, L., Martinod, J., Fucks, E., Iglesias, M., Weill, P., Robin, N., *Uplift of Quaternary shorelines in Eastern Patagonia : Darwin revisited*, en préparation.

♣ Loiselet, C., Braun, J., Husson, L., *Estimates of work required for mantle flows in subduction zones*, en préparation.

♣ Autin, J., Bellahsen, J., Husson, L., Beslier, M-O., Leroy, S., dAcremont, E., *Analogue models of oblique rifting in a cold lithosphere*, en préparation.

Articles Soumis

♣ Loiselet, C., Braun, J., Husson, L., Grudjic, D., Thieulot, C., Le Carlier, C., Yamato, P., *Subducting slabs : jellyfishes in the Earth mantle*, soumis à G3.

♣ Pedoja, K., Husson, L., Cobbold, P.C., Regard, V., Ostanciaux, E., Johnson, M.E., Kershaw, S., Martinod, J., Delcaillau, B., *Relative sea-level fall since the Last Interglacial Maximum : Why are coasts uplifting worldwide ?* , soumis à Earth Science Reviews.

♣ Husson, L., Iaffaldano, G., Bunge, H-P., *Monsoon speeds up Indian plate motion*, soumis à Geology.

Articles Publiés

♣ Husson, L., Brun, J.P., Yamato, P., Faccenna, C., *Episodic slab rollback fosters exhumation of HP-UHP rocks*, Geophysical Journal International, doi : 10.1111/j.1365-246X.2009.04372.x.

♣ Loiselet, C., Husson, L., Braun, J., 2009 : *From longitudinal slab curvature to slab rheology*, Geology, 37, 747-750, doi : 10.1130/G30052A.1.

♣ Yamato, P., Husson, L., Braun, J., Loiselet, C., Thieulot, C., 2009 : *Influence of surrounding plates on 3D subduction dynamics*, Geoph. Res. Lett., 36, doi :10.1029/-2008GL036942.

♣ Conrad, C.P., Husson, L., 2009 : *Influence of dynamic topography on sea level and its rate of change*, Lithosphere, 1, 110-120, doi :10.1130/L32.1.

♣ Guillaume, B., Martinod, J., Husson, L., Roddaz, M., Riquelme, R., 2009 : *Neogene uplift of central-eastern Patagonia : dynamic response to active spreading-ridge subduction ?*, Tectonics, 28, doi :10.1029/2008TC002324.

♣ Husson, L., Conrad, C.P., Faccenna, C., 2008 : *Tethyan Closure, Andean Orogeny, and Westward Drift of the Pacific Basin*, Earth Planet. Sc. Lett., 271, 303-310, doi :10.1016/j.epsl.2008.04.022.

♣ Royden, L., Husson, L. 2009 : *Subduction with variations in slab buoyancy : Models and application to the Banda and Apennine systems*, in : Funiciello, F. & Lallemand, S. (ed), Subduction Zone Geodynamics, Frontiers in Earth Sciences, Springer.

♣ Husson, L., Henry, P., Le Pichon, X., 2008 : *Thermal regime of the NW shelf of the Gulf of Mexico. 1) Thermal and pressure fields* , B.S.G.F., 179, 129-137.

♣ Husson, L., Le Pichon, X., Henry, P., Flotté, N., Rangin, C., 2008 : *Thermal regime of the NW shelf of the Gulf of Mexico. 2) Heat Flow*, B.S.G.F., 179, 138-146.

♣ Rangin, C. Le Pichon, X., Flotté, N., and Husson, L., 2008 : *Cenozoic gravity tectonics in the northern Gulf of Mexico induced by crustal extension. A new interpretation of multichannel seismic data*, B.S.G.F., 117-128.

♣ Flotté, N., Rangin, C., Martinez-Reyes, J., Le Pichon, X., Husson, L., and Tardy, M., 2008 : *The Rio Bravo Fault, a major late Eocene-Oligocene left-lateral shear zone*, B.S.G.F., 147-160.

♣ Husson, L., Conrad, C.P., 2006 : *Tectonic velocities, dynamic topography, and relative sea level*, GRL, doi :10.1029/2006GL026834.

♣ Husson, L., 2006 : *Dynamic topography above retreating subduction zones*, Geology, doi :10.1130/G22436.1.

♣ Royden, L., Husson, L., 2006 : *Trench motion, slab geometry and viscous stresses in subduction systems*, Geophysical Journal International, doi :10.1111/j.1365-246X.2006.03079.x.

♣ Ricard,Y., Husson, L., 2005 : *Propagation of tectonic waves*, GRL, doi :10.1029/-2005GL023690.

♣ Husson, L., Ricard, Y., 2004 : *Stress balance above subduction zones - application to the Andes*; Earth Planet. Sc. Lett., 222(3-4), 1037-1050.

♣ Husson, L., Mugnier, J-L., Leturmy, P., Vidal, G., 2004 : *Kinematics and sedimentary balance of the Subhimalayan range*, W. Nepal ; in : MacClay, K. (ed), Thrust Tectonics and Hydrocarbon Systems, AAPG Memoir 82, 115-130.

♣ Husson, L., Sempere, Th., 2003 : *Thickening the Altiplano crust by gravity-driven crustal channel-flow*; Geoph. Res. Let., 30(5), 124.

♣ Husson, L., Mugnier, J-L., 2003 : *Three-dimensional reconstruction from surface data, restoration, and kinematics of the Baisahi passive-roof duplex*, W. Nepal ; Journal of Structural Geology 25, 79-90.

♣ Husson, L., Moretti, I, 2002 : *Thermal regime of fold and thrustbelts. An application to the Bolivian Sub Andean Zone*; Tectonophysics, 345, 253-280.

♣ Mugnier J-L., Mascle G., Leturmy P., Huygue P., Husson L., Chalaron E., 1999 : *The Siwaliks of Western Nepal : I) Geometry and Kinematics*; Journal of Asian Earth Sciences, 17, 629-642.

Conférences depuis 2006

♣ AGU fall meeting 2009 : Husson and Conrad, *Impact of the Hapagea surpercontinental aggregation on American Cordilleras and the seafloor age distribution.*

♣ Mantle Convection and Lithosphere Dynamics, Braunwald, 2009, Husson and Conrad, *Impact of Hapagea surpercontinental aggregation on American Cordilleras and the seafloor age distribution.*

♣ AGU 2008 : Husson, *The Indian monsoon speeds up plate motion.*

♣ Geomod 2008 : Husson, Brun, Faccenna, Yamato, *Episodic slab rollback makes it easy for HP rocks to be exhumed.*

♣ EGU Vienne 2007 : Husson, Brun, Faccenna, Gueydan, Royden, *Episodic slab rollback as a mechanism for blueschist exhumation.*

♣ AGU fall meeting 2007 : Conrad, Husson, Robinson, *Global Mantle Flow Models Constrained by Observations of Long Term Sea Level Change.*

♣ ACP Workshop, Siofok 2007 : Husson, *Dynamic topography in the Aegean and Pannonian Basins.*

♣ Mantle Convection and Lithosphere Dynamics, Carry-le-Rouet 2007 : Husson, Conrad, Faccenna, *Tethys closure, Andean building, and the Westward drift of the lithosphere.*

♣ MEDUSA Workshop, Delphes 2007.

♣ SUBCO, Montpellier 2007 : Husson, Conrad, Faccenna, *Tethys closure, Andean building, and the Westward drift of the lithosphere.*

♣ Topo-Europe, Rome 2007 : Husson, Royden, Martinod, *Dynamic topography at continental convergent margins.*

♣ EGU Vienne 2007 : Husson, Conrad, Faccenna, *Tethys closure and Andean building cause westward drift of the lithosphere.*

♣ AGU fall meeting 2006 : Husson and Conrad, *Tectonic velocities, dynamic topography, and Relative Sea Level*.

Séminaires depuis 2006

Johns Hopkins University (Baltimore), Geosciences Rennes, LGIT (Grenoble), LMTG (Toulouse), IUEM (Brest), M2C (Caen), Freie Univ. (Berlin), ENS-Lyon, ENS-Paris, Geosciences Rennes, LPG (Nantes), EOST (Strasbourg)

Activités scientifiques pour la communauté

Sessions	**EGU** 2009, **AGU** 2009, **EGU** 2010
Expertise	**Recensions** pour *Geology (5), Earth and Planetary Science Letters (5), Geophysical Journal International (1), Lithoprobe Special Issue (1), Bulletin de la Societe Géologique de France (1)*
Expertise	**Recension** pour Projet INSU 2009

UNIVERSITÉ RENNES 1

Préambule

Le mémoire qui suit est articulé sous la forme d'une compilation de mes recherches effectuées au cours d'une dizaine d'années. Essentiellement construit dans un ordre chronologique -*modulo* quelques adaptations thématiques-, il illustre l'évolution de ma philosophie des Sciences de la Terre, sous la forme de l'élargissement spatial autour de l'objet d'étude qu'à emprunté mon cheminement scientifique dans le temps. J'ai commencé par étudier des structures unitaires sur le front des chaînes de montagnes pour ensuite considérer les chaînes de montagnes comme des bourrelets qui rident la surface de la Terre et enfin développer une réflexion à l'échelle de la géodynamique globale.

Cette évolution s'accompagne d'une migration floue de ma réflexion du *contexte de justification* vers le *contexte de découverte*, c'est-à-dire que ma démarche initialement construite sur un pôle naturaliste, dominée par l'observation de l'objet naturel et son interprétation dans un paradigme existant, s'est orientée vers la formulation physique et la théorisation des processus. En pratique, c'est une combinaison des deux que je développe actuellement.

Mon parcours scientifique m'a permis de participer à des chantiers variés, des relations entre tectonique et sédimentation à la dynamique interne de la Terre, nécessitant l'emploi de méthodologies cohérentes. Animé par la quête d'une vision globale, je ne suis titulaire ni d'une méthodologie particulière ni d'une compréhension aboutie d'un sujet particulier. En conséquence, ce mémoire ne saurait être construit comme une monographie. A l'inverse, il fournit des éléments parfois hétéroclites dont le point de convergence est la dynamique de la lithosphère.

La personnalité scientifique se construit aussi au gré des rencontres. Comme celles d'avec Isabelle Moretti, Yanick Ricard et Wiki Royden.

Table des matières

Chapitre 1

Dynamique orogénique

L'étude des mécanismes de déformation de la lithosphère continentale a subi une évolution graduelle depuis l'essor du concept de tectonique des plaques. Elle était auparavant élaborée de manière confuse, s'appuyant sur des observations biaisées par des concepts sous-jacents parfois erronés. Lorsque la tectonique des plaques fait son entrée à la fin des années soixante, des raisonnements souvent plus simples et logiques clarifient les idées de l'époque sur la formation des chaînes de montagnes en particulier. Il devient alors possible de concilier les observations toujours plus abondantes avec une interprétation physique réaliste. Différents protocoles d'étude des orogènes apparaissent entre les pôles d'observation géologique et de raisonnement physique.

La description structurale et cinématique est un des piliers sur lequel se fonde les interprétations mécaniques. La section 1.1 présente mes contributions apportées à la compréhension de la formation des fronts de chaînes, avec l'exemple du front sud-himalayen. La section 1.2 s'éloigne des structures unitaires et floute la vision des chaînes de montagnes pour n'en conserver que les traits cinématiques et morphologiques principaux afin de proposer un schéma de développement de la croûte épaissie des chaînes de montagnes, étayé sur l'exemple des Andes Centrales. En s'éloignant davantage encore, la lithosphère des chaînes de montagnes devient un bourrelet aux limites de plaques dont la cinématique nous renseigne sur les processus dynamiques entre les plaques. Les aspects que j'ai examinés en particulier sont discutés en section 1.3, en proposant une extension des concepts développés sur la dynamique de la lithosphère aux processus de rifting.

1.1 Tectonique des fronts de chaîne

Les avant-pays plissés sont caractérisés par une déformation qui n'implique pas (ou peu) le socle crustal mais la couverture sédimentaire. Le dépôt des sédiments qui forment cette couverture est souvent synchrone de l'édification de la chaîne dans son ensemble. C'est par exemple le cas des Alpes, de l'Himalaya, et sous une forme un peu plus complexe, celui des Andes. La chaîne interne, ou la croûte sépaissit, est comprise comme une condition cinématique en arrière de la chaîne d'avant-pays, classiquement imagée par le godet d'un bulldozer repoussant un tas de sable, qui se déforme en se propageant vers l'exterieur de la chaîne. Ces déformations sont très caractéristiques ; facilement identifiables dans le paysage, elles ont été largement décrites. En détail, c'est un assemblage de structures plissées. Plusieurs motifs géométriques de ces structures sont récurrents et font l'objet de classifications qui dérivent essentiellement des travaux de Dahlen, Suppe, ou Davis, accompagnées de l'étude de la mécanique associée [Dahlen, 1990, Dahlen et al., 1984, Davis et al., 1983, Suppe, 1983, Suppe & Medwedeff, 1990].

1.1.1 Croissance d'une structure individuelle

Dans le détail, ces structures ont parfois des géométries complexes, comme dans l'exemple qui suit où une structure individuelle est composée de plusieurs écailles imbriquées. Dans la majorité des cas, les données de surface sont indisponibles. Pour déterminer la géométrie de ces structures, le recours à l'équilibrage structural est une possibilité. Les hypothèses qui sous-tendent l'équilibrage sont l'isopacité des couches stratigraphiques, c'est-à-dire que leurs épaisseurs, ou puissances stratigraphiques, mesurées localement sont supposée uniformes sur l'ensemble de la structure. Une simple projection spatiale des mesures de surface permet alors de reconstruire la structure profonde. Cette méthode, classiquement utilisée selon des coupes orthogonales à la direction structurale, est ici etendue en 3D, en collaboration avec J-L. Mugnier. Appliquée à une structure du front sud-himalayen, elle a permis de révéler la structure sous-jacente en duplex. Cette simple technique s'est révélée puissante pour connaître la géométrie des structures et a été abondament utilisée par l'industrie pétrolière.

PERGAMON

Journal of Structural Geology 25 (2003) 79–90

JOURNAL OF STRUCTURAL GEOLOGY

www.elsevier.com/locate/jsg

Three-dimensional horizon reconstruction from outcrop structural data, restoration, and strain field of the Baisahi anticline, Western Nepal

Laurent Husson[a,*], Jean-Louis Mugnier[b,1]

[a]*Ecole Normale Supérieure de Lyon, UMR CNRS 5570, 46 Allée d'Italie, 69364 Lyon cedex 07, France*
[b]*LGCA, UPRESA CNRS 5025, 1381 Rue de la piscine, BP 53, 38041 Grenoble cedex 9, France*

Received 28 February 2001; received in revised form 7 March 2002; accepted 14 March 2002

Abstract

Within many fold and thrust belts, preservation of bed thickness is generally assumed during deformation. A three-dimensional (3D) reconstruction method is proposed from outcrop structural data. This technique accounts for along-strike thickness variations. By a series of 3D spatial projections of dip and strike data, the thickness of strata from any point at the ground surface to reference horizons on stratigraphic columns can be calculated across-strike and projected along the poles of the associated strata, providing sets of dots in space, which represent folded horizons.

The technique is applied to the Baisahi antiform, located on the frontal Subhimalayan thrust. An along-strike deformation gradient is evidenced by two-dimensional cross-section balancing, which shows a passive-roof duplex structure. The 3D geometry of the roof is reconstructed, allowing other approaches such as unfolding to be done. The residual strain field induced by restoration shows distortion features, which are interpreted as internal strain due to the propagation of the fault. © 2002 Elsevier Science Ltd. All rights reserved.

Keywords: 3D reconstruction; Unfolding; Strain; Passive roof duplex; Subhimalayan zone

1. Introduction

The characterization of fold and thrust belt structures is of major relevance world-wide, for both industrial and academic interests. Reconstruction of the three-dimensional (3D) geometry of complex structures still constitutes a major goal for structural geology. The structural description of these areas can be poorly constrained when these zones are remote; in these cases, subsurface geometries are badly documented due to very widely spaced seismic and well data. Two-dimensional (2D) cross-section balancing (Dahlstrom, 1969; Boyer and Elliott, 1982; Woodward et al., 1985) led to major progress in the interpretation of structures at depth. The purpose of this study is to present an original 3D reconstruction method from outcrop structural data. This technique allows the 3D shape of structures to be evaluated in both their eroded and buried parts, only from the measured attitudes of bedding at surface level.

An application to the Baisahi anticline, in the Subhimalayan range of Western Nepal, is presented. Cross-section balancing helps to estimate the geometry and kinematics of the Baisahi structure. The high resolution structural map (Kayastha et al., 1999) provides the data necessary to undertake reconstruction of the Baisahi antiform in 2D and ultimately in 3D. Additionally, unfolding of a 3D reconstructed horizon is used to constrain the evolution of the structure.

The Subhimalayan range of Western Nepal is a southward tapering wedge of syn-orogenic sediments, located in the Himalayan foothills. It is made of several south-verging slices of coarsening upward molasse. Constant bed thickness is a general assumption in this area (e.g. Schelling and Arita, 1991; Mugnier et al., 1992; Schelling, 1992; Powers et al., 1998) and flexural slip hypothesis has been successfully tested on active folding there (Lavé and Avouac, 2000). Moreover, the wedge only underwent a single N10 to N30 horizontal main shortening direction (Jouanne et al., 1999). Numerous structural data were acquired in this zone. Therefore this area is appropriate to apply the proposed 3D reconstruction technique.

2. Geological framework

2.1. Regional setting

The Subhimalayan range constitutes the southern

* Corresponding author. Fax: +33-4-7272-8677.
E-mail addresses: laurent.husson@ens-lyon.fr (L. Husson), mugnier@ ujf-grenoble.fr (J.-L. Mugnier).
[1] Tel.: +33-4-7651-4070; fax: +33-4-7651-4058.

0191-8141/02/$ - see front matter © 2002 Elsevier Science Ltd. All rights reserved.
PII: S0191-8141(02)00044-5

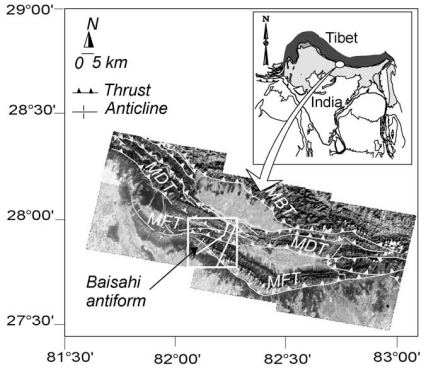

Fig. 1. SPOT spatial imagery and structural sketch of the study area. MFT: Main Frontal Thrust; MDT: Main Dun Thrust; MBT, Main Boundary Thrust. Box: Baisahi reconstructed antiform. Icon: location of the study area. White lines: location of cross-sections. © Cnes 1991—Spot Image Distribution.

foothills of the Himalayas, above the downflexed Indian lithosphere. It is a tectonic wedge of syn-orogenic sediments, fed by the foreland Indo-Gangetic alluvial plain. This wedge accommodates an important part of the Indo-Asian convergence of 50–55 mm/year (Molnar and Tapponnier, 1975; De Mets et al., 1990); shortening rates within the Subhimalayan wedge are estimated to be in the range of 17 ± 5 mm/year (Lyon-Caen and Molnar, 1985; Schelling, 1992; Jackson and Bilham, 1994; Peltzer and Saucier, 1996; Bilham et al., 1997; Mugnier et al., 1999). The Himalayan foothills consist of a few (3–5), mainly south-verging thrust sheets (e.g. Mascle et al., 1986; Leturmy, 1997; Powers et al., 1998), which characterize the thin-skinned pattern of deformation in this intracontinental wedge (Mugnier et al., 1992, 1999; Husson et al., 2002). The faults branch from a major décollement that dips 4–5° to the north (Galahaut and Chandler, 1992; Biswas, 1994; Raiverman et al., 1994). Shortening is accommodated by the Main Boundary Thrust (MBT) at the northern boundary with the Lesser Himalayas, the Main Frontal Thrust (MFT) to the south and the Main Dun Thrust (MDT) in between (Hérail and Mascle, 1980; Mugnier et al., 1992, 1998). The Subhimalayan range has been mainly described as fault propagation folds, duplexes, and north-dipping monoclines (e.g. Banks and Warburton, 1986; Mascle et al., 1986; Powers et al., 1998; Mugnier et al., 1999).

The stratigraphic sequence involved in shortening is primarily composed of coarsening upward molasse. The molasse, or Siwalik Group, is divided into three major units (e.g. Appel and Rosler, 1994): a distal facies of the Lower Siwaliks (LS1 and LS2, Middle Miocene); a wetland-type facies of the Middle Siwaliks 1 and 2 (MS1 and MS2, Upper Miocene); and a proximal facies of the Upper Siwaliks 1 and 2 (US1 and US2, Pliocene to Lower Pleistocene). These facies record the development and southward progradation of the Subhimalayan range (Hérail et al., 1987; Delcaillau, 1997). The basal décollement is located at the base of the Lower Siwaliks Fm. Duplexes are located below an additional décollement within the Lower Siwalik Fm (e.g. Leturmy, 1997; Mugnier et al., 1999).

2.2. The Baisahi antiform and Rapti syncline

The structure described herein is located at the western end of a MFT segment (Fig. 1), which varies along-strike from a north-dipping monocline at the east to a faulted ramp-fold to the west, and terminates as the Baisahi antiform. Thus, it represents the initial stage in the development of a ramp fold, a situation of major relevance for understanding the wedge tectonic regime and kinematics.

A structural map (Fig. 2) has been compiled from both field data and spatial imagery. Fieldwork provided attitudes of bedding along riverbed exposures. Processing of SPOT imagery (Principal Components Analysis and usual directional filters) allows horizons and contacts of the antiformal Baisahi structure to be correlated between the field transects defined by exposures in streambeds, up to its western closure.

The study area is bounded by the southernmost structural feature (MFT), which becomes blind westward; the corresponding tip point of the fault has been located using SPOT imagery and a 1:50,000 scale geological map (Shresta, personal communication). The Rapti syncline, located north of the Baisahi antiform, is offset on its northern edge by the Rapti reverse fault, which displays minor top-to-the-south displacement (Fig. 2). This fault bounds the analyzed structure to the north. Eastward, the reconstructed surface is arbitrarily limited by the 82°20′ meridian. The western edge of the study area is bounded by the periclinal closure, which displays local accommodation structures (minor thrusts and strike-slip faults) as the Baisahi and Rapti folds get increasingly more tightly oppressed between the blind MFT and the Rapti fault. Bedding data (avoiding the pericline) indicate that the structure is cylindrical on average although it can deviate from true cylindricity as the plunge oscillates around an average horizontal axis (Fig. 2).

Fig. 2. Structural map of the study area. Shaded areas are sampling bands for 3D horizon reconstruction, bold solid lines are reference horizons, dashed lines are location of cross-sections. LS: Lower Siwalik Fm.; MS: Middle Siwalik Fm.; US: Upper Siwalik Fm. The Baisahi anticline and Rapti syncline constitute the reconstructed structure. Box: Stereographic projections of outcrop structural data (without the western pericline area). The average cylindrical shape is evidenced by the distribution of the projected poles over a great circle.

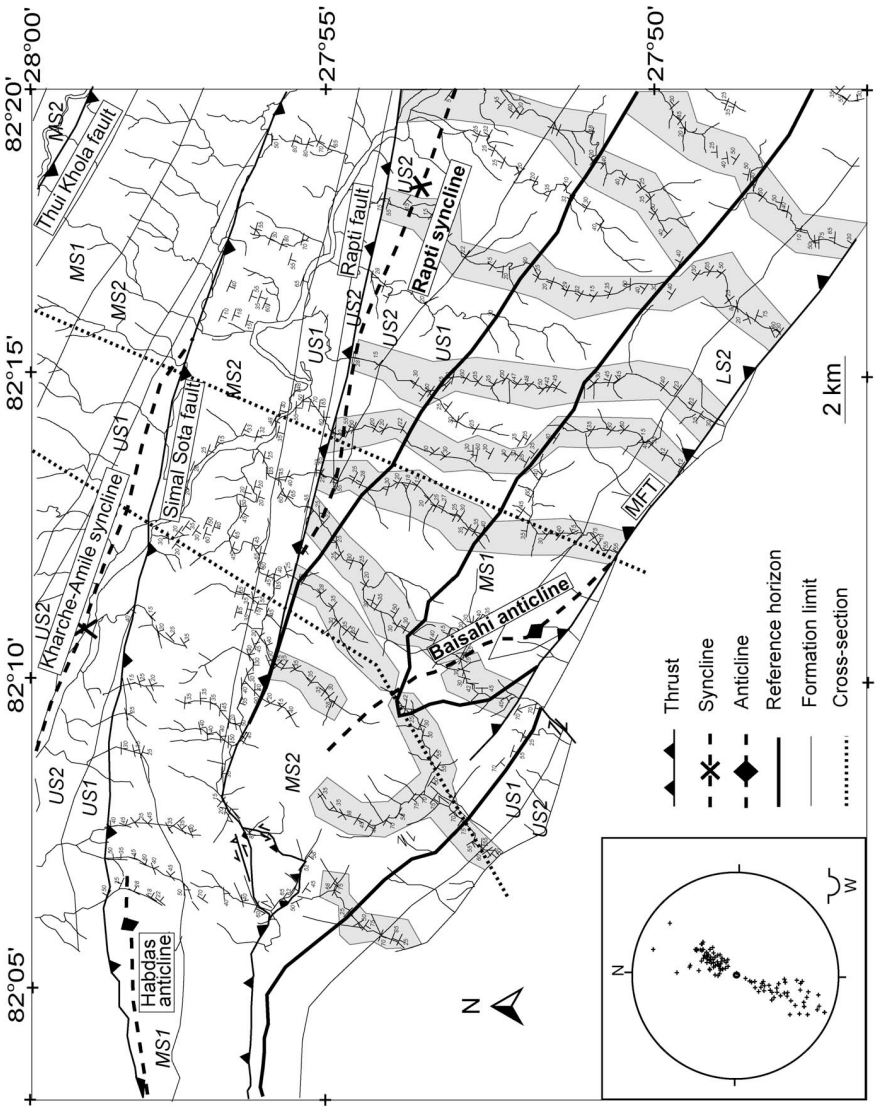

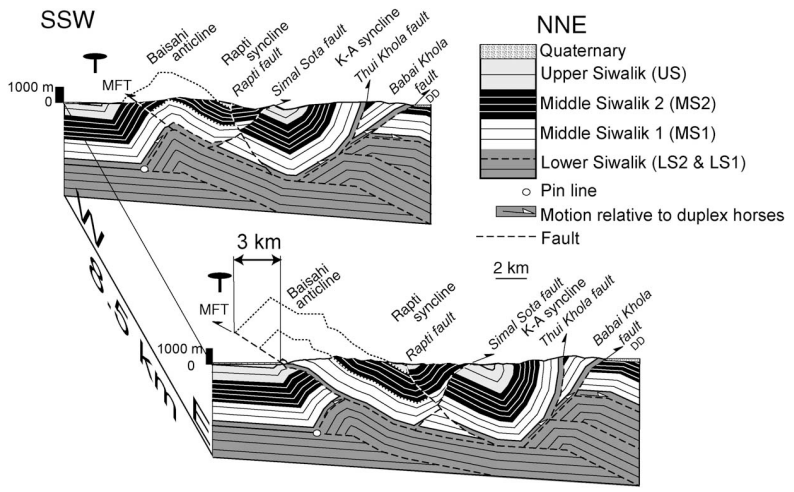

Fig. 3. Balanced cross-sections across the study area. Top: western section; bottom: eastern section. Dashed lines are décollement levels, dotted lines are 3D reconstructed horizons. MFT: Main Frontal Thrust; K.A. Syncline: Kharche–Amile Syncline; DD: Deukhuri Dang. The Thui Khola, Simal Sota and Babai Khola faults are the backthrusts for the passive-roof duplex. Location Fig. 2. The difference in offset between the sections indicates an apparent rotation of the roof of at least 20°.

Structural features in the vicinity of the field area include the Simal Sota and Thui Khola backthrusts in the north and the Kharche–Amile syncline, located between the Thui Khola and Simal Sota backthrusts (Fig. 2). North of the Thui Khola, the structures dip to the south and disappear beneath an alluvial basin (Dang Valley) overthrust by the Babai Khola backthrust. The backthrusts suggest that blind structural features might be hidden beneath the southern Baisahi anticline, stratigraphically within the LS unit.

The measured stratigraphic thickness from one flank to another along a section suggests that constant bed thickness is a correct assumption for 2D reconstruction. Moreover, flexural-slip is assumed to rule the deformation. Two balanced cross-sections have subsequently been constructed on the basis of constant bed lengths and thicknesses and 2D restorability (Dahlstrom, 1969; Woodward et al., 1985) assuming that the section is parallel to the regional displacement vector (Fig. 3). The basal décollement is assumed to gently dip northward at the base of the Lower Siwaliks unit. Such a décollement has already been documented by many authors within the Lower Siwalik Formation (e.g. Schelling and Arita, 1991; Schelling, 1992, Mugnier et al., 1992, 1994, 1999; Acharyya, 1994; Srivastava and Mitra, 1994; Ni and Barraganzi, 1996). The stratigraphic thicknesses are extrapolated from outcrops and estimates from the previous authors. The cross-sections (Fig. 3) are parallel to the average regional compression axis, i.e. between N10° and N30° (Mugnier et al., 1992, 1999; Jouanne et al., 1999). The azimuth of the folds axis is 130°, whereas the overall trend of the Subhimalayan range of Western Nepal is 100–110°. No compressive structure is observed further south, and we assume that shortening is limited southward by the MFT.

Cross-section balancing (Fig. 3) highlights that the base of the MS1 formation beneath the Rapti syncline is 1000–2000 m higher than beneath the Indo-Gangetic plain, indicating that it has been significantly uplifted by blind underlying structures. Moreover, the MFT itself is located close to the top of the LS formation. We interpret these observations as evidence for Lower Siwalik formation horses stacking beneath the Baisahi and Rapti folds. Two décollement levels are assumed to be present, at the base of the entire Siwalik Group and within the Lower Siwalik Fm (LS1/LS2 boundary). Unfortunately no subsurface data is currently available to confirm it. However, duplexes have been described previously, involving similar décollement levels (e.g. Schelling, 1992; Mugnier et al., 1994, 1999; Leturmy, 1997).

Following the assumptions stated above, a passive-roof duplex structure gives a balanced geometry. We are aware that contributions from ancient faults cannot be absolutely rejected to explain the uplift of the Rapti syncline by deforming the base of the young Siwalik Group, but it would not explain the location of the MFT close to the top of the Lower Siwalik formation. Many examples of passive-roof duplexes have been documented world-wide, therefore emphasizing the widespread importance of these blind structures in thrust systems (Suppe, 1980; Price, 1981; Banks and Warburton, 1986; Boyer, 1986; Vann et al., 1986; Wines, 1990; Baby et al., 1992; Medwedeff, 1992; Leturmy, 1997; Mueller and Talling, 1997). Banks and Warburton (1986) defined these as duplexes "whose roof thrust has a backthrust sense and whose roof sequence remains stationary during foreland directed piggy-back style propagation of horses within the duplex". The duplex here involves horses mainly made of the Lower Siwalik LS1 formation; the tendency to form duplexes in the Subhimalayan range is described over the whole Siwalik range (e.g. Biswas, 1994; Mugnier et al., 1994; 1999; Leturmy, 1997). In our interpretation, the Simal Sota, Thui Khola and Babai Khola faults accommodate the passive reverse motion of the duplex roof. Westward, close to the Habdas anticline, the Simal Sota backthrust gradually exhumes deeper levels (up to the upper part of MS1), which indicates that this fault only has a minor throw (increasing westward).

We suggest that north of the Thui Khola fault, other LS duplex slices also associated with the Babai Khola backthrust are required, as shown in Fig. 3. However, as the structure is buried below the Quaternary Deukhuri Dang, the lack of data makes the geometrical interpretation at depth speculative north of the Babai Khola fault. These horses will not be discussed since they are not the focus of the study. The Rapti fault constitutes a late reverse fault with a strike-slip component (deduced from spatial imagery), crosscutting the core of the Rapti syncline. The emerging MFT itself also reflects the late stage evolution of the structure, as it branches off the roof thrust, and thereafter cuts the forelimb of the antiform as a synclinal breakthrough (Suppe and Medwedeff, 1990; Storti and Salvini, 1996). Hence, it post-dates the development of the underlying duplex structure. From terrace uplift (Leturmy, 1997; Lavé and Avouac, 2000), it has been shown that the MFT is the main thrust currently acting in the Siwaliks; it constitutes a discontinuous thrust at the front of the Himalayas (Husson et al., 2001). In the study area, a MFT segment terminates from east to west in the Baisahi anticline.

This stage is similar to the late stage of evolution of fault-propagation folds. The western cross-section displays no slip on the MFT, whereas the eastern one, 8.5 km east, shows a minimum slip of 3 km. It rises the problem of accommodating the difference of displacement between the mature eastern part and the immature western one. High shear strain or extension (Coward and Potts, 1983) are expected hinterland. The Wheeler Ridge, in California, has a very similar evolution (Medwedeff, 1992; Mueller and Talling, 1997), and presents geomorphic evidence for numerous tear faults accommodating the shear strain in this truly cylindrical structure. Another way to accommodate shear strain is to generate extension rather than tear faults.

3. 3D reconstruction methodology

We now describe how a 3D structure can be reconstructed from a simple data set comprising coordinates, height above sea level, strikes and dips of measured strata. This method is somehow close to the Busk reconstruction technique (Busk, 1929). The major assumptions of our horizon projection method are fairly common for fold and thrust belts analysis, generally exposed in 2D. A first order assumption is that bed thicknesses remain invariable during the folding event (flexural slip). Since the data are compiled along sections which are broadly perpendicular to strike, it is also assumed that over the distance required to compile the data along these 'band-sections', bed thickness is constant perpendicularly to the structural trend. These two assumptions imply 2D constant bed thickness across-strike during and after folding, for each independent section, from one fold limb to the other. However, our method accounts for lateral thickness variations along-strike. Each section is independent and has its own stratigraphic thicknesses. Folded structures are generally more elongated than large, and along-strike thickness variations can be found in many settings.

The required input data set contains structural measurements, defined by the absolute spatial coordinates of the datapoints and their strikes and dips. Although surface data are more likely to be used, well data or seismic data can be integrated. The denser the net of structural data, the more accurate the reconstructed surfaces will be. Since this method is based on 3D projections, the additional degree of freedom requires particularly tight data sets. However, the method also takes advantage of this because the 3D projections do not generate any distortion of the original measured data set: dips and strikes are compiled as they are acquired in the field, and are not extrapolated to lay within a vertical plane as it is in 2D. Processing of the digitized data sets provides the output data set for 3D modeling.

3.1. Stratigraphic thickness calculations

The general algorithm is described below:

(i) **Input**: coordinates, dip, strike datafiles for each sampling band (x_i,y_i,z_i,d_i,s_i).
(ii) Fold axis: vector coordinates and spatial location between each adjacent datapoints.
(iii) Trend and plunge of each fold axis.
(iv) Relative and cumulative stratigraphic thicknesses along each sampling band.
(v) Location of the reference horizon along the stratigraphic pole and spatial coordinates.
(vii) **Output**: (x_i',y_i',z_i') dataset. Each dot belongs to the reference horizon.

Roman numbers refer to those given in the following paragraph. The initial data set (i) consists of points P_i defined by their coordinates, and a vector normal to the

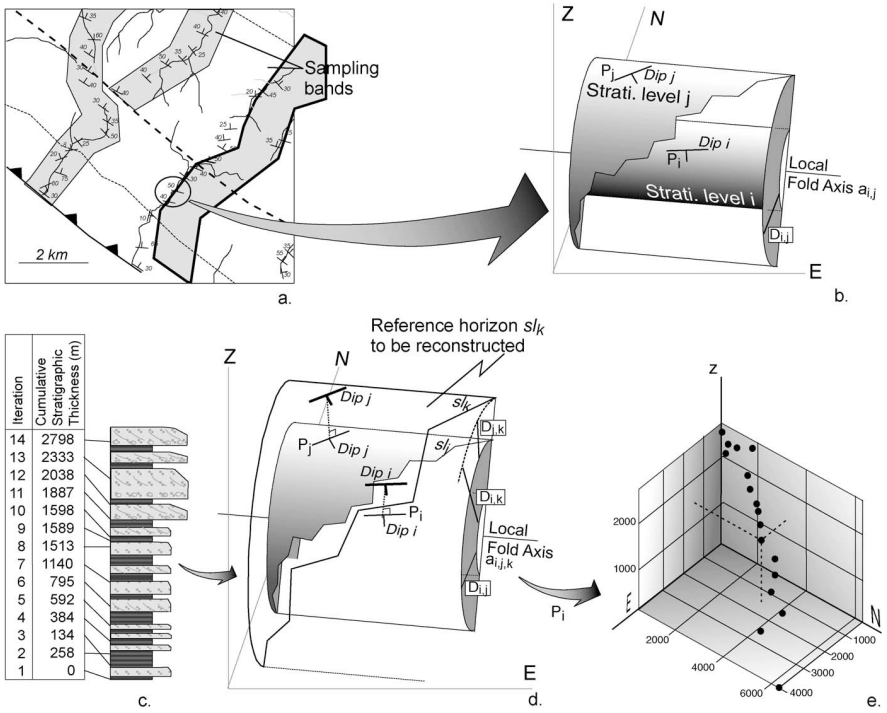

Fig. 4. (a) Sampling strategy for the structural data. Shaded areas are sampling bands, dotted lines are horizon intersections with the surface, dashed lines are the intersections of the reference horizons with the surface. Circled dots are a pair of points P_i and P_j for the next stage; (b) cylindration of the data pairs, where $D_{i,j}$ is the stratigraphic thickness between the data points P_i and P_j; and a_{ij} is the calculated local fold axis; (c) reconstruction of the thickness log corresponding to the cumulate elementary stratigraphic thicknesses for each pair of points; (d) projection of the elementary thicknesses along the poles of the strata. The inner shells ($s.l._i$ and $s.l._j$) are the strata on which structural measurements have been performed, the outer shell ($s.l._k$) is the reference horizon to be reconstructed. Bold dip symbols are the projected dots in space (from the measured strata), which belong to the reference horizon; (e) projection of the data from a sampling band: spatial coordinates of the projected dots.

bed N_i, defined by strikes and dips data from field measurements (Fig. 4a). It is subdivided into sub-sets along isopach sampling bands, striking across the structural trend. Each point belongs to one particular stratigraphic level (most of the time undetermined). The adjacent point within the 'band-section' belongs to another particular stratigraphic level, the strike and dip of which are not necessarily similar to the former. Datapoints can be regarded in pairs (P_i, P_j) in order to define the local folding attitude (Fig. 4b). The latter is assumed locally truly cylindrical. The two data P_i and P_j are considered as belonging to a pair of coaxial cylinders. Each cylinder tangents the bedding surface characterized by its normal N_i. For each pair (P_i, P_j), there is one and only one axis $a_{i,j}$ in space for both coaxial cylinders. The vector product $A_{i,j}$ of the normals N_i and N_j gives the axis orientation. The intersection of the two planes, respectively, defined by P_i, N_i and $A_{i,j}$ and P_j, N_j and $A_{i,j}$ gives the coordinates and location (ii) and trend and plunge (iii) of the cylinders axis $a_{i,j}$. The two radii of the aforesaid cylinders are the respective distances from the datapoints to the fold axis. The difference of these radii is the stratigraphic thickness $D_{i,j}$ between the two datapoints of the pair (iv).

The calculations of $D_{i,i+1}$ are performed successively along each 'band-section'. The total stratigraphic thickness along a sampling band is the sum of each elementary thickness value along the band (iv). This method accounts for both upward and downward calculation within the stratigraphic pile by addition or subtraction of the elementary

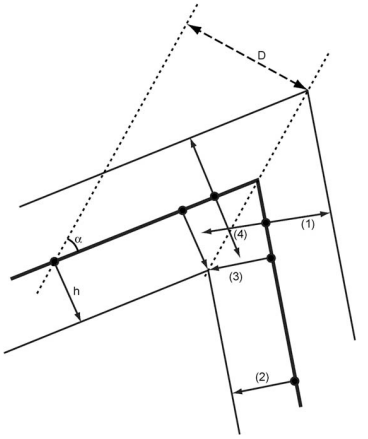

Fig. 5. Projections at the proximity of fold hinges. Dotted lines are bisectors of the kink. When the projection is directed from a horizon (bold) towards external shells (1) or when the source point is far enough from the fold hinge ($h \cos \alpha < D$) towards inner shells (2) and (3), the projections are correct. Where the source point is too close to the hinge ($h \cos \alpha > D$), the projected points are aberrant (4).

calculated thicknesses along a band. The cumulative stratigraphic thicknesses provide synthetic logs for each independent 'band-section' (Fig. 4c), which are parts of the total stratigraphic log of the area. Since no approximation has been done while calculating the thicknesses, the accuracy of the logs only depends on the initial data sets. Additional control is given from one flank to the other, as the cumulative thickness calculated by the projection series across one fold flank has to match with the cumulative thickness deduced from the other flank, otherwise it would generate discrepancies at the level of the hinge.

3.2. Spatial projection of the data sets

Reconstruction of the structure is performed by projecting the structural data onto chosen reference horizons. As the purpose is to characterize the geometry of the structure represented by these surfaces, their intersections with topography have to be accurately described, and particular attention must be paid to periclinal closures.

Once the cumulative stratigraphic thicknesses are calculated, the relative thicknesses $D_{i,j}$ from each datapoint to a reference horizon are assessed on the logs. The output datasets consist of the distances for each datapoint, from its particular strata to the reference horizon (v). Each initial datapoint P_i is projected, along the pole N_i from its original strata to the reference horizon at a distance $D_{i,j}$ (Fig. 4d).

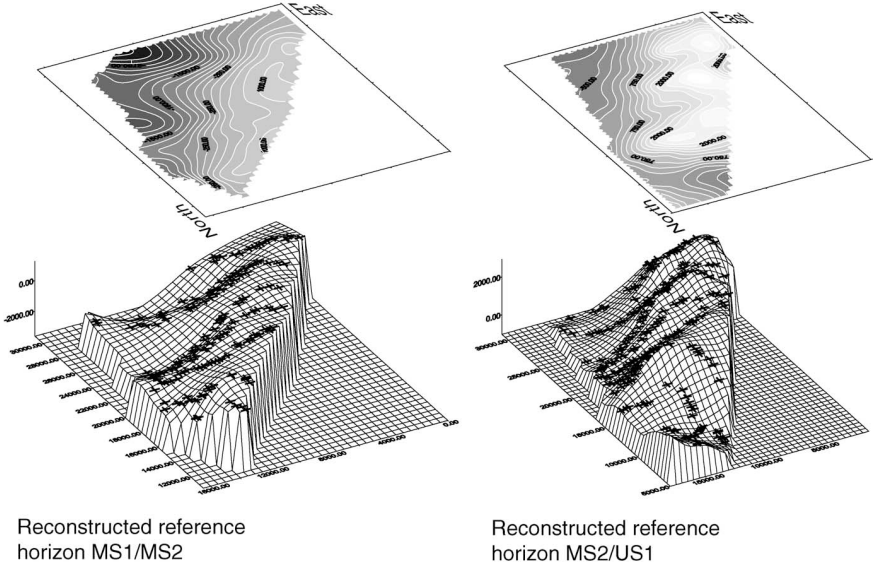

Fig. 6. Interpolated (kriging) reference horizons: MS1/MS2 boundary (left) and MS2/US1 boundary (right). Crosses are the projected structural data.

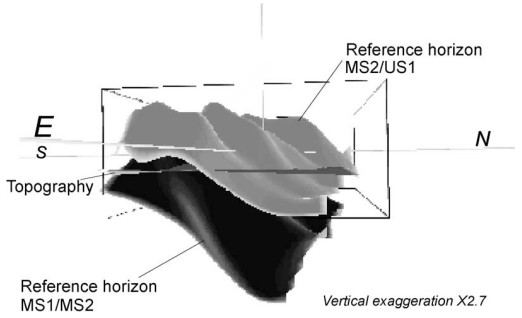

Fig. 7. 3D visualization of the reconstructed horizons with respect to topography.

According to the initial assumptions (flexural slip and constant bed thickness along a band), the resulting dots in space are located on a reference horizon. In fact, the spatial projections of these lengths for each particular 'band-section' define a band in space, which is included within the surface to be reconstructed (Fig. 4e).

Where the curvature is significant, artifacts can be generated. In order to avoid them, it has to be restricted to the cases illustrated in Fig. 5, where the distance D to the hinge is shorter than $h \cos \alpha$, where h is the interstrata thickness and α is the strata/hinge angle. It does not limit the technique to relatively open folds but only projections towards outer shells can be performed close to fold hinges when folds are tight.

This operation is successively realized for each sampling band, producing sets of dots defined by their coordinates, strikes and dips. These sets are located within the reference surfaces (vii). Subsequent interpolation of the data sets provides the 3D geometry of the structure.

4. 3D reconstruction and restoration of the Baisahi and Rapti folds

4.1. Reconstruction

The structural data set is divided into sampling bands, broadly perpendicular to the structural trend (Fig. 2). On the whole, these correspond to the drainage pattern where sampling has been done. As a consequence, the sub-sets comprise tight data within broadly parallel and linear 'band-sections'.

Processing of these sub-sets has to be carried out for each band, in order to reconstruct the two reference horizons between the Middle Siwaliks 1 (MS1) and Middle Siwaliks 2 (MS2) formations, and between the MS2 and Upper Siwaliks 1 (US1) formations. These reference surfaces have been chosen as they are well constrained from the structural analysis from fieldwork and SPOT imagery; moreover, they do not require many projections towards inner shells and artifacts close to fold hinges are avoided. Both horizons belong to the fold above the hanging-wall of the MFT and above the roof thrust of the duplex.

Following the method described above, two data sets (one per horizon) of projected dots are established. After projection, the output data sets are linked to the original map distribution of the input data sets. Interpolation is carried out by kriging. Details on the interpolation procedure can be found in Appendix A. Interpolation grids of the two reconstructed surfaces are represented in Fig. 6. The overall 3D visualization of the structural shape is given by both reference horizons with respect to topography (Fig. 7).

Both the buried part of the structure (Rapti syncline) and the eroded part of it (Baisahi antiform) are reconstructed in 3D. A slight pattern of thalwegs, perpendicular to strike, stands out and suggests that the fold axis varies along-strike. A detailed inspection of the dip and strike of the MS1/MS2 reference horizon in Fig. 2 confirms that the along-strike undulation appears in the initial data. Since the original distribution of the datasets has been accounted for while interpolating, and because the spatial distribution of the perpendicular to strike undulations does not particularly match the spatial distribution of the trends of the projected bands, it is assumed that this pattern reflects the real shape of the folded structure, though some artifacts cannot be locally excluded.

4.2. Unfolding

3D surfaces can be unfolded in order to test their validity and evaluate if they are developable. The reconstructed MS1/MS2 reference horizon is unfolded using Patchwork program (Bennis et al., 1991; Lecomte et al., 1994). The surface is gridded along isoparametric curves, then flattening is performed piecewise. Restoration is realized from a pin line by incremental flattening of the grid surface.

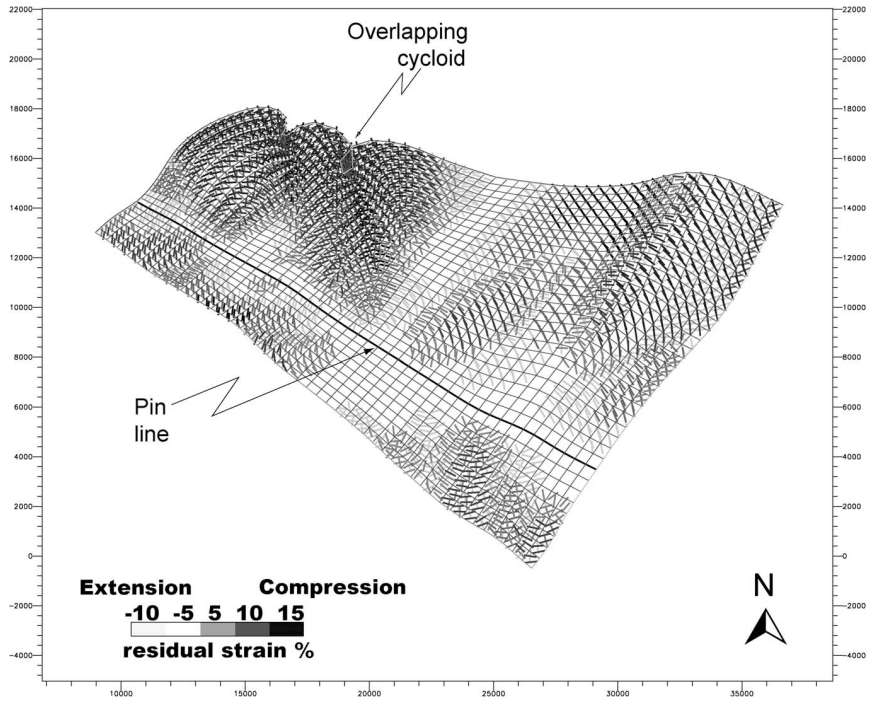

Fig. 8. Unfolded MS1/MS2 reference horizon. Compression and extension are given for the unfolding event. The overlapping cycloid is the representation of an extremely stretched area during folding. In such zones, the initial state cannot be restored; the residual strain field due to unfolding of the antiform measures the difference in shapes of the quadrangles in the folded structure and the flattened quadrangles.

Isoparametric curves of the deformed surface are mapped onto the flattening plane. Geodesic curvature, chords lengths and cross-angles are preserved. The flat quadrangles are recombined by means of rotation and translations, minimizing the misfits between pieces. Gentle distortion of the flattened quadrangles is applied to fill in the misfits (Bennis et al., 1991).

Assumption of pure flexural slip implies that the structure does not undergo major strain during the folding event. The studied structure is roughly cylindrical and shows slight deviations from true cylindricity (see stereoplot Fig. 2). The fold axis slightly undulates, as shown by the 3D view (Fig. 7). It is therefore globally developable (Lisle, 1992), and unfolding should then outline only local anomalies due to internal strain (including small-scale faulting and folding). The pin line is located at the fold crest, where layer-parallel shearing is assumed to be minimal (Suppe and Medwedeff, 1992). Distortion of the quadrangles is illustrated by the 'residual strain field' (Fig. 8), which corresponds to the 2D tensor of distortion required to fill in the misfit of the flattened quadrangles. It measures the differences of shapes between the initial and the final quadrangles. It either indicates local inaccuracy in the 3D surface or internal strain faulting. The NW and the NE zones, respectively, show W–E and NW–SE compressive distortion from the final to the initial state (i.e. during unfolding process). The distortion decreases in magnitude southward and is interpreted as an extensive internal strain hinterland during the lateral propagation of the structure from the initial to the final state. The unfolded MS1/MS2 horizon also features a little 'overlapping cycloid' at the NW of the surface, which is the representation of extremely distorted zones, above the threshold admitted by the program to shorten the pieces while filling in the misfits. It does not represent the actual unfolded state of the area but a local, significantly disturbed zone. Choosing a pin line in the cycloid would significantly

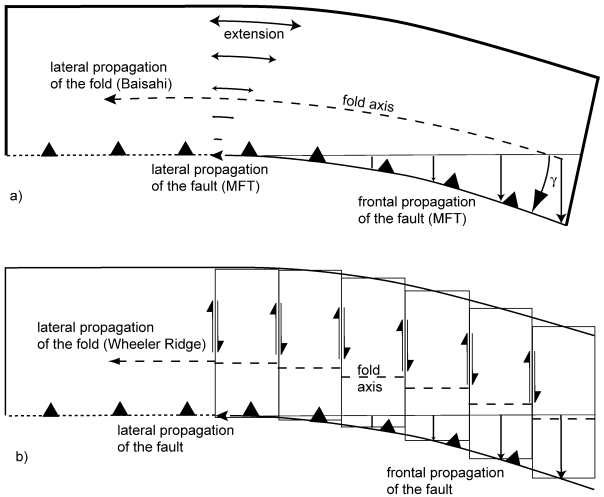

Fig. 9. Hinterland extension induced by the lateral propagation of a structure. (a) Internal strain, Baisahi fold. While the mature part of the structure (right) continues to evolve, along-strike extension is induced on the trailing edge of the fold, accommodated by internal strain. γ is the rotation angle between the mature (right) and immature (left) parts of the structure (20° for the Baisahi anticline). (b) Tear faults, Wheeler Ridge type (after Medwedeff, 1992; Mueller and Talling, 1997). The displacement gradient is there accommodated by block segmentation.

modify the results of the unfolding procedure, although it would not erase the high residual strain in the NW area. To the NW, minor accommodation faults are mapped, west of the cycloid, also indicating that this area underwent high shear strains.

4.3. Discussion

As the thrust propagates southward and westward, there is a rotation of at least 20° clockwise, which induces a shear component hinterland, where the synclinal breakthrough is not initiated yet. It can be accommodated either by hinterland extension (Fig. 9a) or tear faults, parallel to the main shortening axis (e.g. Mueller and Talling, 1997; Fig. 9b). No tear fault has been evidenced in this area from field work and SPOT imagery; this suggests a diffuse shear strain accommodation rather than tear faults, which is furthermore supported by the hinterland compression in the residual strain field (Fig. 8). This mechanism also suggests that shortening is not parallel to the main horizontal stress at the transition between monocline and anticline. However, as soon as this zone propagates laterally, shortening becomes parallel to the main stress axis again.

According to the residual strain field, less than 1 km of shortening is accommodated by internal strain along a cross-section, whereas the total shortening is more than 15 km. Since the differences between regional folding and internal strain are of more than one order of magnitude, we emphasize that in a first order approximation, hinterland along-strike extension does not affect significantly the 2D reconstruction. However, the stratigraphic thicknesses can change laterally. It has been shown that the roof rotates around the migrating Baisahi western pericline, making the motion of the roof slightly oblique to across-strike sections. As the thicknesses appear to change along-strike, they can slightly differ below and above the MFT, making the 3D reconstruction more valid than the 2D sections.

Mueller and Talling (1997) showed that the Wheeler Ridge fold is truly cylindrical. Furthermore, the shear component seems mainly accommodated by tear faults. On the contrary, the Baisahi anticline is not truly cylindrical since its axis undulates and finally plunges towards the NW. In that case, the shear component seems mainly accommodated by internal strain rather than tear faults (Fig. 9). If it is assumed that the internal strain is mainly induced by a simple shear direction of no finite longitudinal extension parallel to the regional transport direction, it would bring about a principal finite extension orientated nearly NNW–SSE to N–S. Furthermore, since a component of extension parallel to the fold axe is described in numerous fold belts (Vialon et al., 1984), an additional NW–SE extension is inferred at the trailing edge of the Baisahi anticline.

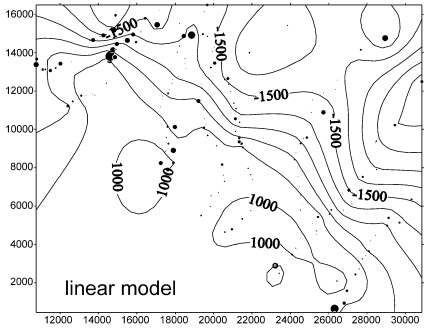

Fig. 10. Geographical repetition of the residuals after interpolation. The distribution is indicated by filled circles; diameter is proportional to the absolute value of the residual. The greatest circle is 250 m. Coordinates are in meters. Elevation in meters above sea level. Parameters of the kriged surface: grid spacing 200 m; linear model: nugget 70; anisotropy ratio 2 in the N105 direction; scale: 1×10^6; length: 12900.

5. Conclusions

The main purpose of the study was to develop an original 3D reconstructing method from outcrop data. This method based on a flexural slip hypothesis is well adapted to fold and thrust belts and may be useful in remote areas of frontal parts of orogenic belts where no subsurface data are available to constrain the geometry of the structures. This technique allows one to reconstruct both the eroded and buried parts of the structures.

By reconstructing two surfaces defined over the Main Frontal Thrust from combined structural fieldwork and spatial imagery, the 3D shape of the eroded Baisahi antiform and the preserved Rapti syncline are characterized with respect to the topography. It has been shown, by the example of the Baisahi anticline, that deformation in fold and thrust belts can deviate from true cylindrical patterns. Since lateral thickness variations are present in many natural settings, additional deviations from a truly cylindrical structure are generated and are accounted for in our method. Hence, this 3D reconstruction technique provides a more accurate description of the shape of the structure than 2D reconstruction.

Additionally, 3D restoration of a reference horizon of the Baisahi antiform has been carried out using Patchwork program in order to test a reconstructed surface. In spite of the globally cylindrical (and hence potentially developable) shape of the structure, unfolding revealed along-strike stretched zones. Bulk shear and extensional internal strain rather than tear faults accommodate the rotation of the hanging wall around the migrating fold pericline.

Acknowledgements

This work was funded by the INSU program PROSE: Himalayan erosion. The manuscript has greatly benefited from reviews by D. Rouby and K. Mueller. We also thank F. Roure for constructive discussions.

Appendix A. Description of the interpolation procedure and parameters

The nugget effect (Nu) has been estimated from the data repeatability: the uncertainty for the geographic position (Po) is in the order of 20 m, the uncertainty on the measurement of the normal to the bedding plane ($\delta\alpha$) is 5° and the mean distance of projection (dist) is 600 m. Therefore the nugget effect is about $Po + \sin(\delta\alpha) \times \text{dist}$, i.e. 70 m. The grid spacing is 200 m. In order to counteract the anisotropic distribution of dots in space and to outline the general trend of the structure, relative weighting has been defined by an anisotropy ratio of two in the N105 direction. The variogram is based on a linear model, with the default parameters proposed by Surfer interpolator (Golden Software, IC). Several other interpolation procedures have been tested but the results do not strongly differ from the result of the linear one. The standard deviation of the residuals between the data and the kriged surface is 62 m and the maximum residual is 250 m. The geographical distribution of the residuals is shown in Fig. 10 by filled circles.

References

Acharyya, S.K., 1994. The Cenozoic foreland basin and tectonics of the eastern Sub-Himalaya: prospects and problems. Himalayan Geology 15, 3–21.

Appel, E., Rosler, W., 1994. Magnetic polarity stratigraphy of the Neogene Surai Khola section (Siwalik, SW Nepal). Himalayan Geology 15, 63–68.

Baby, P., Hérail, G., Salinas, R., Sempere, T., 1992. Geometry and kinematics of passive-roof duplexes deduced from cross-section balancing: example from the foreland thrust system of the southern Bolivian Subandean Zone. Tectonics 3, 523–536.

Banks, C., Warburton, J., 1986. "Passive-roof" duplex geometry in the frontal structures of the Kirthar and Sulaiman mountain belts, Pakistan. Journal of Structural Geology 8, 229–237.

Bennis, C., Vézien, J.M., Iglesias, G., 1991. Piecewise surface flattening for non-distorted texture mapping. Computer Graphics 4, 237–246.

Bilham, R., Larson, K., Freymueller, J., 1997. Idylhim members. GPS measurements of present-day convergence across the Nepal Himalaya. Nature 386, 61–63.

Biswas, S.K., 1994. Status exploration for hydrocarbons in Siwalik basin of India and future trends. Himalayan Geology 15, 283–300.

Boyer, S., 1986. Styles of folding within thrust sheets: examples from the Appalachian and Rocky Mountains of the USA and Canada. Journal of Structural Geology 8, 325–339.

Boyer, S.E., Elliott, D., 1982. Thrust systems. American Association of Petroleum Geologists Bulletin 66, 1196–1230.

Busk, H., 1929. Earth Flexures. Cambridge University Press 186pp.

Coward, M.P., Potts, G.J., 1983. Complex strain patterns developed at the

frontal and lateral tips to shear zones and thrust zones. Journal of Structural Geology 5, 383–399.
Dahlstrom, C.D.A., 1969. Balanced cross-sections. Canadian Journal of Earth Sciences 6, 743–757.
Delcaillau, B., 1997. Les fronts de chaÎne actives—Genèse des reliefs et relations tectonique-érosion-sédimentation. Thèse d'habilitation à diriger des recherches, Université de Caen.
De Mets, C., Gordon, R.G., Argus, D.F., Stein, S., 1990. Current plate motions. Geophysical Journal International 101, 425–478.
Galahaut, V.K., Chandler, R., 1992. On the active tectonics of the Dehra Dun region from observations of ground elevation changes. Journal of the Geological Society of India 39, 61–68.
Hérail, G., Mascle, G., 1980. Les Siwaliks du Népal Central: structures et géomorphologie d'un piedmond en cours de déformation. Bulletin de l'Association Géographique Française 431, 259–267.
Hérail, G., Mascle, G., Delcaillau, B., 1987. Les Siwaliks de l'Himalaya du Népal: un exemple de prisme d'accrétion intracontinental in S.D.L.T.P., Bordet 47, 153–182.
Husson, L., Mugnier, J.L., Leturmy, P., Vidal, G., 2002. Frontal development of the Himalayas: sedimentary record and architecture of the Siwaliks of Western Nepal. In: McClay, K. (Ed.), Thrust Tectonics and Hydrocarbon Systems, AAPG Memoir, in press.
Jackson, M., Bilham, R., 1994. Constraints on Himalayan deformation inferred from vertical velocity fields in Nepal and Tibet. Journal of Geophysical Research 99, 13,897–13,912.
Jouanne F., Mugnier, J.-L., Pandey, M.R., Gamond, J.-F., Le Fort, P., Serrurier, L., Vigny, C., Avouac, J.P., Idylhim members, 1999. Oblique convergence in Himalaya of western Nepal deduced from GPS measurements, 14th Himalaya–Karahorum–Tibet Workshop, Tubingen.
Kayastha, N.B., Pradhan, U.M., Shresta, R.B., Shyam, K.C., Subedi, D.N., Sharma, S., 1999. Geological map of exploration block-3 Nepalganj, Mid-Western, Nepal, Department of Mines and Geology, Kathmandu.
Lavé, J., Avouac, J.-P., 2000. Active folding of fluvial terraces across the Siwaliks Hills, Himalayas of central Nepal. Journal of Geophysical Research 105, 5735–5770.
Lecomte, J.-C., Mondy, J.-F., Bennis, C., Léger, M., 1994. A Balanced Surface Method. A New Way to Improve your Structural Maps Interpretations. AAPG Convention, Denver.
Leturmy, P., 1997. Sédiments et reliefs du front des systèmes chevauchants: Modélisation et exemples du front Andin et des Siwalik à l'Holocène. PhD thesis, Université Joseph Fourier, Grenoble I.
Lisle, R.J., 1992. Constant bed-length folding: three dimensional geometrical implications. Journal of Structural Geology 14, 245–252.
Lyon-Caen, H., Molnar, P., 1985. Gravity anomalies, flexure of the Indian plate, and the structure, support and evolution of the Himalaya and Ganga basin. Tectonics 4, 513–538.
Mascle, G., Hérail, G., Van Haver, T., Delcaillau, B., 1986. Structure et évolution des bassins d'épisuture et de périsuture liés à la chaÎne himalayenne. Société Nationale Elf Aquitaine Production, Bull. Centre Rech. Explor-Prod. 10, 181–203.
Medwedeff, D.A., 1992. Geometry and kinematics of an active laterally propagating wedge thrust, Wheeler Ridge, California. In: Mitra, S., Fisher, G.W. (Eds.), Structural Geology of Fold and Thrust Belts, The John Hopkins Studies in Earth and Space Sciences 5, pp. 1–28.
Molnar, P., Tapponnier, P., 1975. Cenozoic tectonics of Asia: effects of a continental collision. Science 189, 419–426.
Mueller, K., Talling, P., 1997. Geomorphic evidence for tear faults accommodating lateral propagation of an active fault-bend fold, Wheeler Ridge, California. Journal of Structural Geology 19, 397–411.
Mugnier, J.-L., Mascle, G., Faucher, T., 1992. La structure des Siwaliks de l'Ouest Népal: un prisme d'accrétion intracontinental. Bulletin de la Société Géologique de France 163, 585–595.
Mugnier, J.-L., Huyghe, P., Chalaron, E., Mascle, G., 1994. Recent movements along the Main Boundary Thrust of the Himalayas: normal faulting in an over critical thrust wedge? Tectonophysics 238, 199–215.
Mugnier, J.-L., Delcaillau, B., Huyghe, P., Leturmy, P., 1998. The breakback thrust splay of the Main Dun Thrust: evidence of an intermediate displacement scale between earthquake slip and finite geometry of thrust systems. Journal of Structural Geology 20, 857–864.
Mugnier, J.-L., Leturmy, P., Mascle, G., Huyghe, P., Chalaron, E., Vidal, G., Husson, L., Delcaillau, B., 1999. The Siwaliks of Western Nepal. I. Geometry and kinematics. Journal of Asian Earth Sciences 17, 629–642.
Ni, J., Barraganzi, M., 1996. Seismotectonics of the Himalayan collision zone: geometry of the underthrusting Indian plate beneath the Himalaya. Journal of Geophysical Research 89, 1147–1163.
Peltzer, G., Saucier, F., 1996. Present-day kinematics of Asia derived from geologic fault rates. Journal of Geophysical Research 101, 27,943–27,956.
Powers, P.M., Lillie, R.J., Yeats, S., 1998. Structure and shortening of the Kangra and Dehra Dun reentrants, Sub-Himalaya, India. Geological Society of America Bulletin 110, 1010–1027.
Price, R.A., 1981. The Cordilleran fold and thrust belt in the southern Canadian Rocky Mountains. In: McClay, K., Price, N.J. (Eds.), Thrust and Nappe Tectonics, Geological Society Special Publication 9, pp. 427–448.
Raiverman, V., Srivastava, A.K., Prasad, D.N., 1994. Structural style in north-western Himalayan foothills. Himalayan Geology 15, 263–280.
Schelling, D., 1992. The tectonostratigraphy and structure of the eastern Nepal Himalaya. Tectonics 11, 925–943.
Schelling, D., Arita, K., 1991. Thrust tectonics, crustal shortening, and the structure of the far-eastern Nepal Himalaya. Tectonics 15, 851–862.
Srivastava, P., Mitra, G., 1994. Thrust geometries and deep structure of the outer and lesser Himalaya, Kumaon and Garhwal (India): implications for evolution of the Himalayan fold and thrust belt. Tectonics 13, 89–109.
Storti, F., Salvini, F., 1996. Progressive rollover fault-propagation folding: a possible kinematic mechanism to generate regional-scale recumbent folds in shallow foreland belts. Bulletin of the American Association of Petroleum Geologists 80, 174–193.
Suppe, J., 1980. Imbricated structure of western foothills belt, southern central Taiwan. Petroleum Geology Taiwan 17, 1–16.
Suppe, J., Medwedeff, D.A., 1990. Geometry and kinematics of fault-propagation folding. Eclogae Geologicae Helveticae 83, 409–454.
Vann, I.R., Graham, R.H., Hayward, A.B., 1986. The structure of mountain fronts. Journal of Structural Geology 8, 215–227.
Vialon, P., Bonnet, J.L., Gamont, J.F., Mugnier, J.L., 1984. Modélisation des déformations d'une série stratifiée par le déplacement horizontal d'un poinçon. Bulletin de la Société Géologique de France 26, 139–150.
Wines, R.F., 1990. Productive duplex imbrication at the Neuquén basin thrust belt front, Argentina. In: Letouzey, J. (Ed.). Petroleum and Tectonics in Mobile Belts. Technip, Paris, pp. 69–80.
Woodward, N.B., Boyer, S.E., Suppe, J., 1985. An outline of balanced cross-sections. Studies in Geology 11. Department of Geological Sciences, University of Tennessee, Knoxville, 170pp.

1.1.2 Structuration du front de chaîne

L'équilibrage structural prend un sens plus vaste lorsqu'il est replacé dans le contexte dynamique des fronts de chaînes. C'est un support de travail qui permet détayer les interprétations cinématiques. L'enregistrement géologique dans les avant-pays est remarquable, puisque la sédimentation qui accompagne le développement et la progradation des prismes d'avant-pays est souvent préservée, archivant ainsi l'histoire géologique. Des informations sur la chronologie des évènements structuraux et morphologiques du prisme mais également de la chaîne dans son ensemble y sont contenues. Les deux articles suivants, fruits d'une collaboration avec J-L. Mugnier, P. Leturmy et co-auteurs, illustrent l'exploitation de ces reconstructions pour évaluer l'historique de la chaîne himalayenne.

PERGAMON

Journal of Asian Earth Sciences 17 (1999) 629–642

Journal of Asian Earth Sciences

The Siwaliks of western Nepal I. Geometry and kinematics

J.L. Mugnier[a,*], P. Leturmy[a], G. Mascle[a], P. Huyghe[a], E. Chalaron[b], G. Vidal[c], L. Husson[a], B. Delcaillau[d]

[a]*Laboratoire de Geodynamique des Chaines Alpines et UPRESA CNRS 5025, rue Maurice Gignoux, 38031, Grenoble, France*
[b]*Institute of Geological and Nuclear Sciences, New Zealand*
[c]*UMR CNRS 5570 et ENS Lyon, France*
[d]*Département de Géographie, Caen University, 13 rue du milieu, 14000, Caen, France*

Abstract

The Siwalik Group which forms the southern zone of the Himalayan orogen, constitutes the deformed part of the Neogene foreland basin situated above the downflexed Indian lithosphere. It forms the outer part of the thin-skinned thrust belt of the Himalaya, a belt where the faults branch off a major décollement (MD) that is the external part of the basal detachment of Himalayan thrust belt. This décollement is located beneath 13 Ma sediments in far-western Nepal, and beneath 14.6 Ma sediments in mid-western Nepal, i.e., above the base of the Siwalik Group. Unconformities have been observed in the upper Siwalik member of western Nepal both on satellite images and in the field, and suggest that tectonics has affected the frontal part of the outer belt since more than 1.8 Ma. Several north dipping thrusts delineate tectonic boundaries in the Siwalik Group of western Nepal. The Main Dun Thrust (MDT) is formed by a succession of 4 laterally relayed thrusts, and the Main Frontal Thrust (MFT) is formed by three segments that die out laterally in propagating folds or branch and relay faults along lateral transfer zones. One of the major transfer zones is the West Dang Transfer Zone (WDTZ), which has a north-northeast strike and is formed by strike-slip faults, sigmoid folds and sigmoid reverse faults. The width of the outer belt of the Himalaya varies from 25 km west of the WDTZ to 40 km east of the WDTZ. The WDTZ is probably related to an underlying fault that induces: (a) a change of the stratigraphic thickness of the Siwalik members involved in the thin-skinned thrust belt, and particularly of the middle Siwalik member; (b) an increase, from west to east, of the depth of the décollement level; and (c) a lateral ramp that transfers displacement from one thrust to another. Large wedge-top basins (Duns) of western Nepal have developed east of the WDTZ. The superposition of two décollement levels in the lower Siwalik member is clear in a large portion of the Siwalik group of western Nepal where it induces duplexes development. The duplexes are formed either by far-travelled horses that crop out at the hangingwall of the Internal Décollement Thrust (ID) to the south of the Main Boundary Thrust, or by horses that remain hidden below the middle Siwaliks or Lesser Himalayan rocks. Most of the thrusts sheets of the outer belt of western Nepal have moved toward the S–SW and balanced cross-sections show at least 40 km shortening through the outer belt. This value probably under-estimates the shortening because erosion has removed the hangingwall cut-off of the Siwalik series. The mean shortening rate has been 17 mm/yr in the outer belt for the last 2.3 Ma. © 1999 Elsevier Science Ltd. All rights reserved.

1. Introduction

The Siwalik-Ganges foreland basin constitutes a unique present-day active foreland system in a geodynamic context of intracontinental collision, where synorogenic sediments are progressively incorporated into the outer part of the thin-skinned thrust belt. Thus the study of the active Himalayan thin-skinned thrust system may provide useful constraints for interpreting older collisional thrust systems. Therefore we

* Corresponding author.
E-mail address: mugnier@ujf-grenoble.fr (J.L. Mugnier).

1367-9120/99/$ - see front matter © 1999 Elsevier Science Ltd. All rights reserved.
PII: S1367-9120(99)00038-3

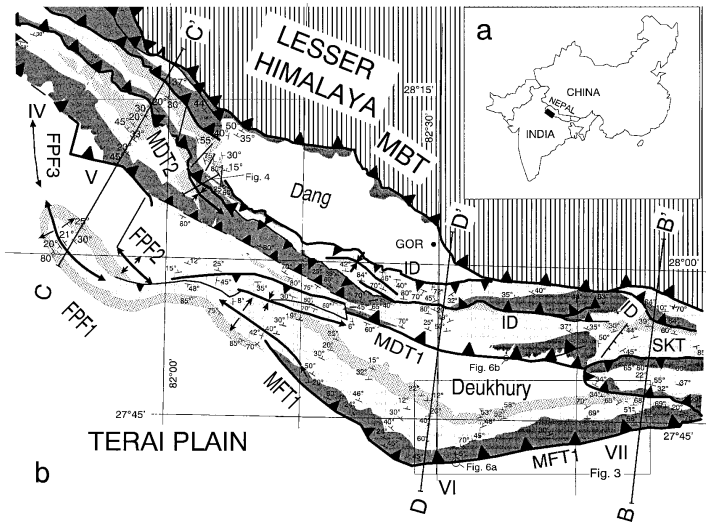

Fig. 1. (a) Regional location map, black domain is the studied area. (b) Structural map of the Siwalik thrust belt of mid-western Nepal. The lithological unit boundaries used for the regional mapping are illustrated on the lithological column of Fig. 3a (Location is VII on the map).

have undertaken a multidisciplinary study of the Siwalik group of western Nepal, combining a geomorphologic analysis of the relief, a study of the geometry of the deposits, and a quantitative study of their deformation. The aim of this paper is to describe the tectonic features that characterize the frontal part of the belt of Nepal in mid-western and far-western Nepal. A companion paper (Mugnier et al., 1999) mainly focuses on the dynamics of the thrust wedge.

2. The Siwalik Group

2.1. Presentation

The Siwalik-Ganges and Indus foreland basin fringes the Himalayan range along more than 2000 km from Assam to Pakistan. The northern edge of this basin is deformed and constitutes the Subhimalayan belt. The Main Boundary Thrust (MBT) is one of the major thrust fault systems along the entire Himalayan range, separating the synorogenic sediments of the Siwalik Group from the Lesser Himalayan formations. The Subhimalayan zone is constituted by a succession of more or less parallel ridges (Figs. 1 and 2). They form the Siwalik hills in India and the Churia hills in Nepal. These hills generally show a gentle northern surface slope and a steeper southern one and their height varies in southern Nepal between 600 and 1500 m. They are sandwiched between the Mahabharat Range in the north, which in Nepal is 2000–2500 m high, and the Terai plains in the south (altitude 90–200 m).

The vertical distribution of facies at the scale of the megasequence of the whole Siwalik Group shows a mean upward coarsening and upward increase in proximity to the thrust front (Delcaillau et al., 1987). The Siwalik Group is informally subdivided into three units (lower, middle and upper Siwaliks) (Figs. 2 and 3a) on the basis of lithostratigraphic criteria (Auden, 1935). Transition from the distal silty and sandy lower Siwalik member to the intermediate to distal sandstone to sandstone–mudstone facies of the middle Siwalik unit occurred away-from-the depocenter setting. The middle Siwalik unit is gradually overlapped southward by the conglomeratic to sandy conglomeratic facies of the upper Siwalik unit, which was deposited in a proximal fluvial mega-fan environment. This upward coarsening of facies reflects the spatial sedimentation pattern in a foreland basin and the progressive southward migration of depositional facies and the location of the thrust front. In the following, results of previous studies of the Surai Khola section are recalled (B-B′, Fig. 1) in order to give a framework for mapping the

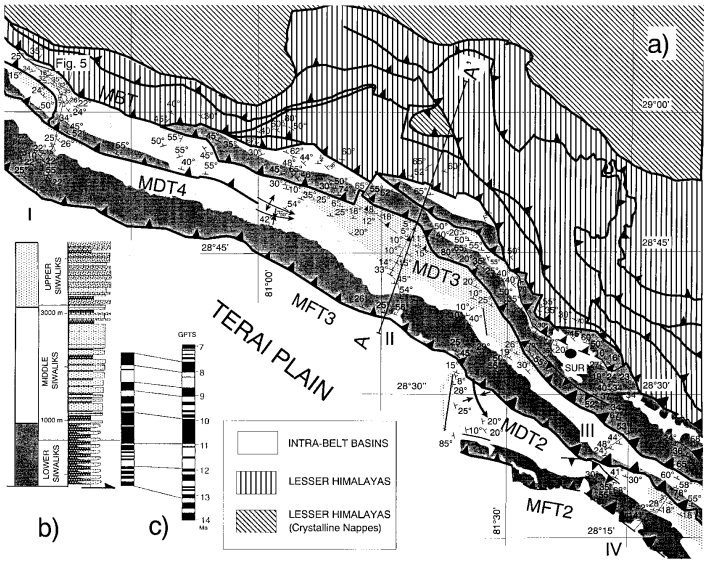

Fig. 2. Structural map of the Siwalik thrust belt of far-western Nepal. The lithological unit boundaries used for the regional mapping are illustrated on the lithological magneto-stratigraphy columns (Location is I on the map) proposed by DeCelles et al. (1998) and based on the scale of Cande and Kent (1995). Note that the lower, middle and upper Siwalik time boundaries defined in Pakistan (Johnson et al., 1985) do not exactly fit with the major lithological boundaries in this area.

Siwalik Group of western Nepal. Furthermore, new structural insights resulting from our field work along the Surai section are presented.

2.2. Sedimentology, stratigraphy and structure of a typical section of western Nepal

The construction of the Mahendra highway in western Nepal has furnished fresh outcrops along the Surai Khola cross-section which have been intensively studied (Corvinus, 1988; Appel et al., 1991; Dhital et al., 1995; Quade et al., 1995). From the base to the top of the sequence (Fig. 3a), several formations are distinguished:

1. The Bankas Formation which is 585 m thick, is made up of fine sandstones and red to brown-purple mudstones that show paleo sols and plant remains. The depositional environment was one of the distal parts of fluvial mega fans characterised by meandering channels (Delcaillau et al., 1987; Tandon, 1990). Fossils suggest that the Bankas formation is of the age of the Chinji stage (Pilgrim, 1917) of the lower Siwalik Group (Corvinus, 1988);
2. The Chor Khola Formation is 1235 m thick and is made of fine to medium, mica-rich sandstones, with dark grey mudstones and locally limestones. Beds coarsen and thicken upward. They are related to floodplain environments with moving bed load meandering channels (Delcaillau et al., 1987; Tandon, 1990; Quade et al., 1995; DeCelles et al., 1998). Abundant leaf prints and woody remains indicate that this formation corresponds to the lower part of middle Siwalik Group (Nagri stage);
3. The 1310 m thick Surai Khola Formation shows very thick layers of medium to coarse grained multistoried, micaceous sandstones (“salt and pepper”) and siltstones. The upper part contains coal, fossil wood fragments, leaf imprints, and freshwater molluscs, which allow correlation with Dhok Pathan stage of middle Siwaliks and Tatrot stage of upper Siwaliks (Corvinus, 1988; Dhital et al., 1995). The depositional environment corresponds to a high bed load with meandering and anastomosing channels (Delcaillau et al., 1987; Tandon, 1990);
4. The Dobatta Formation shows 750 m of light coloured to brown mudstones comprising channels

filled by coarse sandstones, locally cobbles. Numerous remains of vertebrates indicate the Pinjor stage of the upper Siwaliks member. The depositional environment is still of anastomosing channels with high coarse bed load;

5. The Dhan Khola Formation exhibits 1100 m of coarse conglomerate and light-brown sands and volcanic sediments not well consolidated at the top of the sequence. Fossils are rare and do not allow age estimation. The depositional environment corresponds to that of proximal alluvial fans with very close sediment supply (Delcaillau et al., 1987; Tandon, 1990) or to dun gravels (Ranga Rao et al., 1988) deposited in the mobile belt over the upper Siwalik member.

Combining biostratigraphic (Corvinus, 1988) and magnetostratigraphic data (Appel et al., 1991) and considering a continuous stratigraphy, a chronology has been set as follows (Dhital et al., 1995): boundary between Bankas and Chor Khola Formations occurs around 11 Ma, boundary between Chor Khola and Surai Khola Formations occurs around 7 Ma, boundary between Surai Khola units and Dobotta Formations occurs around 4.1 Ma, boundary between Dobotta and Dhan Khola Formations occurs around 1.8–2.3 Ma.

However, our field work has shown that the Surai Khola section is not strictly continuous: (a) an unconformity (Leturmy, 1997, Fig. 3b and c) lies at the base of the Dhan Khola Formation. As there was a lack of chronologic data in this formation (Appel et al., 1991), ages proposed by the magneto-stratigraphy study are not affected by the discovery of this time gap, which could be one of the causes of the age uncertainty (Appel et al., 1991) of boundary between Dobotta and Dhan Khola Formations, i.e., between 1.8 and 2.3 Ma; (b) a décollement level occurred in a marly level of the Chor Khola Formation; displacement is on the order of 10 meters along a meter-scale ramp-flat trajectory. This incipient structure therefore does not affect the magneto-stratigraphy study and indicates the presence of several minor décollements within the Siwalik section.

2.3. Thickness and age of the Siwalik Group

The litho-stratigraphic units described above do not correspond to synchronous deposits along the whole Himalayan front. The boundaries that we have used to map the series in western Nepal (Figs. 1 and 2) are based on the most obvious lithological contrasts, e.g., the occurrence of micaceous sandstone at the bottom of middle Siwaliks, and the occurrence of pebbly sandstone at the bottom of upper Siwaliks. These lithological contrasts do not exactly fit with the Siwalik members boundaries defined in Pakistan (Johnson et al., 1985) if the time lines deduced from magneto-stratigraphic studies (Appel et al., 1991; Cande and Kent, 1995; DeCelles et al., 1998) are used to correlate the sections.

The bottom of the sections in western Nepal refers only to the bottom of thrust sheets, and the lowest part of the lower Siwaliks could actually be located in the footwall of the basal décollement. The age of the bottom of the lower Siwaliks incorporated in the thrust sheets is slightly older than 13 Ma for the Khutia Khola section (DeCelles et al., 1998) and 14.6 Ma for the easternmost section (Appel et al., 1991).

The thickness of the stratigraphic pile involved in the frontal thrust sheets has been estimated from our field work along several sections (Table 1). The stratigraphic thickness of the more external thrust sheets increases from nearly 4000–4300 m in the western part of the studied area to more than 5000 m in the eastern part; this result has already been inferred from the subsurface structure of the Gangetic Plain (Raiverman et al., 1983).

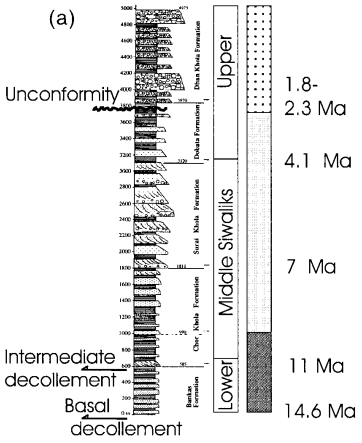

Fig. 3. Regional evidence of discordance including evidence from satellite images. (a) Lithological column (adapted from Dhital et al., 1995) along the Surai Khola in mid-western Nepal showing the location of unconformity and décollement levels (location is VII on Fig. 2). (b) The satellite image (location on Fig. 2) showing the unconformity. (c) Its interpretation.

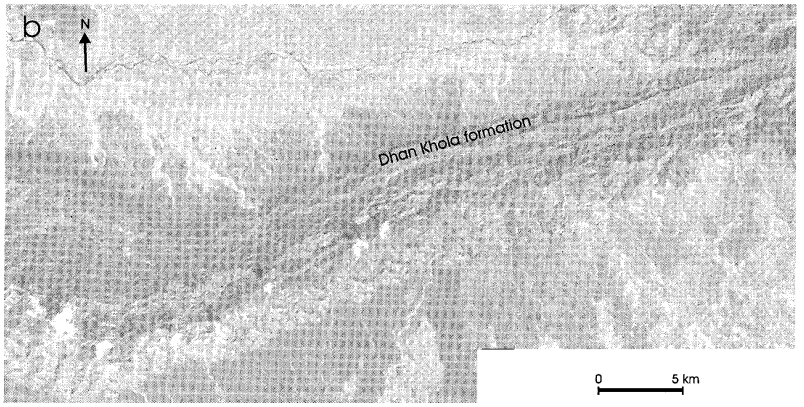

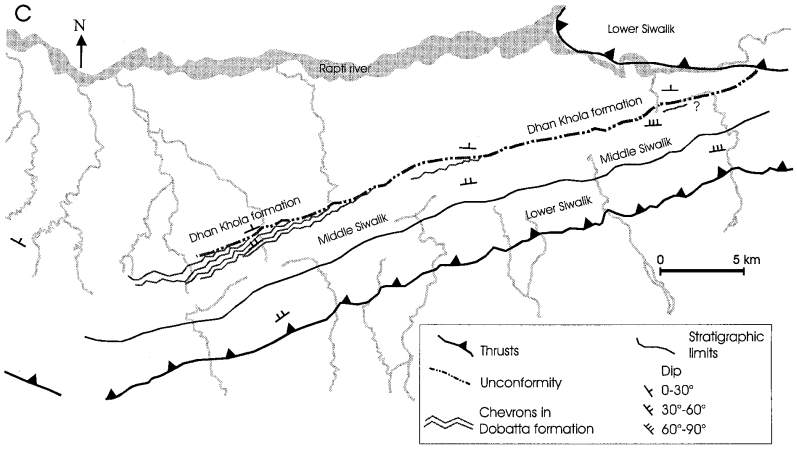

Fig. 3 (*continued*)

This regional thickening is mainly due to a thickening of the middle Siwalik member after 7.6 Ma (after the youngest chron determined in the two sections), as the thickness of the post-7.6 Ma middle Siwaliks of the Surai Khola section and the Khutia Khola section are respectively 3300 and 2100 m.

2.4. Unconformities in the Siwalik Group

Unconformities in the Siwalik units are known from several places of western Nepal. A regional unconformity has been found on satellite views along a N70° trending hill (Fig. 3b; SPOT views KJ 218-294 and KJ 219-294) west of the Surai Khola section (Leturmy, 1997). Beds of the Dobatta Formation (Appel et al., 1991) are characterised by a succession of chevrons (Fig. 3c) whereas the conglomerates of the upper Siwalik member (Dhan Khola Formation) are characterised by a more uniform pattern. In the western part, Dobatta beds are truncated by a surface at the base of the upper Siwalik conglomerates. This surface is interpreted as an erosional discontinuity that affected the upper Siwalik. This erosional discontinuity was not evidenced along the Surai Khola section (Appel et al., 1991) in the western part because it has the same trend as the structures and because it is nearly parallel to the beds.

Unconformities have also been evidenced from field work in several places of western Nepal. Most of them are located at the bottom of conglomerate facies of the upper Siwalik member. Cross-section of Fig. 4 is located west of the Dang Valley (Fig. 1) in the complex zone located to the West of the Dang area, whereas the more than 60° unconformity of Fig. 5 is located above N 150 trending middle Siwalik beds (location on Fig. 2).

The unconformities are particularly well expressed above structures showing an unusual trend respectively to the mean Himalayan one and they probably reflect early stages of the Outer belt deformation. Therefore they suggest that tectonics affected this part of the Siwalik belt since 1.8–2.3 Ma.

3. Geometry of the linked thrust system

3.1. Structural pattern

Structural maps of the far-western area (Fig. 1) and mid-western area (Fig. 2) are based on our field work (time spent in the field by the co-authors is 17 months since 1987) and satellite image interpretation (Multichannel SPOT images). Maps of the Nepali-Canadian project (Scott et al., 1986) at the scale of 1/125 000 and unpublished maps of the Petroleum Project of the Department of Mines and Geology have also been consulted.

Table 1
Stratigraphic thickness within thrust sheets (Location of the sections are I to VII on Figs. 1 and 2)

No. on Figs. 1 and 2	Section	Total thickness
I	Dadheldhura road	4300 m
II	Lower Karnali	4100 m
III	Surkhet road	4100 m
IV	Jhanjhari Khola	4300 m
V	Mungwa Khola	5500 m
VI	Koilabas road	5700 m
VII	Surai Khola	5200 m

Several north dipping thrusts delineate tectonic boundaries between informal upper and lower Siwalik members. Detailed analyses show that there was a succession of laterally relayed thrusts (Hérail and Mascle, 1980; Delcaillau et al., 1987; Mugnier et al., 1992).

The MFT (Main Frontal Thrust) is formed by segments which branch and relay on lateral ramps or die out laterally westward in lateral propagating folds. Three distinct segments from W. to E. of the MFT are identified in mid-western and far-western Nepal. MFT1 is best observed at Koilabas (in India) (Fig. 6a) and MFT2 along the Mungawa Khola. No outcrop of MFT3 is presently known, though Karnali alluvium is clearly faulted at Chisapani. Several fault propagation folds are located to the west of MFT1 (Leturmy, 1997). They are called in order of decreasing size, FPF1, FPF2 and FPF3. The asymmetric anticlinal structure of FPF1 is clearly observed, with a vertical frontal limb and a gentle (i.e., 30 to 20°) northern limb, whereas FPF2 and FPF3 are only characterised by uplifted terraces (90 m above the plain in case of FPF2 and 20 m in case of FPF3). Other blind structures presumably exist beneath the Terai plain (Delcaillau, 1997) ahead of MFT2 and of MFT3 but have not been systematically mapped.

Several thrusts affecting the Siwalik Group lie between the MBT and the MFT. They are grouped together under the name of Main Dun Thrust (MDT). At least 4 distinct segments of the MDT are considered in mid-western and far-western Nepal, and numbered from east to west (Figs. 1 and 2). MDT1 bounds the Deukhury valley to the north (Fig. 6b). It branches to the east on to MFT1 and it dies out to the west in a complex "pop-up" structure mainly characterised by strike-slip motion along its E–W trending borders. MDT2 bounds to the west of the Babai river and is observed in numerous gullies. MDT3 crosses the Bheri and Karnali rivers several times and furnishes amongst the best outcrops of the Siwalik thrust faults (Mugnier et al., 1992, 1998). MDT4 is observed

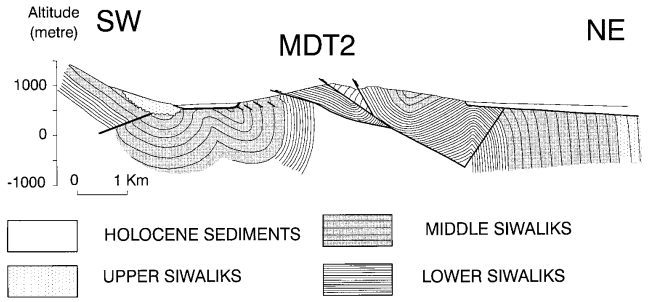

Fig. 4. Cross-section through the West Dang Transfer zone showing a discordance at the base of the conglomerates of the Upper Siwalik unit (location on Fig. 2).

along the Dadeldhura road and presumably dies out to the east in a fault propagation fold.

Several back-thrusts have also been characterised south of the Dang valley, and southward verging thrusts are located at the footwall of the MBT. The stratigraphic separation between footwall and hanging-wall of these faults suggests that they do not cross the whole Siwalik Group, but rather branch off décollement levels located within the lower Siwalik rocks. These faults are linked in numerous cases to the development of duplexes in the lowermost series. The back-thrusts are either duplex roof thrusts that have been tilted, or back-thrusts above tectonic wedges. They are called in this paper Internal Décollement thrusts (ID). These intermediate décollement levels are indicated mainly in the hinterward part of the Siwalik belt, but incipient décollements are also observed along the still continuous stratigraphic piles of the Surai Khola (Fig. 3a) and the lower Karnali. There, the décollement level is expressed by cleavage in clay beds and by local

Fig. 5. Unconformity in the field (location on Fig. 1). Sandstones dip steeply towards SW and the unconformity at the base of conglomerates (see hammer) dips gently towards the North-east.

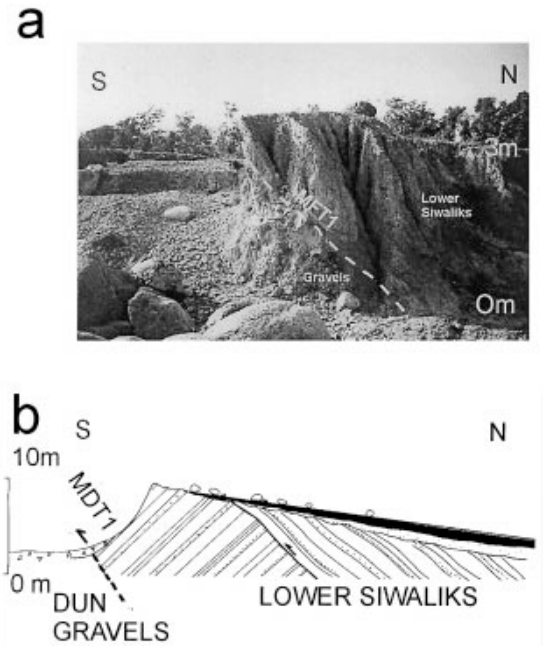

Fig. 6. (a) MFT1 at Koilabas (location on Fig. 1). (b) MDT1 in the Deukhury valley (location on Fig. 1).

(meter scale) ramps through sandstone levels. The succession of all these thrust structures gives a general festooned outcrop pattern to the Siwalik belt of western Nepal (Figs. 1 and 2). Major transverse zones, analysed in a following section, delineate segments in the Siwalik belt.

3.2. Cross-sections through the Siwalik belt

Balanced cross-sections have been constructed parallel to the shortening direction. The use of the kink-fold method (Suppe, 1983) allows us to propose a deeper geometry of the belt from structural field data.

3.2.1. Direction of motion along the faults

The direction of motion along the faults (Fig. 7) is deduced from shear structures in the main fault zones (Mugnier et al., 1998; Huyghe et al., 1999). Where the thrusts do not crop out, the mean shortening direction has been deduced from the statistical analysis of slickensides (Mugnier et al., 1992) measured on minor fractures in the hangingwall of the thrusts. They have been analysed by the right dihedron method (Angelier and Mechler, 1977). It appears that the thrust sheets are mainly displaced from NNE to SSW, and cross-sections have been built parallel to this trend in the rather cylindrical segments of the Siwalik belt. Anomalous shortening directions mainly occur in the zones where displacement is transferred from one branch to another branch of the MDT and MFT.

3.2.2. Typical cross-section formed by forward verging thrusts

The depth of the décollement along the western cross-section (Fig. 8a; AA′ on Fig. 1) is strongly constrained because the horizontal distance between the MFT3 and MDT3 is much greater than the thickness of the thrust sheets. It is suggested that a gently dipping basal décollement is nearly 4 km below the surface in the Bheri-Karnali area. This result agrees with the thickness of the Siwalik Group ahead of the MFT, determined from seismic lines in the Ganga plain (DMG, 1985). The stratigraphic separation between

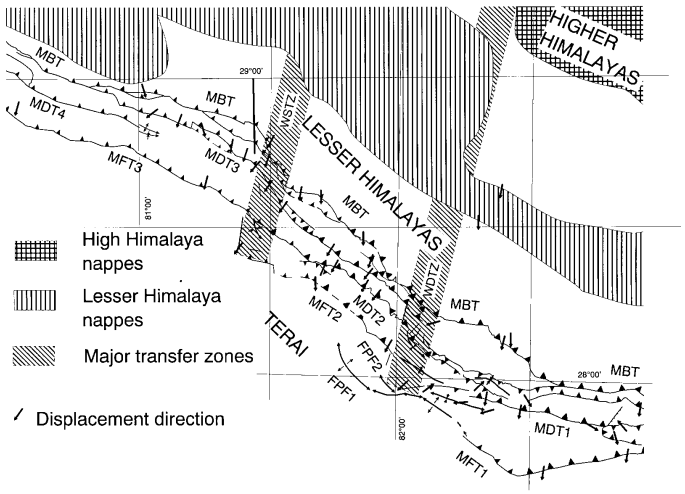

Fig. 7. Displacement direction along major thrusts of the Siwalik belt of western Nepal.

footwall and hangingwall of the Internal Décollement (ID) at the bottom of the inner sheet suggests that it is an intermediate décollement in the upper part of the lower Siwalik unit. Line length balancing implies duplex development in the lower Siwalik rocks at the footwall of the MBT. The cut-off relationships show that a minor out-off sequence (O.F. on Fig. 8a) thrust cuts through previously folded Middle Siwalik beds. The cross-cutting relationships drawn between the MBT and the underlying thrusts (Fig. 8a) show an out-off-sequence reactivation of the MBT, noted in the field by Bashyal (1981) close to the Dadeldhura road.

3.2.3. Cross-sections across back-thrusts

The eastern cross-section (Fig. 8a, BB′ on Fig. 1) is located close to the Surai Khola section and is based on the map of Gautam and Dhital (1994) augmented by our field observations. The hangingwall of the MFT1 is formed by a thick continuous Siwalik section, whereas the hangingwall of MDT1 depicts complex structures formed by a syncline above a forward thrust and a steep back-thrust (“Silling Khola Thrust”, SKT) and large-scale folds with locally overturned limbs. The synclinal structure is not a klippe of a hinterward thrust sheet because it dies out towards the east. The stratigraphic separation between footwall and hangingwall of these forward (MDT1) and backward thrusts (SKT) (respectively juxtaposing the upper part of the lower Siwalik member above upper Siwalik rock and the upper part of lower Siwalik rocks above the middle Siwalik beds) suggests to us that MDT1 branches on an intermediate décollement level at the base of the upper part of lower Siwalik member. A duplex is inferred in the footwall of this décollement to balance the length of lower Siwalik and middle Siwalik. This interpretation suggests that SKT is a roof thrust above a wedge; this geometry is basically analogous to the wedge tectonics described by Price (1986) in the Canadian Cordillera and by Powers et al. (1998) in the Kangra reentrant of the Sub-Himalaya belt. The stratigraphic separation between footwall and hangingwall of the internal décollement (ID) (which places the upper part of lower Siwalik member above upper Siwalik rocks) suggests a décollement at the bottom of the upper part of lower Siwalik beds, whereas line length balancing of lower Siwalik versus middle Siwalik beds suggests a duplex formed by the lowest part of the lower Siwalik member. Such a structure would be hidden beneath the Lesser Himalayas.

3.3. Structural implication of balanced cross-sections

3.3.1. Duplex

The detail of the deep structures is poorly constrained because of the lack of subsurface data, but serial cross-sections strengthen the hypothesis that duplexes are characteristic features in the footwall of the Main Boundary Thrust. They formed between sev-

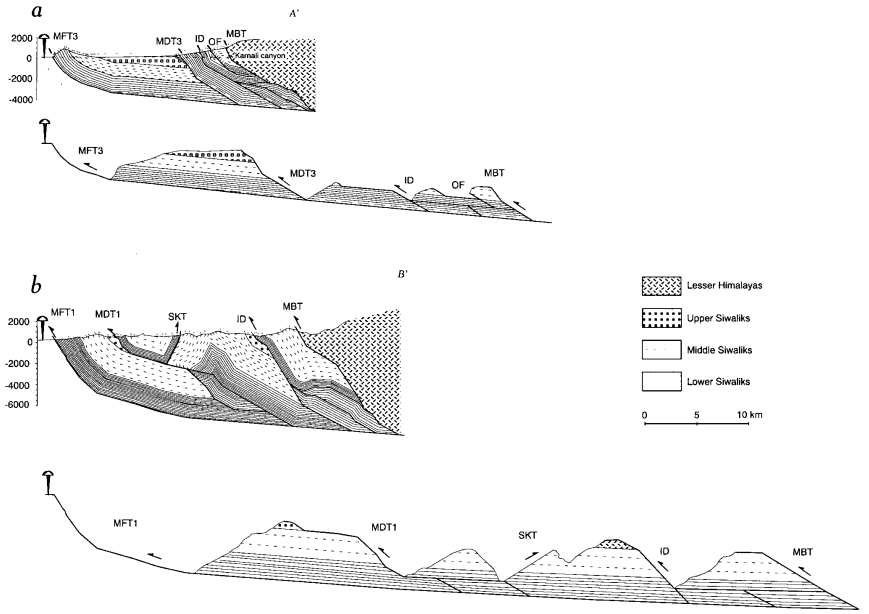

Fig. 8. Balanced cross-sections and restored cross-sections through the Siwalik belt. See text for a description. (a) Cross-section close to the Karnali river (A-A′ on Fig. 2). (b) Cross-section close to the Surai Khola area (B-B′ on Fig. 1).

eral décollements located in the lower Siwalik member. Two kinds of duplex are located in the footwall of the MBT (Fig. 9). Duplexes formed by far travelled horses, as defined by Boyer and Elliott (1982), induce repetition of the lower Siwalik member south of the MBT trace (Fig. 9a). The detail of their geometries is very difficult to decipher because internal deformation is strong and the lithology is rather homogeneous. Far-travelled horses are more clearly recognised in Central Nepal along the Bagmati river (B.N. Upreti, personal communication, 1998) because they incorporate at their bases thin slices of pre-Siwalik series (Hérail and Mascle, 1980). These far travelled horses induce a steepening of the MBT and favour normal sense reactivation (Nakata, 1989) or faulting in the hangingwall. Far-travelled horses and normal sense reactivation are found along the Surkhet–Gorahi fault (SKF on Fig. 9a) between Surkhet (Skt on Fig. 2) and Gorahi (Gor on Fig. 1). Footwall duplexes remain hidden (Fig. 9b) whereas middle to upper Siwalik members rocks crop out south of the Lesser Himalayas series. The details of the duplex geometry are still unknown.

3.3.2. Amount of shortening in the frontal thrust belt

The amount of shortening that affects the whole Siwalik Group is difficult to estimate because of: (1) the lack of subsurface data that would allow the identification of footwall cut-offs and (2) the intense erosion that affects the hangingwall anticlines. Minimum estimates can be proposed. Balanced cross-section A-A′ (Fig. 8) suggests that a minimum of 6 km shortening affects the frontal structure, that a minimum displacement of 6 km acts along the MDT3, and a 5 km displacement along ID. This implies more than 17 km shortening for a section presently 25 km long, i.e., an amount of shortening (total displacement versus initial length) of at least 40%, whereas balanced cross-section B-B′ (Fig. 8) implies more than 40 km shortening for a cross-section presently 33 km long (i.e., 51%). We believe that the difference between the two sections is not meaningful, but is rather linked to

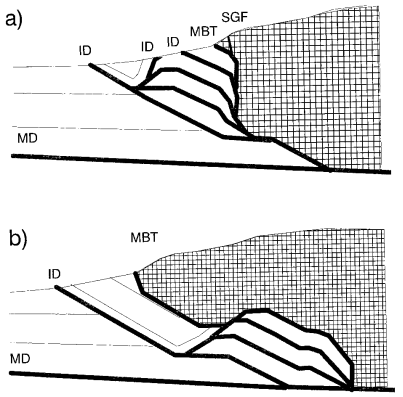

Fig. 9. (a) A sketch of far-travel horses at the footwall of MBT. A duplex formed by far travelled horses induces repetition of the lower Siwalik member south of the MBT trace. (b) A sketch of hidden horses at the footwall of MBT. A duplex is inferred in the footwall of the ID décollement to balance the length of lower Siwalik and middle Siwalik.

an underestimate of shortening due to erosion of hangingwall cut-offs in cross-section A-A′. The 40 km shortening in BB′ is also a minimum, as most of the hangingwall cut-offs are eroded along this section. Considering that the unconformities at the base of the Upper Siwalik member mark the onset of the thrust-related deformation in this part of the fold and thrust belt, a mean minimum shortening rate of 17 mm/yr is calculated for the last 2.3 Ma.

This shortening value is in the range of those proposed by Schelling and Arita (1991) in eastern Nepal (i.e., 20 km shortening for a cross-section presently 30 km long) and by Biswas (1994) in the Siwaliks of north-western India where the amount of shortening greater than 40% was evaluated from sub-surface data. That rate (17 mm/yr) is also very similar to the long-term rate (12–2 Ma) calculated by DeCelles et al. (1998), to the Holocene rate calculated by Lavé and Avouac (1999) and Leturmy (1997) or to the thrust component of convergence calculated in western Nepal from GPS studies (Bilham et al., 1997).

4. Transfer zones and Piggy back basins

4.1. The segmentation of the outer belt

The general segmented pattern of the frontal belt of western Nepal is linked to major transverse zones that delineate several segments in the frontal belt. The westernmost transverse zone is located (Fig. 2) west of the Dadheldura road and mainly affects the extension of the upper Siwalik member and the structures in the hangingwall of MDT4. It is outlined by an angular unconformity between middle and upper Siwalik members that locally exceeds 70° (Fig. 5). The second transverse zone is located west of Surkhet (WSTZ on Fig. 7). The West Dang Transfer Zone (WDTZ) is the major transfer zone that forms the Western boundary of the extension of the large wedge-top basins of mid-western Nepal (Fig. 7). These flat areas are classically called dun valleys.

4.2. The West Surkhet Transfer zone

The West Surkhet Transfer zone forms the western boundary of MFT2, and is outlined by the nearly N–S striking beds that are observed at the outlet of the Babai River in the Terai plain. This second transverse zone affects the trends of the MDT3, MBT and thrusts of the Lesser Himalayas, and also induces bending of the beds in the hangingwall of MFT3-MDT2. This transverse zone forms the boundary between hidden duplexes (in the west compartment) and far travelled horses (in the east compartment) at the footwall of MBT. Gravity data (Department of Mines and Geology, personal communication, 1998) suggest a basement scarp beneath WSTZ.

4.3. The West Dang Transfer zone

The width of the Siwalik belt varies from 25 km west of WDTZ to 40 km east of West Dang Transfer zone. WDTZ is formed by sigmoid folds, sigmoid reverse faults and strike-slip faults (Figs. 2 and 7). The MFT1, MFT2, and MDT3 laterally die out in the WDTZ whereas MDT2 shows a right handed bend. The trajectory of the Main Boundary thrust is hardly affected by WDTZ. It is nonetheless believed that the West Dang Transfer zone affects the geometry of the basal detachment, and is a deep structure that projects to the north (Huyghe et al., 1998), because its continuation forms a pronounced limit of the modern seismicity distribution (DMG, 1997) in the Lesser Himalayas, and the eastward boundary of Greater Himalayan nappes (Fig. 7). Recent tectonic activity that occurs along the MBT (Nakata, 1989) prevents the use of MBT trajectory as a passive marker, and is responsible for its present-day straight pattern. Strike-slip faults also cross the sigmoid structures. As they are difficult to map, we have used morphologic analysis of the drainage pattern (Huyghe et al., 1998) to detect them. Two families are prominent. A first set of tear faults shows a N170° to N10° trend nearly parallel to the mean trend of the WDTZ. A second set shows

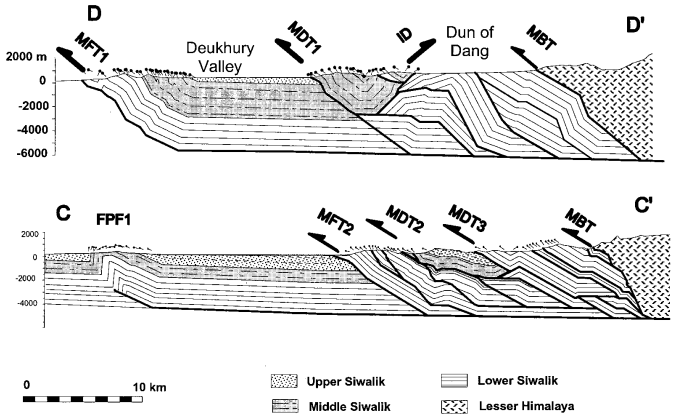

Fig. 10. Cross-sections on each side of West Dang Transfer zone (C-C′ and D-D′ on Fig. 1).

a N60° to N80° trend. This last set is related, close to location of Fig. 4, to strike-slip faults that clearly show a dextral component. These faults could correspond to a set of Riedel fractures that developed during the dextral torsion of the whole structure (fold axes and thrust trajectories) of the WDTZ. Southward, at western end of the Deukhury valley, N90 sinistral strike-slip faults link MDT1 to FPF1. The WDTZ appears as a complex structural zone: the superposition of strike-slip faults, sigmoid folds and sigmoid reverse faults that is observed shows analogies with the cross-strike discontinuities described in the Appalachian overthrust belt above a basement scarp (Wheeler, 1980; Thomas, 1990). Physical models (Calassou et al., 1993) that involve a step in the basal décollement also predict this type of complex structure.

Comparison of balanced cross-sections (Fig. 10) in the western compartment and in the eastern compartment of WDTZ shows: (1) a change of the stratigraphic thickness of the Siwalik beds involved in the thin-skinned thrust tectonics, and particularly of the middle Siwalik bed; (2) an increase of the depth of the décollement from west to east; (3) a transfer of displacement from MFT2 to MFT1 and from MDT3 to ID, whereas the total displacement south of the MBT remains nearly constant (close to 40 km). Those three points are consistent with a step in the basal décollement that controls the differential evolution of the eastern and western thrust belts.

It is suggested that a basement fault controlled the subsidence of the foreland basin during the deposition of the middle Siwalik beds. That feature is presently located beneath the thin-skinned thrust belt.

4.4. The development of the duns

The WDTZ bounds to the West the large wedge-top basins (or duns) of mid-western Nepal (Fig. 1). The Dang valley is one of the largest duns and forms a nearly 1000 km^2 plain within a local drainage basin of less than 3000 km^2. The Deukhury valley forms a nearly 600 km^2 plain within a drainage basin of 6100 km^2. The oldest terrace that crops out in Deukhury valley has been carbon-14 dated at 7000 yr, (Leturmy, 1997) whereas the main phase of infilling in Dang valley is linked to lacustrine sediments more than 20,000 yr old (Yamanaka and Yagi, 1984).

The progressive flattening of the Upper Siwalik beds from the back of the MFT1 hangingwall to the border of the dun suggests a progressive tectonically controlled unconformity (Fig. 8b), though it also could agree with a progressive flattening of the MFT at depth. Furthermore unconformities observed both above WDTZ (Fig. 4) and at the hangingwall of MFT1 (Fig. 3) suggest that the Himalayan front was located south of the dun basins since 2 Ma, and that the WDTZ led the southward shift of the tectonic front at that time. As the tectonic front was located at the tip of the basal décollement, the Dang and Deukhury have been displaced piggy-back above the décollement since 2 Ma. The mechanics of their development is analysed in a companion paper (Mugnier et al., 1999).

5. Conclusion

The geometry of the Outer belt of western Nepal follows the classic rules defined in thin-skinned thrust belts: seven major north dipping thrusts and 3 major south dipping thrusts delineate the thrust sheets. Duplexes have developed between 2 major décollement levels. The thrust sheets of the frontal belt have been displaced from NNE to SSW, perpendicular to the trend of the western Nepal belt since at least 1.8 Ma. The amount of shortening exceeds 40 km. This paper gives new insight in the thrust system kinematics of western Nepal by outlining the importance of: (1) unconformities in the syn-tectonic sediments; (2) out-of sequence thrusting; and (3) the role of duplexes at the footwall of the MBT. It also brings out the importance of two major transfer zones located west of the Dang valley and west of Surkhet. They are probably related to basement scarps that control the geometry of the basal décollement and the distribution of Piggy-back basins. As the frontal belt of the Himalaya is an active tectonic zone, it appears an ideal area to collect field data permitting the estimation of the rates of geological phenomena (shortening rate, sedimentation rate, erosion rate, etc.) and the study of the interactions between the different phenomena and the mechanics of thin-skinned thrust belts.

Acknowledgements

Constructive reading of the manuscript by P. DeCelles and Y. Philippe, B.N. Upreti and K. Burke is gratefully acknowledged. We thank the Institut National des Sciences de l'Univers for the financial support (DBT, IDYL, IT and Prose projects).

References

Angelier, J., Mechler, P., 1977. Sur une méthode graphique de recherche des contraintes principales également utilisable en tectonique et en seismologie: la méthode des dièdres droits. Bulletin Social Géologique France 19, 1309–1318.

Appel, E., Rosler, W., Corvinus, G., 1991. Magnetostratigraphy of the Miocene-Pleistocene Suraï Khola Siwaliks in West Nepal. Journal of Geophysical International 105, 191–198.

Auden, J.B., 1935. Transverse in the Himalayan. Geological Survey of Indian Record 69, 123–167.

Bashyal, R.P., 1981. Geology of Dhangrhi-Dandeldhura road section and its regional significance. Journal of Nepal Geological Society 1, 15–28.

Bilham, R., Larson, K., Freymuller, J., Project IDYLIM members, 1997. Indo-Asian collision rates in the Nepal. Nature 386, 61–64.

Biswas, S.K., 1994. Status of exploration for Hydrocarbons in siwalik Basin of India and Future trends. In: Kumar, R., Ghosh, S.K., Phadtare, N.R. (Eds.), Siwalik Foreland Basin of Himalaya: Dehra Dun, India. IBH, Oxford, pp. 283–301.

Boyer, S.E., Elliott, D., 1982. Thrust systems. American Association of Petroleum Geologists Bulletin 66, 1996–2230.

Calassou, S., Larroque, C., Malavieille, J., 1993. Transfer zones of deformation in thrust wedges: an experimental study. Tectonophysics 221, 325–344.

Cande, S.C., Kent, D.V., 1995. A new geomagnetic polarity time scale for the Late Cretaceous and Cenozoic. Journal of Geophysical Research 100, 6093–6095.

Corvinus, G., 1988. The Mio-Plio-Pleistocene litho- and biostratigraphy of the Surai Khola Siwaliks in West Nepal: first results. C.R. Acad. Sci. Paris 306, 1471–1477.

DeCelles, P.G., Gehrels, G.E., Quade, J., Ojha, T.P., Kapp, P.A., Upreti, B.N., 1998. Neogene foreland basin deposits, erosional unroofing and the kinematic history of the Himalayan fold-thrust belt, Western Nepal. Geological Society of America Bulletin 110, 2–21.

Delcaillau, B., 1997 Les fronts de chaînes actives, Memoir of Habilitation, 335 pp.

Delcaillau, B., Hérail, G., Mascle, G., 1987. Evolution géomorphostructurale de fronts de chevauchements actifs: le cas des chevauchements intra-Siwalik du Népal central. Zeitschrift für Geomorphologie Neue Forschung 31, 339–360.

DMG 1985. (Departement of Mines and Geology, Ministry of Industry His Majesty's Government of Nepal). Nepal Exploration Opportunities Internal Report, 52 pp.

DMG 1997. (Departement of Mines and Geology, Ministry of Industry His Majesty's Government of Nepal). Microseismic Epicenter Map of Nepal Himalaya and adjoining region.

Dhital, M.R., Gajurel, A.P., Pathak, D., Paudel, L.P., Kizaki, K. 1995. Geology and structure of the Siwaliks and Lesser Himalaya in the Surai Khola-Barbanda area, Mid Western Nepal. Bulletin of the Deptartent of Geology, Tribhuvan Univ., Kathmandu, Nepal 4, 1–70.

Gautam, P., Dhital, M.R., 1994. Siwaliks of the Surai Khola-Butwal area. In: Himalayan-Karakorum-Tibet Workshop, 9th Field Trip Guidebook: Kathmandu, Nepal. Geological Society of Nepal, p. 39.

Hérail, G., Mascle, G., 1980. Les Siwalik du Nepal central: structures et géomorphologie d'un piémont en cours de déformation. Bulletin Association Geographique Française 431, 259–267.

Huyghe, P., Galy, A., Mugnier, J.L., 1999. Micro-structures, clay mineralogy and geochimistry of the clay size fraction (< 2 μm) of thrusted zones (Karnali area, Siwaliks of Western Nepal). Journal of Nepal Geological Society 18, 239–248.

Huyghe, P., Mugnier, J.L., Leturmy, P., 1998. Segmentation of the Siwalik thrust belt of Western Nepal and localisation of Piggy-back basins. 13th Himalayan Karakorum Tibet International Workshop, Peshawar, 20–22 April 1998.

Johnson, N., Stix, J., Tauxe, L., Cerveny, P.F., Tahirkheli, A.K., 1985. Paleomagnetic chronology, fluvial processes and tectonics implications of the Siwalik deposits near Chinji village, Pakistan. Journal of Geology 93, 27–40.

Lavé, J., Avouac, J.P., 1999. Abandoned fluvial terraces across the Siwalik Hills (Nepal): Active fault-bend-folding at the Main Frontal Thrust and implications for himalayan seismotectonics, Journal of Geophysical Research (in press).

Leturmy, P. 1997. Sédiments et reliefs du front des systèmes chevauchants: modèlisations et exemples du front andin et des Siwalik (Himalaya) à l'Holocene. PhD thesis, Grenoble university, 229 pp.

Mugnier, J.L., Mascle, G., Faucher, T., 1992. La structure des Siwalik de l'Ouest Népal: un prisme d'accrétion intracontinental. Société Géologique de France, Bulletin 163, 585–595.

Mugnier, J.L., Delcaillau, B., Huyghe, P., Leturmy, P., 1998. The break-back thrust splay of the main dun thrust: evidence of an intermediate displacement scale between earthquake slip and finite

geometry of thrust systems. Journal of Structural Geology 20, 857–864.

Mugnier, J.L., Leturmy, P., Huyghe, P., Chalaron, E., 1999 The Siwaliks of western Nepal: II-mechanics of the thrust wedge, Journal of Asian Earth Sciences 17, 643–657.

Nakata, T., 1989. Active faults of the Himalayas of India and Nepal. In: Malinconico, J., Lille, R. (Eds.), Tectonics of western Himalayas. Geological Society of America Special Paper, 232, 243–264.

Pilgrim, 1917. A preliminary note on some recent mammalian collection from the basal basin of Siwalik. Records of the Geological Survey, India 48, 98–101.

Powers, P.M., Lille, R.J., Yeats, R.S., 1998. Structure and shortening of the Kangra and Dehra Dun reentrants, Sub-Himalaya, India. Geological Society Bulletin 110, 1010–1027.

Price, R.A., 1986. Tectonic wedging in Canadian Cordilliera. Journal of Structural Geology 6, 239–255.

Quade, J., Cater, J.M.L., Ojha, T.P., Adam, J., Harrison, T.M., 1995. Late Miocene environmental change in Nepal and the northern Indian subcontinent: stable isotopic evidence from paleosols. Geological Society of America Bulletin 107, 1381–1397.

Raiverman, V., Kunte, S.V., Mukherjee, A., 1983. Basin geometry, Cenozoic sedimentation and hydrocarbon prospects in northwestern Himalaya and Indo-Gangetic plains. Petroleum Journal of Asia 6, 67–92.

Ranga Rao, A., Agarwal, R.P., Sharma, U.N., Bhalla, M.S., Nanda, A.C., 1988. Magnetic polarity stratigraphy and vertebrate paleantology of Upper Siwalik of the Jammu Hills. Journal of the Geological Society of India 31, 109–128.

Schelling, D., Arita, K., 1991. Thrust tectonics, crustal shortening, and the structure of the far-eastern Nepal Himalaya. Tectonics 10 (5), 851–862.

Scott, S., Nakarmi, S., Dongol, G., Duvadi, A.K., 1986. In: Land Resource Mapping project, Geology report. Kenting Earth Sciences Limited 148 pp.

Suppe, J., 1983. Geometry and kinematics of fault bend folding. American Journal of Science 283, 684–721.

Tandon, S.K., 1990. The Himalayan foreland: focus on Siwalik basin. In: Tandon, S.K., Pant, C.S., Casshyap, S.M. (Eds.), Sedimentary basins of India: tectonic context. Gyanodaya Prakashan Print, Nainital, pp. 171–201.

Thomas, W.A., 1990. Control on location of transverses zones in thrust belts. Ecologae Geologica Helvetica 83, 727–744.

Wheeler, R.L., 1980. Cross-strike discontinuities: possible exploration tool for natural gas in Appalachian overthrust belt. AAPG Bulletin 64, 2166–2178.

Yamanaka, H., Yagi, H., 1984. Geomorphological development of the Dang Dun, Sub-Himalayan zone, southern Nepal. Journal of Nepal Geological Society 4, 151–159.

7

Husson, L., J.-L. Mugnier, P. Leturmy, and G. Vidal, 2004, Kinematics and sedimentary balance of the Sub-Himalayan Zone, western Nepal, *in* K. R. McClay, ed., Thrust tectonics and hydrocarbon systems: AAPG Memoir 82, p. 115–130.

Kinematics and Sedimentary Balance of the Sub-Himalayan Zone, Western Nepal

Laurent Husson[1]

Laboratoire de Géodynamique des Chaînes Alpines et Université Joseph Fourier, Maison des Geosciences, Grenoble Cedex, France

Jean-Louis Mugnier

Laboratoire de Géodynamique des Chaînes Alpines et Université Joseph Fourier, Maison des Geosciences, Grenoble Cedex, France

Pascale Leturmy[2]

Laboratoire de Géodynamique des Chaînes Alpines et Université Joseph Fourier, Maison des Geosciences, Grenoble Cedex, France

Gérard Vidal

Ecole Normale Supéricure de Lyon, Laboratoire des Sciences de la Terre, Lyon, France

ABSTRACT

The Sub-Himalayan Zone constitutes a tectonic wedge of synorogenic sediments along the southern edge of the Himalayan Belt. Sediments are incorporated into the prism from the foreland Indo-Gangetic plain, undergo a tectonic cycle within it, and eventually are eroded. The structural sketch map exhibits westward-plunging arcuate structures on the foremost location of the Outer Belt. Investigations from spatial imagery and digital elevation modeling (DEM), together with kinematic data, allow us to calculate velocities for the geomorphologic development. Four velocities rule the general evolution of the wedge. The foremost geomorphic structure (ridge) is the assemblage of elementary structures. The lateral ridge propagation velocity is estimated to be 40 cm/yr, which supports a general cylindrical development of the Outer Belt, in spite of the asymmetrical development of each independent elbow-shaped structure. The sediment's burial history can be quantified from geometric and kinematic data. We emphasize that because of the cylindrical behavior of the prism, extrapolation of the sediment transfer to the entire western Nepal Siwalik is valid. Burial in the foreland basin takes two times longer than the entire tectonic cycle, which only lasts for about 6.5 m.y. Sediments reaching 6×10^{-5} km^3 per year and per linear kilometer accrete along the Siwalik range.

[1]*Present address*: Collège de France - Chaire de géodynamique, Europôle de l'Arbois - Bat Laennec BP 80, 13545 Aix-en-Provence, France.
[2]*Present address*: Université de Cergy-Pontoise, Avenue du Parc, 8, le Campus 95031 Cergy-Pontoise, France.

About 21% of the flowing material within the wedge is captured and withdrawn from it as subducted duplexes. Assuming a steady-state development of the wedge, and according to the Coulomb-wedge theory for the Siwalik, mean erosion rates are estimated to be about 1.9 mm/yr, which is in accord with previous estimates. We emphasize that this consistency supports the overall estimates for the general development of the wedge.

INTRODUCTION

The critical taper formed by orogenic belts can be divided into various parts in their front zone. As is the case for the Sub-Himalayan Zone of western Nepal, the most frontal deformed part often corresponds to an accretionary wedge of synorogenic sediments incorporated from the foreland basin into the mountain belt. This unit constitutes an open system of material, because sediments are added to the wedge from the foreland and removed from it by erosion. According to Dahlen and Barr (1989), mature continental synorogenic accretionary wedges display critical-taper angles and can be in a volumetric steady state. As a consequence, to keep a balanced volume of sediments throughout time within the unit, the processes that withdraw material from the wedge (erosion or duplex subduction) must be strong enough to remove sufficient material from the wedge. This statement is implicitly constrained by the global energy budget for mature prisms, because increasing the volume of the prism implies an increase of its activation energy. Material within the wedge undergoes a burial cycle, from the fresh sediment in the foreland being incorporated into the prism, to the free, eroded sediment at the surface. This pattern is generally associated with thin-skinned deformation styles.

The main morphotectonic units of the Himalayas south of Tibet include the High Himalayas, which are made of crystalline rocks and are bounded southward by the Main Central Thrust (MCT); and the Lesser Himalayas, which are made of metasedimentary rocks and are separated to the south by the Main Boundary Thrust (MBT). The last unit is the Sub-Himalayan Zone Fold-and-thrust Belt, which forms a Neogene accretionary wedge on the southern foothills of the Himalayas that is deformed in a thin-skinned style (Hérail and Mascle, 1980; Hérail et al., 1986; Schelling, 1992; Mugnier et al., 1992, 1999a; Powers et al., 1998).

Characterization of hydrocarbon maturation, migration, and entrapment in fold-and-thrust belts is often limited by poor knowledge of the kinematics of these areas. The burial history and residential time at depth are the key parameters for such problems, which can only be assessed if the global kinematics of the wedge is well understood (Baby et al., 1994; Moretti et al., 1996). Maturation is closely linked to the time span during which kerogen was maintained at depth; migration depends on the fluid paths, which are controlled by the tectonic regime and associated structure; and eventually, entrapment in foreland fold-and-thrust belts is linked to structural buildup. Although the petroleum potential is rather poor in this area (Bashyal, 1998), the Sub-Himalayan Zone is relevant to our general understanding of the deformation schemes of frontal parts of orogenic belts. Most active mountain belts show similar structural sketches, in which tectonic velocities, sedimentation, and erosion rates are in the same range. These parameters are fundamental for the evolution of petroleum systems in fold-and-thrust belts.

The aim of this chapter is to quantify the geometric and kinematic development of the Sub-Himalayan prism in western Nepal. First, we analyze the structural and morphological evolution of the wedge. Second, we estimate the volume of material incorporated from the foreland, the time of residence within the wedge, and the volume of material removed from the prism undergoing erosion, using across-strike geometric and tectonic velocities together with a structural sketch map. The kinematics cannot be restricted to a 2-D forward cycle, because the lateral growth of the structure also controls the sediment-incorporation mechanisms within the wedge. The morphological evolution helps in documenting the global dynamics of the wedge. The overall development of the wedge is best characterized by its frontal and lateral structural and geomorphological velocities.

GEOLOGIC SETTING

The Sub-Himalayan Fold-and-thrust Belt was created by the deformed synorogenic series of the Siwalik Group (Mugnier et al., 1992, 1994; 1999a; Powers et al., 1998), above the northward-subducting Indian plate. The series is located in the foothills of the Himalayas and comprises a succession of east-southeast–west-northwest-trending ridges that are perpendicular to the N10–N30°E compressional axis (Ni and Baraganzi, 1996; Jouanne et al., 1999).

A few ridges are the geomorphological expression of active thrusts. These faults branch off of a gently north-dipping décollement (Raiverman et al., 1994; Galahaut and Chandler, 1992; Biswas, 1994). Therefore, only a few active thrusts beneath south-verging slices accommodate the shortening in the Sub-Himalayan Zone (Figure 1). The fold-and-thrust belt is bounded by the Main Boundary Thrust (MBT) to the north, and the

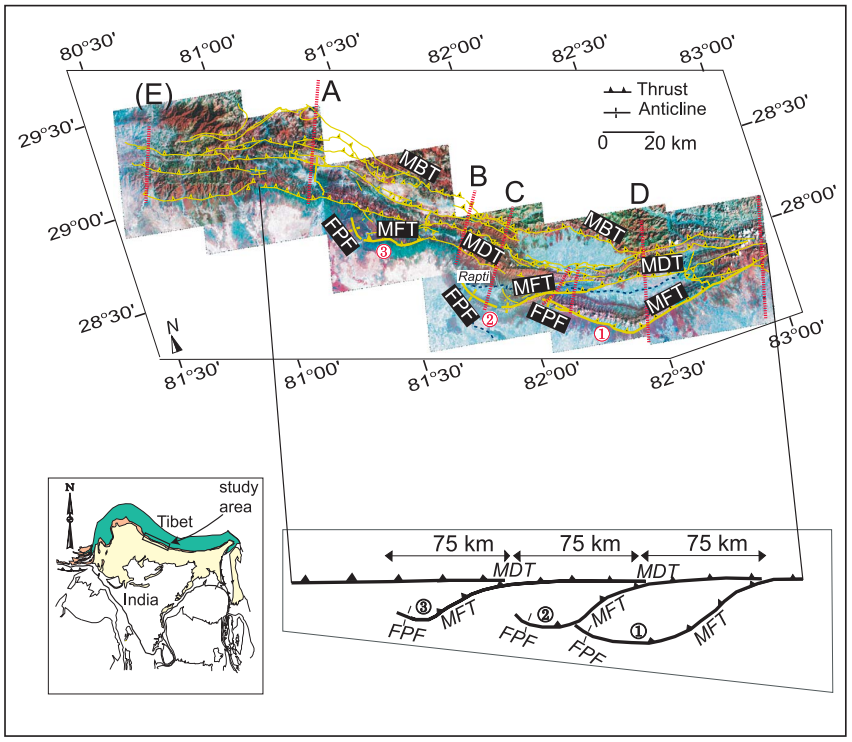

FIGURE 1. Top: Mosaic of SPOT satellite scenes and structural interpretation of the western Nepal Siwalik. Labeled dashed lines A–D are location of balanced cross sections shown in Figure 7. (E) is location of the cross section Figure 6. Unlabelled dashed lines are the locations of other available balanced cross sections. Bottom: Sketch map of west-plunging salients. MDT: Main Dun Thrust; MFT: Main Frontal Thrust; FPF: Fault-related fold (mainly fault-propagation folds).

Main Frontal Thrust (MFT) is the southernmost tectonic feature, characterized by Tertiary sediments overthrusting Quaternary (DeCelles et al., 1998a). Another primary thrust is the Main Dun Thrust (MDT) (Hérail and Mascle, 1980; Delcaillau et al., 1987; Mugnier et al., 1992), which constitutes a succession of laterally relayed thrusts propagating westward as ramp folds. This thrust owes its name to the piggyback basins called duns, which it overthrusts. Previous studies defined the Sub-Himalayan Zone as a fold-and-thrust belt characterized mainly by fault-propagation folds, fault-bend folding, and duplexes (Mascle et al., 1986; Banks and Warburton, 1986; Powers and Lillie, 1996; Powers et al., 1998; Mugnier et al., 1999a).

The prism grows by propagating southward into the foreland Indo-Gangetic plain. The stratigraphic sequence over the Main Décollement (MD) extends from the middle Miocene to the present (Appel and Roesler, 1994; Corvinus, 1994) and consists of a coarsening-upward succession of sandstone and conglomerate as much as 6000 m thick. The Siwalik Group is divided into three informal stratigraphic units. The lower Siwalik unit (middle Miocene) displays paleosols and fluvial channel deposits, the middle Siwalik unit (upper Miocene) is of a flooded-plain to braided-channel type, and the upper Siwalik unit (Pliocene to Pleistocene) is mainly conglomeratic and of a braided-channel type (Hérail et al., 1986; Delcaillau, 1997). This sequence

seems to be diachronous in along-strike and across-strike directions (Appel and Roesler, 1994; Corvinus, 1994, DeCelles et al., 1998a, Ohja et al., 2000) and is interpreted to be the Miocene to Holocene sedimentary record of the Himalayan front's southward migration (Hérail et al., 1986; Delcaillau, 1997; Mugnier et al., 1999a).

STRUCTURAL VELOCITIES IN THE HIMALAYAN OUTER BELT

Structural Development

A mosaic of six (60 km × 60 km) SPOT satellite pictures (Figure 1) taken between longitudes 80°30′E and 83°00′E was compiled to complete the previous field structural investigations and create the structural sketch map along a 300-km-long segment of the Himalayan foothills. Analysis of spatial imagery brought out a peculiar recurrent set of en echelon arcuate structures (salients) that are convex toward the foreland, above the MFT (Figure 1). Information from satellite imagery includes the westward transition from the hinterland to the foreland location of the same continuous structures. They change laterally, from north-dipping MDT monoclines on a hinterland setting to ramp folds showing emergent faults (MFT type), and end up in blind-thrust ramp folds. Previous theoretical and field work emphasized that the fault length increases with greater forward displacement over the fault (Elliott, 1976; Walsh and Waterson, 1988; Jackson et al., 1996; Leturmy, 1997; Mueller and Talling, 1997). In the Sub-Himalayan Zone of western Nepal, all the aforesaid structures become progressively less mature toward their western tips (evolution of MDT monoclines to MFT ramp folds). Along the eastern salient, an early Pliocene cartographic unconformity on the backlimb of the fold disappears toward the west (Leturmy, 1997; Mugnier et al., 1999a). In the central salient, a wind gap (Mueller and Talling, 1997) used to be a main water gap for the Rapti River. The current water gap of the Rapti River bypasses the anticline to the west (Leturmy, 1997, Leturmy et al., 1999).

Because the structures are always less evolved toward the west, and considering the field observations, we infer that the salients propagate westward asymmetrically (from the monoclines toward the anticlines); on a map, the development of the frontalmost structures is not cylindrical but is westward-plunging. Fault tips migrate laterally, perpendicularly to the main deformation axis, as the width of the fault increases with its displacement (Elliott, 1976; Walsh and Waterson, 1988; Marchal et al., 1998). If these statements and observations are correct, they imply that greater displacement occurs over the MDT than over the MFT anticlines, and faults propagate westward.

Structural Velocities Over the Fold-and-thrust Belt

The convergence rate of the Indian plate with the Eurasian plate is about 50–55 mm/yr (De Mets et al., 1990). Only a part of it is accommodated in the Sub-Himalayan Zone. The total shortening rate in this area has been estimated by several methods. To constrain the shortening rate in this area, we review the various published results using various methods. Lyon-Caen and Molnar (1985) used the southward migration of the Tertiary basin depocenter to determine a minimum Indo-Himalayan convergence rate of 10–15 mm/yr and a maximum of as much as 20 mm/yr. By subtracting the shortening accommodated on faults in the High Himalayas from the total Indo-Eurasian convergence, Avouac and Tapponier (1993) arrived at a shortening rate of 18 mm/yr. Peltzer and Saucier's (1996) global kinematic model of Asia suggests a convergence rate of 18 mm/yr between the High Himalayas and the Indian plate. Schelling (1992) and Schelling and Arita (1991) determined a rate of 8.4 to 18.6 mm/yr using minimum shortening estimates from cross-section balancing between the High Himalayas and the MFT in eastern Nepal. DeCelles et al. (1998b) estimated a southward forebulge migration rate of 14 to 33 mm/yr during Eocene-Oligocene time. Lavé and Avouac (2000) used terrace folding to estimate a minimum shortening rate of 21 mm/yr for the Holocene period. All these estimates indicate an average shortening rate of 18 mm/yr for the area between the MCT and the MFT, and this value corresponds to the Indo-Himalayan convergence following the initiation of the MCT (20–22 Ma, according to Hodges et al., 1996). After initiation of the MBT, the total shortening has been partitioned between the Lesser Himalayas and the Sub-Himalayan Zone.

From cross-section balancing in western Nepal, Mugnier et al. (1999a) determined minimum shortening of 40 km in the Sub-Himalayan Zone between the MBT and the MFT. Because the onset of shortening in the present Sub-Himalayan Zone postdates the Pliocene upper Siwalik member (DeCelles et al., 1998a; Mugnier et al., 1999a), shortening-rate estimates are at least 17–20 mm/yr for the various cross sections. In northwest India, Powers et al. (1998) synthesized shortening rates that also had been deduced from various cross-section balancing in the Sub-Himalayan Zone between the MBT and the MFT, and they are in the same range (14 ± 4 mm/yr). Such shortening rates in the Sub-Himalayan Zone in turn implies current minor shortening rates in the Lesser Himalayas.

It can be argued that geodetic data from spirit-leveling (Jackson and Bilham, 1994) or GPS measurements (Bilham et al., 1997; Larson et al., 1999) indicate little current shortening of the Sub-Himalayan zone, the maximum convergence being accommodated in the High Himalayas (about 5 mm/yr, over a total Indo-Himalayan convergence of 19 to 22 mm/yr). However, as several authors have already mentioned (Jackson and Bilham, 1994; Larson et al.,1999; Lavé and Avouac, 2000; and Mugnier et al., 2003), this more likely corresponds to an interseismic period than to the absence of shortening in the Sub-Himalayan Zone. According to Bilham et al. (1997) and Larson et al. (1999), locking below the Lesser Himalayas temporarily precludes foreland shortening, and great earthquakes are expected in order to compensate the lack of rupture south of the MBT. Mugnier et al. (1999c) showed that the mean shortening rate is constant over time (following the onset of deformation in the Sub-Himalayan zone). If correct, these results converge toward a present-day average shortening rate of about 19 mm/yr in the Sub-Himalayan zone, which we consider herein as realistic.

The Sub-Himalayan wedge accommodates shortening by a limited number of thrusts, i.e., the Main Boundary Thrust, the Main Frontal Thrust, and the Main Dun Thrust. Other thrusts currently have minor offsets and do not account for currently important shortening accommodation (see, for example, Mascle et al., 1986; Hérail et al., 1986; Mugnier et al., 1999a).

Scarce short-term velocity estimates are available for the major thrusts. A geomorphological analysis of the ridges overlying the thrusts helps to constrain velocities over the entire wedge. From a 30″ arc DEM (Figure 2a), morphological data are compiled over the ridges overlying the thrusts (Figure 2b). The mean elevation corresponds to the average altitude of each particular thrust-related relief, and the standard deviations of the elevations characterize the distribution of the elevation around this mean value. The morphology of the ridges is directly linked to the tectonic activity (Hurtrez et al., 1999).

The mean elevation increases from the southern MFT periclinal ridge (fault-propagation fold, FPF) to the MFT ridges and to the MDT. The gentle hinterland elevation increase characterizes the average taper geometry of the wedge; it includes the local tectonic activity of the thrusts but also the depth and slope of the Main Décollement, MD, which rules the shape of the wedge as a whole (Davis et al., 1983). The standard deviation of the elevation density characterizes the sharpness of the structures: the lower the standard deviation, the sharper the overlying ridge. In other words, if the elevation densities are concentrated around the mean elevation, the flanks of the ridge are abrupt. The lateral termination of the MFT (FPF of Figure 2) is sharp (standard deviation is 100 m), the MFTs have a smoother shape (standard deviations are 145 m and 148 m for the two studied ridges), and the MDTs have an even smoother morphology (standard deviations are 213 m and 228 m). Hurtrez et al. (1999) showed that because of the rapid erosive processes in the Sub-Himalayan Zone, the structures are in a dynamic equilibrium. Erosion compensates for uplift (Figure 3), and the topographic profiles remain constant through time as long as no tangible change occurs in the tectonic velocities or erosion rates. The topographic profile relates to the thrust velocity. For one particular thrust velocity and ramp geometry, there is one, and only one, associated topographic profile for the overlying ridge. This statement applies to mature ridges when the equilibrium profile is reached. Hence, the sharpness of the FPF probably relates to the growing structure (for which an equilibrium profile is not reached, as shown, by its low mean elevation) rather than to its tectonic activity. If the assumption of a dynamic equilibrium law is correct, the shapes of the MFT and MDT reflect their tectonic activity. Because the MFT and MDT ridge morphologies are globally constant, the previous statement indicates that local estimations of thrust velocities for the major thrusts can be extrapolated laterally.

The MBT presently shows major displacement (rocks of the Lesser Himalayas thrust over the Tertiary sediments of the Sub-Himalayan wedge, according to Upreti, 1990; Mugnier et al., 1992). However, Holocene activation of the MBT has locally minor normal sense slip (0.5 mm/yr; Mugnier et al., 1994), thus suggesting that taper is overcritical in this area, which implies that the MBT is not currently accommodating tangible shortening.

As a consequence, the overall shortening is accommodated mainly by the MDT and the MFT. According to the previous discussion on shortening rates, we assume that shortening over the MCT is minor, and that at least 17–20 mm/yr of shortening occurs within the Sub-Himalayan Zone. Sparse velocity data are available for the Sub-Himalayan thrusts: From terrace uplift inversion, Leturmy et al. (1999) suggested velocities in the range of 7–10 mm/yr for both the MFT and MDT in western Nepal, whereas Lavé and Avouac (2000) calculated a velocity of 21 mm/yr for the MFT and found 0 mm/yr for the MDT in eastern Nepal. These differences can be explained by the distribution of shortening versus time over these thrusts. The MDT displays minor out-of-sequence faults that are overlapped by undeformed sediments (Mugnier et al., 1998; Mugnier et al., 1999a), which indicate a nonpermanent tectonic activity. The ratio between faulted sediments and overlapping sediments is 1:3. We assume that it reflects the periods of relative activity to inactivity of the MDT. If shortening in the Sub-Himalayan Zone is partitioned only over the MDT and MFT, the tectonic activity time span reflects the coeval activation of both thrusts (Leturmy, 1997), whereas inactivity indicates periods of fast activation over the MFT alone (Lavé and Avouac, 2000). Coeval activation exists for a third of the time, hence the MDT tectonic velocity $V_{f\ MDT}$ is one-third of the value given by Leturmy et al. (1999), that is, 2–3 mm/yr. Similar calculations for the MFT indicate a tectonic velocity, $V_{f\ MFT}$, of about 17 mm/yr.

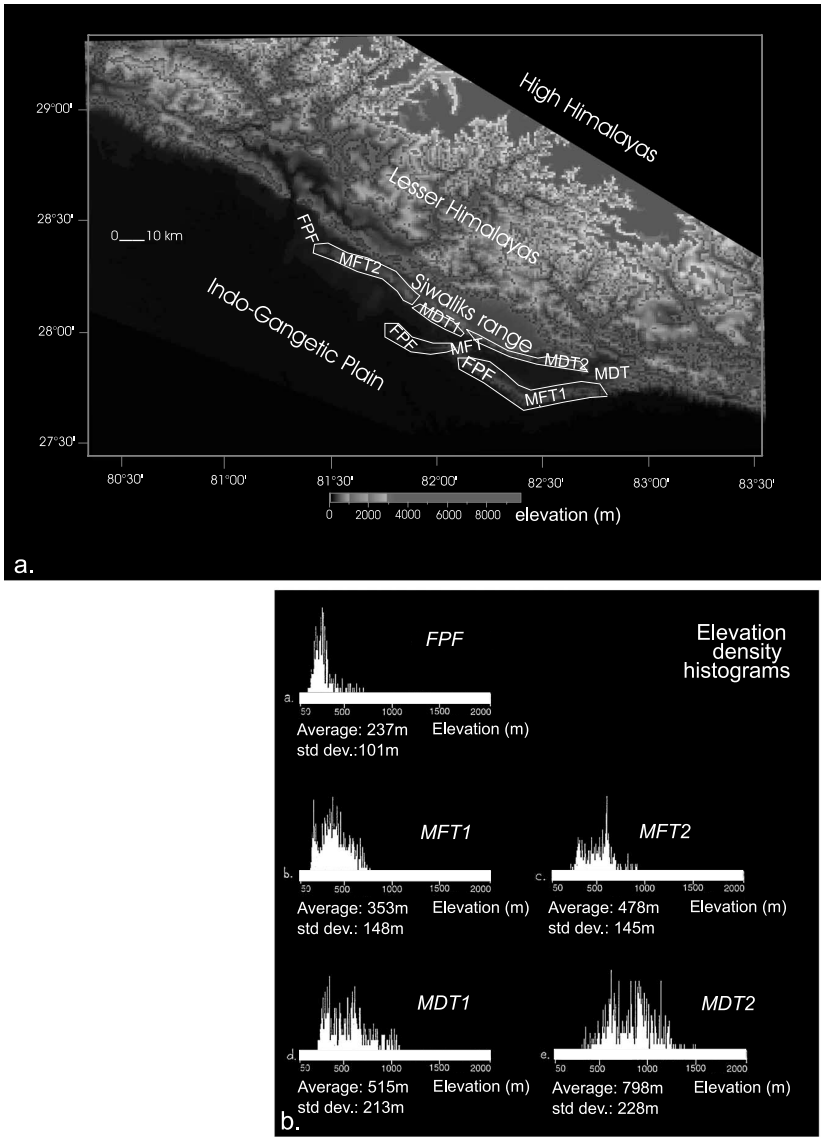

FIGURE 2. (a) 30'' arc DEM of the studied area. Solid white lines represent sampled areas for statistical analysis of elevation. (b) Elevation density histograms of each sampled structure. FPF: fault-propagation fold ridge, MFT1 and 2 : Main Frontal Thrust ridges, MDT1 and 2 : Main Dun Thrust ridges.

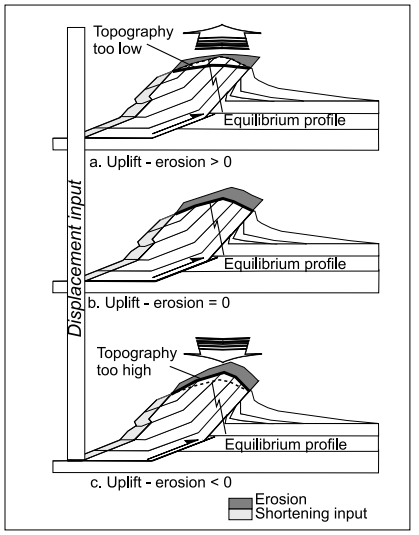

FIGURE 3. Dynamic-equilibrium theory. (a) Topography is too low with respect to the ramp velocity; erosion rates becomes lower than uplift rates. (b) Topography is in a dynamic-equilibrium state, erosion rates balance uplift. (c) Topography is too high, erosion rates become higher than uplift rates. Solid black line is topography, dashed line is equilibrium profile, light gray is the volume input as a result of shortening, dark gray is the erosion response.

Average forward-shortening velocities are available for the main Siwalik thrusts (Figure 4). However, forward velocities do not supply enough information to describe the asymmetrical development of the Sub-Himalayan Zone, and the lateral ramp-fold propagation velocities are needed. Leturmy (1997) calculated lateral-thrust velocities for the structures of the Sub-Himalayan Zone, which are 10 times faster than the forward-thrust velocities. This value is consistent with the observations of average fault displacement versus length given by various authors (Walsh and Waterson, 1988). Therefore, lateral velocity ($V_{l\ MFT}$) for the MFT is in the range of 170 mm/yr. By analogy, as Elliott (1976) previously suggested, the forward and lateral velocities that control the fault propagation can be compared to the ductile edge and screw dislocations, respectively (Figure 5).

$$V_{f_{MFT}} = 17 \text{ mm/yr}$$

$$V_{l_{MFT}} = 170 \text{ mm/yr}$$

For the sake of simplicity, these velocities will further be named V_1 and V_2, respectively.

These structural velocities rule the westward propagation of the salients, which branch off of the MDT. Such a pattern suggests that the development of the most frontal structures is asymmetrical, because propagation only acts toward the west. The remaining question concerns the cylindrical nature of the overall wedge. How do structures and morphology evolve, over time, in the fold-and-thrust belt of western Nepal, where shortening is perpendicular to the global east-southeast to west-northwest trend of the belt and where structures plunge westward?

HOLOCENE MORPHOLOGICAL VELOCITIES OF THE HIMALAYAN FRONT

Lateral Propagation Velocity of the Morphological Structures

Evidence for an asymmetric westward growth of the salients was described previously. It includes ancient unconformities that are located on the eastern part of the salients but that vanish toward the west; a westward transition from water gaps to wind gaps; the distribution of the drainage pattern; and the systematic maturation of the structures, from the eastern monoclines maturing to fault-related folds showing emergent ramps, to the western ends of fault-related folds evolving with blind ramps.

We emphasize that the en échelon pattern of the thrust belt of western Nepal is linked to the lateral propagation of the imbricate thrusting (see Shaw et al., 1999), perpendicularly to the thrust-sheet motion (Mugnier et al., 1999a), and does not reflect any dextral strike-slip component of the front. MFT salients branch eastward on the MDT and propagate westward on the foremost position. The subcontinuous trend of the MFT corresponds to the most frontal ridge, composed of the en échelon fault-related folds. In other words, the envelope of the ridges overlying the MFT is the southernmost

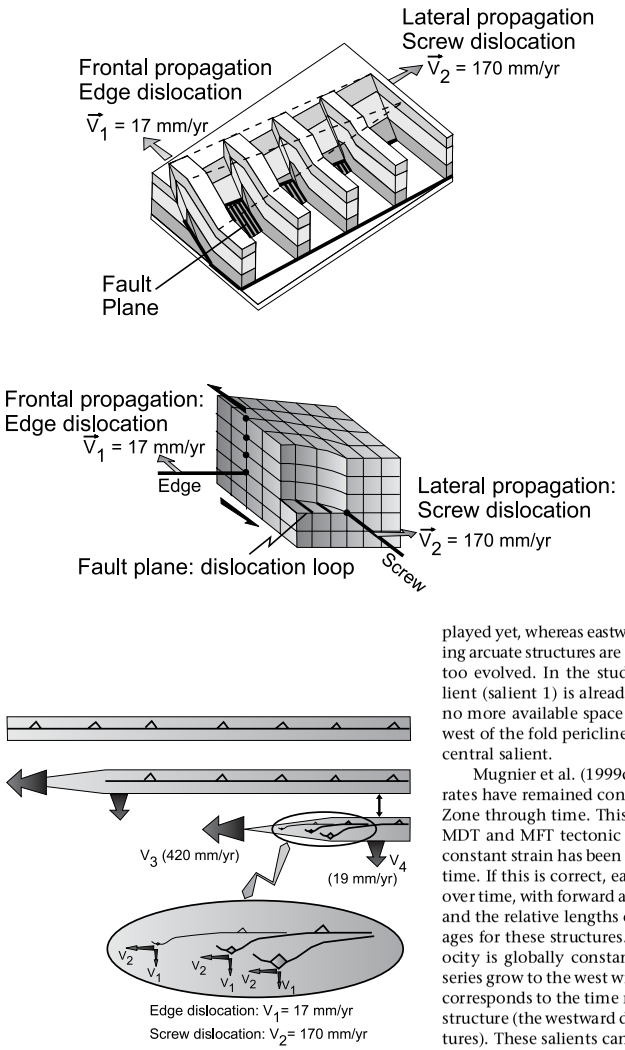

FIGURE 4. Top: Model for fault-propagation fold dynamics (after Suppe and Medwedeff, 1990). V_1 is the MFT forward velocity, V_2 is the MFT lateral propagation velocity. Bottom: analogy with ductile strain dislocations. V_1 is the edge dislocation and V_2 is the screw dislocation.

FIGURE 5. Structural and morphological velocities for the Sub-Himalayan wedge's frontal development. V_1 and V_2 are respectively the frontal and lateral propagation velocities for structural growth, and V_4 and V_3 are frontal and lateral velocities for morphological growth.

morphological feature, elongated along a broad N110°E axis. Each salient is a discrete element belonging to the MFT "chain" (Figure 1).

The salients in the studied area are distributed regularly, with a 75-km spacing (Figure 1), which can be defined as a spatial periodicity of the structures. Over the area, the lengths of the bows (from the beginning of the bend to the tip of the structures) show that they are 30 km shorter on each westward step. On the western side of the area (to the west of 81°20'E), no salient is displayed yet, whereas eastward, although some duns forming arcuate structures are displayed, the system is already too evolved. In the studied area, the easternmost salient (salient 1) is already overmature; that is, there is no more available space for lateral propagation to the west of the fold pericline, because it is bounded by the central salient.

Mugnier et al. (1999c) emphasized that shortening rates have remained constant over the Sub-Himalayan Zone through time. This statement is extended to the MDT and MFT tectonic velocities by assuming that a constant strain has been spread over these thrusts, over time. If this is correct, each frontal salient propagated, over time, with forward and lateral MFT-type velocities, and the relative lengths of the salients provide relative ages for these structures. If the 170 mm/yr lateral velocity is globally constant, salients of the en échelon series grow to the west with a 180,000-yr period, which corresponds to the time required to form a 30-km-long structure (the westward decreased length of these structures). These salients can now be regarded as independent, discrete defects that are gradually emerging westward with an average 180,000-yr period. The MFT ridge is created in this area by the assemblage of these defects. Therefore, this morphological structure propagates laterally with its own velocity, depending only on the

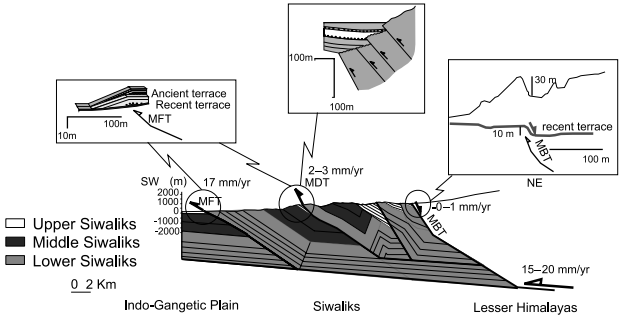

FIGURE 6. Average forward velocities over a typical cross section through the Sub-Himalayan wedge (location in Figure 1). Corresponding values are given by terrace uplift (MFT and MDT, from Leturmy, 1997 and Lavé and Avouac, 2000), sediments seal over out-of-sequence thrusts (MFT and MDT, after Mugnier et al., 1999b), normal-faulted recent terrace (MBT, after Mugnier et al., 1994), and various methods from authors (see text for references).

period of time (180,000 yr) and the spatial offset (75 km) of the independent elements of which it is made. Again, as an analog to the ductile approach, this phenomenon corresponds to dislocation creep. A rough estimate of the lateral morphological propagation velocity (V_3) is now added to the edge and corner structural velocities mentioned above:

$$V_3 = 420 \text{ mm/yr}$$

The morphological ridge, which is an assemblage of the elementary structural defects, propagates laterally more than twenty times faster than the forward structural-propagation velocity and nearly three times faster than the lateral structural-propagation velocity. This, in turn, implies that, even if the structural pattern is asymmetrical (with westward-propagating salients), the overall development of the wedge can be considered to be cylindrical, because the morphological development can be approximated to be instantaneous with respect to structural propagation velocities. However, the proposed value is considered to be a first-order estimate, because we are uncertain about the local structural velocities.

Forward Morphological Propagation Velocity

As for the lateral evolution, the morphological propagation to the south can be defined (Figure 6). Lyon-Caen and Molnar (1985) estimated, from the migration of the flexural Indo-Gangetic plain, that the southward progradation of the deformed area is in the range of 10–15 mm/yr (and is as much as 20 mm/yr). DeCelles et al. (1998a) proposed a southward forebulge migration of 14–33 mm/yr. We assume that the wedge is in a volumetric steady state, and that the taper angle is preserved through time (see Davis et al., 1983 or Dahlen and Barr, 1989). Hence we estimate the southward migration of the morphological front of the foothills to have an average rate of about 19 mm/yr, which is the value we previously debated for the convergence between the Lesser Himalayas and Indian plate. This value is the V_4 forward morphological velocity of the front.

Four velocities thus characterize the development of the Himalayan front. Two structural velocities control the development of individual structures: V_1 = 17 mm/yr, and V_2 = 170 mm/yr.

Two morphological velocities control the topographical evolution of the fold-and-thrust belt: V_3 = 420 mm/yr, and V_4 = 19 mm/yr.

The main observation we can infer from these kinematic estimates is that the overall development of the wedge is very fast laterally and is therefore cylindrical on a first-order approximation, in spite of the surface structural pattern displaying west-plunging fault-related folds. As a consequence, an across-strike evaluation of the sediment cycle within the wedge is adapted and is representative of the behavior of the wedge all along its 300-km strike length.

BURIAL CYCLE OF THE SEDIMENTS WITHIN THE WEDGE

Maximum Residence Time

A set of nine balanced cross sections that were based on surface data has been constructed over the Siwalik (Figure 7) (Leturmy, 1997; Mascle et al., 1998; Mugnier et al., 1999a, b). Assuming an "equivalence" hypothesis, lateral along-strike variations observed in the various cross sections represent different stages of the geometric and kinematic history of the analyzed thrust-related fold. This implies that measurement of fold geometries along each cross section can be used to

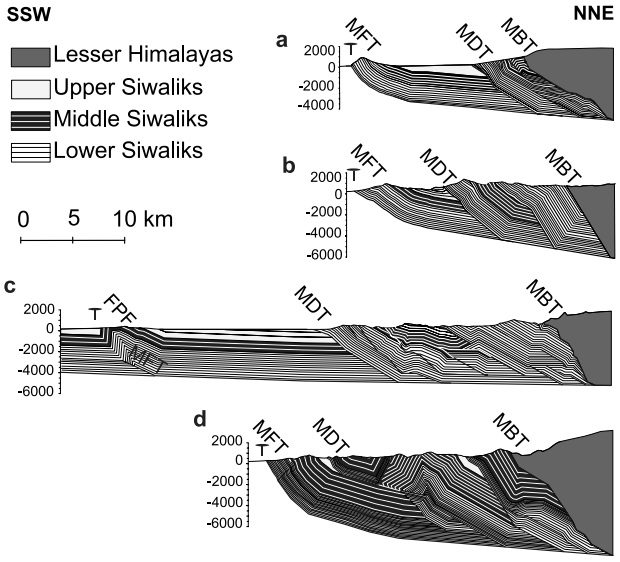

FIGURE 7. Balanced cross sections over the Siwalik (after Leturmy, 1997 and Mugnier et al., 1999a). Other available balanced cross sections are not presented (Mugnier et al., 1999a; Leturmy, 1997, and Husson and Mugnier, 2003). Locations in Figure 1. FPF: fault-propagation fold, MFT: Main Frontal Thrust, MDT: Main Dun Thrust, MBT: Main Boundary Thrust. The pin refers to the point beyond which, it is assumed, no displacement occurred farther south.

determine the kinematics (Poblet et al., 1998). The equivalence hypothesis is extended to all frontal folds, because, it is argued, the kinematics are the same for all the structures in a cylindrical setting. Hence, the whole set of cross sections provides various stages of fault-related fold evolution in the Himalayan fold-and-thrust belt, and together with the tectonic velocities described above, an evolutionary sketch can be constructed (Figure 8). Thrust sheets stack one above the other, with a synchronous development of foreland fault-related folds. New structures develop southward; however, the reactivation of more hinterland thrusts (MDT) implies that hinterland slices gradually tend to be almost entirely eroded (passive remnants are occasionally preserved—see discussion below). Erosion acts as a major control on the evolution of the fold-and-thrust belt. It actually rules the migration of the foremost structures, because it permanently reorganizes the stress field by unloading (Chalaron et al., 1995). Indeed, erosion controls the permanent activation/reactivation regime shifts of the MDT, yielding an average tectonic velocity of 2–3 mm/yr. As soon as a new structure develops toward the south, the previous, juxtaposed hinterland structures enter a reactivation regime. From the geometric analysis, it is estimated that structural growth switches to a foreland fault-propagation fold as soon as the fault begins to crosscut the fold. Suppe and Medwedeff (1990) define this evolution as the breakthrough fault. At this time, both structures are coeval; hinterland structures evolve at low rates (MDT style, at 2–3 mm/yr), whereas the most frontal structures grow at rapid rates (MFT style, at 17 mm/yr). Hence, for a structure, the fast tectonic regime lasts as long as it remains in the foremost position. From the average geometric data obtained from numerous cross sections, we hypothesize that new structures form southward when the ramp is emergent, because two anticlines never coexist along a cross section in the Sub-Himalayan Zone of western Nepal. At least one of the hinges is totally eroded, and only monoclines are preserved.

The burial cycle in such settings can be divided into various stages (Figure 9a), and the associated burial history through time is synthesized in Figure 9b. The residence time presented in the following section is calculated, using average geometries of cross sections and previously described kinematic data, for the tail of a slice implicated in the wedge. Therefore, it corresponds to the maximum residence time within the wedge, because the hinterland part of a thrust sheet is preserved longer.

The first stage of the cycle is the sedimentation in the subsiding foreland basin (stage 1 in Figure 9b), as the Himalayan front migrates toward the south. The Khutia Khola section (Ohja et al., 2000) and the Suraï Khola section (Appel and Roesler, 1994; Corvinus, 1994), on the western edge of the studied area, constitute reference stratigraphic series after the date assignments using magnetostratigraphy (Appel and Roesler, 1994; Ohja et al., 2000) and paleontology (Corvinus, 1994). The sedimentary burial curve used in the present study is derived from the magnetostratigraphic study of Appel and Roesler (1994) and Ohja et al. (2000). Although the ages from magnetostratigraphy show strong variations depending on the sampled lithologies (Ohja et al., 2000), it can be estimated that in the Sub-Himalayan Zone, this phenomenon lasts for about 12 m.y. to 13 m.y., and drives sediments to depths as great as 5000 to 6000 m. Next is the tectonic thickening episode at the footwall of the frontal thrust (stage 2, Figure 9b), when this thrust consumes the foreland sedimentary pile. It gradually moves up the hanging-wall of the décollement to the surface, which corresponds to about 5000 m uplift and is partially compensated in this stage by erosion. Beneath the relief of the frontal crest, it subsequently increases the burial depth by as much as 1000–1500 additional meters. Assuming a vertical uplift of the related fold of about 9–12 mm/yr over the ramp (for ramp dips between 30° and 45° and 5000 m total uplift), this phenomenon lasts for 400,000 to 600,000 years. It is considered to be minor with regard to the total cycle. The following stage corresponds to the instant at which the incorporated sediment enters the dynamic part of the cycle, that is, at which the motion of the sediments is governed by faulting and hence undergoes horizontal displacement. In the Sub-Himalayan Belt, most sediments are incorporated below ramp folds and only a very small amount of sediment accumulates on top of growing structures. During this episode, the sediment is transported over the Main Décollement (stage 3, Figure 9b). The total displacement on the Main Décollement is partitioned between the fast MFT (17 mm/yr) and the low MDT (2.5 mm/yr). These velocities are thus given with regard to the thrust-sheet reference. Sliding on this décollement is split into two stages. When the structure is in the foremost position, transportation over the décollement occurs at 17 mm/yr; afterward, displacement undergoes a reactivation regime at 2.5 mm/yr. As we said above, the former episode of transportation lasts from the ramp's initiation to the breakthrough faulting, and the latter lasts until the slice is totally exhumed on an hinterland location. Average lengths are about 10,500 m for the

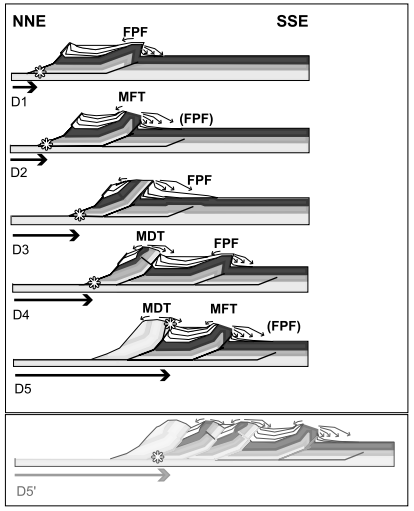

FIGURE 8. Structural evolutionary sketch for the Siwalik of western Nepal, inferred from balanced cross sections. D is the total shortening over the wedge. Stage D5′ (lowest box) is the case where no fault reactivation acts on the wedge (unlike the Sub-Himalayan Zone). Thrust sheets are more numerous, the foremost topographic break is more advanced, the width of the wedge increases. In the Sub-Himalayan Zone, few slices are represented, thus supporting a reactivation hypothesis. White star is the sediment on the tail of the slice. FPF: fault-propagation fold, MFT: Main Frontal Thrust, MDT: Main Dun Thrust.

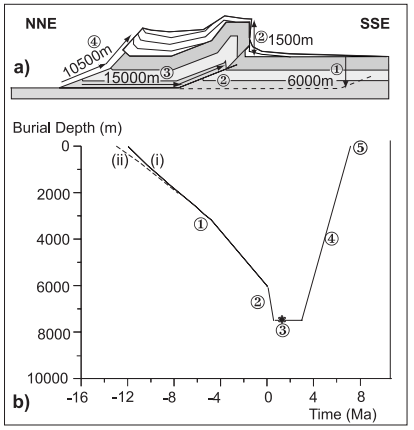

FIGURE 9. Burial evolution of the sediment at the tail of a slice, (a) with regard to the geodetic reference and (b) burial cycle versus time. Stage 1 is sedimentation in the subsiding foreland basin (after (i) Appel and Roesler, 1994 and (ii) Ohja et al., 2000), stage 2 is the tectonic thickening as the sediment is incorporated into the tectonic wedge, stage 3 is slipping on the Main Décollement, stage 4 is exhumation of the sediment in response to erosion. The star represents the instant, during the tectonic cycle, at which velocities change from activation regime (V = 17 mm/yr) to reactivation regime (V = 2.5 mm/yr) for the tail of the slice (not to scale).

ramp and the breakthrough fault, and 15,000 m for the basal dêcollement. On average, this period initially includes a rapid transportation phase of the tail of the slice at 17 mm/yr over about 10,500 m, and secondly, a slow transportation at 2.5 mm/yr, over 4500 m (15,000 minus 10,500 equals 4500 m). During this episode, the vertical-motion component is very small; the burial depth increases only weakly as a result of piggyback sedimentation, whereas a small uplift component is linked to the slip over the gently dipping basal dêcollement. Exhumation (stage 4, Figure 9b) of the tail of the slice starts as soon as it begins to climb over the ramp, when sliding over the basal dêcollement is totally finished and the slice is squeezed between the foremost sheet and the backstop buttress. Average ramp and fault lengths lead to approximately 10,500 m total displacement at that low rate. At that time, new structures have grown forward, and exhumation is realized on both the ramp and the breakthrough fault at low rates of reactivation (2.5 mm/yr). The burial depth subsequently decreases as a function of the ramp and fault angles. An average angle of 45° is used for both the ramp and the fault. The associated vertical displacement gradually leads to the total exhumation and erosion of the thrust sheet. Finally (stage 5 in Figure 9b), surface transportation phenomena are fast enough to be considered instantaneous with respect to the overall cycle.

Therefore, the wedge's development can be described as a steady-state burial cycle, from the incorporation of the foreland sediments to their exhumation and sedimentation in a more distal foreland.

The major burial phase is sedimentation in the foreland, but it lasts fairly long (the average sedimentary rate is only about 500 m/yr). The tectonic thickening, on the other hand, is faster and still increases the burial depth; whereas exhumation is the fastest process of the internal cycle (about 1700 m/m.y. of vertical motion).

The 12-m.y. sedimentation stage in the foreland is about two times longer than the tectonic stage within the wedge. The calculated short time of residence within the prism supports the idea that only a limited number of active thrust sheets control the development of the wedge. Only short-lived slices constitute the actual prism.

Sediment Transfer Balance Within the Wedge

The previously calculated time for the burial/exhumation cycle is an average for the Sub-Himalayan Zone of western Nepal. Using such a sketch of development, we can calculate the material balance within the wedge.

Sediments incorporated from the foreland into the fold-and-thrust belt constitute the main input of material, because piggyback basins represent a weak volume in the Sub-Himalayan Belt. The total input is estimated from kinematic and geometric data, assuming an average velocity of 19 mm/yr of southward migration of the wedge (V_4). In the studied area, the incorporated volume per linear kilometer of the Indo-Gangetic plain (input I), over time, is given by:

$$I = V_4 \times T_s$$

where T_s is the average total thickness of the involved sedimentary pile above the Main Dêcollement (5000 m).

$$I = 9.5 \times 10^5 \text{ km}^3/\text{yr}$$

Given a steady-state regime for the wedge (Dahlen and Barr, 1989), the input volume, I, equals the output volume, O. The main output is erosion. However, geometric observations from the structural sketch map and the balanced cross sections (Leturmy, 1997; Mugnier et al., 1999a) imply some restrictions for the material balance. A part of the wedge's volume is "captured" either as passive remnants of slices, accreted along the footwall of the MBT, or as duplexes, subducted beneath the MBT. Various settings can be distinguished (Figure 10). The lower Siwalik Formation, at the base of the thrust sedimentary pile, often shows duplexes. If duplex horses are located at the hanging-wall of the Main Internal Dêcollement ID (Figure 10a), they are unrelentingly eroded as normal stacked slices; on the contrary, if the duplex is located on the footwall of this dêcollement, it is subducted and consumed by the Lesser Himalayas (Figure 10b) and eventually withdrawn from the prism. Finally, local passive remnants of middle to upper Siwalik sheets are stacked beneath the MBT (Figure 10c) and incorporated into the Lesser Himalayan wedge. Inferences from geometric data (structural sketch map and balanced cross sections) suggest that only subducted duplexes may constitute a significant volume of captured material. On a first-order approximation from geometric data, remnants of slices comprise less than 5% of the total volume of the wedge. On the whole, it can be estimated from the structural sketch map that, within the 300-km length of the studied area, about 55% of the lower Siwalik unit does not reach the surface. In order to keep a balanced structure in the wedge, this unit has to form duplexes, subducted beneath the Lesser Himalayas and subsequently withdrawn from the wedge. Per linear kilometer along the belt, the captured volume (CV) from lower Siwalik duplexes is in the range of:

$$CV = 55\% \times t \times V_4$$

where t is the average stratigraphic thickness of the lower Siwalik unit (2000 m),

$$CV = 2.1 \times 10^5 \text{ km}^3/\text{yr}$$

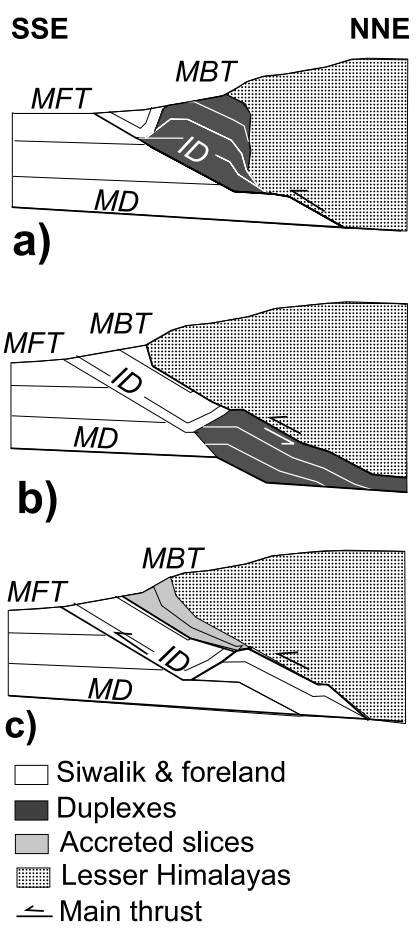

Figure 10. Schematic sketch of the material captured within the Siwalik wedge. (a) Duplex is above the main Internal Dêcollement (ID), and is exhumed and eroded as a normal thrust sheet. (b) Duplex is located beneath the ID, and therefore subducted beneath the Lesser Himalayas and withdrawn from the wedge. (c) Remnants of slices are accreted to the Lesser Himalayas, and subsequently incorporated into them. MD: Main Dêcollement, MFT: Main Frontal Thrust, MBT: Main Boundary Thrust.

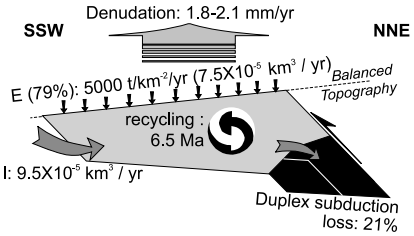

Figure 11. Volume, mass, and time transfer cycle for the sediments within the Siwalik wedge. I is the input of material at the MFT; E is erosion and equals the output minus the loss from duplex subduction. The corresponding average denudation is evaluated assuming a steady state of volume and a critical-taper angle for the wedge. Values are given per linear kilometer at the front of the Sub-Himalayan range.

and hence, the current withdrawn material from subduing duplexes, CV, is therefore approximated to be about 21% of the total volume of the Sub-Himalayan Zone of western Nepal. Again, according to a volumetric steady state (see Dahlen and Barr, 1989) and a critical taper angle (Davis et al., 1983; Mugnier et al. 1992; DeCelles and Mitra, 1995) for the prism, the output has to be equivalent to the input I, as topography remains constant versus time. Hence erosion accounts for about 79% of the input I. Sediments totaling 7.5×10^5 km^3 flow through the wedge per year and per linear kilometer along the belt, in western Nepal.

The average width of the Sub-Himalayan Zone in the studied area is 35–40 km. The average erosion rate for the whole wedge is thus in the range of 1.8 to 2.1 mm/yr.

Previous estimates of erosion from the sediment load in rivers are in the range of 1.5 to 2 mm/yr (Delcaillau, 1997), therefore, they support our estimate of erosion. According to an average density of 2.65, the corresponding eroded mass is about 5000 t/km^2/yr. Delcaillau (1997) calculated specific erosion rates for various drainage areas of the Siwalik in the very wide range of 400 to 9500 t/km/yr, that is, 0.1 to 3.5 mm/yr of erosion. This consistency supports the hypothesis of a steady-state regime for the Siwalik wedge and in turn validates the calculated balance (Figure 11).

CONCLUSIONS

The sediment burial cycle was the main focus of our study. However, across-strike estimates for the Sub-Himalayan Zone's sediment cycle are significant if the behavior of the wedge is similar laterally. Structural

data inferred from balanced cross sections, a structural sketch map, and spatial imagery reveal a laterally orientated development. Further investigations, including geomorphological observations, allowed us to calculate the velocities of the wedge buildup. We see from this study that the lateral morphological growth is much faster than the lateral propagation of the fault-related folds. Morphological structures are the assemblage of independent structures coalescing with time. These structures propagate laterally in an asymmetric pattern, and the envelope of these elementary "defects" propagates fast enough laterally (in the range of 40 cm/yr) to assume an overall cylindrical development on a wedge scale. Hence, estimates of the sediment burial cycle are justified in such a setting. Accretion is the only input of sediments within the fold-and-thrust belt, and it is about 9.5×10^5 km^3/yr at the front of the Himalayan Belt. An average of 21% of the accreted material is withdrawn in the form of subducted duplexes of the lower Siwalik unit beneath the Lesser Himalayas. The maximum residence time within the wedge is estimated to be 6.5 m.y. for sediments undergoing the total burial/exhumation cycle within the wedge. Assuming a steady-state model for the Sub-Himalayan prism, the subsequent volume of material that completes the cycle led to erosion estimates of about 1.8 to 2.1 mm/yr. This is consistent with previous studies and not only supports the erosion rates presently propounded, but also the overall cycle, and hence, the proposed sketch of the wedge's development.

The evolution of foreland petroleum systems is ruled primarily by these parameters (burial, erosion, and tectonic rates), because they control the thermal regime. According to previous studies (Stüwe et al., 1994; Mancktelow and Grasemann, 1997), sedimentation rates such as those found in the Sub-Himalayan Zone would lower the thermal gradient by about 15% at a 5-km depth, whereas erosion rates in the range of those of the Sub-Himalayan Zone would increase the thermal gradient by about 30%. On the other hand, tectonic velocities are not fast enough to induce perturbations on the thermal field. In such settings, the oil window lies at greater depth in the sedimentary basin than it does in the folded belt, where it is significantly shallower. Given these parameters, one can therefore make general assumptions for kerogen maturation in such settings.

REFERENCES CITED

Appel, E., and W. Roesler, 1994, Magnetic polarity stratigraphy of the Neogene Surai Khola section (Siwalik, SW Nepal): Himalayan Geology, v. 15, p. 63–68.

Avouac, J. P., and P. Tapponier, 1993, Kinematic model of active deformation in central Asia: Geophysical Research Letters, v. 20, p. 895–898.

Baby, P., M. Specht, J.Oller, G. Montemuro, B. Colletta, and J. Letouzey, 1994, The Boomerang-Chapare transfer Zone (recent oil discovery trend in Bolivia): structural interpretation and experimental approach, *in* F. Roure, N. Ellouz, V. S. Shein, and I. Skortsov, eds., Geodynamic evolution of sedimentary basins: International symposium, Moscow, p. 203–218.

Banks, C. J., and J. Warburton, 1986, "Passive-roof" duplex geometry in the frontal structures of the Kirthar and Sulaiman mountain belts, Pakistan: Journal of Structural Geology, v. 8/3–4, p. 229–237.

Bashyal, R. P., 1998, Petroleum exploration in Nepal: Journal of the Nepal Geological Society, v. 18, p. 19–24.

Bilham, R., K. Larson, J. Freymueller, J., and Idylhim members, 1997, GPS measurements of present-day convergence across the Nepal Himalaya: Nature, v. 386/6, p. 61–63.

Biswas, S. K., 1994, Status exploration for hydrocarbons in Siwalik basin of India and future trends: Himalayan Geology, v. 15, p. 283–300.

Chalaron, E., J-L. Mugnier, and G. H. Mascle, 1995, Control of the thrust tectonics in the himalayan foothills; a view from a numerical model: Tectonophysics, v. 248, p. 139–163.

Corvinus, G., 1994, The Surai Khola and Rato Khola fossiliferous sequences in the Siwalik Group, Nepal: Himalayan Geology, v. 15, p. 49–61.

Dahlen, F. A., and T. Barr, 1989, Brittle frictional mountain building, 1. Deformation and mechanical energy budget: Journal of Geophysical Research, v. 94, B4, p. 13906–3922.

Davis, D. A., J. Suppe, and F. A. Dahlen, 1983, Mechanics of fold-and-thrust belts and accretionary wedges: Journal of Geophysical Research, v. 88, p. 1153–1172.

DeCelles, P. G., and G. Mitra, 1995, History of the Sevier orogenic wedge in terms of critical taper models, Northeast Utah and southwestern Wyoming: Geological Society of America Bulletin, v. 107, p. 454–462.

DeCelles, P. G., G. E. Gehrels, J. Quade, T. P. Ojha, and P. A. Kapp, 1998a, Neogene foreland basin deposits, erosional unroofing and the kinematic history of the Himalayan fold-and-thrust belt, Western Nepal: Geological Society of America Bulletin, v. 110/1, p. 2–21.

DeCelles, P. G., G. E. Gehrels, J. Quade, and T. P. Ojha, 1998b, Eocene–early Miocene foreland development and the history of Himalayan thrusting, western and central Nepal: Tectonics, v. 17, p. 741–765.

Delcaillau, B., G. Hérail, and G. H. Mascle, 1987, Evolution geomorphostructurale de chevauchements actifs: le cas des chevauchements intra-Siwalik du Népal Central: Zeitschrift für Geomorphologie, Nue Forsch, Bd. 31, p. 339–360.

Delcaillau, B., 1997, Les fronts de chaîne actives— Genèse des reliefs et relations tectonique-érosion-sédimentation: Thèse d'habilitation à diriger des recherches, Université de Caen, 336 p.

De Mets, C., R. G. Gordon, D. F. Argus, and S. Stein, 1990, Current plate motions: Geophysical Journal International, v. 101, p. 425–478.

Elliott, D., 1976, The energy balance and deformation

mechanisms of thrust sheets: Philosophical Transactions of the Royal Society of London, v. 283, p. 289–312.

Galahaut, V. K., and R. Chandler, 1992, On the active tectonics of the Dehra Dun region from observations of ground elevation changes: Journal of the Geological Society of India, v. 39, p. 61–68.

Hérail, G., and G. Mascle, 1980, Les Siwalik du Népal Central: structures et géomorphologie d'un piedmond en cours de déformation: Bulletin de l'Association Géographique Française, v. 431, p. 259–267.

Hérail, G., G. Mascle, and B. Delcaillau, 1986, Les Siwalik de l'Himalaya du Népal: un exemple de prisme d'accrétion intracontinental, in S.D.L.T.P.: Bordet, v. 47, p. 153–182.

Hodges, K. V., R. R. Parrish, and M. P. Searle, 1996, Tectonic evolution of the Central Annapurna Range, Nepalese Himalayas: Tectonics, v. 15, p. 1264–1291.

Hurtrez, J. E., F. Lucazeau, J. Lavé, and J-P. Avouac, 1999, Investigations of the relationships between basin morphology, tectonic uplift and denudation from the study of an active belt in the Siwalik Hills (Central Nepal): Journal of Geophysical Research, v. 104–B6, p. 12,779–12,796.

Husson, L., and J-L. Mugnier, 2003, Three-dimensional reconstruction from surface data, restoration, and kinematics of the Baisahi passive-roof duplex, W. Nepal: Journal of Structural Geology, v. 25, p. 79–90.

Jackson, M., and R. Bilham, 1994, Constraints on Himalayan deformation inferred from vertical velocity fields in Nepal and Tibet: Journal of Geophysical Research, v. 99–B7, p. 13,897–13,912.

Jackson, J. A., R. Norris, and J. Youngson, 1996, The structural evolution of active fault and fold systems in Central Otago, New Zealand: Journal of Structural Geology, v. 16, p. 1041–1059.

Jouanne, F., J-L. Mugnier, M. R. Pandey, J-F. Gamond, P. Le Fort, L. Serrurier, C. Vigny, J-P Avouac, and Idylhim members, 1999, Oblique convergence in the Himalayas of western Nepal deduced from preliminary results of GPS measurements: Geophysical Research Letters, v. 26, p. 1933–1936.

Larson, K. M., R. Bürgmann, R. Bilham, and J. Freymueller, 1999, Kinematics of the Indo-Eurasia collision zone and GPS measurements: Journal of Geophysical Research, v. 104, p. 1077–1093.

Lavé, J., and J. P. Avouac, 2000, Active faulting of fluvial terraces across the Siwaliks Hills, Himalayas of central Nepal: Journal of Geophysical Research, v. 105, p. 5735–5570.

Leturmy, P., 1997, Sédiments et reliefs du front des systèmes chevauchants: Modélisation et exemples du front Andin et des Siwalik à l'Holocène: PhD thesis, UJF-Grenoble I, 235 p.

Leturmy, P., P. Huyghe, J. L. Mugnier, and B. Delcaillau, 1999, An intermediate displacement scale between earthquake slip and finite geometry of thrust systems deduced from a comparison of Quaternary, Holocene and instantaneous rates of shortening in the frontal thrust belt of Himalaya (Western Nepal). Extended abstract in Active Subduction and collision in SE Asia: data and models, Montpellier, May 9–12, Mém. Géosciences— Montpellier, France, v. 14, p. 103–106.

Lyon-Caen, H., and P. Molnar, 1985, Gravity anomalies, flexure of the Indian plate, and the structure, support and evolution of the Himalaya and Ganga basin: Tectonics, v. 4–6, p. 513–538.

Mancktelow, N. S., and B. Grasemann, 1997, Time-dependent effects of heat advection and topography on cooling histories during erosion: Tectonophysics, v. 270, p. 167–195.

Marchal, D., M. Guiraud, T. Rives, and J. Van Den Driessche, 1998, Space and time propagation processes of normal faults, *in* G. Jones, Q. J. Fischer, and R. J. Knipe, eds., Faulting, fault sealing and fluid flow in hydrocarbon reservoirs, Geological Society (London) Special Publication 145, p. 51–70.

Mascle, G., G. Hérail, T. Van Haver, and B. Delcaillau, 1986, Structure et évolution des bassins d'épisuture et de périsuture liés à la chaîne himalayenne: Société Nationale Elf Aquitaine Production, BCREDP 10, Pau, p. 181–203.

Mascle, G., E. Chalaron, A. Gajurel, P. Leturmy, and J-L. Mugnier, 1998, Paleoseismicity in the Siwalik: occurrence of major seismic events in the Himalayas of West Nepal: Bulletin of the Geological Society of Nepal, v. 18, p. 417–430.

Moretti, I., P. Baby, E. Mendez, and D. Zubieta, 1996, Hydrocarbon generation in relation to thrusting in the Sub-Andean Zone from 18 to 22°S, Bolivia: Petroleum Geoscience, v. 2, p. 17–28.

Mueller, K., and P. Talling, 1997, Geomorphic evidence for tear faults accommodating lateral propagation of an active Fault-Bend fold, Wheeler ridge, California: Journal of Structural Geology, v. 19, no. 3–4, p. 397–411.

Mugnier, J. L., P. Huyghe, P. Leturmy, and F. Jouanne, 2004, Episodicity and rates of thrust-sheet motion in Himalayas (western Nepal), *in* K. McClay, ed., Thrust tectonics and hydrocarbon systems: AAPG Memoir 82, this volume, p. 91–114.

Mugnier, J. L., P. Leturmy, G. Mascle, P. Huyghe, E. Chalaron, G. Vidal, L. Husson, and B. Delcaillau, 1999a, The Siwaliks of Western Nepal I: Geometry and kinematics: Journal of Asian Earth Sciences, 17, p. 629–642.

Mugnier, J. L., P. Leturmy, P. Huyghe, and E. Chalaron, 1999b, The Siwaliks of eastern Nepal II: Mechanism of the thrust wedge: Journal of Asian Earth Sciences, 17, p. 643–657.

Mugnier, J-L., P. Leturmy, P. Huyghe, and F. Jouanne, 1999c, A comparison of long-term rate, the Holocene rate and the instantaneous rate of shortening in the frontal thrust belt of Himalaya (Western Nepal): Presented at Thrust Tectonics, Royal Holloway University of London.

Mugnier, J-L., B. Delcaillau, P. Huyghe, and P. Leturmy, 1998, The break-back thrust splay of the Main Dun Thrust: Evidence of an intermediate displacement scale between earthquake slip and finite geometry of thrust systems: Journal of Structural Geology, v. 20, p. 857–864.

Mugnier, J-L., P. Huyghe, E. Chalaron, and G. Mascle, 1994, Recent movements along the Main Boundary Thrust of the Himalayas: normal faulting in an over critical thrust wedge?: Tectonophysics, v. 238, p. 199–215.

Mugnier, J-L, G. Mascle, and T. Faucher, 1992, La structure des Siwalik de l'Ouest Népal: un prisme d'accrétion intracontinental: Bulletin de la Société Géologique de France, v. 163–5, p. 585–595.

Ni, J., and M. Baraganzi, 1996, Seismotectonics of the Himalayan collision zone: geometry of the underthrusting Indian plate beneath the Himalaya: Journal of Geophysical Research, v. 89, p. 1147–1163.

Ohja, T. P., R. F. Butler, J. Quade, P. G. DeCelles, D. Richards, and B. N. Upreti, 2000, Magnetic polarity stratigraphy of the Neogene Siwalik Group at Khutia Khola, far western Nepal: Geological Society of America Bulletin, v. 112, p. 424–434.

Peltzer, G., and F. Saucier, 1996, Present-day kinematics of Asia derived from geologic fault rates: Journal of Geophysical Research, v. 101, B12, p. 27,943–27,956.

Poblet, J., J. A. Munoz, A. Travé, and J. Serra-Kiel, 1998, Quantifying the syntectonic sediments associated with single-layer detachment folds: Journal of Structural Geology, v. 19, p. 369–381.

Powers, P. M., and R. J. Lillie, 1996, Shortening rates within the sub-Himalaya of NW India based on a balanced cross section of the Kangra Dun re-entrant: Himalayan-Karakorum-Tibet Workshop, 11th, Flagstaff, Arizona, p. 120–121.

Powers, P. M., R. J. Lillie, and S. Yeats, 1998, Structure and shortening of the Kangra and Dehra Dun reentrants, Sub-Himalaya, India: Geological Society of America Bulletin, v. 110, p. 1010–1027.

Raiverman, V., A. K. Srivastava, and D. N. Prasad, 1994, Structural style in north-western Himalayan foothills, *in* G. Kumar and N. R. Phadtare, eds.: Siwalik foreland basin of Himalaya, v. 15, p. 263–280.

Schelling, D., 1992, The tectonostratigraphy and structure of the eastern Nepal Himalaya: Tectonics, v. 11–5, p. 925–943.

Schelling, D., and K. Arita, 1991, Thrust tectonics, crustal shortening, and the structure of the far-eastern Nepal Himalaya: Tectonics, v. 10, p. 851–862.

Shaw, J. H., Bilotti, F., and P. A. Brennan, 1999, Patterns of imbricate thrusting: Geological Society of America Bulletin, v. 111, p. 1140–1154.

Stüwe, K., L. White, and R. Brown, 1994, The influence on eroding topography on steady state isotherms. Applications to fission track analysis: Earth and Planetary Science Letters, v. 124, p. 63–74.

Suppe, J., and D. A. Medwedeff, 1990, Geometry an kinematics of fault-propagation folding: Eclogae Geologicae Helveticae, v. 83–3, p. 409–454.

Upreti, B. N., 1990, An outline of the geology of far western Nepal: Journal of Himalayan Geology, v. 1, p. 93–102.

Walsh, J. J., and J. Waterson, 1988, Analysis of the relationship between displacements and dimensions of faults: Journal of Structural Geology, v. 10, p. 239–247.

1.1.3 Structuration d'une zone complexe : le Golfe du Mexique

L'emploi du terme *complexe* est certes peu éloquent de manière générale. Les multiples influences sur la géodynamique du Golfe du Mexique obligent cependant à son emploi. L'héritage des orogénèses Laramide et Sevier, l'évolution de la côte Pacifique d'une marge active vers une marge transformante et le développement du Basin and Range [Atwater, 1970, Sonder & Jones, 1999, Wernicke et al., 1982], la dynamique du système caraïbe et la rotation du Yucatán au sud [Pindell et al., 1988] contrôlent l'ouverture du Golfe du Mexique.

Les conséquences tectoniques et structurales continuent d'être largement discuées, partiellement animées par l'intérêt économique de cette région dont le fort potentiel en hydrocarbures est exploité de longue date. Une revue n'a pas sa place ici, mais quelques points particuliers sur lesquels j'ai travaillé en collaboration avec X. Le Pichon, C. Rangin et N. Flotté peuvent être présentés. Une série d'articles associés est compilée dans un Mémoire du Bulletin de la Société Géologique de France [Rangin et al., 2008]. Une partie du travail portant sur le régime thermique du Golfe du Mexique, présentée dans le chapitre 5, fait écho à ce travail. Dans le premier article présenté ci-dessous, nous examinons le rôle de la faille du Rio Bravo (ou Rio Grande, selon le point de vue) au Tertiaire et sa contribution à l'évolution tectonique tardive et actuelle du Golfe du Mexique. Dans le second article, nous révélons à la lumière de données sismiques multitrace haute pénétration les conséquences d'un épisode de rifting crustal tertiaire dans le Golfe du Mexique sur la tectonique gravitaire.

Bull. Soc. géol. Fr., 2008, t. 179, n° 2, pp. 147-160

The Rio Bravo fault, a major late Oligocene left-lateral shear zone

NICOLAS FLOTTE[1,a], JUVENTINO MARTINEZ-REYES[2], CLAUDE RANGIN[1], XAVIER LE PICHON[1], LAURENT HUSSON[1,b] and MARC TARDY[3]

Key-words. – Rio Bravo fault, Oligocene left-lateral fault, Gulf of Mexico, Burgos basin, SW Texas

Abstract. – It has generally been assumed that the last major compressive deformation in the Sierra Madre Oriental (Mexico) took place during the Laramide orogenesis (Upper Cretaceous – Early Eocene). We have studied the N120° Rio Bravo fault zone probably inherited from the Jurassic opening of the gulf of Mexico. This fault zone is located along the international boundary between United States and Mexico. We demonstrate that it was active mainly during the Oligocene. In the Ojinaga area (Chihuahua), the Sierra Madre Occidental, Oligocene volcanic sequences overlying conformably the sedimentary Upper Cretaceous sequence, are both tightly folded before 30 Ma. We think this folding is associated with motion of a major left-lateral fault, the Rio Bravo left lateral fault. These left-lateral fault system affects also the Sabinas fold-belt and extends below the Burgos bassin. This deformation is also imaged by gravimetric data and the offsets the Palaeocene-Eocene oil fields that are displaced left laterally. We propose that during the Oligocene, this ~1000 km long left-lateral shear zone that might be called the Rio Bravo fault was active during the Oligocene with a total offset of 40-60 km.

La faille du Rio Bravo, une zone de décrochement senestre majeure à l'Oligocène

Mots-clés. – Faille du Rio Bravo, Faille senestre Oligocène, Golfe du Mexique, Sud-Ouest Texas

Résumé. – Il est généralement admis que le principal événement compressif de la Sierra Madre Orientale (Mexique) s'est produit durant l'orogenèse Laramienne (Crétacé terminal-Eocène inférieur). Nous avons étudié la zone de faille du Rio Bravo, structure probablement héritée de l'ouverture du golfe du Mexique au Jurassique. Cette zone de failles est à cheval sur la frontière internationale USA-Mexique. Nous montrons qu'elle est active surtout durant l'Oligocène. Dans la région d'Ojinaga (Chihuahua, Mx) les séries volcaniques oligocènes de la Sierra Madre Occidentale, déposées sont en concordance sur le Crétacé supérieur sédimentaire, ces deux ensembles étant plissés avant 30 Ma. Nous pensons que cette déformation est associée au jeu décrochant senestre qui suit plus ou moins la direction N120° du Rio Bravo. Ce système décrochant senestre affecte également la ceinture plissée de Sabinas et se pousuit vers le SE dans le basin de Burgos. Cette zone de décrochement est imagée dans la gravimétrie, mais aussi par le décalage senestre des champs pétroliers présents dans les séries Eocène-Oligocène de ce bassin. Nous proposons que ce cisaillement crustal senestre long de plus de 1000 km, appelé faille du Rio Bravo, a été actif durant l'Oligocène avec un décalage cumulé de 40 à 60 km.

INTRODUCTION

The Sierra Madre Oriental (SMO) is located along the eastern edge of Mexico (fig.1) and is interpreted as the southern continuation of the Cordilleran deformation belt in northern North America [Campa and Coney, 1983]. The Chihuahua fold-belt and the inverted Sabinas basin belong to this system. In Mexico, this phase is Palaeocene – Lower Eocene in age [Tardy, 1980]. However, the precise dating of the Laramide phase is difficult because, from northern Mexico to Montana (USA), the deformed or undeformed Tertiary continental deposits are not well dated. Initially, the Laramian phase was attributed to the Cretaceous-Tertiary boundary. Here, we document the existence of a major left-lateral fault zone that was active after this tectonic episode, during Late Eocene-Oligocene and linked onshore west-Texas to the Chihuahua – Big Bend area over more than 1000 km. This fault follows part of the Rio Bravo and is called for this reason the Rio Bravo fault. We next discuss its presence along the Texas Lineament where it is localized

1. CNRS-UMR 6635 - CEREGE et Collège de France, Chaire de Géodynamique, Europôle de l'Arbois, BP 80, 13545 Aix-en-Provence, France
2. Centro de Geosciencias-UNAM, Campus Juriquilla, Queretaro, QRO. 76230, Mexico
3. LGCA, Université de Savoie, 73376 Le Bourget du Lac cedex, France
a. now at AREVA, T&D, Tour Areva, 1 place de la Coupole, 92084 Paris La Défense, France
b. now at Geosciences, univ. Rennes 1, Campus de Beaulieu, 35042 Rennes cedex, France
Manuscrit déposé le 20 octobre 2006; accepté après révision le 6 novembre 2007

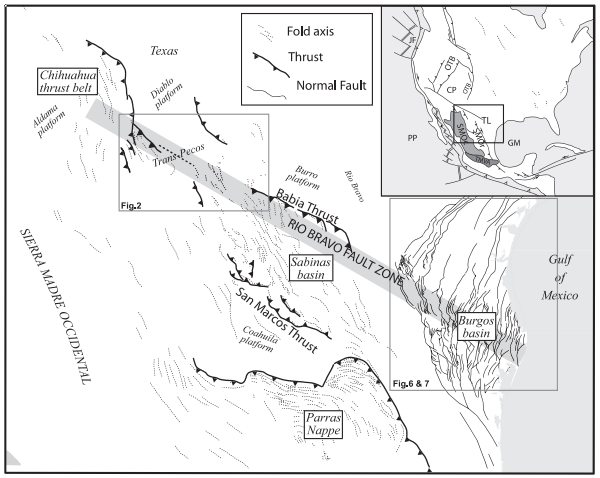

FIG. 1. – Structural sketch map of the studied area in northeastern Mexico and South Texas. Insert shows its location in North America. CP: Colorado plateau, GM: gulf of Mexico, JF: Juan de Fuca plate, OTB: Overthrust belt, PP: Pacific plate, SMOc: Sierra Madre Occidental, SMOr: Sierra Madre Oriental, TL: Texas lineament, TMVA: Trans Mexican volcanic arc.
FIG. 1. – *Schéma structural de la zone d'étude dans le NE du Mexique et le sud Texas. L'encart situe cette zone en Amérique du Nord. CP : plateau du Colorado, GM : golfe du Mexique, JF : plaque Juan de Fuca, OTB : overthrust belt, PP : plaque Pacifique, SMOc : Sierra Madre Occidentale, SMOr : Sierra Madre Orientale, TL : linéament du Texas, TMVA : arc volcanique trans-mexicain).*

within a 30 km-wide corridor and in the Burgos basin and Sabinas fold-belt where deformation is more widely distributed (fig. 1).

THE TEXAS LINEAMENT REGION

The deformation along the Rio Bravo was extensively studied in the Big Bend area, SW-Texas (fig. 2). This region is in a privileged position to study the kinematic evolution of the Texas-Mexico boundary thanks to large Palaeozoic to Neogene outcrops. Based on stratigraphic relationships, Erdlac [1990] studied the Fresno-Terlingua monocline, the only significant "Laramide" (sic) fold, which affects the southwestern rim of the Solitario volcanic caldera (fig. 2).

However there are still controversies about the age of these deformations. Erdlac [1990] proposed that the uplift of this area is at least 50 Ma old and could belong to the main Laramide deformation phase. This interpretation was disputed by Corry *et al.* [1994]. With morphologic and stratigraphic arguments, those authors have proposed that this uplift occurred between 36 and 34 Ma, and does not fit the Laramide climax of deformation. So a pending question is whether the younger strike slip deformation along the Rio Bravo is coeval or not with the Laramide event, or is a late phase of tectonic reactivation along the Texas Lineament. Our data in Mexico suggest a deformation postdating the volcanism of the Sierra Madre Occidental, recognized as post Laramide in Mexico [Tardy 1980]. We present new structural and kinematic data to better constrain this main phase of post Laramide deformation. Our data were collected in northern Chihuahua (Mexico), south of the Rio Bravo. In this area, tightly folded Mesozoic series are well exposed and Mid-Tertiary volcanics are also widespread (fig. 2).

Geological setting of northern Chihuahua

In northern Mexico, Mesozoic basins opened more or less contemporaneously with the Gulf of Mexico. The development of the Sabinas basin and the Chihuahua trough is linked with the early Jurassic rifting of the Gulf of Mexico [Salvador and Green, 1980; Salvador, 1987] and probably reflected extensional or transtensional processes associated with the movement of South America away from North America during the early Mesozoic [Haenggi, 2002; Anderson and Nourse, 2005]. The Chihuahua trough is limited to the east by the Diablo platform, north of the present day Big Bend volcanic province, and to the west by the Aldama platform (fig. 1). The Chihuahua fold belt corresponds to the inverted Chihuahua trough, which was shortened against the buttress-like Diablo platform. The fold belt is formed by large asymmetrical and sigmoidal folds, developed upon a decollement above thick evaporites [Hennings, 1994]. The sigmoidal folds swing from N-S to NW-SE trends, the fold belt extending throughout most of eastern Chihuahua and adjacent parts of Trans-Pecos Texas (figs. 1 and 2). According to Muehlberger [1980] and Haenggi [2002] this left-lateral transpressional tectonic event has renewed motion movement along pre-existing Mesozoic fabric.

FIG. 2. – Geological sketch map of the studied area, south Texas and north Chihuahua. CA: Cerro Alto, CC: Cerro Colorado, MB: Manuel Benavides, MM: Mariscal mountain, Oj: Ojinaga, Pr: Presidio, RC: Rio Conchos, RN: Rio el Nogal, SA: Sierra Azul, S: Solitario volcano, SC: Sierra Santa Cruz, Sec: Santa Elena canyon, SEM: Sierra El Mulato, SEn: Sierra Encantada, SEP: Sierra Peguis, SP: Sierra Ponce, Tm: Terlinga monocline, TMf: Tascotal Mesa fault, TSB: Terlingua-Solitario block.
FIG. 2. – *Carte géologique simplifiée de la zone d'étude, Texas méridional et Chihuahua septentrional.*

Precise dating of the Chihuahua fold belt is difficult because of the lack of syntectonic deposits. As Tertiary volcanic rocks overlie folded Mesozoic strata 150 to 200 km SW of the studied area, McDowell and Maugher [1994] or Reyes-Cortés and Goodell [2000] have proposed an age of 55-45 Ma for this transpressional event. By comparison with the deformation age in New Mexico (USA), Keith and Wilt [1986] also proposed a similar deformation event between 55 Ma an 45 Ma for the Chihuahua fold belt. However, in the Ojinaga region, north of the Rio Conchos, Frantzen [unpublished M.A. thesis, 1958] has proposed that the lowest Oligocene volcanic units are also implicated in this folding (Colquitt syncline) suggesting that the age of the most recent folding could be younger than Laramide.

In the studied area (fig. 2), the main ranges reach high elevations (e.g Sierra El Pegüis: 2000 m or Sierra La Esperanza: 1980 m). The highest elevations correspond with tight anticlines that expose the Lower Cretaceous sequences. Wackstones of the Cuchillo formation (Aptian-Lower Albian) and the massive limestones and sandstones of the Cox, Lagrima and Benavides formations (Albian) are topped by the mudstones and wackstones of the Buda formation (Cenomanian). The Upper Cretaceous is mainly terrigenous and is represented by the Ojinaga formation that recorded an extreme change in depositional environment from shallow water carbonates to marine terrigenous deposits. This thick unit (> 600 m) consists of marine shale, sandstone and limestone interbeds. This abrupt influx of clastic material in the basin is interpreted as related to growth of the Sierra Madre Occidental [Tardy, 1980; Haenggi, 2002]. These strata widely outcrop between the main front of the Chihuahua fold belt and the Rio Bravo valley (fig. 2).

The San Carlos formation (Campanian) marks the progressive marine regression. Numerous patches of sandstones and conglomerates outcrop in the area but cannot be dated. The oldest well-dated Tertiary rocks are volcanics. They are widespread SE of Ojinaga, in the Manuel Benavides area (fig. 2). This volcanic phase in northeastern Chihuahua was initiated with alkalic basalts of uncertain Eocene age [Gunderson *et al.*, 1986]. This volcanism can be compared to the first well-dated Lower Eocene and Middle Eocene volcanic deposits in Texas, which were probably derived from Mexico [Henry *et al.*, 1986; Henry and McDowell, 1986]. The largest volume of igneous rocks erupted between 38 and 32 Ma [Henry and Price, 1984]. The calc-alkalic signature of this volcanism indicates it was related to subduction (subduction of the Farallon plate along the west coast of North America [McDowell and Keiser, 1977]. In northern Chihuahua, widespread volcanic activity occurred between 34 and 33 Ma and 31 and 30 Ma [Gregory, 1981]. Approximately 30 Ma ago, strongly differentiated volcanism began to erupt (rhyodacite and rhyolitic ash-flow

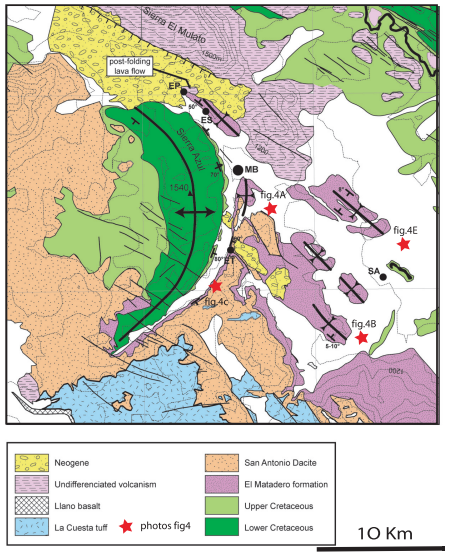

FIG. 3. – Geological sketch map of the Benavides area (location on fig. 2). We have used the volcanic succession proposed by Gunderson *et al.* [1986]. EP: El Pozo, ES: El Saucito, ET: El Tinajon, MB: Manuel Benavides., PA: Paso de San Antonio. Dashed lines: altitude contours 100 m.
FIG. 3. – *Carte géologique simplifiée de la région de Benavides (localisation sur fig. 2). Nous avons adopté la succession volcanique de Gunderson* et al. *[1986]. Contourage topographique tous les 100 m en ligne pointillée.*

tuffs). The arc-related calc-alkalic volcanism was replaced about 26 Ma, by alkalic volcanism associated with the Basin and Range faulting [Henry and Price, 1984; Erdlac, 1990]. These volcanic deposits principally outcrop in the Big Bend area (USA).

Structural data in the Manuel Benavides area

Manuel Benavides (MB fig. 2) is located along the eastern flank of a 20 km-long large and curved anticline, the Sierra Azul (figs 2 and 3). The northern flank of the anticline is parallel to the N140°E trending valley of Benavides where numerous and discrete N120-130°E trending vertical faults cut through the anticline. Exposures are not very good in the valley, but the curved shape of the anticline could indicate that this structure was wrenched along a poorly exposed sinistral strike-slip fault present in the Benavides valley. This direction is the main morpho-structural direction observed along the southern Big Bend area. Northwest of Benavides this fault trend limits sharply the anticline of Sierra El Mulato where Tertiary volcanics are folded. Where the fold is close of the Benavides valley, the northern flank of the anticline is steep, and is locally overturned northward. This is due to proximity of the main fault not exposed in the Benavides valley.

The Tertiary volcanics of the Sierra Azul anticline overlain conformably the Upper Cretaceous terrigenous deposits (Ojinaga formation) which form low and soft morphologies (fig. 3 and 4A). Locally the Upper Cretaceous is overturned like the Lower Cretaceous series but all around this range, the Ojinaga formation is conformably overlain by sedimentary and volcanic unit of the El Matadero formation [Gregory, 1981; Gunderson *et al.*, 1986]. This conformable depositional contact was observed near El Tinajón (fig. 3). Here a basal volcanic conglomerate is overlain by basaltic lava flows (fig. 4C), and a thin ash-flow, the El Matadero tuff [Gregory, 1981; Gunderson *et al.*, 1986] is interbedded within these basalts. The stratigraphic contact between the Ojinaga and the El Matadero formations was not directly observed elsewhere in the Benavides area. Recent colluviums and alluviums cover this contact. However, the high dip observed in the conglomerates and a panoramic view of the eastern flank of the anticline (fig. 4A) lead us to propose that there is no clear angular unconformity between the tightly folded terrigenous Ojinaga formation (Upper Cretaceous) and the El Matadero formation.

Near El Saucito (fig. 3), along the northern flank of the Sierra Azul anticline, the folded El Matadero volcanics formation strikes N150°E and dips 75°N. According to Gunderson *et al.* [1986], these "San Antonio dacites" were unconformably deposited on El Matadero volcanics. We did not observe this disconformity but the San Antonio dacites are deformed into open symmetric folds (fig. 3 and 4B) with the same NW-SE trend as the Benavides anticline.

The youngest volcanic unit described by Gunderson *et al.* [1986], the "La Cuesta Tuff" (fig. 3) is not folded and overlain disconformably older volcanic units.

Age of volcanism and implications on the age of the shortening

The widespread "El Matadero" tuff interbedded with basalts was dated by Gunderson *et al.* [1986] at 33.3 ± 1.0 Ma (K/Ar) and was correlated with the Mule Ear Springs tuff member of the Chisos formation (W-Texas) [Gregory, 1981] that yields 33.06 ± 0.12 and 33.12 ± 0.12 Ma $^{40}Ar/^{39}Ar$ ages [Henry, 1998]. A lateral equivalent of this formation was also dated for this study (sample 9FK). It corresponds to the first volcanic unit overlying conformably the Upper Cretaceous series of the Santa Cruz thust and fold (see below). Our sample yields an age of 33.13 ± 0.4 Ma (see appendix 2). The San Antonio dacites that overlie the El Matadero formation is correlated with the "Tule Moutain trachyandesite" member of the Chisos group dated 31.8 ± 1.3 Ma (K/Ar) by Gregory [1981]. All these ages are concordant and indicate these volcanics were erupted before 30 Ma.

Near El Pozo we have collected a rhyodacite lava flow overlying the El Matadero formation with an angular unconformity (sample 7 FK, fig 3). The K-feldspars were separated and dated 30.98 ± 0.10 Ma ($^{40}Ar/^{39}Ar$, appendix 2). This age fits rather well the age for the youngest volcanic unit outcropping in this area, the "La Cuesta tuff", dated 29.8 ± 0.6 Ma on K-feldspars by Gregory [1981]. All this information indicates the tectonic deformation discussed here occurred during the Oligocene and stopped around 30 Ma in the Benavides area.

North of the Manuel Benavides area, N110°E structural trends are well-developed (fig. 2). Southeast of the Santa Elena canyon, the N110°E trending structural fabric swings to the SSE along N150°E thrusts and folds. The wide El Caballo folds trend (fig. 2) in the Mariscal mountains in Texas

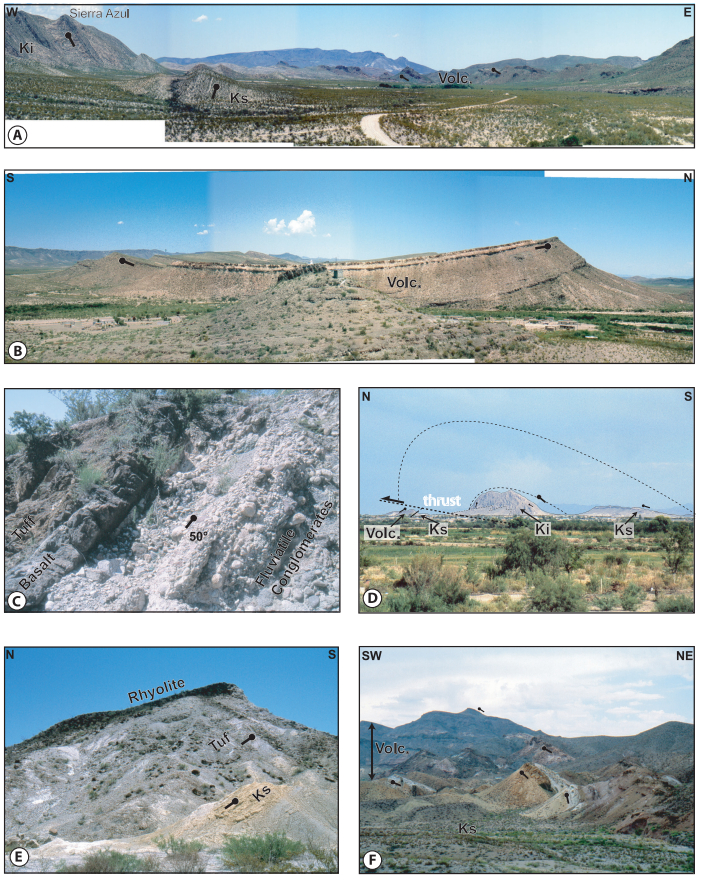

FIG. 4. – Folding of the Oligocene volcanics. Photos are located on figures 2 or 3.
A. Folding in Oligocene volcanics (volc), Early Cretaceous (Ki) and Late Cretaceous (Ks) along the eastern flank of the Benavides anticline. Dip of strata or flows are shown with arrow.
B. Oligocene Matadero formation volcanics affected by open folds.
C. Fluviatile conglomerates, basalts and rhyolites at the base of the Matadero formation.
D. NE verging fold and thrust in Sierra de Santa Cruz. Oligocene volcanics are involved in folding.
E. Depositional conformity of Oligocene volcanics above Late Cretaceous sediments, northern flank of Sierra de Santa Cruz. Small arrows indicate bedding or flows.
F. Folded Oligocene volcanics in Cerro Colorado. Note the NE verging fold.
FIG. 4. – *Plissement du volcanisme Oligocène. Les photos sont localisées sur les figures 2 ou 3.*
A. *Relations entre volcanisme oligocène* (volc), *Crétacé inférieur* (Ki) *et Crétacé supérieur* Ks *sur le flanc oriental de l'anticlinal de Benavides. Le pendage est indiqué par la flèche.*
B. *Plis ouverts dans le volcanisme oligocène de la formation Matadero*
C. *Conglomérat fluviatiles, basaltes et rhyolites à la base de la formation Matadero.*
D. *Plis faille à vergence NE dans la sierra de Santa Cruz. Le volcanisme oligocène est impliqué.*
E. *Flanc nord de la Sierra de Santa Cruz montrant la concordance entre le Crétacé supérieur sédimentaire et le volcanisme oligocène. Les petites flèches indiquent l'attitude des bancs.*
F. *Plissement affectant le volcanisme oligocène au Cerro Colorado. Remarquer le pli déversé vers le NE.*

is interpreted as a sinistral restraining bend along the main N110°E direction of the Rio Bravo fault zone. In their southernmost part, the El Caballo fold trend progressively bends again N110°E, the main direction of the major Rio

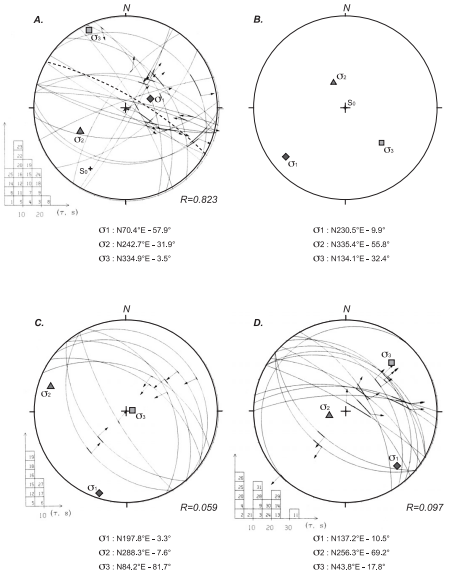

FIG. 5. – Plots of microtectonic striation data collected in El Saucito (A and B) and in Sierra Ponce (C and D)
We have used stereographic projections (Wulf, lower hemisphere) following the Carey-Gailhardis and Mercier [1987] striations inversion method. Azimuths of stress axis is indicated. Stress ratio R= ((2-(1)/((3-(1). On plot A, the dashed line is the stratification of lava flows (S0) in the Matadero formation. The (t-s) angle between the theorical and calculated slip vector is given for each striation. B: orientation of stress main axes alone after rotation of S0. C: older transpressive event. D: younger normal faulting.
FIG. 5. – *Diagrammes microtectoniques de stries collectées à El Saucito (A et B) et Sierra Ponce (C et D).*
Nous avons utilisé la projection stéréographique (Wulf, hémisphère inférieur) suivant la méthode d'inversion des stries de Carey-Gailhardis et Mercier [1987]. L'azimuth des axes de contrainte est indiqué. Rapport de stress R= ((2-(1)/((3-(1). La ligne pointillée indique le S0 (base des coulées de la formation Matadero). (t-s) est l'angle entre le vecteur glissement théorique et calculé pour chaque famille de stries. B: orientation des axes de contrainte seuls après débasculement. C: événement transpressif le plus ancien. D: extension récente.

Bravo fault system. Into the north, in the Mariscal mountain (fig. 2), early geologic mapping combined with field observations led Maxwell *et al.* [1967] and Maxwell and Dietrich [1965] followed by Bumgardner [1976] to propose that sill intrusions in the Mesozoic strata were injected before folding. These sills were dated 37.0 ± 1.3 Ma ($^{40}Ar/^{39}Ar$) by Harlan *et al.* [1995]. Those results demonstrate that deformation is younger than 37 Ma and is probably Late Oligocene in age.

Tectonic evidences for left lateral motion along the Rio Bravo fault

We have made microtectonic observations at many sites because the main fault is buried and poorly exposed and macroscopic observations on this fault are difficult. Microtectonics provide information on the structural fabric of major fault zones when megastructures are not directly observable in the field. The first representative site is "El Saucito", located north of the northern flank of the Benavides anticline (see fig. 3) where conglomerates of the El Matadero formation are locally intensively fractured. We have measured striations on calcareous or volcanic pebbles and on some minor fault planes. The paleostress tensor was calculated by inversion of microtectonic data (fig. 5A) using the Carey-Gailhardis and Mercier [1987] numerical model. The stress tensor is tilted according to the bedding-dip (fig. 4c). Most of the faults are trending N140°E and the maximum principal axis (1 trends N050°E (fig. 5B).

The second representative site for this buried fault zone is along the eastern flank of the Sierra Ponce near Santa Helena Canyon (fig. 2 for localisation). This northward asymmetric recumbent anticline is cored with Lower Cretaceous limestones. Volcanic sills are locally intruded among the strata. The steep NE flank of this anticline is faulted along the Rio Bravo near Santa Helena canyon (fig. 2). Many measurements were made along this fault zone, both on the volcanic rocks and on the Mesozoic calcareous series. Two generations of striations were identified corresponding to two paleo-stress tensors (fig. 5C, 5D). The first generation of faults corresponds to motion along N150°E reverse or strike-slip faults that cut trough Cretaceous carbonates and Cenozoic volcanic sills (fig. 5C). A N020°E-directed σ1 principal axis indicates the main shortening axis.

A second generation of faulting is characterised by normal and a few strike-slip faults (fig. 5D). The stress inversion indicates a NE-SW (N045°E) regional extension compatible with the Miocene Basin and Range extensional direction proposed in northern Mexico [Henry and Aranda-Gomez, 2000] and transtensive Neogene structures described in the Big Bend area [e.g. Henry, 1998] attributed to the Basin and Ranges tectonics.

Like Erdlac [1990] and Henry *et al.* [1998], we conclude that the studied area was affected by two distinct phases of deformation: a shortening phase characterised by a N020°E-N050°E direction of compression followed by an extensive phase with a N045°E direction of extension (Basin and Ranges).

Structural data in the Ojinaga area

This N110 trending left lateral strike slip fault zone observable in the Benavides area where volcanic units are widespread is more difficult to map westward along the Rio Bravo where Paleogene volcanics are poorly exposed.

In the Ojinaga region, the structures within the Chihuahua fold belt are swinging fom N020°E-010°W trending folds (north of the Rio Conchos, fig. 2), to N030°W and locally to N060°W (northern flank of the Benavides anticline). This sigmoidal fabric has controlled the trace of the Rio Bravo (hence the Mexico-USA boundary) between El Paso/Ciudad Juarez and Presidio/Ojinaga. West of the Benavides area, Rio el Nogal (fig. 2) outlines the strike change from N120°E southwards to N140°E-trending folds and NE-verging thrust faults northwards (Ojinaga region) and even N-S thrusts and folds of the Sierras El Peguïs and La Esperanza up to the NE (fig. 2). Upright folds affect the Mesozoic series and the Ojinaga clastic beds make up most

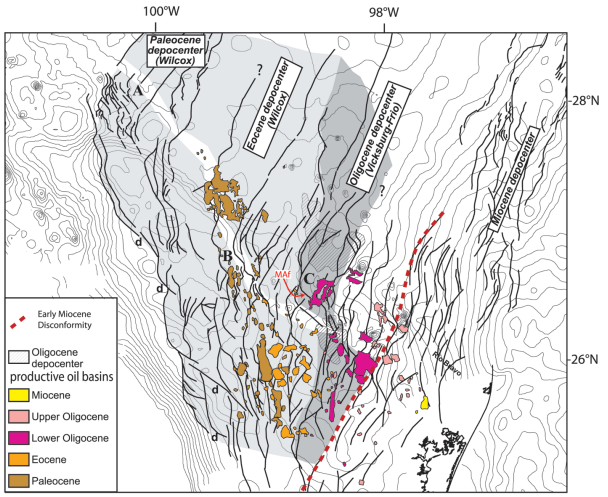

FIG. 6. – Surface trace for growth faults in the Burgos basin and localisation of the main oil splays classified by age (courtesy of PEMEX modified). Thin lines is gravimetric contouring of figure 7. MAf = Mac Allen fault area shown on fig. 9. A,B,C,D, see text for explanation. Note left lateral dragging of listric faults along the Rio Bravo fault. Dotted red line is the surface trace of the Early Miocene disconformity, poorly affected by strike slip motion. d: disconformity at the base of the Burgos basin.
FIG. 6. – *Tracé en surface des failles de croissance dans le bassin de Burgos, et localisation des reservoirs pétroliers classés par âge (courtoisie de PEMEX, figure modifiée). Le contourage en arrière plan est celui des données gravimétriques de la figure 7. MAf= faille de Mc Allen détaillée sur la figure 9. A,B,C,D sont explicités dans le texte. Remarquer l'entraînement en jeu senestre du tracé des failles listriques le long de la faille du Rio Bravo. La ligne rouge pointillée correspond à la trace en surface de la discordance Miocène inférieur peu affectée par le mouvement décrochant.* d : *discordance à la base du bassin de Burgos.*

of the exposures. However in this area a few Cenozoic volcanic rocks outcrops were preserved from erosion.

In the Sierra Santa Cruz, southeast of Ojinaga (fig. 2), Early Cretaceous limestones are folded (figs 2, 4D). The southern flank of the anticline dips 30-40°SW. Here, the Ojinaga late Cretaceous formation is in depositional contact with the early Cretaceous limestones. In contrast, the northern flank of the structure is steeper with 70-80°dips towards the NE (fig. 4D). Here the Early Cretaceous limestones are thrusted over the Ojinaga formation (fig. 4D) and the conformably overlying rhyolitic ash-flow tuff and rhyolitic lava flows (~2 m thick). These volcanic units are correlated with the El Matadero formation of the Benavides area. New dating of this rhyolitic flow was obtained by us as 33.13 ± 0.4 Ma.

Along the Rio Bravo, to the northwest, Cerro Colorado (fig. 2) a similar thrust zone was observed. The Late Cretaceous sequence of the Ojinaga formation is conformably overlain by a red detrital unit (arenites and conglomerates). This unit may be attributed to the detrital base of the El Matadero formation. This continental unit is overlain by the same rhyolitic ash-flow tuff and a rhyolitic lava flow described in the northern flank of the Santa Cruz anticline.

The N140°E trending NE verging thrusts of the Santa Cruz and Cerro Alto can be traced northwestward in the Cerro Colorado, where the Ojinaga formation is conformably overlain by the same red detrital unit cropping out in the northern flank of the Cerro Alto. This detrital unit is overlain by a 200-300 m thick volcanic unit of the El Matadero formation (fig. 4F, location on figure 2).

In the Ojinaga area region, field data show that the observed folding and thrusting are Early Oligocene in age, as previously proposed by Frantzen [1958] and Corry *et al.* [1994] on the other side of the international boundary.

THE BURGOS BASIN

The Burgos basin is located east of the Sierra Madre Oriental front (fig. 1 and fig. 6). Series are continuous from the Paleocene to the Upper Miocene [INEGI, 1980]. In Texas, the Burgos basin is subdivided into three provinces [Diegel *et al.*, 1995] dominated by listric fault soling on subhorizontal shale or salt detachments. The individual detachment provinces are distinguished by age (fig. 6). From west to east, those provinces are the Wilcox fault province of Paleocene-Eocene age, the Vicksburg-Frio province of Oligocene age and the Oligo-Miocene province which extends offshore. A fourth province (Plio-Pleistocene province) is described offshore [Diegel *et al.*, 1995]. A fundamental genetic distinction is made between the detachments that are salt-related (Plio-Pleistocene and Oligo-Miocene) and those that are purely sliding surfaces not directly related to salt withdrawal [Diegel *et al.*, 1995].

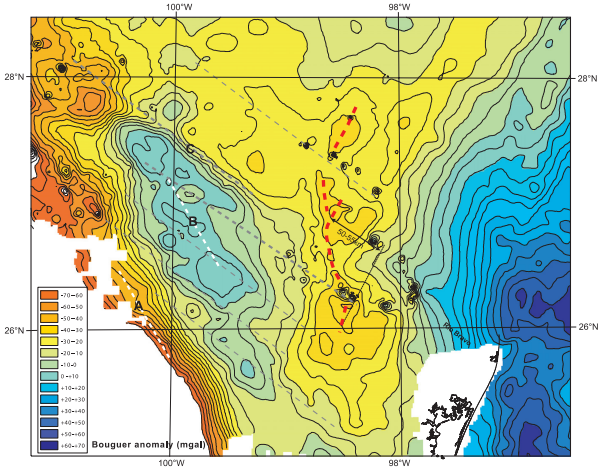

FIG. 7. – Gravimetric map (Bouger anomaly) of the Burgos basin and the western Gulf of Mexico. Dashed black lines are the possible trace of the main strike slip faults offsetting the gravity highs. The 50-55 km left lateral offset of the main Oligocene depocenter is indicated by the red dashed line. A,B,C,D see text for explanation.
FIG. 7. – *Carte des anomalies gravimétriques de Bouger du bassin de Burgos et du golfe du Mexique occidental. Les lignes pontillées noires correspondent au décalage des hauts gravimétriques. Le décalage senestre de 50-55 km du principal dépocentre oligocène est souligné par la ligne pointillée rouge. A,B,C,D sont explicités dans le texte.*

Geometry of normal faults in subsurface

A compilation of structural data on both sides of the Texas-Mexico boundary was made for this study, using an industrial data base provided mainly by PEMEX. We have used both 2D and 3D seismic interpretations to built the structural sketch map of figure 6.

North of the Rio Bravo, Texas faults are N010-020°E trending (fig. 6). The westernmost N045°E faults of the Wilcox province cut through the right bank of the Rio Bravo. To the south, the fault geometry is more complicated (A, fig. 6). The structure is a network of N040°E normal faults that swing rapidly southward to a N120-130°E direction. Southeastward in Texas (zone B, fig. 6), the normal faults of the Wilcox province are also oriented N045°E and show the same structural rotation along the trace of the Rio Bravo. (sector B, fig. 6). On the Mexican side of the river and southward, normal faults are generally trending N160-170°E.

The major fault trend change is also observed in the Oligocene Vicksburg-Frio province (sector C, fig. 6) and the lower Oligocene oil splays are offset left laterally. Figure 9 shows how the Mc Allen fault trace bends along the Rio Bravo with no direct equivalent in Mexico

Gravimetric signature of the Rio Bravo fault discontinuity

The progressive change in the geometry of normal faults along the N120°E main structural direction is interpreted as due to the presence at depth of a major shear fault along the trace of the Rio Bravo.

The Rio Bravo discontinuity is imaged on the Bouguer gravimetric data obtained from Total-USA (fig. 7). The westernmost areas show low negative N150°E anomalies (-70 to -50 mgal) parallel to the structures of the Sierra Madre Occidental (A, fig. 7). They are the result of the thickening at the front of the orogen. East of this anomaly, an

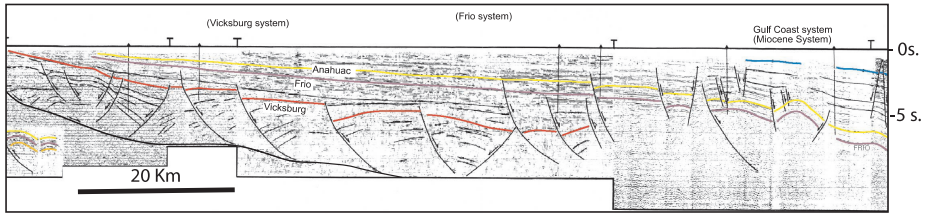

FIG. 8. – E-W seismic section across the Burgos basin [from Perez Cruz, 1992]. The Vicksburg and Frio fault systems are sealed by the Early Miocene Anahuac formation (in yellow). Top Vicksburg fm. in red, top Frio fm. in purple, both affected by faulting.
FIG. 8. – *Coupe sismique E-W dans le bassin de Burgos [Perez Cruz, 1992]. Les failles listriques de Vicksburg et Frio sont cachetées par la formation Anahuac du Miocène inférieur soulignée en jaune. La ligne rouge correspond au sommet de la formation Vicksburg et la ligne violette au sommet de la formation Frio. Ces deux formations sont faillées.*

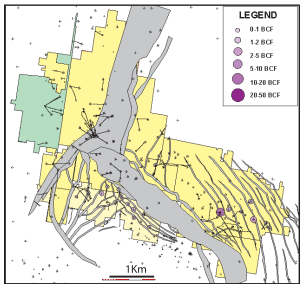

FIG. 9. – The Mac Allen fault scarp (in gray) dragged left laterally along the Rio Bravo fault. The large number of production wells (courtesy of PEMEX) shows the dense control in subsurface for this fault.
FIG. 9. – *L'escarpement de la faille de Mc Allen entraîné par le mouvement senestre de la faille du Rio Bravo. Le grand nombre de puits de production illustre le bon contrôle de subsurface (courtoisie de PEMEX).*

anomaly is well-developed also along a general N150°E direction (B, fig. 7). To the north, this anomaly stops on a N125°E discontinuity (C, fig. 7). This break-up is correlated at the surface with the southwestern termination of the westernmost fault of the Palaeocene Wilcox province (A, fig. 6). As seen above, this termination is characterized by a sinistral network of N020°E faults associated with N120-130°E faults. In the same way, the N020°E Eocene faults (B, fig. 6) change to a N120°E direction. This pattern is correlated with the gravimetric discontinuity described at depth.

Other parallel N120-130°E discontinuities are also observed south of the main Rio Bravo gravimetric discontinuity (dashed gray lines on fig. 7). The magnitude of those discontinuities is less important than for the Rio Bravo one, but they cannot be disregarded. In surface, they are correlated with direction discontinuities of Burgos normal faults (d, fig. 6): the N150-160°E general normal faults trend is locally disrupted by N120-130°E transfer faults. Although the Rio Bravo seems to be the major discontinuity of the area, deformation is distributed along other parallel faults that should not be ignored. To the west, the trend of the Bouguer anomalies is parallel to the N020°E trend of the faults and depocenters of the Burgos basin (red line, fig. 7). North of the Rio Bravo a -30/-50 mgal negative anomaly is well-defined. It is correlated at the surface with the hanging wall of the Vicksburg-Frio Oligocene fault system (C, fig. 6). We interpret this negative anomaly as the main depocenter of the Oligocene sedimentary basin. Although it is not continuous, it can be recognised south of the Rio Bravo. This discontinuity is correlated at the surface with N120°E transfer faults, such as the McAllen fault mentioned above (fig. 6); it also corresponds to the eastward extension of a N125°E discontinuity of the Bouguer anomaly (C, fig. 7). The offset of the depocenter across the Rio Bravo can be estimated at roughly 50-55 km (fig. 7).

At the surface, the -30/-40 mgal negative Bouguer anomaly is also correlated with the main splays (fig. 6) that are exploited in the Oligocene gas and petroleum reservoirs (McAllen petroleum system in Texas and Reynosa petroleum system in Mexico). Using those markers, the sinistral shift across the Rio Bravo can also be estimated at roughly 55-60 km.

We conclude that a major sinistral strike-slip fault system is located along part of the Rio Bravo. We propose a 50-60 km syn/post-Oligocene shift along this structure. As part of the deformation is distributed along secondary N120°E faults, this 50-60 km offset estimate must be considered as a minimum.

The Oligocene depocenter being faulted and shifted left laterally, the deformation is partly syn- or post-Oligocene. E-W seismic sections in Texas and Mexico (fig. 8) show that Oligocene normal faults of the Vicksburg and Frio systems are sealed by the Anahuac formation of Early Miocene age. To the east, the Anahuac is also affected by normal faults in the Burgos offshore delta (fig. 8) but not offset by any left-lateral fault. Onland, Miocene normal faulting is controlled by the Basin and Range only. Consequently the main N120°E Rio Bravo fault was active till latest Oligocene.

Sinistral motion is well argumented both at the deep crustal level and by the offset of oil plays in subsurface. Growth faults were probably developed during this crustal motion as illustrated on figure 9. Sinistral offset at depth along the Rio Bravo fault has destabilized the poorly compacted sedimentary pile of the Burgos basin and delta, with a tendency to slide differentially southeastward. This can be explained by a series of shallow decollements as those described by Diegel *et al.* [1995] in the Burgos basin. In addition, Le Roy and Rangin [2008] have shown that dextral transtension is active during the Neogene south of the Rio Bravo in the Burgos basin. This motion could have favoured faster gravity sliding on the Mexican side than on the Texan one.

THE BABIA FAULT AND THE SABINAS BASIN

General description and geometry

The Sabinas basin is located in northeastern Mexico in the states of Coahuila and Nuevo Leon (fig. 1 and fig. 11). It is accepted as a 200 km-wide Lower Mesozoic transtensional basin associated with the opening of the gulf of Mexico [e.g. Salvador, 1987]. The basin is composed mainly of marine sediments deposited during long-term subsidence. It was limited to the north by the Burro platform and to the south by the Coahuila platform (fig. 11), which were emergent during the Jurassic-Lower Cretaceous. During the late Oligocene deformation discussed here this basin was deformed by

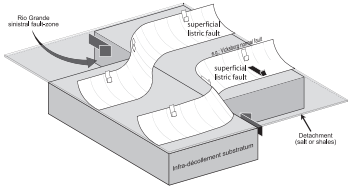

FIG. 10. – Sinistral wrenching of listric faults in the Burgos basin and south Texas above the Rio Bravo sinistral motion at depth.
FIG. 10. – *Crochons senestres des failles listriques du bassin de Burgos et Texas méridional au-dessus du jeu décrochant senestre de la faille du Rio Bravo en profondeur.*

thin-skinned tectonics above a shallow décollement level within the Oxfordian evaporites of the Sabinas basin [e.g. Eguiluz *et al.,* 2001] as in the Chihuahua trough. Tertiary tectonics results in many well-developed N140°E-trending folds. The related N050°E direction of compression is in agreement with the σ1 we have determined in the Manuel Benavides area (fig. 5B). Close to the northern Babia fault (surface trace of the deep Rio Bravo fault defined in the Ojinaga area) and close to the southern San Marcos fault (fig. 11), the folds swing in trend from N140 to N110° along the Babia and San Marcos structure. The sigmoidal geometry of folding within the Sabinas basin is compatible with left-lateral wrenching along a sinistral transpression zone [see modelling of Cobbold *et al.,* 1991]. This interpretation was previously proposed by Charleston [1981] and Padilla y Sanchez [1982] for the deformation of Sabinas fold-belt. Longoria [1985] even proposed the sinistral transpressive model for the deformation of the northern front of the Parras nappe but this is not demontrated by structural data [Tardy, 1980].

This global sinistral en echelon sigmoidal folding in the Sabinas basin (fig. 11) is probably not so simple if we examine the complexity of folds in relation with the trace of basement offsets deduced from the gravity study. The multiple scale sigmoidal shape of these folds suggests left lateral motion at depth along these secondary N120°E trending basement faults.

The Sabinas basin can be simply interpreted as a large sinistral shear band between the Rio Bravo fault in the north and the San Marcos fault in the south. Our detailed study along the Rio Bravo suggests a part of left lateral motion was absorbed along the Rio Bravo fault during the Oligocene, but how much of this deformation was accommodated into the Sabinas basin?

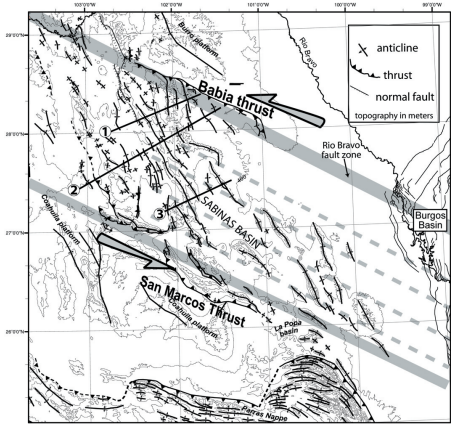

FIG. 11. – Structural sketch map of the left lateral shear band wrenching the Sabins basin between the Rio Bravo fault and San Marcos fault. Topographic contours every 400 m. Dashed gray lines from figure 7. 1,2,3: location of sections figure 12.
FIG. 11. – *Carte structurale synthétique illustrant la bande de cisaillement senestre déformant le bassin de Sabinas entre les failles de Rio Bravo et de San Marcos. Contours topographiques tous les 400 m. Les lignes pointillées grises proviennent de la figure 7. 1,2,3: localisation des coupes de la figure 12.*

Cross-sections in the Sabinas basin

Three SW-NE cross-sections are shown in figure 12. Cross-sections 1 and 2 were constructed for this study and cross-section 3 is from Eguiluz *et al.* [2001]. They illustrate the tectonic style above a décollement level. The depth of the Louann salt is constrained by the thickness of the basin infill estimated from INEGI [1988, 1991]. We use an average depth of 3-4 km below the surface for this horizon. This estimation is equivalent to the average depth proposed by Eguiluz *et al.* [2001]. Above the décollement, Mesozoic series are folded along tight anticlines. Locally the Jurassic evaporites were injected into anticlinal axes (fig. 12-3). On cross-section 12-2 and 12-3, we suppose that the long-wave folds have been formed above a crustal fault cutting the basement.

Shortening was estimated from the cross-sections. It is roughly 10 km on cross-sections 12-1 and 12-3. Cross-section 12-2 has absorbed a shortening of ~20 km. This cross-section is located in the middle part of the Sabinas basin and is more representative of the total accommodated shortening within the basin. However this estimation does not take into account the thrust component absorbed in the Burro (Babia thust) and Coahuila (San Marcos thrust) platforms [INEGI, 1988; SPP, 1982]. We have proposed less than 5 km of NE-SW shortening for the Babia thrust and San Marcos thrust restoring these two thrust zones. Consequently a total NE-SW shortening of 40 to 45 km could have been accommodated in the basin and along its margins. This shortening is interpreted as coeval with the left-lateral strike-slip absorbed along the Rio Bravo fault (fig. 7) that was estimated around 50 km at deph.

Age of deformation

Tardy [1980] proposed a Palaeocene – Early Eocene age (60-52 Ma) for the formation of the Sierra Madre Oriental in the Parras fold and thrust belt. He showed that the youngest deformed series are the Maastrichtian and Dano-Montian pelitic flysch of the Coahuila platform. However, immediately north of the Cohahuila platform (La Popa basin, fig. 11) more recent studies have shown a continuous deposit until the Bartonian (37 Ma) [Vega-Vera and Perilliat, 1989]. For these authors, there is conformity between the Eocene and the underlying Upper Cretaceous – Palaeocene section. This implies that the shortening, in the La Popa basin [Lawton *et al.,* 2001], has gone on till latest Eocene or even later. Unfortunately, in the Sabinas basin, no Tertiary deposits were preserved. This late deformation occurred after in the Sierra de Parras Laramide deformation had ceased. Folds and thrusts of the Parras nappe are covered disconformably by Paleogene continental conglomerates of the Ahuichila formation [Rogers *et al.,* 1961]. West of this area, this sedimentary formation is interbedded with the Upper Eocene-Oligocene volcanic units of the Sierra Madre Occidental [Tardy, 1980]. Moreover, southward in the state of Guanajuato, preserved vertebrates led to propose an Upper Eocene-Lower Oligocene age for this unit [Fries *et al.,* 1955]. We then conclude that the wrench deformation within the Sabinas basin took place during latest Eocene-Early Oligocene.

DISCUSSION

We have shown that the main deformation in the Ojinaga region, south of the Big Bend area, took place during the Oligocene. This transpressive deformation was probably guided at depth by a N120-130°E trending left-lateral strike-slip fault-system. The main compressive stress axis is oriented N040°E to N050°E, consistent with the stress direction proposed by Erdlac [1990]. The system extends eastward along the Babia fault, and further east this fault system cuts through the Burgos basin where Oligocene sinistral wrenching is inferred: sigmoidal folds are cut by the splays of the Rio Bravo fault zone and the depocenters are left laterally offset by a minimum of 50-55 km. Finally this deformation attributed to an Oligocene deformation event is much younger than the Laramide event. The structures were locally sealed by Lower Miocene deposits. Thus the Rio Bravo fault zone was active along the 1000 km of its mapped length during the Middle Tertiary.

The deformation of the Sabinas basin implies contraction across a 200 km wide shear zone extending from the Babia fault into the north to the San Marcos thrust into the south. From stratigraphic data [Vega-Vera and Perilliat, 1989], the Sabinas basin was deformed during the Bartonian 38-40 Ma. Northwest of the Sabinas basin, our structural data in the Ojinaga area have evidenced an early Oligocene main phase of deformation south of the Trans-Pecos. Both deformations are sub-contemporaneous (Upper Eocene and Lower Oligocene). Moreover directions of shortening are similar (N050°E in the Sabinas basin and N010°E to N050° in the Ojinaga area). Because of the similarities between ages and directions of shortening, these structures cannot be separated.

In the Burgos basin, the deformation is mainly localized along the Rio Bravo fault. However, part of the left-lateral strike-slip is accommodated along parallel faults that can be traced below the Sabinas basin. The strike-slip deformation may be considered to be distributed within the Burgos basin. The fundamental difference with the Sabinas basin is the absence of salt and the superimposed gravity-driven extensive tectonism.

The Sabinas basin started to wrench and N140-160°E folds developed above a shallow salt décollement within the Middle Jurassic series. The geometry characterizes a sinistral wrench along the N120°E trend. This inversion is responsible of the overthrust of the pelagic series of the Sabinas basin over the Mesozoic Coahuila platform to the south and the Burro platform to the north. The total shortening accommodated by folds within the basin and by the lateral thrusts is estimated to be at least 40 km. This quantity is of the same order than the Upper Eocene–Lower Oligocene 50 km total offset estimated along the Rio Bravo fault in the Burgos basin.

Consequently total cumulated left lateral strike-slip motion along the large shear band can be estimated to be a minimum of 70 to 80 km at the crustal level.

Deformation was probably distributed from the San Marcos fault to southern Texas before being localized along the Rio Bravo fault. The 50 km absorbed along the Rio Bravo fault alone are sufficient to absorb the same quantity of rifting offshore Texas during the Oligocene [Rangin *et al.,* 2008].

The Upper Eocene-Lower Oligocene period of deformation can be related to the evolution of the western margin of the Gulf of Mexico (and of the Burgos basin). From the Paleocene to Lower Eocene, sedimentation was mainly clastic with important sediment influx connected to Laramide tectonic pulses s.s. [Galloway *et al.*, 2000]. During the Middle Eocene, depositional episodes were minor, reflecting a continental tectonic quiescence [Galloway *et al.*,

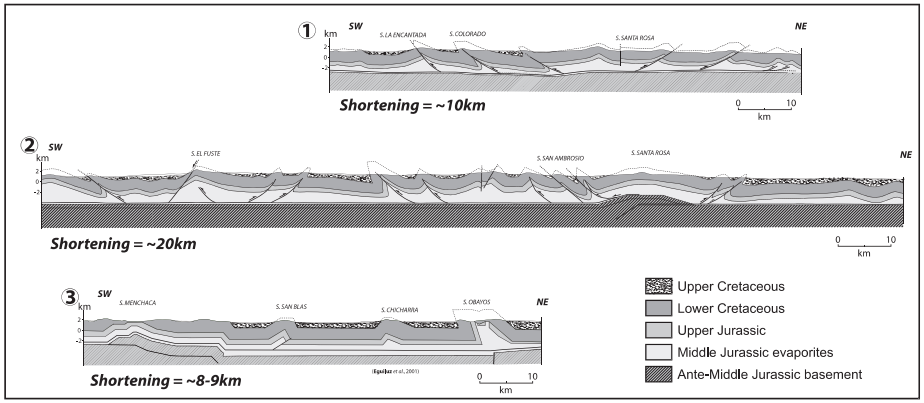

FIG. 12. – Shortening across the Sabinas basin estimated on cross sections. Section 3 is from Eguiluz *et al.* [2001]. Thickness of the Mesozoic series is estimated on the basis of INEGI 1/250.000 geological maps, Montclova (1991), Nueva Rosita (1991), San Miguel (1982), Tlahualilo de Zaragoza (1988), Ocampo (1990). Section location on figure 11.
FIG. 12. – *Raccourcissement du bassin de Sabinas estimé sur coupes. La coupe 3 est d'Eguiluz* et al. *[2001]. L'épaisseur des séries mésozoïques est estimée sur les cartes géologiques 1/250,000 de l'INEGI. Localisation des coupes sur figure 11.*

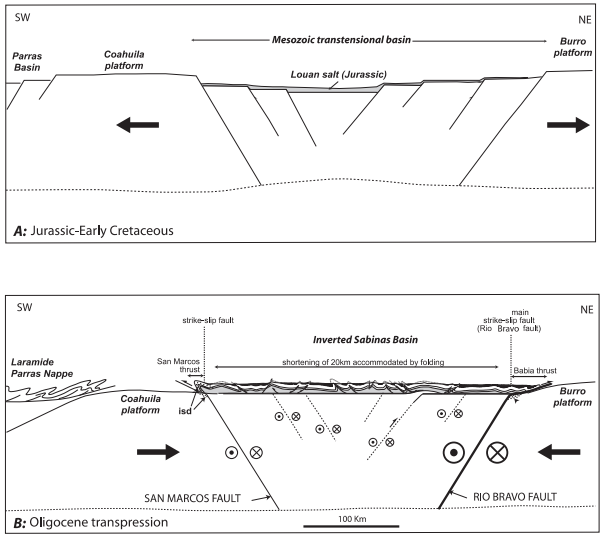

FIG. 13. – Schematic section of the Sabinas basin and its margins. A: before Oligocene inversion. B: transpresional inversion in the basin.
FIG. 13. – *Section schématique du bassin de Sabinas et de ses marges. A: avant l'inversion Oligocène, B: après l'inversion en transpression.*

2000]. On the other hand, the Upper Eocene–Lower Oligocene period witnessed significant changes. This period was a time of massive sediment influx [Galloway *et al.*, 2000]. The Oligocene depocenter is dramatically shifted toward the east, indicating a major reorganization of source areas. Moreover, from thermochronological data from the Sierra Madre Oriental, Gray *et al.* [2001] show a 5-7 km exhumation of the Laramide foreland basin during the late Oligocene (< 30 Ma), extended probably within the Sabinas basin [Ewing, 2003]. This exhumation is centered on the Sierra Madre Oriental where large open folds and uplift were described by Tardy [1980] and tentatively

TABLE I. – Ar/Ar plateau ages of dated samples GOM 7 and GOM 9 discussed in text. We are very grateful to Gilbert Féraud (Géoscience Azur, Nice-Sofia Antipolis) to have conducted these analisis.
TABL. I. – *Age plateau Ar/Ar des échantillons GOM 7 et GOM 9 discutés dans le texte. Nous remercions Gilbert Féraud (Géoscience Azur, Nice-Sofia Antipolis) pour avoir effectué ces analyses.*

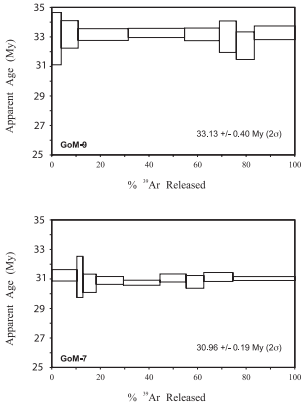

TABLE II. – Analytical results of samples GOM 7 (7 FK; H292) and GOM 9 (9FK H291) discussed in text.
TABL. II. – *Résultats analytiques des échantillons GOM 7 (7 FK; H292) and GOM 9 (9FK H291) discutés dans le texte.*

Step n°	Atmospheric contamination (%)	^{39}Ar (%)	$^{37}Ar_{Ca}/^{39}Ar_K$	$^{40}Ar^*/^{39}Ar_K$		Age (My)	
9 FK (H291)							
1	4.579	3.87	0.187	4.842	32.884	±	1.771
2	0.318	6.97	0.005	4.885	33.173	±	0.932
3	0.110	20.63	0.004	4.883	33.162	±	0.399
4	0.000	23.12	0.003	4.899	33.270	±	0.309
5	0.000	14.37	0.004	4.885	33.175	±	0.426
6	0.000	6.92	0.003	4.861	33.016	±	1.068
7	3.147	7.42	0.003	4.771	32.408	±	0.935
fuse	0.235	16.70	0.002	4.901	33.281	±	0.462
				Integrated age= 33.13 ± .20 Ma			
7 FK (H292)							
410	1.978	10.30	0.028	4.605	31.250	±	0.388
430	0.000	2.48	0.027	4.589	31.143	±	1.393
446	1.251	5.48	0.029	4.524	30.709	±	0.618
462	1.137	11.22	0.030	4.553	30.899	±	0.266
476	0.841	15.02	0.029	4.530	30.746	±	0.171
490	0.000	10.77	0.028	4.578	31.068	±	0.272
510	0.703	7.24	0.027	4.538	30.803	±	0.432
587	0.000	12.01	0.027	4.586	31.138	±	0.303
1111	0.511	25.49	0.028	4.572	31.031	±	0.133
				Integrated age= 30.98 ± .10 Ma			

dated Miocene. The Late Oligocene is a large diastrophic period in northern Mexico.

Moreover, this period also corresponds to a maximum volcanic activity in Trans-Pecos [e.g. Henry and McDowell, 1986], along the inferred Rio Bravo fault. In the Burgos basin, hydrovolcanic series intercalated within the Upper Eocene to Oligocene deposits probably indicate the existence of this tectonic event.

CONCLUSIONS

After a period of tectonic quiescence following the Laramide between the Paleocene and the Middle Eocene, the Upper Eocene (?)-Oligocene period corresponds to a major wrenching episode along the Sabinas basin and left lateral strike slip motion along the Rio Bravo. This left lateral motion, linked to crustal extension offshore Texas (Corsair rift) [Rangin *et al.*, 2008; Husson *et al.*, a and b, 2008], marks a major tectonic event in northern Mexico, decoupled from Texas.

The geodynamic explanation for such 80 km of left lateral motion in northern Mexico is probably related to fast northwards decrease of subduction along the Farallon North America boundary during the middle part of the Tertiary. Straving of volcanism along the Sierra Madre Occidental during this period support this hypothesis.

References

ANDERSON T. H. & NOURSE J. A. (2005). – Pull-apart basins at releasing bends of the sinistral Late Jurassic Mojave-Sonora fault system. *In*: T.H. ANDERSON, J. A. NOURSE, J. W. MCKEE AND M. B. STEINER, Eds., The Mojave-Sonora megashear hypothesis: Development, assessment, and alternatives. – *Geol. Soc. Amer. Sp. Paper*, **393**, 97-122.

BUMGARDNER J. E. (1976). – Geology of the gabbro sill surrounding Mariscal Mountain, Big Bend National Park, Texas. – Univ. of Texas, Austin, PhD Thesis.

CAREY-GAILHARDIS E. & MERCIER J.-L. (1987). – Numerical model for determining the state of stress using focal mechanisms of earthquake population: application to Tibetan teleseisms and microseismicity of southern Peru. – *Earth Planet. Sci. Lett.*, **82**, 165-177.

CHARLESTON S. (1981). – A summary of the structural geology and tectonics of the State of Coahuila, Mexico. *In*: C. SMITH and S. KATZ, Eds, Lower Cretaceous stratigraphy and structure, northern Mexico. – *West Texas Geol. Soc. Publ.*, **81-74**, 28-36.

COBBOLD P. R., GAPAIS D. & ROSSELLO E. A. (1991). – Partitioning of transpressive motions within a sigmoidal foldbelt: the Variscan Sierras Australes, Argentina. – *J. Struct. Geol.*, **13**(7), 743-758.

CAMPA M.F. & CONEY P. (1983). – Tectonostratigraphic terranes and mineral resources distribution in Mexico. – *Can. J. Earth Sci.*, **20**, 1040-1051.

CORRY C. E., STEVENS J. B. & HERRIN E. (1994). – A laramide push-up block: the structures and formation of the Terlingua-Solitario structural block, Big Bend Region, Texas: Discussion and reply. – *Geol. Soc. Amer. Bull.*, **106**, 553-559.

DIEGEL F., KARLO J., SCHUSTER D., SHOUP R. & TAUVERS P. (1995). – Cenozoic structural evolution and tectonostratigraphic framework of the northern Gulf coast continental margin. *In*: F. DIEGEL *et al.*, Eds, Salt tectonics: A global perspective. – *AAPG Memoir* **65**, 109-151.

EGUILUZ A. S. (2001). – Geologic evolution and gas resources of the Sabinas basin in northeastern Mexico. *In*: C. BARTOLINI, R. T. BUFFLER and A. CANTU-CHAPA (Eds), The western Gulf of Mexico basin: Tectonics, sedimentary basins, and petroleum systems. – *AAPG Mem.*, **75**, 241-270.

ERDLAC R. J. (1990). – A Laramide-age push-up block: the structure and formation of the Terlingua-Solitario structural block, Big Bend region, Texas. – *Geol. Soc. Amer. Bull.*, **102**, 1065-1076.

EWING T.E. (1991). – Structural framework. In: A. SALVADOR, Ed., The Gulf of Mexico basin. – Geol. Soc. Amer., Decade of North American geology, vol. **J**, 31-52.

FRANTZEN D. R. (1958). – Oligocene folding in Rim Rock country, Trans-Pecos Texas. – Unpublished M.A. Thesis thesis, University of Texas at Austin.

FRIES C. J., HIBBART C. W. & DUNKLE D. H. (1955). – Early Cenozoic vertebrates in the red conglomerate at Guanajuato, Mexico. – *Smiths. Misc. Coll.*

GRAY G.G., POTTORF R.J., YUREWICZ D.A., MAHON K.I., PEVEAR D.R. & CHUCHLA R.J. (2001). – Thermal and chronological record of syn- to post-Laramide burial and exhumation. Sierra Madre Oriental, Mexico. *In*: C. BARTOLINI, R.T. BUFFLER & A. CANTÚ-CHAPA, Eds, The western Gulf of Mexico basin: Tectonics, sedimentary basins and petroleum systems. – *AAPG Mem.*, **75**, 159-181.

GALLOWAY W. E., GANEY-CURRY P. E., X. LI & BUFFLER R. T. (2000). – Cenozoic depositional history or the gulf of Mexico basin. – *AAPG Bull.*, **84**(II), 1743-1774.

GREGORY J. L. (1981). – Volcanic stratigraphy and K-Ar ages of the Manuel Benavides area, northeastern Chihuahua, Mexico, and correlations with the Trans-Pecos Texas volcanic province. – PhD Thesis, University of Texas.

GUNDERSON R., CAMERON K. & CAMERON M. (1986). – Mid-Cenozoic high-K calc-alkalic and alkalic volcanism in eastern Chihuahua, Mexico: Geology and geochemistry of the Benavides-Pozos area. – *Geol. Soc. Amer. Bull.*, **97**, 737-753.

HAENGGI W. T. (2002). – Tectonic history of the Chihuahua trough, Mexico and adjacent USA, Part II: Mesozoic and Cenozoic. – *Bol. Soc. Geol. Mex.*, **LV**(1), 38-94.

HARLAN S. S., GEISSMAN J. W., HENRY C. D. & ONSTOTT T. C. (1995). – Paleomagnetism and Ar/Ar geochronology of gabbro sills at Mariscal Mountain anticline, southern Big Bend National Park, Texas: implications for the timing of Laramide tectonism and vertical axis rotations in the southern Cordilleran orogenic belt. – *Tectonics*, **14**(2), 307-321.

HENNINGS P. H. (1994). – Structural transect of the southern Chihuahua Fold Belt between Ojinaga and Aldama, Chihuahua, Mexico. – *Tectonics* **13**, 1445-1460.

HENRY C. D. (1998). – Geology of the Big Bend Ranch State Park, Texas. – University of Texas at Austin, Bureau of Economic Geology, Guidebook **27**.

HENRY C. D. & PRICE J. G. (1984). – Variations in caldera development in the Tertiary volcanic field of Trans-Pecos Texas. – *J. Geophys. Res.*, **89**, 8765-8786.

HENRY C. D. & MCDOWELL F. W. (1986). – Geochronology of magmatism in the Tertiary volcanic field, Trans-Pecos Texas. *In*: J. G. PRICE, C. D. HENRY, D. F. PARKER & D. S. BARKER, Eds, Igneous geology of Trans-Pecos Texas, field trip guide and research articles. – University of Texas at Austin, Bureau of Economic Geology, Guidebook **23**, 360p.

HENRY C. D., MCDOWELL F. W., PRICE J. G., PRICE J. G. & SMYTH R. C. (1986). – Compilation of potassium-argon ages of Tertiary igneous rocks, Trans-Pecos Texas. – Univ. of Texas-Austin, Bur. Econ. Geol., Geological circular n°**86-2**, 34p.

HENRY C. D., KUNK M. J., MUEHLBERGER W. R. & MCINTOSH W. C. (1997). – Igneous evolution of a complex laccolith-caldera, the Solitario, Trans-Pecos Texas: Implications for calderas and subadjacent plutons. – *Geol. Soc. Amer. Bull.,* **109**(8), 1036-1054.

HENRY C. D. & ARANDA-GOMEZ J. J. (2000). – Plate interactions control middle-late Miocene, proto-gulf and Basin and Range extension in the southern Basin and Range. – *Tectonophysics,* **318**, 1-26.

HUSSON L., HENRY P. & LE PICHON X. (2008). – Thermal regime of the NW shelf of the Gulf of Mexico. A) Thermal and pressure fields – *Bull. Soc. géol. Fr.,* **179**, 2, 129-137.

HUSSON L., LE PICHON X., HENRY P., FLOTTE N. & RANGIN C. (2008). – Thermal regime of the NW shelf of the Gulf of Mexico. B) Heat flow density. – *Bull. Soc. géol. Fr.,* **179**, 2, 139-145.

INEGI (1980). – Geological map of Mexico 1/1,000,000.

INEGI (1988). – Geological map of Tlahualilo de Zaragoza 1/250,000

INEGI (1991). – Geological map of Monclova 1/250,000.

KEITH S. B. & WILT J. C. (1986). – Laramide orogeny in Arizona and adjacent regions: a strato-tectonic synthesis. – *Arizona Geol. Soc. Digest,* **16**, 502-554.

LAWTON T. F., GILES K. A., VEGA F. J. & ROSALES-DOMINGUEZ C. (2001). – Stratigraphy and origin of the La Popa basin, Nuevo Leon and Coahuila, Mexico. *In*: C. BARTOLINI, R.T. BUFFLER & A. CANTÚ-CHAPA, Eds, The western Gulf of Mexico basin: Tectonics, sedimentary basins and petroleum systems. – *AAPG Mem*., **75**, 219-240.

LE ROY & RANGIN C. (2008). – Cenozoic crustal deformation of the offshore Burgos basin region (NE Gulf of Mexico), a new interpretation of deep penetration multi-channel seismic reflection lines. – *Bull. Soc. géol. Fr.,* **179**, 2, 161-174.

LONGORIA J.F. (1985). – Tectonic transpression in the Sierra Madre Oriental, northeastern Mexico; an alternative model. – *Geology*, **13**, 7, 453-456.

MAXWELL R. A. & DIETRICH J. W. (1965). – Geology of the Big Bend area, Texas. – *Publ. West Tex. Geol. Soc.,* **65-51**, 196 p.

MAXWELL R. A., LONSDALE J. T. & HAZZARD R. T. (1967). – Geology of Big Bend National Park, Brewster county, Texas. – *Publ. Univ. Tex. Texas Bur. Econ. Geol.,* **67-11**, 320 p.

MCDOWELL F. W. & KEIZER R. P. (1977). – Timing of mid-Tertiary volcanism in the Sierra Madre Occidental between Durango city and Mazatlan, Mexico. – *Geol. Soc. Amer. Bull.,* **88**, 1479-1487.

MCDOWELL F. W. & MAUGHER R. L. (1994). – K-Ar and U-Pb zircon chronology of Late Cretaceous and Tertiary magmatism in central Chihuahua State, Mexico. – *Geol. Soc. Amer. Bull.,* **106**, 118-132.

MUEHLBERGER W. R. (1980). – Texas lineament revisited. *In*: Trans-Pecos Region. – New Mexico Geol. Soc., *31st Field Conference Guidebook*, 113-121.

PADILLA Y SANCHEZ R. J. (1982). – Geologic evolution of the Sierra Madre Oriental between Linares, Concepcion del Oro, Saltillo, and Monterrey, Mexico. – University of Texas.

REYES-CORTÉS I. A. & GOODELL P. C. (2000). – Geological setting and mineralization: Sierra Peña Blanca, Chihuahua, Mexico. *In*: *Cuarta Reunion Sobre la Geologia del Noroeste de Mexico y Areas Adyacentes, Estacion Regional del Noroeste*. – UNAM, Inst. Geologia, Estacion Regional del Noroeste, Publicaciones Ocasionales, **101**.

RANGIN C., LE PICHON X., FLOTTÉ N. & HUSSON L. (2008). – Tertiary extension in the northern Gulf of Mexico, a new interpretation of multi-channel seismic data. – *Bull. Soc. géol. Fr.,* **179**, 2, 117-128.

ROGERS C. L., DE CSERNA Z., OJEDA J., TAVERA E. & VAN VLOTEN R. (1961). – Reconocimiento geologico y depositos de fosfatos del Norte de Zacatecas y areas adyacentes en Coahuila, Nuevo Leon y San Luis Potosi. – *Consejo Recursos naturales no renovables Bol.,* **56**.

SALVADOR A. (1987). – Late Triassic–Jurassic paleogeography and origin of Gulf of Mexico basin. – *AAPG Bull.,* **7**, 419-451.

SALVADOR A. & GREEN A. (1980). – Opening of the Caribbean Tethys (origin and development of the Caribbean and the Gulf of Mexico). *In:* J. AUBOUIN, J. DEBELMAS & M. LATREILLE, coord., *Géologie des chaînes alpines issues de la Téthys, Geology of the Alpine chains born of the Tethys. – Mém. BRGM,* **115**, 224-229.

SPP (1982). – Geological mal of San Miguel, 1/250.000.

TARDY M. (1980). – Contribution à l'étude géologique de la Sierra Madre orientale du Mexique. Stratigraphie, évolution paléogéographique et évolution tectonique sur un profil du secteur transverse de Parras. Organisation et géodynamique de la Sierra Madre orientale au passage domaine alpin-caraïbe – Cordillère ouest-américaine. – Unpublished Thèse d'état thesis, Univ. Pierre et Marie Curie.

VEGA-VERA F. J. & PERRILLIAT M. (1989). – La presencia del Eoceno marino en la cuenca de la Popa (Grupo Difunta), Nuevo Leon: orogenia post-Ypresiana. – *Universidad Nacional Autonoma de Mexico*, **8**, 67-70.

Bull. Soc. géol. Fr., 2008, t. 179, n° 2, pp. 117-128

Cenozoic gravity tectonics in the northern Gulf of Mexico induced by crustal extension. A new interpretation of multichannel seismic data

CLAUDE RANGIN[1], XAVIER LE PICHON[1], NICOLAS FLOTTÉ[2] and LAURENT HUSSON[3]

Key-words. – Gravity tectonics, Cenozoic rifting, Gulf of Mexico, Texas, Northeast Mexico.

Abstract. – The Gulf of Mexico margin in Texas is one of the most impressive examples of starved passive margin gravity collapse systems. Growth faults developed upslope and are compensated down slope by toe folding and thrusting. On the basis of new multi-channel seismic data with high penetration (down to 11 s-twtt) we present evidences for deep crustal extension and rifting that have enhanced superficial sliding. This hypothesis is supported by a significant heat flow anomaly and crustal thinning independently deduced from gravity data. This Cenozoic rifting episode is tectonically linked to left lateral motion along the Rio Bravo fault, a reactivated branch of the Texas lineament.

Extension crustale tertiaire dans le nord du golfe du Mexique à l'origine de la tectonique gravitaire. Une nouvelle interprétation de données de sismique multitraces

Mots-clés. – Tectonique gravitaire, Rifting tertiaire, Golfe du Mexique, Texas, Mexique du Nord-Est.

Résumé. – La marge du golfe du Mexique au Texas est une des marges passives fossiles où les glissements gravitaires sont les plus connus. Des failles de croissance developpées en haut de pente se voient compensées en bas de pente par des plissements et des chevauchements. Sur la base de données de sismique multitrace haute pénétration (jusqu'à 11 std), nous montrons qu'un épisode de rifting crustal a pu provoquer ces glissements superficiels. Cette hypothèse semble renforcée par un flux de chaleur significativement élevé, l'extension crustale étant indépendamment déduite des données gravimétriques. Cet épisode de rifting cénozoïque est structuralement lié au déplacement senestre le long de la faille du Rio Bravo, une branche du linéament du Texas réactivée.

INTRODUCTION

Rifting of the Gulf of Mexico was initiated at the Triassic-Jurassic boundary probably along tectonic zones of weakness inherited from the Late Paleozoic Ouachita Orogeny [Marton and Buffler, 1994]. A simple shear model [Wernicke, 1985] has been often proposed for the early evolution of the Texas margin [Watkins, 1978; Simmons, 1992]. During middle Jurassic times thinning of the crust was coeval with sedimentation of thick evaporites (Louann salt). Spreading of this basin occurred briefly during the Late Jurassic [Salvador, 1987; Buffler, 1991]. A series of transfer fault zones with sinistral offset are part of the rifting fabric [Tardy, 1980; Anderson and Nourse, 2005; Lister *et al.,* 1986]. Offshore Texas these faults are represented by the Brazos and Matagorda transfer faults [Simmons, 1992]. They have segmented this old passive margin during the rifting but no clear evidences were found for similar transform faults during spreading except maybe for the Mojave Sonora megashear [Silver and Anderson, 1974]. Thermic subsidence affects this basin during the Cretaceous with development of carbonate reefs [Buffler, 1983]. A stratigraphic synthesis of this post rift history was presented by Feng and Buffler [1996] and Rowan *et al.* [1999]. A significant event was the accumulation of a thick clastic sequence in southern Texas during the Paleocene, probably related to the fast erosion of the Laramide Orogeny in northeastern Mexico [Galloway *et al.,* 2000; Tardy, 1980]. During the Eocene, a 4000 m thick depocenter extended from South Texas to the Mexican-USA border [Salvador, 1987]. During the Oligocene, large deltas were developed in Texas (the Vicksburg and Frio formations). A thick regressive wedge was developed during the Miocene and the Pliocene with a noticeable sedimentary hiatus during the early Pliocene.

Despite this long thermal relaxing history, Nagihara and Jones [2005] have recently documented an abrupt transition in heat flow at the oceanic crust-thinned crust boundary proposed by Marton and Buffler [1994] just offshore the Mississippi delta. Reed [1994] had suspected Cenozoic rifting offshore Texas. The thick sedimentary pile of sediments blanketing the western margin of the Gulf of Mexico affected by recent extension involving the whole sedimentary package was usually interpreted in terms of gravity tectonics over a Triassic salt sole or other shales detachement horizons. References are numerous on this subject and difficult to synthesize here. According to most authors, the early stages of salt tectonics in the northern Gulf of Mexico basin

1. CNRS-UMR 6635, CEREGE, Chaire de Géodynamique du Collège de France, BP 80, Europôle de l'Arbois, 13545 Aix en Provence cedex, France.
2. AREVA T&D, Tour Areva, 1 place de la Coupole, 92084 Paris la Défense, France
3. Géosciences Rennes, CNRS-UMR 6118, Univ. Rennes 1, Campus de Beaulieu, 35042 Rennes cedex, France.
Manuscrit déposé le 29 janvier 2007 ; accepté après révision le 6 novembre 2007

were related to differential thermal subsidence resulting from Early-Middle Jurassic rifting. Salt sheets formation and evacuation basinward of autochthonous Jurassic salt is however considered by most authors as Cenozoic in age, this process being driven by gravitational instabilities caused by the slope gradient after intense sedimentary loading of the margin. This type of gravity driven thin-skinned tectonics was intensively studied [Rowan *et al.*, 1999] and constrained by numerous models [i.e. Jackson and Galloway, 1984; Vendeville and Cobbold, 1987; Vendeville and Jackson, 1992a and b].

This salt tectonics processes were clearly imaged and modelled for the Sigsbee abyssal plain but tectonic processes are less well understood along the middle and upperslope where large active or recent faults are reported. We think that these gravity processes now active along the Sigsbee scarp were enhanced by crustal rifting during the Cenozoic along the upper margin of Texas. This conclusion is based on a new interpretation of industrial seismic lines with deep penetration made available to us in this area.

A set of these shortly spaced multi-channel seismic lines covering offshore Texas were used. Some depth converted sections extending onshore were also used to calibrate the offshore time sections. Most of the lines have a time penetration of 13 s-twtt, except at the boundary with Mexico where penetration does not exceed 8 s-twtt. We have also used information of wells to calibrate some of the offshore time sections.

In the first part of this paper we describe reference lines embracing the onshore and offshore regions (fig. 1). These sections provide a global view of the Texas margin structure. We have added complementary information on the basis of additional onshore seismic lines.

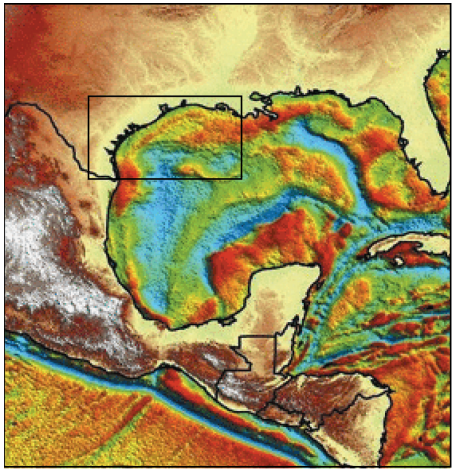

FIG. 1. – The Texas passive margin in the northern Gulf of Mexico localized on a free air gravity anomaly map of the gulf and surrounding regions.
FIG. 1. – *La marge passive du Texas dans le nord du golfe du Mexique localisée sur une carte des anomalies gravimétriques à l'air libre du golfe et regions avoisinantes.*

The second part of this paper deals specifically with the most significant crustal extensional fault, the Corsair fault offshore Texas. This fault system was mapped and its relationships with the deep basement reflectors are presented.

The third part of the present paper presents a possible interpretation of the nature of the "basement" reflectors taking into account the results of the thermal companion study of this project [see Husson *et al.*, 2008 a, b]. We also discuss the tectonic model for detachment at the base of the crust adopting a ductile crust interpretation for the "basement" above the Moho. Space and time relationships between crustal extension at depth and gravity sliding in the sedimentary package are discussed.

REGIONAL SEISMIC LINE DESCRIPTION

Seismic composite line 1

This composite seismic line is used as a reference line (fig. 2). It extends from the onshore Wilcox fault zone (WFZ), the northernmost extensive fault system, to the Corsair fault zone (CFZ). This composite seismic line is discussed here from NW to SE.

1) Northwest of the WFZ, Mesozoic to Eocene series are gently dipping offshore and are not affected by any large fault (sector 1).

2) The Wilcox fault zone is the westernmost significant extensional fault system known onshore. The Cretaceous series are offset by a SE-dipping normal fault system (sector 2). Thickening of the Paleocene sequence and associated roll over structures indicate a syn-Paleocene deformation (sectors 2 and 3). Locally this early deformation is sealed by the late Paleocene-early Eocene deposits (sector 2). A major normal fault cuts through the Cretaceous and may connect at depth with the Jurassic salt. A main decollement is localized at the Cretaceous/Paleocene sequence boundary (sector 3).

3) The Vicksburg fault zone (VFZ) is located SE of the WFZ. It is characterized by a decollement level located at about 4 s-twtt, at the roof of the Paleocene sequence. This decollement branches upwards into the Eocene and locally above. Syn-rift geometries within the Eocene deposits (thickening toward the fault) and the sub-continuity of the Oligocene reflector show that the deformation occurred mainly during the Eocene. Below this decollement, faulting of the reflectors (Cretaceous?) and the fan geometries observed within the Paleocene, both indicate that deformation occurred on top of a lower decollement at the roof of the Mesozoic. The geometry of the faults within the Cretaceous sequence has been interpreted by White *et al.* [1986] as connecting onto a 9 s-twtt deep decollement not imaged on the seismics studied here. However, the nature of the horizons below this decollement remains undetermined (fig. 2).

4) The Frio fault zone is located SE of the VFZ. It is characterized by normal faults connected at depth (5 to 5.5 s-twtt) onto the top Paleocene decollement level, the SE extension of the decollement described below the VFZ that gently dips to the SE. The huge thickness of Oligocene deposits in the hanging wall of the major fault (F1) demonstrates that the deformation mainly occurred during the Oligocene. F1 connects with a main decollement level (reflector B, fig. 2) located at the top of the Paleocene sequence. However part of the deformation is accommodated along F2 and continues during the Miocene. A progressive basinward migration of the deformation is then suspected within this fault zone, and the progression of this migration extended south to the Corsair fault system (CFZ).

Below the decollement, other normal faults affect the Paleocene sequence and the underlying undetermined crust. These faults may be related with the Paleocene deformation defined within the Wilcox fault zone. However, some faults as F3, may connect deeper than the 8/9 s-twtt. Other faults such as F4, connect at its base with this deep undetermined sequence.

5) The Corsair fault zone (CFZ) is the southernmost and younger fault system observable on this composite seismic line. It can be described as formed by two main fault segments: the Wanda fault (F5) and the Corsair fault itself (F6).

F5 connects onto F2 described above. The thickening of the Miocene sequence along the hanging wall of F5 indicates a Miocene activity that extends into the Pliocene. Southeastward, this fault cuts through the Paleocene series and connects at 9 s-twtt onto the deepest decollement level (reflector A). The origin of this decollement is discussed below using a depth converted profile.

In the hanging wall of the Corsair fault, a huge thickening of well-dated Miocene series indicates a main Miocene faulting episode. However, we cannot exclude that part of the deformation may have begun in the Upper Oligocene because the deep series are not dated. The hanging wall of the Corsair fault is also characterized by numerous secondary faults accommodating the rollover and ramp syncline.

Nature of reflector A

An interpretation of the significance of this section must take into account the actual depths. We have used two main sources of information to establish the depth image of the time section presented in figure 2.

– The first source of information is the refraction data presented by Ebeniro *et al.* [1988]. These data were collected along a composite N-S profile located south of Galveston between 29°N and 25.5°N, from the shelf to a depth of 1500 m on the slope. This composite profile is based on 5 transverse OBS sections. Two of these, (n°5 at 1500 m water

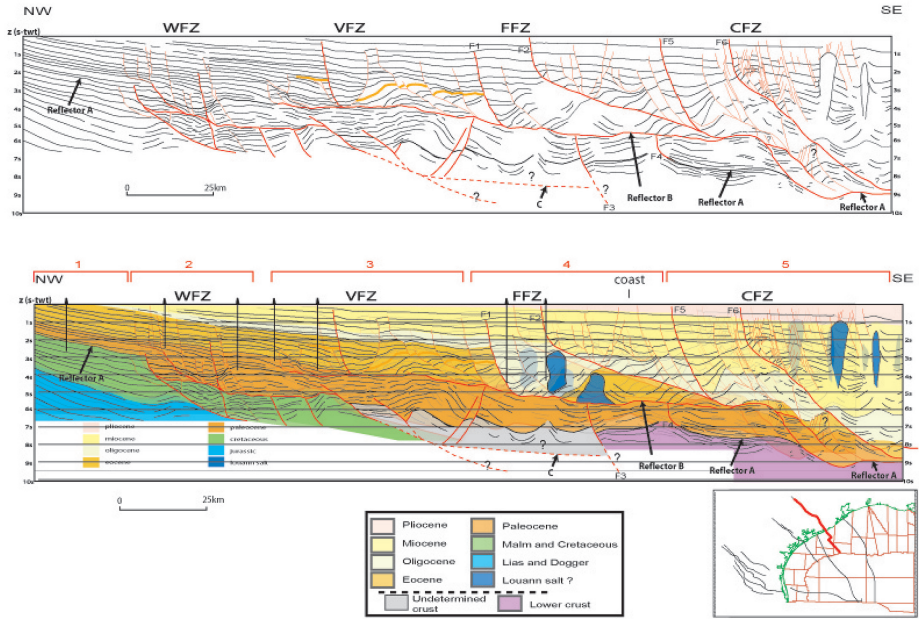

FIG. 2. – Interpreted line drawing of a composite onshore-offshore seismic section across the central part of the GOM margin (red line for location on insert). The main seismic sequences are classified by ages according to well information shown on figure. Reflectors A, B, C are discussed in text. WFZ : Wilcox fault zone, VFZ : Vicksburg fault zone, FFZ : Frio fault zone, CFZ : Corsair fault zone. Individual faults F1 to F5 are discussed in text. Red sectors 1 to 5 are also discussed in text.
FIG. 2. – *Tracé interprétatif d'une section sismique composite terre-mer au droit de la partie centrale de la marge du GOM (ligne rouge pour localisation dans l'encart). Les principales séquence sismiques sont présentées par tranches d'âge en accord avec les données de puits indiqués sur la figure. Les réflecteurs sismiques* A, B, C, *sont discutés dans le texte. Les failles individuelles F1 à F5 sont discutées dans le texte. Les secteurs 1 à 5 figurés en rouge sont également discutés dans le texte.*

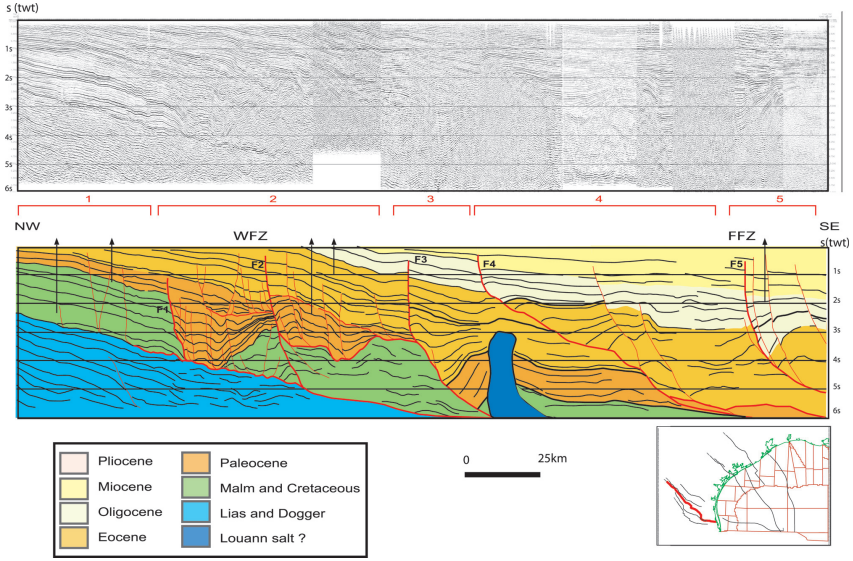

FIG. 3. – Interpreted line drawing of onland seismic section #2 illustrating decollement on the salt layer. Same legend as figure 2.
FIG. 3. – *Tracé interprétatif de la ligne sismique terrestre #2 illustrant le décollement sur le niveau salifère. Même légende que la figure 2.*

depth and n°3 at 750 m water depth) have a well defined Moho 20-22 km deep. Ebeniro *et al.* section n°1 is located just south of the Corsair FZ. It provides an average velocity slightly below 3 km/s for the upper 6 s of the section, and an average velocity of 5.25 km/s between 6 s and 10.7 s where is the deepest reflector at 7.2 km/sec.

– The second source of information is the Bouguer gravity map that we have inverted for the Moho using an average depth of 22 km for this crustal/mantle boundary. This depth is rather well established on the slope by the refraction work of Ebeniro *et al.* [1988] [See also Husson *et al.*, 2008 a and b]. This inversion shows that the Moho stays at a nearly constant depth of 20-22 km under the whole shelf. Thus the velocities of 7.2 to 7.4 km/s found at 20-22 km under lines 1 and 2 of Ebeniro *et al.* [1988] actually correspond to the gravimetric Moho. There is no reason to assume the existence of a 10 km thick 7.2-7.4 km/s crust between 20 and 30 km. It is not justified by seismic refraction arguments and is not compatible with gravity data.

Thus we can conclude that the deep decollement (reflector A) described above at the southeastern end of the profile could be located at a depth of 18 km to 19 km, whereas the Moho is localized at 21-22 km. The 3 km thick layer located between the reflector A above and the Moho below, potentially includes the Cretaceous, Jurassic and Triassic sequences known, plus the pre-Mesozoic basement and the brittle crust.

We thus have two options: either we assume that there is no igneous crust and that the Cretaceous and Jurassic lie directly on top of the mantle that is possibly serpentinized, or we assume that there are no Mesozoic sequences extending downslope, and that the Cenozoic sequences lie directly on top of the lower crust. We prefer the second hypothesis and propose that the 9 s-twtt decollement level connects onto the top of the lower crust. In any case, at the depth of 18 km, where the decollement is located below the Corsair rift, the estimated temperature is about 500°C and the material, whatever its composition must be metamorphosed and ductile. We believe that the style of the reflectors seen at this depth (see below in this paper) is compatible with a brittle-plastic transition crustal zone between 6 and 8 s-twtt

Consequently, the oldest deformation is Paleogene in the Wilcox fault zone and is located far to the NW of the present gulf margin. It corresponds geometrically to normal faults connecting onto a décollement level generally attributed to the Middle Jurassic salt layer as presented in figure 3. In figure 2 the Eocene seals the deformation there. This deformation extends toward the SE where it can be described below the Vicksburg and Frio fault zones.

During the Eocene, the deformation migrated SE of the WFZ. New normal faults connected onto a shallower décollement localized at the top of the assumed Paleocene sequence. This décollement was active during the Eocene in the VFZ and during the Oligocene and earliest Miocene in the FFZ. Consequently, a southeastward migration of the normal faults activity is rather well documented, but part of this early deformation remains active during the Neogene.

Balance between rates of early and late Tertiary deformation is difficult to estimate.

The younger fault system is clearly located along the CFZ. This system was mainly active during the Miocene and may continue to be active during the Pliocene and the Quaternary**.** It is associated with a deepening of the décollement level that connects onto the top of the lower crust at 18-19 km depth. The extrapolated temperature at this depth is about 500°C, well beyond the brittle-ductile limit.

Seismic line 2

This onshore seismic line is located in South Texas, close to the Mexico/USA boundary with a WNW-ESE trend, parallel to the Rio Bravo (fig. 3).

1) This northwesternmost zone corresponds to the undeformed Jurassic to Eocene deposits which are relatively conformable. The whole sequence gently dips basinward. This zone is the equivalent to the northwesternmost zone of composite seismic line 1 (fig. 2).

2) The Wilcox fault zone is the oldest extensional area. The normal fault F1 cuts through the Cretaceous sequence. It connects at depth onto a gently SE-dipping decollement level parallel to the Lower and Upper Jurassic seismic reflectors. This decollement is assumed to be localised within the Middle Jurassic salt as for the composite seismic line 1. Thickening of the Early and Middle Paleocene sequence in the hanging wall of F1 and continuity of Early Eocene strata both indicate that the fault was active during the Paleocene. The geometry of the Paleocene sequence is compatible with tilted normal faults connected onto the assumed Middle Jurassic salt-decollement.

Fault F2 is located southeastward of F1. It cuts through the Cretaceous seismic sequence and connects onto the Middle Jurassic salt décollement. A second décollement level is located at the Cretaceous-Paleocene boundary. It is responsible for the rollover geometry of the Paleocene deposits. F2 was active during the Paleocene and part of Early Eocene.

3) F3 is located SE of F2. This listric normal fault connects at depth (~6 s-twtt) onto the assumed Middle Jurassic décollement level. The rollover geometry is in

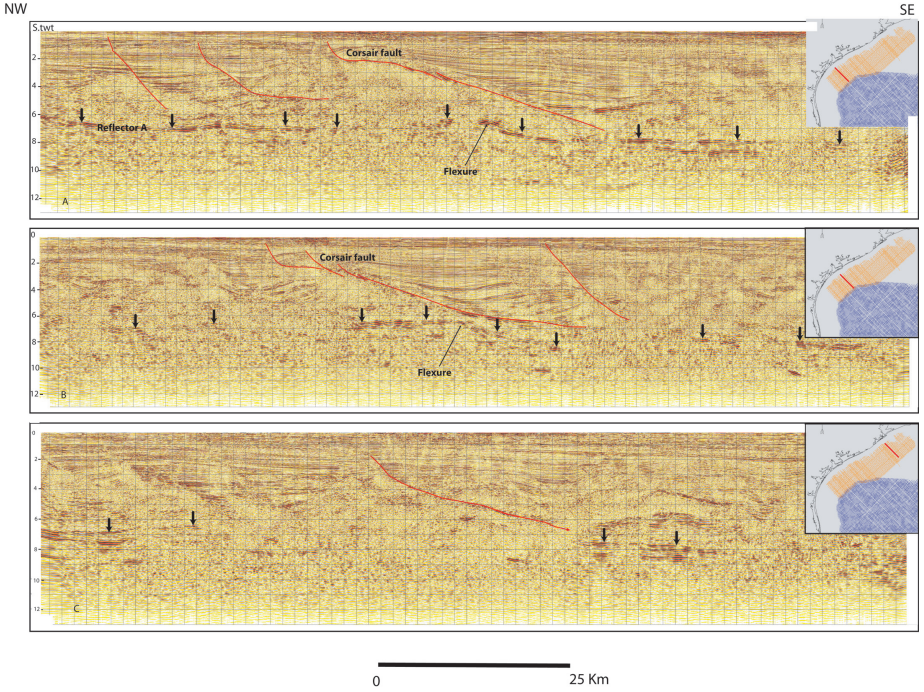

FIG. 4. – Selected cross-sections across the offshore Texas margin, illustrating the brittle Corsair fault (in red) merging down on reflector A (shown by arrows) interpreted as the top of the ductile crust.
FIG. 4. – *Selection de sections sismiques au travers de la marge marine du Texas, montrant le trace de la faille Corsair (en rouge), venant se raccorder vers le bas sur le reflecteur A (surligné par des flèches), et interprété comme le toit de la croûte ductile.*

agreement with the listric character of this fault. The thickening of deposits indicates that this fault was mainly active during the Eocene and the Early Oligocene.

4) F4 is a major listric fault that connects at depth onto a décollement localized at what appears to be the southeast extension of the Cretaceous-Paleocene boundary identified on figure 2. According to the discussion above this reflector merges downslope with the top of the lower crust. Thickening of the Eocene and Oligocene deposits indicates that F4 was active during this time.

5) F5 corresponds to the Frio fault zone, that is the main Oligocene fault system in this area. Its activity results in the thickening of Oligocene seismic sequence but the base of the Miocene sequence is also affected.

In summary, this composite seismic line depicts the same evolution as the composite seismic line 1 onshore Texas (fig. 2).

The earliest deformation occurred along the Wilcox fault system. Here normal faults are generally assumed to connect at depth onto the Middle Jurassic salt layer that would have acted as a main décollement level. Within the Wilcox fault zone, this deformation is sealed by the Middle Upper Eocene seismic sequence.

As into the north, and during the Eocene, the deformation has migrated southeastwards, and WFZ normal faults connect at depth onto the SE extension of the Jurassic décollement. Farther SE, the Eocene fault F4 roots on a shallower décollement level (~6 s-twtt) onto a horizon attributed to the Cretaceous-Paleocene boundary interpreted here as the top of the lower crust by analogy with section of figure 2.

The FFZ is the younger fault system illustrated on this inland composite section. It was mainly active during the Oligocene. Consequently a southeastward migration of normal faults activity also characterizes this composite line.

GEOMETRIES OF DEEP STRUCTURES IN THE CORSAIR FAULT AREA

Modelling of the thermal regime of the Texas shelf [Husson *et al.*, 2008 a, b] has shown that a positive thermal anomaly is centered below the Corsair fault zone and led us to assume a late Cenozoic crustal thinning in this area. No seismic evidence for recent volcanism was found on the seismic lines. For this reason, we will first focus our attention on the deep structures (> 8 s-twtt) below the CFZ illustrated by three deep (12 s-twtt) seismic lines (fig. 4).

From NW to SE, lines A, B, C, a major deep reflector (shown by arrows on figure 4) was observed between 7 s-twtt and 9 s-twtt. This reflector is marked by a high acoustic impedance (high seismic energy) that clearly contrasts with the above reflectors. This observation is limited to these lines that have a 13 s-twtt penetration. The southernmost available lines close to the Mexico-USA international boundary are limited to 6-6.5 s-twtt penetration only, and consequently the southward continuity of this reflector cannot be proven southwards. In sections A and B (fig. 4) the middle part of the sections shown in figure 4, reflector A shows a clear flexure. This is particularly evident on sections a and b. The Corsair fault shown in red uses this flexure as a ramp and merges downslope on the deepest décollement at 8 s-twtt.

With a simple velocity model equivalent to the one used above (i.e. 3.3 km/s between 0-6 s-twtt, and 5.5 km/s below, a composite of 5.2 and 6 km/sec), 7 and 9 s-twtt correspond respectively to 12-13 and 18-19 km. At these depths, the present temperatures are estimated to be 375°C and 500°C. Thus, the material below must be under a ductile regime. Consequently the Corsair fault merges down onto the roof of the ductile crust.

Southeastward of line 4B (fig. 5), the depth of the reflector A increases progressively and reaches roughly 9 s-twtt (i.e. ~18-19 km). The SE-dipping Corsair fault does not cut through this reflector but flattens onto it. This sub-continuous reflector A shows high wavelength undulations and is located at an average time-depth of 7 s-twtt (i.e. ~13 km, see above). We interpret this reflector as a sub-horizontal décollement localized at the top of the lower crust as the Moho is situated at a depth of about 21-22 km (see above). This décollement would then have acted at the boundary of the ductile crust interface.

The sub-continuous reflector described above shows between lines A and B (fig. 4) a systematic flexure just below the Corsair fault. This flexure shows in detail how the

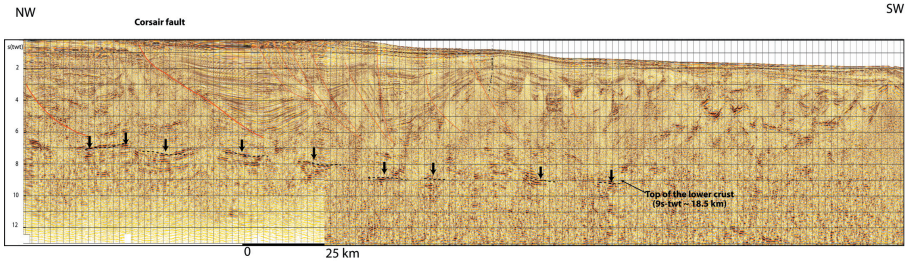

FIG. 5. – Time section across the Corsair fault showing an undulated reflector (arrows) interpreted as the top of the ductile crust located at 9 s-twtt or 18.5 km depth.
FIG. 5. – *Section temps au droit de la faille Corsair montrant un réflecteur ondulé (flèches), interprété comme le toit de la croûte ductile localisée à 9 std ou 18,5 km de profondeur.*

Corsair fault bends at depth along the supposed top of the ductile crust (seismic profiles A, B, C on fig. 6).

This flexure was mapped on figure 7. The map was constructed by interpolation of the picking of the major Cretaceous-Paleocene boundary reflector. It shows that the flexure has a regional NE-SW trend, just SE of the trace of the Corsair fault on the mud line. Southward (close to the US-Mexican border), the reflector was not picked up due to the poor quality of the seismic data and the shallow penetration. To the NE, the flexure extends till the trace of the Brazos transfer zone mentioned by Huh *et al.* [1996]. The flexure below the Corsair fault system is not continuous from Louisiana to the Mexico-USA boundary. It is particularly clear southwest of the Brazos transfer fault and can be followed southwestward over a length of 120 km. Its southern limit is correlated with the change in direction (NE-SW to N-S) of the Corsair fault system close to the trace of the Matagorda transfer zone.

Consequently, the flexure observed below the Corsair fault trends NE-SW and extends from the Brazos to the Matagorda transfer faults along a distance of 120 km. It appears to be directly correlated with the NE-SW segments of the Corsair fault system. The flexure is the northern limit of the zone of extreme thinning of the crust that increases in thickness from 2-3 km at its minimum to more than 7 km landward of the flexure. Thus we interpret the flexure as the

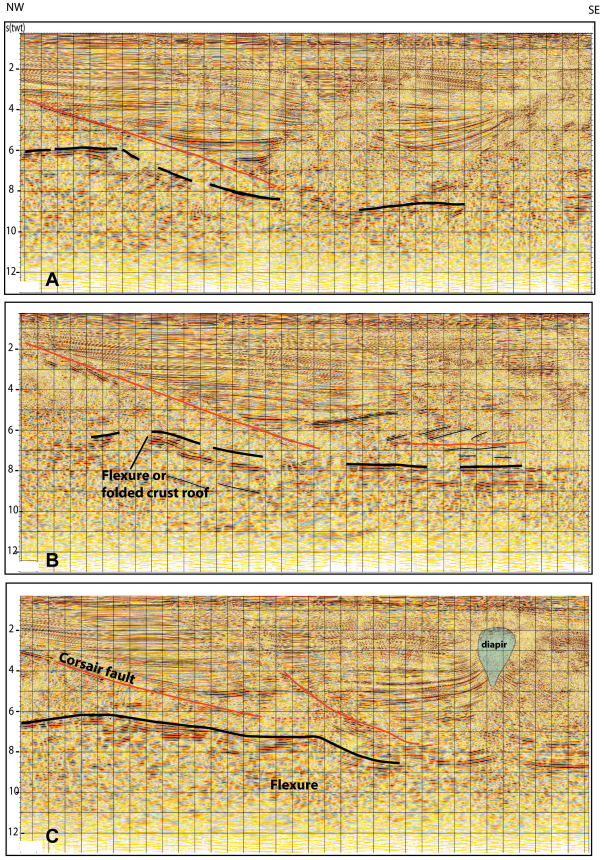

FIG. 6. – Detailed images of the flexure of the ductile crust layer (in black) just below the brittle Corsair fault above (in red).
FIG. 6. – *Images détaillées de la flexure du niveau de la croûte ductile (en noir) juste en dessous de la faille Corsair cassante (en rouge).*

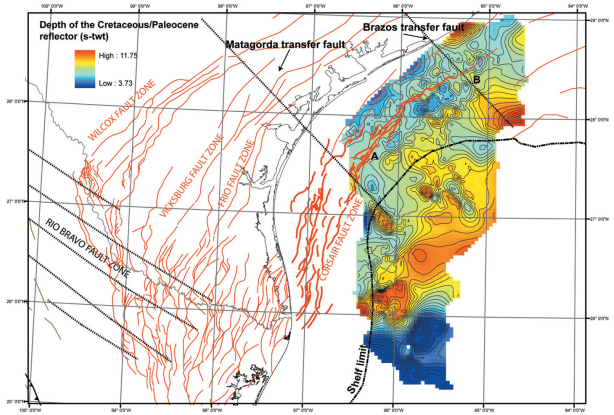

FIG. 7. – Time map of the Cretaceous/Palaeocene boundary showing the flexure of this deep reflector; the mud line trace of the Corsair fault is shown with thick red lines. The Brazos and Matagorda transfer fault traces are shown by dashed lines in Texas. On land Texas main faults are shown in red as well as the most significant faults in the Burgos basin on the Mexican side. Here the trace of the Rio Bravo fault zone is suggested with black dashed lines.
FIG. 7. – *Carte temps de la limite Crétacé-Paléocène montrant la flexure de ce réflecteur profond. La trace en surface de la zone de faille Corsair est indiquée en rouge épais. La trace des failles de transfert Brazos et Matagorda est figurée en lignes pointillées. A terre, au Texas, les failles principales sont figurées en rouge aussi bien que les failles les plus significatives du bassin de Burgos côté mexicain. Ici le tracé de la zone de failles du Rio Bravo est suggérée par des lignes pointillées noires.*

elastic shoulder of the Corsair rift that was mostly formed during the Lower Miocene. This would explain why it stops at each extremity on a fault.

ORIGIN, MEANING AND DEPTH OF THE DEEP REFLECTORS AND DECOLLEMENT

Heat flow below the Frio and Corsair fault systems

Basement heat flow data computed in the thermal study were extracted along the NW-SE transect of seismic line 1 (fig. 8) [see also Husson *et al.*, 2008 a, b for details on the thermal regime]. The heat flow progressively increases rapidly across this fault zone from 30 mW/m^2 to 55 mw/m^2. This increase is correlated with the zone of rapid thinning to the minimum 2-3 km crustal thickness below the CFZ and has been interpreted in terms of Upper Cenozoic crustal extension to account for the thermal anomaly

Moho topography

The Moho topography has been estimated from Bouguer anomaly data (fig. 9). The gravity inversion has been performed following Parker [1977] and Oldenburg [1974]. It has been solved in the frequency domain. The reference depth is set to 22 km according to previous estimates from refraction data [Ebeniro *et al.*, 1988]. The crustal density is fixed to 2700 kg/m^3 and the mantle density to 3300 kg/m^3.

The Moho depth was extracted along a cross-section corresponding to seismic cross-section composite 1 (fig. 2). The thickness of Jurassic and basement corresponds to the margin created during the Middle Jurassic extension. This extension led to accretion in the centre of the Gulf of Mexico.

Onshore Texas, the crust (Jurassic and basement) is 17 km thick (fig. 9). The crust thickness progressively decreases basinward. Below the offshore Texan zone defined by thermal anomalies (fig. 8) and the Corsair fault zone (CFZ), the combined thickness of the basement and Mesozoic series is less than 3 km. This thickness is lower than the 7-9 km average thickness of the oceanic crust [Ranalli, 1995]. This reduced thickness is also associated with a 1.5 km upwelling of the Moho. To account for the thermal anomaly, we have to assume that the anomalous thinning below the CFZ occurred during the Upper Cenozoic, and most probably during Lower Miocene, as explained above.

Interpretation of the nature of the deep reflectors

Their origins will be discussed using composite seismic line 1 (fig. 2).

The deep reflector A (fig. 2) is generally interpreted as the same Upper Cretaceous level over the whole length of the section, deepening from less than 2 s-twtt (3 km) to the northwest to 9 s-twtt to the southeast. It is indeed more or less continuous below the Frio and Vicksburg fault zones. Only few diapirs or normal faults related to the Paleocene extension affect its continuity. To the southeast, the Corsair fault connects onto it at a depth of 9 s-twtt (18-19 km).

At such a depth, pressure and temperature imply a ductile behaviour [see Husson *et al.,* 2008 a]. Moreover the Moho is localized at about 21-22 km. Thus the seismic sequence sandwiched between the Tertiary depocenter of the Corsair fault and the upper mantle is only 3 km thick. This seismic sequence is then best interpreted as a thin lower

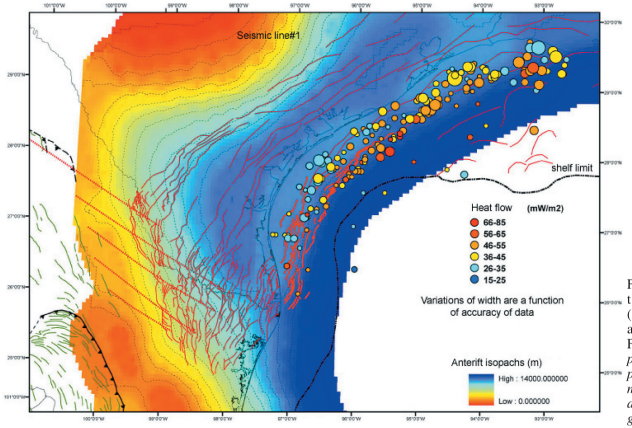

FIG. 8. – Heat flow data (in mW/m^2) plotted on the trace of the Corsair fault. Ante-rift isopachs (in m) are showed by dashed lines. Other legends are the same than figure 7.
FIG. 8. – *Données du flux de chaleur (en mW/m^2) portées sur la trace de la faille Corsair. Les isopaques des sédiments anté-rift sont indiqués en mètres et sont figurés par des pointillés fins. Les autres légendes sont identiques à celles de la figure 7.*

crust with a ductile behaviour and the top of the lower crust would correspond to the high reflective seismic reflector deepening toward the southeast from 7 to 9 s-twtt (reflector A). If this is correct, the nature of reflector A changes from northwest to southeast from the top of the Cretaceous sedimentary layer to the top of the lower ductile crust.

Depth prior to the Oligo-Miocene sedimentation

Below the Frio fault zone (FFZ, composite seismic line fig. 2), reflector A (top of the lower crust) is localized at roughly 7 s-twtt (i.e. 13 km with a mean velocity of 3.3 km/s between 0 to 6 s-twtt and 5.5 km/s below). Below the Corsair fault zone, this reflector reaches 9 s-twtt (i.e. 18-19 km). Removing the thickness of the Oligo-Miocene series and a continuous thickness of Eocene to Paleocene, the reflector was localized at 4 to 4.5 s-twtt (i.e. 7-8 km) during the lowest Oligocene. This rough estimate does not take into account the isostatic process due to the sedimentary loading.

In the same way, the upper main décollement (reflector B), onto which FFZ normal faults connect, was localized at a depth of about 4-4.5 km.

The assumed lower decollement (C on fig. 2) would be localized within the crust. During its time of activity within the Paleocene, subtracting the thickness of the Eocene to present deposits, we obtain an approximate 7 km depth for this décollement.

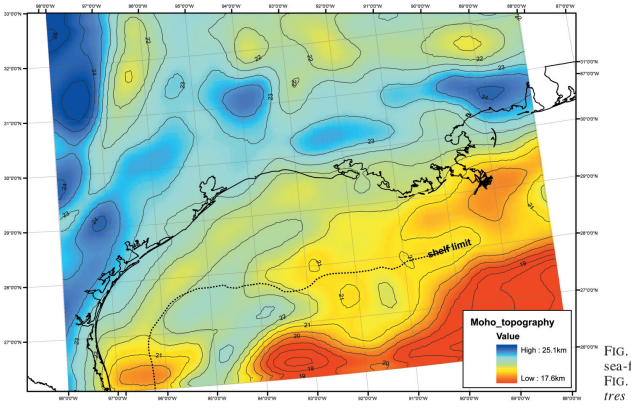

FIG. 9. – Moho depth map in kilometres below sea-floor.
FIG. 9. – *Carte de la profondeur du Moho en kilomètres sous le fond de la mer.*

GEOMETRY OF THE RECENT EXTENSIONAL ZONE OFFSHORE TEXAS

A systematic tectonic analysis of the seismic lines of the Gulf of Mexico offshore region is here presented (fig. 10) along sections selected along the Corsair fault zone. A main decollement zone can be identified between 6 and 9 s-twtt and separates two distinct mega-seismic sequences. This depth zone is the one predicted above to coincide with the brittle-ductile regime. The upper seismic sequence (0 to 9 s-twtt) is affected by dominant SE facing listric faults and images clastic sediments of probable Cenozoic age.

The lower seismic sequence is interpreted as ductile crust and is characterized by dominantly flat or gently SE dipping reflectors (S) and NW dipping discontinuities (C). This could image possible foliation (S) and semi brittle shear planes (C) respectively. At the regional scale this possible geometry in apparent S/C flat shear bands is interpreted as characteristic of the fabric in the stretched lower crust.

This geometry suggests that the upper sequence, mainly formed by Cenozoic sediments, is directly lying or detached above a stretched crust affected by an asymmetrical shearing process. The supposed age of the sediments (not older than Paleocene) suggests a Cenozoic detachment age.

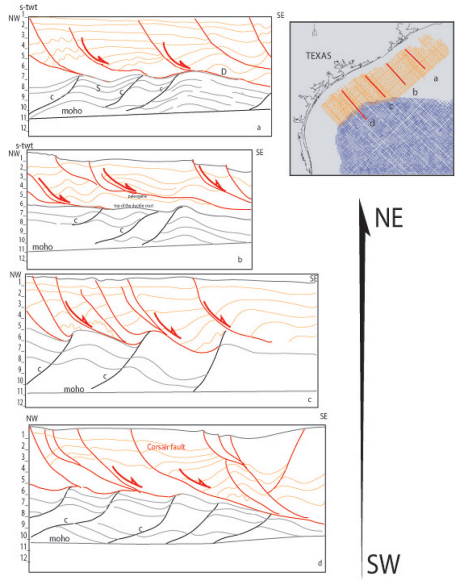

FIG. 10. – Simplified line drawings selected along the Corsair fault of the Texas margin. The sediments above the decollement are directly in contact with the ductile crust with S internal reflectors and affected by C semi-brittle faults.

FIG. 10. – *Tracés simplifiés de lignes sismiques temps sélectionnées au long de la marge texane au droit de la faille Corsair. Les sediments décollés de la séquence sismique supérieure, reposent dirtectement sur la croûte ductile affectée par des réflecteurs S et par des failles ductiles-cassantes C.*

In term of brittle and semi-brittle faulting, a clear opposed asymmetry was systematically observed between the upper and lower mega-seismic sequences separated by a decoupling (decollement) surface that can be traced all over the offshore Texas margin. The upper sedimentary sequence with some possible preserved rafts of upper crust or Mesozoic-Paleozoic sequences are locally suspected and are characterized by strong reflectivity. However these rafts are systematically affected by basin-ward gravitational sliding with the upper sedimentary sequence. On the contrary, the lower crust shows an opposite geometry with NW facing ductile to semi-ductile normal faults. Similar opposed polarity between the upper and lower parts of the crust was observed in the North Sea area, where a marked decoupling exists between the brittle and ductile crust.

On these time sections, we have placed the Moho depth between 10 and 11 s-twtt on the basis of refraction data and gravity modelling (see above). The overlying crustal thickness decreases rapidly from 5 s-twtt close to the coast to less than 2 s-twtt below the Corsair rift.

Between the Matagorda and Brazos transfer fault zones, the average gentle dip of the roof of the crust is affected by a pronounced flexure (see above). This flexure fits rapid thinning of the crust just below the Corsair fault. In some places basinward, the lower crust may be missing and the sedimentary mega-sequence would then be directly detached on the Moho. Between the Matagorda and Brazos transfer fault zones the roof of the ductile crust is gently tilted southeastwards. The roughness of this surface increases northeastwards along the rift zone and is particularly smooth close to the Mexican border, approaching the Rio Bravo fault.

Stretched crust when partially exhumed and cooled (i.e. in metamorphic complexes inland or mega-mullions along the oceanic spreading zones) shows ductile faults that evolve rapidly to semi-brittle faults with the same dip as potential C shear planes. Here the roughness of this sequence boundary fits with the emergence of these C reflectors that affect the décollement surface. We interpret these NW discontinuities as crustal semi-ductile NE facing normal faults that offset up to 1 s-twtt the decollement surface. Development of these brittle-ductile C planes provides the observed irregularity to the roof of the crust. These C planes also bound SE tilted crustal blocks identified by their pervasive SE dipping S foliation.

This type of structure into the lower crust was mainly observed at the NE termination of the Texas rift where the crust was moderately stretched and probably had time to cool during the stretching. On the contrary, along most of the length of the rift these tilted blocks are missing, the roof of the crust is flat and smooth particularly at the SW termination of the rift at its junction with the Rio Bravo transfer fault. This could indicate that the ductile crust remained relatively hot and was never affected by the transition to brittle crust. If a direct relationship exists between the roughness vs. smoothness of the roof of the crust, and the extensional rate into the lithosphere, we could locate the maximum extension at the junction with the Rio Bravo fault and along the Corsair fault. This extension could have been less pronounced at the NE termination of the rift in offshore Louisiana. This could indicate a NE propagating rift zone connected southwestwards to the left-lateral Rio Bravo fault.

The SE facing listric faults of the upper seismic mega-seismic sequence generally flatten on the decollement surface. Where this surface is smooth, the listric faults merge with the decollement with a small angle. Where the roof of the crust is rough and bumpy, the deepest part of these faults shows intensively folded reflectors or transparent seismic sequences interpreted as dysharmonically folded sedimentary sequences. Most of the time this folding in the sedimentary pile is located at the hanging wall of the NW facing fault planes that bound these crustal blocks. Up sequence, it is often the place for shale compaction and related formation of mud diapirs that locally can reach the mud line. At depth, most of the listric faults that affect the sedimentary pile flatten along the SE dipping surface of the crustal blocks. The Corsair fault is one of these and is apparently guided by the presence of large SE tilted fault blocks particularly developed along the crustal flexure.

CONCLUSION

If we accept the seismic sequence interpretation presented in figure 11, most of the gravitational collapse of the sedimentary pile above the 9 s-twtt decollement could be related to stretching of the crust below, down to the Moho.

The brittle crust can be missing locally. Estimated temperature exceeding 600°C at the Moho surface demonstrates that this thin ductile crust is still very hot, and still behaves as a ductile layer, at least in its thinnest part, just SE of the Corsair fault as figured on figure 11. The Cenozoic thinned crust is probably located inside the previously attenuated crust during the Jurassic. Possible rafts of this Jurassic attenuated crust are preserved offshore between the Corsair rift and the Jurassic oceanic crust as indicated on figure 11 below. No direct observations were made because the extensive presence of salt diapirism in the Sigsbee plain. Recent oil discoveries in this area could support this hypothesis.

The continuity of the Corsair fault from the roof of the thin crust up to the mud line suggests that extension was continuous from the Oligocene (?)-Lower Miocene up to present time with some decrease in fault activity during the Pliocene-Pleistocene (a discrete unconformity moderately affected by faulting was observed on numerous seismic lines particularly into the eastern part of the margin).

At depth, the upper seismic sequence moves along a main detachment surface, located most of the time between 7 to 8 s-twtt upslope down to 9 s-twtt down slope where the crust is thinner. This fits the upper surface of the crust, but other minor detachment surfaces were observed in the sedimentary pile in the Eocene or the Paleocene.

We then propose that the lithosphere extension started during the Paleogene and was maximal during the Oligocene but lasted at least until the uppermost Miocene and even to the present time. It may still be active if we consider that the Corsair fault affects the mud line and connects at depth with the top of the crust. We think that the ductile

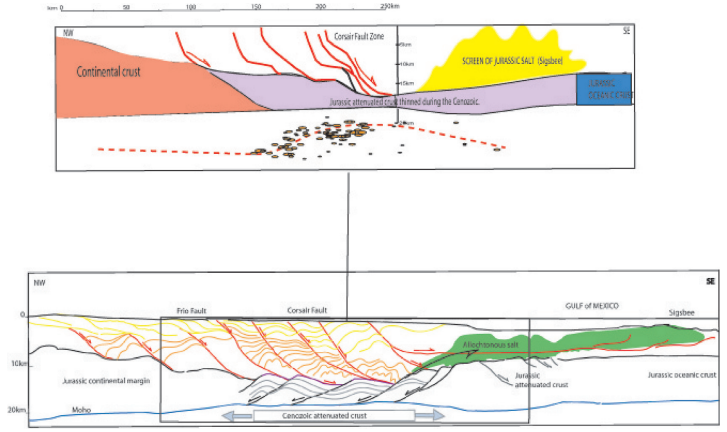

FIG. 11. – A : Simplified section across the Texas margin. The Cenozoic attenuated crust is shown in violet. Sediments above the main decollement have been omitted. This thinned continental crust during the Cenozoic is thinner than the Jurassic oceanic crust (shown in blue) in the deepest part of the GOM.
B : Schematic cross section of the Texas margin incorporating the section above and observations of figure 10. The Cenozoic thinned crust is located inside the Jurassic attenuated crust. This drifted Jurassic attenuated crust is poorly observable because it is covered by allochthonous salt of the Sigsbee.

FIG. 11. – A : *Section simplifiée de la marge texane. La croûte atténuée au Cénozoïque est figurée en violet. Les sédiments situés au dessus du décollement principal ont été omis. Cette croûte amincie au Cénozoïque est plus mince que la croûte océanique Jurassique (indiquée en bleu) dans la partie la plus profonde du GOM.*
B : *Section schématique de la marge texane incorporant la section ci-dessus et les observations de la figure 10. La croûte amincie au Cénozoïque est localisée dans la croûte atténuée du Jurassique indiquée en bleu. Cette partie de croûte riftée est difficilement observable car recouverte du sel allochtone de la Sigsbee.*

crust did participate fully to the deep decollement process and probably still does.

The lithosphere extension of the Texas rift initiated during the middle Paleogene was mostly transferred southwards on land to the left lateral Rio Bravo fault zone mainly during the Paleogene [Flotté *et al.*, 2008], and part of this extension was transferred to the Mexican margin [see Le Roy and Rangin, 2008 and Le Roy *et al.*, 2008]. Here the tectonic slip of the Rio Bravo fault zone is considered to be partially sealed by the Anawak formation, at the Oligocene-Miocene boundary [see Flotté *et al.*, 2008]. If this is correct, then subsequent extension into the crust remained active along the Mexican GOM offshore margin only during the Neogene up to present time.

Acknowledgements. – This work was possible with the collaboration of Total USA in Houston providing us dense coverage seismic profiles grids as well as wells information and gravity data. Sylvain Calassou from Total was a key person for the development of the ideas developed here.

References

ANDERSON T.H. & NOURSE J.A. (2005). – Pull-apart basins at releasing bends of the sinistral Late Jurassic Mojave-Sonora fault system. – *Geol. Soc. Amer. Sp. Paper,* **393**, 97-122p.

BUFFLER R.T. (1983). – Structure of the Mexican ridges foldbelt, southwest Gulf of Mexico. *In*: A. W. BALLY, Ed., Seismic expression of structural styles: a picture and work atlas. – *Am. Assoc. Petrol. Geol.*, Tulsa, Okla., vol. 2, 16-21,

BUFFLER R.T. (1991). – Seismic stratigraphy of the deep gulf of Mexico Basin and adjacent margins. *In*: A. SALVADOR, Ed., The gulf of Mexico basin. – GSA, The Geology of North America J, 353-387.

EBENIRO J., NAKAMURA Y., SAWYER D. & O'BRIEN W. (1988). – Sedimentary and crustal structure of the northwestern gulf of Mexico. – *J. Geophys. Res.,* **93**(B8). doi: 10.1029/88JB00421.

FLOTTÉ N., MARTINEZ J., RANGIN C., HUSSON L., TARDY M. & LE PICHON X. – The Rio Bravo fault, a major late Eocene-Oligocene left-lateral shear zone. – *Bull. Soc. géol. Fr,* **179**, 2, 147-160.

FENG J. & BUFFLER R. T. (1996). – Post Mid-Cretaceous depositional history, gulf of Mexico basin. – *GCAGS Trans.,* **XLVI**, 9-25.

GALLOWAY W. E., GANEY-CURRY P. E., LI X. & BUFFLER R. T. (2000). – Cenozoic depositional history of the gulf of Mexico basin. – *AAPG Bull.,* **84**(11), 1743-1774.

HUH S., WATKINS J. S., KASANDE R., FIDUK J.C., BRYANT S., SILVER K.E., BRADSHAW B.E., XUE F. & XI J. (1996). – Regional structure and tectonics of the Texas shelf. – *GCAGS Trans.,* **XLVI**, 39-51.

HUSSON L., HENRY P. & LE PICHON X. (2008). – Thermal regime of the NW shelf of the gulf of Mexico. (part 1): Thermal and pressure fields. – *Bull. Soc. géol. Fr,* **179**, 2, 129-137.

HUSSON L., LE PICHON X., HENRY P., FLOTTÉ N. & RANGIN C. (2008). – Thermal regime of the NW shelf of the gulf of Mexico. Part 2. Heat Flow. – *Bull. Soc. géol. Fr,* **179**, 2, 139-145.

JACKSON M. & GALLOWAY W. (1984). – Structural and depositional styles of Gulf Coast Tertiary continental margins: application to hydrocarbon exploration. – *AAPG Educ. Course Notes*, **25**, 4-150.

LE ROY C. & RANGIN C. (2008). – Cenozoic crustal deformation of the offshore Burgos basin region (NE Gulf of Mexico), a new interpretation of deep penetration multi-channel seismic reflection lines. – *Bull. Soc. géol. Fr,* **179**, 2, 161-174.

LE ROY C., RANGIN C., LE PICHON X., HAI NGUYEN THI NGOC, ANDREANI L. & ARANDA-GARCÍA M. (2008). – Neogene crustal shear zone along the western Gulf of Mexico margin and its implications for gravity sliding processes: Evidences from 2D and 3D multichannel seismic data. – *Bull. Soc. géol. Fr,* **179**, 2, 175-185.

LISTER G.S., ETHERIDGE M.A. & SYMONDS P.A. (1986). – Detachment faulting and the evolution of passive continental margins. – *Geology*, **14**, 246-250.

MARTON G. & BUFFLER R.T. (1994). – Jurassic reconstruction of the Gulf of Mexico basin. – *Internat. Geol. Rev.,* **36**, 545-586.

NAGIHARA S. & JONES K.O. (2005). – Geothermal heat flow in the northeast margin of the Gulf of Mexico. – *AAPG Bull.*, **89**, 821-831

OLDENBURG D.W. (1974). – The inversion and interpretation of gravity anomalies. – *Geophysics,* **4**, 526–536.

PARKER R.L. (1977). – Understanding inverse theory. – *Ann. Rev. Earth planet. Sci.*, **5**, 35-64.

RANALLI G. (1995). – Rheology of the Earth 8 (2nd edition). – Chapman and Hall, London, 413 pp.

REED J.M. (1994). – Probable Cretaceous to Recent rifting in the Gulf of Mexico basin. Part 1. – *J. Petrol. Geol.,* **17**, 4, Z9-629 666.

ROWAN M.G., JACKSON M.P.A. & TRUGDHILL B.D. (1999). – Salt-related fault families and fault welds in the northern Gulf of Mexico. – *AAPG Bull.,* **83**, 1454-1484.

SALVADOR A. (1987). – Late Triassic-Jurassic paleogeography and origin of Gulf of Mexico basin.– *AAPG Bull.,* **71**, 419–451.

SILVER L.T. & ANDERSON T.H. (1974). – Possible left-lateral early to middle Mesozoic disruption of the southwestern North American craton margin. – *Geol. Soc. Amer. Abstr. Progr.,* **6**, 7, 955-956.

SIMMONS G.R. (1992). – The regional distribution of salt in the northwestern Gulf of Mexico: styles of emplacement and implications for early tectonic history. – Unpub. Ph.D. Dissert., Texas A & M Univ., 180p.

TARDY M. (1980). – Contribution à l'étude géologique de la Sierra Madre Orientale du Mexique. – Thèse de Doctorat d'Etat, Univ. Pierre et Marie Curie de Paris, France, 459 p. (Unpublished).

VENDEVILLE B. & COBBOLD P. R. (1987). – Syn-sedimentary gravitational sliding and listric normal growth faults: Insights from scaled physical models. – *C. R. Acad. Sci.,* Paris, **305**, IIa, 1313-1319.

VENDEVILLE B. & JACKSON M.P.A. (1992a). – The fall of diapirs during thin skinned extension. – *Mar. Petrol. Geol.,* **9**, 331-353.

VENDEVILLE B. & JACKSON M.P.A. (1992b). – The rise of diapirs during thin skinned extension. – *Mar. Petrol. Geol.,* **9**, 354-371

WATKINS L.S., LADD W.J., BUFFLER T.R., SHAUB F., HOUSTON H. & WORZEL L.J. (1978). – Occurrence and evolution of salt in deep gulf of Mexico. – *AAPG Bull.*, **43**, 65, 629-666.

WERNICKE B. (1985). – Uniform-sense normal simple shear of the continental lithosphere. – *Can. J. Earth Sci.*, **22**, 108-125.

WHITE W.A., CALNAN T.R., MORTON R.A., KIMBLE R.S., LITTLETON T.G., MCGOWEN J.H., NANCE H.S. & SCHMEDES K.E. (1986). – Submerged lands of Texas, Brownsville-Harlingen area: sediments, geochemistry, benthic macroinvertebrates, and associated wetlands. – Bur. Econ. Geol., The Univ. Texas at Austin, 138 pp. + maps.

1.2 Croissance crustale des chaînes de montagnes : le cas des Andes Centrales

Si l'hypothèse d'isopactité prévaut dans les avant-pays plissés, elle ne s'applique pas dans les parties plus internes où la croûte est épaissie. Cette assertion se vérifie simplement en comparant les épaisseurs crustales et le raccourcissement mesuré en surface, comme dans les Andes Centrales, ainsi qu'il est montré dans l'article suivant. L'explication mécanique est la dépendence en température de la rhéologie. Les observations indirectes -cinématiques en particulier- avaient permis d'envisager cette dépendence ; elles ont été ultérieurement corroborées par des mesures directes [Goetze, 1978, Hirth & Kohlstedt, 1995a,b, Kirby, 1983, Kirby & Kronenberg, 1987]. Bien que ces mesures restent naturellement insatisfaisantes puisque les facteurs d'échelles spatiale et temporelle ne permettent pas d'extrapoler avec certitude, elles illustrent une dépendence de type Arrhenius de la viscosité. Les croûtes épaisses, réchauffée par leurs propres productions radiogéniques, atteignent des températures suffisantes pour faire chuter la viscosité effective de la croûte de plusieurs ordres de grandeur. La décroissance exponentielle de la viscosité devient primordiale sur la dynamique lorsque les croûtes deviennent épaisses [Bird, 1991]. Les vitesses caractéristiques de fluage de la croûte inférieure, excité par les contraintes gravitationelles dues aux variations d'épaisseur crustale, deviennent alors grandes au regard de sa vitesse de raccourcissement. La croûte ne s'épaissit plus mais la chaîne de montagne se propage latéralement, conduisant à la formation d'un haut plateau. Les cas du Tibet [Clark & Royden, 2000, Royden et al., 1997] ou des Andes [Gerbault et al., 2005, Yang et al., 2003] sont symptomatiques, celui des Andes est développé dans l'article suivant, en collaboration avec T. Sempere.

Thickening the Altiplano crust by gravity-driven crustal channel flow

L. Husson and T. Sempere

Institut de Recherche pour le Développement, Lima, Perú

Received 4 January 2003; revised 4 February 2003; accepted 6 February 2003; published 12 March 2003.

[1] In the Central Andes, crustal thickness is not well correlated to upper crustal shortening. Only little shortening is documented in the upper crust of the 60–65 km-thick Altiplano plateau, whose thickening and uplift were delayed with respect to earlier and greater thickening in the adjacent Western and Eastern Cordilleras. Because crustal thickness variations induce horizontal stress gradients and cause crustal flow, a thickness-dependent channel flow is modeled here and applied to the Central Andes. *In situ* thickening is assumed for both cordilleras, while the Altiplano crustal thickening is generated by lateral flow from these overthickened adjacent domains. A $\sim 8.10^{18}$ Pa s viscosity channel is predicted for crustal thicknesses exceeding 45–50 km to match the estimated topographic evolution of the Central Andes. Thickening in the cordilleras was sufficient to generate a flow of 6.10^9 m^3 per unit length toward the initially ~30–35 km-thick Altiplano. *INDEX TERMS:* 3210 Mathematical Geophysics: Modeling; 5104 Physical Properties of Rocks: Fracture and flow; 8164 Tectonophysics: Evolution of the Earth: Stresses—crust and lithosphere; 8102 Tectonophysics: Continental contractional orogenic belts; 8122 Tectonophysics: Dynamics, gravity and tectonics. **Citation:** Husson, L., and T. Sempere, Thickening the Altiplano crust by gravity-driven crustal channel flow, *Geophys. Res. Lett.*, *30*(5), 1243, doi:10.1029/2002GL016877, 2003.

1. Introduction

[2] The origin of the Altiplano plateau is poorly understood. In the Bolivian Orocline, i.e. the central segment of the Central Andes, upper crustal shortening estimates do not correlate well with total crustal thickness [*Kley and Monaldi*, 1998]. The largest deviation is found for the 60–65 km-thick [*Beck et al.*, 1996] Altiplano crust: in this domain, the pre-Neogene total crustal thickness was ~30–35 km [*Sempere et al.*, 2002] and only minor (<10–15%) upper crustal shortening has occurred during the Neogene [*Rochat et al.*, 1999]. This profound discrepancy means that homogeneous crustal shortening cannot have been responsible for the Altiplano crustal growth. We address this issue by testing the hypothesis that the Bolivian Orocline has developed heterogeneously from gravity-driven channel flow of crustal material injected from overthickened areas of the Western and Eastern Cordilleras towards the Altiplano.

2. Relevant Characteristics of the Bolivian Orocline

[3] The Bolivian Orocline (BO) is commonly divided into a number of geomorphic zones (Figure 1), among which the Altiplano plateau is the most characteristic due to its 3600 m mean elevation and 60–65 km crustal thickness [*Isacks*, 1988; *Beck et al.*, 1996]. The Altiplano is bounded by the Eastern Cordillera (EC), which originated mainly from tectonic shortening [e.g., *Sheffels*, 1990], and by the Western Cordillera (WC), where cluster the volcanoes of the subduction arc. Both EC and WC crustal thicknesses are, at least locally, over 70 km [*Beck et al.*, 1996], but there is no evidence that the WC, unlike the EC, originated from tectonic contraction only. West of the WC, which is largely covered by Late Neogene volcanics, the Coastal Belt displays a west-tapering 65–0 km-thick crust [*ANCORP Working Group*, 1999] and a complex history. In contrast, the EC has resulted from the Oligocene-Miocene tectonic inversion of a Triassic-Jurassic rift system [*Sempere et al.*, 2002]. East of the EC, between 18°S and 23°S, the Subandean Zone (SAZ) is a Neogene fold-and-thrust belt, the foredeep of which underlies the Chaco plain [e.g., *Dunn et al.*, 1995].

[4] Models of Andean uplift [*Gregory-Wodzicki*, 2000; *Kennan*, 2000] consider that the onset of the WC uplift occurred 60 Ma ago, and that the EC uplift developed later and slower (Figure 2a). This first stage of mountain growth last until the Late Paleogene, when the WC and EC reached elevations of ~2000 m and ~1000 m respectively. Uplift rates of both cordilleras have increased since 20 Ma, leading to the present-day high elevations. Located between them, the Altiplano uplift mainly occurred during the last 20–10 Ma, and thus was delayed with respect to the cordilleras.

3. Discrepancies Between Shortening Rates and Crustal Thicknesses

[5] The present-day crustal thickness in the EC can be explained by intense inversion and tectonic contraction of previously thinned crust [*Sempere et al.*, 2002]. According to shortening estimates [e.g., *Rochat et al.*, 1999], bulk strain in the EC is ~0.4, in agreement with its 70 km crustal thickness. In the SAZ, minimum bulk strain is ~0.45, but its overall crustal thickening has been only moderate due to its thin-skinned deformation.

[6] The high crustal thickness of the WC has not been satisfactorily explained yet: tectonic shortening, magmatism, and possibly other in-situ crustal growth processes (see, *Lamb and Hoke* [1997] for a review) have contributed to crustal growth.

[7] Figure 3 compares the actual crustal thickness and the crustal thickness predicted by assuming *in situ* crustal thickening correlated to upper crustal bulk strain across the BO. The SAZ presents a large excess of crustal volume, whereas the Altiplano is characterized by a significant deficit (bulk strain ~0.12). Because this discrepancy cannot be explained by homogeneous crustal deformation, we explore the hypothesis that thickening of the Altiplano crust

Copyright 2003 by the American Geophysical Union.
0094-8276/03/2002GL016877$05.00

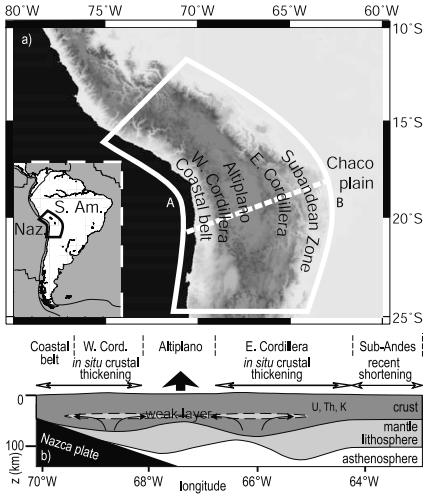

Figure 1. Location map of the considered area of the Central Andes and b) schematic lithospheric cross-section (after *Beck et al.*, 1996; *Myers et al.*, 1998, *Yuan et al.*, 2000).

originated by viscous flow from the overthickened WC and EC crusts.

4. Viscous Mid/Lower Crustal Channel Flow

[8] Laboratory experiments suggest that the viscosity exponentially decreases with temperature [e.g., *Goetze*,

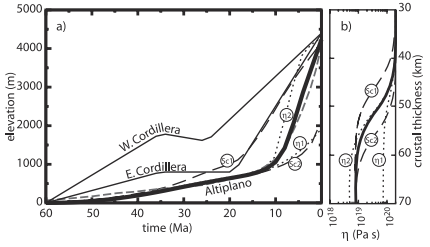

Figure 2. a) Observed uplift for the E. and W. Cordilleras (solid lines) and Altiplano (gray dashed) [*Kennan*, 2000], and predicted Altiplano uplift for the thickness-dependent viscosity attitudes shown in b). Only EC and WC uplifts are inputs for the model, Altiplano is given as a reference. Heavy black curve is the best fit model, dashed lines and dotted lines show the effect of varying *Sc* and η_{min}, respectively. Predicted Altiplano elevations are given at its center.

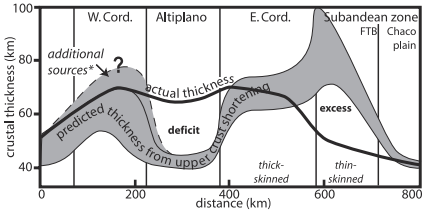

Figure 3. Deviation between the actual crustal thickness (solid line, after *Beck et al.*, 1996) and crustal thickness predicted from estimates of *in situ* crustal growth in the Central Andes (gray area); *additional sources* refer to other processes for crustal growth (e.g. magmatism, underplating).

1978; *Kirby*, 1983]. Thus viscosity strongly decreases at some critical depth in thick crusts. This in turns help to understand why the upper crust is more likely described by an elastic/brittle behavior and the lower crust by a ductile behavior. Following *Bird* [1991], models have demonstrated that a lateral flow in the middle to lower crust may explain geological observations [e.g., *Royden*, 1996; *McQuarrie and Chase*, 2000; *Clark and Royden*, 2000]. We model the response of a low-viscosity material flowing into a channel under a topographic load. Lateral flow variations induce vertical injection from the mid/lower crust and crustal thickness variations. The flow Q is assumed to occur within a channel of constant thickness C and can be described by a Poiseuille flow for a Newtonian fluid [e.g., *Turcotte and Schubert*, 1982], by the equation

$$Q = \frac{C^3}{12\eta}\frac{\partial P}{\partial x}, \qquad (1)$$

where η is the viscosity, and $\frac{\partial P}{\partial x}$ the lateral pressure gradient. We assume that the lateral pressure gradient only depends on the lateral density variations related to crustal thickness. The change in crustal thickness S through time is given by the flow lateral variation and writes

$$\frac{\partial S}{\partial t} = g\rho_c \frac{C^3}{12}\frac{\partial}{\partial x}\left(\frac{1}{\eta}\frac{\partial h}{\partial x}\right), \qquad (2)$$

where g is the gravitational acceleration and h the predicted elevation (h varies through time by Airy-type isostasy with $\frac{\partial h}{\partial t} = \frac{\rho_m - \rho_c}{\rho_m}\frac{\partial S}{\partial t}$), where ρ_m and ρ_c are the mantle and crust densities, of 3300 kg m^{-3} and 2800 kg m^{-3} respectively). Changes in crustal thickness are calculated assuming incompressibility ($\nabla\vec{v}$ where $\vec{v}$ is the velocity). In our model, the negative lateral flow variations from the zones which tend to collapse are instantaneously compensated, *i.e.* the net balance of flowing material is always positive and the total volume increases through time due to shortening in the cordilleras. We assume that the warm flowing material, while injected in a thinner crust, cools and retrieves the viscosity of the material embedding the channel (*i.e.* undeformable). The channel thickness may range from 5 km to 25 km [*Wernicke*, 1990]; here C is fixed to 15 km (see discussion). Viscosity exponentially relates to the thermal

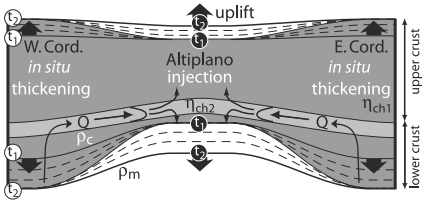

Figure 4. Conceptual model for the lateral injection of mid-lower crust below the Altiplano.

field; as the thermal regime of a thick crust increases due to radiogenic heat production, we now assume that the viscosity of the channel is a direct function of the crustal thickness (neglecting any delay for thermal relaxation). On this basis, the viscosity strongly decreases around a critical depth S_c, and a low-viscosity layer appears within thick crusts. We subsequently define the channel viscosity η_{ch} as a function of crustal thickness S by

$$\eta_{ch} = \eta_{\min} - \frac{(\eta_{\max} - \eta_{\min})}{2}\left(1 + \tanh\frac{(S - S_c)}{\Delta_\eta}\right), \qquad (3)$$

5. Modeling the Altiplano Crustal Growth

[9] We now apply our model to the BO, in order to characterize the critical thickness S_c for which a strong viscosity decrease occurs, the length parameter over which it occurs Δ_η, and to give estimates of the maximum and minimum viscosities η_{min} and η_{max} (see profiles Figure 2b).

[10] As the crust thickens (*in situ* thickening, from t_1 to t_2, Figure 4), its base gradually melts as a function of thickness, and melted fractions are incorporated into the mid-lower crust, lowering its average viscosity to η_{ch}; this layer may correspond to the partially molten zone inferred within the Andean crust [e.g. *Yuan et al.*, 2000, Figure 1]. The channel is bounded laterally by the subducting Brazilian craton and Nazca plate. Density contrasts due to lateral thickness variations drive the channel-flow Q described by equation (1) into the thinner Altiplano crust, inducing its uplift without any shortening.

[11] We calibrate the viscosity variations using the present-day topography together with uplift estimates from *Kennan* [2000] and *Gregory-Wodzicki* [2000]. Uplift rates are converted into *in situ* crustal growth rates from isostasy for both WC and EC (Figure 2a). The best fit between estimates and the predicted evolution of the overall topography occurs for a viscosity decrease from 2.10^{20} Pa s to 8.10^{18} Pa s, for a critical crustal thickness S_c of 47 km, over a 10 km step Δ_η (Figure 2b). Uncertainty on WC and EC elevation input values is ~500 m (L. Kennan, personal communication, 2002) inducing variations in the Altiplano predicted elevation also of ~500 m. Uncertainties in input elevations correspond to variations in both *Sc* and $\Delta\eta$ by ~5 km for similar Altiplano uplift rates.

[12] This predicted viscosity also matches the results of previous depth-dependent or temperature-dependent models, with a strong viscosity decrease (10^{19} Pa s in the channel) for crusts thicker than 40–50 km [*Clark and Royden*, 2000; *McQuarrie and Chase*, 2000; *Medvedev and Beaumont*, 2001]. Viscosity estimates from full-2D models involving more complex rheologies [e.g., *Beaumont et al.*, 2001] are also in the same range. The low viscosity found for the channel is expected for temperatures higher than 600–700°C, consistent with the observations of partially molten rocks within the crust of high plateaus.

6. Discussion

[13] Various processes have been suggested for plateau formation, but they seldom explain all observations when applied to the Andes. Other studies that favor that "blind" brittle shortening would have occurred below the Altiplano as deep as ~26–44 km [e.g., *McQuarrie and DeCelles*, 2001] are contradicted by laboratory experiments [e.g., *Goetze*, 1978; *Kirby*, 1983] and by seismological data, which both suggest that the lower crust is ductile, at least locally as shallow as 18 km [e.g., *Yuan et al.*, 2000]. Mantle delamination [e.g., *Platt and England*, 1994] is insufficient to produce major uplift (<800 m, *Husson* [2001]) and does not induce crustal thickening. Thickening by magmatic addition [*Kay and Mpodozis*, 2001] on the time scale of an orogenesis would involve considerable heat advection, which would appear on the surface heat flow signal. Eventually, homogeneous crustal deformation is incompatible with the observed upper crust shortening.

[14] Although the average viscosity of the lithosphere is generally considered to be about 10^{21} to 10^{22} Pa s [e.g., *England*, 1986; *Wdowinski et al.*, 1989] the viscosity of the crust is highly variable with depth due to the elevated crustal geotherm. Conversion of rheological envelopes (after e.g., *Ranalli and Murphy* [1987]) into Newtonian viscosity profiles indicates that viscosity in thick crust is low (<10^{19} Pa s) at depth for typical geotherms. Our model supports the theoretical results for mid-lower crustal flow within high plateaus. Significant channel weakening (<10^{19} Pa s) occurs for critical crustal thickness of 40 to 50 km, while normal (e.g. 35 km thick) crust channel viscosity would be higher than 2.10^{20} Pa s. Note that a higher channel viscosity for normal crust does not affect our results as most of the predicted Altiplano uplift occurred when both cordilleras had thickened up to 40–50 km, and 2.10^{20} Pa s is thus a lower bound. As emphasized by *Clark and Royden* [2000], due to the uncertainty in channel thickness, the results for channel viscosity are nonunique, as they scale with C^3/η. Variations in C from 10 to 20 km must be balanced by variations in η_{min} and η_{max} from 2.4 10^{18} Pa s to 1.9 10^{19} Pa s and from 6.10^{19} Pa s to 9.5 10^{20} Pa s, respectively, giving a range of channel viscosities of almost one degree of magnitude. Our estimates for the viscosity profile are based on the assumption that temperature, and thus viscosity, is a function of crustal thickness. But apart from radiogenic heating, various thermal processes are heterogeneously distributed in orogens. Full-2D models could more likely integrate these processes. However, our poor knowledge of the distribution of heat sources limits integrative analysis, and simple models with restricted number of free parameters yield more informative results.

[15] In the Central Andes, the heat flow is globally correlated to crustal thickness [*Springer and Forster*, 1998; *Husson and Moretti*, 2002]. To a first order approximation, viscosity may be more conveniently described as

thickness-dependent (rather than truly temperature-dependent). Our model suggests that the present-day Altiplano crust has been almost equally fed by both cordilleras (3.10^9 m^3 per unit length flowing eastward and as much westward), but an uneven distribution of thermal sources could locally limit or enhance weakening and imply an asymmetric flow (only the cumulative flows are equal as they vary through time).

[16] About volume balance in the Central Andes, we propose that: (i) Large amounts of excess crustal volume flow from the SAZ to the EC lower crust. For a 30 km-thick basement shortened by 70 km to 150 km [e.g., *Dunn et al.*, 1995; *Rochat et al.*, 1999], the volume accreted to the EC ranges between 2.1 10^9 and 4.5 10^9 m^3 per unit length. (ii) The EC shows a fair correlation between upper crustal strain and crustal thickness. However, the expected excess crustal material incorporated from the SAZ is difficult to evidence as crustal mass also flows from the EC into the Altiplano. (iii) No significant *in situ* crustal growth can be invoked for the Altiplano, and its crustal volume represents the injected mass from the middle and lower crusts of the adjacent cordilleras. This interpretation is supported by the timing (Altiplano uplift delayed with respect to the cordilleras), which illustrates the time span necessary for viscous processes to develop, and by its crustal growth without significant upper crustal shortening. (iv) Ductile crust was likely to flow into the Altiplano from the WC. In this area early shortening was possibly larger than currently evaluated and that more recent strain was low; additional processes like magmatic addition or underplating might have contributed to its crustal growth.

[17] The recent vertical uplift of the coastal area of southern Peru and northern Chile can also be explained by a similar process of lateral crustal flow from the overthickened WC toward the coast. The issue of the Altiplano crustal thickening should also be considered in 3D, as along-strike ductile crustal flow may have participated in crustal thickening of the northern and southern Central Andes.

[18] **Acknowledgments.** This study is a contribution of IRD's UR 104 (*Continental Lithospheric Deformation in Convergence Zones and Material Transfers*). We acknowledge S. Wdowinski and S. Medvedev for their reviews.

References

ANCORP Working Group, Seismic reflection image revealing offset of Andean subduction-zone earthquake locations into oceanic mantle, *Nature*, *397*, 341–344, 1999.

Beaumont, C., R. A. Jamieson, M. H. Nguyen, and B. Lee, Himalayan tectonics explained by injection of a low-viscosity crustal channel coupled to focused surface denudation, *Nature*, *414*, 738–742, 2001.

Beck, S. L., G. Zandt, S. C. Maers, T. C. Wallace, P. G. Silver, and L. Drake, Crustal scale variations in the central Andes, *Geology*, *24*, 407–410, 1996.

Bird, P., Lateral extrusion of lower crust from under high topography, in the isostatic limit, *J. Geophys. Res.*, *96*, 10,275–10,286, 1991.

Clark, M. K., and L. H. Royden, Topographic ooze: Building the eastern margin of Tibet by lower crustal flow, *Geology*, *28*, 703–706, 2000.

Dunn, J., K. G. Hartshorn, and P. W. Hartshorn, Structural styles and hydrocarbon potential of the sub Andean thrust belt of southern Bolivia, in *Petroleum Basins of South America*, edited by R. Tankard, S. Suarez, and H. J. Welsink, *AAPG Mem.*, *62*, 523–543, 1995.

England, P., Comment on "Brittle failure in the upper mantle during extension of continental lithosphere" by Dale S. Sawyer, *J. Geophys. Res*, *91*, 10,487–10,490, 1986.

Goetze, C., The mechanisms of creep in olivine, *Philos. Trans. R. Soc. London, Ser. X*, *288*, 99–119, 1978.

Gregory-Wodzicki, K. M., Uplift history of the central and northern Andes: A review, *Geol. Soc. Am. Bull.*, *112*, 1091–1105, 2000.

Husson, L., Dynamique et régime thermique des chaînes de montagnes—Application aux Andes centrales, Ph.D. thesis École Normale Supérieure de Lyon, France, 2001.

Husson, L., and I. Moretti, Thermal regime of fold and thrust belts-An application to the Bolivian Sub Andean Zone, *Tectonophysics*, *345*, 253–280, 2002.

Isacks, B. L., Uplift of the central Andean plateau and bending of the Bolivian orocline, *J. Geophys. Res.*, *93*, 3211–3231, 1988.

Kay, S., and C. Mpodozis, Central Andean ore deposits linked to shallow subduction systems and thickening crust, *GSA Today*, *11*, 4–9, 2001.

Kennan, L., Large-scale geomorphology of the Andes: Interrelationships of tectonics, magmatism and climate, in *Geomorphology and Global Tectonics*, edited by M. A. Summerfield, pp. 167–199, John Wiley, New York, 2000.

Kirby, S. H., Rheology of the lithosphere, *Rev. Geophys.*, *21*, 1458–1487, 1983.

Kley, J., and C. R. Monaldi, Tectonic shortening and crustal thickness in the central Andes: How good is the correlation?, *Geology*, *26*, 723–726, 1998.

Lamb, S. H., and L. Hoke, Origin of the high plateau in the central Andes, Bolivia, South America, *Tectonics*, *16*, 623–649, 1997.

McQuarrie, N., and C. G. Chase, Raising the Colorado plateau, *Geology*, *28*, 91–94, 2000.

McQuarrie, N., and P. DeCelles, Geometry and structural evolution of the central Andean backthrust belt, Bolivia, *Tectonics*, *20*, 669–692, 2001.

Medvedev, S., and C. Beaumont, Models for mid and lower crustal channel flows (abstract), *Eos Trans. AGU*, *82*(47), Fall Meet. Suppl., Abstract T12D-0937, 2001.

Meyers, S. C., S. Beck, G. Zandt, and T. Wallace, Lithospheric-scale structure across the Bolivian Andes from tomographic images of velocity and attenuation for *P* and *S* waves, *J. Geophys. Res.*, *103*, 21,233–21,252, 1998.

Platt, J. P., and P. C. England, Convective removal of lithosphere beneath mountain belts: Thermal and mechanical consequences, *Am. J. Sci.*, *294*, 307–336, 1994.

Ranalli, G., and D. C. Murphy, Rheological stratification of the lithosphere, *Tectonophysics*, *132*, 281–295, 1987.

Rochat, P., G. Hérail, P. Baby, and G. Mascle, Bilan crustal et contrôle de la dynamique erosive et sédimentaire sur les mécanismes de formation de l'Altiplano, *C. R. Acad. Sci., Ser. X*, *328*, 189–195, 1999.

Royden, L., Coupling and decoupling of crust and mantle in convergent orogens: Implications for strain partitioning in the crust, *J. Geophys. Res.*, *101*, 17,679–17,705, 1996.

Sempere, T., et al., Late Permian-Middle Jurassic lithospheric thinning in Peru and Bolivia and its bearing on Andean-age tectonics, *Tectonophysics*, *345*, 153–181, 2002.

Sheffels, B. M., Lower bound on the amount of crustal shortening in the central Bolivian Andes, *Geology*, *18*, 812–815, 1990.

Springer, M., and A. Forster, Heat flow density across the central Andean subduction zone, *Tectonophysics*, *291*, 123–139, 1998.

Turcotte, D. L., and G. Schubert, *Geodynamics: Applications of Continuum Physics to Geological Problems*, 450 pp., John Wiley, New York, 1982.

Wdowinski, S., R. O'Connell, and P. England, A continuum model of continental deformation above subduction zones: Application to the Andes and the Aegean, *J. Geophys. Res.*, *94*, 10,331–10,346, 1989.

Wernicke, B. P., The fluid crustal layer and its implications for continental dynamics, in *Exposed Cross-Sections of the Continental Crust*, edited by M. H. Salisbury and D. M. Fountain, pp. 509–544, Kluwer Acad., Norwell, Mass., 1990.

Yuan, X., et al., Subduction and collision processes in the central Andes constrained by converted seismic phases, *Nature*, *408*, 958–961, 2000.

L. Husson, Laboratoire de Géologie, Ecole Normale Supérieure, 24 rue Lhomond, 75231 Paris cedex 05, France. (husson@geologie.ens.fr)

T. Sempere, I. R. D.-Perú, casilla 18-1209, Lima 18, Peru. (sempere@terra.com.pe)

1.3 Les chaînes de montagnes aux frontières de plaques

Dans le chapitre précédent, la stabilité crustale était perçue dans un cadre où les forces aux limites sont implicites, apparaissent comme le résultat d'une dynamique plus globale, mais ne sont pas analysées. C'est en dé-zoomant de nouveau que la chaîne de montagne devient au premier ordre un bourrelet à la frontière entre deux plaques et peut être appréhendée dans le cadre de la tectonique des plaques. Cette idée n'est pas nouvelle et peut être considérée comme relevant des travaux séminaux d'Argand [1924] : une chaîne de montagne ne saurait être maintenue en équilibre sans l'existence de forces aux limites dont la magnitude est comparable aux forces gravitationelles.

1.3.1 Les montagnes, contrebalancier des forces aux limites

Une originalité de l'approche que nous développons ici avec Y. Ricard est, en considérerant la dynamique de la lithosphère comme une réponse à la sollicitation par les forces aux limites, d'utiliser les observations cinématiques et morphologiques pour quantifier ces mêmes forces. Les contraintes gravitationnelles n'équilibrent pas totalement les contraintes aux limites (sans quoi il n'y aurait aucune déformation permettant même d'édifier la chaîne de montagnes) : les contraintes visqueuses contribuent -dans une moindre mesure que les contraintes gravitationelles- à équilibrer le système dynamique des orogènes. Les montagnes sont alors perçues comme un contrebalancier aux forces aux limites qui animent la tectonique des plaques. Puisque les forces inertielles sont négligeables dans les processus tectoniques, la géométrie et la cinématique des chaînes de montagnes témoignent directement de ces forces tectoniques aux limites : les zones où la convergence entre les plaques est animée par des forces élevées s'accompagnent de montagnes élevées. Les montagnes doivent donc être comprises comme des indicateurs dynamiques et non cinématiques. Ce concept apparaît dans les vitesses de convergence à la surface de la Terre, qui varient peu tandis que les forces de flottabilité dans les chaînes de montagnes (que l'ont peut inférer à partir de leur géométrie, *c.f.* article ci-dessous et fig. 4.2) varient de plus d'un ordre de grandeur. En d'autres termes, en supposant une mécanique linéaire, il ressort que les montagnes modulent les vitesses tectoniques lorsque le régime permanent de la

convergence est atteint. Une illustration est la diminution de la vitesse de convergence entre les plaques Indienne et Eurasienne lorsque la collision himalayenne prend place [Allègre et al., 1984, Patriat & Achache, 1984]. D'apparence triviale, cette base de reflexion n'est en fait que peu prise en considération dans la vaste majorité des études de la dynamique orogénique, pour lesquelles les modèles - conceptuels ou physiques- sont pilotés par des conditions aux limites en vitesses et non en contraintes. Les résultats de modèles classiques [Avouac & Burov, 1996, Beaumont et al., 2001, Willett, 1999] sont biaisés pour cette raison. Ce concept est un pilier de mes travaux sur la géodynamique globale présenté en section 4, dans laquelle je met en évidence la rétroaction de la dynamique orogénique sur la tectonique des plaques et la circulation mantellique à l'échelle globale.

Techniquement, l'approximation de la lithosphère à une plaque mince uniformement visqueuse est pertinente à cette échelle. Cette méthode a été essentiellement introduite par England & McKenzie [1982, 1983] au début des années 80. En intégrant la mécanique sur l'épaisseur de la lithosphère, le problème perd une dimension. Les contraintes aux limites peuvent être introduites normalement à l'épaisseur de la lithosphère (comme dans la majorité des études en plaques minces, [England & Houseman, 1985, England & McKenzie, 1982, 1983]) et/ou comme un cisaillement alternativement moteur ou résistant à la base de la lithosphère, comme dans l'exemple proposé ci-dessous. Les contraintes visqueuses sont calculées à partir du taux de déformation et de la viscosité effective de la lithosphère, pour laquelle nous proposons en retour une valeur. Enfin, les contraintes de flottabilité sont exprimées en introduisant un terme ayant la dimension d'un moment et du nombre d'Argand Ar, en référence aux travaux précurseurs de Emile Argand au début du $20^{\text{ème}}$ siècle [Argand, 1924]. Au regard de sa simplicité, cette méthode s'est montrée puissante pour mettre en évidence les mécanismes de déformation de la lithosphère [e.g., England & Houseman, 1985].

Dans l'article suivant, le cas des Andes en particulier est examiné. Les contraintes aux limites sont extraites à partir de la cinématique de déformation de la chaîne de montagne, et une quantification de la valeur de la viscosité effective de la lithosphère est proposée.

Available online at www.sciencedirect.com

SCIENCE DIRECT®

Earth and Planetary Science Letters 222 (2004) 1037–1050

EPSL

www.elsevier.com/locate/epsl

Stress balance above subduction: application to the Andes

L. Husson*, Y. Ricard

Ecole Normale Supérieure de Lyon, Laboratoire des Sciences de la Terre, 46 allée d'Italie, 69364 Lyon Cedex 07, France

Received 19 November 2003; received in revised form 23 March 2004; accepted 26 March 2004

Abstract

The frequent changes in tectonic and morphological evolutions of active plate margins suggest that similar processes drive apparently antagonistic tectonics. We address the problem by a thin viscous sheet approach where the governing stresses are restricted to interplate traction, buoyancy and viscous stresses. Various cases are explored, from compression to extension, leading to dismiss corner-flow-driven models and to favor interplate traction-driven models. From the topography of the Andes, we determine the magnitude and profiles of the current stresses beneath the Andes at various locations. The total transmitted force is about 9×10^{12} N m^{-1}. Shear stresses at the boundaries of the deforming lithosphere range between 25 and 110 MPa and almost balance the buoyancy stresses due to crustal thickening, the remaining difference being the viscous stresses. The deviatoric stress is less than 10 MPa and the effective viscosity of the Andean lithosphere is as low as $\sim 3 \times 10^{21}$ Pa s. Maximum compression is located in the Eastern side of the Andes, matching the geological observations, but we find that the current stress regime is insufficient to explain the present-day elevation. This suggests that interplate traction was slightly stronger in the past when the Neogene plate convergence was faster, and this decrease in interplate traction implies that high and steep parts of the Andes cannot be sustained anymore. The shape of the Altiplano can be explained by a weak lateral variation of the viscosity, which allows the high plateau to be constructed in the characteristic time span of Andean building.
© 2004 Elsevier B.V. All rights reserved.

Keywords: subduction; stress; topography; crustal deformation; fluid dynamics

1. Introduction

Although the main characteristics of subductions are similar anywhere, their morphological and tectonic expressions vary from intensely compressive to extensive through intermediate settings, so that the intraplate stress field has been intensively discussed and remains the focus of many studies (e.g. [1]). Within cratons, the intraplate stress field is mainly neutral or compressive, but it is fairly common to see combined extensional and compressional settings in convergent systems. The Aegean sea and the Tonga trench display extensional patterns, the Japan sea and Italy show coeval extensional and compressional features, while the Andes undergo compression with some areas of neutral/extensional regimes. The tectonic regime also varies through time: for instance the Basin and Range evolved from the Laramide compression to the present-day extension [2]. These changes of tectonic regimes suggest that the physical processes governing deformation differ only slightly from one geodynamic setting to another.

* Corresponding author. Present address: Collège de France, Chaire de Géodynamique, Europôle de l'Arbois 13545, Aix-en-Provence, France.

E-mail address: husson@cdf.u-3mrs.fr (L. Husson).

0012-821X/$ - see front matter © 2004 Elsevier B.V. All rights reserved.
doi:10.1016/j.epsl.2004.03.041

Topography is the consequence of stresses applied to tectonic plates and of their evolution through time. All stresses in Earth are the consequences of lateral variations in the internal density. Plate-driving stresses are mostly resisted by basal shear on the asthenosphere. The role of crustal or lithospheric density variations has been emphasized by many authors [3–11]. Using the thin viscous sheet approximation, Wdowinski et al. [12] concluded that the Andean topography is the consequence of a basal shear induced by corner-flow circulation while the internal sources of stresses due to crustal thickening were neglected. We propose herein an alternative mechanism for mountain building where forces acting on the plate boundaries are balanced by internal stresses arising from crustal thickness variations. We first address the problem using theoretical cases to decipher which forces can be responsible for various geodynamic settings. We then use the observed topography to quantify the stresses acting on the Andean margin, and evaluate the results by considering a time-dependent model.

2. The model

2.1. Thin viscous sheet approximation

The derivation of the thin viscous sheet model for the lithosphere has been discussed in detail in various papers dealing with continental deformation (e.g. [4,13]) and we only briefly discuss the assumptions. The thin sheet model is based on the vertical integration of the Navier–Stokes equations coupled with mass conservation. The lithosphere is stiff enough with respect to the underlying mantle that the vertical variations of the horizontal velocity can be neglected. The lithosphere is also thin enough with respect to the scale of the deformations under consideration that the horizontal gradients of the stresses are negligible with respect to the vertical gradients [14].

In the lithosphere we define σ_{ij}, τ_{ij} and P to be the total stress tensor, the deviatoric stress tensor and the pressure, respectively (i or j stand for x or y as we only derive a two-dimensional model),

$$\sigma_{ij} = \tau_{ij} - P\delta_{ij}. \tag{1}$$

We assume that the lithosphere behaves like an incompressible viscous fluid with

$$\tau_{ij} = \eta\left(\frac{\partial u_i}{\partial x_j} + \frac{\partial u_j}{\partial x_i}\right), \tag{2}$$

where the average effective viscosity of the lithosphere η can be constant, laterally variable or even some non-linear function of the stress tensor. u_i either represents the horizontal velocity or the vertical velocity.

Assuming that the bottom of the lithosphere is subjected to a shear stress Σ (we choose $\Sigma = -\sigma_{xz}$ ($z=0$) so that $\Sigma>0$ on the left margin of the plate induces compression) while the upper surface is stress free. Within the thin sheet approximation, integrating the vertical force balance equation, the vertical equilibrium becomes

$$\frac{1}{2}\frac{(z-L-h)^2}{L+h}\frac{\partial \Sigma}{\partial x} + \sigma_{zz}(z) = \int_{L+h}^{z} \rho g \, \mathrm{d}z, \tag{3}$$

where ρ is the density, g the gravitational acceleration and z the depth measured from the bottom of lithosphere of thickness L. The upper surface topography is at the position $L+h$ ($z \le L+h$). In the following, we set L to 100 km, assuming that the lithospheric mantle diffuses thermally faster than its vertical growth (Fig. 1).

In the usual thin plate approximation, basal tractions are assumed not to be significant. When accounted for, the first term on the left of Eq. (3) is often neglected as the horizontal stress variations are assumed to be with much longer wavelengths than the lithospheric thickness, but this approximation would not be very good for steep mountain belts such as the Andes, where there must be significant tractions.

We integrate vertically the equation expressing the horizontal equilibrium over the lithosphere thickness. One gets

$$\frac{\partial}{\partial x}\int_0^{L+h} \sigma_{xx} \mathrm{d}z + \Sigma = 0. \tag{4}$$

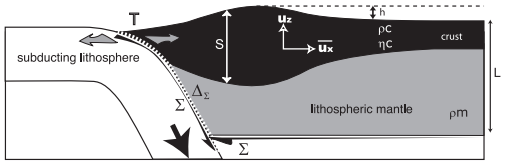

Fig. 1. Sketch model of the subduction zone. See text for legends.

The horizontal total stress σ_{xx} can now be replaced by the sum of the deviatoric and vertical total stresses; $\sigma_{xx} = \tau_{xx} - \tau_{zz} + \sigma_{zz}$. Using Eqs. (2) and (3), we obtain

$$4L\frac{\partial}{\partial x}\bar{\eta}\frac{\partial \bar{u}}{\partial x} + \Sigma = -\frac{\partial}{\partial x}\int_0^{L+h}\mathrm{d}z\int_{L+h}^{z}\rho g \, \mathrm{d}z' - \frac{1}{6}\frac{\partial^2 \Sigma}{\partial x^2}L^2 \tag{5}$$

which describes the horizontal equilibrium (leaving out in the Σ derivatives the terms of lower importance, in h^2 and hL), averaged over the thickness of the lithosphere. Wdowinski et al. [12] implicitly neglected the second order term $(L^2/6)$ $(\partial^2\Sigma/\partial x^2)$. The influence of the density variations only arises from crustal thickness variations and density variations between the lithospheric mantle and asthenosphere are neglected. We can therefore define an isostatic crustal thickness $S = h\rho_m/(\rho_m - \rho_c)$, where ρ_m and ρ_c are the mantle and crust densities, respectively. h is defined with respect to a crust of null thickness (i.e. $h=0$ when $S=0$, and a continent with a typical crustal thickness $S_0 = 35$ km corresponds to a topography of 4375 m). For simplicity, we omit the averaging symbol (overline) for vertically averaged quantities ($\bar{u}$ and $\bar{\eta}$ in Eq. (5)) in the following. After some algebra Eq. (5) gives the following horizontal stress balance equation

$$4L\frac{\partial}{\partial x}\eta\frac{\partial u}{\partial x} = \frac{\rho_c g}{2}\left(1 - \frac{\rho c}{\rho m}\right)\frac{\partial S^2}{\partial x} - \Sigma - \frac{1}{6}\frac{\partial^2 \Sigma}{\partial x^2}L^2. \tag{6}$$

It couples the basal shear Σ, the deviatoric stress $T = -4\eta\partial u/\partial x$ ($T>0$ corresponds to compression), and the buoyancy forces related to S^2. The fact that S^2 (or Sh) rather than S controls the deformation is sometimes called the density moment rule [15].

A non-dimensionalization of Eq. (6) can be performed (e.g. using the length scale L and reference velocity and viscosity, u_0 and η_0) which leads to the introduction of the Argand number Ar [16], which writes accordingly to [4]

$$Ar = \frac{\rho_c g L^2}{2\eta_0 u_0}\left(1 - \frac{\rho_c}{\rho_m}\right). \tag{7}$$

Ar indicates the capability of the lithosphere undergoing buoyancy forces to deform. However, non-dimensional quantities do not simplify the following discussions and we keep dimensional values.

Additionally, for incompressible fluids, the time-dependence of the crustal thickness S is given by:

$$\frac{\partial S}{\partial t} + S\frac{\partial u}{\partial x} + u\frac{\partial S}{\partial x} = 0. \tag{8}$$

By multiplying Eq. (8) by $2S$, one obtains the transport equation of the density moment [17],

$$\frac{\partial S^2}{\partial t} + 2S^2\frac{\partial u}{\partial x} + u\frac{\partial S^2}{\partial x} = 0. \tag{9}$$

Eqs. (6) and (9) are the governing equations of the model (see also [18]).

2.2. General comments

The transport Eq. (9) assumes local mass conservation. This assumption may be flawed in situations with erosion, sedimentation or magmatic addition. Mass variations could be taken into account by a source term in Eq. (8) to account for the net material addition or removal and by a diffusive term to represent transport with erosion and sedimentation.

We do not discuss these processes which affect the velocities (Eq. (9)) but not the stress balance (Eq. (6)).

We only account for lateral variations of density due to changes in crustal thickness. In fact, a dense lithospheric mantle would favor gravitational instabilities. Considering a lithospheric mantle with thickness $L-S$ has a density ρ_L slightly larger than the asthenospheric mantle density ρ_M, the Argand number Ar (Eq. (7)) should be written

$$Ar = \frac{gL^2}{2\eta_0 u_0}\left[\rho_c\left(1-\frac{\rho_c}{\rho_m}\right)+\rho L\left(1-\frac{\rho L}{\rho_m}\right)\frac{(L-S)^2}{S^2} + 2\rho_c\left(1-\frac{\rho L}{\rho_m}\right)\frac{(L-S)}{S}\right]. \quad (10)$$

Ar now includes the lithospheric mantle and is positive as long as $L \leq 4S$ (assuming $\rho_c = 2800$ kg m^{-3}, $\rho_m = 3200$ kg m^{-3} and $\rho_L = 3225$ kg m^{-3}). If $L < 4S$, the dynamics remains qualitatively similar to that described herein although the stabilizing role of internal loads becomes less important. If $L > 4S$, the lithosphere becomes unstable by Rayleigh–Taylor instability. The long-term stability of continents suggests that Ar generally remains positive.

The existence of strong crustal variations between two tectonic units of different crustal thicknesses has to be associated with a change in deviatoric stresses. The x-integration of Eq. (6) across a discontinuity $\Delta S^2 = S^2(0^+) - S^2(0^-)$ of the crustal density moment (strictly speaking, the approximations imply that the crustal density moment change must occur over distances larger than the lithosphere thickness), implies a jump in the deviatoric stress $\Delta T = T^- - T^+$,

$$T^- - T^+ = \frac{\rho_c g}{2L}\left(1-\frac{\rho_c}{\rho_m}\right)(S^2(0^+) - S^2(0^-)), \quad (11)$$

(provided that the two units have similar lithospheric thicknesses L). Indeed, at a passive margin, the assymetry in crustal thickness is equivalent to an extensive stress applied at the continent boundary (~ 20 MPa for $L = 100$ km and a continental crust thickness $S = 35$ km). This extensive stress along the passive margins of South East Asia favors the southeastward extrusion along the collision of India with Asia. The tendency of thick continents to be under extension may be partially counteracted by their dense lithospheric roots that reduces the effective Ar.

By the horizontal integration of Eq. (6) between two tectonic units a and b of same crustal thickness, one gets

$$-L(T^a - T^b) = \int_a^b \Sigma + \frac{1}{6}\frac{\partial^2 \Sigma}{\partial x^2} L^2 \mathrm{d}x. \quad (12)$$

It shows that the change of stress between two tectonic units of same crustal thickness only depends on the basal friction. For instance, the stress change between the two sides of a mountain belt does not depend on the topography of the belt itself.

The system of Eqs. (6) and (9) can have motionless solutions (a zero vertically averaged horizontal velocity u) when the basal shear stress imposed beneath the lithosphere are exactly resisted by the stresses due to variations in the crustal structure.

$$\Sigma + \frac{1}{6}\frac{\partial^2 \Sigma}{\partial x^2} L^2 = \frac{\rho_c g}{2}\left(1-\frac{\rho_c}{\rho_m}\right)\frac{\partial S^2}{\partial x}. \quad (13)$$

In this case of steady state, the stresses at the base of the lithosphere can be deduced from the surface topography.

The lithosphere of the Earth is not in steady state and we will in the following discuss several time-dependent scenarii involving different distributions of stresses. They include compression/tension T at the plate boundary, and traction Σ at its base, either driving or resisting. At this stage, no attempt is made to reproduce a given geological setting.

2.3. Theoretical cases: mountain building at plate margin

We now consider situations where the crust has a uniform thickness S_0 at time $t = 0$ and where the viscosity is uniform and constant. A few experiments introducing a non-linear rheology in our model gave results that differ from the standard runs less than the obvious uncertainty due to the inhomogeneous structure of the lithosphere. To maintain the crust at a steady state, an initial deviatoric stress T_0 has to be applied $T_0 = \rho_c g/(2L)\ (1-\rho_c/\rho_m)\ S_0^2$ at $x = 0^-$. The simplest way to deform the lithosphere is to apply at the plate margin ($x = 0^-$) a deviatoric stress $T_0 + \delta T$ without any shear beneath the lithosphere, $\Sigma(x>0) = 0$. According to (11) the deviatoric stress at $x = 0^+$ is

$$T^+ = \delta T + \frac{\rho_c g}{2L}\left(1-\frac{\rho_c}{\rho_m}\right)(S_0^2 - S^2(t,x^+)). \quad (14)$$

The two deviatoric stresses T^+ and δT are identical at $t = 0$ but then, T^+ decreases with $S^2(t,x^+)$. The horizontal plate velocity is set to 0 at a distance D away from the free border of the plate. Without bottom shear ($\Sigma = 0$), Eq. (6) implies that the deviatoric stress is uniform and according to Eq. (8), the crustal thickness varies in the first time steps as

$$\frac{\mathrm{d}S}{S} = \frac{T^+}{4\eta L}\mathrm{d}t. \quad (15)$$

A normal stress at a plate boundary (e.g. in a collision situation) does not deform the plate locally but uniformly. The situation of uniform deformation is unlike most everyday situations where the dynamics is dominated by inertia and where the application of a normal stress tends to produce local deformation (a car hit in the front deforms in the front). Note that because T^+ decreases when S increases, the final height is reached when $T^+ = 0$.

A situation where the basal traction Σ decreases from the edge toward the hinterland roughly mimics interplate traction at subduction zones. In the first time steps, the deviatoric stress increases with the distance to the trench (again, thickening occurs away from the trench),

$$\frac{\mathrm{d}S}{S} = \frac{\Sigma}{4\eta L}\mathrm{d}t. \quad (16)$$

A similar situation is obtained in Fig. 2 where the shear below the lithosphere exonentially decreases as $\Sigma = \Sigma_0\ \exp(-x/\Delta_\Sigma)$. The crust has an initial uniform thickness S_0. A topography is generated (Fig. 2) over the basal shear zone, with a -quasi-exponentially decreasing slope according to Eq. (16). Away from the zone undergoing interplate traction, a high plateau develops with a final elevation $H \sim \int_0^x (\Sigma + \frac{L^2}{6}\frac{\partial^2 \Sigma}{\partial x^2})\mathrm{d}x/\rho_c g S_0$. The deviatoric stress (Fig. 2) evolves from compressive to neutral when the steady state (Eq. (13)) is reached.

To explain a topography near the plate margin, a basal shear stress toward the trench can be invoked. A corner-flow has indeed been mentioned for mountain building at plate margins (e.g. [12]). This situation corresponds to that depicted in Fig. 3 where we used the same parameters as in Fig. 2, with an exponentially increasing traction toward the trench, although traction for the corner-flow model is often described as proportional to $1/x$. A zero velocity at the trench is required. It implies that a deviatoric stress can build up at the plate margin, resisting the rising stresses induced by the growing topography. As previously, the deviatoric stress decreases during the orogeny (Fig. 3).

In real Earth, the plate motion is resisted by a drag at the lithosphere/asthenosphere boundary. To simulate a subduction zone, we add a resistive stress proportional to the lithospheric velocity u to the previously considered driving basal shear stress, so that Σ is now replaced by $\Sigma - ku$. The shear stress $-ku$ could mimic the traction at the base of the lithosphere of the Couette flow induced by the lithospheric motion [18]. Eq. (6) becomes accordingly

$$4L\frac{\partial}{\partial x}\eta\frac{\partial u}{\partial x} = \frac{\rho_c g}{2}\left(1-\frac{\rho_c}{\rho_m}\right)\frac{\partial S^2}{\partial x} - \Sigma + ku - \frac{L^2}{6}\frac{\partial^2(\Sigma - ku)}{\partial x^2}, \quad (17)$$

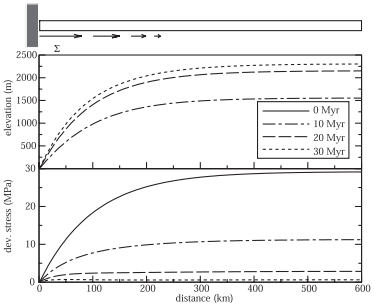

Fig. 2. Elevation and deviatoric stress induced by a basal traction $\Sigma = \Sigma_0 e^{-x/\Delta\Sigma}$ (toward the hinterland), with $\Sigma_0 = 25$ MPa, $\Delta_\Sigma = 100$ km, $L = 100$ km, $\eta = 5\times10^{21}$ Pa s, $\rho_c = 2800$ kg m^{-3} and $\rho_m = 3200$ kg m^{-3}. The initial crustal thickness is $S_0 = 35$ km and the plate length $D = 7000$ km.

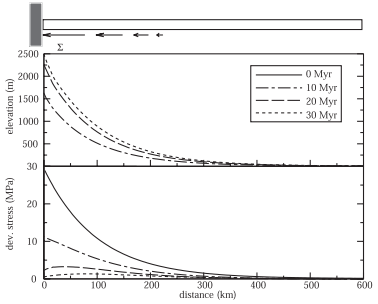

Fig. 3. Deviatoric stress and elevation induced by a basal traction $\Sigma = -\Sigma_0 \exp(-x/\Delta_\Sigma)$ (toward the trench) below the overriding plate. This traction roughly mimics the effect of a corner-flow circulation. Parameters are those of Fig. 2.

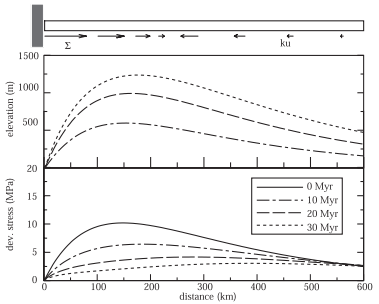

Fig. 5. Elevation and deviatoric stress induced by an exponentially decreasing interplate traction below the overriding plate (as in Fig. 2), resisted by a passive drag at the base of the lithosphere. Parameters are those of Fig. 4.

When Σ is directed toward the trench ($\Sigma<0$, corner-flow, Fig. 4), the simulations are fairly similar to those of Fig. 3. However, the motion of the plate is now resisted by a passive drag of the mantle, and a depression associated with extension is expected hinterland. If the shear stress is directed toward the trench ($\Sigma>0$, interplate traction, Fig. 5), the deviatoric stress first increases and then drops when the passive drag gets higher than the transmitted stress. A relief builds up at the plate margin and only compression is expected. A neutral stress is achieved when the steady state is reached.

When the basal traction is directed away from the trench, the maximum velocity is produced next to the trench and decreases toward the hinterland (Fig. 6, top). The corner-flow model predicts velocities directed toward the trench, of lower magnitudes (Fig. 6, bottom). A velocity peak is reached where the resistance gets stronger than the corner-flow shear and extension is then induced hinterland.

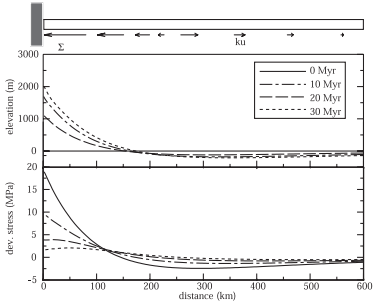

Fig. 4. Elevation and deviatoric stress induced by a corner-flow driving traction below the overriding plate (as in Fig. 3), resisted by a passive drag ku at the base of the lithosphere. The resistance k is 3.9×10^{16} Pa s m^{-1} (i.e. 10 MPa at 0.8 cm/year). Other parameters are those of Fig. 2.

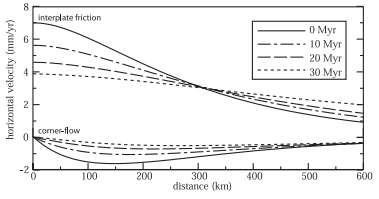

Fig. 6. Horizontal velocities when tectonics is driven by interplate traction (top) and when tectonics is driven by corner-flow (bottom). Positive velocities are directed toward the right hand side. The situations are those depicted in Figs. 4 and 5.

These theoretical cases highlight the sensitivity of the predicted topography on different models. One is the corner-flow model [12], and the other suggests that interplate traction is responsible for mountain building. The main difference between these models is the sense of the basal shear traction (toward the trench in the first model, toward the hinterland in the second). The corner flow model pulls the upper plate toward the trench while interplate traction pushes the overriding plate toward its hinterland. In [12], there is no interaction between the lithosphere and the mantle far from the subduction corner (i.e. they implicitly assume $k=0$) and no extension is then induced hinterland. In our simulation, on the contrary, a passive drag implies a bulk extension of the overriding plate hinterland comparable in magnitude to the bulk shortening across the orogen. Geodetic measurements over the Andes [19–21] and the Himalayas [22,23] as well as the global intraplate stress map [1] indicate a compression rather than extensional stress regime behind mountain belts associated with subduction zones, supporting the notion that interplate tractions play a more important role than counterflow in deformational dynamics in these areas.

2.4. Theoretical cases: from gravitational collapse to back-arc opening

Subduction zones can also be associated with extension rather than with compression when the stresses at or near the plate margin either decrease and cannot support furthermore a preexisting topography, or become intrinsically extensive. This change of boundary conditions may be related to the slowing down of the normal subduction rate (South Tibet [24] and South Peru [25]), to the stopping of subduction (Basin and Range [2]) or to back-arc opening (Aegean sea [26]).

Gravitational collapse can be illustrated by decreasing the compressive stresses. In Fig. 7, we compute the evolution of the topography of Fig. 5 when the interplate traction is suddenly reduced to zero at time $t=30$ Ma. The initial situation depicted by a solid line in Fig. 7 corresponds to the last situation (dashed line) of Fig. 5. During the transition toward a new equilibrium state, the tectonic

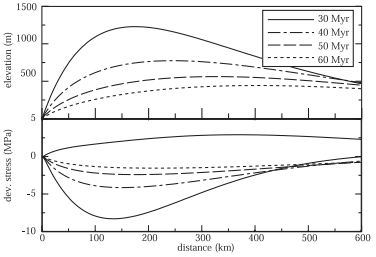

Fig. 7. Elevation and deviatoric stress for a collapsing pre-existing topography. The situation at 30 Ma in Fig. 5 is suddenly submitted to zero interplate traction ($\Sigma=0$). Solid lines show the situation just before and after the shear stress is set to zero. Other parameters remain as in Fig. 5.

stresses become extensive and the mountain range collapses. The maximum extension is located where the mountain reaches its highest elevation. The existence of a deviatoric stress at the plate margin able to sustain a 35-km-thick crust precludes any further thinning. A more quantitative illustration of this process focussed on South Peru will be presented in the following.

A further evolution toward an oceanic domain can occur when the deviatoric stress at the plate margin can no longer sustain the thickness of the continental crust. In the previous models, only basal traction was assumed. In order to account for slab retreat, an extensional deviatoric stress, T^+, can be imposed at the trench level (Fig. 8). During the first stage, the deviatoric stress is extensive next to the trench ($T^+<0$) but can remain compressive hinterland as in this simulation if $LT^+ + \int_0^x (\Sigma + L^2/6\partial^2\Sigma/\partial x^2)\mathrm{d}x > 0$. As the topography gently increases, stresses gradually become neutral hinterland as a marginal basin widens. Such scenario may explain the mild extensive situations at plate margins (e.g. in the Longitudinal Valley of Chile).

Nevertheless, we neglected significant specificities that are beyond the scope of this paper, such as local mass conservation which does not hold anymore due to magma production in back arcs situations. In an end member situation, the total amount of extension correspond to magma production rather than to crustal

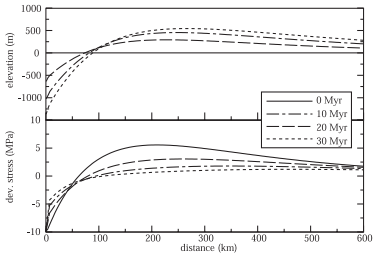

Fig. 8. Elevation and deviatoric stress induced by an exponentially decreasing interplate traction below the overriding plate, resisted by the drag at the base of the lithosphere as in Fig. 5. In addition, a − 10 MPa normal deviatoric stress is imposed as a right boundary condition. Such forcing mimics the effects of trench suction. Parameters are those of Fig. 5.

thinning. Still, it would affect the velocities but not the stress balance.

3. Application to the Andes

3.1. Fitting the topography

The Andean belt is located over the eastward subduction of the Nazca plate below South America. It is characterized by a thick crust up to 70 km below the Eastern Cordillera of Bolivia that compensates the topography (e.g. [27,28]).

Let the interplate traction and the deformation velocity have sigmoidal variations with x, as

$$\Sigma = \frac{\Sigma_0}{2}\left(1 - \tanh\frac{(x - x_\Sigma)}{\Delta_\Sigma}\right), \tag{18}$$

$$u = \frac{u_0}{2}\left(1 - \tanh\frac{(x - x_u)}{\Delta_u}\right). \tag{19}$$

These profiles allow Σ and u to decrease from Σ_0 and u_0 at the trench to zero hinterland over the lengths Δ_Σ and Δ_u. The distance at which the traction and velocities are halved are x_Σ and x_u. Any monotonic function decreasing from a maximum near the trench to zero hinterland could have been used but a sigmoidal variation for the velocity field is in agreement with the velocity profiles inferred from direct measurements (e.g. [29]).

Assuming isostasy, we compute from the observed topography S the term of Eq. (17) related to the density moment $1/2\rho_c g(1-\rho_c/\rho_m)\partial S^2/\partial x$ and deduce the quantities Σ_0, x_Σ, Δ_Σ, u_0, x_u, Δ_u, η and k by a generalized least square adjustment of Eq. (17) for various Andean profiles (Table 1).

The viscosity η is considered as uniform. We choose four topographic profiles perpendicular to the trench (averaged over 200 km large bands, see Fig. 9). The case of South Peru where extensive tectonics is observed will be discussed separately. The topographies are depicted in Fig. 10 (left column). The associated $1/2\rho_c g(1-\rho_c/\rho_m)\partial S^2/\partial x$ functions related to crustal variations are shown in the right column (thick lines). In each case, these functions are initially positive (along the western flank of the Andes) then abruptly change sign, become moderately negative and eventually reach zero. The interplate traction term (dashed lines), deduced from the inversion, closely fits the western segment of positive $\partial S^2/\partial x$. The resistive term (dotted lines) balances the negative part of $\partial S^2/\partial x$. The remaining term proportional to $\partial^2 u/\partial x^2$ (long dashed) is always very small. It represents the variations of the deviatoric stresses. The stress balance of the orogen naturally evolves toward a cancellation of this term.

3.2. Quantifying the stresses

Interplate traction varies along-strike as both its amplitude and the width of the traction zone are directly related to the distance to the trench of the maximum elevation (Fig. 10). Interplate traction

Table 1
Deduced parameters from the inversion of the Andean topography, Eqs. (17), (18) and (19)

	Peru	Altiplano	N. Chile	S. Chile
Σ_0 (MPa)	108	26	70	27
x_Σ (km)	26	175	55	20
Δ_Σ (km)	50	80	100	47
u_0 (mm/year)	5	7	3.5	2
x_u (km)	280	650	280	380
Δ_u (km)	120	100	80	200
η (Pa s)	2.15×10^{21}	1.66×10^{21}	4.28×10^{21}	4.8×10^{21}
k (Pa s m^{-1})	2.2×10^{17}	5.4×10^{16}	3.2×10^{17}	1.0×10^{17}

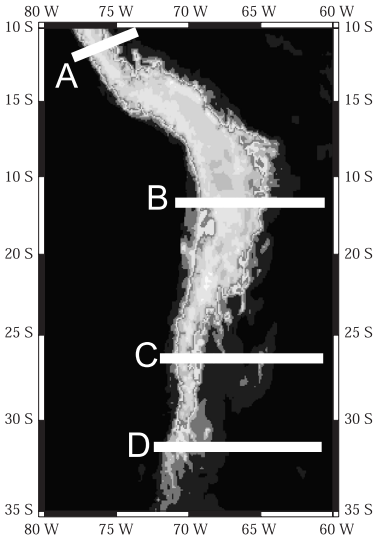

Fig. 9. Topography of the Andes. Location of the four reference profiles (across Central Peru (A), North (B), Central (C), and South (D) Chile).

ranges between 25 and 110 MPa, consistent with [30,31]. The shorter wavelength of the Peruvian Andes requires a stronger traction over a shorter distance Δ_Σ than below the Altiplano section. The total transmitted force from the subducting plate, $\int_0^\infty (\Sigma + \frac{t^2}{6}\frac{\partial^2\Sigma}{\partial x^2})\,dx$ is similar for the three mature profiles A, B and C ($\sim 9\times10^{12}$ N m^{-1}), and only for D this force is lower ($\sim 2.3\times10^{12}$ N m^{-1}).

The Andean subduction is commonly divided along-strike into several panels which correspond to the subduction angle of the Nazca plate. North and South of the Altiplano high plateau (18°S to 28°S), the slab segments subduct with a shallow angle (A and C). At the level of the Altiplano (B) and also beneath South Chile (D), the slab subducts with a steep angle. The traction profiles are not correlated to the present-day inclination of the Benioff–Wadatti zone at greater depth. Because slab bending changed through time in the Andes [32], the present-day stress balance reflects an average of the whole history of interplate traction.

The deviatoric stresses associated with the present-day tectonic deformation are given by $4\eta\partial u/\partial x$. For the four profiles, the deviatoric stresses are less than 10 MPa (see Fig. 11). The maximum compression and the width of the compressive zone are free parameters for the inversion. Maximum compression occurs in the Sub-Andean Zone, in agreement with geological observations (e.g. [33]).

From the previous inversion we have obtained the shape of the horizontal velocity and the amplitude of the deviatoric stresses (Fig. 11). Geodetic GPS measurements in the Andes confirm a maximum shortening in the foreland. They indicate a maximum East–West shortening across the belt of about 4 cm/year but the secular deformation is less than 1 cm/year [29,21]. A similar value can be estimated from geological records. Total Neogene shortening is assumed to range between 190 and 250 km in the Central Andes [33,34], which corresponds to 7 to 9 mm/year average deformation for 27 Ma, and probably 10 mm/year for the last 10 Ma [29].

Combining this velocity information with the deviatoric stresses, we estimate a viscosity in the range of 1.5 to 5×10^{21} Pa s, only a couple of orders of magnitude larger than the underlying mantle (4×10^{19} Pa s [35]). It represents an effective rheology averaged over the lithosphere, accounting for the softening of the lithosphere due to crustal faulting, fracturation and décollement levels. England [36], based on strain rates in extensional areas, mentioned that the lithosphere viscosity has to be about 10^{22} Pa s, and Wdowinski et al. [12] suggested that it can even be as low as 10^{21} Pa s in some places. We explain the low effective visosity of the Andean lithosphere by its pre-Andean history. The western margin of South America underwent several extensional events that thermally and mechanically weakened the lithosphere, particularly between 18°S and 28°S [37–39].

3.3. Time evolution

The previous inversions provide the current stress balance in the Andes, but may not reflect the past stress balance responsible for the overall growth of the

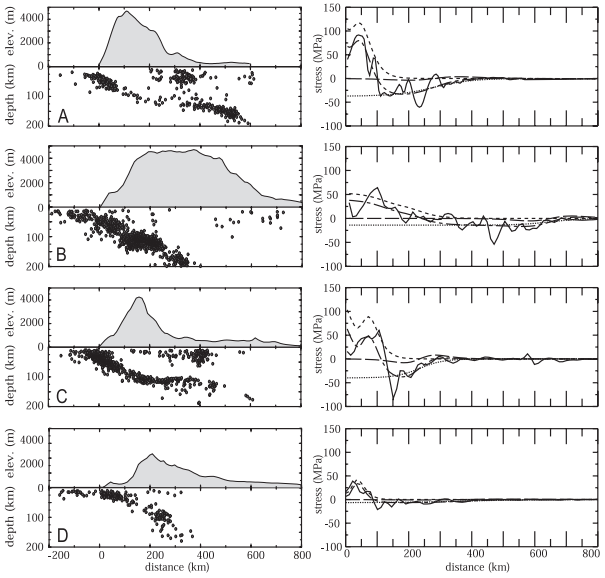

Fig. 10. Left column: topographic profiles A, B, C and D corresponding to Fig. 9. Earthquake epicenters underlining Benioff zone of the Nazca plate are also plotted. Right column: $1/2\rho_c g(1-\rho_c/\rho_m)\partial S^2/\partial x$ profiles (solid lines). These profiles can be balanced by the sum of an interplate traction (dashed lines), a resistive basal shear (dotted lines) and an internal deviatoric stress term (long dashed) computed from a generalized least-squares fit of Eq. (6). The sum of the three last terms (dotted-dashed) give good fits to the observations (solid lines).

Andes. Indeed, interplate traction profiles may have changed during the orogeny. We now test whether or not the present-day boundary conditions are appropriate to reconstruct the present-day situation, starting with an homogeneous plate and integrating Eqs. (6) and (9) through time. For each section, we take the parameters Σ, x_Σ, Δ_Σ, k and η deduced from the previous fits (Table 1). Contrarily to the previous sections, the velocity profiles are not constrained to have a priori sigmoidal shapes but are deduced from time integration.

3.3.1. General models for the Andes

Choosing the present-day traction profiles as constant boundary conditions through time allows the Andean belt to be reconstructed; however, in order to reproduce the current topography in the time range of the Andean orogeny (i.e. $\sim$ 27 Ma), the present-day interplate traction profiles are too low and have to be increased by 7 to 30 MPa (Fig. 12). Profile B, across the Altiplano presents a tangible misfit as the high plateau shape cannot be reproduced. In S. Chile (C), the Longitudinal Valley on the western side is neglected.

The convergence rate between the Nazca and South American plates strongly increased since 27 Ma and gradually decreased until present [40,41]. One can assume that interplate traction during the Andean orogeny decreased accordingly to the convergence rate. The fact that our time-dependent simulations

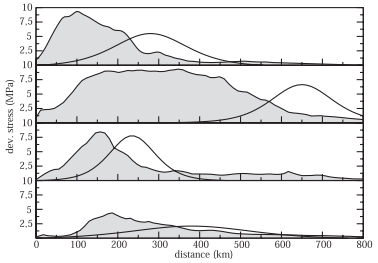

Fig. 11. Predicted deviatoric stresses for the four sections, according the stress balance shown in Fig. 10. In all cases the largest compressive stresses at present-day occur in the eastern fold and thrust belt. The topography is shown in shadings.

requires larger interplate tractions than at present-day reflects such an evolution.

3.3.2. High plateaus: the Altiplano example

A better fit to the observed topography of the Altiplano than in Fig. 12 could be obtained by weakening the rheology of the Andean lithosphere in order to confine and enhance the deformation of the Eastern Cordillera. A thermally thinned lithosphere has indeed been invoked to explain the building of the Altiplano [42–44]. Moreover, an Early Neogene lithospheric stretching has been active at the level of the Altiplano [37]. Fig. 13 shows the predicted topography after 27 Ma, using a moderate lateral viscosity increase under the eastern edge of the Cordillera (from 2.1×10^{21} to 6.3×10^{21} Pa s). The variation of the effective viscosity is also a way to account for the strong décollement, in the brittle deformation domain, where the Brazilian craton subducts.

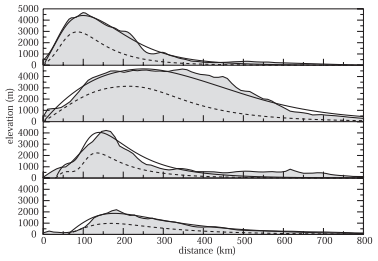

Fig. 12. Forward modeling of the four sections. In each case, the lines show the topographic profile at 10 (dashed) and 27 Ma (solid). Boundary conditions and viscosities (from 1.5×10^{21} to 5×10^{21} Pa s) are deduced from the inversion of the topography (Fig. 10) except interplate tractions that have been raised by 7 to 30 MPa, accounting for the decrease in the convergence rate.

3.3.3. Extension in active mountain belts: the South Peruvian example

A neutral state of stress has been evidenced by the coeval normal and inverse tectonic regimes in mountain belts such as the Alps (e.g. [45]), the Andes [46,47,25], or Tibet [24]. In the Andes, it has been described between 13°S and 18°S. This segment is the most oblique to the present-day convergence direction. Although still controversial, paleomagnetic data (e.g. [48,49]) indicate that this segment probably rotated counterclockwise. Although the setting is obviously 3D this situation can be simulated assuming that the segment rotated 30° counterclockwise for the last 10 Ma and that only the traction component normal to the belt affects the 2D stress balance. The traction is then a function of the convergence angle between the two plates. After being Σ between 27 and 10 Ma, we reduce the interplate traction by cos θ where θ varies from 0 at 10 Ma to 30° at present. Fig. 14a depicts the evolution of interplate traction and of the associated maximum elevation through time. Boundary conditions are those given for the Peruvian segment (panel A, Figs. 9 and 10).

The deviatoric stress at present (after 27 Ma of orogeny) well matches the observations of extension in the high Andes and compression in the Sub-Andean

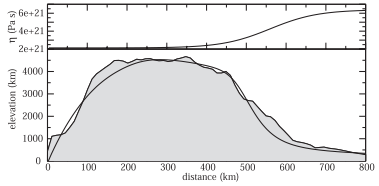

Fig. 13. Forward modeling of the Altiplano area at 27 Ma (bottom) introducing a lateral variation of viscosity (top). The interplate traction profile corresponds to that depicted in Fig. 10 panel B.

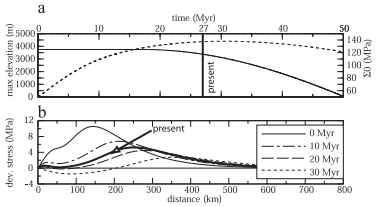

Fig. 14. Forward modeling for South Peru. Boundary conditions are the same as in Fig. 10 panel B. (a) Interplate traction (solid line) is assumed to decrease as the plate rotates at constant rate after 17 Ma (30° in 10 Ma). Until 25–30 Ma, the maximum elevation (dashed line) increases. (b) Deviatoric stress through time. The deviatoric stress becomes extensive where the elevation is maximum but remains compressive on the edges of the mountain belt. The present-day situation should correspond to 27 Ma, where the deviatoric stress cancels on the western side of the belt.

Zone (Fig. 14b). Of course, in our 2D model the extension can only be perpendicular to the belt while the observations indicate a significant along-strike component. If we assume arbitrarily that the rotation of the belt will continue in the future, the simulation predicts a general collapse of the topography. The tectonic stresses will be extensive everywhere but in the Brazilian craton where, according to Wdowinski et al. [12], the prevailing compressive stresses imposed by the subduction will still be acting.

The slowing down of the Nazca subduction should have the same impact and tends to shift the tectonic regime toward extension. It may be the case for the Quaternary extension in the North Peruvian segment.

So far we have neglected the Longitudinal Valley in the southern Andes, which becomes a significant feature in the southernmost section (D). This area features extensive focal mechanisms associated with the depression. The decrease in the convergence rate is likely associated to a decrease in the normal stress at the plate margin, leading to the onset of a situation comparable to that depicted Fig. 8.

4. Conclusions

Most tectonics settings and surface morphologies of plate margins can be understood and reconstructed using a thin sheet approximation. Interplate traction and resistive drag at the base of the lithosphere are the main controls of the tectonic regime at plate margins. The topography (more likely the crustal thickness variations) gives a first order feedback on the evolution of tectonics at plate margins.

Our model considers that topography is entirely supported by isostasy, and does not account for other forces like those arising from the elastic flexure of the downgoing lithosphere. The model also aims at reducing an intrinsically 3D problem to 2D: only across-strike deformation is considered and is averaged over the lithosphere thickness. A limitation comes from the assumption of local mass conservation that neglects erosion, delamination and magmatism. Corner-flow as a driving mechanism for Andean type tectonics can be discarded as it induces an extensive stress regime on the overriding plate.

The stress balance equation can be used to invert the topography and predict the present-day magnitudes and along-strike profiles of the stresses responsible for mountain building. In the Andes, we find that interplate traction range between 25 and 110 MPa. The total transmitted force is about 9×10^{12} N m^{-1} for the mature parts of the belt, consuming a significant amount of the plate tectonics driving forces. The topography of the Andes can be achieved in 25 to 30 Ma with a lithospheric viscosity between 1.5×10^{21} and 5×10^{21} Pa s, but only if the interplate traction is increased by 7 to 30 MPa with respect to the present-day stress balance. It outlines that the current topography reflects the history of the transmitted force as plate convergence was more vigorous in earlier periods of Andean orogeny.

Particular settings such as extension or high plateaus can often be reproduced by mild improvements of the model. In South Peru, the N–S extension can be explained by the increasing obliquity to the convergence of this segment of the Andes through time, which reduces the interplate traction. In fact, a slight change in the boundary conditions has an immediate impact as the tectonic equilibrium prevails (as outlined by the viscous stresses, which are almost one order of magnitude lower than the other stresses). This explains the frequent extensional tectonic regimes observed in various orogens. We also show in the case of the Altiplano that a very slight lateral viscosity variation is required for high plateaus to develop.

Acknowledgements

This work was supported by the Institut Français Pétrole. We wish to thank D. Coblentz and Ph. England for their reviews. This work also benefited from S. Medvedev's extreme meticulousness. ***[EB]***

References

[1] J. Reinecker, O. Heidbach, B. Mueller, 2003. The 2003 release of the World Stress Map (www.world-stress-map.org).
[2] T. Atwater, Implications of plate tectonics for the Cenozoic tectonic evolution of western North America, Bull. Geol. Soc. Am. 81 (1970) 3513–3536.
[3] E.V. Artyushkov, Stresses in the lithosphere caused by crustal thickness inhomogeneities, J. Geophys. Res. 78 (1973) 7675–7708.
[4] P. England, D. McKenzie, A thin viscous sheet model for continental deformation, Geophys. J. R. Astron. Soc. 70 (1982) 295–321.
[5] P. England, D. McKenzie, Correction to: a thin viscous sheet model for continental deformation, Geophys. J. R. Astron. Soc. 73 (1983) 523–532.
[6] L. Fleitout, C. Froidevaux, Tectonic stresses in the lithosphere, Tectonics 2 (1983) 315–324.
[7] G. Houseman, P. England, Crustal thickening versus lateral expulsion in the Indian–Asian continental collision, J. Geophys. Res. 98 (1993) 12233–12249.
[8] B. Wuming, C. Vigny, Y. Ricard, C. Froidevaux, On the origin of deviatoric stresses in the lithosphere, J. Geophys. Res. 97 (1992) 11729–11737.
[9] D. Coblentz, R.M. Richardson, M. Sandiford, On the gravitational potential energy of the Earth's lithosphere, Tectonics 13 (1994) 929–945.
[10] C.H. Jones, J.R. Unruh, L.J. Sonder, The role of gravitational potential energy in active deformation in the southwestern United States, Nature 381 (1996) 37–41.
[11] C.H. Jones, L.J. Sonder, J.R. Unruh, Lithospheric graviational potential energy and past orogenesis: implications for conditions of initial Basin and Range and Laramide deformation, Geology 26 (1998) 639–642.
[12] S. Wdowinski, R.J. O'Connell, P. England, A continuum model of continental deformation above subduction zones: application to the Andes and the Aegean, J. Geophys. Res. 94 (1989) 10331–10346.
[13] S. Medvedev, Yu. Podladchikov, New extended thin-sheet approximation for geodynamic applications: I. Model formulation, Geophys. J. Int. 136 (1999) 567–585.
[14] L. Fleitout, C. Froidevaux, Tectonics and topography for lithosphere containing density heterogeneities, Tectonics 1 (1982) 21–57.
[15] C. Froidevaux, B. Isacks, The mechanical state of the lithosphere in the Altiplano–Puna segment of the Andes, Earth Planet. Sci. Lett. 71 (1984) 305–314.
[16] E. Argand, La tectonique de l'Asie, Congrès Géologique International, Comptes-rendus de la XIII Session, 596 pp., Brussels, 1924.
[17] C. Lémery, Y. Ricard, J. Sommeria, A model for the emergence of thermal plumes in Rayleigh–Bénard convection and infinite Prandtl number, J. Fluid Mech. 414 (2000) 225–250.
[18] S. Ellis, P. Fullsack, C. Beaumont, Oblique convergence of the crust driven by basal forcing: implication for length-scales of deformation and strain partitioning in orogens, Geophys. J. Int. 120 (1995) 24–44.
[19] L. Leffler, S. Stein, A. Mao, T. Dixon, M.A. Ellis, L. Ocola, I.S. Sacks, Constraints on present-day shortening rate across the central eastern Andes from GPS data, Geophys. Res. Lett. 24 (1997) 1031–1034.
[20] M. Bevis, R. Smalley, T. Heering, J. Godoy, F. Galban, Crustal motion north and south of the Arica deflection: comparing recent geodetic results from the Central Andes, G^3, 1 (1999).
[21] G. Khazaradze, J. Klotz, Short- and long-term effects of GPS measured crustal deformation rates along the south central Andes, J. Geophys. Res. 108 (2003) 2289, doi: 10.1029/2002JB001879.
[22] R. Bilham, K. Larson, J. Freymueller, Idylhim members, GPS measurements of present-day convergence across the Nepal Himalaya, Nature 386 (1997) 61–63.
[23] K.M. Larson, R. Burgmann, R. Bilham, J. Freymueller, Kinematics of the Indo-Eurasian collision zone and GPS measurements, J. Geophys. Res. 104 (1999) 1077–1093.
[24] R. Armijo, P. Tapponnier, J.L. Mercier, H. Tonglin, Quaternary extension in southern Tibet: field observations and tectonic implications, J. Geophys. Res. 91 (1986) 13803–13872.
[25] J.L. Mercier, M. Sébrier, A. Lavenu, J. Cabrera, O. Bellier, J.F. Dumont, J. Machare, Changes in the tectonic regime above a subduction zone of Andean type: the Andes of Peru and Bolivia during the Pliocene–Pleistocene, J. Geophys. Res. 97 (1992) 11945–11982.
[26] L. Jolivet, C. Faccenna, Mediterranean extension and the Africa–Eurasia collision, Tectonics 19 (2000) 1095–1106.
[27] D.E. James, Andean crustal and upper mantle structure, J. Geophys. Res. 76 (1971) 3247–3271.
[28] S.L. Beck, G. Zandt, S.C. Myers, T.C. Wallace, P.G. Silver, L. Drake, Crustal-thickness variations in the central Andes, Geology 24 (1996) 407–410.
[29] E. Klosko, S. Stein, D. Hindle, J. Kley, E. Norabuena, T. Dixon, M. Liu, Comparison of GPS, seismological, and geological observations of Andean mountain building, in: S. Stein, J. Freymueller (Eds.), Plate Boundary Zones, Geodynamics Series vol. 30, A.G.U., Washington, 2002, pp. 123–134.
[30] R.M. Richardson, D. Coblentz, Constraint on the intraplate stress magnitudes from stress modeling in the Andes of South America, J. Geophys. Res. 99 (1994) 22015–22025.
[31] D. Coblentz, R.M. Richardson, Analysis of the South American intraplate stress field, J. Geophys. Res. 101 (1996) 8643–8657.
[32] G.A. Yañez, C.R. Ranero, R. von Huene, J. Diaz, Magnetic anomaly interpretation across the southern central Andes (32°–34°S): the role of the Juan Fernández Ridge in the late Tertiary evolution of the margin, J. Geophys. Res. 106 (2001) 6325–6345.

[33] P. Baby, P. Rochat, G. Mascle, G. Hérail, Neogene shortening contribution to crustal thickening in the back-arc of the Central Andes, Geology 25 (1997) 883–886.
[34] J. Kley, C.R. Monaldi, Tectonic shortening and crustal thickness in the Central Andes: how good is the correlation? Geology 26 (1998) 723–726.
[35] L.M. Cathles, The Viscosity of the Earth's Mantle, Princeton Univ. Press, Princeton, NJ, 1975.
[36] P. England, Comment on "Brittle failure in the upper mantle during extension of continental lithosphere" by Dale S. Sawyer, J. Geophys. Res. 91 (1986) 10487–10490.
[37] T. Sempere, G. Hérail, J. Oller, M.G. Bonhomme, Late Oligocene–Early Miocene major tectonic crisis and related basins in Bolivia, Geology 18 (1990) 946–949.
[38] T. Sempere, Phanerozoic evolution of Bolivia and adjacent regions, in: A.J. Tankard, R.J. Suarez, H.J. Welsink (Eds.), Petroleum Basins of South America, A.A.P.G. Memoir vol. 62, (1995) 207–230.
[39] S. Lamb, L. Hoke, L. Kennan, J. Dewey, Cenozoic evolution of the Central Andes in Bolivia and northern Chile, in: J.P. Burg, M. Ford (Eds.), Orogeny Through Time, Spec. Pub.-Geol. Soc., vol. 121, 1997, pp. 237–264.
[40] F. Pardo-Casas, P. Molnar, Relative motion of the Nazca (Farallon) and South American plates since Late Cretaceous time, Tectonics 6 (1987) 233–248.
[41] E. Norabuena, L. Leffler-Griffin, A. Mao, T. Dixon, S. Stein, I.S. Sacks, L. Occola, M. Ellis, Space geodetic observations of Nazca–South America convergence across the Central Andes, Science 279 (1998) 358–362.
[42] B. Isacks, Uplift of the central Andean plateau and bending of the Bolivian orocline, J. Geophys. Res. 93 (1988) 3211–3231.
[43] S. Wdowinski, Y. Bock, The evolution of deformation and topography of high elevated plateaus: 2. Application to the Central Andes, J. Geophys. Res., (1994) 7121–7130.
[44] L. Husson, T. Sempere, Thickening the Altiplano crust by gravity-driven crustal channel-flow, Geophys. Res. Lett. 30 (2003) 1243 (doi:10.1029/2002GL016877).
[45] C. Sue, P. Tricart, F. Thouvenot, J. Fréchet, Widespread extension in the core of the western Alps revealed by earthquake analysis, J. Geophys. Res. 104 (1999) 611–622.
[46] M. Sébrier, J.L. Mercier, F. Mégard, G. Laubacher, E. Carey-Gailhardis, Quaternary normal and reverse faulting and the state of stress in the Central Andes and South Peru, Tectonics 4 (1985) 739–780.
[47] M. Assumpçao, The regional intraplate stress field in South America, J. Geophys. Res. 97 (1992) 11889–11903.
[48] M.E. Beck, R.R. Burmester, R.E. Drake, P.D. Riley, A tale of two continents: some tectonic contrasts between the Central Andes and the North American Cordillera, as illustrated by their paleomagnetic signatures, Tectonics 13 (1994) 215–224.
[49] I. Coutand, A. Chauvin, P.R. Cobbold, P. Gautier, P. Ropperch, Vertical axis rotations across the Puna plateau (northwestern Argentina) from paleomagnetic analysis of Cretaceous and Cenozoic rocks, J. Geophys. Res. 104 (1999) 22965–22984.

Dans le cas des Andes présenté ci-dessus, la morphologie de la chaîne est présentée comme une réponse directe à la friction interplaque : sa morphologie vient équilibrer cette friction pour une vitesse de convergence donnée. Il existe cependant une rétroaction de la morphologie de la chaîne de montagne sur la vitesse de convergence. Iaffaldano et al. [2006] ou Meade & Conrad [2008] ont ansi montré qu'au premier ordre la convergence entre les plaques Nazca et Amérique du Sud ralentit à mesure que les Andes se développent. L'examen de la convergence Inde-Asie est éloquent pour examiner les ordres supérieurs. En collaboration avec G. Iaffaldano et H-P. Bunge, nous montrons dans l'article suivant que si la convergence entre les deux plaques est au premier ordre ralentie par la croissance himalayenne et tibétaine, le second ordre révèle l'impact du climat. La mousson, focalisée sur l'est himalayen, stimule l'érosion de façon asymmétrique sur la chaîne, et par conséquent détériore localement l'équilibre statique des forces au profit d'un équilibre dynamique : la convergence est accélérée à l'est, où l'épaisseur crustale est limitée par l'érosion. C'est en revanche la cinématique globale indienne qui est affectée. Cette cinématique particulière fournit une explication à l'altitude atypiquement élevée du Népal Central, qui ne peut se justifier en deux dimensions que par un nombre d'Argand très faible.

Monsoon speeds up Indian plate motion

Laurent Husson[1,2*], Giampiero Iaffaldano[3], Hans-Peter Bunge[4]

[1]CNRS UMR6118, Géosciences Rennes, France,
[2]CNRS UMR 6112, Laboratoire de Planétologie et Géodynamique de Nantes, France,
[3]Department of Earth and Planetary Science, Harvard University, Massachusetts, USA,
[4]Department of Earth and Environmental Science, LMU Munich, Germany.
[*]To whom correspondence should be addressed; E-mail: laurent.husson@univ-rennes1.fr

September 8, 2009

Abstract

The short-term plate motion variations, on the order of a few Myrs, are a powerful probe into the nature of plate boundary forces, as mantle related buoyancy forces evolve over longer time-scales. Here we relate the recent counter-clockwise rotation of India to increased erosion and lowered elevation of the eastern Himalayas following monsoon intensification. The along-strike elevation Himalayan profile is used to infer the competing contributions from mountain building and erosion. Monsoonal erosion in the Eastern Himalayas locally decreased the gravitational potential energy. Coupled mantle/lithosphere models show that it lowered the ability of the orogen to resist convergence of the Indian plate towards Eurasia sufficiently to foster convergence along the eastern Himalayas. It ultimately converts into an additional component of counter-clockwise rotation of India about a Euler pole located North of the Carlsberg ridge, unusually close from the boundary between the converging plate pair. The modified stress balance along the entire Himalayas provides an unusual setting in which the extremely elevated Central Himalayas, that would normally collapse under their own weight, can be sustained.

Introduction

A prominent feature of the Himalayan morphology is the along-strike parabolic profile of its elevation (Fig. 1a). Topography increases eastward from $\sim$3 km in Kashmir and Ladakh towards the summits of Nepal, where most of the world's highest peaks cluster at a mean altitude

of more than 6 km, and gently decreases back to a mean elevation of 3 km further east. Several lines of evidence relate the Miocene intensification of aridity in Tibet to a strengthening of the monsoon, with a stepwise increase at ∼10 Myrs, although uncertainties affect such estimate by 2 Myrs or so (e.g., Zhisheng et al., 2001; Fan et al., 2006; Dettman et al., 2003). The monsoon intensification led to moisture concentration at the Himalayan front when Tibet became sufficiently high to block northward air fluxes, indicative of an interplay between morphology and climate (e.g., Molnar et al., 1993).

The Indian monsoon appears to have been particularly efficient in eroding the eastern Himalayas. In fact, mean precipitation increases 3-fold from 1 to more than 3 m/yr (Fig. 1b) as one moves eastward along the belt, a regime that prevailed for several Myrs in the recent past (Fluteau et al., 1999). Higher rainfall in an orogen fosters erosion, and a new steady morphological equilibrium (Beaumont et al., 1992; Willett, 1999) is reached typically over a time scale of less than 3 Myrs (Whipple & Meade, 2006). While fast erosion (Galy & France-Lanord, 2001) and exhumation of metamorphic rocks (Burg et al., 1998; Thiede et al., 2004; Finlayson et al., 2002; Clift et al., 2008) have been observed in the Himalayas at the range scale, higher strain rates are reported in the eastern Himalayas (see Kreemer & Holt, 2001). However, the faster flux of eroded material within the wedge is a recent feature, for bulk shortening across the range since the onset of the collision at ∼50 Myrs is higher in western Nepal (DeCelles et al., 2002). Thus it is reasonable to assume that stronger erosion induced by monsoon intensification over the past 10 Myrs contributed to shape the along-strike profile of topography, and that the present-day relief of the Himalayas has been achieved only within the past few Myrs.

The evolution of Himalayan morphology has, of course, implications for the dynamics of the India/Eurasia convergent system because the gravitational potential energy stored in thick crusts of mountain belts yields forces comparable to the driving and resisting forces available in plate tectonics (Husson & Ricard, 2004; Iaffaldano & Bunge, 2008). Forces arising from

large orogenic belts are capable to deform the interior of plates, for instance in the Indian ocean following the rise of the Tibetan plateau (e.g., Chamot-Rooke et al., 1993), or to reduce the convergence between overriding and subducting plates (Iaffaldano et al., 2006; Molnar & Stock, 2009). Likewise, the recent episode of plateau formation in the Andes decreased the convergence rate between the Nazca and South American plates and profoundly affected plate kinematics within the broader Pacific and Atlantic ocean basins (Husson et al., 2008; Iaffaldano & Bunge, 2009), consistent with the notion of a weak asthenosphere (Richards et al., 2001).

Important constraints exist on past plate motion for the Indian Ocean basin. Indian continental crust entered subduction 60 to 50 Myrs ago, resulting in a marked decrease of convergence from ∼20 cm/yr to ∼4 cm/yr (Patriat & Achache, 1984). On its southwestern side, the Carlsberg ridge divides India from Africa since the Miocene. Moreover, the separation of India from the Indo-Australian plate might have initiated as early as 18 Myrs (Gordon et al., 1998), but only at ∼8 Myrs did plate motion in the Indian ocean became steady (Merkouriev & DeMets, 2006). Here we take advantage of sets of plate-pair finite rotations (Horner-Johnson et al., 2005; Merkouriev & DeMets, 2006; Royer et al., 2006; Torsvik et al., 2008) to map the motion of India over the past 20 Myrs (Figs. 2 and 3). Specifically, we solve for the entire India-Somalia-Nubia-Eurasia plate circuit (see supporting material) to compute the convergence history of India towards Eurasia, as well as the sequence of Euler poles for the spreading of India with respect to Somalia, averaged within four stages.

The resulting history of plate kinematics shows an intriguing temporal behaviour: first we note the overall decrease in plate convergence over the past 20 Myrs which may be explained by an increase in mean elevation of the Tibetan plateau (Molnar & Stock, 2009), or alternatively by separation of the Indian and Australian plate occurring between 10 and 20 Myrs ago (Iaffaldano & Bunge, 2009). Far more interesting, however, is that India appears to undergo a counterclockwise rigid rotation over the past 10 Myrs. In particular, during the last stage from 6 Myrs

to present-day the motion of India shifts westward relative to Eurasia (Fig. 2, arrows). We note furthermore that the path of Euler poles describing India/Somalia relative motion moves eastward from its general NE-SW trend no later than ∼10 Myrs ago (Fig. 2, dots). In spherical geometry, as the Euler pole moves closer to a plate one can show that the plate undergoes a more spinning motion rather than translation on the globe. Our observations thus provide evidence that India underwent a rigid rotation about a pole located relatively close to - if not within - India itself, in addition to its convergence towards Eurasia. The distinct kinematic signature of this rotation stands out further if one decomposes the total convergence (Fig. 3a) into their trench-normal and trench-parallel components (Fig. 3b and 3c). While for the past 20 Myrs total convergence has been systematically ∼0.5 cm/yr faster in the eastern part relative to the west, the partition of normal and parallel components changed significantly only over the past 6 Myrs or so. While long-term tendencies for both normal and trench parallel components is a decrease by 0.05 to 0.1 mm/yr/Ma (0.08 and 0.25 mm/yr/Ma for total convergence in the northwestern and northeastern corners of India) until ∼6 Ma, the trench-normal component increased during the most recent stage by ∼0.5 cm/yr across the eastern margin, and the parallel component increased by an almost equal amount along the western margin at the same time (Fig. 3b and 3c).

There is no obvious reason for mantle related driving forces to have evolved rapidly enough to explain this variation (Bunge et al., 1998). Similarly, the large Tibetan plateau was already mature at 10 Myrs (Tapponnier et al., 2001). Furthermore, the Carlsberg ridge does not display any anomalous morphology that would reflect a heterogeneous cooling or subsidence history in the ocean floor. In this study we therefore suggest that monsoon intensification has modified the morphology of the eastern Himalayas, decreasing its elevation and crustal thickness sufficiently to affect plate motion. Specifically, we test the hypothesis that lower gravitational potential energy on the northeastern edge of the Indian plate induced by intensified monsoon and erosion

allowed for faster convergence across the eastern margin, thus triggering counter-clockwise rigid rotation of India with respect to both Eurasia and Somalia.

Models and results

While estimates of paleo-elevation in the eastern Himalayas are necessarily subject to uncertainty, the present-day morphology obviously results from a dynamic equilibrium between processes responsible for mountain building and rates at which material is eroded. Here we make no attempt to decipher the complex paths that relate large-scale rainfall and morphology of high plateaus through erosion and *vice-versa*. Rather we consider the actual morphology and precipitation in the Himalayas (Fig. 1a and 1b) as a result of such interplay, with insights on paleo-elevations potentially available through empirical correlations between present-day erosion, precipitation and relief (e.g., Summerfield & Hulton, 1994).

In the morphological equilibrium that shapes orogens, erosion can be regarded as a "negative" contribution to elevation, whereas mountain building is its "positive" counterpart, the sum of the two resulting in the actual relief. The present-day morphology of the Himalayan orogen can be used to test and support such view. A quadratic regression of rainfall Q as a function of distance along the trench (Fig. 1b) accounts for the drastic eastward increase in precipitation and neglects second-order terms. In the Himalayas, erosion is higher where precipitation is highest, even when elevation is rather low, indicating that erosion is controlled more by rainfall than relief (Grujic et al., 2006). We use a simple functional relationship between precipitation P and erosion E, with $E = \alpha P^n + C$, where α, n, and C are unknown constants. Similarly, we evaluate the shear stresses at the plate interface responsible for mountain building M as a function of plate convergence V. That is, $M = \beta V^m$, where β and m are further constants (see Whipple & Meade, 2004, and references therein).

We explore a combination of relationships where *n=1* or *n=3/2*, in order to account for

the inferred stronger erosional power of loaded rivers, while *m=1* or *m=1/2* accounts for the mountain-building contribution (Meade & Conrad, 2008). All fits to the present-day along-strike profile of topography give almost equally satisfying results (Fig. 1a) and do not allow further selection of optimal values. In all cases erosion works more efficiently in the eastern Himalayas and lowers the total elevation by 6 to 9 km more with respect to the western margin (Fig. 1c). Therefore erosion decreases the total elevation from west to east relative to the elevation that would be achieved without erosion but with an equal convergence rate. Of course the latter situation is of theoretical interest only, because we expect both convergence and mountain building to decrease as soon as elevation increases. However, based on our inferences and considering that erosion strengthened since the time of monsoon intensification, it is reasonable to assume that elevation of eastern Himalayas was higher in the recent past compared to present-day, possibly yielding elevations of $\sim$ 6 km before monsoon intensification.

We test how reduced topography in the eastern Himalayas affects Indian plate motion by using global numerical models of the coupled mantle/lithosphere system (Kong & Bird, 1995; Bunge et al., 1997; Iaffaldano & Bunge, 2009). The models solve the momentum balance and account explicitly for the global relief of continents and oceans, as well as realistic mantle related driving forces and plate configurations to compute instantaneous global plate velocities (see supporting material). This allows us to test our hypothesis directly as a set of initial and final scenarios - that is, to compute plate velocities for conditions of topography immediately before monsoon intensification and at present-day. Specifically, we balance all contributions to momentum in the lithosphere, including the gravitational spreading of topography and high plateaus, and perform two distinct simulations of global plate velocities: in one we assume present-day elevation at the global scale, particularly in the Himalayas and Tibetan plateau (Fig. 4a). In our second simulation we modify the assumed relief in the eastern Himalayas only, in accord with our hypothesis of higher elevation there immediately prior to monsoon

intensification (Fig. 4b). We compute global plate velocities for both scenarios. Finally, we estimate the impact of eroded topography on plate motion as the difference between the two velocity fields.

In addition, our ability to include plate configurations directly through distinct finite-element boundaries within the computational grid allows us to investigate the role of the separation between India and Australia. In one model, India and Australia are considered as a single plate while in a second model, we cast India and Australia as two individual plates separated by a plate boundary according to published observations of the Indian ocean-floor (Stein & Okal, 1978; Weissel et al., 1980). With separate Indian and Australian plates, we predict a velocity change for India of $\sim$0.5 cm/yr, directed normal- and parallel-to-trench in the eastern and western margin, respectively (Fig. 5, black arrows), compatible with our reconstructions of Indian motion over the past 10 Myrs (see Fig. 3). More importantly, we confirm the induced velocity change is indeed a rigid body rotation, well described by an Euler pole of magnitude 0.066 °/Myr located at about E57°, N14° (Fig. 5, black star). Because crustal thickness along eastern Himalayas is the sole varying parameter between the two simulations, our results link the observed rotation of India explicitly to the local release of potential energy along the eastern India/Eurasia plate boundary following intensification of monsoon. When India and Australia are assumed as a single plate, our simulations predict a velocity change for the larger Indo-Australian plate as small as $\sim$0.1 cm/yr (Fig. 5, gray arrows), and the predicted velocity fails to be described by a single Euler pole.

Discussion

Our results support the notion that faster erosion in the eastern Himalayas, induced by monsoon intensification some 10 Myrs ago, decreased elevation locally thus reducing tectonic resistance against India/Eurasia plate convergence in this region. Consequently, Indian plate motion in-

creased by ∼0.5 cm/yr along the eastern end of the margin. This is equivalently described by a counter-clockwise rigid rotation of India about a pole located north of the Carlsberg ridge, in the vicinity of India itself. In other words, topographic variations and in particular the peculiar along-strike elevation profile of the Himalayas are sufficient to explain the recent rotation of India. The fact that no solid body rotation is predicted if we assume a single Indo-Australian plate lends support to independent evidence that India must have been a separate tectonic unit prior to monsoon intensification (Stein & Okal, 1978; Weissel et al., 1980; Wiens et al., 1985; Gordon et al., 1998). Our result should be of no surprise: the Indo-Australian plate offers a larger basal area for mantle shear tractions, as well as subduction related forcing along the Java-Sumatra trench, plate boundary forces in the southwest Pacific, and forcing related to spreading along the Carlsberg and Indian ridges. Reduced gravitational potential energy along the eastern Himalayas, representing only a small portion of the entire boundary of the larger Indo-Australian plate, would thus more likely be balanced by internal deformation rather than a rigid rotation of a joint Indo-Australian plate.

Further support for our conclusions comes from the observed path of the India/Somalia rotation pole over the past 20 Myrs. Our models explain the shift of the path eastward from its general NE-SW trend after monsoon intensification (Fig. 2 and 5). Adding the monsoon-induced rotation of India computed from our models (located in the vicinity of the northern Carlsberg ridge, see black star in Fig. 5) to the observed India/Somalia spreading pole 10 to 16 Myrs ago yields a prediction for the pole (white circle, Fig. 5) that compares with the observed locations after monsoon intensification.

It is intriguing that lateral variations in plate coupling may arise as a consequence of climate phenomena. Since climate is often affected in turn by geologic processes at plate margins, such as mountain building, this implies continuous feedback mechanisms between climate dynamics and plate motions, where at times one controls the others and *vice-versa*. Plate convergence

should therefore not be regarded as a steady boundary condition of orogenic belts. Rather it undergoes variations related, among others, to climate-controled morphological processes. This opposes most dynamic models that explore the relationships between climate and morphology by imposing velocity rather than stress boundary conditions (e.g., Willett, 1999; Whipple & Meade, 2006).

Two more implications are worth noting. Spreading along mid ocean ridges is often regarded as a process where rate, geometry and degree of asymmetry are determined, at least in part, by local ridge-mantle (Yale & Phipps Morgan, 1998) or ridge-plume (Müller et al., 1998) interactions. Instead, our results link the recent spreading history along the Carlsberg ridge explicitly to variations of the tectonic regime at a distant convergent margin. This agrees with findings which relate spreading variations in the southern Pacific and Atlantic over the past 10 Myrs to plateau formation in the Andes (Husson et al., 2008; Iaffaldano & Bunge, 2009), supporting the view that far-field effects must be considered in the spreading history of ocean basins (Iaffaldano et al., 2007).

A second implication concerns the location of Euler poles. Commonly one can describe the relative motion of plate pairs through an Euler pole located far away from the plate boundary they share, as far away as ∼90° (Müller et al., 2008), resulting in mostly translational relative motion between the plates. But plate pairs sharing a diffuse boundary - that is, a deformation zone usually hundreds to thousands of kilometres wide - tend to locate their Euler pole within their wide boundary (Gordon, 1998), a feature that has been linked to geometrical effects minimising the net torque along the shared boundary (Zatman et al., 2001). Our findings suggest an additional cause for rigid rotation, namely time-dependent lateral variations in plate-boundary forces. This means that plate boundary forces have the ability to sufficiently modify the net torque between two adjacent plates to generate a rotational component with an Euler pole located in the vicinity of both plates, even when they share a narrow margin.

On a final note, the parabolic elevation profile results from the fact that rainfall and erosion are focussed on the eastern Himalayas, whereas plate convergence increases linearly because India rotates as a rigid body. This distributes the evolving stress boundary conditions onto the entire plate, and not only where erosion is high. It thus also fosters plate convergence in the Central Himalayas and supplies additional shear stress that may in turn balance the very large gravitational potential energy. Our model thus provides an explanation for the existence of the extremely high elevation in central Nepal that is home to the high peaks of the Annapurnas and Mount Everest.

Acknowledgements

L.H. acknowledges S. Bonnet, D. Lague and P. Davy for stimulating discussions. G.I. acknowledges support from a Reginald A. Daly Postdoctoral Fellowship at Harvard University.

References

Beaumont, C., Fullsack, P., & Hamilton, J., 1992. Erosional control of active compressional orogens, in *Thrust Tectonics*, pp. 1–18, ed. McClay, K., Chapman and Hall.

Bunge, H.-P., Richards, M., & Baumgardner, J., 1997. A sensitivity study of 3-D spherical mantle convection at 10exp8 Rayleigh number: Effects of depth dependent viscosity, heating mode and an endothermic phase change, *J. Geophys. Res.*, **102**, 11991–12007.

Bunge, H.-P., Richards, M., Lithgow-Bertelloni, C., Baumgardner, J., Grand, S., & Romanovicz, B., 1998. Time scales and heterogeneous structures in geodynamic earth models, *Science*, **280**, 91–95.

Burg, J.-P., Nievergelt, P., Oberli, F., Seward, D., Davy, P., Maurin, J.-C., Diao, Z., & Meier, M., 1998. The namche barwa syntaxis: evidence for exhumation related to compressional crustal folding, *Journal of Asian Earth Sciences*, **16**(2-3), 239–252.

Chamot-Rooke, N., Jestin, F., & de Voogd, B., 1993. Intraplate shortening in the central indian-ocean determined from a 2100-km-long north-south deep seismic-reflection profile, *Geology*, **21**(11), 1043–1046.

Clift, P., Hodges, K., Heslop, D., Hannigan, R., Long, H. V., & Calves, G., 2008. Correlation of himalayan exhumation rates and asian monsoon intensity, *Nature Geoscience*, **1**(12), 875–880.

DeCelles, P., Robinson, D., & Zandt, G., 2002. Implications of shortening in the Himalayan fold-thrust belt for uplift of the Tibetan Plateau, *Tectonics*, **21**(6), 1062.

Dettman, D. L., Fang, X., Garzione, C. N., & Li, J., 2003. Uplift-driven climate change at 12 ma: a long [delta]18o record from the ne margin of the tibetan plateau, *Earth and Planetary Science Letters*, **214**(1-2), 267–277.

Fan, M., Song, C., Dettman, D. L., Fang, X., & Xu, X., 2006. Intensification of the asian winter monsoon after 7.4ma: Grain-size evidence from the linxia basin, northeastern tibetan plateau, 13.1ma to 4.3ma, *Earth and Planetary Science Letters*, **248**(1-2), 186–197.

Finlayson, D. P., Montgomery, D. R., & Hallet, B., 2002. Spatial coincidence of rapid inferred erosion with young metamorphic massifs in the himalayas, *Geology*, **30**(3), 219–222.

Fluteau, F., Ramstein, G., & Besse, J., 1999. Simulating the evolution of the asian and african monsoons during the past 30 myr using an atmospheric general circulation model, *Journal of Geophysical Research*, **104**, 11995–12018.

Galy, A. & France-Lanord, C., 2001. Higher erosion rates in the himalaya: Geochemical constraints on riverine fluxes, *Geology*, **29**(1), 23–26.

Gordon, R., 1998. The plate tectonic approximation: plate non-rigidity, diffuse plate boundaries, and global plate reconstructions, *Annual Review of Earth and PLanetary Sciences*, **26**, 615–642.

Gordon, R. G., DeMets, C., & Royer, J.-Y., 1998. Evidence for long-term diffuse deformation of the lithosphere of the equatorial indian ocean, *Nature*, **395**(6700), 370–374.

Grujic, D., Coutand, I., Bookhagen, B., Bonnet, S., Blythe, A., & Duncan, C., 2006. Climatic forcing of erosion, landscape, and tectonics in the bhutan himalayas, *Geology*, **34**(10), 801–804.

Horner-Johnson, B. C., Gordon, R. G., Cowles, S. M., & Argus, D. F., 2005. The angular velocity of nubia relative to somalia and the location of the nubia-somalia-antarctica triple junction, *Geophysical Journal International*, **162**(1), 221–238.

Husson, L. & Ricard, Y., 2004. Stress balance above subduction: application to the andes, *Earth and Planetary Science Letters*, **222**(3-4), 1037–1050.

Husson, L., Conrad, C. P., & Faccenna, C., 2008. Tethyan closure, andean orogeny, and westward drift of the pacific basin, *Earth and Planetary Science Letters*, **271**(1-4), 303–310.

Iaffaldano, G. & Bunge, H.-P., 2008. Strong plate coupling along the nazca–south america convergent margin, *Geology*, **36**(6), 443–446.

Iaffaldano, G. & Bunge, H.-P., 2009. Relating rapid plate motion variations to plate boundary forces in global coupled models of the mantle/lithosphere system: effects of topography and friction, *Tectonophysics*, **474**, 393–404.

Iaffaldano, G., Bunge, H.-P., & Dixon, T., 2006. Feedback between mountain belt growth and plate convergence, *Geology*, **34**, 893–896.

Iaffaldano, G., Bunge, H.-P., & Buecker, M., 2007. Mountain belt growth inferred from histories of past plate convergence: A new tectonic inverse problem, *Earth and Planetary Science Letters*, **260**, 516–523.

Kong, X. & Bird, P., 1995. Shells: a thin-shell program for modeling neotectonics of regional or global lithosphere with faults, *Journal of Geophysical Research*, **100**, 22129–22131.

Kreemer, C. & Holt, W., 2001. A no-net-rotation model of present-day surface motions, *Geophysical Research Letters*, **28**, 4407–4410.

Meade, B. J. & Conrad, C. P., 2008. Andean growth and the deceleration of south american subduction: Time evolution of a coupled orogen-subduction system, *Earth and Planetary Science Letters*, **275**(1-2), 93–101.

Merkouriev, S. & DeMets, C., 2006. Constraints on indian plate motion since 20 ma from dense russian magnetic data: Implications for indian plate dynamics, *Geochemistry Geophysics Geosystems*, **7**, Q02002.

Molnar, P. & Stock, J., 2009. Slowing india's convergence with eurasia since 20 ma and its implications for tibetan mantle dynamics, *Tectonics*, **28**, 357–396.

Molnar, P., England, P., & Martinod, J., 1993. Mantle dynamics, uplift of the tibetan plateau, and the indian monsoon, *Reviews of Geophysics*, **31**(4), 357–396.

Müller, R., Roest, W., & Royer, J.-Y., 1998. Asymmetric sea-floor spreading caused by ridge-plume interactions, *Nature*, **396**, 455–459.

Müller, R., Sdrolias, M., Gaina, C., & Roest, W., 2008. Age, spreading rates and spreading asymmetry of the world's ocean crust, *Geochemistry, Geophysics, Geosystems*, **9**(4), Q04006.

Patriat, P. & Achache, J., 1984. India-eurasia collision chronology has implications for crustal shortening and driving mechanism of plates, *Nature*, **311**(5987), 615–621.

Richards, M., Yang, W., Baumgardner, J., & Bunge, H.-P., 2001. Role of a low-viscosity zone in stabilizing plate tectonics: Implications for comparative terrestrial planetology, *Geochemistry Geophysics Geosystems*, **2**.

Royer, J.-Y., Gordon, R. G., & Horner-Johnson, B. C., 2006. Motion of nubia relative to antarctica since 11 ma: Implications for nubia-somalia, pacific-north america, and india-eurasia motion, *Geology*, **34**(6), 501–504.

Stein, S. & Okal, E., 1978. Seismicity and tectonics of the ninetyeast ridge area: Evidence for internal deformation of the indian plate, *Journal of Geophysical Research*, **83**, 2233–2245.

Summerfield, M. & Hulton, N., 1994. Natural controls of fluvial denudation rates in major world drainage basins, *Journal of Geophysical Research*, **99**, 13871–13883.

Tapponnier, P., Zhiqin, X., Roger, F., Meyer, B., Arnaud, N., Wittlinger, G., & Jingsui, Y., 2001. Oblique stepwise rise and growth of the tibet plateau, *Science*, **294**, 1671–1677.

Thiede, R. C., Bookhagen, B., Arrowsmith, J. R., Sobel, E. R., & Strecker, M. R., 2004. Climatic control on rapid exhumation along the southern himalayan front, *Earth and Planetary Science Letters*, **222**(3-4), 791–806.

Torsvik, T., Mueller, R., Van der Voo, R., Steinberger, B., & Gaina, C., 2008. Global plate motion frames: Toward a unified model, *Reviews of Geophysics*, **46**, RG3004.

Weissel, J., Anderson, R., & Geller, C., 1980. Deformation of the indo-australian plate, *Nature*, **287**, 284–291.

Whipple, K. X. & Meade, B. J., 2004. Controls on the strength of coupling among climate, erosion, and deformation in two-sided, frictional orogenic wedges at steady state, *Journal of Geophysical Research*, **109**(F1), F01011.

Whipple, K. X. & Meade, B. J., 2006. Orogen response to changes in climatic and tectonic forcing, *Earth and Planetary Science Letters*, **243**(1-2), 218–228.

Wiens, D. A., DeMets, C., Gordon, R. G., Stein, S., Argus, D., Engeln, J. F., Lundgren, P., Quible, D., Stein, C., Weinstein, S., & Woods, D. F., 1985. A diffuse plate boundary model for indian ocean tectonics, *Geophysical Research Letters*, **12**(7), 429–432.

Willett, S. D., 1999. Orogeny and orography: The effects of erosion on the structure of mountain belts, *Journal of Geophysical Research*, **104**(B12), 28957–28981.

Willmott, C., Robeson, S., & Feddema, J., 1994. Estimating continental and terrestrial precipitation averages from rain-gauge networks, *International Journal of Climatology*, **14**(4), 403–414.

Yale, M. & Phipps Morgan, J., 1998. Asthenosphere flow model of hotspot-ridge interactions: a comparison of iceland and kerguelen, *Earth and planetary science letter*, **161**, 45–56.

Zatman, S., Gordon, R., & Richards, M., 2001. Analytic models for the dynamics of diffuse oceanic plate boundaries, *Geophysical Joutnal International*, **145**, 145–156.

Zhisheng, A., Kutzbach, J. E., Prell, W. L., & Porter, S. C., 2001. Evolution of asian monsoons and phased uplift of the himalaya–tibetan plateau since late miocene times, *Nature*, **411**, 62–66.

Figure captions

Figure 1. (a) Mean along-strike elevation of the Himalayas at present-day (gray). Elevation is fit by the sum of a positive contribution from plate convergence V, namely mountain building $M = \beta V^m$, and a negative contribution from intensified precipitation P, namely erosion $E = \alpha P^n + C$. (red: $n = 1$, $m = 1/2$, blue: $n = 3/2$, $m = 1/2$, green: $n = 3/2$, $m = 1$, black: $n = 1$, $m = 1$. (b) Present-day precipitation rate along the India/Eurasia convergent margin (solid blue, after Willmott et al. 1994) and quadratic interpolation (dashed blue). Total India/Eurasia convergence rate (solid red) along the margin, averaged over the past 20 Myrs and $\sim 5\,10^{-3}\,mm\,yr^{-1}/km$ longitudinal linear increase trend (dashed red). (c) Contributions to elevation from mountain building and erosion, plotted as along-strike increment from the relative minimum (colors as in panel a).

Figure 2. India (IN) convergence towards Eurasia (EU) over the past 20 Myrs (arrows, see text and supporting material) within four stages identified by different colours. Dots locate the Euler pole for the spreading of India with respect to Somalia (SO) at the same stages (right-hand rule). Present-day plate boundaries in black, oceans in white, continental topography above and below 4 km in gray-scale and light-gray respectively. AR: Arabia, NU: Nubia, AU: Australia.

Figure 3. Total (a), normal-to-trench (b), and parallel-to-trench (c) components of India/Eurasia convergence over the past 20 Myrs (see text and supporting material). Components are sampled at E95° (dashed gray) and E75° (solid black) along the convergent margin (see inset map), and averaged within four stages.

Figure 4.. (a) Present-day elevation of Himalayas and the Tibetan plateau. (b) Inferred elevation prior to monsoon intensification (see text and supporting material).

Figure 5. Model predictions for Indian plate motion change triggered by monsoon-driven elevation change in the Eastern Himalayas (black arrows). Black star denotes the Euler pole of the additional rotational component of convergence after monsoon intensification. Gray arrows show the model predicted plate motion change with merged India and Australia into a unique plate (gray arrows). Present-day plate boundaries in black, oceans in white, continents in gray. Acronyms as in Fig. 2.

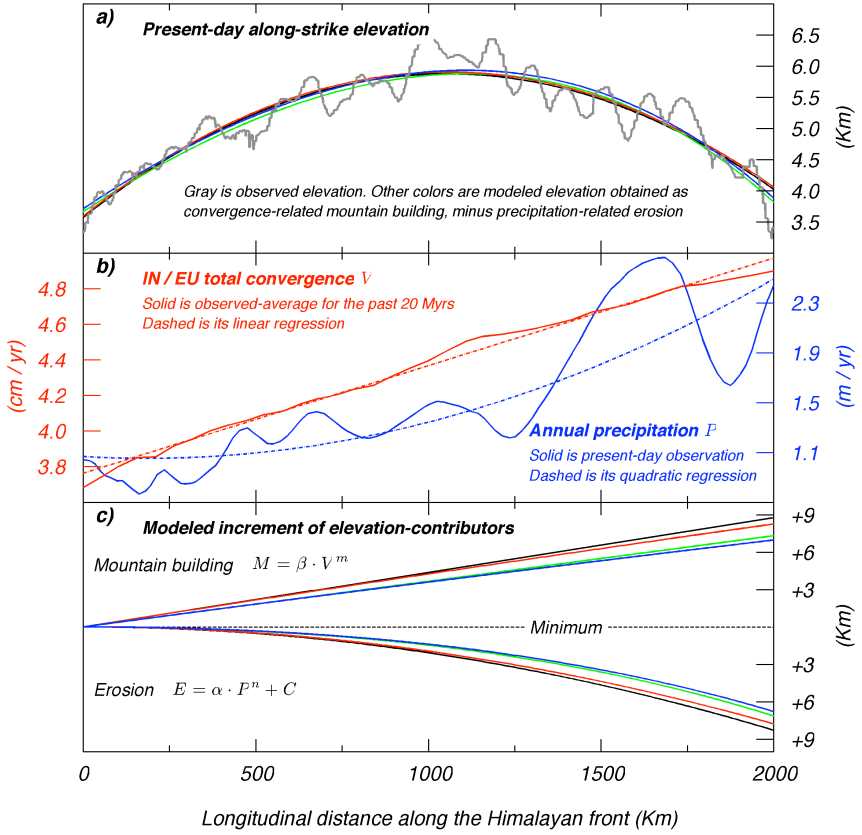

Figure 1:

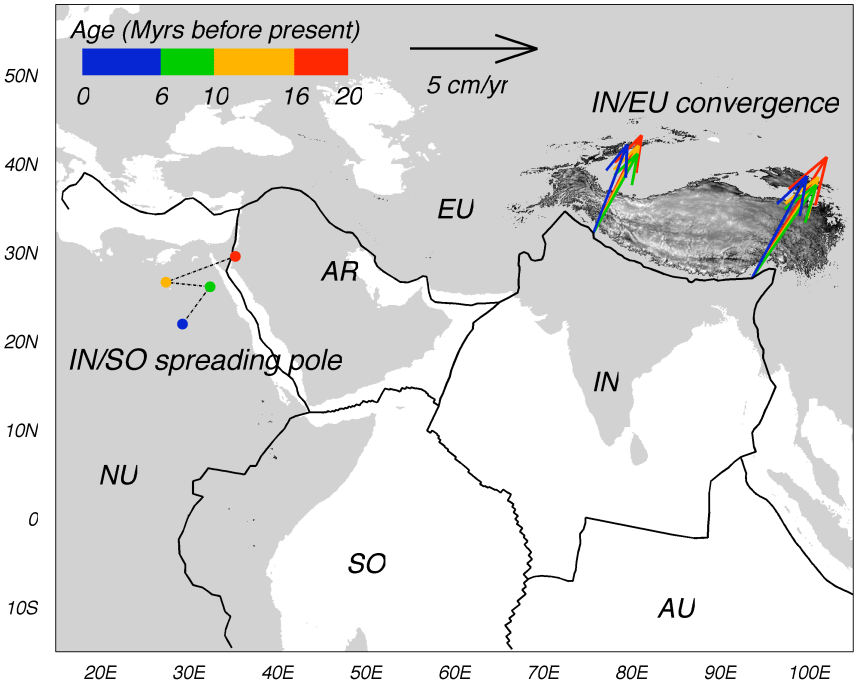

Figure 2:

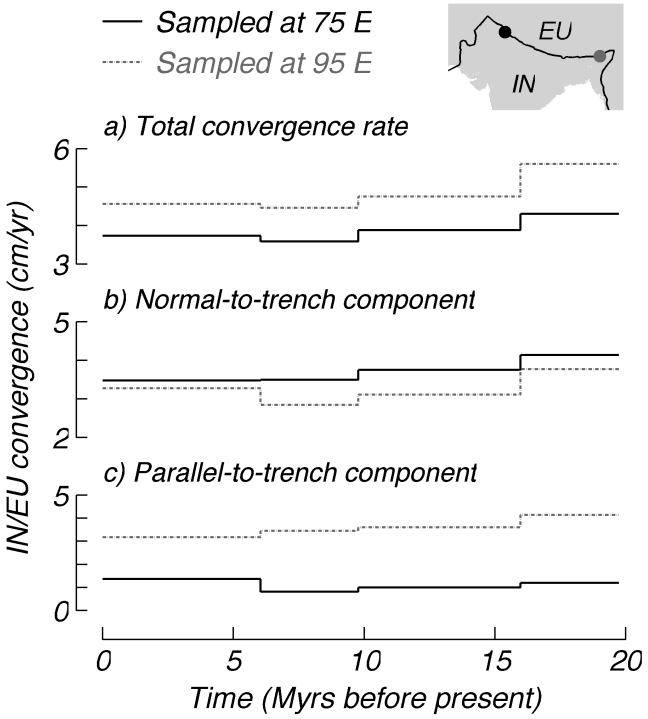

Figure 3:

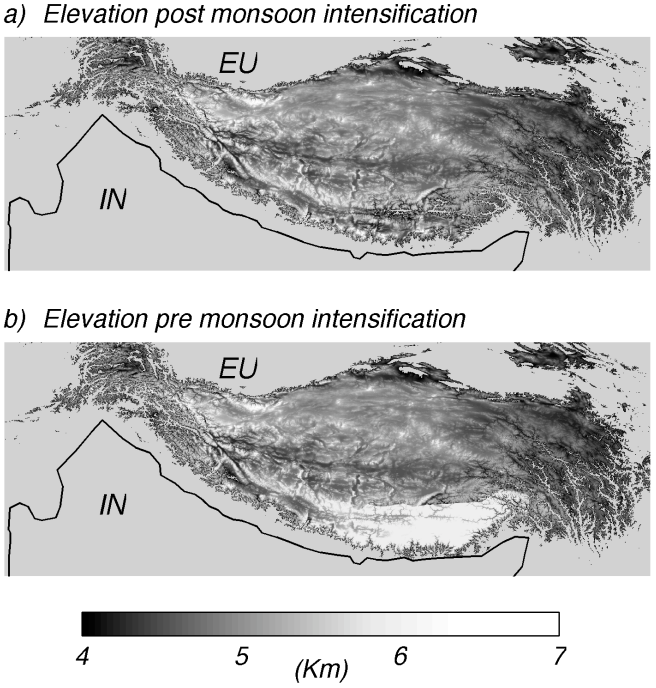

Figure 4:

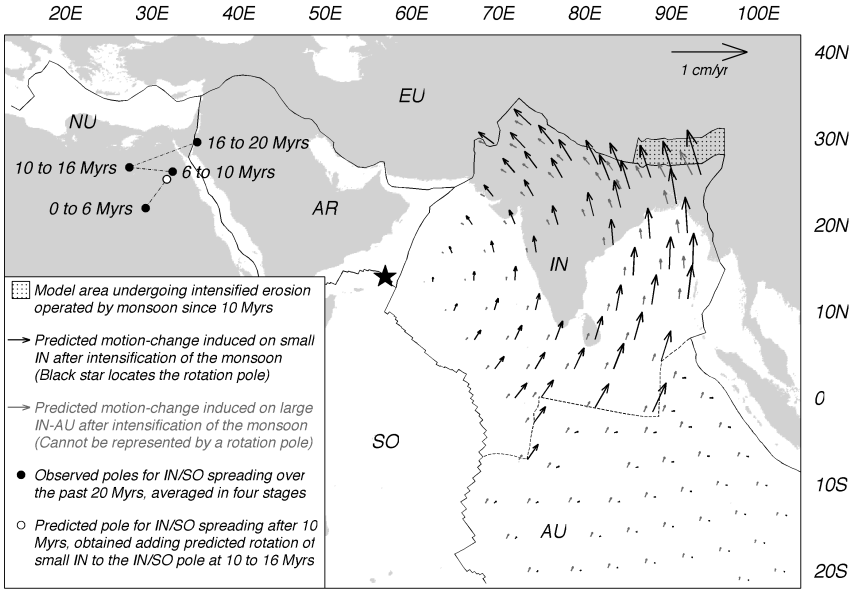
20E
30E
40E
50E
60E
70E
80E
90E
100E
40N
30N
20N
10N
0
10S
20S
1 cm/yr
EU
NU
AR
IN
SO
AU
16 to 20 Myrs
10 to 16 Myrs
6 to 10 Myrs
0 to 6 Myrs
Model area undergoing intensified erosion operated by monsoon since 10 Myrs
Predicted motion-change induced on small IN after intensification of the monsoon (Black star locates the rotation pole)
Predicted motion-change induced on large IN-AU after intensification of the monsoon (Cannot be represented by a rotation pole)
Observed poles for IN/SO spreading over the past 20 Myrs, averaged in four stages
Predicted pole for IN/SO spreading after 10 Myrs, obtained adding predicted rotation of small IN to the IN/SO pole at 10 to 16 Myrs

Figure 5:

behave as an individual plate. On its southwestern side, India separated from Africa thanks to the expansion of the Carlsberg ridge before the split of Africa into the two sub-plates of Nubia and Somalia (DeMets et al., 2005) along the East African Rift, which started spreading during Miocene (e.g., Pik et al., 2008). Estimates of the long-term convergence therefore shouldn't neglect the development of the East African rift. The evolution of India/Eurasia convergence can thus rigorously be evaluated by solving for the entire India-Somalia-Nubia-Eurasia plate circuit. We do so for the period that covers from present-day back to 20 Ma, taking advantage of previously published collections of plate-pairs finite-rotations (Horner-Johnson et al., 2005; Merkouriev & DeMets, 2006; Royer et al., 2006; Torsvik et al., 2008). Note that we compute Euler poles for the relative motion of each pair of adjacent plates, at the temporal resolution available from the associated compilation of finite rotations (see table 1). Such resolution may of course change for different plate-pairs, depending on the number of isochrons identified and/or reposted within each of the studies we refer to. We then compute a weighted average within the stages 0-6 Ma, 6-10 Ma, 10-16 Ma, and 16-20 Ma (see table 2).

India-Somalia

We reconstruct the sequence of Euler poles for the separation of India relative to Somalia over the past 20 Myrs from a recent compilation of finite rotations (Merkouriev & DeMets, 2006) (see table 1), the high resolution of which allows us speculating on the time-dependency of motion. Spreading rates decrease from 20 to 9 Ma, possibly indicating ongoing separation between India and Australia, and therefore a gradually stronger resistance of Tibet upon a smaller Indian plate (Iaffaldano & Bunge, 2009) or an increase in the resistance from the growing Tibetan plateau (Molnar & Stock, 2009). Spreading rates gradually tend to be even along the Carlsberg ridge from 20 to 9 Ma (it increases towards the Southeast from 27 to 30 mm/yr, on average along the ridge), after which it becomes much faster in the Southeast than in the Northwest

(from 23 to 36 mm/yr). Finally, we note that a change in the general pattern of spreading is also evident from India/Somalia polar wander, showing an eastward shift from its general NE-SW trend around 10 Ma (see Fg. 1 in the main text).

Somalia-Nubia

The kinematics of rifting between Nubia and Somalia is available at stages from present-day to 3.2 Ma, as well as from 3.2 to 11 Ma (Horner-Johnson et al., 2005; Royer et al., 2006), during which the Euler pole is rather stable (the magnitude varies by only 0.03 °/Myr between the two stages and the location of the pole wanders by only few degrees, see table 1). Recent evidences support the notion that the East African Rift begun spreading during the mid-Miocene (Pik et al., 2008; Bonini et al., 2005), and there appears to be no obvious reason for a different spreading regime during Early Miocene, or even for stronger activity. Unlike Molnar & Stock (2009), we therefore keep the simplest assumption that spreading remained constant, and deliberately extend the Euler pole of the stage 3.2 to 11 Ma, back to 20 Ma. The contribution of the East African rift to the plate circuit we solve for is essentially to translate the Carlsberg ridge and Indian plate northeastward. However, considering the small variation of Somalia/Nubia spreading, this converts into a negligible clockwise contribution to India/Eurasia convergence along the Himalayan front.

Nubia-Eurasia

During Neogene the pole of rotation of Nubia with respect to Eurasia remained relatively stable over the past 20 Myrs (Torsvik et al., 2008), in the vicinity of Cape Verde, with only few degrees of wander between 0 and 20 Ma and no significant variation in magnitude (see table 1). At the location of the Himalayas, such small degree of time-depencency contributes to vary the rate of India/Eurasia convergence by less than 0.1 cm/yr over the time period of interest.

We add the Euler poles of plate-pairs composing the India-Somalia-Nubia-Eurasia circuit to compute the sequence of Euler poles of India toward Eurasia, averaged within four stages spanning the past 20 Myrs (see table 2). In the recent period, convergence is characterized by significant counter-clockwise rotation of India. Along the Himalayas, the normal-to trench component of convergence increases by $\sim$0.5 cm/yr eastward, while the parallel-to-trench component increases by an almost equal amount in the Northwestern syntax (see Fg. 1 and 2 in the main text). Note that within the India-Somalia-Nubia-Eurasia plate circuit, the Carlsberg ridge bears most of the variability. Changes in the spreading regime of the Carlsberg ridge can either be related to a change in convergence between India and Eurasia, upstream in the plate circuit, or a change in the motion of Africa with respect to Eurasia, downstream. However, the kinematics of other plate-pairs composing the circuit support the former hypothesis.

Modelling the rotational convergence

Plate velocities and their time-dependence result from the evolving balance of momentum within the lithosphere. Such balance includes both shallow and deep-rooted contributions from forces related to subducting slabs, gravitational collapse of large topographic features, friction along faults and plate boundaries, deviatoric stresses associated with lateral variations of crust and lithosphere thicknesses, and shear tractions from the convecting mantle acting at the base of tectonic plates. Over the past decades there has been much but unrelated progress in developing numerical models of mantle and lithosphere dynamics. By merging these two independent classes of models we simulate the coupled mantle convection/plate tectonic system, where key components of the momentum-balance are simultaneously accounted for. Ultimately, we compute global plate velocities and associated equilibrium forces by coupling two independent

	Stage (Ma)	Longitude (°E)	Latitude (°N)	ω (°/Myr)
India-Somalia	20 to 18	35.2	37.4	0.49
	18 to 17.2	30.1	23.4	0.60
	17.2 to 16	38.7	25.0	0.60
	16 to14.6	30.6	26.7	0.46
	14.6 to 12.4	28.7	29.4	0.41
	12.4 to 11	29.7	24.2	0.42
	11 to 9.8	17.1	23.9	0.34
	9.8 to 9.1	23.7	41.1	0.30
	9.1 to 8.1	30.3	27.7	0.40
	8.1 to 6.7	30.5	25.5	0.39
	6.7 to 6	41.6	16.2	0.50
	6 to 5.2	8.4	19.2	0.30
	5.2 to 3.6	25.6	28.7	0.36
	3.6 to 2.6	39.6	12.8	0.53
	2.6 to 1.8	30.0	25.6	0.39
	1.8 to 0.8	33.5	24.1	0.41
	0.8 to 0	27.9	19.0	0.45
Somalia-Nubia	20 to 11	-172.5	51.8	0.13
	11 to 3.2	-172.5	51.8	0.13
	3.2 to 0	-177.2	44.7	0.08
Nubia-Eurasia	20 to 16	-15.9	11.4	0.12
	16 to 10	-21.2	19.2	0.12
	10 to 6	-25.4	19.1	0.12
	6 to 0	-26.9	17.9	0.12

Table 1: Euler poles for pairs of adjacent plates composing the India-Somalia-Nubia-Eurasia circuit. First plate rotates with respect to the second (see references in the text).

	Stage (Ma)	Longitude (°E)	Latitude (°N)	ω (°/Myr)
India-Eurasia	20 to 16	28.6	40.4	0.62
	16 to 10	18.9	40.4	0.48
	10 to 6	21.7	42.0	0.47
	6 to 0	19.1	35.7	0.46

Table 2: Reconstructed Euler poles for convergence of India towards Eurasia over the past 20 Myrs, averaged within four stages. First plate rotates with respect to the second.

models of mantle flow and lithosphere dynamics, described in the following.

The global mantle convection code TERRA (Bunge et al., 1997) solves for the conservation equations of mass, momentum, and energy to compute temperature and velocity fields throughout the mantle. Local finite-elements enable achieving sufficient spatial resolution to fully resolve the dynamically-important thermal boundary-layers of convective motion in the Earth's mantle: more than 100 million grid points are used, equivalent to a grid spacing of 10 to 20 km. Furthermore, high resolution allows for strong radial variations of mantle viscosity. Here we use a viscosity of $10^{21}\ Pa\,s$ for the upper mantle, increasing 40-fold in the lower mantle. Finally, we constrain our convection models with history of surface subduction (Lithgow-Bertelloni & Richards, 1998) to yield global mantle flow models.

The code SHELLS (Kong & Bird, 1995) is designed to model global lithosphere dynamics. Based on a 2D thin-shell spherical grid, it solves for the instantaneous balance of momentum to predict global plate velocities and associated force fields at equilibrium. SHELLS features a finite-element computational grid that explicitly accounts for geological faults and plate boundaries through interfaces between finite elements (Bird, 1998, 1999). Scalar values for topography, heat-flow, crustal and lithosphere thicknesses estimated through Airy compensation are assigned at each node. Stress sources contributing to momentum in the lithosphere include global topography and its lateral variations, lateral differences in crustal and lithospheric thicknesses, as well as shear stresses from the convecting mantle at the base of plates. No vertical shear traction is assumed on vertical planes so that vertical normal stresses are lithostatic at all nodes, and equal to the weight of the overburden per unit area. A temperature vertical profile at each node is computed in order to define the rheological properties of the deep crust and lithosphere. Thermal conductivity and radioactive heat generation are uniform and constant throughout the model lithosphere. Dip angles of faults and plate boundaries cast within the numerical grid are constrained from seismological observations. The rheological properties of

faults and plate boundaries are accounted for by assigning weaker rheologies to selected interfaces between elements, that follow realistic plate-boundary configurations. Specifically the code computes temperature, pressure and strain rate along the dipping fault plane to assign the rheological law - between frictional (Mohr-Coulomb) faulting or dislocation creep - that provides the lowest shear stress. The model accounts for friction ceofficients at plate boundaries ranging from 0.03 to 0.15, much lower than suggested by Byerlees law for non-faulted material (0.85), and in agreement with recent geometrical constraints on the internal and basal strength of faults (Suppe, 2007). When dislocation creep prevails, stress σ is proportional to strain rate $\dot{\epsilon}$ and depends on temperature θ and depth z: $\sigma = A\,\dot{\epsilon}^{\frac{1}{n}}\,exp^{\frac{B+Cz}{\theta}}$, with A, B and C being constants. We set the following values for the crust and lithospheric mantle layers, respectively to $A = 3.2\,10^{7}\,Pa\,s^{1/3}$ and $3.4\,10^{4}\,Pa\,s^{1/3}$, $B = 10048\,K$ and $21340\,K$, $C = 0\,K\,m^{-1}$ and $0.0233\,K\,m^{-1}$, $n = 3$ within both layers. Such values are selected within the range of observations (Bird, 1998; Hickman, 1991) so that, at the average computed strain-rate, we obtain the same effective viscosity within the asthenospheric parts of mantle and lithosphere models.

The two models are coupled by using asthenosphere velocities derived from mantle circulation models (MCMs) as a velocity boundary condition at the base of plates in the lithosphere model. Plate basal-tractions are then computed through the dislocation creep rheology of olivine, where strain rate equals the vertical gradient of the asthenosphere velocity pattern from MCMs. Therefore we explicitly include in the momentum balance of lithosphere realistic mantle buoyancy forces, that arise from MCMs constrained with history of subduction. However, the coupling is not fully reciprocal for we assign a kinematic boundary condition in MCMs.

References

Bird, P., 1998. Testing hypotheses on plate-driving mechanisms with global lithosphere models including topography, thermal structure, and faults, *Journal of Geophysical Research*, **103**, 10115–10129.

Bird, P., 1999. Thin-plate and thin-shell finite element programs for forward dynamic modeling of plate deformation and faulting, *Computers and Geosciences*, **25**, 383–394.

Bonini, M., Corti, G., Innocenti, F., Manetti, P., Mazzarini, F., Abebe, T., & Pecskay, Z., 2005. Evolution of the Main Ethiopian Rift in the frame of Afar and Kenya rifts propagation, *Tectonics*, **24**, C1007+.

Bunge, H.-P., Richards, M., & Baumgardner, J., 1997. A sensitivity study of 3-D spherical mantle convection at 10exp8 Rayleigh number: Effects of depth dependent viscosity, heating mode and an endothermic phase change, *J. Geophys. Res.*, **102**, 11991–12007.

Chemenda, A. I., Burg, J.-P., & Mattauer, M., 2000. Evolutionary model of the himalaya-tibet system: geopoem: based on new modelling, geological and geophysical data, *Earth and Planetary Science Letters*, **174**(3-4), 397–409.

Conder, J. A. & Forsyth, D. W., 2001. Seafloor spreading on the southeast indian ridge over the last one million years: a test of the capricorn plate hypothesis, *Earth and Planetary Science Letters*, **188**(1-2), 91–105.

DeMets, C., Gordon, R. G., & Royer, J.-Y., 2005. Motion between the indian, capricorn and somalian plates since 20 ma: implications for the timing and magnitude of distributed lithospheric deformation in the equatorial indian ocean, *Geophysical Journal International*, **161**(2), 445–468.

Gordon, R., Argus, D., & Royer, J.-Y., 2008. Space geodetic test of kinematic models for the indo-australian composite plate, *Geology*, **36**(10), 827–830.

Gordon, R. G., DeMets, C., & Royer, J.-Y., 1998. Evidence for long-term diffuse deformation of the lithosphere of the equatorial indian ocean, *Nature*, **395**(6700), 370–374.

Hickman, S., 1991. Stress in the lithosphere and the strength of active faults, *Reviews of Geophysics*, **29**, 759–775.

Horner-Johnson, B. C., Gordon, R. G., Cowles, S. M., & Argus, D. F., 2005. The angular velocity of nubia relative to somalia and the location of the nubia-somalia-antarctica triple junction, *Geophysical Journal International*, **162**(1), 221–238.

Iaffaldano, G. & Bunge, H.-P., 2009. Relating rapid plate motion variations to plate boundary forces in global coupled models of the mantle/lithosphere system: effects of topography and friction, *Tectonophysics*, **474**, 393–404.

Kong, X. & Bird, P., 1995. Shells: a thin-shell program for modeling neotectonics of regional or global lithosphere with faults, *Journal of Geophysical Research*, **100**, 22129–22131.

Lithgow-Bertelloni, C. & Richards, M., 1998. Dynamics of cenozoic and mesozoic plate motions, *Reviews of Geophysics*, **36**, 27–78.

Merkouriev, S. & DeMets, C., 2006. Constraints on indian plate motion since 20 ma from dense russian magnetic data: Implications for indian plate dynamics, *Geochemistry Geophysics Geosystems*, **7**, Q02002.

Molnar, P. & Stock, J., 2009. Slowing india's convergence with eurasia since 20 ma and its implications for tibetan mantle dynamics, *Tectonics*, **28**, 357–396.

Patriat, P. & Achache, J., 1984. India-eurasia collision chronology has implications for crustal shortening and driving mechanism of plates, *Nature*, **311**(5987), 615–621.

Pik, R., Marty, B., Carignan, J., Yirgu, G., & Ayalew, T., 2008. Timing of East African Rift development in southern Ethiopia: Implication for mantle plume activity and evolution of topography, *Geology*, **36**(2), 167–170.

Royer, J.-Y. & Gordon, R. G., 1997. The Motion and Boundary Between the Capricorn and Australian Plates, *Science*, **277**(5330), 1268–1274.

Royer, J.-Y., Gordon, R. G., & Horner-Johnson, B. C., 2006. Motion of nubia relative to antarctica since 11 ma: Implications for nubia-somalia, pacific-north america, and india-eurasia motion, *Geology*, **34**(6), 501–504.

Suppe, J., 2007. Absolute fault and crustal strength from wedge tapers, *Geology*, **35**(12), 1127–1130.

Torsvik, T., Mueller, R., Van der Voo, R., Steinberger, B., & Gaina, C., 2008. Global plate motion frames: Toward a unified model, *Reviews of Geophysics*, **46**, RG3004.

Wiens, D. A., DeMets, C., Gordon, R. G., Stein, S., Argus, D., Engeln, J. F., Lundgren, P., Quible, D., Stein, C., Weinstein, S., & Woods, D. F., 1985. A diffuse plate boundary model for indian ocean tectonics, *Geophysical Research Letters*, **12**(7), 429–432.

1.3.2 Les instabilités lithosphériques et la propagation des hauts plateaux

L'évolution morphologique des chaînes de montagnes semble, d'après les exemples disponibles, être caractérisée par la croissance d'une chaîne peu large localisée au niveau de la marge, dont l'altitude s'accroît jusqu'à un maximum, suivi d'une propagation de la déformation vers l'intérieur du continent chevauchant. L'étape ultime est l'écroulement du haut plateau ainsi formé. Les Alpes, les Andes, les Himalaya-Tibet, puis la Cordillière nord-américaine peuvent être vu comme des étapes de cette progression. Les causes mécaniques restent débattues, et s'établissent autour de deux modèles conceptuels limites. Le premier, dans lequel la lithosphère est comprise comme une plaque cassante s'épaississant par un écaillage à l'échelle de la lithosphère [Tapponnier et al., 2001] bute sur la jusitification d'une rhéologie permettant une pareille évolution. Le second, qui fait intervenir un fluage visqueux de la croûte et du manteau lithosphérique [Royden et al., 2008], permet d'expliquer une vaste partie des observations en respectant les contraintes rhéologiques. Cependant, la propagation à des distances de l'ordre de 1500 km, au Tibet ou en Amérique du Nord, reste difficile à expliquer sans l'existence d'une chaîne excessivement haute au niveau de la fosse.

Le nombre d'Argand Ar relie les contraintes gravitationelles et la viscosité. Il donne ainsi une mesure de la capacité d'un orogène à maintenir une altitude sans fluer, c'est-à-dire à s'épaissir plus vite qu'il ne s'écroule sous son propre poids. Dans les gammes de paramètres raisonables géologiquement, il ressort -sans surprise ?- que les montagnes peuvent atteindre des altitudes maximales qui sont comparables à celles observées sur la Terre actuelle (notons que cette valeur a changé depuis l'Archéen à mesure que la Terre se refroidit [Rey & Houseman, 2006]). Cependant, la propagation latérale des chaînes de montagnes au profit d'un développement en hauts plateaux reste difficile a percevoir dans ce contexte. Ce travail, qui fait suite au précédent (également en collaboration avec Y. Ricard), examine le rôle favorable des instabilités gravitationelles de la lithosphère thermique dans le développement des hauts plateaux.

Dans la section précédente, seules les contraintes gravitationelles dues aux variations d'épaisseur crustale sont considérées, négligeant la possibilité d'une contribution par des hétérogénéités thermiques ou chimiques siégeant dans le manteau lithosphérique. La différentiation chimique du manteau implique probablement l'existence d'hétérogénéités de densité dans la lithosphère, dont l'importance est mal connue. Une autre source d'hétérogénéité est d'origine thermique. Le manteau lithosphérique est par définition plus froid que l'asthénosphère sous-jacente. Il existe donc dans la lithosphère une compétition entre l'effet du moment crustal -qui tend à restaurer une épaisseur uniforme- et le moment thermique lithosphérique, instable qui tend à destabiliser la lithosphère et à l'entraîner dans la convection mantellique (fig. 1.1). Le comportement gravitaire de la couche lithosphérique limite thermique a largement été étudié en termes d'instabilités de Rayleigh-Taylor, et apppliqué à une très large gamme de contextes géologiques, en particulier par Molnar et Houseman [Conrad & Molnar, 1999, Houseman et al., 1981, Molnar et al., 1998]. Cependant, peu d'études examinent la compétition avec la croûte dont la flottabilité est positive et qui pour le moins ralentit la destabilistation du système [Molnar & Houseman, 2004].

Cette compétition entre la stabilisation par la croûte et la déstabilisation par la lithosphère thermique est remarquable dans le cas des Andes Centrales, où la déformation s'accélère sous la Cordillière Orientale à mesure qu'une instabilité lithosphérique se développe dans le manteau. Celle-ci est imagée par la tomographie sismique [Baumont et al., 2002], et la conversion des vitesses de propagation des ondes S en anomalies de température puis en densité révèle la présence d'une forte anomalie de densité sous la Cordillière Orientale (fig. 1.2). En termes de moments, il ressort que les variations latérales du moment thermique lithosphérique sont comparables en magnitude aux variations latérales du moment crustal, minéralogique. Les contraintes de flottabilité qui en résultent sont en conséquence également comparables (fig. 1.3). L'incidence sur la dynamique lithosphérique de la racine lithosphérique apparaît significative : elle pourrait être capable de stimuler la tectonique dans la Cordillière Orientale.

Afin d'évaluer l'impact sur l'histoire tectonique de la chaîne, j'ai introduit progressivement le moment thermique dans un modèle du même type que ceux présentés

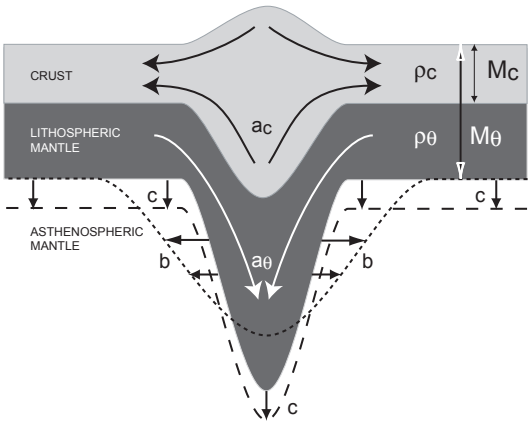

FIG. 1.1: Compétition entre les forces de flottabilité dans la croûte, qui tendent à stabiliser le système, et les forces de flottabilité de la lithosphère thermique, qui tendent à destabiliser le système. L'efficacité de l'instabilité de Rayleigh-Taylor de la lithosphère est modulée par la croûte, moins dense que le manteau lithosphérique sous-jacent. *Competition between the stabilizing crustal buoyancy forces and the lithospheric thermal destabilizing buoyancy forces. The efficiency of the Rayleigh-Taylor instability is modulated by the crust, less dense than the underlying lithospheric mantle.*

en section 1.3.1. Il est introduit *ad-hoc* (bien qu'étayée par l'enregistrement géologique de la convergence entre les Andes Centrales et le bouclier brésilien) dans l'équilibre du système en supposant une croissance linéaire dans le temps de la racine lithosphérique entre 27 Ma et 0 Ma. A l'inverse des modéles qui prennent uniquement en compte la cinématique, les processus s'accélèrent à mesure que le moment négatif de la lithosphère thermique prend de l'ampleur (fig. 1.4). Cette accélération de la tectonique andine est plus fidèle aux enregistrement géologiques de la croissance andine (comme les paléo-altimètres, largement utilisés et débattus dans les Andes Centrales, voir Garzione et al. [2008] ou Sempere et al. [2006] pour une revue).

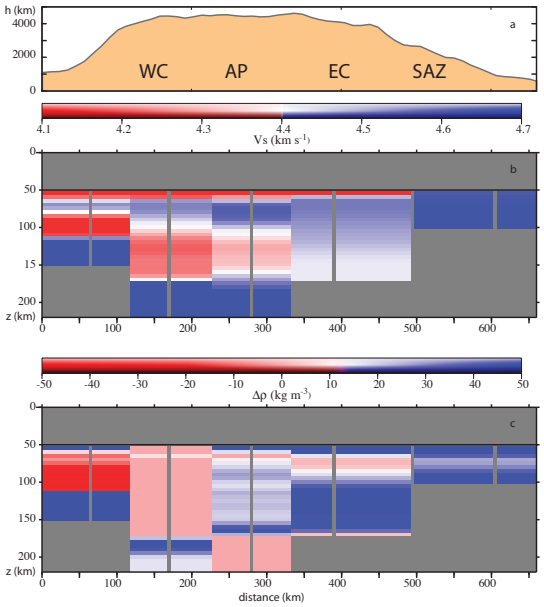

FIG. 1.2: Anomalies de vitesses de propagations des ondes S sous les Andes Centrales (22°S) [Baumont et al., 2002], et conversion en anomalies de densité. La conversion est réalisée avec $\partial V_s/\partial T = 3.3\,10^{-4}$ [Lee, 2003], une expansion thermique $\alpha = 2.4\,10^{-5}\,K^{-1}$ [Turcotte & Schubert, 2002], et une densité de référence $\rho_0 = 3225\,kg\,m^{-3}$. *S-wave velocity anomalies in the Central Andes (22° S)[Baumont et al., 2002], and conversion into density anomalies (assuming* $\partial V_s/\partial T = 3.3\,10^{-4}$ *[Lee, 2003], a thermal exansion* $\alpha = 2.4\,10^{-5}\,K^{-1}$ *[Turcotte & Schubert, 2002], and a reference density* $\rho_0 = 3225\,kg\,m^{-3}$.

Dans l'article qui suit, nous examinons avec Y. Ricard cette compétition en utilisant toujours le formalisme des plaques minces visqueuses, en couplant les moments lithosphériques thermiques M_θ et minéralogiques M_c (siégeant ici uniquement dans la croûte). Le problème est traité en 2 dimensions. L'étude de stabilité révèle bien sûr un mode dans lequel l'hétérogénéité thermique domine et déstabilise la lithosphère et un mode dans lequel la croûte stabilise la lithosphère. Un mode plus inattendu correspond à une propagation spatiale, sous forme d'ondes tectoniques, qui conduisent à la progradation de la déformation très à l'intérieur des plaques, sous forme de trains d'ondes. La vitesse de groupe est de l'ordre de 0.5 mm/yr, comparable à la vitesse de propagation des hauts plateaux comme le Tibet [Royden et al., 2008, Tapponnier et al., 2001]. Ce modèle continu peut alors être proposé

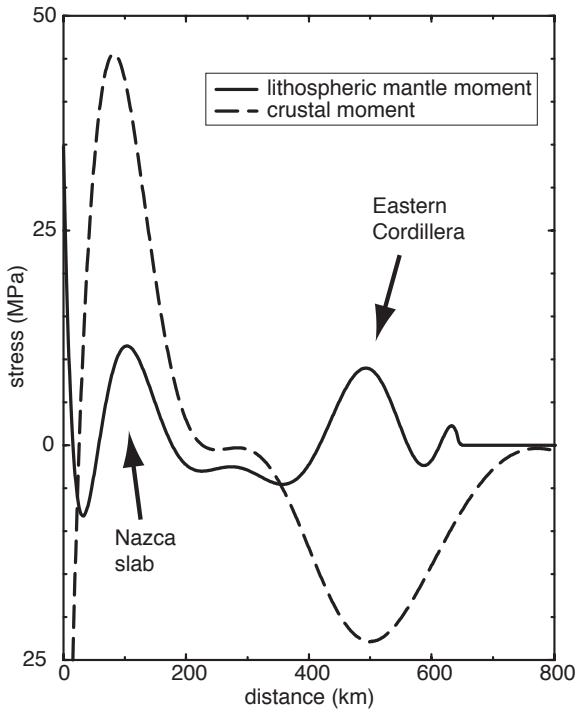

FIG. 1.3: Contraintes de flottabilité dans les Andes Centrales (22°S) inférées d'après la vitesse de propagation des ondes S [Baumont et al., 2002] pour la composante thermique lithosphérique (tiretés), et sur la base d'un modèle isostatique pour la composante crustale, tel que $\rho_c = 2800\,kg\,m^{-3}$ et $\rho_m = 3225\,kg\,m^{-3}$. *Buoyancy forces in the Central Andes (22° S) inferred from the S-wave propagation velocity [Baumont et al., 2002] for the lithospheric thermal component (dashed line) and on the basis of an isostatic model for the crustal component (solid), with* $\rho_c = 2800\,kg\,m^{-3}$ *and* $\rho_m = 3225\,kg\,m^{-3}$*).*

comme une alternative au mode de propagation discontinu proposé par Tapponnier et al. [2001] sur la base d'interprétations très discutées des résultats de la tomographie sismique de Griot et al. [1998]. Un régime oscillatoire comparable dans la lithosphère *a priori* stable des cratons a été récement mis en évidence par Jaupart et al. [2007]. Cette étude diffère cependant dans le traitement des instabilités thermiques qui sont atténuées par diffusion à mesure que les instabilités se développent.

Propagation of tectonic waves

Y. Ricard[1]
Department of Geology and Geophysics, Yale University, New Haven, Connecticut, USA

L. Husson
Earth, Atmospheric and Planetary Sciences, Massachusetts Institute of Technology, Cambridge, Massachusetts, USA

Received 10 June 2005; revised 2 August 2005; accepted 10 August 2005; published 13 September 2005.

[1] Mountain building depends on the disequilibrium between boundary stresses, either at the base of the deforming lithosphere or its lateral boundaries, and buoyancy stresses arising form lateral density variations within the lithosphere itself. On the basis of the thin viscous sheet approximation, we propose a model which accounts for both crustal and lithospheric thickness variations. The deformation is controlled by the sum of the moments of density anomalies (i.e. density anomalies times depth) of compositional and thermal origins. The transport of the compositional moment is obtained from the continuity equation while the transport of the thermal moment is obtained from the heat equation. The resulting set of equations controls the coupled behavior of the crust and lithosphere. It shows that various type of solutions can exist: unstable, stable and propagating. When propagation occurs, the crustal and the lithospheric thickness variations are out of phase. The tectonic waves propagate with velocities around 5 mm yr^{-1} that increase with the crustal thickness and decrease with the lithospheric viscosity. We discuss these solutions and argue that continents may in large part be in a domain of propagating tectonic waves. **Citation:** Ricard, Y., and L. Husson (2005), Propagation of tectonic waves, *Geophys. Res. Lett.*, *32*, L17308, doi:10.1029/2005GL023690.

1. Introduction

[2] The fundamental role of crustal thickness variations in the stress balance has been acknowledged since [*Argand*, 1924], and almost all tectonic models account for it. The lithosphere is a thermal boundary layer and its lateral thickness variations in time and space during an orogenesis are also associated with density variations. Whereas the crust constantly tends to approach a uniform thickness because it is lighter than the underlying mantle, the cooling lithospheric mantle is denser than the underlying asthenosphere and may become unstable [e.g., *Houseman et al.*, 1991; *Neil and Houseman*, 1999; *Conrad*, 2000]. The dynamics of orogenesis results from the balance between competing processes of crustal and lithospheric thickening.

2. The Model

[3] A thin viscous sheet approximation has been extensively used to describe the dynamics of the crust, [e.g., *England and McKenzie*, 1982; *Houseman and England*, 1993; *Husson and Ricard*, 2004]. This approximation is based on the vertical integration of the Navier-Stokes equations, coupled with mass conservation of the crust which controls the time evolution of the model. *Lémery et al.* [2000] have extended this approach in the case of thermal density variations to derive a boundary layer model of convection at very large Rayleigh number. In the present paper we couple these approaches to take into account both compositional and thermal heterogeneities in the deforming lithosphere.

[4] The main assumption of the thin sheet viscous models is that the vertical variations of the horizontal velocity can be neglected within the lithosphere. This holds when the lithosphere is stiff enough with respect to the underlying asthenosphere and when the deformations occur at wavelengths larger than the lithospheric thickness.

2.1. Stress Balance

[5] We assume that the lithosphere behaves like an incompressible viscous fluid of viscosity η and that isostasy holds across the whole lithosphere. If the upper and lower boundaries of the lithosphere are traction free, the horizontal equilibrium equation relates the lateral density variations to the viscous stresses by

$$4L_0 \frac{\partial}{\partial x} \eta \frac{\partial u}{\partial x} = \frac{\partial M}{\partial x}, \tag{1}$$

where u denotes the vertically average velocity and L_0 the uniform averaged thickness of the mechanical lithosphere [*Lémery et al.*, 2000]. The quantity M is the moment of the lithospheric mass anomalies and is written [*Artyushkov*, 1973; *Fleitout and Froidevaux*, 1982]

$$M = \int_0^{+\infty} \delta\rho g z \, dz, \tag{2}$$

where $\delta\rho$ is the lateral density variation, g the gravitational acceleration, z the depth measured downward from sea level. This equation assumes that below some compensation depth the density heterogeneities $\delta\rho$ vanish so that equation (2) remains finite.

[6] In the lithosphere, the total moment M can be divided into a compositional component M_c which relates to the difference between crustal and mantle densities ρ_c and ρ_m, and a thermal moment M_θ

$$M_c = \frac{1}{2}\rho_c g \left(1 - \frac{\rho_c}{\rho_m}\right) S^2, \qquad M_\theta = \int_0^{+\infty} z \rho_m g \alpha \theta \, dz, \tag{3}$$

[1] Permanently at Laboratoire des Sciences de la Terre, UMR5570, Université de Lyon 1, Villeurbanne, France.

Copyright 2005 by the American Geophysical Union.
0094-8276/05/2005GL023690$05.00

where S is the nonuniform crustal thickness, α the thermal expansion coefficient and θ the temperature of the lithosphere minus the deep mantle temperature (i.e. θ and M_θ are negative). Using (3), we make the approximation that the products expansivity times density are the same in the crust and in the lithosphere.

[7] The crustal moment M_c depends on the squared crustal thickness S [*England and McKenzie*, 1982, 1983]. If the vertical temperature gradient is constant across a thermal lithosphere of thickness L, the thermal moment writes

$$M_\theta = -\frac{1}{3}\rho_m \alpha \Delta\theta g L^2, \tag{4}$$

where $\Delta\theta$ is the temperature increase across the lithosphere. The thermal moment is therefore related to the squared lithospheric thickness.

[8] By isostasy the surface topography h can be expressed in terms of S and L (or in terms of M_c and M_θ using (3))

$$h = \frac{\rho_m - \rho_c}{\rho_m} S - \frac{1}{2}\alpha \Delta\theta L. \tag{5}$$

The lithospheric contribution to isostasy is generally small compared to the crustal contribution.

2.2. Transport

[9] The time-dependence of the crustal moment is obtained by assuming crustal mass conservation:

$$\frac{\partial M_c}{\partial t} + u\frac{\partial M_c}{\partial x} + 2M_c\frac{\partial u}{\partial x} = 0, \tag{6}$$

the coefficient 2 in the last term of the left hand side of (6) comes from the fact that $M_c \propto S^2$ (see (2)). The heat equation multiplied by z and integrated vertically yields the transport of the thermal moment [*Lémery et al.*, 2000]

$$\frac{\partial M_\theta}{\partial t} + u\frac{\partial M_\theta}{\partial x} + 2M_\theta\frac{\partial u}{\partial x} = \kappa\frac{\partial^2 M_\theta}{\partial x^2}, \tag{7}$$

(κ is the thermal diffusivity). The third term of the left hand side expresses the fact that the lithosphere can become thinner by developing cold downwelling instabilities. In equation (7) we have neglected the secular increase in lithospheric thickness due to the difference between surface cooling (a term which goes as $-\kappa\rho_m g\alpha\Delta\theta$ in *Lémery et al.* [2000]) and internal radioactive mantle production. In other terms we assume that the planet surface heat flux equals the rate of radiogenic heat production. The secular cooling term is uniform and keeping a modest cooling rate in the equations would not affect our conclusions.

3. Dynamics of the Lithosphere

[10] The dynamics of the lithosphere is therefore controlled at long wavelength by equations (1), (6) and (7). The stability/instability of the crust-lithosphere combination on top of the mantle is akin to that of a light/heavy fluid layer on top of another fluid, namely akin to Rayleigh-Taylor instability. However, due to the thermal diffusive term in the transport equation in (7) but not in (6), the coupled dynamics of the crust and lithosphere yields some surprising behavior with respect to the classical Rayleigh-Taylor instability.

3.1. Stability Analysis

[11] In order to solve our system of equations we can replace x, t, u, M_c, M_θ by $L_0\tilde{x}$, $(L_0^2/\kappa)\,\tilde{t}$, $(\kappa/L_0)\tilde{u}$, $(\eta\kappa/L_0)\tilde{M}_c$, $(\eta\kappa/L_0)\tilde{M}_\theta$ where the $\sim$ variables are now dimensionless. To study the stability of our system, let us assume that the solution consists in a uniform state without any tectonic velocity plus infinitesimal perturbations, $\tilde{M}_c = M_c^0 + \epsilon m_c(\tilde{x}, \tilde{t})$, $\tilde{M}_\theta = M_\theta^0 + \epsilon m_\theta(\tilde{x}, \tilde{t})$, $\tilde{u} = \epsilon u(\tilde{x}, \tilde{t})$, where M_c^0 and M_θ^0 are the uniform dimensionless moments and $\epsilon \ll 1$. Assuming all terms of order ϵ go as $\exp(ik\tilde{x} + \sigma\tilde{t})$, our governing equations (1), (6) and (7) yield to first order in ϵ

$$\begin{aligned} 4uk + i(m_c + m_\theta) &= 0, \\ \sigma m_c + 2ikM_c^0 u &= 0, \\ \sigma m_\theta + 2ikM_\theta^0 u + k^2 m_\theta &= 0. \end{aligned} \tag{8}$$

Solving for σ leads to the dispersion relation

$$2\sigma^2 + \sigma\left(M_\theta^0 + M_c^0 + 2k^2\right) + k^2 M_c^0 = 0. \tag{9}$$

Depending of the sign of the discriminant of this second degree equation, σ can either be real or imaginary. Let us define k_1 and k_2

$$k_1 = \frac{\left(\sqrt{|M_\theta^0|} - \sqrt{M_c^0}\right)}{\sqrt{2}}, \quad k_2 = \frac{\left(\sqrt{|M_\theta^0|} + \sqrt{M_c^0}\right)}{\sqrt{2}}. \tag{10}$$

If $0 < k < |k_1|$ or $k > k_2$, the two roots of the dispersion equation are real and the growth rate σ is

$$\sigma = \frac{1}{2}\left(k_1 k_2 - k^2\right) \pm \frac{1}{2}\sqrt{\left(k_1^2 - k^2\right)\left(k_2^2 - k^2\right)}. \tag{11}$$

On the contrary, when $|k_1| < k < k_2$, the roots are imaginary numbers (i.e. $\sigma = Real(\sigma) + i\omega$),

$$Real(\sigma) = \frac{1}{2}\left(k_1 k_2 - k^2\right), \ \omega = \frac{1}{2}\sqrt{\left(k^2 - k_1^2\right)\left(k_2^2 - k^2\right)} \tag{12}$$

[12] The roots of the dispersion equation are depicted in Figure 1. When $M_\theta^0 + M_c^0 > 0$ (dashed lines, $k_1 < 0$) the lithosphere is everywhere stable. On the contrary, when $M_\theta^0 + M_c^0 < 0$ (solid lines, $k_1 > 0$) long wavelength perturbations ($k < k_1$) are unstable (the two σ roots are positive). This is the typical case of Rayleigh-Taylor instabilities with a dense fluid on top of a lighter fluid. However, the dynamics are different from the Rayleigh-Taylor situation at shorter wavelengths. For the shortest wavelengths ($k > k_2$), lithospheric thermal anomalies are erased by thermal diffusion and any perturbation vanishes. For $0 < k_1 < k < k_2$, a propagating unstable mode becomes a propagating stable mode as k increases. This tectonic wave propagates as a plane wave at phase velocity ω/k and

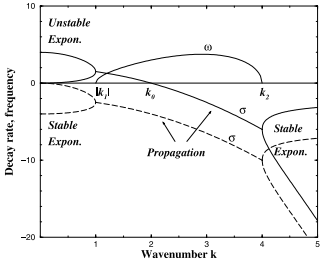

Figure 1. Decay rate σ and angular frequency ω of a perturbation of the crust or the lithospheric thicknesses as a function of the wave number k. The solid line corresponds to a case where the lithosphere is globally unstable. As the wave number increases, the dynamics shifts from unstable to stable. Between $|k_1|$ and k_2 propagating tectonic waves are excited. The dashed line is for a stable lithosphere. For the clarity of the plot, we used the geologically nonrelevant values $k_1 = 1$ and $k_2 = 4$ (solid line) and $k_1 = -1$ and $k_2 = 4$ (dashed lines).

physically, as it is a dispersive wave, at the group velocity $d\omega/dk$. When $Real(\sigma) = 0$, a pure propagating mode of constant amplitude exists with wave number and angular frequency

$$k_0 = \sqrt{k_1 k_2}, \quad \text{and} \quad \omega = \frac{1}{2}k_0(k_2 - k_1). \tag{13}$$

This particular wave propagates with the maximum phase velocity and its group and phase velocities are equal. Its velocity that can easily be expressed in dimensional units by

$$v_p = \frac{1}{2}\sqrt{\frac{\kappa\rho_c(\rho_m - \rho_c)g}{L_0\eta\rho_m}}S. \tag{14}$$

[13] The existence of a propagating mode is surprising in a context where only diffusive processes occur (diffusion of momentum and diffusion of heat). The propagation occurs while the undulations of the crust and the lithosphere are not in phase. This can be shown by solving (8) which implies that the ratio of the crustal and lithospheric deformations is a complex number,

$$m_\theta = -\frac{m_c}{(k_1 - k_2)^2}\left(\left(k_1^2 + k_2^2 - 2k^2\right) + 4i\omega\right). \tag{15}$$

[14] We can compare to real geological situations by redimensionalizing our results. The only parameter value whose value is debatable is the lithospheric viscosity. We choose a rather low stiffness of the lithosphere, $L_0 = 50$ km, $\eta = 2\ 10^{21}$ Pa s, which is however the kind of values commonly used to model orogeny [*England*, 1986; *Husson and Ricard*, 2004]. The other parameters are standard and yield $k_1 = 0.1$ and $k_2 = 12$ for $S = 40$ km and $L = 83$ km (see parameters in the caption of Figure 2). The compositional and lithospheric moment have opposite signs and similar amplitudes, $M_c^0 = 71$, $M_\theta^0 = -73$. With this parameters, propagation takes place for wavelengths between 26 km and 3140 km. This suggests that much of continental tectonics is either in the unstable regime or in the propagating regime. Only the shortest wavelengths are stable (wavelengths less than 26 km). In this uninteresting domain, however, our long wavelength approximation breaks down.

[15] As seen in Figure 2, the phase and group velocities have typical values from 5 to 10 which in real units corresponds to 3.2 to 6.4 mm yr^{-1}. With the same parameters, $S = 40$ km and $L = 83$ km, propagation at constant amplitude occurs for a wavelength of 287 km and a velocity of 3.7 mm yr^{-1} (see (14)).

3.2. Nonlinear Solutions

[16] The previous results have been obtained in the linear stability approximations where the nonlinear terms have been neglected. We can also compute the whole nonlinear solution using a standard finite difference algorithm with periodic boundary conditions and explicit time-stepping.

[17] In Figure 3, we depicted the solutions for three different cases. The lithospheric thickness has been reduced from Figures 3a to 3c (86, 83 and 80 km thick), so that the dynamics for a wavelength of 1250 km corresponds to unstable, propagating unstable and propagating stable cases, respectively. The initial interfaces are depicted by dashed lines, the final interfaces are depicted by solid lines.

[18] In the case of a thick lithosphere (Figure 3a), the instability rapidly destabilizes the whole layer and leads to a finite time singularity analog to that discussed by *Lémery et al.* [2000]. In Figures 3b and 3c the propagation to the right of a wave-like deformation is clearly noticeable. The maxima of the lithospheric thickness are shifted to the right with velocities of order 5 mm yr^{-1} in agreement with the marginal stability study. Due to the asymmetry of the lithospheric thickening of Figure 3b, lithosphere evolves toward what could be interpreted as a series of subduction zones.

[19] The physics of the topography propagation is easy to understand (see Figure 4): the thickness variations of the lithosphere are in advance to those of the crust, in the direction of propagation. They induced a compression and thus a thickening on the right hand side of the mountain

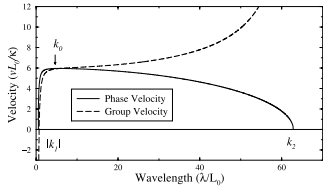

Figure 2. Phase (solid line) and group (dashed line) velocity of a tectonic wave as a function of the normalized wavelength. We use the following parameters: $S = 40$ km, $L = 83$ km, $\eta = 2\ 10^{21}$Pa s, $\kappa = 10^{-6}$ m^2 s^{-1}, $L_0 = 50$ km, $\rho_c = 2800$ kg m^{-3}, $\rho_m = 3200$ kg m^{-3}, $g = 9.8$ m s^{-2}, $\alpha = 3\ 10^{-5}$ K^{-1}, $\theta_m = 1350$ K). With real units, a normalized velocity of 6 corresponds to 3.7 mm yr^{-1}.

ranges that collapse on their left hand side. Thermal diffusion controls the maximum of the lithospheric thickness and mitigates the overall instability. In the simulations of Figure 3, the difference of phase is difficult to see as it only amounts to about 2° according to (15).

4. Conclusions

[20] The long wavelength tectonic waves exist when the compositional and thermal moments have somewhat similar amplitudes. This balance is however the typical situation of a mature lithosphere that thickens ($M_\theta + M_c > 0$) until it starts destabilizing ($M_\theta + M_c < 0$). The tectonic wave have velocities given by (14). These velocities are increasing with the average crustal thickness, S and decreasing with the root mean square resistance of the lithosphere, $\sqrt{L_0\eta}$. This traveling mode of tectonics should at any rate be present on Earth or on other planets taking into account the large range of crust and lithosphere thicknesses that can be found.

[21] In orogenic places like Andes and Tibet, the crust is very thick and the lithosphere rather weak, which should significantly increase the propagation velocity of our tectonic waves. The eastward migration of the compressive front of the Central Andes [*Lamb et al.*, 1997] and the ongoing acceleration of the deformation in the Eastern Cordillera [*Kennan*, 2000] relate to the emplacement of the cold and dense mantle root evidenced in seismic tomography [*Baumont et al.*, 2002]. In Tibet, the northeastward development of the plateau during Tertiary and the accompanying thickening of the lithosphere mantle *Tapponnier et al.* [2001] can be elegantly explained by the situation described in Figure 3b.

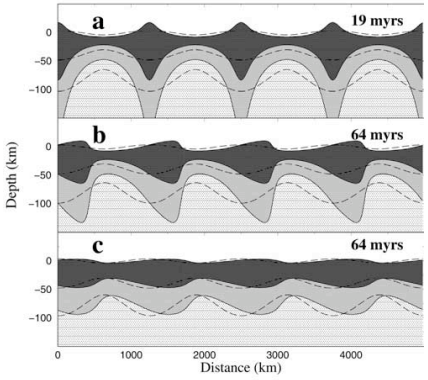

Figure 3. Evolution of the crust and lithosphere with time. The initial sinusoidal interfaces are depicted with dashed lines, the final interfaces with solid lines. The crust, mantle lithosphere and asthenosphere are shaded (darker, intermediate and lighter shades). The initial wavelength is in the domain of unstable (Figure 3a, with an initial lithospheric thickness of 86 km), propagating (Figure 3b, initial lithospheric thickness of 83 km), and stable (Figure 3c, 80 km) regime. For clarity the surface topography has been multiplied by a factor 5. The final solutions have been computed after (a) 19 myr and (b) and (c) 64 myr.

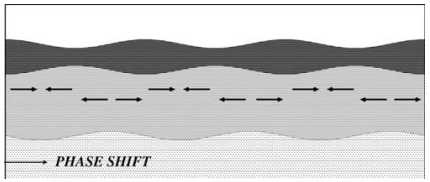

Figure 4. In the propagating mode, the crustal and lithospheric thickening are out of phase, this induces a compression on one side of the mountains, an extension on the other side. This peculiar tectonic setting can then propagate.

[22] The model is based on a long wavelength analytical model that could be improved to include higher order terms [*Medvedev and Podladchikov*, 1999]. It seems however that a natural development of this study should now use a complete numerical model to take into account the short wavelength deformations and to couple the mechanical lithosphere (here of uniform thickness L_0) to the variable thermal lithosphere.

[23] **Acknowledgments.** The first author thanks the Yale university where he spends a sabbatical year. The manuscript benefits from discussion with M. Brandon and D. Bercovici and a review by J. Braun. Support was obtained from the CNRS and the Garon Foundation for Supine Geophysics. The second author thanks the M.I.T. for technical support.

References

Argand, E. (1924), *Comptes-Rendus du 13ème Congrès Géologique International*, 596 pp., Brussels.

Artyushkov, E. V. (1973), Stresses in the lithosphere caused by crustal thickness inhomogeneities, *J. Geophys. Res.*, *78*, 7675–7708.

Baumont, D., A. Paul, G. Zandt, S. L. Beck, and H. Pedersen (2002), Lithospheric structure of the central Andes based on surface wave dispersion, *J. Geophys. Res.*, *107*(B12), 2371, doi:10.1029/2001JB000345.

Conrad, C. P. (2000), Convective instability of thickening mantle lithosphere, *Geophys. J. Int.*, *143*, 52–70.

England, P., and D. McKenzie (1982), A thin viscous sheet model for continental deformation, *Geophys. J. R. Astron. Soc.*, *70*, 295–321.

England, P., and D. McKenzie (1983), Correction to: A thin viscous sheet model for continental deformation, *Geophys. J. R. Astron. Soc.*, *73*, 523–532.

England, P. (1986), Comment on "Brittle failure in the upper mantle during extension of continental lithosphere" by D. Sawyer, *J. Geophys. Res.*, *91*, 10,487–10,490.

Fleitout, L., and C. Froidevaux (1982), Tectonics and topography for lithosphere containing density heterogeneities, *Tectonics*, *1*, 21–57.

Houseman, G., and P. England (1993), Crustal thickening versus lateral expulsion in the Indian-Asian continental collision, *J. Geophys. Res.*, *98*, 12,233–12,249.

Houseman, G. A., D. P. McKenzie, and P. Molnar (1991), Convective instability of a thickened boundary layer and its relevance for the thermal evolution of continental convergent belts, *J. Geophys. Res.*, *86*, 6115–6132.

Husson, L., and Y. Ricard (2004), Stress balance above subduction zones: Application to the Andes, *Earth Planet. Sci. Lett.*, *222*, 1037–1050.

Kennan, L. (2000), Large-scale geomorphology of the Andes: Interrelationships of tectonics, magmatism and climate, in *Geomorphology and Global Tectonics*, edited by M. A. Summerfield, pp. 167–199, John Wiley, New York.

Lamb, S. H., L. Hoke, L. Kennan, and J. Dewey (1997), The Cenozoic evolution of the central Andes in Bolivia and northern Chile, in *Orogeny Through Time*, edited by J. P. Burg and M. Ford, *Spec. Publ. Geol. Soc. London*, *121*, 237–264.

Lémery, C., Y. Ricard, and J. Sommeria (2000), A model for the emergence of thermal plumes in Rayleigh-Bénard convection and infinite Prandtl number, *J. Fluid Mech.*, *414*, 225–250.

Medvedev, S., and Y. Podladchikov (1999), New extended thin-sheet approximation for geodynamic applications -I. Model formulation, *Geophys. J. Int.*, *136*, 567–585.

Neil, E. A., and G. A. Houseman (1999), Rayleigh-Taylor instability of the upper mantle and its role in intraplate orogeny, *Geophys. J. Int.*, *138*, 89–107.

Tapponnier, P., X. Zhiqin, F. Roger, B. Meyer, N. Arnaud, G. Wittlinger, and Y. Jingsui (2001), Oblique stepwise rise and growth of the Tibet Plateau, *Science*, *294*, 1671–1677.

L. Husson, EAPS, MIT, 77 Massachusetts Avenue, Cambridge, MA 02139, USA. (lhusson@mit.edu)

Y. Ricard, Laboratoire des Sciences de la Terre, UMR5570, Université de Lyon 1, Bat Géode, F-69622 Villeurbanne, France. (ricard@ens-lyon.fr)

1.3.3 Généralisation : l'exemple du rifting

De manière générale, le comportement dynamique de la lithosphère est piloté par les trois sources de contraintes qui se résument aux hétérogénéités de densité liées à la minéralogie (essentiellement dans la croûte), aux hétérogénéités de densité liées au champ thermique, et aux contraintes aux limites, ou lointaines, ou encore "tectoniques". Les applications précédentes suggèrent que dans un contexte de collision, il est possible d'être prédictif sur l'évolution des chaînes de montagnes en prenant en compte ces sources de manière simple. De la même manière, la dynamique de la lithosphère dans un contexte extensif répond aux mêmes processus.

En collaboration avec les géologues de Paris 6 -N. Bellahsen en particulier- nous avons choisi d'examiner la dynamique du rifting par une approche similaire. Le cas d'étude est le rift d'Aden (fig. 1.5). Dans l'état actuel, l'épaisseur crustale décroit depuis les plaques Arabe au nord et Somalie au sud pour atteindre une épaisseur nulle au centre du rift. Les contraintes de flottabilité liées à ces variations d'épaisseur crustale (fig. 1.5) sont calculées sur la base d'un modèle isostatique et atteignent sur les marges passives ± 30 MPa (fig. 1.6). Intégrées depuis le centre du rift, ce sont des forces de l'ordre de 2.5 $10^{12} N\,m^{-1}$ qui tendent à restaurer une épaisseur uniforme au système. Celles-ci doivent être équilibrées soit par les forces aux limites de la lithosphère, soit par les forces de flottabilité thermique de la lithosphère amincie. En fait, nous pouvons montrer que, pour une rhéologie visqueuse linéraire de la lithosphère, l'amincissement initial de la lithosphère par le manteau sous-jacent suffit à conduire à l'amincissement de la croûte et à l'ouverture du rift, sans nécessité de forces tectoniques aux limites. L'expérience peut être réalisée en utilisant le formalisme des plaques minces décrit précédement. Une croûte de faible densité relative et d'épaisseur uniforme est associée à une lithosphère dont le moment thermique est plus faible au centre (fig. 1.7). Cette hétérogénéité initiale suffit à initier une dynamique extensive globale au centre du rift et compressive sur les épaules du rift, conformément aux observations géologiques [Bellahsen et al., 2006, Fournier et al., 2004]. Les variations latérales du moment thermique croissent dans le temps à mesure que le système se déstabilise et entraîne la croûte en la comprimant. Des résultats comparables ont été obtenus par Huismans et al. [2001]. Ce modèle entièrement actif suffit à expliquer les traits principaux de l'ouverture d'un rift. Dans ce modèle, les forces aux limites qui conduisent non pas à l'amincissement, mais à la séparation des

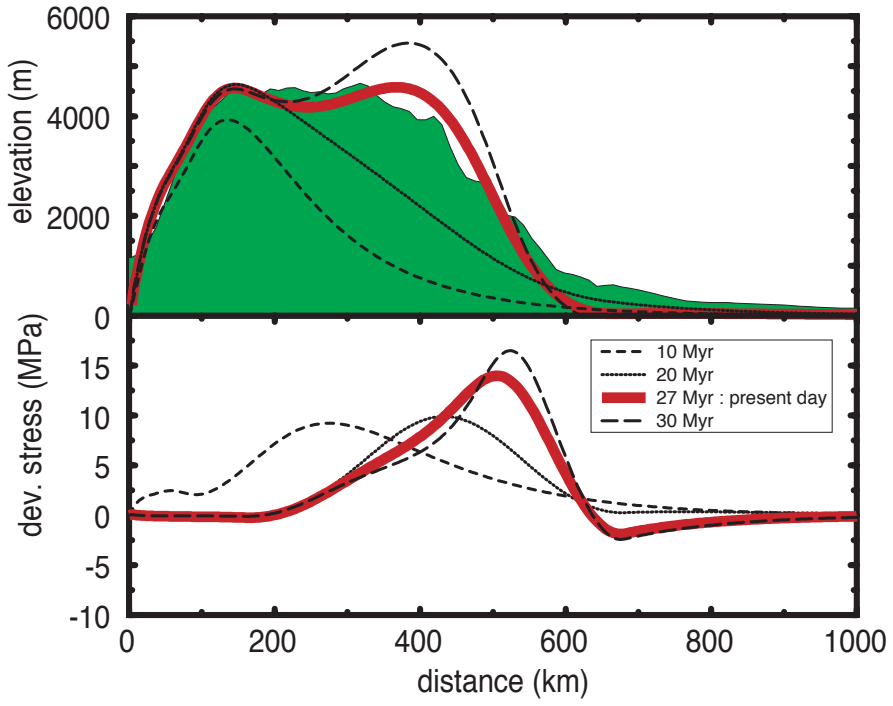

FIG. 1.4: Evolution de la topographie des Andes Centrales, lorsque une anomalie de densité liée à la racine lithosphérique sous la Cordillière Orientale est introduite dans le modèle. La topographie actuelle est donnée en vert. 27 Myrs correspond au temps de croissance andine déduit de l'enregistrement géologique (la courbe rouge donne la situation actuelle, prédite par le modèle). *Predicted time evolution of the Andean elevation when a negative buoyancy anomaly that mimicks the lithospheric root is introduced in the model. Current topography is given at 27 Myrs, approximately the characteristic time of orogenic growth inferred from the geological record.*

plaques, ne sont pas prises en compte.

Les études tectoniques et structurales dans le Golfe d'Aden, à terre et en mer [Bellahsen et al., 2006, d'Acremont et al., 2005, Fournier et al., 2004] permettent d'examiner plus en détail l'évolution du champ de contraintes dans le temps. En effet, une particularité du Golfe d'Aden est l'obliquité forte ($\sim 50°$) de la direction axiale du Golfe ($\sim$ N75°) par rapport à la direction d'ouverture du système ($\sim$ N25°). Il ressort que les déformations liées aux variations latérales du moment thermique ou crustal devraient avoir pour direction structurale $\sim$ N75°, reflétant l'amincissement de la lithosphère et de la croûte, et les déformations liées aux

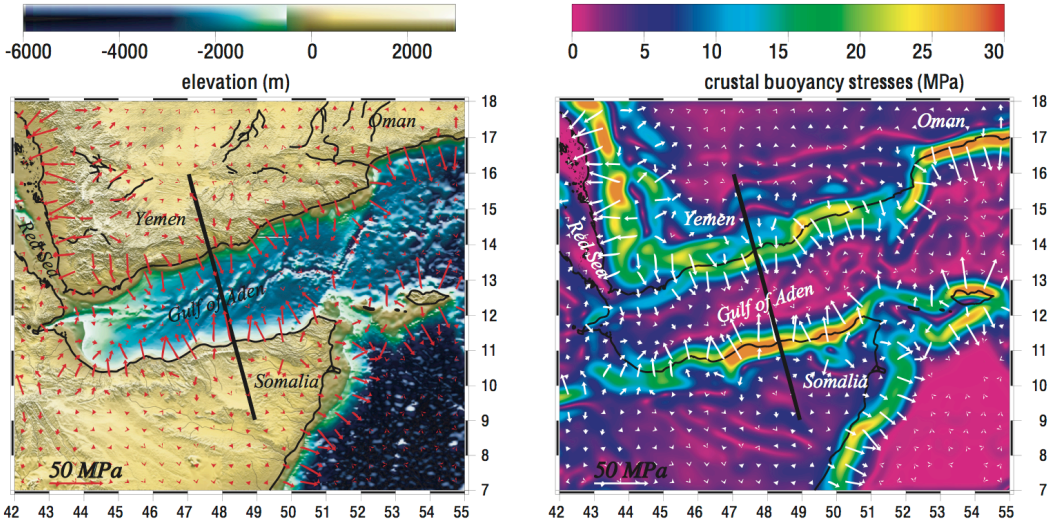

FIG. 1.5: Topographie du Golfe d'Aden et valeur absolue des contraintes de flottabilité calculées sur la base d'un modèle isostatique crustal. Le tracé noir correspond au profil de la figure 1.6. *Gulf of Aden, topography (left) and absolute value of the crustal buoyancy stresses (right) calculated assuming local isostasy. Black line is the profile of fig. 1.6.*

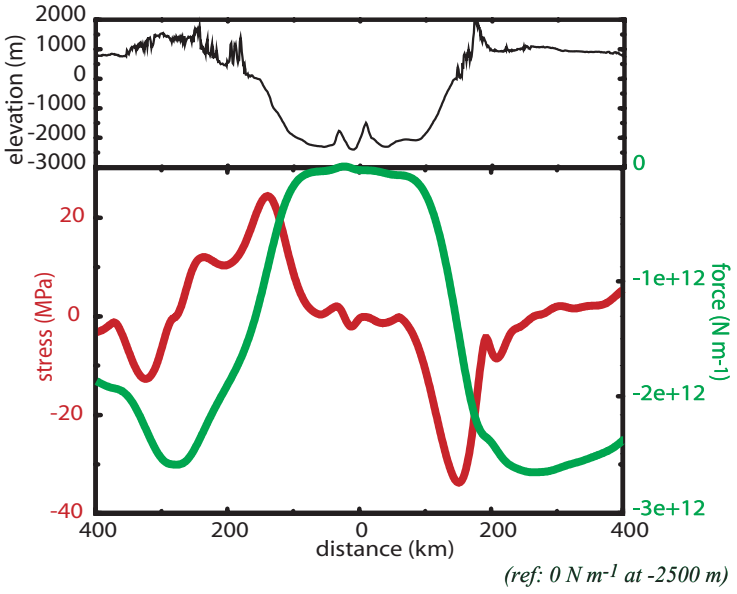

FIG. 1.6: Topographie (noir), contraintes de flottabilité (rouge), et force résultante (vert) calculées sur un profil orthogonal au Golfe d'Aden (localisation fig. 1.5). *Gulf of Aden, toopography (black), crustal buoyancy stresses and resulting force, calculated along a NNW-SSW profile (loc. fig. 1.5).*

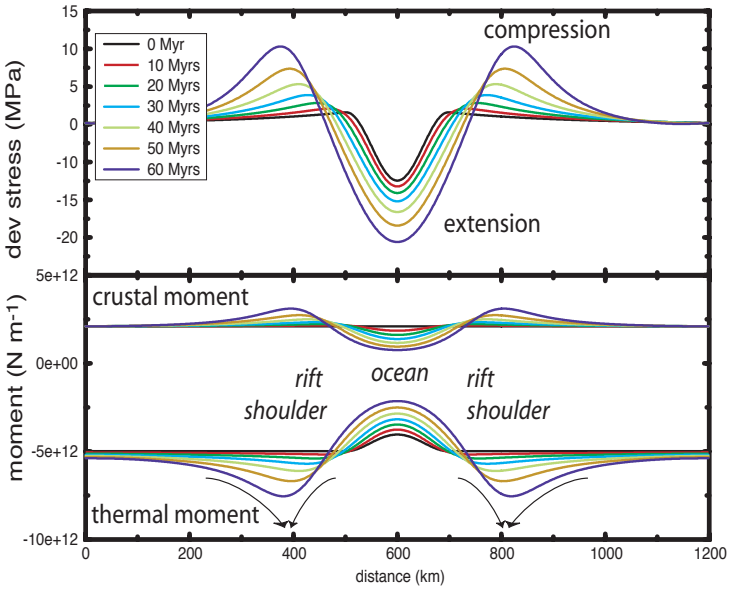

FIG. 1.7: Modèle d'évolution active d'un rift. Les contraintes aux limites sont nulles, seules les forces de flottabilité thermique et crustale sont actives. *Time evolution model of an active rift. Lateral boundaries are stress free, only the thermal negative buoyancy of the lithospheric mantle is driving the model.*

forces aux limites, $\sim$ N115°, orthogonalement à la direction d'ouverture observée, et parallèlement à la direction des segments de rift dans le Golfe. Les études structurales révèlent l'existence des deux directions principales d'extension attendues, N20° et N160° pour les failles normales synchrones du rifting. La chronologie des évènements est débattue par les mêmes auteurs [Bellahsen et al., 2006, Fournier et al., 2004]. Il demeure que l'existence des deux systèmes de failles est cohérent avec les prédictions des modèles présentés ci-dessus.

Afin d'examiner la généalogie des systèmes faillés, nous avons mis au point des expériences analogiques au laboratoire de Rome-3, en collaboration avec F. Funiciello et C. Faccenna. Ces modèles permettent en particulier d'examiner de façon plus réaliste que les modèles en plaques minces le rôle de la rhéologie sur le développement des failles. Les résultats sont présentés dans leur application au Golfe d'Aden dans l'article suivant.

Analogue models of oblique rifting in a cold lithosphere

[1]Julia Autin, [1]Nicolas Bellahsen, [2]Laurent Husson, [3]Marie-Odile Beslier, [1]Sylvie Leroy, [1]Elia d'Acremont

[1] CNRS-UMR 7072, Laboratoire de Tectonique, UPMC, Case 129, 4 place Jussieu, 75252 Paris Cedex 05, France

[2] CNRS-UMR 6118, Géosciences Rennes, Univ. Rennes 1, Campus de Beaulieu, 35042 Rennes cedex, France

[3] CNRS-Géosciences Azur-UMR 6526, OOV, B.P. 48, 06235 Villefranche-sur-Mer cedex, France

Abstract

New lithospheric analogue models of oblique rifting provide insights into the fault evolution, basin segmentation, and mantle exhumation during rift localization and capture main characteristics of natural oblique rifts. We present two models of oblique rifting: an oblique rift (obliquity about 50°) with a pre-existing lithospheric weakness (heterogeneous model) and one homogeneous. The main results are: (i) The fault populations, especially in early stages of deformation, are composed of faults that are, in strike, intermediate between the rift-parallel trend and the perpendicular to the opening direction. This fault population is characteristic of oblique rifts as in previous studies. (ii) In later stages, faults parallel to the rift become numerous in both models, even if in the homogeneous model displacement-normal faults also play a major role. Local stresses due to variations of thickness in the crust during the rift localization are certainly important during the rift localization and control the formation of rift-parallel faults. (iii) During final stages of extension, in the heterogeneous model, the crust is deformed by rift-parallel faults, and in the basins, displacement-normal faults compose the small scale deformation pattern. In the homogeneous model though, displacement-normal faults tend to accommodate most of the extension and control the final stages of extension. They would probably control the formation of the ocean-continent transition, mantle exhumation if any, and the geometry of oceanic accretion centres. Those results may provide insights into the possible evolution of the Gulf of Aden conjugate margins.

1. Introduction

Oblique rifting are usually seen to requires a pre-existing lithospheric weakness, which localizes the rift obliquely relatively to the displacement/opening direction. Thus, it is the

consequence of a multiphase tectonic history, such as, for example, two successive rifting events [e. g. Viking Graben, *Brun and Tron*, 1993; *Faerseth et al.*, 1997].

The rheological structure of a strong and cold lithosphere can be simplified at first order by a brittle-ductile 4-layer (brittle/ductile crust over a brittle/ductile lithospheric mantle). In such a multilayered structure, the uppermost brittle mantle is the most resistant part of the lithosphere. The occurrence of a pre-existing weakness in this layer has thus a great influence on the whole lithosphere strength, and is an efficient way to initiate oblique rifting.

A major consequence of these considerations is that the system can be simplified to an extending crust influenced by a basal zone of deformation (extension in the sub-Moho mantle) that acts as the major boundary condition. This has been successfully used in analogue models, as the systems become pretty simple to model. Analogue models of an extending crust above an oblique velocity discontinuity provided several insights about the fault patterns in such contexts [*Clifton et al.*, 2000; *Mart and Dauteuil*, 2000; *McClay and White*, 1995; *Sokoutis et al.*, 2007; *Tron and Brun*, 1991; *Withjack and Jamison*, 1986]. A major result of such modelling, for moderate obliquity (from 30° to 60°), is the occurrence of one main fault population that strikes oblique to both the rift trend and the perpendicular to the opening direction. Withjack and Jamison [1986] effectively showed analytically that, in case of oblique rifting, seen as transtension, opening direction and direction of extension are not parallel. In some experiments cited above, rift-parallel faults develop [*Mart and Dauteuil*, 2000; *Tron and Brun*, 1991], while in other they do not [*Clifton et al.*, 2000; *McClay and White*, 1995; *Withjack and Jamison*, 1986]. In all of them however, no opening perpendicular faults initiate.

Applying those models to nature leads to different results. For oceanic ridges, the models seem in great accordance with observations, as faults population observed in nature are well predicted by the models [*Clifton et al.*, 2000; *Clifton and Kattenhorn*, 2006; *Dauteuil et al.*, 2001; *Mart and Dauteuil*, 2000]. The homogeneity of the (newly created) crust at a localized and narrow extension zone probably explains that the models closely resemble the nature. However, in continental rifts, it seems more problematic. For the Viking Graben, two rifting events are documented, the first one providing a lithospheric weakness used by the second one. While Faerseth et al. (1997) propose, for the second one, an (dextral) oblique rifting kinematics, Brun and Tron (1993) propose different kinematics, based on their analogue model results. This might highlight some problems comparing the published analogue models to continental rifts. For the Gulf of Aden, an oceanic basin that has undergone an oblique rifting, two problems arise. First, opening perpendicular faults compose a main fault

population [*Bellahsen et al.*, 2006; *Fournier et al.*, 2004; *Huchon et al.*, 1991; *Huchon and Khanbari*, 2003; *Lepvrier et al.*, 2002], not predicted by analogue models as noted by Bellahsen *et al.* [2006]. Second, no lithospheric weakness is recognized at the scale of the Gulf with the correct orientation (trend of the Gulf: N070°E approximately). In order to take into account these particularities or unexplained characteristics of the Gulf of Aden, and because mantle exhumation is suspected in the ocean-continent transition, we have performed models at the scale of the whole continental lithosphere to capture the evolution of the whole system.

Recent analogue models of oblique rifting in a (hot) extending lithosphere [*Sokoutis et al.*, 2007] show that opening-perpendicular faults initiate in such oblique rifts. The deformation patterns are relevant to the so-called “wide rifting” mode of extension. Localised thinning in the brittle crust is accompanied by ductile doming of both lower crust and mantle. It may become a potential locus for achieving mantle exhumation. Models of volcanic passive margins [*Callot et al.*, 2002] show that very oblique faults (rift-parallel) can initiate without any linear weaknesses (but only local) controlling the rift localization. Thus, it appears that the processes of oblique rifting must be studied at the scale of the whole lithosphere.

We here present new analogue models of oblique rifting. The rheology is a four-layer lithosphere ("cold" lithosphere) resting on a low viscosity asthenosphere. The rifting obliquity is ensured by lateral offset velocity discontinuity with and without a weakness in the lithosphere. We thus think that an oblique rift can develop in a “homogeneous” lithosphere. We present first the experimental procedure and the results for two models (homogeneous and heterogeneous) and then compare them to previous models of oblique and orthogonal rift (i.e. rift perpendicular to the opening direction) and to the margin structure of the Gulf of Aden.

2. Model Setting and data processing

2.1. Model geometry

It is now widely accepted that an extending continental lithosphere with a normal crustal thickness (about 35 km) and a stable geotherm can be considered as a brittle-ductile multilayer (Kirby, 1983) and can be simplified at first order by a four-layer type strength profile [e.g., *Davy and Cobbold*, 1988; *Davy and Cobbold*, 1991]. In the laboratory, such a multi-layer is modelled using sand and silicone. Here, we used a microsphere mix (see below) as an analogue of brittle layers, and silicone putties as analogue of ductile layers. The models

are constructed in a deforming box (56 X 30 X 30 to 50 cm3, fig. 1), which consists of a drawer without bottom sliding in a rectangular box. The drawer is pulled by a screw jack, which represent the direction of extension. The drawer arms are of different lengths, so that they create two lateral velocity discontinuities imposing an oblique direction of deformation (fig. 1).

Our models represent the oblique extension of a non-thickened resistant lithosphere, as we can observe in cratons. Consequently, they are made of an upper brittle crust, a ductile lower crust, an upper brittle lithospheric mantle and a lower ductile lithospheric mantle (see fig. 2 and table 1 for details). The modelled lithosphere overlies a low viscosity, higher density glucose syrup that represents the asthenosphere.

2.2. Scaling

The microsphere mix is composed of 4/5 of glass microspheres and 1/5 of hollow aluminium microspheres. The glass microspheres have a density of 1.49 and a frictional angle of 31.5° (D. Rossi, personal communication). The hollow aluminium microspheres have a density of 0.39 and a frictional angle of 24.7° [*Rossi and Storti*, 2003]. This mix allow using very well rounded and spherical materials with a density of 1.2, similar to other analogue materials [*Benes and Davy*, 1996; *Davy and Cobbold*, 1991]. It has a frictional angle of ~30°, similar to Earth materials in terms of friction. The approximated cohesion of such material is very low (mix 100 Pa, glass microspheres: 155 Pa, aluminium microspheres: 6 Pa). This material is used to model the upper crust (1.5 cm, see table 1 and fig. 2) and the lithospheric mantle (0.8 cm, see table 1 and fig. 2).

The silicone putty (SGM36, manufactured by Rhône-Poulenc) was enriched with Iron (III) oxide or Lead (II) carbonate in order to reach suitable scaled densities and viscosities. The "red silicone" (Fe-oxide enriched) has a density of 1.33 and a Newtonian viscosity of 7.104 Pa.s and corresponds to the ductile upper mantle (2 cm, see table 1 and fig. 2). The "white silicone" (Lead carbonate enriched) has a density of 1.25 and a Newtonian viscosity of 4.104 Pa.s and corresponds to the ductile lower crust (0.7 cm, see table 1 and fig. 2).

Thicknesses, viscosities, densities, and strain rates are appropriately scaled to simulate an extending continental lithosphere. Scaling of the models to the natural prototype was achieved by maintaining similarity in geometry, dynamics, kinematics and rheology [*Hubbert*, 1937; *Ramberg*, 1981]. The brittle materials are scaled with the equation (1):

$$\sigma^* = \rho^*.g^*.L^* \quad (1)$$

where σ* is the adimensional stress ratio (model over nature), ρ* is the density ratio, g* is the gravity ratio, L* is the model length ratio. The models were intended to represent a geometrical scale of L* = Lmodel/Lnature = 0.75*10-6 (where Lmodel and Lnature are the corresponding lengths in model and nature, respectively), i.e. 1.5 cm in the experiment corresponds to 20 km in nature. For example, the upper crust of 1.5 cm thick corresponds to 20 km. The adimensional gravity ratio is g*= 1 since both models and nature undergo the same gravity field. The density ratio is around 0.4 (0.41 in the brittle crust and 0.36 in the brittle mantle). Thus, the stress ratio is set to σ* = ρ*.g*.L* = 3.10-7. Thus, the cohesion of an analogue material representing the upper crust (cohesion around 30 to 100 MPa) should have a cohesion around 10 to 30 Pa. Our analogue material for the brittle crust has a cohesion between few Pa and about 150 Pa. This cohesion might be a little high. In any case, the cohesion evaluated in the rock mechanics for natural rocks might be higher than the effective one in nature. Thus, this scaling of the cohesion is approximated and valid at the first order.

The time scaling for the ductile material writes:

□□ ρ*.g*.L□ . □

where □is the viscosity ratio, ρ* is the density ratio, g* is the gravity ratio, L* is the model length ratio, □is the time ratio. The viscosity ratio is of 4.10-17 (natural lower crust: 1021 Pa.s and model lower crust: 4.104 Pa.s). Thus, the time ratio is around 0.75*10-10 at the lower crust scale (1 hour in the model corresponds to 0.85 Ma in nature).

The experiments are performed with an extension velocity of V = 5 cm/h. Although too fast for rifting processes, this velocity, which corresponds to about 6 cm/yr in nature, is nonetheless comparable to the velocities applied in previous studies [*Benes and Davy*, 1996; *Brun and Beslier*, 1996; *McClay and White*, 1995; *Sokoutis et al.*, 2007].

2.3. Experiments

From a set of 13 experiments, we particularly investigated two configurations of oblique extension: a) an experiment in stratified lithosphere of uniformly thick layers (hereafter referred to as "homogeneous model"), where the obliquity is induced by the lateral velocity discontinuities; b) an experiment where a weakness zone (a locally thinner lithospheric mantle designed prior to the experiment) trends parallel to the direction of obliquity imposed by the lateral velocity discontinuities, and joins them ("heterogeneous model"). The obliquity, i.e. the angle between the direction of extension and the rift trend, is 50° and is constant for both models. The total displacement is 10 cm in all experiments, corresponding to an amount of

extension of 20% throughout the entire model and about 130% throughout the rift, for both models. In order to allow for a better observation of fault patterns, no extra sedimentation was applied during the experiments, which in turns prevented the identification of fault activity during the whole duration of the experiment. This was achieved by comparing top photographs (taken from above) at successive steps of the experiment.

2.4. Data Processing

2.4.1. Line drawing of faults

Surface photographs and laser scans were acquired during model evolution with a 2 minutes interval (figs. 3 and 4). We define a fault segment as a fault part of uniform orientation, which we interpret as a uniform state of stress. We hand picked the fault segments on the top views (figs. 5 and 6) at each step until the information became too complex to be deciphered (~ 30 minutes, 5% extension). Afterwards, models are investigated using the processing of the DEM only (see below). The segment lengths and azimuths are thus determined at each step of extension. We calculated the number of segments of each fault segment populations through time (fig. 7). We also calculated the amount of the total fault length for each population through time, as well as their total length (fig. 7). Defining North as the opening direction, three main fault populations are observed: (1) N050°-060°E oriented faults are called rift-parallel faults, (2) N060-080°E oriented faults are called intermediate faults, (3) N080-100°E oriented faults are called displacement-normal faults. Zooms of the rift centre are also displayed in order to better observe the relation between the fault populations (figs. 8 and 9).

2.4.2. Laser scan processing

The DEM have a resolution of 0.25 mm in x, y, z. After surface interpolation, each DEM was subtracted to the previous one in time (Figs. 10 and 11) in order to get differential vertical movements, and hence to deduce which faults are active during a specific time interval. The surface topography is displayed either in map view or cross-section (fig. 12).

2.4.3. Topography corrections for cross-sections

Supplementary photographs and laser scans were recorded during the dismantling of models, providing DEM of each interface after gradual stripping of the above layers (surface, top ductile crust, top brittle mantle and top ductile mantle). The removal of each overlying layer of variable thickness brings each surface to a new isostatic equilibrium. Taking advantage of the changing isostatic equilibrium, we restored the shape of the interface prior to its readjustment. We have realised two final lithospheric cross-sections on each model (fig. 13), which are extension-parallel and rift-normal.

3. Results

3.1. Homogeneous model

In the homogeneous model (model 5), faults significantly initiate after ~1% of extension (fig. 5 and 7, stage 2). First, displacement-normal (red) and intermediate (green) faults initiate (fig. 5 and 7-A). Those faults localize at the model borders, near the lateral velocity discontinuities. Thus, faults propagate toward the centre of the model away from the discontinuities (fig. 5, steps until 2-3%). The geometry consists of two en-echelon basins that do not overlap, defining a relay zone in the centre of the model. As the model evolves, the two first basins continue to accommodate the applied extension (figs. 5, stage 2). The faults forming are mainly intermediate ones and displacement-normal ones, then mainly intermediate ones (fig. 7-A)

At an extension rate of about 2 to 3%, the relay zone breaks through and rift-parallel faults initiate (fig. 8-a). The number of fault segments increases more rapidly than during earlier stages (fig. 7-A, stage 3), but with relatively shorter lengths. On figure 7-A the evolution of the relay zone can be followed precisely: during stage 3, intermediate faults first dominate, followed by displacement-normal faults in an increasing amount, and eventually rift-parallel faults. Rift-parallel faults mainly develop in the centre of the model and with short lengths. The relative length amount of intermediate segments tends to decrease during stage 3 as the two other ones increase (fig. 7-B). The total length of each fault population follows the same evolution (fig. 7-C).

During a fourth stage, the rate of fault segment initiation decreases (it even stops for the rift-parallel and displacement perpendicular ones). The faults are active, accommodate extension and gently propagate but no new segments are created (fig. 10-c). Indeed, the total fault length keeps increasing whereas the number of segmentss remains constant (figs. 3, 7-A and C).

A fifth stage can be observed on figure 7-A, with a slight increase and then a decrease in total measured length. This could be an interpretation artefact of the complex fault pattern in which faults coalesce and scarps collapse.

After this first structuration, the model is not easily interpretable. The following evolution can be observed on top views (fig. 3 and fig. 8) and topographic profiles (fig. 12-A). After 4% bulk extension (fig. 8-c), the development of relay zone is completed and all major faults are formed. The topographic profiles show little vertical movements. Then the deformation is mainly accommodated by displacement-normal fault formation or reactivation (figs. 8-d and e, ~5-6%). Horsts and grabens develop but the elevation of the rift shoulders approximately remains constant (fig. 12-A). Then the development of rift-parallel faults is observed on the edges of the rift (fig. 8-f and g, ~7-13%). The final structure, with four horsts and five grabens in the displacement-normal direction, is achieved after ~12% extension (fig. 12-A). The vertical displacements are progressively increased. Nevertheless, in the rift centre, the continuous extension is accommodated by displacement-normal faults, which progressively destruct the rift-parallel and intermediate oriented horsts (fig. 8-g and h, 13-15%). The rift shoulders finally reach an elevation of 3.7 mm above the mean elevation along the profiles (at 19.24% extension), whereas the maximal subsidence reaches 2.9 mm depth (fig. 12-A).

A major observation of the oblique models is the progressive rotation of crustal blocks (fig. 3). The rotated blocks are formed along the rift borders with a rift-parallel to intermediate direction. Then they progressively undergo a clockwise rotation, which separates the block from the rift border forming a scissor-like shaped graben. The maximal observed rotation exceeds 20°. Small blocks are more prone to high rotations. In the homogeneous model, rotation zones from opposite borders interact in the rift centre and lead to highly deformed areas. As rotations are always clockwise, these areas correspond to left-lateral shear zones.

In cross-sections (fig. 13), the major shifts in the scanned surfaces are interpreted as faults in the brittle crust layer and as boudins in the sub-Moho mantle. As in the experiments of Brun and Beslier [1996], the two brittle-ductile systems (crust and mantle) are in opposition of phase, i.e. the thinned brittle crust is above the thickened brittle mantle and conversely (fig. 13). In other terms, surface grabens correspond at depth to a boudin of brittle mantle and the horsts, to shear zones. In Brun and Beslier's [1996] models, the ductile crust undergoes horizontal shear and therefore constitutes a decollement zone between the upper crust and the mantle. Maximum thinning of the brittle mantle, which represents the main resistance of the lithosphere, occurs beneath the northernmost major horst.

3.2. Heterogeneous model

In the heterogeneous model (model 4), faults start to develop after about 1.5% bulk extension (fig. 6). They localize at the lateral velocity discontinuities. Two basins form, especially on the "right" discontinuity. At the very beginning, faults are mainly displacement-normal (fig. 7-E). Until 2.5% extension, the rate of fault segment creation is approximately constant (fig. 7-D, stage 2). The displacement-normal faults are actually concentrated at one of the lateral displacement. It appears that in the rest of the model, those faults are not dominant. Very few displacement-normal faults initiate (fig. 6 and fig. 7-D). The faults initiate mainly parallel to the rift and in an intermediate orientation (fig. 7-E). Fault spacing is large (1,5 cm) and the faults are globally longer than in the previous model. The rift is narrow and the rift-parallel structuration is well observed. The stage 2 is shorter than in the homogeneous model since faulting occurs at higher extension amount and stage 3 starts earlier.

After about 2.5% bulk extension, there is a slight increase in segment creation rate. This could be a stage 3 as in the previous experiment. We interpret this as the equivalent of the relay break through of the previous experiment, i.e. the time when the deformation propagates through the centre of the model. First intermediate segments initiate, followed by rift-parallel and displacement-normal ones (fig. 7-D). The relative length of displacement-normal faults is largely decreased, showing that those faults are significant at one lateral discontinuity but not very important in the main part of the model (fig. 7-E). Moreover, the total length of rift-parallel faults becomes higher than that of the displacement-normal faults, which indicates an early prominence of rift-parallel faults. This stage, which corresponds to the deformed zones connection, occurs earlier in the heterogeneous model (2% vs. 2,5% extension).

After that, segment creation slows down, corresponding to a stage 4 (fig. 7), where fault segments are active and gently propagate without creation of new segments. Extension is accommodated by the existing segments (fig. 11-c). Nevertheless, the model 4 still presents a slight increase of rift-parallel faults during this step (figs. 7-D and F). The rift-parallel faults become even more numerous than the displacement-normal ones (fig. 7-F). A stage 5 can be observed with a slight amount of segment creation, but this could rather be seen as the continuation of stage 4.

After this first structuration, we can observe the model evolution through top-views (fig. 4 and fig. 9) and topographic profiles (fig. 12-B). The deformed zones connection is achieved after 3% extension (fig. 4-b). After ~4.5% extension, rift-parallel faults form on the rift borders and in the rift centre limiting a central rift-parallel horst. The rift is then composed of rift-parallel structures, composed of two grabens separated by a major horst, which is finally individualised after 6% extension (fig. 4-d). These structures are clearly identifiable on the topography after 5.15% extension (fig. 12-B). The rift borders are first structured by

intermediate faults then by rift-parallel ones after 6% extension (fig. 9-b-c-d). After 10% extension, the central horst starts to be re-faulted by numerous intermediate faults on its edges. Small horsts are separated from the rift edges (fig. 9-d and e) and are observed on the topographic profiles (fig. 12-B, ~10%). Then, the three horsts and four grabens observed will constitute the rift structuration until the final state. The small horsts are re-faulted by displacement-normal faults in the deep lateral grabens (fig. 9-f) and are thus less elevated on the topographic profiles. The central horst is finally destructed by rift-parallel faults (fig. 9-g and h). The final state (fig. 9-h) shows that the main horst and rift borders are re-faulted by rift-parallel faults whereas the in-graben structures are re-faulted by displacement-normal faults. The rift shoulders reaches an elevation of 1.8 mm above the mean elevation along the profiles (at 19.48% extension), whereas the maximal subsidence reaches 4.2 mm (fig. 12-B). But it seems that higher elevation stand laterally to the profiles.

Rotations are not as frequent in heterogeneous model as it is in the homogeneous model. Indeed, the central horst limits the structures length and their rotation. Nevertheless, the central horst initiates in a rift-parallel direction (fig. 4-c) and is finally in a nearly intermediate orientation at the end of the experiment (fig. 4-h). Small scissor-like shaped grabens can be observed on the rift borders too.

The final cross-section of the heterogeneous model (fig. 13) shows that the central horst is directly located above the ductile mantle heterogeneity. As in the model 5 and the model of Brun and Beslier [1996], the two brittle-ductile systems (crust and mantle) are in opposition of phase. A remarkable observation is the break-up of the brittle mantle. This feature can be observed on the brittle mantle in top-view too (fig. 14). The discontinuity in the brittle mantle layer, which is the zone of highest strength in the model, allows the contact between the ductile mantle and the ductile crust. The models by Brun and Beslier (1996) display comparable characteristics and lead to the ductile mantle exhumation at the surface.

3.3. Synthesis

As in previous studies [*Clifton et al.*, 2000; *McClay and White*, 1995; *Tron and Brun*, 1991], our models of oblique rifts present highly segmented borders with an en échelon organisation. In both models, regardless of the amount of extension, intermediate faults are the most abundant. In both models, rift-parallel faults initiate and become an important fault set in latter stages, becoming as numerous as displacement-normal faults in the homogeneous model and more numerous than them in the heterogeneous one.

However, several differences are noteworthy. In the homogeneous model, the total number of segments is twice as numerous as in the heterogeneous model. In the homogeneous model, the horsts are more numerous and rise above the mean elevation, whereas there are few horsts in the heterogeneous model and they lie under the mean elevation except for the rift shoulders. The grabens of the heterogeneous models are deeper. The homogeneous model displays a distributed deformation in the whole lithosphere with a slight asymmetric thinning. Whereas the heterogeneous model displays a rather symmetric pattern with a central break-up of the brittle mantle, which can lead to ductile mantle exhumation.

In the homogeneous model, displacement perpendicular faults control the final stage of extension. In the heterogeneous model, large active rift-parallel faults control the deformation, even if some displacement-perpendicular ones can be observed in the centre of the basin.

Rotations are systematic in both models but less important in the heterogeneous one. In the homogeneous model rotation can lead to left-lateral shear zones in the rift centre, whereas they poorly affect the deformation of the central horst in the heterogeneous model.

4. Discussion

4.1. Intermediate faulting in the early stage of oblique rifting

In the heterogeneous model, the fault pattern initiates with intermediate and displacement-normal faults in the vicinity of the lateral velocity discontinuities (fig. 6). Displacement-normal faults were not observed in previous models [*Clifton et al.*, 2000; *McClay and White*, 1995; *Tron and Brun*, 1991] (fig. 15). This population is likely due to the lateral discontinuities, which localise the deformation that is not much influenced by the lithospheric weakness in the mantle, as stresses are directly transmitted to the crust, before the propagation of the rift toward the model centre, strongly influenced by the weakness. Intermediate faults start to develop in the model centre with an en-echelon pattern and through a wide oblique zone (fig. 6, 2.14%).

In the homogeneous model, intermediate faults and many displacement-normal faults initiate at the lateral discontinuities (fig. 5). The lateral deformed zones are wider than in the heterogeneous model. They propagate toward the centre of the model with an intermediate to displacement-normal direction. The deformed zones reach the centre of the model at 2.25% extension (fig. 5) without being connected.

Thus, in both analogue models presented here, during the early stages (less than ~3% of extension), the main fault population is composed by faults with intermediate strike (intermediate between the perpendicular to extension and the parallel to the rift axis). This is consistent with previous analogue models [*Clifton et al.*, 2000; *McClay and White*, 1995; *Tron and Brun*, 1991]. As shown by Withjack and Jamison [1986], from analogue and analytic models, oblique rift firstly develops under a transtensional regime that induces a slight rotation of the minimal main stress σ_3 in the applied zone of obliquity. σ_3 is thus slightly oblique to the direction of extension (opening direction). The resulting fault pattern mainly displays faults with an intermediate azimuth. Other analogue models of oblique rifting [*Clifton et al.*, 2000; *McClay and White*, 1995; *Tron and Brun*, 1991] model the crust overlying a basal velocity discontinuity and show the same pattern. Figure 15 shows the azimuthal distribution of faults under similar obliquity for the models of Tron and Brun (1991), Clifton *et al.*, (2000), our models and for Gulf of Aden onland major faults (Bellahsen et al., 2006). In good agreement with the prediction of Withjack and Jamison [1986], all models and data present an important peak of intermediate faults (60° to 75° from the displacement direction). This good agreement between data and models (performed both at crustal and lithospheric scales) suggests that the analogue models reproduce well the early stages of oblique continental rifting, and that this early evolution is well constrained. The analogue models with a crust over a basal velocity discontinuity [*Clifton et al.*, 2000; *McClay and White*, 1995; *Tron and Brun*, 1991] thus succeed in capturing the main structural characteristics of oblique rifting with a basal discontinuity instead of the whole lithosphere, but probably only in early stages. As we will discuss later, the following stages of rifting are probably more complicated.

4.2. Development of local stresses

The fault pattern evolves with ongoing extension, when the two lateral deformed zones connect toward the centre of the model. Intermediate and rift-parallel new faults develop rather than displacement-normal faults (fig. 7-D and E). However, their initiation seems to have different stress origins in the heterogeneous and the homogeneous models.

In the heterogeneous model, the lateral deformed zones are rapidly connected along the weakness with en échelon intermediate and rift-parallel faults (fig. 6, since 2.58%). Then, rift-parallel faults begin to accommodate a large amount of the applied extension (fig. 9-a-d, 3.09 to 6.21%). The initiation and propagation of such faults are interpreted to be due to local stresses induced by variation of crustal thickness across the rift [*Artyushkov*, 1973; *Fleitout and Froidevaux*, 1982]. These local stresses are controlled by the oblique heterogeneity, which localizes mantle thinning and thus crustal thinning. In such zones with local stresses, the oblique reactivation of displacement-normal faults might occur, even if oblique slip cannot be constrained in our models.

In the homogeneous model, the lateral deformed zones connect by rift-parallel faults on a very narrow width (fig. 5, 2.90%). These faults form a relay zone between the two shifted discontinuities, and thus the deformed zones. The first rift-parallel faults initiate when this relay breaks through. In this relay zone, as few extension has been accommodated so far at this step, the lack of significant variation in crustal thickness suggests another origin for fault obliquity. Local stresses may also be invoked, but in this case they are due to stress rotation typical of relay zones. Such mechanism was suggested by Huchon et al. (2003) to explain rift-parallel faults and rift perpendicular extension direction. The authors also noticed that this could not be a valid explanation for the whole rift, but only for local places. Our results tend to confirm such a hypothesis: relay faults might form in some places between en-echelon basins. Once such faults are active and start thinning the crust, local stresses due to crustal thickness variation (as in the heterogeneous model) can also act to enhance such faults. In such zone, the local stresses will be perpendicular to the deformed zone controlled by early relay faults.

In previous crustal-scale models [*Clifton et al.*, 2000; *McClay and White*, 1995; *Tron and Brun*, 1991], faults tend to be of intermediate trend in the rift centre and to approach rift-parallel direction on the rift borders. Thus, to explain rift-parallel faults, local stresses due to crustal thickness variation might also play a minor role in the fault pattern geometry. This fault population is not prominent except in Tron and Brun‘s (1991) experiments (fig. 15). In the latter experiments, rift-parallel faults initiate only above the border of the basal silicone layer, which underlies the sand (fig. 3 in Tron and Brun, 1991). This may explain the presence of a peak in the population of faults and its scarcity in the other models (fig. 15).

The heterogeneous model, as one can foresee, has more efficiently localizes deformation than the homogeneous model. Indeed, less segments and horsts are created and grabens are deeper. The deformation is thus accommodated by large offset on less numerous faults. In the homogeneous model, displacement-normal faults are more developed than rift-parallel faults, whereas rift-parallel faults become more important in the heterogeneous model. Moreover, displacement-normal faults are proportionally more numerous in the homogeneous model

than in the heterogeneous model (fig. 7). The final fault distribution shows a peak of displacement-normal faults in the homogeneous model. In the heterogeneous model, the heterogeneity seems to develop rift-parallel faults at the expense of displacement-normal faults.

4.3. Rift localization

In both models, once the rift localizes, the rate at which new fault segments initiate tends to decrease and the deformation is mostly accommodated following the same ongoing activity and by propagating segments formed during earlier stages. However, once the rift is mature (fig. 8 and 9), the formation of new segments resumes though at this stage, the fault pattern becomes too complex to be accurately deciphered from models photographs. There is indeed no evidence of a dominating fault population.

In the heterogeneous model, intermediate and rift-parallel faults cut the rift-parallel structures (fig. 9). This is especially clear in the central horst and on the rift borders. Then, displacement-normal faults localize in the main deep grabens as we can see on the final line-drawing (fig. 16).

In the homogeneous model, displacement-normal faults cut the intermediate and rift-parallel structures, except on the rift borders, where rift-parallel faults are still active (fig. 8). This is consistent with other analogue models where the faults close to rift-parallel direction are border faults (here referring to the faults at the margin of the deformed zone, see Figure 3 of Tron and Brun, 1991 or of McClay and White, 1995).

In both models, displacement-normal faults (perpendicular to the far-field extensional stress) initiate only in the centre of the rifted zone. This is likely due to much lower local stresses than at the previous stage (see section 4.2), because of low crustal thickness variations in this zone of high crustal thinning. Moreover, as the thinned parts of the lithosphere localise the deformation, the development of the rift-parallel faults on the rift borders stop early.

4.4. Initiation of a possible mantle exhumation

The differences between the two models show that the behaviour of the brittle mantle is prominent. As shown in section 3.2, the complete breakup of the uppermost brittle mantle occurs in the heterogeneous model, while it is not achieved in the homogeneous one in the time lapse of the experiment (fig. 13 and 14-B). It would however have eventually occurred. This shows that the heterogeneous setting favours an earlier breakup of the uppermost brittle mantle. This is a consequence of the heterogeneity introduced in the initial model, which

decreases the strength of the brittle mantle, and hence of the whole lithosphere, and leads to an early localisation of the deformation at depth.

In the four-layers orthogonal models of Brun et Beslier (1996) (fig. 13), the break-up of the brittle upper mantle also occurs. It is a consequence of the boudinage of the high strength uppermost brittle mantle and the localisation of the deformation in one of the neck zone as extension proceeds. The breakup of the brittle mantle leads to the superposition of two conjugate normal shear zones, one in the ductile lower crust and one the ductile mantle. The localisation of the deformation in this lithospheric weakness zone induces the necking of the whole lithosphere, and a high thinning of the crust and eventually its breakup leading to the exhumation of the mantle.

In the same way, it is most probable that brittle mantle breakup in our models is an initial step of the exhumation of the mantle. The models cross-sections (fig. 13) are compared to the four-layers orthogonal model of Brun and Beslier [1996]. The analogue materials, layer thicknesses and extension velocities are comparable. While models 4 and 5 undergo an extension twice as high as Brun and Beslier's [1996] model (~20% vs. 10% in Brun and Beslier, 1996), the ductile mantle does not reach the surface, even when the breakup of the brittle mantle is achieved (heterogeneous model, fig. 13). The difference seems thus to be due to the rift obliquity in our models. Indeed, in the homogeneous model, the obliquity induces an en-echelon pattern of the thinned zones of the lithosphere, and especially in the brittle mantle (Fig. 14). Thus, the localisation of thinning along a continuous zone is more difficult, the localisation of the deformation at depth occurs lately, and the deformation is more diffuse in the brittle crust, leading to a much wider rifted zone. Nevertheless, analogue modelling suggests that the presence of an oblique heterogeneity could allow for mantle exhumation after larger extension than in orthogonal extension.

In our models, as well as in most previous analogue modelling studies, we used a newtonian viscosity. There is little doubt that a non-newtonian viscosity would have favoured even more rift localization and mantle exhumation, regardless of the chosen type of model. This could also explain the difference between models and observations.

4.5. Block rotations

Block rotations are observed in both models, but are larger in the homogeneous model than in the heterogeneous one. In all models, the rotations are clockwise, consistent with the kinematics of the oblique rift (right lateral). Some horsts rotate from an intermediate direction to a displacement-normal one (rotations up to 20°). Rotations induce the opening of scissor-

like shaped grabens (fig. 3 and 4), which are wider toward the East on the northern flank of the rift and wider toward the West on the southern flank. Consequently, there is a differential amount of extension along-strike the grabens, the extension being higher in the widest parts of the grabens, near the rift centre. In the rift centre, block rotations induce the formation of left-lateral steep shear zones, especially observed on the top view of the brittle mantle (fig. 13-A). These shear zones can be the initiation of future zones of transfer and maybe transform faults, which dissect the oblique rift. Their spacing would thus be linked to the scale of the rotated blocks.

The rotations are less expressed in model 4 and no transverse steep shear zones are observed at surface level and at depth. Thus, the homogeneous model favours block rotation, probably because all faults have mainly dip slip displacements inducing rotations. On the contrary, the heterogeneous model favour rift-parallel faults those probably have oblique slip, preventing from block rotations.

As a consequence, block rotations dissect the horst and graben structures in the rift centre. The extensional features are then shorter and more discontinuous near the rift centre than on the rift borders. These observations have noteworthy implications for the comprehension of the structure of conjugate margins issued of oblique rifting. Analogue modelling strongly suggests that faults presently observed in the distal parts of such passive margins, near the ocean-continent transition, do not show their initial orientation, whereas the more proximal parts of the margins, especially the emerged parts, may have better preserved the initial faults trends until the end of the rifting.

4.6. Application: the oriental Gulf of Aden

Scaled physical models have been used to interpret the geometry and evolution of fracture populations that form on mid-ocean ridges and continental rifts during oblique extension [*Clifton et al.*, 2000; *Dauteuil et al.*, 2001; *Mart and Dauteuil*, 2000; *McClay and White*, 1995; *Sokoutis et al.*, 2007; *Tron and Brun*, 1991; *Withjack and Jamison*, 1986]. The Gulf of Aden structure and evolution were already studied in the light of the clay analogue and analytical models of Withjack and Jamison (1986). They noted that the intermediate fault population was an important one in the Gulf, in good agreement with their models and corroborated by our models. However, both onshore and offshore data were rather scarce at the time of their study. New data are now available [*Bellahsen et al.*, 2006; *d'Acremont et al.*, 2005; *Fournier et al.*, 2004; *Huchon and Khanbari*, 2003] that confirm the above conclusions but also show some complexities that can be understood in the light of our models.

The Gulf of Aden trends along a N070°E direction. It formed under the influence a N020°E trending far field extension, of the Afar hot spot in the west, and maybe of the propagating Carlsberg ridge in the east. The obliquity is thus around 50°. The far field extension direction is due to a complex evolution of the converging northern margin of the Bitlis-Zagros-Makran. Around 30-40 Ma ago, the still active subduction of the Tethyan Ocean under the Zagros and Makran, with the starting collision in the Bitlis, could have provided extensional stresses to the African plate (Bellahsen et al. 2003). The Gulf opened along an orientation that does not seem to be inherited, and thus seems to be newly created as discussed in Bellahsen et al. [2003].

Three fault populations (extension-normal, rift-parallel, intermediate) are observed on the onshore margins [*Bellahsen et al.*, 2006; *Fournier et al.*, 2004; *Fournier et al.*, 2007; *Huchon et al.*, 1991; *Huchon and Khanbari*, 2003; *Lepvrier et al.*, 2002]. Moreover, microstructural studies show several extension directions and their relative chronology. Accordingly, both counter clockwise rotations (N020°E extension toward N160°E extension, [*Autin*, 2008; *Bellahsen et al.*, 2006; *Huchon and Khanbari*, 2003; *Lepvrier et al.*, 2002] or clockwise rotations (N160°E extension toward N020°E extension, [*Autin*, 2008; *Fournier et al.*, 2004] occur during the rifting.

The Gulf of Aden is highly segmented with first order and second order segmentations [*d'Acremont et al.*, 2005]. Offshore, near the ocean-continent transition, the structures exhibit more displacement-normal directions [*d'Acremont et al.*, 2005]. On the oriental northern margin, offshore grabens present scissor-like morphology with an opening and deepening toward the East [*Autin*, 2008]. The ocean-continent transition seems to exhibit exhumed serpentinised mantle in some local area [*Leroy et al.*, subm.].

The models presented in this study were elaborated to be consistent with the obliquity of the Gulf of Aden, which results in a 50° oblique rift. The four-layer rheology corresponds to a cold lithosphere, deformed during the Tertiary rifting of the Gulf of Aden. However, this rheology is only applicable in the oriental Gulf of Aden, since the western part deformed under the influence of the Afar hot spot. Lateral velocity discontinuities are rather experimental tricks, and have no real geological analogue, but it is a way to induce oblique (or orthogonal) rifts in homogeneous lithosphere scale models without preexisting weaknesses. As suggested by the model of Bellahsen et al. (2003), the obliquity of the Gulf of Aden does not seem to depend of inherited lithospheric heterogeneity.

The fault pattern in the homogeneous model is comparable to the fault pattern described on the Gulf of Aden margins (fig. 17-3 and fig. 18). Three fault populations initiate in this

model: rift-parallel faults rather on the rift borders and displacement-normal faults in the rift centre. The models may thus provide keys for the interpretation of the Gulf of Aden faults interpretation.

(i) The observed anticlockwise rotation of the direction of extension may results from local stresses due to crustal thickness variation on the rift border as suggested by Bellahsen *et al.* [2006]. In such a state of stress (extension N160°E, perpendicular to the rift axis) rift-parallel faults may activate and displacement-normal may be reactivated obliquely as observed in some places in the field [*Bellahsen et al.*, 2006; *Huchon and Khanbari*, 2003].

(ii) The observed clockwise rotation of the extension direction can be related to a late rotation of stresses in the rift centre. In such zone, the crust is highly thinned and thickness variations become smaller, inducing a subsequent decrease in local stresses. Thus, the stress regime is again dominated by far field boundary conditions, i.e. N-S to N020°E as suggested in d'Acremont et al. (2006).

(iii) The high segmentation of the Gulf of Aden (fig. 18) may be due to the rift obliquity that induces stress rotations as discussed above and to block rotations that have two consequences: (1) the initiation of steep shear or transfer zones initiated in the rift centre and (2) rotated blocks are faulted by ongoing deformation resulting in short horsts (shorter than in orthogonal rifts). One can hypothesize that those transfer faults can localize the transfer zones that seem to initiate during the ocean-continent transition formation and deformation and/or during the final stages of rifting [*Autin et al.*, subm.]. Those steep faults are indeed parallel to the opening direction and well oriented to become transfer faults and maybe transform faults. The second structural characteristic is the short length of horsts in the distal margin (fig. 18), which may be a consequence, as in the models, of block rotations. Thus, we could suggest that the highly non-cylindrical structures imaged by reflection seismic data (fig. 18) are due to block rotations and horsts re-faulting.

(iiii) Finally, the model displays grabens with scissor-like morphology. Such grabens are observed on the northern margin [*Autin et al.*, subm.] (fig. 18) and could result from blocks rotations. In particular, in the ocean-continent transition, a scissor-like morphology is observed. In such location, mantle exhumation, if any, might occur on short length in the en-échelon structured margin. Final stages of rifting and possible mantle exhumation are thus in en-échelon zones, controlled by displacement normal faults as mentioned earlier. This morphology controls the beginning of oceanic accretion that occurs in non-oblique but opening perpendicular segments of a few tens of kilometres each [*d'Acremont et al.*, subm.].

Conclusions

We have presented two analogue models where an oblique rifting is simulated in two ways. In one experiment, the lithosphere is heterogeneous, thanks to a zone of weakness in the lithospheric mantle. In this model, the obliquity of the rift is forced by the obliquity of the weakness and lateral velocity discontinuities (offset in plane view). In the second model, the lithosphere is homogeneous. In this model, the rift is oblique only because the lateral velocity discontinuities are offset.

In both models, the evolution of the fault pattern indicates how the rift localizes. In a first stage, intermediate faults are the main ones, especially in the heterogeneous model. This is due to the overall kinematics of the oblique rift. Those were predicted by previous analogue models.

In a second stage, the rift localizes along the oblique zone especially though the initiation of rift-parallel faults, probably due to local stresses (extension perpendicular to the rift axis) due to crustal thickness variations.

Once the rift has thinned enough, the deformation localizes in the rift centre where no crustal thickness variation are significant. In the homogeneous models, no local stresses perturb the far field one. Faults perpendicular to the far field extension initiate. The result is that the zones of extreme thinning are still disposed en-echelon. Those are believed to be the one that will control the ocean-continent transition structure (not seen in our models) and the geometry of the accretion centres. In the heterogeneous model, faults perpendicular to the far field extension as well as rift-parallel ones control the late stages of deformation. Thus, in this case the zone of extreme thinning is aligned with the rift axis.

These characteristics allow to explain the structures observed in the Gulf of Aden and their evolution and, in particular, argue that the obliquity of the rifting in this area was most probably not due to a pre-existing lithospheric weakness.

Acknowledgements

We thank F. Funiciello and C. Faccenna for their advices, comments and help in the Laboratory of experimental geology of the University of Rome III. We also thank J.P. Brun for stimulating discussions. We would like to thank D. Rossi for useful personal communication. Figures 5, 6, 10, 11, 12 and 13 were produced with the GMT software package (Wessel & Smith 1995). This study is part of the GDR "Marges" and the "Action Marges" projects.

			Nature	Model
Crust	Upper crust	Thickness	20 km	1.5 cm
		Density	2.8 g.cm^{-3}	1.2 g.cm^{-3}
	Lower crust	Thickness	10 km	0.7 cm
		Density	2.9 g.cm^{-3}	1.25 g.cm^{-3}
		Viscosity	10^{21} Pa.s	4.10^{4} Pa.s
Mantle	Lithospheric brittle mantle	Thickness	~ 12 km	0.8 cm
		Density	3.3 g.cm^{-3}	1.2 g.cm^{-3}
	Lithospheric ductile mantle	Thickness	~ 50 km	2 cm
		Density	3.3 g.cm^{-3}	1.33 g.cm^{-3}
		Viscosity	10^{23} Pa.s	7.10^{4} Pa.s
	Asthenosphere	Density	3.2 g.cm^{-3}	1.41 g.cm^{-3}
		Viscosity	10^{19} Pa.s	10 Pa.s

Table 1: Main physical properties of natural and analogue materials.

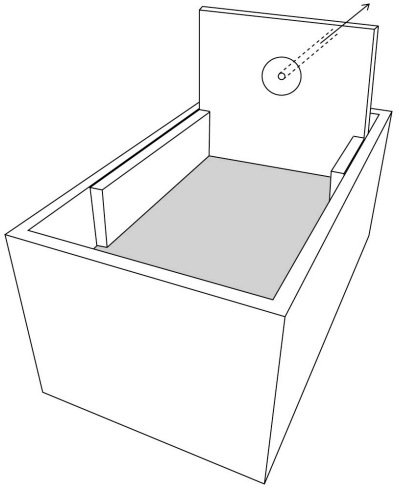

Figure 1: Strength profiles of the lithosphere and heterogeneity in experiments.

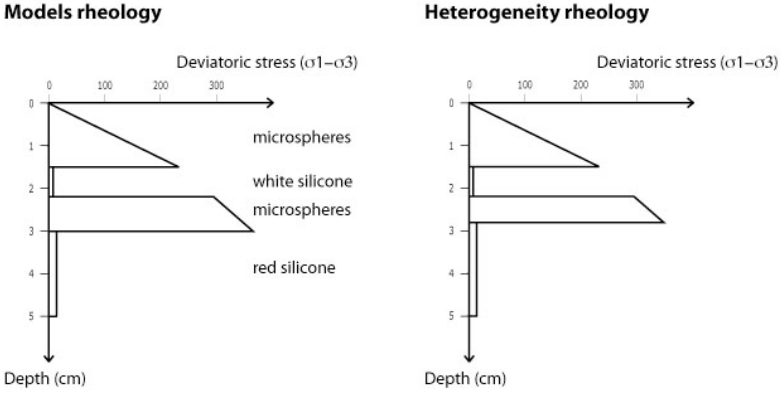

Figure 2: Strength profiles for the experimental lithosphere and the heterogeneity.

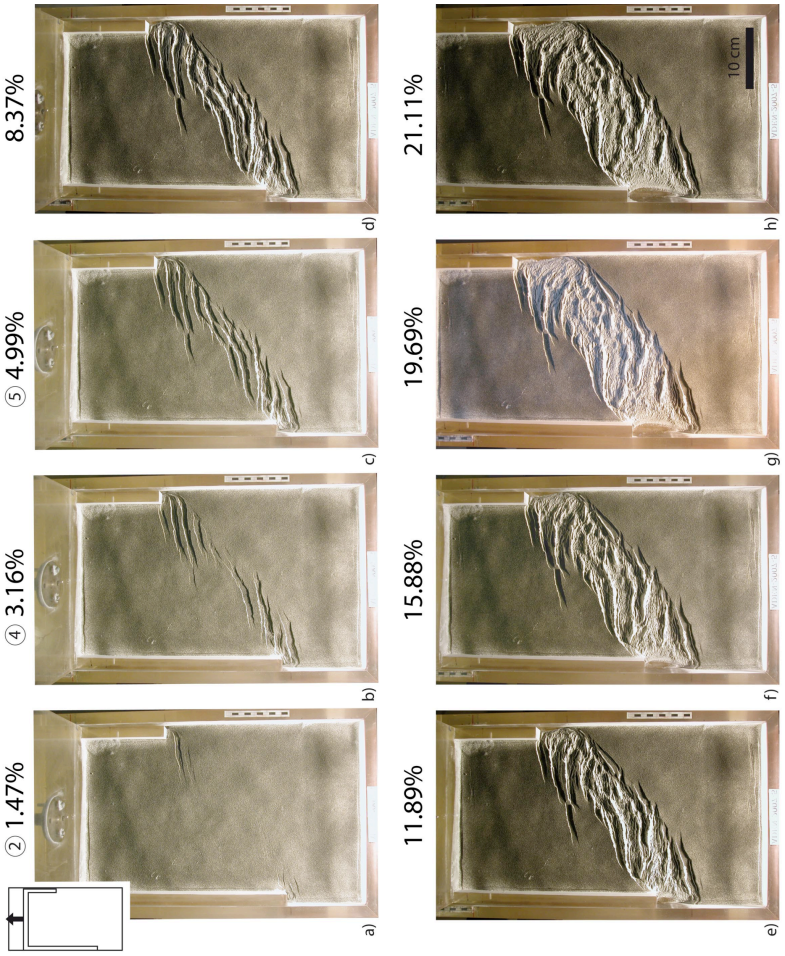

Figure 3: Top views of the homogeneous model during extension. Circled numbers correspond to the stages of figure 7.

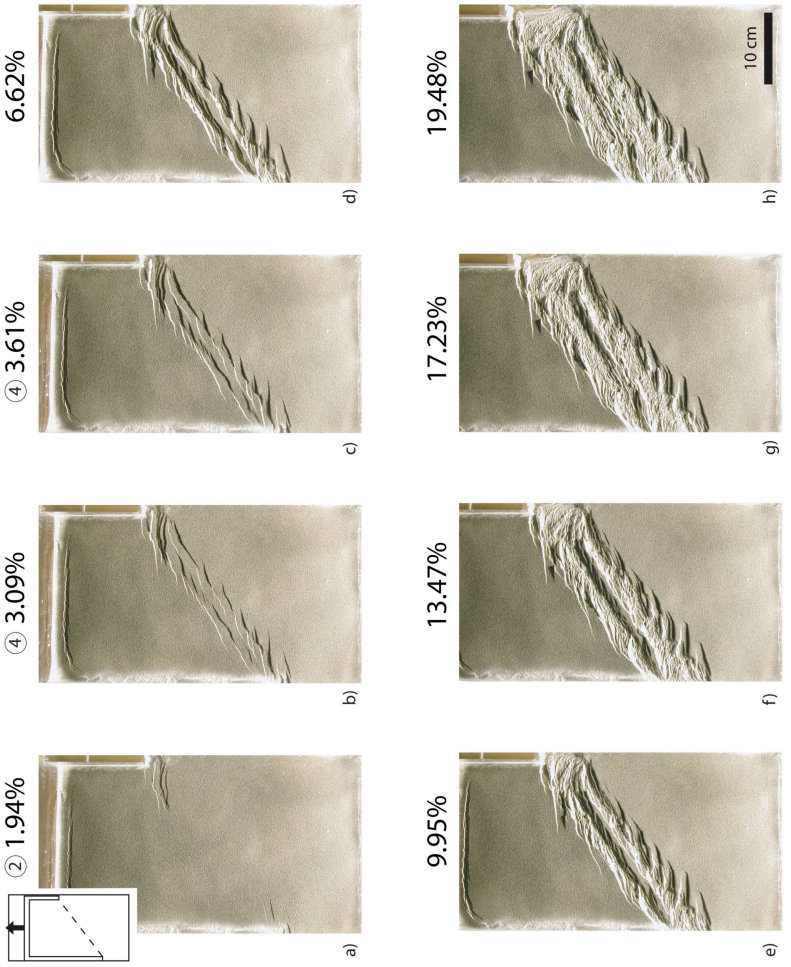

Figure 4: Top views of the heterogeneous model during extension. Circled numbers correspond to the stages of figure 7.

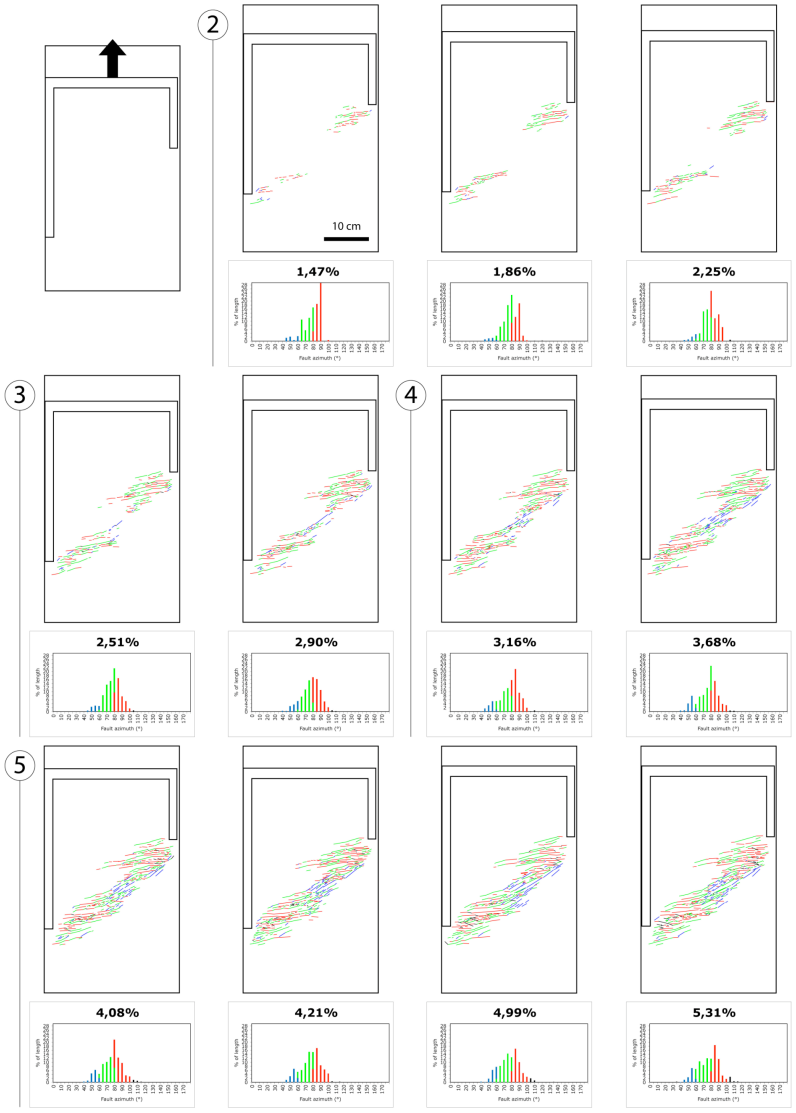

Figure 5: Line-drawing of the first stages of the model homogeneous and azimuthal distribution of the percentage of total length for each segment population. Blue: rift-parallel segments. Green: intermediate segments. Red: displacement-normal segments. Circled numbers correspond to the stages of figure 7.

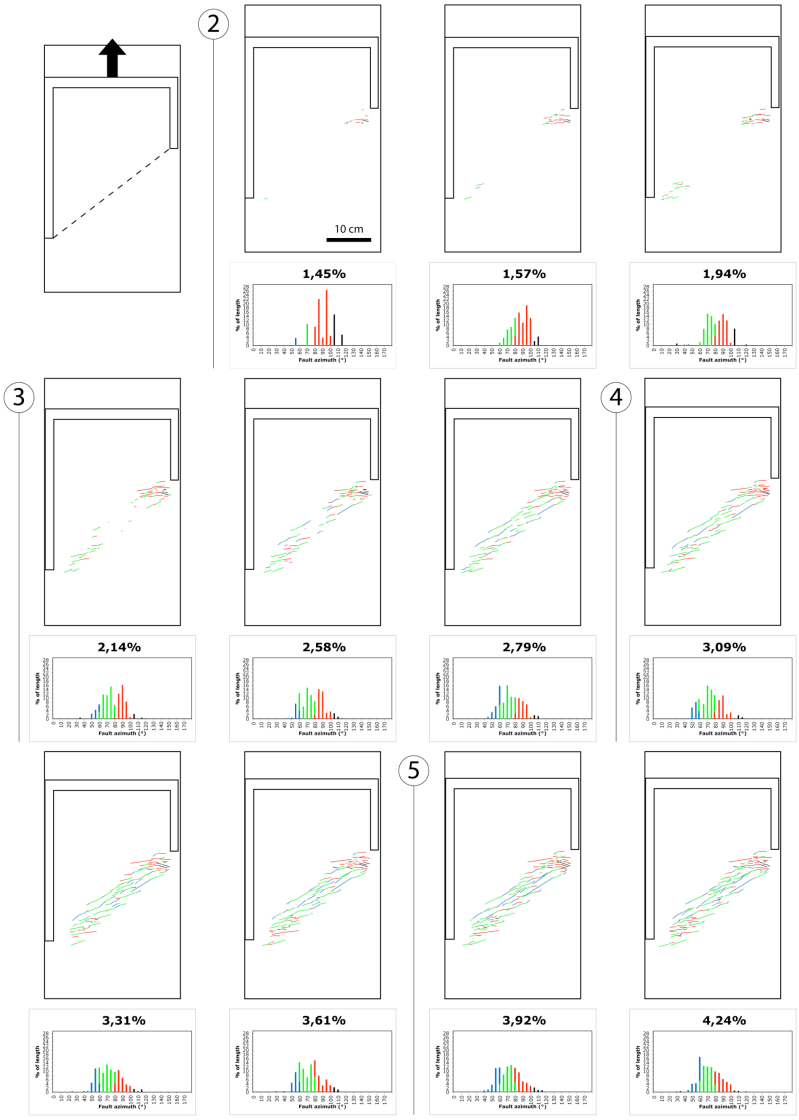

Figure 6: Line-drawing of the first stages of the model heterogeneous and azimuthal distribution of the percentage of total length for each segment population. Blue: rift-parallel segments. Green: intermediate segments. Red: displacement-normal segments. Circled numbers correspond to the stages of figure 7.

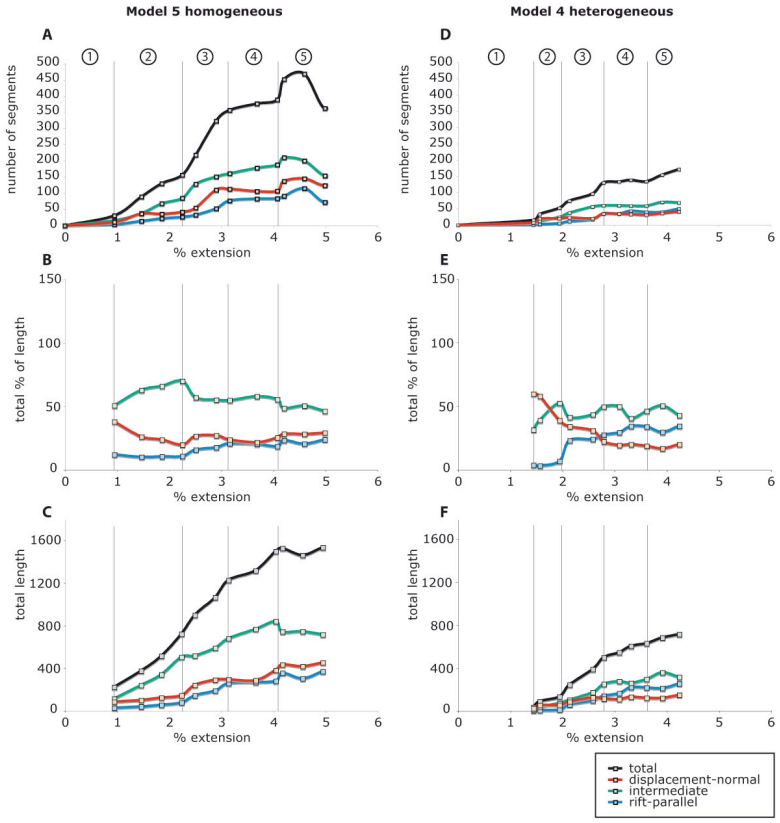

Figure 7: Time-evolution of the fault population during the first stages of development of the homogeneous (left) and heterogeneous (right) models with increasing extension. Blue: rift-parallel segments. Green: intermediate segments. Red: displacement-normal segments. A-D: number of segments evolution. B-E: total cumulated length percentage. C-F: total cumulated length.

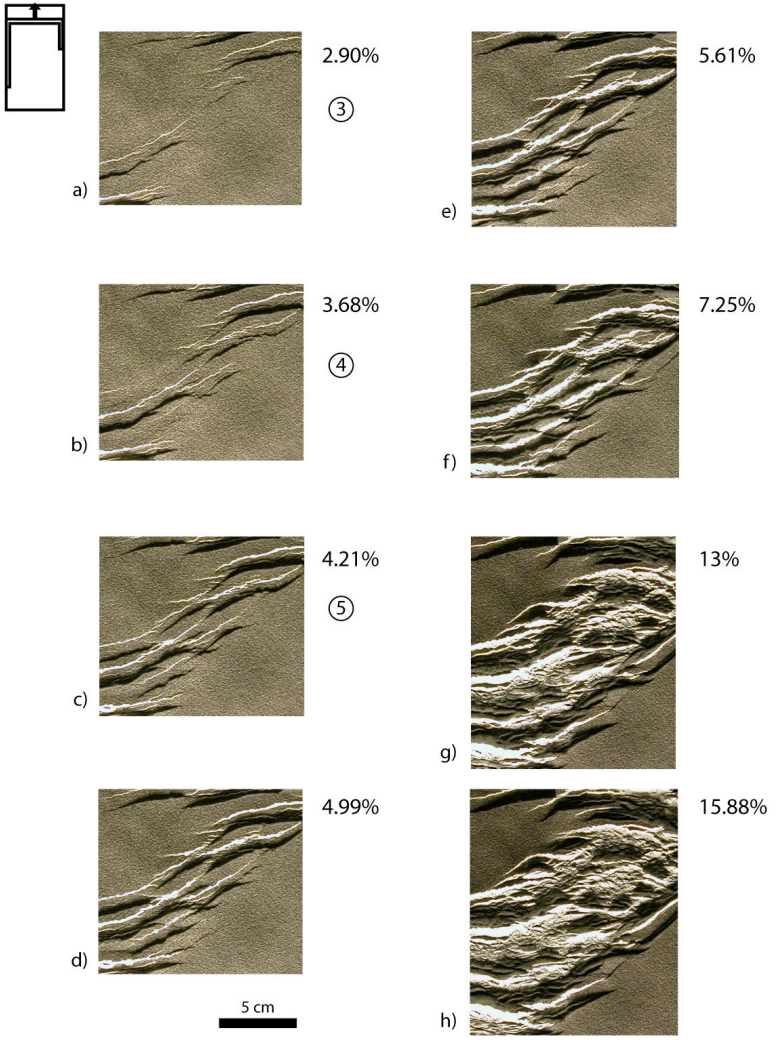

Figure 8: Time evolution of the centre of the homogeneous model. Circled numbers correspond to the stages of figure 7.

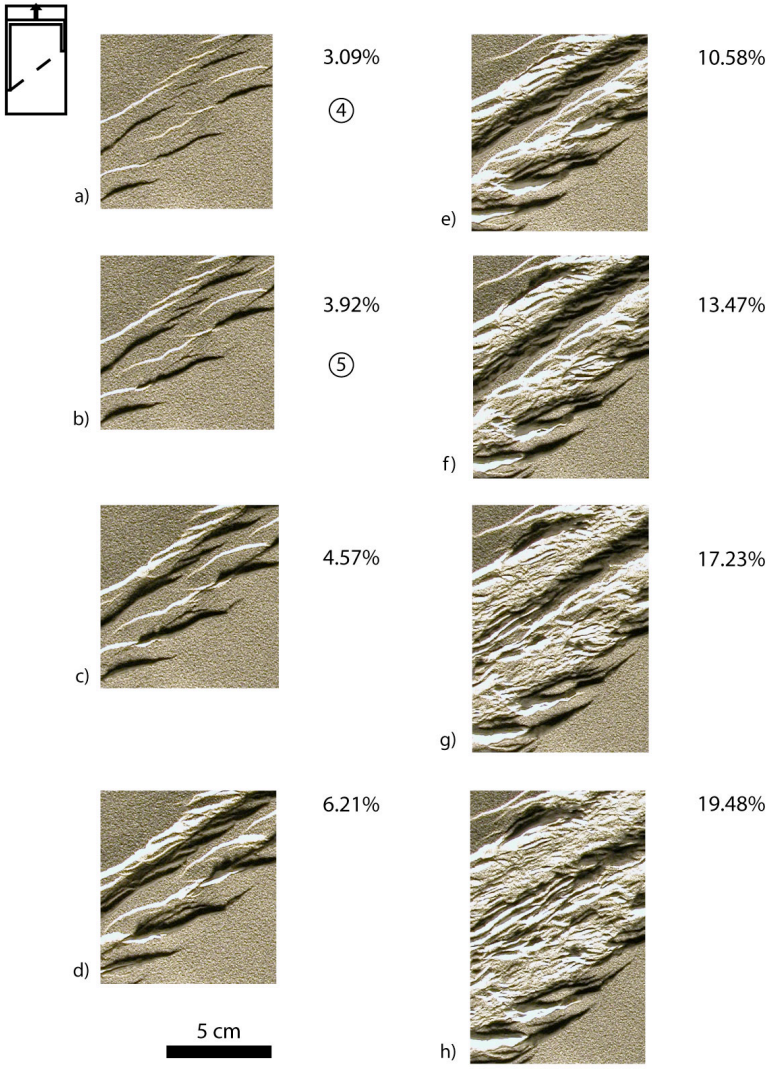

Figure 9: Time evolution of the centre of the heterogeneous model. Circled numbers correspond to the stages of figure 7.

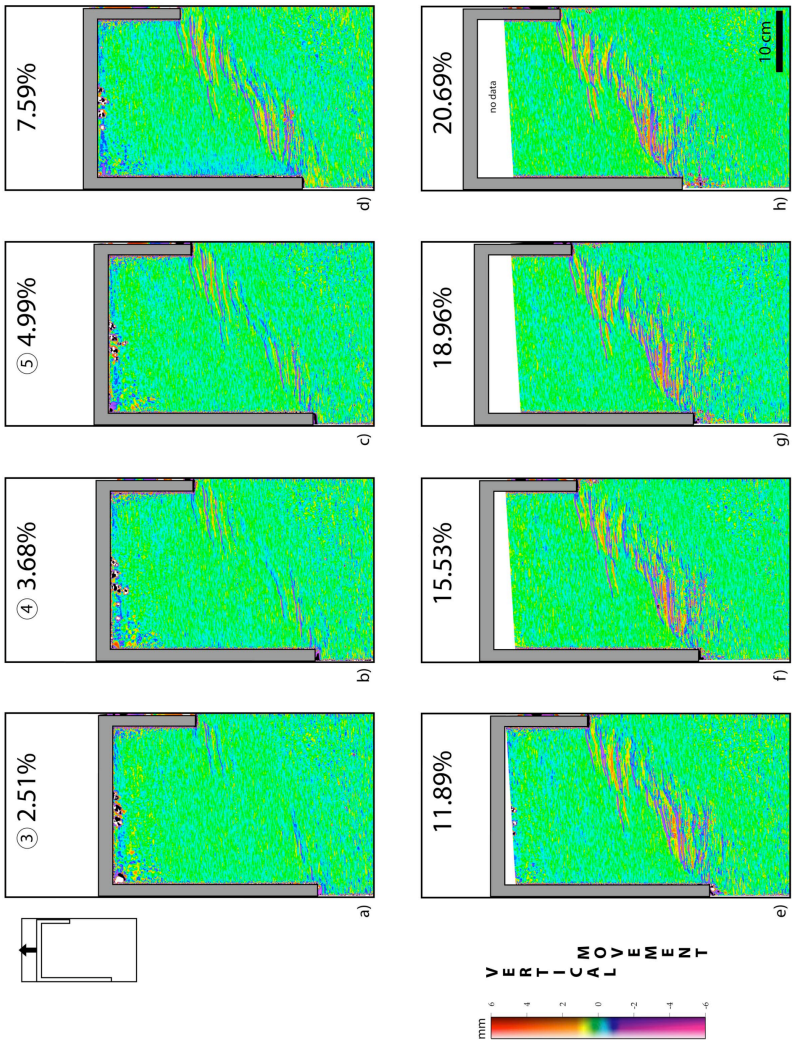

Figure 10: Differential topography (2 min spaced) of the homogeneous model for increasing extension amount. Circled numbers correspond to the stages of figure 7.

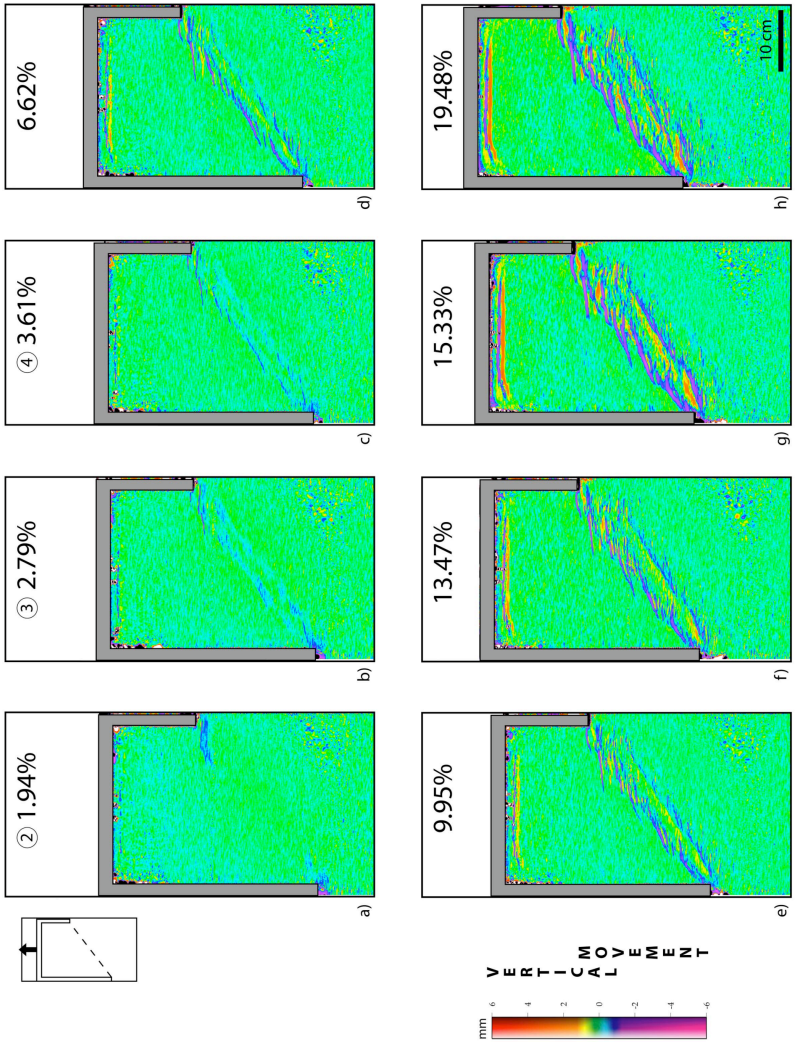

Figure 11: Differential topography (2 min spaced) of the heterogeneous model for increasing extension amount. Circled numbers correspond to the stages of figure 7.

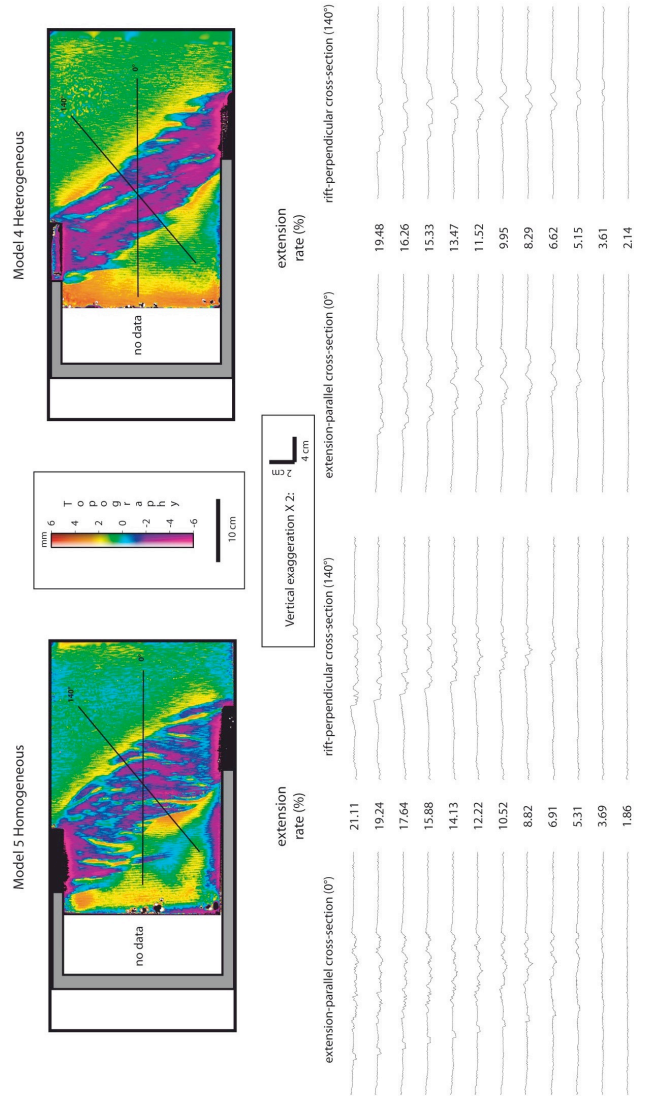

Figure 12: Evolution of the topography (from laser scan data) for the homogeneous and heterogeneous models along two profiles: extension-parallel and rift-perpendicular cross-sections. See profiles localisation on the topographic maps.

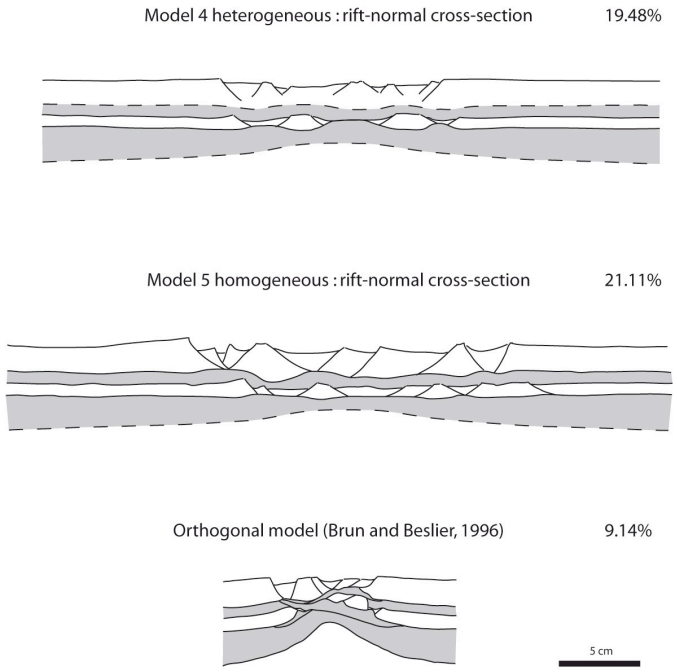

Figure 13: Model cross-sections and comparison with the model of Brun and Beslier (1996), where the rift is perpendicular to the opening direction.

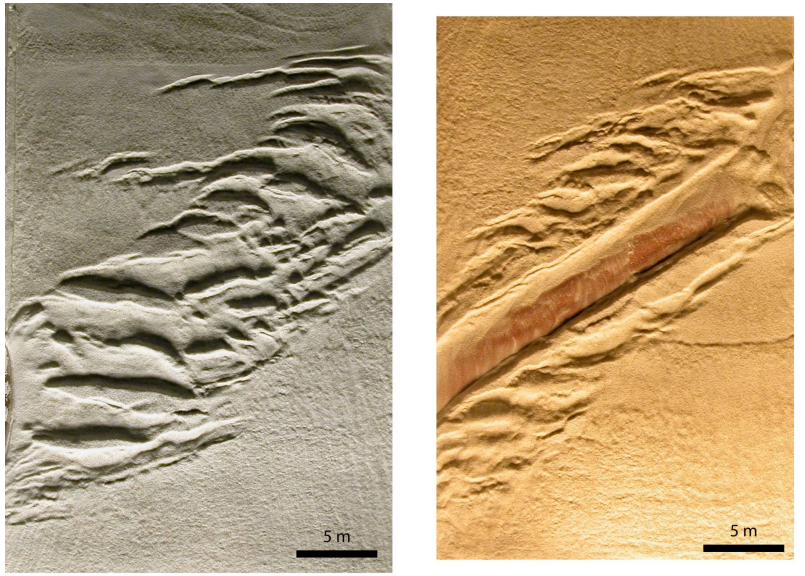

Figure 14: Photographs of the top of the brittle mantle for homogeneous model 5 and heterogeneous model 4, taken after the removal of the brittle and ductile crust layers. Note the exhumation of the reddish ductile mantle in the center of the rift in model 4.

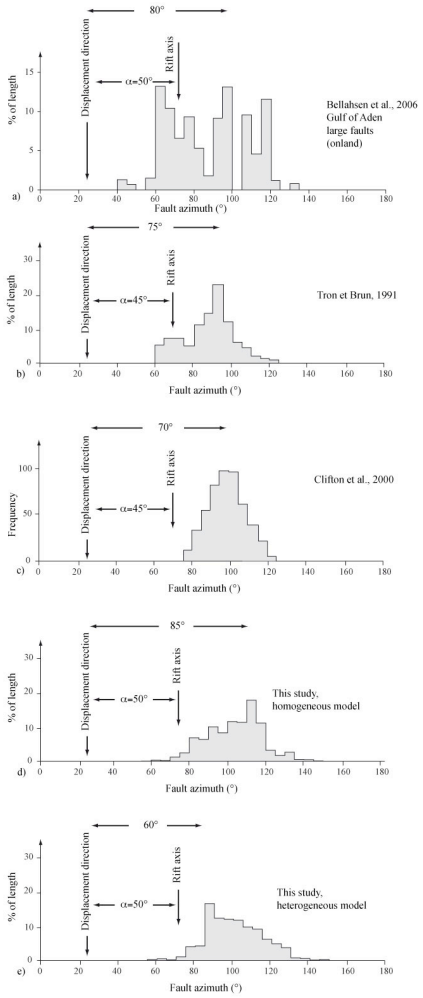

Figure 15: Fault distribution (percentage of total length vs. fault azimuth) for different analogue models of oblique rifting and comparison to the Gulf of Aden (measured faults onland).

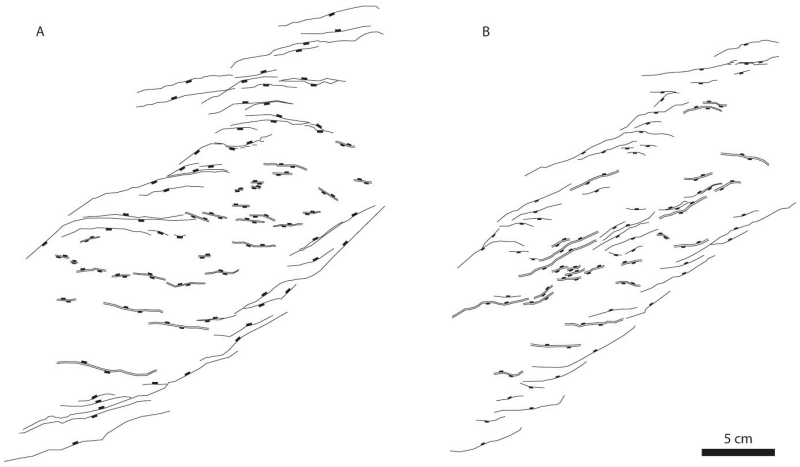

Figure 16: Line drawing of the homogeneous (A) and heterogeneous (B) models after 20% extension. Only major faults are reported.

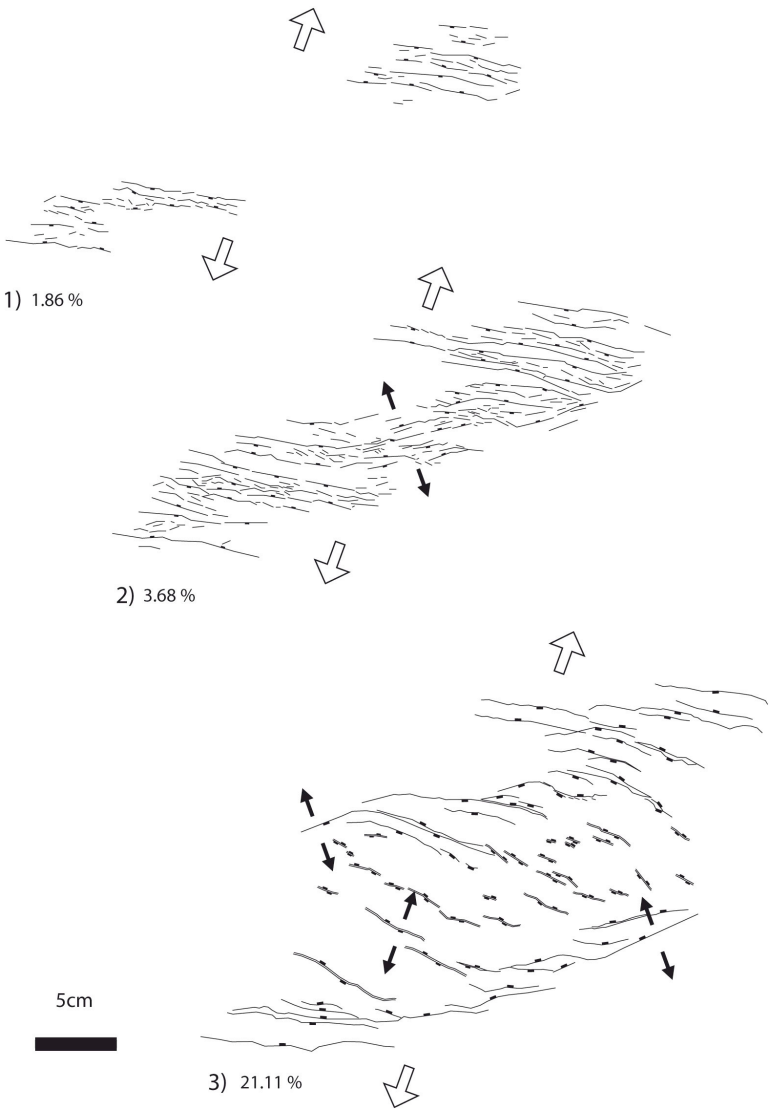

Figure 17: Line-drawing of the three main steps in the evolution of the homogeneous model. Drawings are rotated in order to fit the opening direction of the Gulf of Aden (N020°E, white arrows). Black arrows represent the local stresses induced by thickness variation.

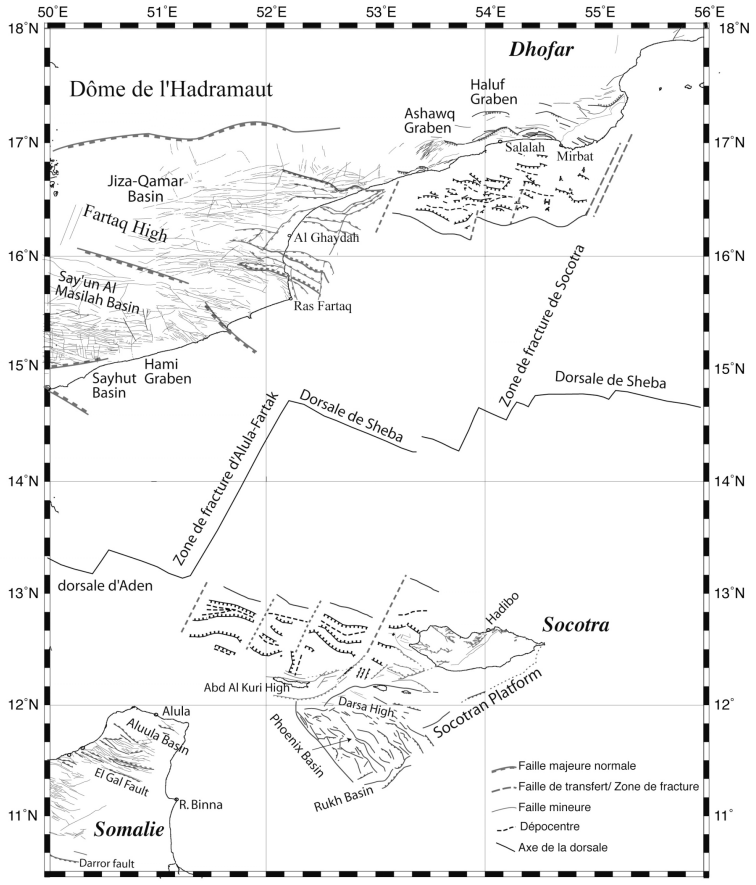

Figure 18: Structural map of the conjugate margins of the oriental Gulf of Aden. Synthesis from field work and seismic reflection data ([*Autin et al.*, subm.; *Bellahsen et al.*, 2006; *Beydoun and Bichan*, 1969; *Birse et al.*, 1997; *Brannan et al.*, 1997; *d'Acremont et al.*, 2005; *Fantozzi*, 1996; *Khanbari*, 2000; *Lepvrier et al.*, 2002; *Menzies and al.*, 1994; *Morrison et al.*, 1997; *Platel and Roger*, 1989; *Roger et al.*, 1989; *Roger et al.*, 1992; *Samuel et al.*, 1997; *Watchorn et al.*, 1998].

References

Artyushkov, E. V. (1973), Stresses in the lithosphere caused by crustal thickness inhomogeneities, *J. Geophys. Res.*, *78*.

Autin, J. (2008), Déchirure continentale et segmentation du golfe d'Aden oriental en contexte de rifting oblique, PhD thesis, Université Paris VI, France.

Autin, J., et al. (subm.), Continental break-up history of a deep magma-poor margin from seismic reflection data (northeastern Gulf of Aden margin, offshore Oman), *submitted to Geophysical Journal International*.

Bellahsen, N., et al. (2003), Why did Arabia separate from Africa? Insights from 3-D laboratory experiments., *Earth and Planetary Science Letters*, *216*, 365-381.

Bellahsen, N., et al. (2006), Fault reactivation and rift localization: the northeastern Gulf of Aden margin, *Tectonics*, *25*, 14 p.

Benes, V., and P. Davy (1996), Modes of continental lithospheric extension: experimental verification of strain localization processes, *Tectonophysics*, *254*, 69-87.

Beydoun, Z. R., and H. R. Bichan (1969), The geology of Socotra Island, Gulf of Aden, *Q.J.geol. Soc. Lond.*, *125*, 413-446.

Birse, A. C. R., et al. (1997), The Mesozoic and early tertiary tectonic evolution of the Socotra area, eastern Gulf of Aden, Yemen, *Marine and Petroleum Geology*, *14*(6), 675-684.

Brannan, J., et al. (1997), Tectono-stratigraphic development of the Qamar basin, eastern Yemen, *Marine and Petroleum Geology*, *14*(6), 701-730, IN707-IN712.

Brun, J.-P., and M.-O. Beslier (1996), Mantle exhumation at passive margins, *Earth and Planetary Science Letters*, *142*, 161-173.

Brun, J. P., and V. Tron (1993), Development of the North Viking Graben: inferences from laboratory modelling, *Sedimentary Geology*, *86*(1-2), 31-51.

Callot, J. P., et al. (2002), Development of volcanic passive margins: three-dimensional laboratory models, *Tectonics*, *21*(6), 1052.

Clifton, A. E., et al. (2000), Influence of rift obliquity on fault-population systematics: results of experimental clay models, *Journal of Structural Geology*, *22*, 1491-1509.

Clifton, A. E., and S. A. Kattenhorn (2006), Structural architecture of a highly oblique divergent plate boundary segment, *Tectonophysics*, *419*(1-4).

d'Acremont, E., et al. (2005), Structure and evolution of the eastern Gulf of Aden conjugate margins from seismic reflection data, *Geophys. J. Int.*, *160*, 869-890.

d'Acremont, E., et al. (subm.), Anomalous ridge Structure between Alula-Fartak and Socotra FZ (eastern Gulf of Aden) from bathymetry, gravity and magnetic data: Segmentation evolution and implications for accretion processes, *submitted to Geophysical Journal International.*

Dauteuil, O., et al. (2001), Propagation of an oblique spreading center: the western Gulf of Aden, *Tectonophysics*, *332*, 423- 442.

Davy, P., and P. R. Cobbold (1988), Indentation tectonics in nature and experiment. I: Experiments scaled for gravity, *Bulletin of the Geological Institution of the University of Upsala*, *14*, 129-141.

Davy, P., and P. R. Cobbold (1991), Experiments on shortening of a 4-layer model of the continental lithosphere, *Tectonophysics*, *188*(1-2), 1-25.

Faerseth, R. B., et al. (1997), Oblique rifting and sequential faulting in the Jurassic development of the northern North Sea, *Journal of Structural Geology*, *19*(10), 1285-1302.

Fantozzi, P. L. (1996), Transition from continental to oceanic rifting in the Gulf of Aden: structural evidence from field mapping in Somalia and Yemen, *Tectonophysics*, *259*(4), 285-311.

Fleitout, L., and C. Froidevaux (1982), Tectonics and topography for a lithosphere containing density heterogeneities, *Tectonics*, *1*(1), 21-56.

Fournier, M., et al. (2004), Oblique rifting and segmentation of the NE Gulf of Aden passive margin, *Geochemistry, Geophysics, Geosystems*, *5*(11), 24 p.

Fournier , M., et al. (2007), Segmentation and along-strike asymmetry of the passive margin in Socotra, eastern Gulf of Aden: Are they controlled by detachment faults?, *Geochemistry Geophysics Geosystems*, *8*(3).

Hubbert, M. K. (1937), Theory of scale models as applied to the study of geologic structures, *Bulletin of the Geological Society of America*, *48*(10), 1459-1519.

Huchon, P., et al. (1991), Extensional deformation in Yemen since Oligocene and the Africa-Arabia-Somalia triple junction, *Annales Tectonicae*, *V*, p.141-163.

Huchon, P., and K. Khanbari (2003), Rotation of the syn-rift stress field of the northern Gulf of Aden margin, Yemen, *Tectonophysics*, *364*(3-4), 147-166.

Khanbari, K. (2000), Propagation d'un rift océanique: Le Golfe d'Aden
Ses effets structuraux sur la marge yéménite, 204 pp, Laboratoire de Géologie, Ecole Normale Supérieure, Paris, Paris.

Lepvrier, C., et al. (2002), Cenozoic extension in coastal Dhofar (southern Oman) :

implications on the oblique rifting of the Gulf of Aden, *Tectonophysics*, *357*, 279– 293.

Leroy, S., et al. (subm.), Constrasted styles of rifting in the eastern Gulf of Aden, *submitted to Nature*.

Mart, Y., and O. Dauteuil (2000), Analogue experiments of propagation of oblique rifts, *Tectonophysics*, *316*, 121–132.

McClay, K. R., and M. J. White (1995), Analogue modelling of orthogonal and oblique rifting, *Marine and Petroleum Geology*, *12*(2), 137-151.

Menzies, M., and al. (1994), Geology of the Republic of Yemen, in *The Geology and Mineral Resources of Yemen*, edited, pp. 21-48, eds McCombe, D.A. Fernette, G.L & Alawi. A.J.

Morrison, J., et al. (1997), The Cretaceous sequence stratigraphy of the Socotran Platform, the Republic of Yemen, *Marine and Petroleum Geology*, *14*(6), 685-699.

Platel, J. P., and J. Roger (1989), Evolution dynamique du Dhofar (Sultanat d'Oman) pendant le Crétacé et le Tertiaire en relation avec l'ouverture du Golfe d'Aden, *Bull. Soc. Geol. Fr.*, *8*(2), 253-263.

Ramberg, H. (1981), *Gravity, Deformation and the Earth's Crust*, Academic Press New York.

Roger, J., et al. (1989), Données nouvelles sur la stratigraphie et l'histoire géologique du Dhofar (Sultanat d'Oman), *Bull. Soc. Géol. France*, *2*, 265-277.

Roger, J., et al. (1992), Geological Map of Hawf with Explanatory Notes; sheet NE 39-16, *Ministry of Petroleum and Minerals, Directorate General of Minerals, Oman*.

Rossi, D., and F. Storti (2003), New artificial granular materials for analogue laboratory experiments: aluminium and siliceous microspheres, *Journal of Structural Geology*, *25*(11), 1893-1899.

Samuel, M. A., et al. (1997), Field observations from the Socotran platform: their interpretation and correlation to Southern Oman, *Marine and Petroleum Geology*, *14*(6), 661-673.

Sokoutis, D., et al. (2007), Modelling the extension of heterogeneous hot lithosphere, *Tectonophysics*, *444*(1-4), 63-79.

Tron, V., and J. P. Brun (1991), Experiments on oblique rifting in brittle–ductile systems, *Tectonophysics*, *188*, 71–84.

Watchorn, F., et al. (1998), Rift-related sedimentation and stratigraphy, southern Yemen (Gulf of Aden). in *Sedimentation and Tectonics in the Rift Basins Red Sea- Gulf of Aden.*, edited by B. Purser and D. Bosence, pp. 165- 189, Chapman & Hall, London.

Withjack, M. O., and W. R. Jamison (1986), Deformation produced by oblique rifting, *Tectonophysics*, *126*(2-4), 99-124.

Chapitre 2

Subductions

Le concept de subduction est intimement associé d'une part à celui de tectonique des plaques et d'autre part à celui de convection mantellique. Cette situation est source d'ambiguités et de mécompréhension, puisque d'aucuns isolent implictement la tectonique des plaques de la convection mantellique. On trouve fréquement un paradigme d'étude des subductions vues depuis la surface vers l'intérieur, où la convergence entre les plaques et la disparition de ces plaques dans le manteau sont considérées en isolement de l'écoulement mantellique sous-jacent. Un paradigme réciproque (de l'intérieur vers la surface) est aussi fréquent, dans lequel la subduction est perçue comme le courant descendant d'une cellule de convection. La lithosphère en subduction y est décrite comme une couche limite thermique instable qui ne saurait être empêchée par la tectonique de surface. Il s'agit respectivement du point de vue *du géologue* et du point de vue *du physicien*.

Cette dualité est héritée de la période d'avènement de la tectonique des plaques [Le Pichon, 1968, McKenzie & Parker, 1967, Morgan, 1968] qui a vu l'entrée de la physique dans la conceptualisation des sciences de la Terre. Elle a été très fructueuse dans les décennies qui ont suivi puisqu'elle a permis de documenter la tectonique des plaques et la subduction en particulier par les observations géologiques tout en développant parallèlement une comprénsion physique des processus. Elle a atteint ses limites dès lors que d'une part les principes physiques élémentaires qui pilotent la subduction ont été compris, et que que les observables de surface en termes de tectoniques ont été bien décrits. Les divergence entre prédictions et observations, d'un point de vue comme de l'autre, ne sauraient être expliquée sans une

approche conjointe. C'est dans ce cadre que je base mes travaux sur la subduction.

De manière générale, les études portant sur les zones de subduction portent sur des tentatives de corrélations -peu satisfaisantes- entre observables cinématiques et propriétés mécaniques intrinsèques de la zone de subduction [Heuret & Lallemand, 2005, Jarrard, 1986, Lallemand et al., 2005], et sur la modélisation de la dynamique des zones de subduction prises comme systèmes indépendants.

2.1 Subductions de lithosphères hétérogènes

La subduction des plaques lithosphériques est dans son acception générale entendue comme celle de plaques homogènes qui descendent dans le manteau moins dense en régime permanent. Cette idée a été largement véhiculée par les travaux essentiels en modélisation analogique, en particulier de Faccenna et Funiciello [e.g., Bellahsen et al., 2005, Funiciello et al., 2003, Schellart, 2004] (fig. 2.1), accompagné par pléthore de modèles numériques [e.g., Capitanio et al., 2007, Christensen & YuenN, 1984, Di Giuseppe et al., 2008, Stegman et al., 2006]. Ces modèles, qui explorent les propriétés intrinsèques des subductions ont permis d'avoir une compréhension claire des mécanismes qui opèrent pour une subduction isolée, mais prédisent des comportements qui ne sont que partiellement comparables aux observations. Cette divergence s'explique par le traitement des zones des subductions en tant que systèmes isolés. Les zones de subductions prises dans un contexte global sont traitées dans la section 4.

En réalité, il semble peu probable que le régime permanent s'applique systématiquement à la Terre, puisque les structures en densité et en rhéologie des panneaux plongeants sont très souvent hétérogènes. Dans les expériences et applications présentées dans les articles suivants, nous proposons un modèle semi-analytique pour examiner le comportement dynamique des subductions faisant intervenir des panneaux plongeants hétérogènes (J. Martinod et co-auteurs [Martinod et al., 2005] avaient envisagés cette possibilité, fig. 2.1) et explorons la possibilité que cette hétérogénéité soit responsable de la divergence presque systématique entre

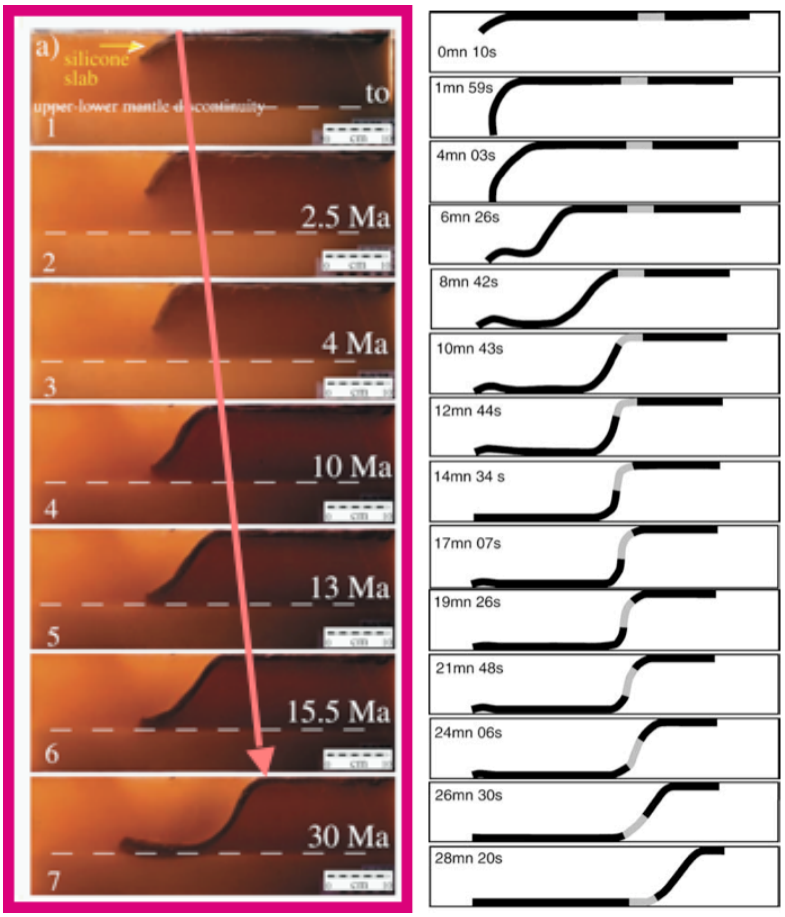

FIG. 2.1: Modélisation analogique de la migration de type *rollback* du panneau plongeant, vers un régime permanent (à gauche, expérience F. Funiciello et C. Faccenna) et en régime transitoire lors de l'introduction d'une lithosphère hétérogène (à droite, évolution schématique [Martinod et al., 2005]). *Analogue modeling of a rollback type subduction, towards a steady state (left, experiment by F. Funiciello and C. Faccenna) and in transient state (right, sketch evolution [Martinod et al., 2005]).*

théories et observations. Les subductions y apparaissent alors comme une successions de régimes transitoires. Les cinématiques variées qui en résultent correspondent mieux aux observations que les modèles en régime stationnaire.

La vaste majorité des modèles de subductions sont soit analogiques, soit numériques. Dans le premier cas, les processus physiques qui opèrent sont supposés compris et l'expérience permet de les tester, mais sans pouvoir isoler facilement les différentes contributions à la dynamique du système. Les modèles numériques discrétisent le système, permettant d'introduire une complexité et une résolution

parfois supérieure aux modèles analogiques. Là encore, l'impact des processus physiques n'est pas toujours identifiable. Alternativement , il est possible de simplifier les problèmes afin d'avoir accès à une expression analytique, dont la résolution est limitée par le nombre d'itérations. Cette approche semi-analytique permet d'examiner indépendament chaque contribution.

Geophys. J. Int. (2006) doi: 10.1111/j.1365-246X.2006.03079.x

Trench motion, slab geometry and viscous stresses in subduction systems

Leigh H. Royden and Laurent Husson

Department of Earth, Atmospheric and Planetary Sciences, M.I.T., Cambridge MA 01890*, USA. E-mails: lhroyden@mit.edu; lhusson@mit.edu*

Accepted 2006 May 18. Received 2006 May 2; in original form 2006 February 7

SUMMARY

A semi-analytic, 3-D model for subduction within a Newtonian viscous upper mantle provides a dynamically consistent means of computing viscous stress, trench motion and slab geometry in subduction systems. Although negative slab buoyancy provides the basic driving force for subduction, slabs that extend from the surface to the base of the upper mantle are oversupported by viscous stresses in the shallow (<100–150 km) mantle and undersupported by viscous stresses at greater depth in the upper mantle. These deeper parts of the subduction system act as an 'engine' for subduction while shallower parts act as a 'brake' on trench motion; trench migration rates and slab geometry reflect a competition between these two effects. During steady-state subduction, trench migration rates vary approximately linearly with slab buoyancy and model rates of trench motion are in good agreement with the range of observed rates for a two layer upper mantle viscosity of $\sim 2 \times 10^{20}$ Pa s above 300 km and $\sim 5 \times 10^{20}$ Pa s below. Steady-state slab dip increases as slab density decreases, especially for very low-density slabs, which dip significantly more steeply than high-density slabs. The horizontal velocity at the top of the lower mantle, measured relative to the foreland, has a very large effect on trench migration rates, rivalling or even exceeding that of slab buoyancy. Slab width, parallel to the trench, also has a significant effect on trench migration rates due to the viscous pressure of toroidal flow around the slab. The stiffness of the subducting lithosphere does not exert a significant effect on trench migration rates or slab geometries for rigidities compatible with oceanic lithosphere. Very stiff slabs, with elastic plate thicknesses more that ~40 km or viscosities in the range of 10^{25}–10^{26} Pa s, subduct significantly more slowly than weak slabs, with trench migration rates in the range of half to a third that of weak slabs. Large, unexpected effects on trench migration rates and slab geometry are exerted by the structure and density of the frontal prism and overriding plate, indicating that local geology can exert important constraints on slab dynamics. During non-steady-state subduction, rates of trench migration respond rapidly as variably buoyant lithosphere penetrates into the asthenosphere. In the absence of other driving forces for convergence, trench migration rates can change by a factor of two or more in as little as 2–3 Myr, for example, from 35 to 70 mm yr^{-1} when an oceanic piece of slab follows a continental one into the subduction system. Subduction of variable-buoyancy lithosphere is accompanied by changes in slab dip with depth and through time.

Key words: asthenosphere, geodynamics, lithosphere, subduction zone, trench migration.

INTRODUCTION

Subduction systems embody the local interplay between slab buoyancy and mantle viscosity, embedded within the global convective system (e.g. McKenzie 1969; Forsyth & Uyeda 1975; Chapple & Tullis 1977; Richter & McKenzie 1978; Hager 1984). On a global scale there exist important feedbacks among slab buoyancy, plate geometry, plate motions and convective flow in the upper and lower mantle (Turcotte & Oxburgh 1967; Richter 1977; Hager & O'Connell 1981; Davies 1989; Ricard *et al.* 1993; King & Hager 1990; Becker & O'Connell 2001; Bercovici 2003). For example, the rapid subduction of the Pacific plate and its convergence with Eurasia is largely attributable to the great length of subduction boundary along its northern and western margins, where high-density lithosphere sinks rapidly into the less dense upper mantle (Forsyth & Uyeda 1975; Solomon & Sleep 1974; Richards & Lithgow-Bertelloni 1996; Lithgow-Bertelloni & Richards 1998; Conrad & Lithgow-Bertelloni 2002, 2004).

Within this interactive dynamic system, the factors that determine the motion of the trenches are poorly understood. Only a handful of

© 2006 The Authors
Journal compilation © 2006 RAS

studies have incorporated more-or-less self-consistent trench motion into the scheme of subduction (Zhong & Gurnis 1995a,b; Han & Gurnis 1999; Becker *et al.* 1999; Gurnis *et al.* 2000; Funiciello *et al.* 2003a,b; Enns *et al.* 2005); most define trench motion *a priori* (e.g. Griffiths *et al.* 1995; Christensen 1996; Olbertz *et al.* 1997). In fact, the rate of trench motion depends on a subtle balance between the local density and geometry of the subducting slab and the viscosity structure of the surrounding mantle, as well as on mantle-flow induced by far-field events (Cross & Pilger 1982; Becker *et al.* 1999; Zhong & Gurnis 1995a,b). The failure to incorporate self-consistent trench motion into dynamic models for subduction affects the results of subduction-zone models and limits our understanding of the subduction process.

This paper was largely motivated by the desire to understand the evolution of subduction systems in which variable slab densities and variable rates of trench motion appear to play a primary role in the regional tectonics, for example within the Mediterranean region (e.g. Malinverno & Ryan 1986; Wortel & Spakman 1992; Royden 1993a,b; Jolivet & Faccenna 2000; Faccenna *et al.* 2003). In the process of our investigations, we discovered that, although many quantitative analyses of subduction exist, few were framed in a way that could be readily adapted to the subduction of narrow, variable-density slabs (exceptions include works by Dvorkin *et al.* 1993; Stegman *et al.* 2006). Eventually, we decided develop an analytical approach that was applicable to steady-state and time-dependent systems, beginning with analysis and quantification of the stresses that act on subducting lithosphere and the way in which these stresses are related to the evolving slab geometry and trench velocity.

THE PROBLEM

The dynamic behaviour of subduction systems is governed by the balance between stresses induced by the buoyancy of the slab and by the viscous flow of mantle adjacent to the slab (e.g. Turcotte & Oxburgh 1967; McKenzie 1969; Davies 1977; Stevenson & Turner 1977). In general, mantle flow related to subduction is 3-D and cannot be readily captured by 2-D flow models (e.g. Funiciello *et al.* 2003a,b; Billen & Gurnis 2001; Billen *et al.* 2003). In this paper, we consider the case where the subducting slab may migrate laterally through the surrounding asthenosphere and where subduction is sufficiently far advanced that the slab extends to the base of the upper mantle (Fig. 1). Because the lower mantle is too viscous to flow at rates comparable to the upper mantle, slab migration must be accompanied by lateral flow of material around the edges of the slab (toroidal flow), as well as by downdip flow parallel to the slab (poloidal flow). This means that the buoyancy stresses arising from the downgoing slab are resisted by a viscous mantle with important components of flow in three-dimensions (see model results of Funiciello *et al.* 2006).

3-D numerical codes now exist with the resolution to model flow for subduction zones of limited lateral extent (e.g. Stegman *et al.* 2006). However, few numerical models are equipped to determine 'self-consistent' trench motion (see Enns *et al.* 2005, for a discussion). One of the difficulties in allowing for self-consistent trench motion is that most finite-element models of convection cannot allow for a truly stress-free upper surface. Instead, a vertical component of velocity, usually zero, is specified at the upper surface of the model. In practice, this means that trench location must be specified explicitly and that it is difficult to allow for trench migration in a natural, self-consistent manner. Partially for this reason, laboratory experiments of subduction have been used to generate insight into trench migration as a self-consistent feature arising from subduction (Bellahsen *et al.* 2005; Faccenna *et al.* 1996; Funiciello *et al.* 2003a; Schellart 2004a; Shemenda 1993; Shemenda & Groholsky 1994).

There is also much to be learned from simple algorithms that approximate the interactions of a slab with the surrounding mantle and allow self-consistent trench motion. One such 3-D approach was used by Dvorkin *et al.* (1993), where analytical results from Hele Shaw models of viscous flow were used to analyse viscous stresses acting on narrow slabs with prescribed dips and velocities. A second example is the work of Buiter *et al.* (2001, 2002), who used 2-D analysis of short slabs to estimate the slab pull force and computed consistent trench velocities. We use a somewhat similar approach, but one that does not depend *a priori* on specified forces, slab geometries or rates.

In the following sections we develop a dynamically consistent approach to subduction that involves coordination of several algorithms, or modules, each of which describes the behaviour of one part of the system. One module describes stresses due to the poloidal flow of mantle above the slab, another describes the stresses due to toroidal circulation of mantle around the slab, yet another describes the rheologic behaviour of the slab itself, etc. While each module is based on an analytic algorithm, the subduction process is simulated by linking all the modules at one time and time stepping through the subduction process. We stress that, if desired, any particular module can be reformulated without changing the overall approach to the problem. For example, the slab could be modelled using either a viscous or elastic thin-sheet rheology, a different approximation could be used for flow and stresses within the circulating mantle, etc. In the following sections we go through the physics of each element of the subduction problem, beginning with the stresses that act on the subducting lithosphere.

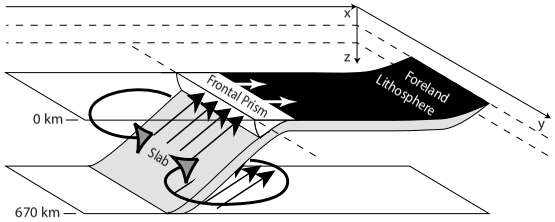

Figure 1. Schematic slab geometry, showing trench migration (white arrows), toroidal flow around slab (grey-shaded arrow heads) and direction of net mantle flux within viscous wedges above and below the plate (black arrowheads).

© 2006 The Authors, *GJI*
Journal compilation © 2006 RAS

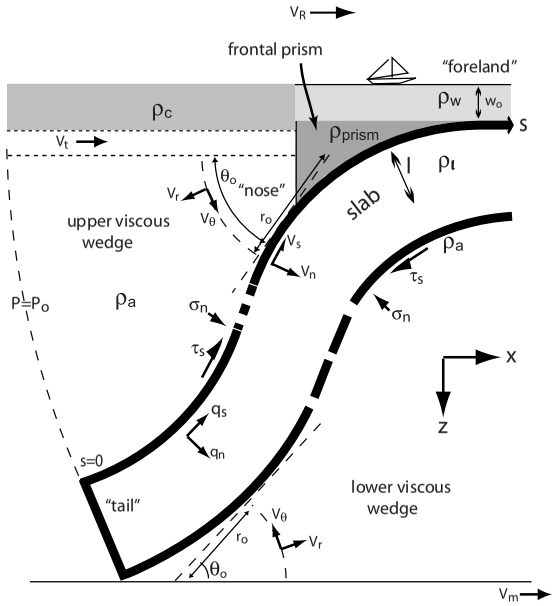

Figure 2. Slab geometry and conventions used in the text, particularly convention for positive directions of slab velocities (v_s, v_n), total force per unit area on the slab surfaces (q_s, q_n), and viscous normal and shear stress (σ_n, τ) on upper and lower slab surface. v_R is the velocity of the trench relative to the foreland. See Table 1 and text for definition of other variables.

SOURCES OF STRESS ON THE SLAB

For ease of reference, we shall use the term 'mantle wedge' or 'viscous wedge' to refer to the sublithospheric mantle material that forms an approximately triangular wedge above or below the subducting slab (Fig. 2). The narrowest portion of the upper wedge will be referred to as the 'asthenospheric nose' (after Kincaid & Sacks 1997). The end of the subducted slab near the upper mantle/lower mantle interface will be referred to as the 'slab tail'. The approximately triangular (and, in the model, undeforming) region in front of the asthenospheric nose, extending from the surface to the top of the slab, is referred to as the 'frontal prism'. The frontal prism includes the accretionary prism as well as volcanic rocks, oceanic or/and continental crust, and mantle lithosphere. We also use the common geologic term 'foreland' to describe the part of the subducting plate that has not yet been subducted.

Slab buoyancy

The driving force for subduction derives from the negative buoyancy of the subducted lithosphere and is equal to $(\rho_l - \rho_a)gl$, where ρ_l is the average density of the slab, ρ_a that of the asthenosphere, and l is the thickness of the slab (see Table 1 for a listing of all symbols and variables). The buoyancy of a particular piece of lithosphere can be readily estimated from its bathymetry before it nears the trench by applying a simple Airy balance:

$$(\rho_l - \rho_a)lg = (\rho_a - \rho_w)(w_0 - w_a)g, \tag{1}$$

where w_o is the pre-subduction water depth of the lithosphere, w_a is the water depth of an isostatically compensated column of asthenosphere (without crust) under no-flow conditions and ρ_w is the density of sea water. Eq. (1) indicates that the initial water depth of the slab can be equated with an average density difference between slab and asthenosphere. For example, each kilometre change in the initial water depth of a 100-km-thick slab translates to a change in mean density of 23 kg m^{-3}. Because most mid-ocean spreading centres are essentially a compensated column of asthenosphere, overlain by only a thin veneer of basaltic crust, their mean depth of ~2500 m below sea level should be a fair estimate of w_a.

Slabs with pre-subduction water depths of 6+ km are extremely dense and have the buoyancy of old oceanic lithosphere. Slabs with pre-subduction water depths near zero, typical of much continental lithosphere, have a buoyancy of approximately the same magnitude, but opposite sign. (Note that this method of estimating buoyancy refers only to the lithospheric material that is actually subducted. If, for example, sedimentary layers were stripped off the top of the slab prior to subduction, the buoyancy of the subducted slab would be determined by isostatically removing the sediments from the basement and calculating the resultant water depth; such backstripping of sedimentary sequences is a common technique in basin analysis).

© 2006 The Authors, *GJI*
Journal compilation © 2006 RAS

Table 1. Model parameters.

Variable	Definition	Value[a]	Remarks
Lengths			
x	Horizontal distance, across strike		See Fig. 3
y	Horizontal distance, along strike		See Fig. 3
z	Depth (relative to geoid)		
s	Distance along slab from tail		See Fig. 2
w	Vertical deflection of the slab		
w_0	Pre-subduction water depth (proportional to slab buoyancy)		See Fig. 2
w_a	Mid-ocean ridge depth	2.5 km	See eq. (1)
d_w	Water depth above frontal prism	$d_w = w_0^a$	See Fig. 2
l	Thickness of the slab	100 km[a]	See Fig. 2
l_p	Thickness of viscously competent part of slab	50 km[a]	See eq. (C9)
	Thickness of upper plate lithosphere	50 km[a]	
a	Slab half-width along strike	1000 km[a]	See Fig. 3
λ	Thickness of sublithospheric mantle	$\lambda + l = 670$ km	See Fig. 2
r	Radial distance in mantle wedge		See Appendix B
r_o	Radial distance to point on slab	$r_o = r$ on slab	See Fig. 2
Density			
$\rho\,(z)$	Density as a function of depth		
ρ_a	Density of the asthenosphere	3300[a] kg m^{-3}	
ρ_c	Density of the crust	2800[a] kg m^{-3}	
ρ_l	Density of the slab		
ρ_w	Density of water	1000 kg m^{-3}	
ρ_{prism}	Density of the frontal prism	2800[a] kg m^{-3}	
Stress			
P_{lith}	Lithostatic pressure		See eq. (2)
P_{visc}	Viscous pressure		Written as P in Appendices A and B
τ	Viscous shear stress		See Appendix B
σ	Viscous normal stress		See Appendix B
P_{static}	Static pressure of asthenosphere		See eq. (3)
P_0	Viscous pressure due to toroidal component of flow		See Fig. 2 and eq. (7)
q_i	Stress (minus P_{static}) acting on slab surfaces		See Fig. 2
Velocity			
v_i	Velocity in i-direction		
v_t	Upper plate velocity	$v_t = v_R^a$	Measured with respect to foreland; See Fig. 2
v_m	Lower mantle velocity	0[a]	Measured with respect to foreland; See Fig. 2
v_R	Velocity of trench		Measured with respect to foreland; See Fig. 2
Rheology			
μ	Viscosity of the upper mantle (not including slab or lithosphere)	2×10^{20} Pa; $z < 300$ km[a] 5×10^{20} Pa; $z > 300$ km[a]	May be a function of depth
μ_p	Viscosity of viscously competent part of slab		Eq. (C9)
D	Flexural rigidity of slab	10^{19} N m[a] when slab is elastic	10^{19} N m $\sim$ 1 km elastic plate thickness; See Appendix C
Other			
g	Acceleration of gravity	9.81 m s^{-2}	
θ	Angle from horizontal in mantle wedge		See Fig. 2
θ_o	Angle locally tangent to slab		See Fig. 2
n	Index normal to the slab		See Fig. 2
s	Index tangential to the slab		See Fig. 2
t	Index for top surface of slab		See eq. (8)
b	Index for bottom surface of slab		See eq. (8)
f_i	Functions for layered viscosity		Defined in Appendix A
g_i	Functions for layered viscosity		Defined in Appendix B

[a]Default values unless otherwise specified.

© 2006 The Authors, *GJI*
Journal compilation © 2006 RAS

Lithostatic and static pressure

Lithostatic pressure is simply defined as the pressure generated by the weight of all overlying material:

$$P_{\text{lith}} = \int_{z_{\text{surface}}}^{z} \rho(z) g \, dz, \tag{2}$$

where z is the depth relative to the geoid. We can also define a 'static pressure' of the mantle, which is the lithostatic pressure of an isostatically compensated column of asthenosphere under static (no flow) conditions:

$$P_{\text{static}} = \rho_a g (z - w_a) + \rho_w g w_a. \tag{3}$$

Thus static pressure is strictly a function of depth relative to the geoid. Under static, or no-flow, conditions, the lithostatic pressure in the asthenosphere will be equal to the static pressure. Where viscous flow occurs within the asthenosphere, the lithostatic pressure is the sum of the static pressure and the pressure of viscous flow. Beneath the upper mantle wedge, the total stress on the upper surface of the slab is equal to the stress of viscous flow plus the static asthenospheric pressure. The lower surface of the slab always lies within sublithospheric mantle, so that the stress on it is everywhere equal to the stress of viscous flow plus the static asthenospheric pressure.

Within the frontal prism, we assume that the deformation is negligible, so that total stress within the frontal prism is equal to the lithostatic pressure. Under this assumption, the total normal stress on the upper surface of the slab beneath the frontal prism is equal to the lithostatic pressure and can be computed from Eq. (2). Similarly, the shear stress on the upper surface of the slab beneath the frontal prism is zero. (These assumptions can easily be modified to include an explicit rheology for the frontal prism, so that the stress it applies to the top of the slab will include lithostatic pressure and the stress of deformation).

For simplicity we assume, unless otherwise noted, that the frontal prism is filled with material of crustal density ($\rho_{\text{prism}} = \rho_c = 2800$ kg m^{-3}). We also assume that the bathymetry of the upper surface of the frontal prism is equal to the initial water depth of the incoming plate so that no bathymetric trench is formed (either of these two assumptions can be easily modified, as desired).

Viscous stresses

The viscous stresses related to subduction can be approximately subdivided into the long wavelength, or background, stresses that are related to large-scale flow of mantle material around the slab, and the highly localized stresses that are related to the flux of material into the narrow portions of the upper and lower mantle wedges (Figs 1–3). This subdivision is useful because the large-scale flow of mantle material around the slab can, at long wavelength, be approximated by 2-D flow in the $x - y$ plane, while the influx of material into the narrow mantle wedges can, away from the edges of the slab, be approximated by 2-D flow in the x–z plane. Hence a difficult 3-D problem can be approximated by two simpler problems in 2-D flow.

Background stress of toroidal flow around the slab

Let us first consider the viscous stresses due to toroidal flow of mantle material around a vertically subducting slab of half-width a centred at $y = 0$ (Fig. 3). The frame of reference is a point on the foreland located far from the subduction boundary, so that the slab moves downwards and laterally at a rate v_R. The lower mantle moves in the x-direction with velocity v_m and the overriding plate moves with velocity v_t. For simplicity, the velocity of the overriding plate was set equal to the velocity of the trench, so that no deformation occurs within the overriding plate. However, other assumptions can be made, the effects of which are mentioned in the results section of this paper.

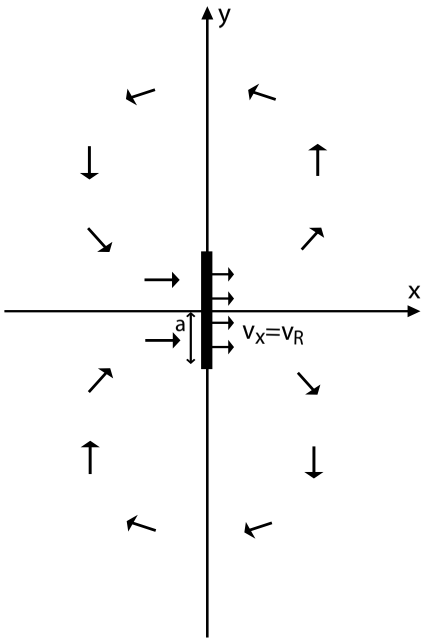

Figure 3. Plan view of Hele-Shaw flow field used to approximate viscous pressure of toroidal flow around a slab of half-width a, moving in the horizontal plane at a rate v_R.

(Note that our convention of denoting velocities with respect to the foreland lithosphere is different from the usual convention of computing velocity with respect to the top of the lower mantle or some other reference frame, e.g. no net rotation).

The resulting velocities and viscous stresses for this fundamentally 3-D flow are not amenable to analytic solution, but there is an easily derived approximation for the velocity and stress that is valid at some distance from the slab. First, we note that at the wavelengths of interest for toroidal flow around the subduction system as a whole, horizontal velocities away from $x = 0$ can be approximated by Hele-Shaw flow in a thin viscous gap, where the viscous gap corresponds to the sublithospheric portion of the upper mantle with thickness λ (Batchelor 1967; Acheson 1990; Furbish 1997). Appendix A gives a derivation for the Hele-Shaw flow around a vertical slab embedded in a layered-viscosity mantle. We show that, along the midline of the slab, at distances of $x < 2a$ from the slab, the viscous pressure due to toroidal flow in a uniform viscosity mantle can be approximated

© 2006 The Authors, *GJI*
Journal compilation © 2006 RAS

as:

$$P_{\rm visc}(x,0) = \frac{12\mu a}{\lambda^2}\left[v_R - \left(\frac{v_t + v_m}{2}\right)\right] e^{-9(x/a)^{0.8}}, \quad (4)$$

and derive a similar, but more complex, expression for viscous pressure for a mantle within a horizontally layered viscous mantle (Appendix A, eq. A9). Because the assumptions that we used to derive viscous stress break down for narrow slabs, we estimate that eq. (4) should not be used for slabs whose total width is much less than the thickness of the upper mantle, giving a minimum bound on slab half-width of $a = 300$ km.

Local stress in the mantle wedges

In the wedge of viscous mantle that overlies the slab, the local flow pattern and related viscous stresses will be fundamentally different from the overall toroidal flow pattern, as material is fluxed from thicker to thinner parts of the wedge (Fig. 1). This is particularly the case within the narrow portions of the wedge near the asthenospheric nose where flow is severely constricted by the plates above and below. (Viscous stresses in this domain are important not only in understanding rates of trench migration but also for lattice preferred orientation of olivine in the mantle wedge (e.g. Kaminski *et al.* 2004). We address this local flow pattern in two-dimensions using a variant of the corner-flow solution as derived in Turcotte & Schubert (1982). We note, however, that the 2-D solution breaks down near the edges of the slab where even local flow is fundamentally 3-D.

We cannot use the precise analytical solution for corner flow because the mantle wedge is not infinite in extent, because its geometry changes with distance along the wedge, and because the normal and shear velocities imparted by the subducted slab also change with distance along the wedge. However, we can estimate these viscous stresses by deriving an approximate flow velocity along circular arcs within the viscous wedge (Fig. 2). An approximate solution for flow and viscous stress in the viscous upper and lower mantle wedges is derived in Appendix B for a layered viscous rheology. For a uniform viscosity wedge, the shear stress, τ_s, and the along-slab gradient of viscous normal stress, $\partial\sigma_n/\partial s$, acting on the top of the slab are:

$$\frac{\partial\sigma_n}{\partial s} = \frac{-12\mu}{r_o^3\theta_o^3}\int_0^s v_n\,ds + \frac{6\mu(v_t + v_t)}{r_o^2\theta_o^2}, \quad (5)$$

$$\tau_s = -r_o\theta_o\frac{\partial\sigma_n}{\partial s} + \frac{\mu(v_t - v_s)}{r_o\theta_o}, \quad (6)$$

where v_n and v_s are the normal and shear components of slab velocity and θ_o is the local dip of the slab (Fig. 2). The variable r_o is as shown is Fig. 2 and is defined as the local thickness of the upper mantle wedge, measured in the z-direction, divided by $\sin\theta_o$. Expressions for viscous stresses with a non-uniform mantle viscosity, and analogous expressions for the lower mantle wedge, are derived in Appendix B.

The viscous normal stress on the slab can be computed from eq. (5) by integrating from the slab end ($s = 0$) to the point of interest:

$$\sigma_n(s) = P_o + \int_0^s \frac{\partial\sigma_n}{\partial s}\,ds, \quad (7)$$

where P_o is defined as the viscous pressure at the open end of the wedge (Fig. 2). P_o should be approximately equal to the viscous pressure related to large-scale flow of mantle around the subducted slab as given by eq. (4). Because the circular arc that defines the open ends of the upper viscous wedge is not a uniform distance from the slab, we define x as the average distance of the circular arc from the slab. Typically, the average distance from the circular arc through $s = 0$ to the slab will be approximately $\sim\lambda/2$, where λ is the thickness of the upper mantle, but its value depends in detail on the geometry of the slab.

SUBDUCTION MODEL

Building on the relationships between slab velocity, geometry and stress established in the preceding sections and the appendices, we can construct an algorithm for the behaviour of the subducted slab, where the externally applied stresses and the slab buoyancy are united via the rheology of the subducted slab and the surrounding mantle.

Mantle viscosity

For a given slab geometry and rate of trench migration, the viscous stresses on the slab will vary with the viscosity of the sublithospheric mantle, and *vice versa*. In our model results (presented below) there is only a narrow range of values for upper mantle viscosity that yield subduction rates consistent with observed rates of subduction (around 2–3 10^{20} Pa s, Fig. 4.) However, there is considerable latitude in our model of how viscosity may vary with depth. Published estimates of the viscosity of the upper mantle suggest that its lower part may be several to perhaps 10 times more viscous than its upper part (e.g. Mitrovica & Forte 1997; Steinberger & O'Connell 1998; Steinberger 2000; Steinberger *et al.* 2004).

In general, we use a two-layer viscosity structure with an asthenospheric viscosity of 2.0×10^{20} Pa s above 300 km depth, and a viscosity of 5.0×10^{20} Pa s below 300 km depth (Fig. 4). For comparison, we also give some results for a uniform viscosity upper mantle of 3.2×10^{20} Pa s (chosen because this gives trench

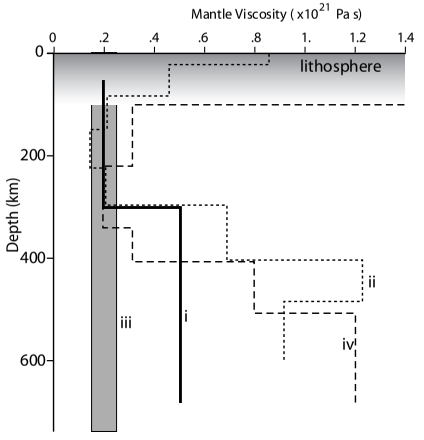

Figure 4. Two-layer upper mantle viscosity structure used in this paper (i) compared to viscosity structure determined by (ii) Mitrovica & Forte (2004), (iii) Lambeck & Chappel (2001), (iv) Steinberger *et al.* (2004) and O'Connell, personal communication (2005).

© 2006 The Authors, *GJI*
Journal compilation © 2006 RAS

velocities comparable to the two-layer case) and cases where upper and lower mantle viscosity vary by up to a factor of 10. The viscosity of the lower mantle (beginning at 670 km depth) is assumed to be very much greater than that of the upper mantle (e.g. Hager 1984; Ricard & Wuming 1991; Steinberger 2000; Forte & Mitrovica 2001) and we implicitly treat its viscosity as infinite. The top surface of the upper mantle wedge coincides with the base of the upper plate lithosphere, assumed to be 50 km thick unless otherwise noted; the basal surface of the lower mantle wedge coincides with the upper mantle/lower mantle boundary. The crust of the overriding plate is 11.5 km thick with a density of 2800 kg m^{-3} and the density of the mantle lithosphere is equal to the asthenospheric density of 3300 kg m^{-3}. These values were chosen because they give a water depth of zero for an isostatically compensated upper plate.

Slab rheology

We quantify the flexure of the slab in response to bending stresses as that of a thin flexurally competent sheet. In general we treat the slab as a thin elastic sheet with flexural rigidity D, but also examine several cases where the slab is a thin viscous sheet (see Appendix C). The slab is able to transmit extensional and compressional stresses along its length, consistent with studies that suggest that the slab may be able to support much of its weight within the upper mantle (e.g. Elsasser 1969; Spence 1987; Zhong 2001; Conrad & Lithgow-Bertelloni 2002, 2004; Billen *et al.* 2003; Schellart 2004a,b). The downdip length of the slab is not allowed to change during bending. Unless otherwise noted, we use a minimal flexural rigidity of 10^{19} N m, which is equivalent to an elastic plate thickness of $\sim$1 km. Thus slab rigidity has a negligible effect on slab behaviour as compared to the zero-strength case but its inclusion helps to maintain numerical stability in the computations because it prevents kinking of the slab. (In the results section we will show that slab rigidity has negligible effect on subduction geometry or rates until it exceeds an effective elastic thickness of 30–40 km, with similar results for a viscous slab).

Force balance

The external stresses acting on the slab surface can be summed to find the total externally applied stresses, with q_n and q_s being the total stress in directions normal and parallel to the slab (see Fig. 2 for conventions). We also denote q_x and q_z as the horizontal and vertical components of stress on the slab. Using the superscripts t and b to denote stresses acting on the top and bottom surface of the slab respectively, these force components can be written:

$$\begin{aligned} q_n &= \sigma_n^t + P_{\rm static}^t - \sigma_n^b - P_{\rm static}^b \\ q_s &= \tau^t - \tau^b \\ q_2 &= q_n\cos\theta_o - q_s\sin\theta_o \\ q_x &= q_n\sin\theta_o + q_s\cos\theta_o. \end{aligned} \quad (8)$$

Note that q_n and q_s depend on the viscous stress on the top and bottom of the slab, and so are related to the velocity of the slab [e.g eqs (6) and (7)]. Appendix C combines the external and gravitational stresses acting on the slab with an equation that includes the bending stresses internal to the slab. By setting the total horizontal and vertical forces acting on each slab element equal to zero, we derive one equation that links all the external stresses on the slab to the velocity and geometry of the slab (eq. C7).

Defining the asthenospheric nose and slab tail and interactions with the lower mantle

Of great importance is where to terminate the narrow end of the viscous wedge above the slab because stresses near the asthenospheric nose become extremely high. For example, Winder & Peacock (2001), note that stresses 'become infinite as the nose radius approaches zero, and [. . . .] there is no clear reason to pick one radius over another'. However, in our description, there is a natural way to choose the location of the asthenospheric nose using the concept that stresses must be continuous throughout the region modelled. Thus the total pressure in the asthenospheric nose should be comparable to the total pressure in the adjacent part of the frontal prism. In other words, the pressure immediately in front of the viscous wedge needs to be sufficiently low that viscous asthenospheric material is drawn into the narrow part of the wedge by the lateral pressure gradient. (More correctly, the total stress must be continuous, but given uncertainties in the precise configuration of the asthenospheric the probable gradational transition from asthenosphere to lithosphere, assuming a continuous pressure field should be a sufficiently accurate condition for internal consistency of stresses).

This requirement can be met approximately if the pressure at the base of the frontal prism (Fig. 2) is equal to the pressure within the asthenospheric nose, or

$$P_{\rm visc\ (nose)} + P_{\rm static\ (nose)} = P_{\rm lith\ (frontal\ prism)}, \quad (9)$$

where $P_{\rm static}$ is the pressure that would be present if there were no viscous flow in the mantle and is given by eq. (3). The viscous pressure in the asthenospheric nose is effectively equal to the viscous normal stress on the slab (Appendix B), so that this relationship becomes:

$$\begin{aligned} \sigma_n + [\rho_a g(w + w_o - w_a) + \rho_w g w_a] = [\rho_{\rm prism} g(w + w_o - d_w) \\ + \rho_w g d_w], \end{aligned} \quad (10)$$

where σ_n is the viscous normal stress on the top of the slab at the narrow end of the asthenospheric wedge and $(w + w_o)$ is the total depth of the slab relative to the geoid. The right-hand side of eq. (9) is the lithostatic pressure at the thick end of the frontal prism, assuming that the water depth above the prism is d_w and that the density of the prism is $\rho_{\rm prism}$.

At each time step we solve for the location of the front of the asthenospheric nose by finding the slab depth for which eq. (9) is satisfied. More specifically, we compute σ_n everywhere along the slab using values of slab velocity, v_s and v_n, and slab geometry from the previous time step. (In practice, v_s and v_n are a weighted average of the slab velocities for the previous 0.1–1.0 Myr, or 10–100 time steps. This damping process prevents oscillation in the results due to overshooting of the correct values of velocity and stress.) We then find the location on the slab where eq. (9) is satisfied, and denote that position as the front of the asthenospheric nose.

Somewhat more problematic is how to treat the narrow end of the viscous wedge below the subducting slab and the interaction of the subducting slab with the lower mantle. This narrow wedge end lies at the junction of the downgoing plate and the upper mantle/lower mantle boundary. Almost certainly, the subducting slab does not behave as a coherent plate at these depths (e.g. Ito & Sato 1991; Christensen 2001). This issue becomes especially important when there is relative motion between the foreland lithosphere and the top of the lower mantle.

It is useful to distinguish here between two different, but related, effects that result from motion of the upper mantle/lower mantle boundary with respect to the foreland lithosphere. First, velocities

© 2006 The Authors, *GJI*
Journal compilation © 2006 RAS

at the base of the upper mantle (e.g. Gripp & Gordon 1990) result in flow within the upper mantle. The motion of the slab will be affected by this flow. The second effect results from the deep slab becoming anchored, or partly anchored, to the lower mantle due to the high viscosity in the lower mantle. The latter presents problems if the slab is not allowed to undergo longitudinal strain and if the slab is still strong enough to act as a stress guide, as in our slab model. In this case, stress transmission along the slab may interfere with the subduction processes near the surface in a manner that we believe to be physically unrealistic.

In order to avoid having to deal with the interaction of the slab with the high-viscosity lower mantle, we truncate the downgoing slab where the lower surface of the slab has descended to 95 per cent of the total depth of the upper mantle, approximately 30 km above the top of the lower mantle. This forms the slab 'tail'. For similar reasons, we also truncate the slab where its dip falls below 12° and the base of the slab has reached a depth that is 75 per cent of the total depth of the upper mantle, approximately 150 km above the top of the lower mantle. Thus, in all the formulations and results in this paper, the slab is not attached to the lower mantle in any way.

Computation of slab motion

Slab motion at each time step was derived by solving eq. (C8) or (C11) for new values of $w(s)$ that provide consistent velocities and stresses without longitudinal strain along the slab. Solution is via a fourth-order finite difference scheme with implicit differencing. The fourth order and second order spatial derivatives of $w(s)$ as well as values of w(s) and the time derivative of $w(s)$ that enters these equations via q_n are calculated simultaneously for the next time step. The new values of $w(s)$ are calculated by inversion of a five-band diagonal matrix. Time steps used were typically 0.01 Myr and the distance between spatial nodes along the slab was 5 km. The sufficiency of these values was checked using time steps as small as 0.001 Myr and node spacing as small as 1 km.

We begin each computation by inserting a sufficiently long length of slab into the subduction system and allowing the system to evolve until steady state is reached. We define the rate of slab migration as the rate at which the slab profile moves laterally at 100 km depth, measured relative to the stable foreland lithosphere.

GENERAL RESULTS

Steady-state subduction occurs when the geometry of the slab (slab profile) and the rate of subduction remain unchanged through time and can only occur when the slab has a uniform buoyancy. Unless otherwise noted, the velocity of the lower mantle relative to the foreland is zero and the half-width of the slab (or half the trench length, a) is 1000 km.

Slab buoyancy, geometry and retreat rate

Slab buoyancy is the fundamental driving force for subduction, although subduction processes are enhanced and modified by a variety of other factors. This is illustrated in Fig. 5(a), which shows that the rate of steady-state trench migration varies almost linearly with the

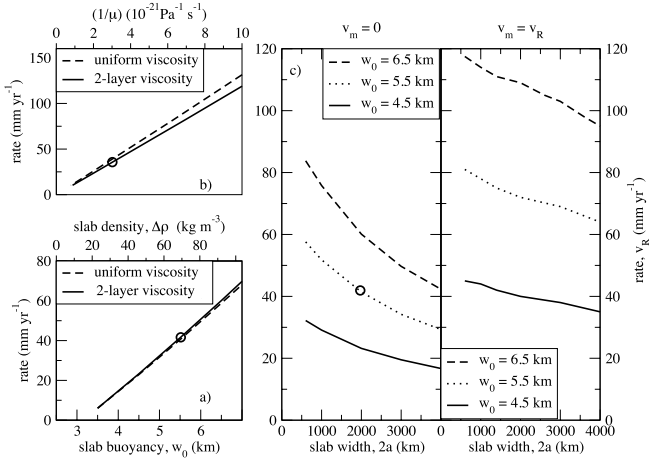

Figure 5. (a) Trench migration rates as a function of slab buoyancy for one-layer (3.2×10^{20} Pa s - solid line) and two-layer (2×10^{20} for $z < 300$ km, 5×10^{20} for $z > 300$ km - dashed line) upper mantle viscosity profiles. Slab buoyancy is parametrized by pre-subduction water depth w_o (and by $\Delta\rho$ for a 100 km thick slab). (b) Trench migration rates as a function of the reciprocal of viscosity, for uniform (solid line) and two-layer (dashed line) upper mantle viscosity structure. For two-layer viscosity, the viscosity below 300 km depth is 2.5 times the viscosity above 300 km depth; the value plotted is their weighted arithmetic mean. (c) Trench migration rates as a function of slab width parallel to the trench, for initial water depths of 4.5, 5.5 and 6.5 km and $v_m = 0$ (foreland stationary with respect to top of lower mantle). (d) Trench migration rates as a function of slab width parallel to the trench, for initial water depths of 4.5, 5.5 and 6.5 km and $v_m = v_R$ (trench stationary with respect to top of lower mantle). Circles show reference case. Trench migration rate is measured relative to the foreland lithosphere.

© 2006 The Authors, *GJI*
Journal compilation © 2006 RAS

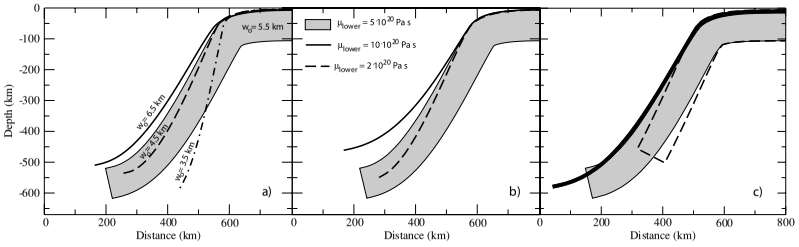

Figure 6. Steady-state subduction geometry. In all panels the shaded slab corresponds to the reference case with an initial water depth of $w_0 = 5.5$ km and a viscosity of 2.0×10^{20} Pa s above 300 km depth and 5.0×10^{20} Pa s below. (a) Slab geometry as a function of slab buoyancy; solid, dashed, and dot-dashed lines are the geometry of the upper slab surface for slabs with initial water depths of 6.5, 4.5, and 3.5 km pre-subduction depths, respectively; (b) Slab geometry as a function of mantle viscosity. Viscosity above 300 km is 2.0×10^{20} Pa s. Geometry of upper slab surface for: viscosity of 2.0×10^{20} Pa s below 300 km (dashed line) and viscosity of 2.0×10^{21} Pa s below 300 km (solid line). (c) Slab geometries with all parameters the same as the reference case except: slab is 10 km thick, but with unchanged buoyancy (thin black slab), or: slab is truncated at a 500 km depth in the upper mantle (dashed outline).

increasing density contrast between the slab and the surrounding mantle (actually with density contrast times slab thickness). The computed migration rate for a very dense slab, with an equivalent pre-subduction water depth of 6 km, is 60 mm yr^{-1}. With all other parameters held fixed, the rate of trench migration varies linearly with the reciprocal of mantle viscosity (Fig. 5b).

Fig. 6(a) shows the steady-state slab geometries attained for subduction of slabs with buoyancies corresponding to initial water depths of 4.5, 5.5 and 6.5 km (or $(\rho_l - \rho_a)$ equal to 46–92 kg m^{-3} and $l = 100$ km). Slab geometry is characterized by gradually increasing dip from the surface down to ∼100 km depth. Between 100 and 500 km depth, dips are nearly uniform, being between 50° and 70°. Slab buoyancy has little effect on steady-state slab geometry except for very low density slabs ($w_0 = 3.5$ km). The increase in dip for these less dense slabs occurs because, with decreasing slab density, the retreat rate of the trench slows proportionately more than the motion of the deep slab through the mantle. Increasing the viscosity of the mantle below 300 km causes the slab dip to become shallower, especially near the base of the upper mantle (Fig. 6b). For a uniform viscosity upper mantle, slab dips remain fairly steep to the base of the upper mantle (Fig. 6b). For viscosities below 300 km depth that are 2.5–10 times larger than viscosities above 300 km, the slab dip flattens significantly near the base of the upper mantle.

The gradual increase in slab dip above 100 km depth does not result from flexural properties of the subducted slab because of the very low values of rigidity used in constructing Fig. 6. Instead, it results from the high stresses that act on the subducted plate near the asthenospheric nose. These stresses are due to viscous flow in the mantle wedge and to the lithostatic stresses due to the low-density material contained in the frontal wedge. For the two-layer viscosity structure assumed in this paper, the vertical (upwards) component of viscous stress on the slab is many times larger in the top 100 km of the subduction system than between 100–500 km depth (Fig. 7).

Fig. 6(c) shows the effects of two assumptions about slab geometry that we have made in our model. In general, we assume that the slab is 100 km thick and is truncated when its lower surface descends to 95 per cent of the depth to the base of the upper mantle. If the slab is instead truncated where its lower surface attains a depth of 75 per cent of the depth to the base of the upper mantle, the geometry of the slab above 200 km is virtually unchanged, the dip below 200 km increases modestly, and the rate of trench migration remains nearly unchanged, increasing from 41 to 43 mm yr^{-1}. (As before, no viscous flow of mantle occurs through the gap between the end of the slab and the top of the lower mantle. The purpose of this exercise is not to model a short slab *per se*, but to show the sensitivity of our results to assumptions about exact position of the slab tail).

If the slab is assumed to be only 10 km thick, rather than the 100 km that we generally assume, the slab geometry is virtually unchanged (dark line on Fig. 6c). The rate of trench migration increases slightly from 41 to 43 mm yr^{-1}. This indicates that it is slab buoyancy, as opposed to thickness or density, that controls the slab geometry and rate of trench migration.

Stresses on the slab

Fig. 7 shows the stresses that act on and along the subducted slab. The normal stresses in this plot are computed as the total normal stress on the slab minus the static pressure of the asthenosphere, as defined in eq. (3). Stresses on the top of the slab have the largest magnitude at shallow depth beneath the asthenospheric nose, while those on the lower surface of the plate have the largest magnitude in the deep mantle, above the narrow end of the lower mantle wedge. This occurs because, for a given flow rate in the viscous wedge, larger magnitude stresses are generated where the wedge is narrower. The prominent kink in the normal stress acting on the upper surface of the slab occurs where the asthenospheric nose abuts the frontal prism. The kink occurs because the normal stress on the top of the slab beneath the frontal prism become more negative, relative to static asthenospheric pressure, with increasing slab depth (because material within the frontal prism has a lower average density than the asthenosphere). Normal stresses on the top of the slab beneath the asthenospheric wedge, relative to static asthenospheric pressure, become less negative with decreasing slab depth. The two are required to be equal where the frontal prism meets the asthenospheric nose and are large, with magnitudes typically in excess of 100 MPa.

Fig. 7(b) also shows the extensional stress transmitted longitudinally along the slab. (Extensional stress is plotted as a function of depth to the midline of the slab and assumes that extensional stress is distributed evenly across a 100-km-thick slab). Extensional

© 2006 The Authors, *GJI*
Journal compilation © 2006 RAS

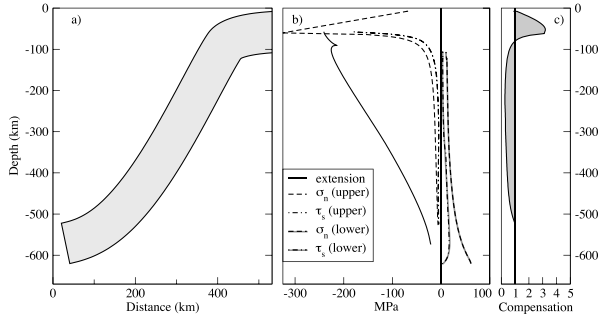

Figure 7. (a) Geometry of reference slab, $w_0 = 5.5$ km. (b) Normal and shear stress acting on the upper and lower surface of the slab as a function of depth. Normal stresses are computed relative to P_{static}, the lithostatic pressure in a static column of asthenosphere (eq. 3). Stresses on the upper slab surface are plotted as a function of depth of upper surface, stresses on the lower slab surface are plotted as a function of depth of the lower slab surface, extensional stress plotted as a function of depth of the centre of the slab. (c) Slab compensation, defined as the vertical component of stresses on the upper and lower surfaces of the slab (minus P_{static}) divided by slab buoyancy. Compensation plotted as a function of depth to the top of the slab.

stress reaches a maximum near the surface, where it is typically several hundred MPa. For the cases examined in this paper, approximately 60–70 per cent of the slab buoyancy integrated, along the slab from the surface to the base of the lower mantle, is supported by viscous stresses on the slab. The remaining 30 to 40 per cent of the slab buoyancy is supported by transmission along the slab to the surface. This is consistent with the result obtained by Conrad & Lithgow-Bertelloni (2004), who showed from their study of global plate motions and dynamics that some slabs are highly coupled to the trailing plate (foreland). This figure is also consistent with results obtained by Royden (1993a) from gravity modelling of Mediterranean subduction systems.

For ease of reference, we define a parameter called 'slab compensation', equal to the vertical component of stress applied to the top and bottom surfaces of each slab element divided by the slab buoyancy for that element (normal stress has the static pressure of the asthenosphere subtracted from it), Where slab deflection is less than ∼100 km, the slab compensation is typically greater than one. Between 100 and 500 km depth, slab compensation is typically less than one. This is a general feature of subducting slabs: compensation is greater than one above ∼100–150 km and less than one at greater depths. This means that slabs are overcompensated in the shallow mantle and undercompensated at greater depth. The overcompensation at shallow depth does not make up for all of the undercompensated material at depth, and the residual is transmitted to the foreland lithosphere and produces a horizontal force on the foreland.

Deep 'engine'; shallow 'brakes'

The evolution and geometry of a subduction system depends on the competition between the undersupported slab at depths greater than ∼100–150 km and the oversupported slab at shallower depths. The deep undersupported portion of the slab can be regarded as the engine for subduction because the net vertical force on this part of the slab is downwards. The shallow oversupported portion of the slab can be regarded as the brakes for the subduction process because the net vertical force on this part of the slab is upwards.

The competing effects of the slab engine and slab brakes can be best illustrated by considering two different hypothetical subduction systems, one with a mantle viscosity of 10^{20} above 260 km depth and 10^{21} Pa s below 260 km depth, and a second with the viscosity structure reversed. For $w_o = 5.5$ km, both viscosity structures yield the same trench retreat rate of ∼34 mm yr^{-1}. In the first case (weak uppermost mantle corresponding to the gently dipping slab in Figs 8a and b) the slab is overcompensated above ∼75 km depth and the vertical component of stress on the slab surfaces averages approximately twice the slab buoyancy. Below ∼75 km, the slab is undercompensated and the vertical component of viscous stress decreases to less than half the slab buoyancy, then increases to become approximately equal to slab buoyancy at the base of the upper mantle. In the second case (strong uppermost mantle and steeply dipping slab in Figs 8b and c), the slab is overcompensated above ∼125 km depth, with the vertical component of stress on the slab surfaces averaging about 2.5 times the slab buoyancy. Below ∼125 km depth, slab compensation drops to 0.5 and then to 0.1, increasing only marginally at the base of the upper mantle.

Using the analogy of engine and brakes, the engine is relatively weak in the case where the mantle below 260 km is highly viscous so that it can support a large fraction of the negative slab buoyancy. The brakes are weak because the low viscosity at shallow depth produces relatively low-magnitude stresses in the asthenospheric nose. In the other case, where the mantle below 260 km has a low viscosity, the engine is strong and the low-viscosity mantle supports only 10 per cent of the negative slab buoyancy. The brakes are strong because the high viscosity at shallow depth produces large magnitude stresses in the asthenospheric nose. Thus a weak engine coupled with weak brakes produces the same trench retreat rate as a strong engine coupled with strong brakes. However, the differing stress distributions produce very different slab geometries. Slab dip in the first case is 45–50° between 100 and 300 km depth then decreases to ∼12° at the base of the upper mantle. Slab dip in the second case is ∼75° throughout most of the upper mantle.

In conceptual terms the brakes and the engine for a subduction system can be thought of as the extent to which the slab is overcompensated at shallow depth and undercompensated at large depth. If one were to increase the strength of the brakes, the rate of motion

© 2006 The Authors, *GJI*
Journal compilation © 2006 RAS

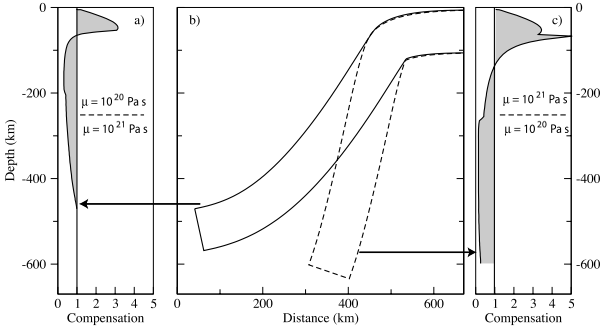

Figure 8. Steady-state slab geometry and slab compensation, defined as the vertical component of stress acting on the upper and lower surfaces of the slab (minus P_{static}) divided by the slab buoyancy. (a) slab compensation for the gently dipping slab with mantle viscosity 10^{20} Pa s for $z < 260$ km and 10^{21} Pa s for $z > 260$ km. (b) slab geometries; (c) slab compensation for the steeply dipping slab with mantle viscosity 10^{21} Pa s for $z < 260$ km and 10^{20} Pa s for $z > 260$ km.

of the trench would slow and the dip of the slab would steepen. This occurs because the strength of the brakes correlate not only with the vertical component of stress acting on the slab surfaces, but also correlate loosely with the horizontal component of stress acting on the slab surfaces. Hence an increase in the strength of the brakes acts to retard the vertical and horizontal slab velocity at shallow depth.

Note, however, that the strength of the engine and the brakes are not independent quantities and there is a complex interplay between them. First of all, they are defined here as the extent to which the slab is under or overcompensated at each point. Integration of slab compensation over the total length of the slab (but not over slab depth, which how compensation is plotted in Figs 7 and 8) must be equal to the integrated slab buoyancy. Otherwise the total vertical force acting on the slab will not be zero, as is required by static force balance. (Integration of our results showed this to be the case for our slabs to better than 1 per cent uncertainty). Thus the engine and brakes must integrate to zero along the slab; it is not possible to change one integral without the other. However, the distribution of compensation along the slab can be varied provided that the integral requirement is met.

How does this work? For example, let us increase the strength of the brakes by lowering the density of the material filling the frontal prism, thus producing a more negative normal stress on the top of the slab at shallow depth. The rate of trench migration slows, slab dip steepens and the magnitude of viscous stresses on the slab is reduced due to the slower motion of the slab through the mantle. As viscous stresses decrease on the deep slab, the engine also becomes stronger, contributing to a further increase in slab dip. Thus a change on either part of the system affect the other because, among other effects, it changes the rate of trench retreat and hence the viscous stresses throughout the system.

OTHER PARAMETERS AFFECTING SUBDUCTION

Apart from slab buoyancy, a variety of other factors exert significant effects on the subduction process. We can characterize these factors through their effects on trench migration rates and slab geometry.

Relative motion of the upper mantle/lower mantle boundary

Rates of trench motion are affected by horizontal motion of the lower mantle because it induces horizontal flow in the upper mantle relative to the foreland lithosphere; for example, this probably occurs under the Pacific plate, which is thought to be moving rapidly westward relative to the lower mantle (e.g. Gripp & Gordon 1990). The horizontal flow induced by the relative motion of the lithosphere and the lower mantle is often referred to as the 'asthenospheric wind'. Hager & O'Connell (1978) used this concept to help explain slab dip angles. The velocity of the asthenospheric wind should be an important variable in subduction systems because it will change the magnitude of the viscous stresses on the slab.

Fig. 9 shows the variation in the rate of trench migration (relative to the foreland lithosphere) for a wide range of imposed velocities (v_m) at the upper/lower mantle boundary. The dependence of subduction rate on lower mantle velocity rivals that of slab buoyancy. The rate of trench motion varies approximately linearly with v_m with a proportionality constant of approximately 1/2. For example, when $v_m = 0$, a slab with an initial water depth of 6.5 km and a half-width of 1000 km exhibits a rate of trench motion relative to the foreland of $v_R = 60$ mm yr^{-1} (Fig. 9a). If v_m is increased until the trench velocity and the lower mantle velocity are equal (trench stationary in lower mantle reference frame), then the rate of trench migration is $v_R = 110$ mm yr^{-1} (see Fig. 2 for sign conventions). If v_m is reversed to -50 mm yr^{-1}, the rate of trench migration with respect to the foreland slows to 35 mm yr^{-1} (although the rate of trench migration with respect to the lower mantle is 85 mm yr^{-1}).

In general, we find that when the half-width of the slab is greater than about 1000 km, v_R is approximately equal to $(v_o + v_m/2)$, where v_R is the velocity of the trench relative to the foreland, v_m is the velocity of the top of the lower mantle relative to the foreland, and v_o is the velocity of the trench for $v_m = 0$. These results suggest that subduction will not occur when v_m approaches $-2v_o$. We would expect the proportionality constant (1/2) to decrease for narrow slabs, because narrower slabs are less affected by the pressure of toroidal flow around the slab. For slabs with a half-width of 300 km, v_R is approximately equal to $(v_o + v_m/3)$.

© 2006 The Authors, *GJI*
Journal compilation © 2006 RAS

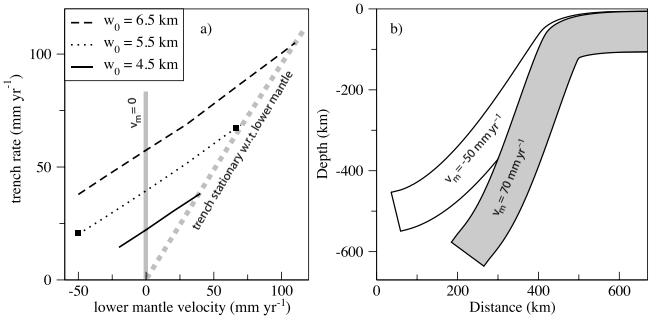

Figure 9. (a) Rate of trench migration as a function of the velocity at the top of the lower mantle v_m and slab buoyancy w_0. Trench migration rates are measured relative to the foreland lithosphere. Shaded solid line indicates $v_m = 0$ (foreland stationary relative to the top of the lower mantle). Shaded dashed line indicates $v_m = v_R$ (trench stationary relative to the top of the lower mantle). Squares show cases for slab geometries plotted in (b). (b) Slab geometry with all parameters being the same as the reference case except v_m. Shaded slab is $v_m = 70$ mm yr^{-1} (trench stationary with respect to the top of the lower mantle). White slab is $v_m = -50$ mm yr^{-1}.

There is an important relationship between lower mantle velocity and slab dip (Fig. 9b), with negative lower mantle velocities producing flatter slabs and positive lower mantle velocities producing steeper slabs. The effects of lower mantle velocity on trench migration rate and slab geometry can be readily understood from the perspective of engine and brakes within the subduction system. Increasing the lower mantle velocity with respect to the foreland increases the strength of the engine because, for the same rate of trench migration relative to the foreland, smaller rates of viscous flow are required in the mantle. This decreases the magnitude of the viscous stress acting on the plate at depth. The effect is greatest near the base of the upper mantle and negligible near the top. This increases the strength of the engine for subduction. Hence slab dip and trench migration rates increase.

Slab width (trench length)

The rate of trench migration, relative to the foreland, increases with decreasing slab width (trench length), because the background stress of large-scale toroidal flow around the slab is greater in magnitude for wider slabs (eqs 4 and 7 and Fig. 5). There is approximately a factor of two difference in the retreat rate of wide slabs (half-width of 2000 km, or total trench length of 4000 km) and narrow slabs (half-width of 300 km, or total trench length of 600 km). For the densest slabs ($w_o = 6.5$ km), retreat rates vary from about 43 to 88 mm yr^{-1}. For less dense slabs ($w_o = 4.5$ km), retreat rates vary from about 17 to 32 mm yr^{-1}. These results are similar qualitatively to what was found by Dvorkin *et al.* (1993) who computed the magnitude of viscous stresses exerted on slabs of varying width, and found that narrower slabs were consistent with faster rates of trench motion. However, they were only able to estimate an upper bound on the rate of trench motion for narrow slabs ($\sim$230 mm yr^{-1}), approximately two to three times the rates computed for dense slabs in this paper, depending on the value assumed for lower mantle velocity (see above).

The effect of slab width is less pronounced for slabs where the lower mantle velocity is equal to the trench velocity ($v_m = v_R$), so that the trench is stationary in the lower mantle reference frame. For example, for a dense slab ($w_o = 6.5$ km), trench migration rates decreased from 117 mm yr^{-1} to 95 mm yr^{-1} when the slab half-width was increased from 300 to 2000 km. The corresponding decrease in rates is from 81 mm yr^{-1} to and 64 mm yr^{-1} for $w_o = 5.5$ km and from 45 mm yr^{-1} to 35 mm yr^{-1} for $w_o = 4.5$ km. Our results are compatible with the analogue results of Bellahsen *et al.* (2005), who showed that subduction rates decrease with increasing slab width, although there was a moderate amount of scatter in their results. Our results are also generally consistent with the numerical results of Stegman *et al.* (2006) who obtained comparable decrease in trench migration rates for thick (more negatively buoyant plates) provided that the slabs were wider than 600 km, but little variation of trench migration rates for thin (less negatively buoyant) slabs as a function of increasing slab width.

Correlating observed rates of subduction with observed slab width can be problematic because for some slabs, such as or the northern and western boundaries of the Pacific plate, the width of possible slab segments is not obvious, but the full slab-width appears to be larger than 1000 km. In other cases, the width of the slab is clearly defined; for example, the Scotia and Hellenic arcs. Although observed rates of trench migration are consistently within or near the range of rates predicted by our model, several studies have concluded that there is not a clear correlation between observations of trench rates and a suite of parameters that characterize the subduction system (Jarrard 1986; Lallemand *et al.* 2005). Why this should be the case may be partly explained by some of the other features that affect subduction, as described in the following sections.

Slab flexure

Lithosphere has flexural strength, probably composed of some mixture of elasticity combined with viscous and brittle yielding (Brace & Kohlstedt 1980). The bending strength of the lithosphere is commonly characterized by an effective elastic plate thickness (e.g. Walcott 1970). Effective elastic plate thickness decreases with increasing slab bending because of brittle and ductile yielding of the slab (McNutt & Menard 1982). The oceanic lithosphere is observed to have an upper bound of around 35 km effective elastic

© 2006 The Authors, *GJI*
Journal compilation © 2006 RAS

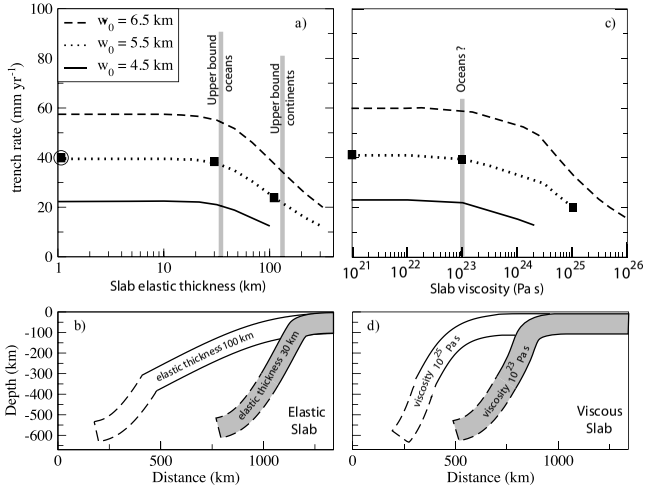

Figure 10. (a) Rates of trench migration as a function of effective elastic plate thickness (elastic plate thickness of 1 km corresponds to a flexural rigidity of 10^{19} N m). Circle shows reference case and squares correspond to the slab geometries plotted in (b). (b) Slab geometries for 1 km, 30 km and 100 km elastic plate thicknesses (30 km and 1 km effective elastic plate thicknesses give nearly identical geometries and the weaker slab case is hidden). (c) Rates of trench migration as a function of slab viscosity, assuming that viscous bending stresses are important only in a uniform viscosity layer 50 km thick. Squares correspond to the slab geometries in plotted in (d). (d) Slab geometries for plate viscosities of 10^{21}, 10^{23} and 10^{25} Pa s thicknesses (10^{21} Pa s and 10^{23} Pa s give nearly identical geometries and the weaker slab case is hidden). Dashed outlines indicate that slabs are assumed to be weak below 300 km depth—see text.

plate thickness, although the elastic limit of the lithosphere is probably exceeded in subduction systems (Billen & Gurnis 2005). Most continental lithosphere has elastic plate thicknesses of around 50 km or less, but some cratons have values as high as $\sim$150 km (McNutt *et al.* 1988; Watts & Burov 2003).

Fig. 10 shows the effects of elastic plate strength on slab geometry and trench retreat. Below 300 km depth, we prescribe a minimal elastic plate thickness of 1 km (or a flexural rigidity of 10^{19} Nm), because it is unlikely that flexural strength of the slab is preserved at these depths and because a stiff slab at the base of the upper mantle causes the slab to be supported by resting on the top of the lower mantle. For effective elastic plate thicknesses of $\sim$30 km or less, there is virtually no effect on slab geometry or trench migration rate. Thus it is very unlikely that slab rigidity in the range of that observed for oceanic lithosphere will have a significant effect on the subduction process relative to a slab with no flexural strength. Above $\sim$50 km elastic plate thickness, rates of trench retreat decrease approximately linearly with increasing elastic plate thickness, reaching about one third of their zero-thickness value at 300 km elastic plate thickness, with a dramatic flattening of the slab profile (Fig. 10b). However, such stiff slabs are unlikely to be subducted to significant depth.

In areas of high curvature, brittle and viscous yielding become the dominant mechanism supporting flexural stresses within the plate. In these cases it is more appropriate to treat the bending lithosphere as a viscous sheet. The effective bending viscosity for the oceanic lithosphere is not well constrained, and depends on the thickness of the viscous layer and the distribution of viscosity within that layer. A reasonable estimate is that the viscously strong part of the lithosphere is perhaps 50 km thick, with a viscosity somewhere in the neighbourhood of 10^{23} Pa s (Conrad & Hager 1999b; Steinberger *et al.* 2004). Fig. 10 shows the effects of viscous flexural strength on slab geometry and trench retreat. The bending strength in the slab is assumed to be contained in a 50-km-thick viscous layer (see Appendix C). Below 300 km the viscosity of this layer decreases by one order of magnitude for every 20 km in depth, until it reaches a minimum value of 10^{21} Pa s.

For plate viscosities less than 10^{23} Pa s, there is little effect of viscosity on slab geometry or trench migration rate. For plate viscosities up to 2×10^{24} Pa s, there are almost no changes in migration rate but fairly significant changes in slab geometry, with shallower dips above 100 km depth and steeper dips between 100 and 400 km depth. However, such high values of viscosity are probably unreasonably large for oceanic lithosphere. Thus it seems likely that slab viscosity will not have a significant effect on subduction, provided that the slab does not undergo significant longitudinal strain.

Our results are compatible with the numerical results of Stegman *et al.* (2006) and the analogue results of Bellahsen *et al.* (2005), both of whom showed that stiffer plates undergo slower rates of trench migration than weaker plates. Bellahsen *et al.* (2005) also showed that stiffer plates display a larger radius of curvature than weaker plates, comparable to the results we obtained for a stiffer elastic and viscous slabs.

Velocity of upper plate lithosphere

In this paper, there is no explicit coupling of normal stress across the vertical interface between the frontal prism and the upper plate

© 2006 The Authors, *GJI*
Journal compilation © 2006 RAS

lithosphere. However, stress coupling between them is implicit because the upper plate is coupled to the underlying viscous wedge and applies shear and normal stresses to the top of the viscously flowing region. The viscously deforming mantle is then coupled to the frontal prism by requiring that the normal stress across the intervening interface be equal, or at least equal at the base of the frontal prism. (There is no coupling of shear stresses across this boundary, since shear stress is assumed to be negligible in the frontal prism and not in the asthenospheric nose.) Thus changes in the kinematically prescribed velocity of the upper plate lithosphere will change the stresses acting within the frontal prism by changing the thickness of the prism and the stress that the prism exerts on the slab.

Although a more proper stress coupling between upper plate lithosphere and the frontal prism is beyond the scope of this paper, the stress transmission that is implicitly included in the model is sufficient to cause significant changes in trench retreat rate as a function of upper plate velocity. For example, compared to our reference case, where upper plate velocity (at 41 mm yr^{-1}) was taken equal to the rate of trench migration, a reduction in the upper plate velocity to zero while holding all other variable fixed produced a slowing of trench migration rates from 41 to 32 mm yr^{-1}. Slab dip increased only marginally, by a few degrees. This indicates that there is significant coupling between the upper plate lithosphere and the slab, despite the lack of explicit stress transmission across the vertical boundary between the upper plate and the frontal prism. The significant slowing of the trench migration rates computed here are consistent with analogue results of Shemenda (1993), although we do not compute the significant changes in slab dip observed in their study, possibly because their study included a variety of other processes affecting the upper plate.

Structure of upper plate lithosphere

The density distribution within the frontal prism depends on the geologic construction of the prism from sediments, volcanic material, oceanic and mantle lithosphere. Decreasing the density of material in the frontal prism leads to a reduction in trench retreat rate because it decreases the normal stress acting on the slab beneath the frontal prism. Examination of eq. (9) shows that this also reduces the value on the left-hand side of this equation. This means that at the front of the asthenospheric nose, the viscous normal stress on the slab will become more negative, thus increasing the strength of the brakes on the subduction system. This decreases the rate of trench migration and steepens the dip of the slab.

Fig. 11(b) shows that as the density of the frontal prism varies from 2000 kg m^{-3} to 3200 kg m^{-3}, while the thickness of the upper

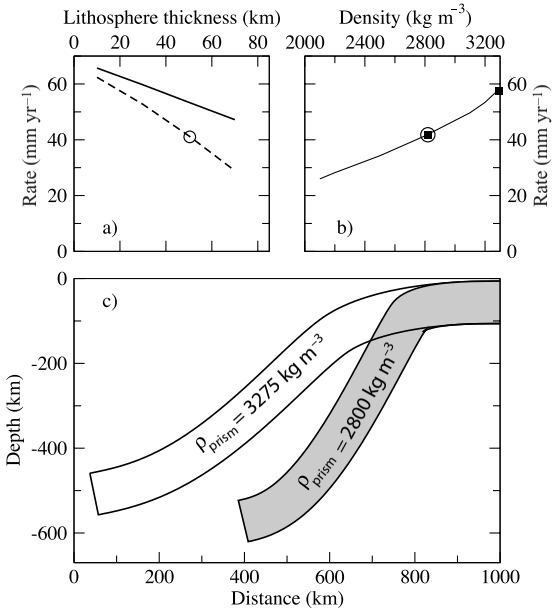

Figure 11. (a) Rates of trench migration as function of the thickness of the overriding plate lithosphere, for frontal prism density of 2800 kg m^{-3} (dashed line) and frontal prism density of 3200 kg m^{-3} (solid line). (b) Rates of trench migration as a function of density of the frontal prism, assuming a lithospheric thickness of 50 km for the overriding plate. (c) Slab geometries for frontal prism densities of 2800 kg m^{-3} (shaded slab) and 3275 kg m^{-3} (no shading). Circles in (a, b) show reference case; squares in (b) correspond to the slab geometries in (c). All parameters the same as for reference case except thickness of upper plate lithosphere and density of the frontal prism.

© 2006 The Authors, *GJI*
Journal compilation © 2006 RAS

plate lithosphere is held fixed at 50 km, the rate of trench migration increases from 26 mm yr^{-1} to 58 mm yr^{-1}. The density of material in the frontal prism affects the geometry of the slab at depth, particularly when the mean density of the prism begins to approach that of the asthenosphere. Fig. 11c shows the geometry of two otherwise identical slabs overlain by frontal prisms with densities of either 2800 kg m^{-3} or 3275 kg m^{-3}. In the latter case, the dip of the slab is quite gentle throughout the upper mantle.

In the examples used so far, the lithosphere of the overriding plate has been assumed to be 50 km thick. This constrains the asthenospheric wedge to have an upper surface at 50 km depth and a lower surface that corresponds to the top of the subducting slab, and controls the distribution of engines and brakes. Changing the thickness of the upper plate lithosphere allows us to investigate the effect of moving the top of the viscous wedge to larger or smaller depth. Conceptually, this changes the rate of trench retreat because decreasing the maximum thickness of low-density material in the frontal prism will decrease the magnitude of the viscous normal stress at the front of the asthenospheric (see eq. 9, with similar reasoning as above). Varying the lithospheric thickness of the upper plate from 10 to 70 km decreases the rate of trench migration from 62 mm yr^{-1} to 30 mm yr^{-1}, an ∼50 per cent reduction in trench rate (Fig. 11c). This assumes that the entire frontal prism has a uniform density of 2800 kg m^{-3} and extends to a depth equal to the thickness of the lithosphere. If a mantle-type density of 3200 kg m^{-3} is assumed for the frontal prism, the reduction in trench rate is less, from 66 to 48 mm yr^{-1}, or a ∼25 per cent reduction in trench rate.

TIME-DEPENDENT SUBDUCTION: VARIATIONS IN SLAB BUOYANCY

Some subduction systems display large temporal variability in trench migration rates; in many of the same systems, geologic data indicate variability in the character of the subducted lithosphere. For example, it is not unusual for subduction of dense oceanic lithosphere to be followed by entry of continental lithosphere into the trench and, commonly, by slowing or cessation of subduction (e.g. India/Eurasia convergence, Patriat & Achache 1984; Mediterranean region, Malinverno & Ryan 1986; Wortel & Spakman 1992). These subduction systems involving lithosphere of variable buoyancy are of interest because they demonstrate the spatial and temporal scales over which subduction systems respond to changes in slab buoyancy.

A full investigation of the effects of variable slab buoyancy is beyond the scope of this paper, but we can investigate the timescales over which the subduction responds to variations in slab buoyancy by examining a foreland lithosphere with periodic strips of high- and low-buoyancy lithosphere. While such regular variation in slab buoyancy is unlikely to occur in nature, there are a variety of tectonic settings in which subduction may involve a foreland lithosphere with a mixture of high- and low-density terrains, such as in the Mediterranean region in Late Cenozoic time (e.g. Royden 1993a,b; Jolivet & Faccenna 2000; Faccenna *et al.* 2001, 2003; Lonergan & White 1997). Here, we observe deep-water and shallow-water domains that are typically a few hundred kilometres in extent, so that the question of how rapidly subduction and trench migration rates respond to subduction of variable density lithosphere can be reasonably addressed through modelling of a subducting slab composed of alternating stripes of high- and low-density lithosphere.

Fig. 12(a) shows the oscillating rate of trench migration for slabs composed of alternating strips of high-density (w_o = 6.5 km) and low-density (w_o = 3.5 km) lithosphere, each strip being 200 km wide in a direction perpendicular to the trench. During subduction, the rate of trench migration oscillates with a period of ∼10 Myr and the rate of trench migration changes from ∼70 mm yr^{-1} to ∼35 mm yr^{-1}, and *vice versa*, within less than a few million years (Abrupt kinks in the trench-velocity curve are due largely to truncation of the slab tail near the top of the lower mantle, and reflect the lack of subtlety with which we apply boundary conditions at the slab end. The kinks are not numerical instabilities in the code.) These rapid oscillations in trench migration rates highlight the sensitivity of subduction to stresses in the shallow part of the mantle wedge. The associated geometry of the slab also oscillates in time (Fig. 12b). The most buoyant portions of the slab exhibit the shallowest slab dips, and the difference in dip between buoyancy segments reaches more than 30°.

Our results are highly compatible with the analogue studies of Martinod *et al.* (2005), who examined the effect of subducting a single low-density plateau embedded within a higher density oceanic foreland. Their study showed a dramatic reduction in subduction velocity as the buoyant block entered the subduction boundary, and an equally dramatic increase in rates as the dense portion of the slab followed the buoyant block into the subduction zone.

DISCUSSION

Trench migration is the surface expression of subduction. As such, it is an integral part of the subduction process and arises naturally from the forces that govern subduction. A proper, dynamically consistent, treatment of trench migration, such as we have attempted in this paper, provides insights into the subduction process that are not obvious from models with kinematic constraints on trench motion.

Several studies of subduction have demonstrated that slab dip varies as a function of trench migration rate (Griffiths *et al.* 1995; Olbertz *et al.* 1997; Lallemand *et al.* 2005). This statement is commonly associated with the misperception that high-density slabs dip more steeply than low-density slabs (e.g. Luyendyk 1970). This is correct if trench migration rates (which we measure relative to the foreland lithosphere, not to the lower mantle) are held fixed while the buoyancy of the subducting slab is varied. However, our results show that, in a dynamically consistent framework, there is little variation in steady-state slab geometry as a function of slab buoyancy except for low-buoyancy slabs, which dip more steeply than high-buoyancy slabs. This occurs because rates of trench migration are not independent from slab buoyancy but naturally decrease with increasing slab buoyancy. Other authors have envisaged that entry of more buoyant lithosphere into a subduction boundary might provide a mechanism to explain short-lived periods of flat subduction (e.g. Gutscher *et al.* 1999; Yáñez *et al.* 2001). Our study indicates that entry of buoyant lithosphere into a subduction boundary cannot, by itself, cause flat-slab subduction.

During steady-state subduction, slab dip reflects the angle, as a function of depth, at which all parts of the slab profile migrate horizontally at the same rate. In general, slab dip increases downwards to ∼100 km depth and then remains relatively uniform until near the base of the upper mantle. This steepening of the slab is not due to flexural rigidity of the slab lithosphere because we have used near-zero values of rigidity in most of our calculations. Instead, steady-state slab dip reflects the magnitude of viscous stresses acting on the slab at each depth. For a zero rigidity slab, the viscous normal stresses on each section of slab must be equal to the slab buoyancy multiplied by the cosine of the slab dip. Thus the slab

© 2006 The Authors, *GJI*
Journal compilation © 2006 RAS

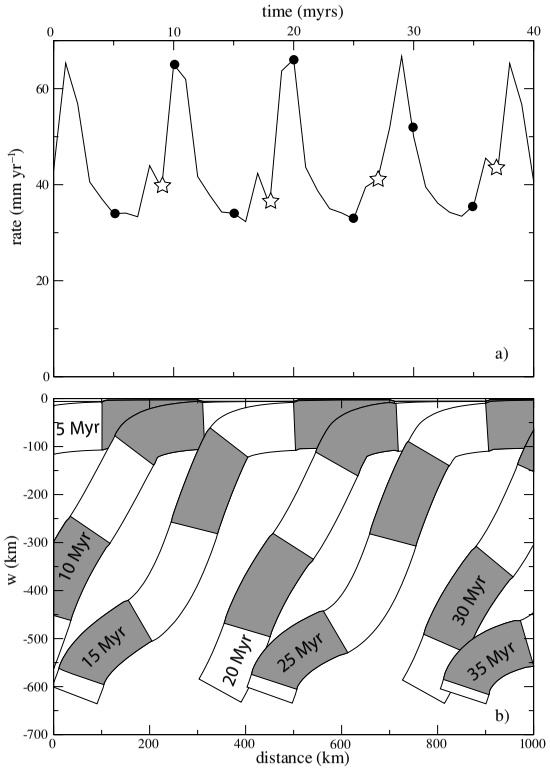

Figure 12. Rates of trench migration for subduction of alternating strips of high density ($w_o = 6.5$ km, unshaded) and low density ($w_o = 3.5$ km, shaded) lithosphere and geometry of the subducted slab through time. Time interval between slab positions is 5 Myr Solid dots in (a) correspond to the times at which the slab geometry is plotted.

profile migrates laterally at a uniform rate despite depth-dependent variation in viscous stress on the slab.

The importance of viscous stresses at shallow level is evident from the depth-dependence of viscous stress on the slab. During steady-state subduction there is a systematic mismatch between viscous stress and buoyancy along the length of the slab. The vertical component of viscous stress applied to the surfaces of the slab averages several times the slab buoyancy in the upper ∼100 km of the mantle. Below this depth, the vertical component of viscous stress typically averages much less than the slab buoyancy. We define slab compensation as the vertical component of stress applied to the surface(s) of the slab divided by the slab buoyancy, We conclude that subducted slabs are generally overcompensated at depths less than ∼100 km and undercompensated throughout the rest of the upper mantle. Conceptually, this can be viewed as subduction systems having a deep driving portion (engine) and a shallow resisting portion (brakes). It is the interplay between the 'engine' and the 'brakes' that determines the slab geometry and the rate of trench retreat.

Because viscous stresses within the shallow 'resisting' part of the subduction zone are extremely large, the rate of trench migration is very sensitive to factors that affect the slab at shallow depth, like the structure and density of the frontal prism and the thickness of the upper plate lithosphere. As yet, there is no consensus among geophysicists as to how to define the model thickness or geometry of the asthenospheric nose in a physically realistic manner. We propose that this problem can be satisfactorily resolved by requiring stress continuity from the frontal prism into the asthenospheric nose. This constrains the pressure within the asthenospheric nose to be approximately equal to the pressure within the deepest part of the frontal prism. This emphasizes the importance of the interaction between shallow level lithospheric processes and deeper viscous processes in controlling slab geometry and trench migration rates.

© 2006 The Authors, *GJI*
Journal compilation © 2006 RAS

The importance of toroidal flow around the slab is illustrated by the dependence of trench migration rate on the width (parallel to the trench) of the subducting slab, with approximately a factor of two decrease in rate as the width of the slab increases from 600 to 2000 km. In the latter case, the stresses related to toroidal flow are much less than in the former case because the upper mantle must flow for a greater distance around the slab. There is little effect of slab width on the dip of the slab. However, if the top of the lower mantle is allowed to move at sufficient velocity that the trench becomes stationary with respect to the lower mantle, the effect of slab width is very much less. The corresponding variation in subduction rates as the slab width changes from 300 to 2000 km is only 25 to 30 per cent.

The relative velocity between the foreland lithosphere and the top of the upper mantle has a large effect on the rate of trench migration, measured relative to a point on the foreland lithosphere. The rate of trench migration, relative to the foreland, varies almost linearly with the velocity of the top of the lower mantle with respect to the foreland. In comparison to a reference case where there is no relative velocity between the foreland lithosphere and the top of the lower mantle, changing the velocity of the lower mantle until the trench is stationary in the lower mantle reference frame nearly doubles the rate of trench motion, measured relative to the foreland. When the direction of motion of the lower mantle is reversed (so that its velocity is from the foreland towards the trench), rates of trench motion, measured relative to the foreland, are reduced.

There is a nearly linear relationship between the velocity of the trench relative to the foreland lithosphere and the velocity of the trench relative to the lower mantle. For a half-slab width of 1000 km, v_R is approximately equal to $(v_o + v_m/2)$, where v_R is the velocity of the trench relative to the foreland, v_m is the velocity of the top of the lower mantle relative to the foreland, and v_o is the velocity of the trench when the foreland lithosphere is fixed with respect to the top of the lower mantle. The proportionality constant should depend on the slab width, being somewhat smaller for narrower slabs—our results suggest around 1/3 for slab widths of 600 km. Our results suggest that subduction probably will not occur when v_m is in the neighbourhood of $-2v_o$.

Slab rheology exerts a strong effect on slab morphology and trench migration rates, but only for relatively strong slabs, stronger than the upper bounds on oceanic lithosphere. For a purely elastic slab, effective elastic plate thicknesses must exceed 30–40 km before geometry or migration rates become appreciably different from a slab with a minimal elastic plate thickness of 1 km. For a purely viscous slab, the viscosity of a slab with a viscously competent layer 50 km thick must reach $\sim 10^{24}$ Pa s before there is a significant change in slab geometry. At much higher slab viscosities, the rate of trench migration slows markedly. For a dense slab ($w_o = 6.5$ km), trench migration rates for a slab with a viscosity of 10^{26} Pa s, more than 5 orders of magnitude greater than the viscosity of the upper mantle, are approximately one fourth of the trench migration rate for a weak slab, with all other parameters held fixed.

These results, are somewhat inconsistent with the proposal of Conrad & Hager (1999a), who argued that the high energy dissipation associated with bending slabs that are more than about 4 orders of magnitude greater than the surrounding mantle will shut down subduction. In fact, much of the slowing of subduction at a viscosity of 10^{26} Pa s does not derive from stresses involved in bending the slab because slab curvature is reduced at high viscosities. Instead, it comes from the increased strength of the 'brakes' applied to the subduction system by the low-density material in the frontal prism, which becomes very wide as the slab becomes stiffer. If the density of the frontal prism material is increased to 3200 kg m^{-3}, the rate of trench migration is ∼50 mm yr^{-1} at a slab viscosity of 10^{26} Pa s and ∼15 mm yr^{-1} at a slab viscosity of 10^{27} Pa s. The primary difference between our results and theirs stems from the slab curvature, which they impose on the slab but which we calculate as inherent to the subduction system. Our slab curvature is much lower than the one that they impose. Thus we find that very stiff slabs inhibit subduction, but only at viscosities about 2 orders of magnitude greater than those proposed by Conrad & Hager (1999a).

A number of authors have tried, with little success, to correlate a variety of subduction parameters with trench retreat rates or with the presence or absence of upper plate extension or shortening (e.g. Jarrard 1986; Lallemand *et al.* 2005). Our results suggest several first-order reasons why this may be the case, such as the dependence on the geologic structure of the upper plate. These crustal and lithospheric-level processes above the slab exert strong controls on the subduction process largely through their effects on flow within the crucial area of the asthenospheric nose. Thus geologic features of the subduction zone are important controls on the subduction process and can be comparable to mantle viscosity and slab buoyancy in their effect on trench migrations rates and slab geometry. The development of topography above the frontal prism, which we have neglected here, should have similarly important effects on the behaviour of the subduction system.

The timescale over which subduction rates respond to variations in slab buoyancy appears to be very short and even narrow (200 km) strips of anomalously buoyant lithosphere greatly affect subduction rates. We show that rapid fluctuations in the rate of trench motion, by a factor of two or more, can occur in as little as 3 Myr, with similarly rapid changes occurring in slab geometry. This process could account for intermittent extensional and/or compressional events within the leading edge of the upper plate of many subduction systems. For typical rates of oceanic subduction (50–100 mm yr^{-1}), such events might typically occur over time periods of 5–10 Myr and at rates of extension or compression of a few tens of millimetres per year. This is consistent with the timescales observed for events like opening of the Japan or Aegean Seas and provides a natural mechanism for the opening and closing of marginal seas throughout the life of an oceanic subduction system. Clearly, an important test of our results will be the integration of observed slab geometry, subduction history and geologic constraints on slab buoyancy for subduction systems that have experienced variable rates of subduction and upper plate deformation.

ACKNOWLEDGMENTS

We would like to thank Clint Conrad and Riad Hassani for helpful and constructive reviews, as well as Thorsten Becker, Claudio Faccenna and Francesca Funiciello for helpful discussions and comments. This project was carried out as part of project MEDUSA, funded by the NSF Continental Dynamics Program, grant EAR-0409373.

REFERENCES

Acheson, D.J., 1990. *Elementary Fluid Dynamics*, Clarendon Press, New York, 397 pp.

Batchelor, G.K., 1967. *An Introduction to Fluid Dynamics*, Cambridge University Press, Cambridge, 615 pp.

© 2006 The Authors, *GJI*
Journal compilation © 2006 RAS

Becker, T.W., Faccenna, C., Giardini, D. & O.Connell, R.J., 1999. The development of slabs in the upper mantle: insights from numerical and laboratory experiments, *J. geophys. Res.,* **104,** 15 207–15 226.
Becker, T.W. & O'Connell, R.J., 2001. Predicting plate motions with mantle circulation models, *Geochem. Geophys. Geosyst.,* **2**, doi:2001GC000171.
Bellahsen, N., Faccenna, C., Funiciello, F., Daniel, J.-M. & Jolivet, L., 2003. Why did Arabia separate from Africa? Insights from analogue modeling, *Earth planet. Sci. Lett.,* **216,** 316–381.
Bellahsen, N., Faccenna, C. & Funiciello, F., 2005. Dynamics of subduction and plate motion in laboratory experiments: insights in to the 'plate tectonics' behavior of the earth, *J. geophys. Res.,* **110**, doi:10.1029/2004JB002999.
Bercovici, D., 2003. The generation of plate tectonics from mantle convection, *Earth planet. Sci. Lett.,* **205,** 107–121.
Billen, M.I. & Gurnis, M., 2001. Comparison of dynamic flow models for the Central Aleutian and Tonga-Kermadec subduction zones, *Geochem. Geophys. Geosyst.,* **4,** 1035.
Billen, M.I., Gurnis, M. & Simons, M., 2003. Multiscale dynamics of the Tonga-Kermadec subduction zone, *Geophys. J. Int.,* **153,** 359–388.
Billen, M.I. & Gurnis, M., 2005. Constraints on subducting plate strength within the Kermadec trench, *J. geophys. Res.,* **110**, doi:10.1029/2004JB003308.
Brace, W.F. & Kohlstedt, D.L., 1980. Limits on lithospheric stress imposed by laboratory experiments, *J. geophys. Res.,* **85,** 6248–6252.
Buiter, S.J.H., Govers, R. & Wortel, M.J.R., 2001. A modelling study of vertical displacements at convergent plate margins, *Geophys. J. Int.,* **147,** 415–427.
Buiter, S.J.H., Govers, R. & Wortel, M.J.R., 2002. Two-dimensional simulations of surface deformation caused by slab detachment, *Tectonophysics,* **354,** 195–210.
Chapple, W.M. & Tullis, T.E., 1977. Evaluation of the forces that drive plates, *J. geophys. Res.,* **82,** 1967–1984.
Christensen, U., 1996. The influence of trench migration on slab penetration into the lower mantle, *Earth planet. Sci. Lett.,* **140,** 27–39.
Christensen, U., 2001. Geodynamic models of deep subduction, *Phys. Earth planet. Sci. Inter.,* **127,** 25–34.
Conrad, C.P. & Hager, B.H., 1999a. Effects of plate bending and fault strength at subduction zones on plate dynamics, *J. geophys. Res.,* **104,** 17 551–17 571.
Conrad, C.P. & Hager, B.H., 1999b. The thermal evolution of an earth with strong subduction zones, *Geophys. Res. Lett.,* **26,** 3041–3044.
Conrad, C.P. & Lithgow-Bertelloni, C., 2002. How mantle slabs drive plate tectonics, *Science,* **298,** 207–209.
Conrad, C.P. & Lithgow-Bertelloni, C., 2004. The temporal evolution of plate driving forces: importance of 'slab suction' versus 'slab pull' during the Cenozoic, *J. geophys. Res.,* **109**, doi:10.1029/2004JB002991.
Cross, T.A. & Pilger, R.H. Jr., 1982. Controls of subduction geometry, location of magmatic arcs, and tectonics of arc and back-arc regions, *Geol. soc. Am. Bull.,* **93,** 545–562.
Davies, G.F., 1977. Viscous mantle flow under moving lithospheric plates and under subduction zones, *Geophys. J. R. astr. Soc.,* **49,** 557–563.
Davies, G.F., 1989. Mantle convection model with a dynamic plate: Topography, heat flow and gravity anomalies, *Geophys. J. Int.,* **98,** 461–464.
Dvorkin, J., Nur, A., Mavko, G. & Ben-Avraham, Z., 1993. Narrow subducting slabs and the origin of backarc basins, *Tectonophysics,* **227,** 63–79.
Elsasser, W.M., 1969. Convection and stress propagation in the upper mantle, in *The Application of Modern Physics to the Earth and Planetary Interiors*, pp. 223–246, ed. Runcorn, S.K., Wiley-Interscience, Hoboken, New Jersey.
Enns, A., Becker, T.W. & Schmeling, H., 2005. The dynamics of subduction and trench migration for viscosity stratification, *Geophys. J. Int.,* **160,** 761–775.
Faccenna, C., Davy, P., Brun, J.P., Funiciello, R., Giardini, D., Mattei, M. & Naples, T., 1996. The dynamics of back-arc extensions: An experimental approach to the opening f the Tyrrhenian sea, *Geophys. J. Int.,* **126,** 781–795.
Faccenna, C., Becker, T.W., Lucente, F.P., Jolivet, L. & Rossetti, F., 2001. History of subduction and back-arc extension in the central Mediterranean, *Geophys. J. Int.,* **145,** 809–820.
Faccenna, C., Jolivet, L., Piromallo, C. & Morelli, A., 2003. Subduction and the depth of convection in the Mediterranean mantle, *J. Geophys Res.,* **108**, doi:10.1029/2001JB001690.
Forsyth, D. & Uyeda, S., 1975. On the relative importance of the driving forces of plate motion, *Geophys. J. R. astr. Soc.,* **43,** 163–200.
Forte, A.M. & Mitrovica, J.X., 2001. Deep-mantle high-viscosity flow and thermochemical structure inferred from seismic and geodynamic data, *Nature,* **410,** 1049–1056.
Funiciello, F., Faccenna, C., Giardini, D. & Regenauer-Lieb, K., 2003a. Dynamics of retreating slabs: 1. Insights from three-dimensional laboratory experiments, *J. geophys. Res.,* **108,** 2207, doi: 10.1029/2001JB000896.
Funiciello, F., Morra, G., Regenauer-Lieb, K. & Giardini, D., 2003b. Dynamics of retreating slabs: 2. Insights from two-dimensional numerical experiments, *J. geophys. Res.,* **108,** 2207, doi: 10.1029/2001JB000898.
Funiciello, F., Moroni, M., Piromallo, C., Faccenna, C., Cenedese, A. & Bui, H.A., 2006. Mapping mantle flow during retreating subduction: laboratory models analyzed by feature tracking, *J. geophys. Res.,* **111**, doi:10.1029/2005JB003792.
Furbish, D.J., 1997. *Fluid Physics in Geology*, Oxford University Press, New York, 476 pp.
Gripp, A.E. & Gordon, R.G., 1990. Current plate velocities relative to the hotspots incorporating the NUVEL-1 global plate motion model, *Geophys. Res. Lett.,* **17,** 1109–1112.
Griffiths, R.W., Hackney, R.I. & van der Hilst, R.D., 1995. A laboratory investigation of effects of trench migration on the descent of subducted slabs, *Earth planet. Sci. Lett.,* **133,** 1–17.
Gurnis, M., Zhong, S. & Toth, J., 2000. On the competing roles of fault reactivation and brittle failure in generating plate tectonics from mantle convection, in *The History and Dynamics of Global Plate Motions, Geophysical Monograph*, Vol. 201, pp. 73–94, eds Richards, M.A., Gordon, R.G. & van der Hilst, R.D., AGU, Washington, DC.
Gutscher, M.A., Malavieille, J., Lallemand, S. & Collot, J.Y., 1999. Tectonic segmentation of the North Andean margin : impact of the Carnegie Ridge collision, *Earth planet. Sci. Lett.,* **168,** 255–270.
Hager, B.H., 1984. Subducted slabs and the geoid: Constraints on mantle rheology and flow, *J. geophys. Res.,* **89,** 6003–6015.
Hager, B.H. & O'Connell, R.J., 1978. Subduction zone dip angles and flow driven by plate motion, *Tectonophysics,* **50,** 111–133.
Hager, B.H. & O'Connell, R.J., 1981. A simple global model of plate dynamics and mantle convection, *J. geophys. Res.,* **86,** 4843–4867.
Han, L. & Gurnis, M., 1999. How valid are dynamic models of subduction and convection when plate motion are prescribed?, *Phys. Earth planet. Inter.,* **110,** 235–246.
Ito, E. & Sato, H., 1991. Aseismicity in the lower mantle by superplasticity of the descending slab, *Nature,* **351,** 140–141.
Jarrard, R.D., 1986. Relations among subduction parameters, *Rev. Geophys.,* **24,** 217–284.
Jolivet, L. & Faccenna, C., 2000. Mediteranean extension and the Africa-Eurasia collision, *Tectonics,* **19,** 1095–1106.
Kaminski, E., Ribe, N.M. & Browaeys, J.T., 2004. D-Rex, a program for calculation of seismic anisotropy due to crystal lattice preferred orientation in the convective upper mantle, *Geophys. J. Int.,* **158,** 744–752.
Kincaid, C. & Sacks, I.S., 1997. Thermal and dynamical evolution of the upper mantle in subduction zones, *J. geophys. Res.,* **102,** 12 295–12 315.
King, S.D. & Hager, B.H., 1990. The relationship between plate velocity and trench viscosity in Newtonian and power-law subduction calculations, *Geophys. Res. Lett.,* **17,** 2409–2412.
Lallemand, S., Heuret, A. & Boutelier, D., 2005. On the relationships between slab dip, back-arc stress, upper plate absolute motion, and crustal nature in subduction zones, *Geochem. Geophys. Geosyst.,* **6**, doi: 10.1029/2005GC000917.
Lambeck, K. & Chappel, J., 2001. Sea level change through the last glacial cycle, *Science,* **292,** 679–686.
Lithgow-Bertelloni, C. & Richards, M.A., 1998. The dynamics of Cenozoic and Mesozoic plate motions, *Rev. Geophys.,* **36,** 27–78.

© 2006 The Authors, *GJI*
Journal compilation © 2006 RAS

Lonergan, L. & White, N.J., 1997. The origin of the Betic Rif mountain chains, *Tectonics,* **16,** 504–522.
Luyendyk, B.P., 1970. Dips of downgoing lithospheric plates beneath island arcs, *Geol. soc. Am. Bull.,* **81,** 3411–3416.
Malinverno, A. & Ryan, W., 1986. Extension in the Tyrrhenian sea and shortening in the Apennines as result of arc migration driven by sinking of the lithosphere, *Tectonics,* **5,** 227–245.
Martinod, J., Funiciello, F., Faccenna, C., Labanieh, S. & Regard, V., 2005. Dynamical effects of subducting ridges: insights from 3-D laboratory models, *Geophys. J. Int.,* **163,** 1137–1150.
McKenzie, D., 1969. Speculations on the consequences and causes of plate motions, *Geophys. J. R. astr. Soc.,* **18,** 1–32.
McNutt, M.K. & Menard, H.W., 1982. Constraints on yield strength in the oceanic lithosphere derived from observations of flexure, *Geophys. J. R. astr. Soc.,* **71,** 363–395.
McNutt, M.K., Diament, M. & Kogan, M.G., 1988. Variations in elastic plate thickness at continental thrust belts, *J. geophys. Res.,* **93,** 8825–8838.
Mitrovica, J.X. & Forte, A.M., 1997. Radial profile of mantle viscosity: Results from the joint inversion of convection and postglacial rebound observables, *J. geophys. Res.,* **102,** 2751–2769.
Mitrovica, J.X. & Forte, A.M., 2004. A new inference of mantle viscosity based upon a joint inversion of convection and glacial isostatic adjustment data, *Earth planet. Sci. Lett.,* **225,** 177–189.
Olbertz, D., Wortel, M. & Hansen, U., 1997. Trench migration and subduction zone geometry, *Geophys. Res. Lett.,* **24,** 221–224.
Patriat, P. & Achache, J., 1984. India-Eurasia collision chronology has implications for crustal shortening and driving mechanism of plates, *Nature,* **311,** 615–621.
Regard, V., Faccenna, C., Martinod, J., Bellier, O. & Thomas, J.-C., 2003. From subduction to collision: Control of deep processes on the evolution of convergent plate boundary, *J. geophys. Res.,* **108**, doi:10.1029/2002JB001943.
Ricard, Y. & Wuming, B., 1991. Inferring the viscosity and the 3-D density structure of the mantle from geoid, topography and plate velocities, *Geophys. J. Int.,* **105,** 561–571.
Ricard, Y., Doglioni, C. & Sabadini, R., 1993. Differential rotation between lithosphere and mantle: a consequence of lateral mantle viscosity variations, *J. geophys. Res.,* **96,** 8407–8415.
Richards, M.A. & Lithgow-Bertelloni, C., 1996. Plate motions changes, the Hawaiian-Emperor bend, and the apparent success and failure of the geodynamic models, *Earth planet. Sci. Lett.,* **137,** 19–27.
Richter, F.M., 1977. On the driving mechanism of plate tectonics, *Tectonophysics,* **38,** 61–88.
Richter, F.M. & McKenzie, D., 1978. Simple plate models of mantle convection, *J. Geophys.*, **44,** 441–471.
Royden, L.H., 1993a. The tectonic expression of slab pull at continental convergent boundaries, *Tectonics,* **12,** 303–325.
Royden, L.H., 1993b. Evolution of retreating subduction boundaries formed during continental collision, *Tectonics,* **12,** 629–638.
Schellart, W.P., 2004a. Quantifying the net slab pull force as a driving mechanism for plate tectonics, *Geophys. Res. Lett.,* **31,** 5.
Schellart, W.P., 2004b. Kinematics of subduction and subduction-induced flow in the upper mantle, *J. geophys. Res.,* **109,** B07401, doi:10.1029/2004JB002970.
Shemenda, A.I., 1993. Subduction of lithosphere and back-arc dynamics: insights from physical modeling, *J. geophys. Res.,* **98,** 16 167–16 185.
Shemenda, A.I. & Groholsky, A.L., 1994. Physical modeling of slow spreading, *J. geophys. Res.,* **99,** 9137–9153.
Solomon, S.C. & Sleep, N.H., 1974. Some simple physical models for absolute plate motions, *J. geophys. Res.,* **79,** 2557–2567.
Stegman, D.R., Freeman, J., Schellart, W.P., Moresi, L. & May, D., 2006. Influence of trench width on subduction hinge retreat rates in 3-D models of slab rollback, *Geochem. Geophys. Geosyst.,* **7**, doi:10.1029/2005GC001056.
Spence, W., 1987. Slab pull and the seismotectonics of subducting lithosphere, *Rev. Geophys.,* **25,** 55–69.
Steinberger, B. & O'Connell, R.J., 1998. Advection of mantle viscosity and plume distribution, *Geophys. J. Int.,* **132,** 412–434.
Steinberger, B., 2000. Plumes in a convecting mantle: models and observations for individual hotspots, *J. geophys. Res.,* **105,** 11 127–11 152.
Steinberger, B., Sutherland, R. & O'Connell, R., 2004. Prediction of Emperor-Hawaii seamount locations from a revised model of plate motion and mantle flow, *Nature,* **430,** 167–173.
Stevenson, D.J. & Turner, J.S., 1977. Angle of subduction, *Nature,* **270,** 334–336.
Turcotte, D.L. & Oxburgh, E.R., 1967. Finite amplitude convective cells and continental drift, *J. Fluid Mech.,* **28,** 29–42.
Turcotte, D.L. & Schubert, G., 1982. *Geodynamics, Applications of Continuum Physics to Geological Problems*, John Wiley, New York, 450 pp.
Walcott, R.I., 1970, Flexural rigidity, thickness and viscosity of the lithosphere, *J. geophys. Res.,* **75,** 3941–3954.
Watts A.B. &Burov, E.B., 2003. Lithospheric strength and its relationship to the elastic and seismogenic layer thickness, *Earth planet. Sci. Lett.,* **213,** 113–131.
Winder, R.O. & Peacock, S.M., 2001. Viscous forces acting on subducting lithosphere, *J. geophys. Res.,* **106,** 21 937–21 951.
Wortel, M.J.R. & Spakman, W., 1992. Subduction and slab detachment in the Mediterranean-Carpathian region, *Science,* **290,** 1910–1917.
Yáñez, G., Ranero, C.R., von Huene, R. & Díaz, J., 2001. Magnetic anomaly interpretation across a segment of the southern Central Andes (32°–34°S): implications on the role of the Juan Fernández ridge in the tectonic evolution of the margin during the upper Tertiary, *J. geophys. Res.,* **106,** 6325–6345.
Zhong, S. & Gurnis, M., 1995a. Mantle convection with plates and mobile, faulted plate margins, *Science,* **267,** 838–842.
Zhong, S. & Gurnis, M., 1995b. Towards a realistic simulation of plate margins in mantle convection, *Geophys. Res. Lett.,* **22,** 981–984.
Zhong, S., 2001. Role of ocean-continent contrast and continental keels on plate motion, net rotation of lithosphere, and the geoid, *J. geophys. Res.,* **106,** 703–712.

APPENDIX A

Background stress of toroidal flow around the slab

In the Hele-Shaw approximation for flow in a Newtonian viscous channel, horizontal flow is assumed to have a parabolic profile with depth and the horizontal pressure gradient is invariant with depth. Pressure gradient is related to horizontal flow velocity as:

$$\frac{\partial P}{\partial x} = \frac{\partial}{\partial z}\left(\mu \frac{\partial v_x}{\partial z}\right), \tag{A1}$$

and similarly for the pressure gradient in the y-direction.

© 2006 The Authors, *GJI*
Journal compilation © 2006 RAS

For computation of Hele-Shaw flow in a viscous medium with viscosity variations in the z-direction, it is useful to define the functions:

$$f_1(z) = \int_0^z \frac{dz'}{\mu(z')} \qquad f_2(z) = \int_0^z \frac{z'dz'}{\mu(z')}$$

$$f_3(z) = \int_0^z \frac{(z-z')}{\mu(z')}dz' \qquad f_4(z) = \int_0^z \frac{z'(z-z')}{\mu(z')}dz'$$

Integrating (A1) with respect to z, dividing by μ, and integrating again with respect to z yields an expression for velocity as a function of depth for a layered medium:

$$v_x(x,y,z) = \left[\frac{v_t f_1(\lambda) + (v_m - v_t)f_1(z)}{f_1(\lambda)}\right] + \frac{\partial P}{\partial x}\left[\frac{f_1(\lambda)f_2(z) - f_2(\lambda)f_1(z)}{f_1(\lambda)}\right], \tag{A2}$$

where v_t and v_m are the velocities in the x-direction of the upper and lower surface of the channel, respectively. For the case of uniform viscosity, eq. (A2) simplifies to the more familiar:

$$v_x(x,y,z) = \left[\frac{v_t(z-\lambda) + v_m z}{\lambda}\right] + \frac{\partial P}{\partial x}\left(\frac{z(z-\lambda)}{2\mu}\right). \tag{A3}$$

(A2) can be integrated over z to obtain the total flux in the x-direction due to viscous flow in the channel:

$$\int_0^\lambda v_x\,dz = \left[\frac{v_t\lambda f_1(\lambda) + (v_m - v_t)f_3(\lambda)}{f_1(\lambda)}\right] - \frac{\partial P}{\partial x}\left[\frac{f_2(\lambda)f_3(\lambda) - f_1(\lambda)f_4(\lambda)}{f_1(\lambda)}\right], \tag{A4}$$

which, for uniform viscosity, reduces to:

$$\int_0^\lambda v_x\,dz = \lambda\left(\frac{v_t + v_m}{2}\right) - \frac{\partial P}{\partial x}\left(\frac{\lambda^3}{12\mu}\right). \tag{A5}$$

Analogous expressions can be written for flow velocity and integrated flux in the y-direction.

The net flux in the x- and y-directions must satisfy the continuity equation if the channel thickness (equated here with the upper mantle) is to remain constant through time. Therefore, P must satisfy Laplace's equation everywhere except along the vertical slab surface, at points $-a < y_i < a,\ x_i = 0$. Over this set of points, P does not need to satisfy the Laplace equation but the velocity in the x-direction must equal the horizontal slab velocity, v_R. (In the Hele-Shaw approximation, only the net flux orthogonal to an obstacle is set to zero at the surface of the obstacle. The details of the flow as a function of depth and the flux parallel to the boundary are not constrained. This is a standard approximation in fluid mechanics and works well as long as one is a moderate distance from the obstacle relative to the channel depth. See, e.g. Batchelor 1967).

A solution for P that satisfies Laplace's equation everywhere except at (x_i, y_i) is:

$$P_i(x,y) = \frac{A_i(x - x_i)}{(x-x_i)^2 + (y-y_i)^2}, \tag{A6}$$

where A_i is a constant. Taking the derivative with respect to x and substituting into eq. (A4) to find corresponding flux in the x-direction, we obtain:

$$\int_0^\lambda v_x\,dz = \left[\frac{v_t\lambda f_1(\lambda) + (v_m - v_t)f_3(\lambda)}{f_1(\lambda)}\right] + A_i\frac{\left[(x-x_i)^2 - (y-y_i)^2\right]}{\left[(x-x_i)^2 + (y-y_i)^2\right]^2}\left[\frac{f_2(\lambda)f_3(\lambda) - f_1(\lambda)f_4(\lambda)}{f_1(\lambda)}\right], \tag{A7}$$

and for uniform viscosity:

$$\int_0^\lambda v_x\,dz = \lambda\left(\frac{v_t + v_m}{2}\right) + \frac{(x-x_i)^2 - (y-y_i)^2}{\left[(x-x_i)^2 + (y-y_i)^2\right]}\left(\frac{A_i\lambda^3}{12\mu}\right). \tag{A8}$$

If we choose $x_i = 0$ and $-a \le y_i \le a$, then eqs (A6–A8) satisfy Laplace's equation everywhere except on the slab surface. The brute-force approach, used here, is to choose a set (x_i, y_i) along the slab surface and invert to find the values of A_i that yield the desired x-velocity at those points. We chose 100 evenly spaced points at $x_i = 0$ and y_i between 0 and a, required the distribution of A_i's to be symmetrical about $y_i = 0$, and inverted for the A_i's. The resulting velocity along the y-axis and pressure along the x-axis are shown in Fig. A1.

It is not clear if it is more appropriate to characterize the background stresses on the slab by averaging P between $y = \pm a$, or by taking the maximum value of P at $y = 0$ (it makes little difference to ours results). Here we choose to use the value of P at $y = 0$. This yields a background stress due to toroidal flow around the slab that is a function of distance from the slab. Fig. A1 shows that a good empirical approximation for the pressure at $y = 0$ is:

$$P(x,0) = \left\{\frac{a[v_R\lambda f_1(\lambda) - v_t\lambda f_1(\lambda) - (v_m - v_t)f_3(\lambda)]}{f_2(\lambda)f_3(\lambda) - f_1(\lambda)f_4(\lambda)}\right\}e^{-.9(x/a)^{0.8}}. \tag{A9}$$

For uniform viscosity, this reduces to a simpler equation given in (4) in the main text.

© 2006 The Authors, *GJI*
Journal compilation © 2006 RAS

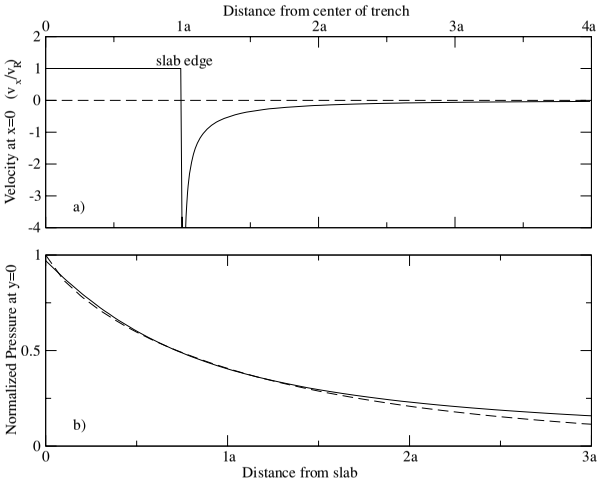

Figure A1. (a) Model velocity of viscous flow in x-direction (orthogonal to the trench) plotted along y-axis (y-axis lies along the trench as shown in Fig. 3). Velocity is the average velocity in a vertical column through the upper mantle, as described in Appendix A, and is constrained to be v_R on the slab surface. (b) Pressure of viscous flow along the axis of symmetry through the centre of the slab (x-axis), plotted as a function of distance from the slab and normalized to 1 on the slab surface. Solid line shows the model solution as described in Appendix A, dashed line is the empirical approximation used in our subduction model, eqs (4) and (A9).

APPENDIX B

Local stress in the mantle wedge

In cylindrical coordinates, the continuity equation is be expressed as:

$$0 = \frac{\partial(r v_r)}{\partial r} + \frac{\partial v_\theta}{\partial\theta}, \tag{B1}$$

where r is the radius and θ the angle from the horizontal (see Fig. 2 for signs and conventions). Viscous stresses are related to velocity by:

$$\tau_{r\theta} = \mu\left[\frac{1}{r}\frac{\partial v_r}{\partial\theta} + r\frac{\partial}{\partial r}\left(\frac{v_\theta}{r}\right)\right], \tag{B2}$$

$$\tau_{rr} = -\tau_{\theta\theta} = 2\mu\frac{\partial v_r}{\partial r}, \tag{B3}$$

and the pressure gradient in the radial and tangential direction can be expressed in terms of these viscous stresses:

$$\frac{\partial P}{\partial r} = \frac{1}{r}\left[\frac{\partial(r\tau_{rr})}{\partial r} - \tau_{\theta\theta} + \frac{\partial\tau_{r\theta}}{\partial\theta}\right], \tag{B4}$$

$$\frac{\partial P}{\partial\theta} = \frac{\partial\tau_{\theta\theta}}{\partial\theta} + \tau_{r\theta} + \frac{\partial(r\tau_{r\theta})}{\partial r}. \tag{B5}$$

We wish to use these expressions to derive an approximate flow profile for v_r as a function of θ, without requiring information about how v_r or v_θ vary in the r-direction. Let us assume that v_r and v_θ vary much more rapidly with $r\theta$ than with r. Then their derivatives with respect to r can be ignored. Likewise, τ_{rr} and $\tau_{\theta\theta}$ can be ignored, as can all other derivatives with respect to r in (B2–B5), yielding the approximate relations:

$$\tau_{r\theta} = \frac{\mu}{r}\frac{\partial v_r}{\partial\theta}, \tag{B6}$$

$$\frac{\partial\sigma_{\theta\theta}}{\partial r} = \frac{\partial P}{\partial r} = \frac{1}{r}\frac{\partial\tau_{r\theta}}{\partial\theta}, \tag{B7}$$

© 2006 The Authors, *GJI*
Journal compilation © 2006 RAS

$$\frac{\partial \sigma_{\theta\theta}}{\partial \theta} = \frac{\partial P}{\partial \theta} = \tau_{r\theta} + \frac{\partial (r\,\tau_{r\theta})}{\partial r}, \tag{B8}$$

where $\sigma_{\theta\theta}$ is the total normal stress related to viscous flow in the θ direction. Taking the derivative of eq. (B7) with respect to θ and the derivative of eq. (B8) with respect to r, equating the right-hand sides, and dropping derivatives with respect to r gives:

$$\frac{1}{r}\frac{\partial^2 \tau_{r\theta}}{\partial \theta^2} = \frac{\partial}{\partial r}\left[\tau_{r\theta} + \frac{\partial (r\,\tau_{r\theta})}{\partial r}\right] = 0. \tag{B9}$$

From eqs (B9) and (B7) we find that the approximate dependence of shear stress on θ is:

$$\tau_{r\theta}(r) = A(r)\theta + B(r) = r\theta\,\frac{\partial \sigma_{\theta\theta}}{\partial r} + \tau_t(r), \tag{B10}$$

where τ_t is the shear stress at $\theta = 0$, which is not known *a priori*. (We also have assumed implicitly that $\sigma_{\theta\theta}$ is approximately a constant for fixed r_o).

We define four useful functions:

$$g_1(\theta) = \int_0^\theta \frac{d\theta'}{\mu(\theta')} \qquad g_2(\theta) = \int_0^\theta \frac{\theta' d\theta'}{\mu(\theta')}$$

$$g_3(\theta) = \int_0^\theta \frac{(\theta - \theta')}{\mu(\theta')}\,d\theta' \qquad g_4(\theta) = \int_0^\theta \frac{\theta'(\theta - \theta')}{\mu(\theta')}\,d\theta'$$

Using the expression for shear stress given in (B10), we can see by inspection that a solution for v_r in eq. (B6) is given by:

$$v_r = \left(r^2 \frac{\partial \sigma_{\theta\theta}}{\partial r}\right) g_2(\theta) + \tau_t r\, g_1(\theta) + C(r), \tag{B11}$$

where C is an arbitrary function of r. Finally, integrating eq. (B1) over r and θ and substituting for v_r from (B11) yields:

$$\int^r v_\theta\, dr = -\left(r^3 \frac{\partial \sigma_{\theta\theta}}{\partial r}\right) g_4(\theta) - r^2 \tau_t(r) g_3(\theta) - rC(r)\theta - D(r), \tag{B12}$$

where D is also an arbitrary function of r.

We can use (B10)–(B12) to find approximate expressions for viscous stress within the viscous wedge, beginning with the stress on the upper surface of the slab. Consider the flow across a circular arc within the upper mantle wedge, as shown in Fig. 2. The lower straight-line segment of the slice is locally tangent to the subducted slab (making an angle θ_o with the horizontal) and the upper straight-line segment is horizontal and coincides with the upper surface of the viscous wedge. If the vertical thickness of the wedge at this point is d_t, then the circular arc has a radius of curvature $r_o = d_t/\sin\,\theta_o$ and an arc length $\theta_o d_t/\sin\,\theta_o$. We solve for the three arbitrary constants in (B11) and (B12) and for $d\sigma_{\theta\theta}/dr$ by applying velocity boundary conditions at $\theta = 0$ and $\theta = \theta_o$. Using the conventions given in Fig. 2, at $\theta = 0$ the radial and tangential velocities are $v_\theta = 0,\ v_r = -\,v_t$. Thus:

$$D(r) = 0 \qquad C(r) = -v_t$$

At $\theta = \theta_o$ the radial and tangential velocities are $v_\theta = v_n,\ v_r = -\,v_s$. In addition, we replace the integral over r with an integral over s along the slab surface, noting that locally $dr = -\,ds$. Thus:

$$-v_s = -r_o^2\, g_2(\theta_o)\frac{\partial \sigma_n}{\partial s} + r_o \tau_t(r_o) g_1(\theta_o) - v_t, \tag{B13}$$

$$\int_0^s v_n\, ds = r_o^3\, g_4(\theta_o)\frac{\partial \sigma_n}{\partial s} - r_o^2 \tau_t(r_o) g_3(\theta_o) + v_t r_o \theta_o, \tag{B14}$$

and:

$$\tau_t = \frac{(v_t - v_s)}{r_o\, g_1(\theta_o)} + \frac{\partial \sigma_n}{\partial s}\left[\frac{r_o\, g_2(\theta_o)}{g_1(\theta_o)}\right], \tag{B15}$$

$$\frac{\partial \sigma_n}{\partial s} = -\frac{\partial \sigma_n}{\partial r} = \frac{-g_1(\theta_o)\int_0^s v_n\, ds + r_o\, g_3(\theta_o)(v_s - v_t) + v_t r_o \theta_o\, g_1(\theta_o)}{r_o^3[g_2(\theta_o) g_3(\theta_o) - g_1(\theta_o) g_4(\theta_o)]}, \tag{B16}$$

where σ_n is the value of $\sigma_{\theta\theta}$ evaluated on the surface of the slab (although $\sigma_{\theta\theta}$ is implicitly assumed to be a constant for fixed r_o). Values for shear stress and velocity as a function of θ can be obtained by substituting (B15) and (B16) into B(10)–B(12). For uniform viscosity the expressions for pressure gradient and shear stress along the top of the slab reduce to the expressions found in eqs (5) and (6) in the main text, while velocities within the upper mantle wedge are

$$v_r = -\frac{r_o^2 \theta^2}{2}\frac{\partial \sigma_n}{\partial s} + \tau_t r_o \theta - v_t, \tag{B17}$$

$$v_\theta = \frac{\partial}{\partial s}\left[-\frac{\partial \sigma_n}{\partial s}\left(\frac{r_o^3 \theta^3}{6}\right) + \tau_t\left(\frac{r_o^2 \theta^2}{2}\right) - v_t r_o \theta\right]. \tag{B18}$$

© 2006 The Authors, *GJI*
Journal compilation © 2006 RAS

We can find analogous solutions for viscous stresses on the base of the slab by considering flow across a circular arc within the lower mantle wedge, as shown in Fig. 2. The upper straight-line segment of the slice is locally tangent to the subducted slab (making an angle θ_o with the horizontal) and the lower straight-line segment is horizontal and coincides with the lower surface of the viscous wedge. If the vertical thickness of the wedge at this point is d_b, then the circular arc has a radius of curvature $r_o = d_b/\sin\theta_o$ and an arc length $\theta_o d_b/\sin\theta_o$. We proceed as before, solving for the three arbitrary constants in (B11) and (B12) and for $\partial\sigma_n/\partial r$ in the lower mantle wedge by applying velocity boundary conditions at $\theta = 0$ and $\theta = \theta_o$. Using the conventions given in Fig. 2, at $\theta = 0$ the radial and tangential velocities are $v_\theta = 0,\ v_r = v_m$. At $\theta = \theta_o$ the radial and tangential velocities are $v_\theta = -v_n,\ v_r = v_s$. In addition, we replace the integral over r with an integral over s along the slab surface $\partial\sigma_n/\partial s$.

Thus for the lower mantle wedge we find the analogous expressions to (B15) and (B16):

$$\tau_m = \frac{(v_s - v_m)}{r_o g_1(\theta_o)} - \frac{\partial \sigma_n}{\partial s}\left[\frac{r_o g_2(\theta_o)}{g_1(\theta_o)}\right], \tag{B19}$$

$$\frac{\partial \sigma_n}{\partial s} = \frac{\partial \sigma_n}{\partial r} = \frac{-g_1(\theta_o)\int_0^s v_n\, ds + r_o\, g_3(\theta_o)(v_s - v_m) + v_m r_o \theta_o\, g_1(\theta_o)}{r_o^3[g_2(\theta_o) g_3(\theta_o) - g_1(\theta_o) g_4(\theta_o)]}, \tag{B20}$$

where τ_m is the shear stress on the base of the upper mantle. In the case of uniform viscosity, the analogous expressions to (5), (6), (B17) and (B18) are, for the lower mantle wedge:

$$\frac{\partial \sigma_n}{\partial s} = \frac{-12\mu}{r_o^3 \theta_o^3}\int_0^s v_n\, ds + \frac{6\mu(v_s + v_m)}{r_o^2 \theta_o^2}, \tag{B21}$$

$$\tau_s = \frac{\mu(v_s - v_m)}{r_o \theta_o} - r_o \theta_o \frac{\partial \sigma_n}{\partial s}, \tag{B22}$$

$$v_r = \frac{r_o^2 \theta^2}{2}\frac{\partial \sigma_n}{\partial s} + \tau_m r_o \theta + v_m, \tag{B23}$$

$$v_\theta = \frac{\partial}{\partial s}\left[-\frac{\partial \sigma_n}{\partial s}\left(\frac{r_o^2 \theta^3}{6}\right) - \tau_m\left(\frac{r_o^2 \theta^2}{2}\right) - v_m r_o \theta\right]. \tag{B24}$$

The accuracy of this approximation can be tested numerically, but a reasonable idea can be obtained by comparing the shear stresses and pressure gradient along a uniformly dipping slab, of infinite extent, with uniform velocity on the slab and zero velocity at the surface and at the base of the upper mantle ($v_t = v_m = 0$). The results of this calculation are shown for a slab in steady state with a dimensionless rate of trench retreat of one, so that on the upper surface of the slab $v_r = 1 - \cos(\theta_o)$, $v_\theta = \sin(\theta_o)$. Fig. B1 shows that the accuracy of the approximate solution is excellent for small angles and worsens as the angle increases. For an angle of 60°, which is typical for many of the model slabs produced for this paper, the approximate shear stress and viscous pressure gradient are approximately 20 per cent greater than the exact solutions.

More exact approximations can be readily developed. However we found that building explicit assumptions about how velocity depends on r into the approximation could cause problems in the computation of subduction dynamics because it tended to force a particular kind of behaviour on the slab. Thus the simple solutions presented here, although less accurate for a uniform, linear wedge than others we derived, had the advantage of being versatile and working reasonably well for all kinds of slab geometries and velocity distributions on the slab.

APPENDIX C

Static force balance on slab elements

Denoting the internal compression directed along the axis of the slab as C and the internal shear forces acting on planes orthogonal to the axis of the slab as V, then a static force balance on a slab element of length ds yields

$$\frac{\partial}{\partial s}(V\cos\theta) + \frac{\partial}{\partial s}(C\sin\theta) + q_z + \rho_l g = 0, \tag{C1}$$

$$\frac{\partial}{\partial s}(V\sin\theta) + \frac{\partial}{\partial s}(C\cos\theta) + q_x = 0, \tag{C2}$$

where eqs (C1) and (C2) correspond to the vertical and horizontal components of force, respectively. Assuming no compressional or shear stress at the slab end (at $s = 0$), these can be integrated over s:

$$(V\cos\theta) + (C\sin\theta) + \int_0^s (q_z + \rho_l g l)\,ds = 0, \tag{C3}$$

$$(V\sin\theta) - (C\cos\theta) + \int_0^s q_x\, ds = 0. \tag{C4}$$

© 2006 The Authors, *GJI*
Journal compilation © 2006 RAS

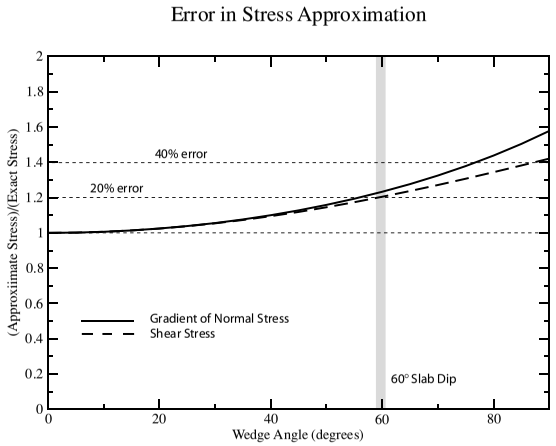

Figure B1. Accuracy of approximate solution for shear stress (τ_s) and gradient of normal stress ($\partial\sigma_n/\partial s$) on the surface of a slab below a viscously deforming wedge. Solutions are for a steady-state 'upper plate' wedge of infinite extent with a 'trench retreat rate' of one and a stationary upper surface. Lines show ratio of approximate stress computed using the equations of Appendix B divided by the exact analytical solution for a uniform viscosity wedge. The approximate method overestimates the shear stress and normal stress gradient along the slab surface by comparable amounts, reaching ~20 per cent for typical slab dips of 60°.

Multiplying eqs (C3) and (C4) by $\cos\theta$ and $\sin\theta$ respectively, and combining them to eliminate C, rearranging, and taking the derivative with respect to s yields

$$\frac{\partial V}{\partial s} + \frac{\partial \sin\theta}{\partial s}\int_0^s q_x\,ds + \frac{\partial \sin\theta}{\partial s}\int_0^s (q_z + \rho_l g l)\,ds + \rho_l g l\cos\theta + (q_x\sin\theta + q_z\cos\theta) = 0. \tag{C5}$$

Using a thin elastic sheet approximation to relate V to bending moment, M, and thence to slab deflection gives

$$V(s) = -\frac{\partial M}{\partial s} = -\frac{\partial}{\partial s}\left(\frac{D}{\cos\theta}\frac{\partial^2 w}{\partial s^2}\right), \tag{C6}$$

where D is the flexural rigidity. Noting that slab dip is related to deflection by

$$\sin\theta = -\frac{\partial w}{\partial s} \qquad \cos\theta = \left[1 - \left(\frac{\partial w}{\partial s}\right)^2\right]^{1/2}$$

and substituting into eq. (C5) yields an equation that governs the behaviour of the slab in response to externally applied stresses and internal density variations:

$$\frac{\partial^2}{\partial s^2}\left(\frac{D}{\cos\theta}\frac{\partial^2 w}{\partial s^2}\right) + \frac{\partial^2 w}{\partial s^2}\left(\int_0^s q_x\,ds - \tan\theta\int_0^s (q_z + \rho_l g l)\,ds\right) - q_n - \rho_l g l\cos\theta = 0. \tag{C7}$$

For the top of the slab beneath the frontal prism, we define:

$$q_n^t = (w_{\text{next}} + w_o - d_w)\rho_{\text{prism}} g$$

and for the top and bottom of the slab within the sublithospheric mantle:

$$q_n^t = \sigma_n^t\left[\frac{(w_{\text{next}} - w)\cos\theta}{v_n}\right] + P_{\text{static}}$$

$$q_n^b = \sigma_n^b\left[\frac{(w_{\text{next}} - w)\cos\theta}{v_n}\right] + P_{\text{static}},$$

© 2006 The Authors, *GJI*
Journal compilation © 2006 RAS

eq. (C7) is solved at each time step by formulating it as:

$$\frac{\partial^2}{\partial s^2}\left(\frac{D}{\cos\theta}\frac{\partial^2 w_{\text{next}}}{\partial s^2}\right) + \frac{\partial^2 w_{\text{next}}}{\partial s^2}\left(\int_0^s q_x\,ds - \tan\theta\int_0^s (q_z + \rho_l g l)\,ds\right) - \left(q_n^t + q_n^b\right) - \rho_l g l\cos\theta = 0, \tag{C8}$$

where w_{next} is the slab depth to be solved for at the next time step. We then solve eq. (C8) for w_{next} by fast inversion of a five-band matrix using values of all other variables as computed from the previous time step(s). The location of the asthenospheric nose is computed at each time step as described in the main text.

For the case of a viscous slab, with viscosity μ_p and thickness l_p, the equivalent expression to (C7) is:

$$\frac{\partial^2}{\partial s^2}\left(\frac{\mu_p l_p^3}{12\cos\theta}\frac{\partial^3 w}{\partial s^2 \partial_t}\right) + \frac{\partial^2 w}{\partial s^2}\left(\int_0^s q_x\,ds - \tan\theta\int_0^s (q_z + \rho_l g l)\,ds\right) - q_n - \rho_l g l\cos\theta = 0. \tag{C9}$$

This can solved as:

$$\frac{\partial^2}{\partial s^2}\left[\frac{\mu_p l_p^3}{12\Delta t\cos\theta}\frac{\partial^2(w_{\text{next}} - w)}{\partial s^2}\right] + \left[\frac{\partial^2(w_{\text{next}} - w)}{\partial s^2} + \frac{\partial^2 w}{\partial s^2}\right]\left(\int_0^s q_x\,ds - \tan\theta\int_0^s (q_z + \rho_l g l)\,ds\right) - \left(q_n^t + q_n^b\right) - \rho_l g l\cos\theta = 0. \tag{C10}$$

However, at viscosities above 10^{24} to 10^{25} Pa s, the algorithm developed from (C10) had numerical difficulties in its implementation. At these higher viscosities, we substituted another algorithm. Writing the viscous dw/dt in eq. (C9) as $v_R\,\partial w/\partial s$, then eq. (C9) can be written as a fifth order differential equation:

$$\frac{\partial^2}{\partial s^2}\left(\frac{\mu_p l_p^3 v_R}{12\cos\theta}\frac{\partial^3 w_{\text{next}}}{\partial s^3}\right) + \frac{\partial^2 w_{\text{next}}}{\partial s^2}\left(\int_0^s q_x\,ds - \tan\theta\int_0^s (q_z + \rho_l g l)\,ds\right) - \left(q_n^t + q_n^b\right) - \rho_l g l\cos\theta = 0. \tag{C11}$$

The algorithms corresponding to (C10) and (C11) yield virtually identical results for steady-state subduction over the range of viscosities for which we could obtain results from eq. (C10), with less than 1 per cent difference in trench migration rates and indistinguishable slab geometries.

© 2006 The Authors, *GJI*
Journal compilation © 2006 RAS

Subduction with Variations in Slab Buoyancy: Models and Application to the Banda and Apennine Systems

Leigh H. Royden and Laurent Husson

Abstract Temporal variations in the buoyancy of subducting lithosphere exert a first-order control on subduction rate, slab dip and the position of the associated volcanic arc. We use a semi-analytic, three-dimensional subduction model to simulate "unforced" subduction, in which trench motion is driven solely by slab buoyancy. Model rates of subduction and model slab dip respond almost immediately to changes in the buoyancy of the subducting lithosphere entering the trench; as more buoyant slab segments correlate with slower subduction rates and steeper slab dip. The results are largely consistent with observations from the Banda and southern Apennine subduction systems, where subduction slowed and ended shortly after the entry of continental lithosphere into the trench. Over a 2 m.y. period, model subduction rates decrease from ~70 mm/year to ~30 mm/year for the Banda Arc, and from ~40 mm/year to ~20 mm/year for the Apennine Arc. Increases in model slab dip and decreases in arc-trench distance are likewise consistent with hypocenter locations and volcanic arc position along the Banda and Sunda arcs. In contrast, a time period of ~10 m.y. is needed for model subduction rates to slow to near zero, much longer than the ~3 m.y. upper bound on the observed slowing and cessation of trench motion in the Apennine and Banda systems. One possible explanation is that slab break-off, or the formation of large slab windows, occurred during the last stages of subduction, eliminating toroidal flow around the slab and allowing the slab to steepen rapidly into its final position.

1 Introduction

Slab buoyancy provides the primary driving force for subduction (e.g., Forsyth and Uyeda, 1975; Chapple and Tullis 1977; Conrad and Lithgow-Bertelloni, 2004). However, several studies have revealed a poor correlation between observed slab buoyancy and subduction kinematics (Jarrard, 1986; Doglioni et al., 1999; Lallemand et al., 2005). This may reflect the importance of other factors that affect subduction rate and has led to a number of studies that explore a wide range of factors that might affect subduction (e.g., Kincaid and Olson, 1987; Funiciello et al., 2003; Schellart, 2004, Bellahsen et al., 2005; Royden and Husson, 2006; Capitanio et al., 2007; Billen and Hirth, 2007, Stegman et al., 2006). Alternatively, it may be that temporal variations in slab buoyancy exert a short-term effect on subduction that is as important as the mean buoyancy.

L.H. Royden
Department of Earth, Atmospheric and Planetary Sciences, M.I.T., Cambridge, MA 02139, USA, lhroyden@mit.edu

S. Lallemand and F. Funiciello (eds.), *Subduction Zone Geodynamics,*
DOI 10.1007/978-3-540-87974-9, © Springer-Verlag Berlin Heidelberg 2009

Temporal variations in slab buoyancy occur commonly during subduction, for example when oceanic plateaus, seamounts or fragments of continental crust enter a subduction system. Thus by examining the relationship between slab density, slab geometry and subduction rate from theoretical models, and comparing these results to the time-history of subduction and magmatism in natural systems, we can begin to understand how variations in slab density may control a host of geological phenomenon. Yet, despite the extensive literature on subduction process, only a handful of studies have examined the role of variable slab buoyancy in the subduction process. These have generally aimed at examining the role of slab buoyancy in controlling slab shape (i.e., van Hunen et al., 2004) and arc curvature (i.e., Morra et al., 2006). In contrast, Martinod et al. (2005) use an analog approach to show that buoyant slab material entering the subduction system both steepens the slab angle and reduces the velocity of the trench. In this paper we investigate more systematically the length and time-scales over which variations in slab buoyancy control on subduction velocity, slab geometry and subduction dynamics, with a brief comparison to two natural subduction systems.

2 Subduction Model

We use a semi-analytical model updated from Royden and Husson (2006) that includes a Newtonian viscous mantle and a slab of finite width, as measured parallel to the trench. Figure 1 shows the geometry and primary sources of stress on the slab. This model uses approximate solutions for toroidal flow around the slab and for flow above and beneath the slab. This provide a reasonable approximation of stress on the slab at distances of more than ~100 km from its side boundaries (Royden and Husson, 2006). We have neglected possible curvature of the trench and slab along strike, which also affects stress on the slab near the side boundaries.

A uniform viscosity is assigned to the slab, making up a viscously competent zone that is 50 km thick and localized within the upper (cold) portion of the slab (Table 1). Subduction is assumed to be "unforced," in that the rate of subduction and trench migration are determined only by the negative buoyancy of the subducted lithosphere and viscous stresses induced in the slab and surrounding mantle. In the model, far-field motions of the plates do not contribute to the subduction process nor play a role in trench migration. Unless otherwise specified, the foreland (unsubducted lithosphere in front of the trench) is assumed to be stationary relative to the underlying lower mantle; therefore the rate of trench motion is equal to the rate of subduction (see later portions of this paper and Royden and Husson, 2006, for alternative assumptions). This is equivalent to the analog models that fix the end of the slab to the sidewall of the tank (e.g., Kincaid and Olson, 1987).

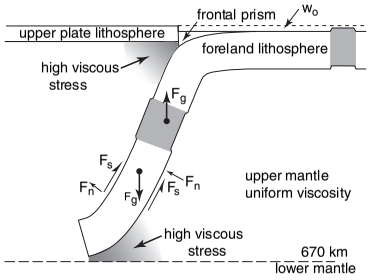

Fig. 1 Schematic diagram of the model subduction zone. *Shaded areas* within the slab denote low-density (high buoyancy) slab segments. F_g, F_n and F_s are gravitational force, and normal and tangential components of viscous forces, respectively. w_0 is pre-subduction water depth of the foreland. *Shaded areas* in the upper mantle outside of the slab denote areas of high viscous stress on the slab due to the flux of mantle in or out of this constricted region

Table 1 Model parameters for Figs. 2 and 3

w_a	Mid-ocean ridge depth	2.5 km
l	Thickness of slab	100 km
	Trench length	600 km
	Thickness of upper plate	50 km
ρ_a	Density of the asthenosphere	3,300 kg m^{-3}
ρ_c	Density of the crust/frontal prism	2,800 kg m^{-3}
ρ_w	Density of water	1,000 kg m^{-3}
	Viscosity of the upper mantle (excluding slab and lithosphere)	2.5×10^{20} Pa
	Viscosity of slab "core"	10^{23} Pa s
	Thickness of slab "core"	50 km

Subduction is "mature" in that the end (or "tail") of the slab extends to the top of the lower mantle, treated in this paper as a rigid boundary. This condition prevents mantle flow beneath the slab tail (Garfunkel et al., 1986). Note, however, that the position of the slab tail is determined only by viscous forces within the slab and upper mantle. The slab position is not *a priori* fixed with respect to the top of the lower mantle. This differs from tank models where the deep slab becomes fixed onto the base of the tank (see Funiciello et al., 2003). Because the process of slab deformation within the transition zone is poorly known, it is not clear which, if either, of these assumptions is more correct. There should be little difference between them when the foreland lithosphere, and thus the slab tail, is relatively stationary with respect to the top of the lower mantle. However, differences in predicted behavior could become large when there is rapid relative motion between them.

Prior to subduction, slab buoyancy can, to first order, be linearly equated with the bathymetry of the soon-to-be-subducted lithosphere (its "pre-subduction" water depth, w_o). For a slab thickness of 100 km and an asthenospheric density of 3300 kg/m^3, each kilometer change in pre-subduction water depth translates to a change in mean slab density of ~23 kg/m^3. Slab buoyancy is neutral if w_o equals ~2.5 km, very negative if w_o is ~6.5 km (e.g., old oceanic lithosphere), and very positive if w_o is ~0 km (e.g., typical continental lithosphere). (See Royden and Husson, 2006, for further discussion of buoyancy and bathymetry.) Note, however, that slab buoyancy is a function only of the lithospheric material that is actually subducted and the density of that material as it is subducted. If sediments or crust are stripped from the slab as it enters the subduction zone, or if phase changes occur during subduction, the slab buoyancy changes accordingly. In this paper we ignore both of these effects, although they could easily be included with appropriate changes in slab density with depth.

3 Subduction of a Model Foreland

In Figs. 2 and 3 we show results for subduction of a model foreland consisting of a deep oceanic domain (w_0 = 6.5 km) embedded with several contrasting buoyancy domains, including a continental island (250 km wide, w_0 = 0 km), an oceanic plateau (800 km wide, w_0 = 3.5 km), and a continental margin (w_0 = 0 km) (Fig. 2a). Slab buoyancy is varied in a direction normal to the trench while all other parameters are held constant.

After subduction of oceanic lithosphere has achieved a steady-state geometry and rate (at ~70 mm/year), the contrasting buoyancy domains reach the trench and are subducted sequentially. When the continental island

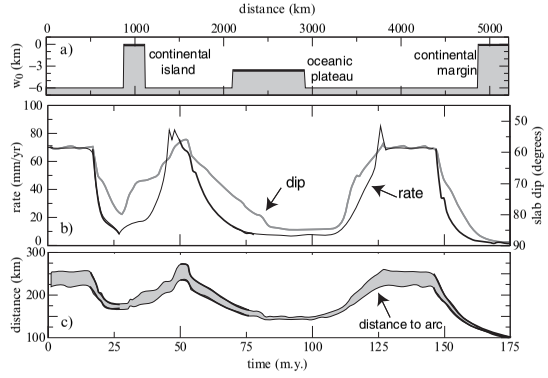

Fig. 2 (**a**) Pre-subduction water depth for the model foreland to be subducted, as a function of horizontal distance. Large water depths are equated with large negative slab buoyancy, see text for details. *Thick solid lines* represent more buoyant segments of the foreland, consistent in all panels. (**b**) Subduction rate (*black line*) and slab dip at 100 km depth (*gray line*) as a function of time. (**c**) Distance from the trench to the volcanic arc, taken as the horizontal distance over which slab deflection increases from 2 to 100 km (lower value) or to 150 km (higher value)

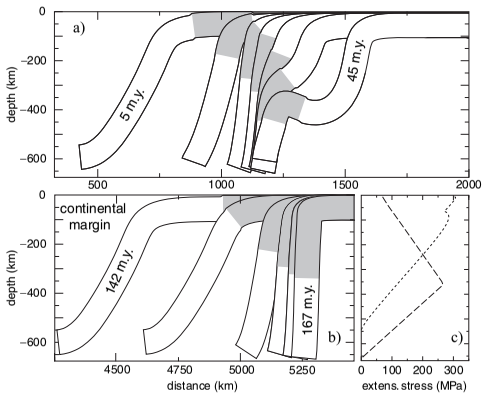

Fig. 3 Slab geometries corresponding to two subduction events of Fig. 2: (**a**) subduction of the continental island and (**b**) subduction the continental margin. *Shaded slab* units denote continental lithosphere. The time interval between slab positions is 5 m.y. with beginning and ending times as indicated. (**c**) Extensional stress along the subducted slab for steady-state subduction of oceanic lithosphere and after subduction of a continental margin

enters the trench and reaches the uppermost asthenosphere (~65 km depth), the rate of subduction drops abruptly and trench retreat slows to 5–10 mm/year (Fig. 2b). Subsequently, as the leading edge of the next oceanic segment enters the trench and reaches the uppermost asthenosphere, the subduction rate increases again to ~70 mm/year. A similar pattern of decreasing and increasing rate occurs with subduction of the oceanic plateau. Finally, rates slow and subduction is terminated when the continental margin enters the system; its leading edge is ultimately subducted to ~300 km depth km (Fig. 3, see also Ranalli et al., 2000; Regard et al., 2003).

The time-scale over which subduction rates respond to changes in slab buoyancy is generally on the order of just a few million years. When subduction rates change in response to slab buoyancy, the rates of change can be rapid only when the subduction rate is rapid. This is because each new lithospheric segment, with new buoyancy, enters the system at the rate of subduction, and the subduction system adjusts to the new slab buoyancy accordingly. Thus rapid changes in subduction rate can only occur when the subduction velocity is high; when subduction velocity is low, changes in subduction rate must occur slowly, but the rate of change can become rapid as the subduction rate speeds up.

Model steady-state subduction of the dense oceanic slab occurs at an average dip of ~60–65° (Figs. 2b and 3). When continental or plateau lithosphere enter the system, the slab steepens to more than 80° because the buoyant part of the slab at shallow depth resists sinking and slows the rate of trench retreat; meanwhile the deeper, denser part of the slab continues to sink at a faster rate. Flattening of the shallow slab occurs when dense lithosphere follows buoyant lithosphere into the trench because the dense slab at shallow depth sinks more rapidly than the buoyant material at greater depth. Thus there is a strong correlation between slab dip and trench migration rate (Fig. 2b). For narrow, highly buoyant slab segments, the dip of the slab may become inverted at depth, with a local depth-minimum coinciding with the buoyant slab segment (Fig. 3a).

Equating the distance from the subduction boundary to the volcanic arc with the horizontal distance over which slab deflection increases from 2 to 100 and 150 km, the distance from the subduction boundary to the volcanic arc is ~220–250 km during steady-state oceanic subduction for the parameters used in this paper (Fig. 2c). This decreases to ~150–170 km during subduction of the continental island and oceanic plateau areas. The greatest change in the location of the volcanic arc occurs when subduction terminates

against the continental margin and the distance from the thrust belt to the volcanic arc is decreased to ~100 km. The precise distance to the arc is highly sensitive to factors like the density of material in the frontal prism (Fig. 1), but the significant decrease in arc-trench distance during slowing of subduction is a robust feature of the model results.

4 Case Studies: Banda and Apennine Systems

The subduction model used here supposes that subduction occurs solely as a result of negative slab buoyancy, so the model results are not applicable to orogenic belts like the Himalaya, which accommodate rapid inter-plate convergence driven largely by far-field forces (e.g., Conrad and Lithgow-Bertelloni, 2004). It is best applied to unforced subduction systems that display upper-plate extension concurrent with subduction, such as those of the Mediterranean region (e.g., Malinverno and Ryan, 1986; Wortel and Spakman, 2000; Royden, 1993a, b; Jolivet and Faccenna, 2000; Faccenna et al., 2003), and the region extending eastward from Indonesia to the Pacific plate (Hall, 1996; Charlton, 2000; Daly et al., 1991; Rangin et al., 1990; Hinschberger et al., 2000). The Apennine and Banda Sea systems offer excellent opportunities to compare model results with observations in systems where subduction has terminated following entry of continental lithosphere into the subduction zone. Conversely, there are also subduction systems where an increase in subduction rate can be correlated with entry of denser lithosphere into the trench, but the amount of geologic information needed to document rates and timing renders such comparisons beyond the scope of this paper.

4.1 Geological Settings

Subduction of Australian lithosphere northward beneath the Banda Arc occurred prior to Pliocene time at a rate of ~70 mm/year (Fig. 4a, after Hinschberger et al., 2000). The pre-subduction depth, w_o, of the subducted oceanic lithosphere was probably similar to that observed today in the adjacent Indian Ocean, ~5.7 km. During Pliocene time, the eastern end of the subduction system encountered the continental margin of northwestern Australia and arc-continent collision occurred diachronously from west to east. During subduction of the margin, w_o decreased to its current value of ~0.05 km. The rate of subduction dropped to zero by 0.5–1.0 Ma while to the west (Sunda arc), subduction of oceanic lithosphere continues at ~70 mm/year (Kreemer et al., 2000; Richardson and Blundell, 1996; Hughes et al., 1996). Thus the Banda Sea offers an excellent opportunity to observe the reaction of subduction system to the entry of continental material into the trench, and at the same time to observe steady-state subduction of oceanic lithosphere (Sunda arc) that is probably similar to that of the Banda arc prior to collision.

The Late Cenozoic Apennine system consumed mixed oceanic and continental lithosphere along a west-dipping subduction system (Fig. 4b). Reconstruction of the southern Apennines suggests a Late Miocene subduction rate of ~30–50 mm/year or perhaps higher (e.g., Patacca et al., 1990; Fig. 5b, detailed rates taken from the unpublished work of P. Scandone, pers. com., 2006, average rate from Faccenna et al., 1997). The apparent oscillations in rate are probably artifacts of an incomplete geological record, and the maximum rates are probably the more significant. In any case, we choose a rate of 40 mm/year as the pre-collisional rate of subduction for the Apennine system. In Pliocene time, the southern Apennine trench encountered the continental Adriatic lithosphere and thrusting and subduction had

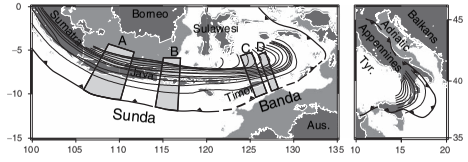

Fig. 4 Location maps for the Banda Arc and Apennine subduction systems. *Boxes* show locations of swath profiles for earthquake hypocenters in Fig. 6. Slab contours are 50 km isodepths, adapted from Sambridge and Gudmundsson (1998). Light gray domains are shallow water domains. *Solid and dashed bold curves* indicate active and fossil trench locations

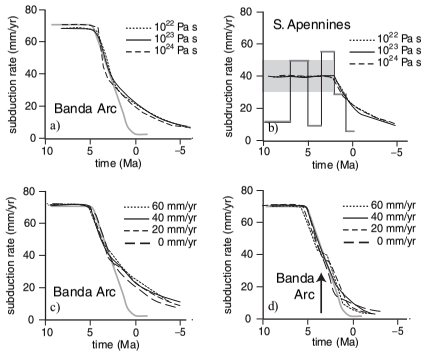

Fig. 5 Observed (*gray curves*) and model (*black curves*) rates of subduction for the Banda arc the Southern Apennines. Parameter values are given in Table 2. (**a**), (**b**) Subduction rate versus time following entry of continental lithosphere into the trench at 5 Ma. Foreland velocity relative to the top of the lower mantle is zero. *Labeled curves* correspond to different values of slab viscosity. (**c**) Subduction rate versus time for the Banda Arc following entry of continental lithosphere into the trench at ~5 Ma. *Labeled curves* correspond to different imposed values foreland velocity (from foreland toward trench) relative to the top of the lower mantle. (**d**) Same as (**c**) except that slab detachment occurs at 470 km depth at the time indicated by the *vertical arrow*

Table 2 Parameters for Figs. 5 and 7

	Pre-subduction water depth	Northward foreland velocity (relative to lower mantle)	Slab viscosity	Mantle viscosity
Figure 5a (Banda)	5.7 km	0 mm/year	10^{22} Pa s	1.9×10^{20} Pa s
	5.7 km	0 mm/year	10^{23} Pa s	1.8×10^{20} Pa s
	5.7 km	0 mm/year	10^{24} Pa s	1.5×10^{20} Pa s
Figure 5b (Apennines)	5.0 km	0 mm/year	10^{22} Pa s	2.4×10^{20} Pa s
	5.0 km	0 mm/year	10^{23} Pa s	2.2×10^{20} Pa s
	5.0 km	0 mm/year	10^{24} Pa s	1.8×10^{20} Pa s
Figure 5c,d (Banda)	5.7 km	0 mm/year	10^{22} Pa s	1.9×10^{20} Pa s
	5.7 km	20 mm/year	10^{22} Pa s	2.1×10^{20} Pa s
	5.7 km	40 mm/year	10^{22} Pa s	2.4×10^{20} Pa s
	5.7 km	60 mm/year	10^{22} Pa s	2.7×10^{20} Pa s
Figure 7	5.7 km	0 mm/year	10^{23} Pa s	1.8×10^{20} Pa s
	5.7 km	0 mm/year	10^{24} Pa s	1.5×10^{20} Pa s

ended by Quaternary time (see e.g., Patacca et al., 1990; Faccenna et al., 2001; Jolivet and Faccenna, 2000).

4.2 Model Parameters

The transition from oceanic to continental foreland was modeled for these two systems using the same parameters as in Fig. 2 and Table 1, except as noted in Table 2. In particular, the pre-subduction water depth of oceanic lithosphere subducted in the Banda region was estimated from the depth of the adjacent ocean basin (5.7 km for the Banda Arc). The pre-subduction water depth for the deepwater portions of the Apennine slab is unknown, so we chose a moderate depth of 5 km. In both cases the pre-subduction water depth of continental portion of the lithosphere is set to sea-level. A range of slab viscosities, from 10^{22} to 10^{24} Pa s, were used in the model runs, with the viscosity of the surrounding mantle chosen in each case to provide a subduction velocity of ~70 mm/year for the Banda system and ~40 mm/year for the Apennine system.

4.3 Subduction Rates

Model rates of subduction are in excellent agreement with the rapid termination of subduction within the Apennine and Banda systems for the initial period of slow-down, with velocities slowing down from ~70 to ~30 mm/year over a 2 m.y. period for the Banda Sea model, and from ~40 to ~20 mm/year over a 2 m.y. period

for the Apennine system (Fig. 5a and b). This indicates that the timescale over which subduction initially responds to changes in slab buoyancy is similarly rapid in the natural systems and in the model, and is largely independent of slab viscosity. However, for all slab viscosities, the latter stages of subduction termination are significantly faster in the observed systems than in the model results. In particular, the slowing of model subduction from 20 to 0 mm/year occurs over at least 10 m.y., with a gradual slowing of rate, while subduction in the Apennine and Banda systems terminates abruptly.

One possible source of the mismatch between observed and model results is the imposed velocity of the foreland relative to the top of the lower mantle (see e.g., Schellart, 2005). The foreland lithosphere for the Apennine subduction system is approximately stationary, or at least not moving very rapidly, in the hot spot reference frame (e.g., Gordon and Jurdy, 1986). Its motion with respect to the top of the lower mantle is, presumably, similar. However, the Indian-Australian plate (the foreland for the Banda subduction system) is moving northwards in the hotspot reference frame at ~60 mm/year, bringing into question the importance of the absolute velocity of the foreland with respect to the top of the lower mantle.

Figure 5c shows the model decrease in subduction rate expected for imposed foreland velocities, relative to the top of the lower mantle, ranging from 0 to 60 mm/year, in a direction orthogonal to and toward the trench. In order to match the initial subduction velocity of ~70 mm/year and to keep the initial slab buoyancy consistent with a pre-subduction water depth of 5.7 km, the viscosity of the mantle had to be adjusted for each individual case (Table 2). With these constraints, there is little predicted variation in the rate at which subduction slows as a function of imposed foreland velocity, indicating that this is probably not the cause of the misfit between observations and model in the latter stages of subduction termination. This result is consistent with the Apennine and Banda systems exhibiting the same rapid termination in subduction regardless of foreland velocity. It appears that some process, not included in our subduction model, must be responsible for the rapid termination of subduction in the latter stages of continental margin subduction, as we discuss further below.

4.4 Slab Dip and Migration of the Volcanic Arc

A robust result of the model is that the slab dip steepens as buoyant material enters and descends into the subduction system. For example, Fig. 3 shows the model slab dip steepening from about 60–65° during steady-state subduction of oceanic lithosphere to 85° or more after buoyant lithosphere enters the trench. This compares favorably to the slab geometries indicated by earthquake hypocenters from the Sunda and Banda arcs (Fig. 6); the average slab dip in the Sunda arc, where oceanic lithosphere is being subducted in steady-state is ~55–60° between 200 and 400 km depth. The slab dip along the Banda arc, where subduction has ceased, is ~75–80°. Both model and observations show an increase in slab dip of about 20° during entry of the continental margin into the subduction system. The modern slab dip beneath the Apennines is also very steep, perhaps 80° or more (Lucente et al., 1999; Piromallo and Morelli, 2002).

Another robust result from the model is the migration of the volcanic arc (equated in the model with a depth of 100–150 km at the top of the subducted slab) toward the trench during subduction of buoyant lithosphere. Thus there is a strong correlation between subduction rate and the location of the volcanic arc. The modern position of the volcanic arc within the Southern Apennines is ~100 km from the thrust front, similar to

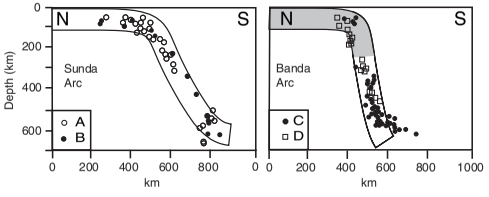

Fig. 6 Observed earthquake hypocenters (*dots*) from the Banda and Sunda arcs as given by Schoffel and Das (1999) and Das (2004). Swath locations shown in Fig. 4. *Solid lines* show model slab profiles from Fig. 3, for steady-state subduction of oceanic lithosphere (*left panel*) and following entry of the continental lithosphere (*shaded region*) into the subduction boundary (*right panel*, geometry corresponding to 152 m.y. in Fig. 2)

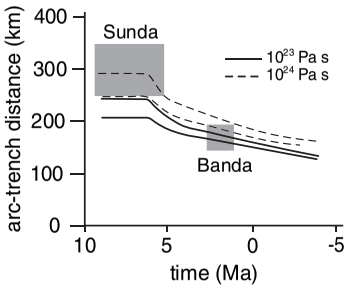

Fig. 7 Observed distance from the Banda and Sunda volcanic arcs to the adjacent trench or frontal thrust belt (*shaded squares*) as a function of time following entry of the continental lithosphere into the subduction boundary at ~5 Ma. *Lines* show model distances from trench to the front and back of the volcanic arc for the viscosities shown. Front and back of the model volcanic arc are equated with the positions where the upper slab boundary descends below 100 and 150 km depth, respectively

the model results of Fig. 2c after subduction of the continental margin. Within the Banda-Sunda arc system, the volcanic arc is ~250–350 km from the Sunda trench but only ~150–200 km from the inactive Banda thrust front. Using the Sunda arc as a proxy for the Banda arc prior to its interaction with the Australian continental margin, there appears to have been a 100 km decrease in the distance from the thrust front to the volcanic arc that is associated with subduction of the margin (Fig. 7). While we cannot rule out that some of the decrease in arc-trench distance might be due to shortening in the fore-arc region after the eruption of the last volcanic arc rocks at ~3 Ma, the fact that the slab dip is steeper slab the Banda region than in the Sunda region is also consistent with a decrease in the arc-trench distance during slowing and cessation of subduction.

5 Slab Detachment?

A number of authors (e.g., Buiter et al., 2002; Wortel and Spakman, 2000) have suggested that during the entry of continental lithosphere into a subduction zone, the lower part of the slab detaches from the upper part, in a process commonly referred to as "slab break-off" or "slab detachment." This process has been specifically suggested for both the Apennine (Buiter et al., 1998) and Banda arc (Elburg et al., 2004) systems. While a detailed investigation of this process is beyond the scope of this paper, we can make a preliminary assessment of whether this process could lead to a sufficiently rapid termination of the last stages of subduction, as indicated in Fig. 5.

Figure 5d shows the results for a simulated slab break-off at the time indicated by the vertical arrow. Although our model does not really allow for proper slab break-off, we simulate instantaneous slab break-off by truncating the slab at 470 km depth and setting the viscous stresses on the bottom of the slab to zero. This somewhat *ad hoc* modification of the forces on the slab eliminates the high stress area beneath the lower part of the slab (Fig. 1) and also eliminates the viscous stresses that result from toroidal flow around the slab (because mantle can flow through the region formerly occupied by the deep part of the slab). The results indicate a very rapid transition from slow subduction to no subduction, in good agreement with observations from the Banda Sea (Fig. 5d) and the Apennines (not shown but similar to Fig. 5d). Although not a precise simulation of slab break-off, these results suggest that slab break-off may provide a mechanism whereby the last stages of subduction occur very quickly.

Importantly, the reduction in weight of the deep slab is not the most important factor in causing rapid cessation of subduction. Rather, it is the creation of a shortcut for mantle flow that is critical in enabling rapid steepening of the slab into its final, stationary position. In particular, the creation of gaps in the slab enables rapid flow out of the geometrically confined, high-stress region beneath the deep slab (Fig. 1), thereby allowing for rapid motion of the deep slab.

6 Discussion and Conclusions

In general, rates of subduction and trench motion respond rapidly to changes in slab buoyancy. Subduction rates respond more rapidly to changes in slab buoyancy when the subduction rate is fast, and less rapidly when subduction rates are slow. Because subduction rates are faster for more negatively buoyant slabs, there is a discrepancy between the amount

of time that various buoyancy domains spend in the shallow part of the subduction system and their original extent within the foreland. In Fig. 2, continental lithosphere and oceanic plateau regions initially make up ~25% of the foreland, but account for ~55% of the subduction time. Thus the duration of events within a thrust belt cannot be used as a direct measure of the original extent of various buoyancy or facies domains because the low buoyancy regions will be over-represented in the duration of thrusting.

The dip of subducted slabs at shallow depth (~100 km) tracks closely with the rate of trench migration. For the parameters used in this paper, very dense slabs (old ocean) subduct at angles of ~60–65° whereas more buoyant lithospheres, like the oceanic plateau modeled in Fig. 2, subduct at steeper angles. (The precise slab dip depends on a variety of parameters and may vary from system to system even if slab buoyancy is identical). When all other parameters are held constant, the correlation between subduction rate and slab dip at 100 km depth is surprisingly good. This is counter to the common misconception that high-density slabs dip more steeply than low-density slabs (e.g., Luyendyk, 1970). The latter is correct if the trench retreat rate is held constant while slab buoyancy is varied, but not when both subduction rate and trench-migration rate are controlled by the negative buoyancy of the slab. This agrees with the fact that little correlation is found between observed slab dip and slab density (e.g., Jarrard, 1986; Heuret and Lallemand, 2005).

Because arc-magmas are generated above subducted slabs at depths of 100–150 km, there is also a correlation between the slab buoyancy, slab dip and location of the volcanic arc. As slab dips steepen, the volcanic arc should move closer to the trench (or front of the thrust belt). This occurs most markedly during subduction of a continental margin or other large buoyant object and is illustrated by the Banda/Sunda subduction system (Fig. 2). Equating the distance from the trench to the volcanic arc with the horizontal distance over which the slab depth increases from 10 to 100 km, the model distance from the trench to the volcanic arc decreases by ~100 km during subduction of the continental margin.

When subduction terminates, the viscous stresses on the slab disappear and the stresses on the slab arise only from its buoyancy. If subduction is terminated by subduction of a continental margin or other buoyant object, the depth to which the leading edge of the buoyant lithosphere can be subducted depends on its buoyancy and the buoyancy of deeper, denser portions of the slab. This is reflected in the extensional stresses transmitted along the slab (Fig. 3c). For a uniformly buoyant slab subducting in steady-state, the extensional stress along the slab increases toward the surface. (Note that extensional stress is not necessarily zero at the surface; only the vertical component of stress, integrated along the slab, must be zero.) When subduction terminates after subducting a continental margin, the extensional stress within the subducted slab is greatest at the former ocean-continent transition. This result is intuitive because at that stage there are no longer stresses on the slab from viscous flow in the surrounding mantle. Thus the extensional stress on the slab increases upwards to the point where the density of the slab is less that the density of the surrounding mantle. This suggests slab attenuation and possible slab detachment may be most likely to occur at this site (see Fig. 3c and Wortel and Spakman, 2000; Regard et al., 2003).

Our results apply largely to unforced subduction systems, where trench motion is controlled by slab buoyancy and not by far-field constraints on relative plate velocities. Modeling studies (e.g., Hassani et al., 1997) and observations (e.g., on the Nazca subduction zone, Gutscher et al., 1999) indicate that velocities imposed on the upper plate can play a large role in determining slab geometry and kinematics. For this reason, we have chosen natural examples where the upper plate lithosphere experienced extension during the subduction process, suggesting relatively little stress coupling between the over-riding and downgoing plates.

Nevertheless, some of the general concepts developed here may be extrapolated more broadly. We suggest that, for large plates like the Pacific, local and short-term variations in upper plate deformation, such as in the Japan or Kurile regions, may be more closely related to temporal and spatial variations in slab buoyancy than to the mean buoyancy of the slab. Even small variations in slab buoyancy result in speeding or slowing of trench motion. Although the change in rate may be but a minor fraction of the total trench velocity, even a change in rate of 5 mm/year over 10 m.y. can result in significant stretching or shortening of the upper plate. If this interpretation is correct, it helps to explain the apparent contradiction that slab buoyancy is the most important driver of subduction, yet there appears to be a lack of correlation between local slab buoyancy and associated upper plate deformation.

References

Bellahsen, N., Faccenna, C., and Funiciello, F., 2005, Dynamics of subduction and plate motion in laboratory experiments: Insights into the "plate tectonics" behavior of the Earth, J. Geophys. Res., 110, doi:10.1029/2004JB002999.

Billen, M.I. and Hirth, G., 2007, Rheologic Controls on Slab Dynamics, Geochem. Geophys. Geosyst. (G3), 8, Q08012, doi:101029/2007GC001597.

Buiter, S.J.H., Wortel, M.J.R., and Govers, R., 1998, The role of subduction in the evolution of the Apennines foreland basin, Tectonophysics, 296, 249–268.

Buiter, S.J.H., Govers, R., and Wortel, M.J.R., 2002, Two-dimensional simulations of surface deformation caused by slab detachment, Tectonophysics, 354, 195–210.

Capitanio, F.A., Morra, G., Goes, S., 2007, Dynamic models of downgoing-plate buoyancy driven subduction: Subduction motions and energy dissipation, Earth Planet. Sci. Lett., 262, 284–297.

Chapple, W.M., and Tullis, T.E., 1977, Evaluation of the forces that drive the plates, J. Geophys. Res., 82, 1967–1984.

Charlton, T.R., 2000, Tertiary evolution of the Eastern Indonesia collision complex, J. Asian Earth Sci., 18, 603–631.

Conrad, C.P., and Lithgow-Bertelloni, C., 2004, The temporal evolution of plate driving forces: Importance of "slab suction" versus "slab pull" during the Cenozoic, J. Geophys. Res., 109, doi:10.1029/2004JB002991.

Daly, M.C., Cooper, M.A., Wilson, I., Smith, D.G. and Hooper, B.G.D., 1991, Cenozoic plate tectonics and basin evolution in Indonesia, Mar. Pet. Geol., 8, 2–21.

Das, S., 2004, Seismicity gaps and the shape of the seismic zone in the Banda Sea region from relocated hypocenters, J. Geophys. Res., 109, doi:10.1029/2004JB003192.

Doglioni, C., Harabaglia, P., Merlini, S., Mongelli, F., Peccerillo, A., and Piromallo, C., 1999, Orogens and slabs versus their direction of subduction, Earth Sci. Rev., 45, 167–208.

Elburg, M.A., van Bergen, M.J., and Foden, J.D., 2004, Subducted upper and lower continental crust contributes to magmatism in the collision sector of the Sunda-Banda Arc, Indonesia, Geol. Soc. Am., 32, 41–44.

Faccenna, C., Mattei, N., Funiciello, R., and Jolivet, L., 1997, Styles of back-arc extension in the Central Mediterranean, Terra Nova, 9, 126–130.

Faccenna, C., Becker, T.W., Lucente, F.P., Jolivet, L., and Rossetti, F., 2001, History of subduction and back-arc extension in the central Mediterranean, Geophys. J. Int., 145, 809–820.

Faccenna, C., Jolivet, L., Piromallo, C., and Morelli, A., 2003, Subduction and the depth of convection in the Mediterranean mantle, J. Geophys Res., 108, doi:10.1029/2001JB001690.

Forsyth, D. and Uyeda, S., 1975, On the relative importance of the driving forces of plate motion, Geophys. J.R. Astr. Soc., 43, 163–200.

Funiciello, F., Faccenna, C., Giardini, D., and Regenauer-Lieb, K., 2003, Dynamics of retreating slabs: 2. Insights from three-dimensional laboratory experiments, J. Geophys. Res., 108, 2207, doi:10.1029/2001JB000896.

Garfunkel, C., Anderson, A., and Schubert, G., 1986, Mantle circulation and the lateral migration of subducted slab, J. Geophys. Res., 91, 7205–7223.

Gordon, R.G., and Jurdy, D.M., 1986, Cenozoic global plate motions, J. Geophys. Res., 91, 12389–12406.

Gutscher, M.-A., Olivet, J.-L., Aslanian, D., Eissen, J.-P., and Maury, R., 1999, The "lost Inca plateau": Cause of flat subduction beneath Peru?, Earth Planet. Sci. Lett., 171, 335–341.

Hall, R., 1996, Reconstructing Cenozoic SE Asia, in Hall, R., and Blundell, D., eds., Tectonic Evolution of SE Asia: Geol. Soc. Lond. Spec. Pub., 106, p. 203–224.

Hassani, R., Jongmans, D., and Chéry, J., 1997, Study of plate deformation and stress in subduction processes using two-dimensional numerical models. J. Geophys. Res., 102, 17951–17965.

Heuret, A., and Lallemand, S., 2005, Plate motions, slab dynamics and back-arc deformation, Phys. Earth Planet. Int., 149, 31–51.

Hinschberger, F., Malod, J.A., Réhault, J.P., Villeneuve, M., Royer, J.Y., Burhanuddin, S., 2000, Late Cenozoic geodynamic evolution of eastern Indonesia, Tectonophysics, 404, 91–118.

Hughes, B.D., Baxter, K., Clark, R.A., and Snyder, D.B., 1996, Detailed processing of seismic reflection data from the frontal part of the Timor trough accretionary wedge, eastern Indonesia, in Hall, R., and Blundell, D., eds., Tectonic Evolution of SE Asia: Geol. Soc. Lond. Spec. Pub., 106, 75–83.

Jarrard, R.D., 1986, Relations among subduction parameters, Rev. Geophys., 24, 217–284.

Jolivet, L. and Faccenna, F., 2000, Mediteranean extension and the Africa-Eurasia collision, Tectonics, 19, 1095–1106.

Kincaid, C., and Olson, P., 1987, An experimental study of subduction and slab migration, J. Geophys. Res., 92, 13, 832–13,840.

Kreemer, C., Holt, W.E., Goes, S., and Govers, R., 2000, Active deformation in eastern Indonesia and the Philippines from GPS and seismicity data, J. Geophys. Res., 105, 663–680.

Lallemand, S., Heuret, A., and Boutelier, D., 2005, On the relationship between slab dip, back-arc stress, upper plate absolute motion, and crustal nature in subduction zones, Geochem. Geophys. Geosyst., 6, Q09006, doi:10.1029/2005GC000917.

Lucente, F.P., Hiarabba, C.C., and Imini, G.C., 1999, Tomographic constraints on the geodynamic evolution of the Italian region, J. Geophys. Res., 104(B9), 20307–20327.

Luyendyk, B.P., 1970, Dips of downgoing lithospheric plates beneath island arcs, Geol. Soc. Am. Bull., 81, 3411–3416.

Malinverno, A., and Ryan, W., 1986, Extension in the Tyrrhenian sea and shortening in the Apennines as result of arc migration driven by sinking of the lithosphere, Tectonics, 5, 227–245.

Martinod, J., Funiciello, F., Faccenna, C., Labanieh, S., and Regard, V., 2005, Dynamical effects of subducting ridges: Insights from 3-D laboratory models, Geophys. J. Int., 163, 1137–1150.

Morra, G., Regenauer-Lieb, K., and Giradini, D., 2006, Curvature of oceanic arcs, Geology, 34, 877–880.

Patacca, E., Sartori, R. and Scandone, P., 1990, Tyrhennian basin and Apenninic arcs: Kinematic relations since late Tortonian times, Mem. Soc. Geol. Ital., 45, 425–451.

Piromallo, C., and Morelli, P., 2002, P-wave tomography of the mantle under the Alpine-Mediterranean area, J. Geophys. Res., 108, doi:10.1029/2002JB001757.

Ranalli, G., Pellegrini, R., and d'Affizi, S., 2000, Time-dependence of negative buoyancy and the subduction of continental lithosphere, J. Geodyn., 30, 539–555.

Rangin, C., Jolivet, L., and Pubellier, M., 1990, A simple model for the tectonic evolution of southeast Asia and Indonesian region for the past 43My, Bull. Geol. Soc. France 8, 889–905.

Regard, V., Faccenna, C., Martinod, J., Bellier, O., and Thomas, J.C., 2003, From subduction to collision: Control of deep processes on the evolution of convergent plate boundary, J. Geophys. Res., 108, doi:10.1029/2002JB001943.

Richardson, A.N., and Blundell, D.J. 1996, Continental collision in the Banda Arc. in Hall, R., and Blundell, D., eds., Tectonic Evolution of SE Asia: Geol. Soc. Lond. Spec. Pub., 106, p. 47–60.

Royden, L.H., and Husson, L., 2006, Trench motion, slab geometry and viscous stresses in subduction systems, Geoph. J. Int., doi: 10.1111/j.1365-246X.2006.03079.x.

Royden, L.H., 1993a, The tectonic expression of slab pull at continental convergent boundaries, Tectonics, 12, 303–325.

Royden, L.H., 1993b, Evolution of retreating subduction boundaries formed during continental collision, Tectonics, 12, 629–638.

Sambridge, M., and Gudmundsson, O., 1998, Tomography with irregular cells, J. Geophys. Res., 103, 773–781.

Schellart, W.P., 2004, Kinematics of subduction and subduction-induced flow in the upper mantle, J. Geophys. Res., 109, B07401, doi:10.1029/2004JB002970.

Schellart, W.P., 2005. Influence of the subducting plate velocity on the geometry of the slab and migration of the subduction hinge, Earth Planet. Sci. Lett., 231, 197–219.

Schoffel, H.-J. and Das, S., 1999, Fine details of the Wadati-Benioff zone under Indonesia and its geodynamic implications, J. Geophys. Res., 104, 13,101–13,114.

Stegman, D.R., Freeman, J., Schellart, W.P., Moresi, L., and May, D., 2006, Influence of trench width on subduction hinge retreat rates in 3-D models of slab rollback, Geochem. Geophys. Geosyst., 7, Q03012, doi:10.1029/2005GC001056.

van Hunen, J., van den Berg, A.P., and Vlaar, N.J., 2004, Various mechanisms to induce shallow flat subduction: A numerical parameter study, Phys. Earth Planet. Int., 146, 179–194.

Wortel, M.J.R., and Spakman, W., 2000, Subduction and slab detachment in the Mediterranean-Carpathian region, Science, 290, 1910–1917.

2.2 Le *rollback* est-il une vue de l'esprit ?

Les modèles de subduction ont souvent été appréhendé avec l'idée sous-jacente de *rollback*, c'est-à-dire de la migration de la fosse vers l'avant-pays de la plaque en subduction dans un référentiel absolu. Un tel régime semble compatible avec les subductions de taille modeste, comme les nombreuses subductions méditerranéennes (fig. 2.2). De fait, la notion de *rollback* a été largement porpagée par les géologues interessés par les subductions méditerranéenes, et hellénique en particulier [Faccenna et al., 1996, 2001, Jolivet & Faccenna, 2000, Royden, 1993]. C'est autour de l'exemple hellénique qu'a été tentée la généralisation du concept, étayée par des arguments indirects, comme la courbure des panneaux plongeants (fig. 2.3), la chimie des laves d'arrière-arc qui indiquent une contamination du reservoir mantellique localisé devant le panneau plongeant par le reservoir situé en arrière du slab [Pearce et al., 2001] ou l'anisotropie sismique dans le prisme mantellique dont la magnitude augmente avec la vitesse de migration de la fosse [Long & Silver, 2008].

Les tentatives de généralisation du concept de *rollback* passent par la confrontation aux données cinématiques, en particulier les vitesses de migration des fosses de subduction [Heuret & Lallemand, 2005, Schellart et al., 2007, Sdrolias & Müller, 2006]. Les fosses ont des vitesses de migration distribuées de façon presque uniforme entre un recul (jusqu'à 130 mm/an pour la subduction Tonga) et une avancée (jusqu'à 50 mm/an) (fig. 2.4). Ce constat remet en cause l'acception générale du *rollback*, qui ne prévoit pas la possibilité d'avancée de la fosse. (Ces vitesses ne sont pas indépendantes du référentiel absolu choisi pour le mouvement des plaques ; le référentiel choisi ici, basé sur la fixité des points chauds du Pacifique [Gripp & Gordon, 2002], est le plus dramatique. Les autres référentiels minimisent les vitesses d'avancée des fosses mais conservent la même dispersion des valeurs).

En prenant du recul sur les subductions, en *dé-zoomant*, le point de vue de la convection mantellique pourrait fournir des éléments de réponse. Malheureusement, les modèles les plus aboutis de convection [e.g., Foley & Becker, 2009] ne permettent pas encore de représenter de manière réaliste la tectonique des plaques et ne sont à présent d'aucun secours. Une alternative est la description analytique de la convection. La lithosphère océanique y est décrite comme une couche limite

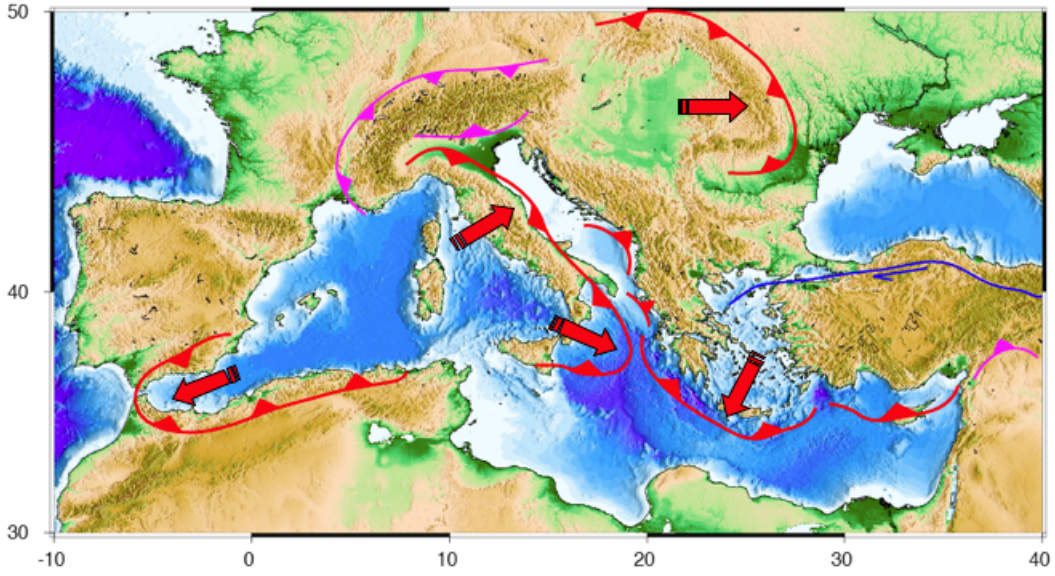

FIG. 2.2: Carte de la Méditerranée illustrant les subductions dont le comportement est en *rollback*. *Map of the Mediterranean domain showing rollback typ subduction zones (in red).*

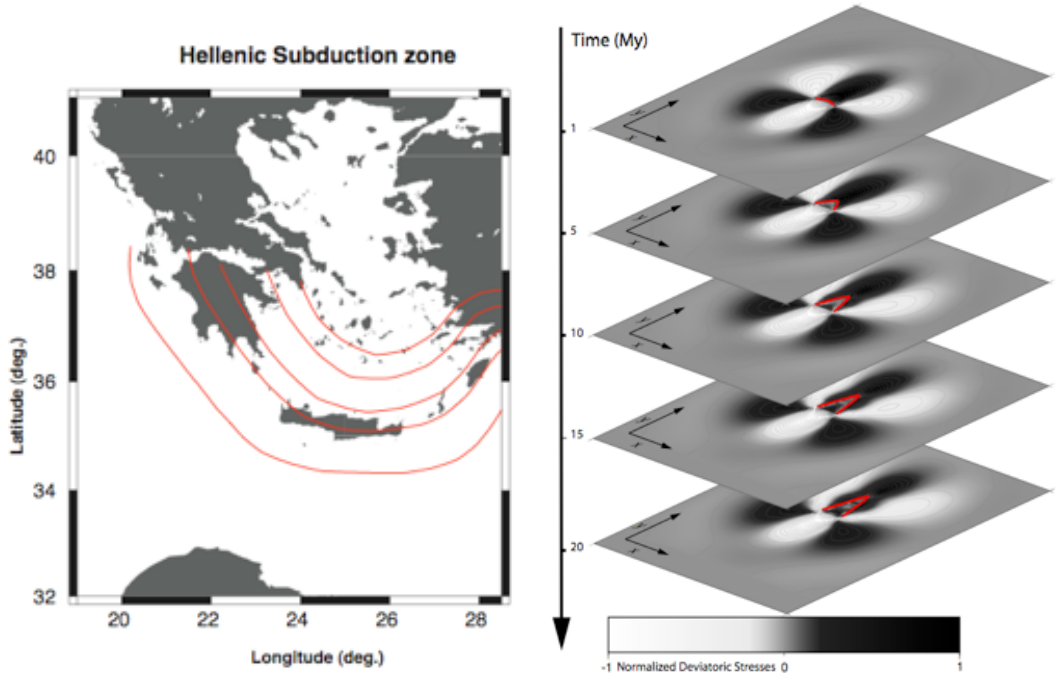

FIG. 2.3: Géométrie du panneau plongeants hellénique (isocontours 50 km [Gudmundsson & Sambridge, 1998]) et modèles de déformation d'un slab en retrait (le trait rouge indique la courbure du slab, voir section 2.4 [Loiselet et al., 2009]). *Interpolated geometry of the hellenic slab (isocontours every 50 km [Gudmundsson & Sambridge, 1998]), and models of slab deformation during rollback (red curve outlines slab curvature, see section 2.4 [Loiselet et al., 2009].*

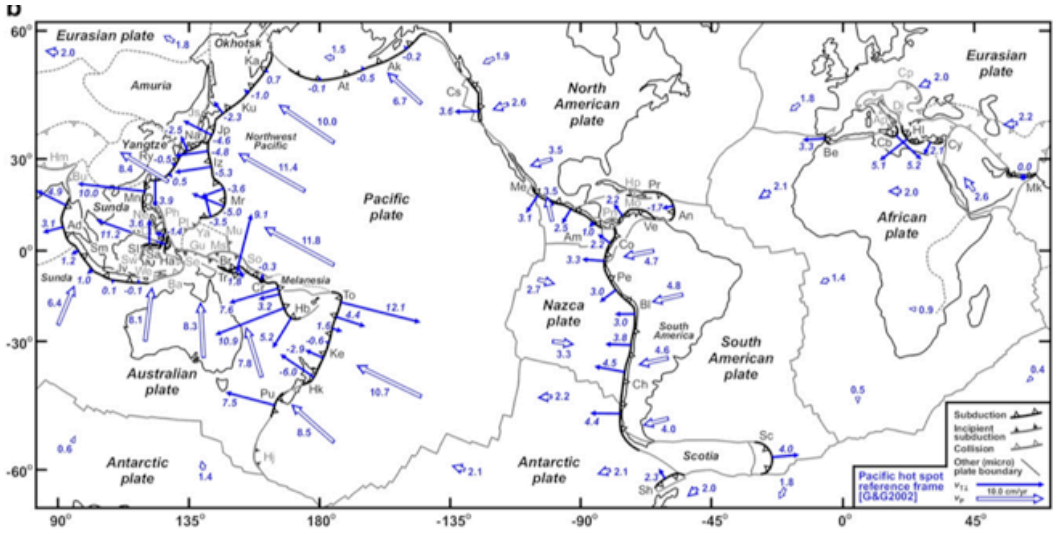

FIG. 2.4: Vitesses de migration des fosses de subduction dans le référentiel NUVEL1-HS3 (fixité des points chauds Pacifique [Gripp & Gordon, 2002]) [Schellart et al., 2007]. *Trench migration rates in the Pacific hotspots based reference frame NUVEL1-HS3 [Gripp & Gordon, 2002], [Schellart et al., 2007].*

thermique dont la subduction ne saurait se produire avant un âge critique et ne saurait subsister à la surface de la Terre au delà de cet âge, en contradiction avec les observations de distribution "triangulaire" des âges de la lithosphère océanique [Parsons, 1982, Rowley, 2002], c'est-à-dire que la probabilité de subduction est en apparence indépendante de l'âge de la lithosphère (fig. 2.5). La flottabilité de la lithosphère module efficacement les vitesses de *rollback* et pourrait expliquer ces divergences : une lithosphère dont la flottabilité est fortement négative devrait subducter plus efficacement. Les observations contrarient de nouveau la théorie, puisque c'est l'inverse qui est enregistré, dans l'acceptation de l'âge de la lithosphère océanique comme *proxy* pour sa flottabilité (fig. 2.6).

Au regard des divergences entre théorie et observations, il paraît nécéssaire d'élargir le champ d'investigation de la dynamique des subductions. La modélisation des subductions prises comme systèmes fermés reproduit de manière insatisfaisante la majorité des observations cinématiques. Dans le chapitre 4, je discute de l'impact de la circulation des plaques et du manteau à l'échelle globale sur la dynamique de subduction. Les plaques adajcentes á la plaque en subduction semblent jouer un rôle primordial dans la circulation globale de la lithosphère et du manteau. En particulier, elles affectent la dynamique du système Pacifique dans son ensemble, qui de par sa dimension porte l'essentiel des signaux cinématiques observés. Les

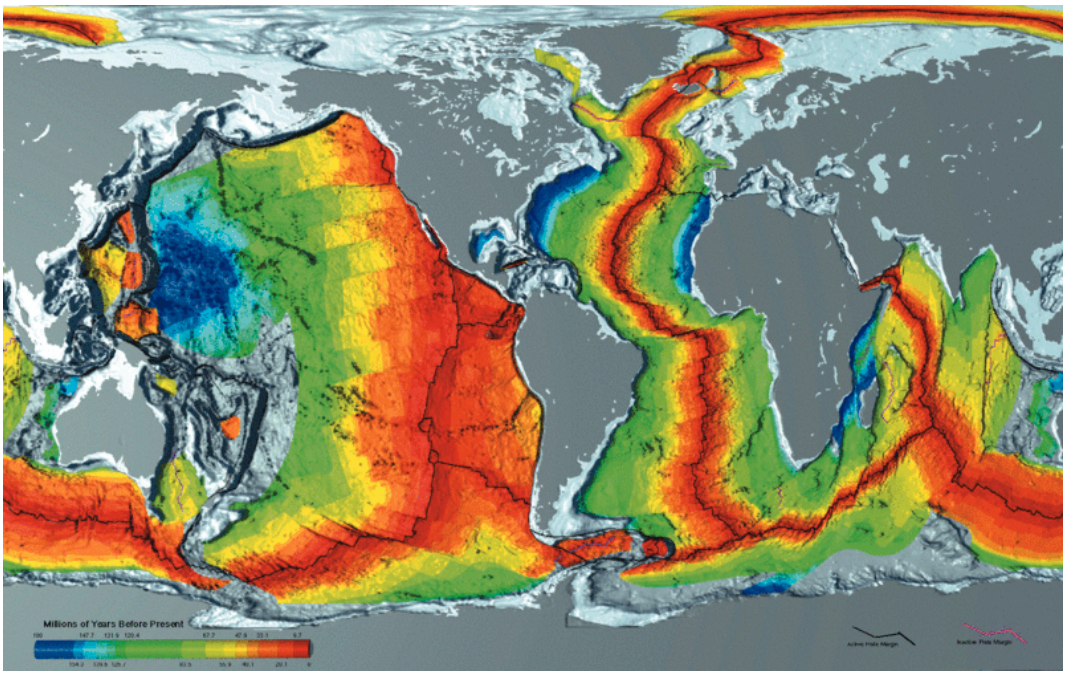

FIG. 2.5: Distribution des âges de la lithosphère océanique [Müller et al., 2008]. *Seafloor age map* [Müller et al., 2008].

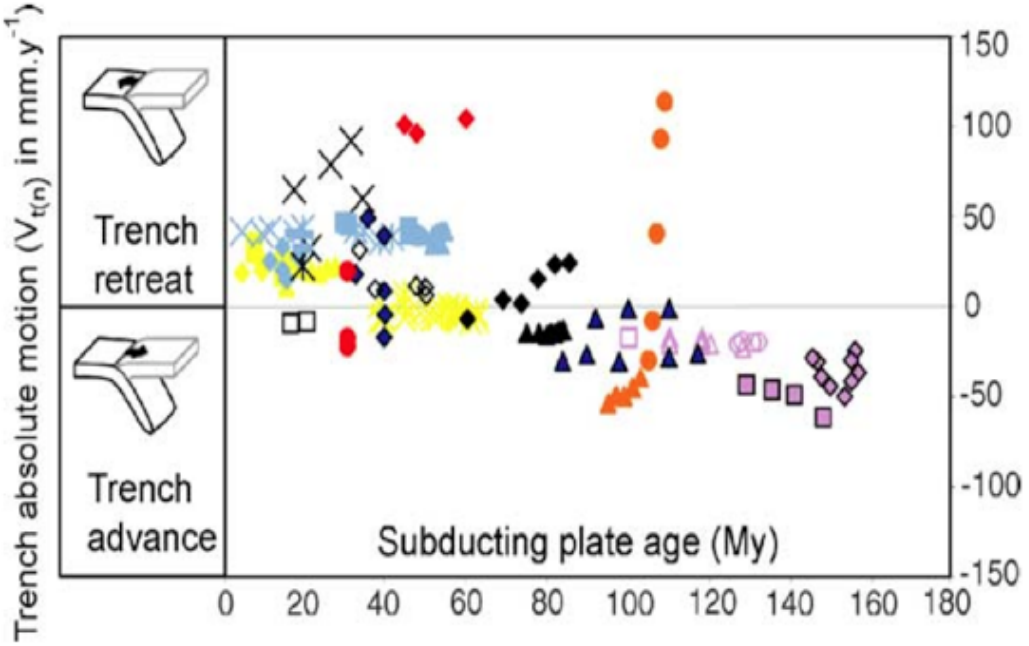

FIG. 2.6: Vitesses de migration des fosses en fonction de l'âge de la lithosphère pris comme *proxy* pour sa flottabilité [Heuret & Lallemand, 2005], dans le référentiel NUVEL1-HS3 [Gripp & Gordon, 2002]. *Trench migration rates as a function of lithosphere age, taken as a proxy for lithospheric buoyancy [Heuret & Lallemand, 2005], in the NUVEL1-HS3 reference frame [Gripp & Gordon, 2002].*

conséquences de la dynamique propre des plaques adjacentes, excitées par des l'ouverture des océans, l'entraînement par le manteau en convection, et les subductions adjacentes, sont multiples. Dans la section 2.3, deux exemples de cette incidence sont proposés à l'échelle de la subduction, puis à l'échelle de l'orogénèse.

A l'échelle de la Terre, le processus de *rollback* existe et il reste raisonnable de le considérer comme le comportement naturel, spontanné, des subductions. Cependant, la finitude de la Terre fait qu'il ne s'applique convenablement que à des systèmes privilégiés. Les conditions requises sont essentiellement (i) un isolement spatial de la zone de subduction des autres subductions et des forts courants mantelliques et (ii) un contrôle suffisament faible de la dynamique des plaques adjacentes sur la zone de subduction. Ceci s'applique à certaines subductions ayant un bassins d'arrière-arc suffisament développé pour que la cinématique de la plaque supérieure n'interagisse pas avec la subduction (Scotia par exemple) ou lorsque la plaque supérieure accompagne naturellement le retrait de la fosse à une vitesse comparable. C'est le cas unique de la subduction hellénique, où la plaque anatolienne poussée partiellement par la plaque arabe et coulissant le long de la faille nord-anatolienne, migre vers la fosse hellénique de manière à n'exercer que des contraintes faibles sur le contact entre les plaques (ceci se vérifie par le faible taux de déformation actuel de la mer Egée). Ainsi, la mer Egée, qui est le cas d'étude privilégié du mécanisme de *rollback*, est aussi l'exemple unique qui a conduit à la formalisation du concept. Ce raisonnement partiellement circulaire qui s'est établi sur les deux dernières décennies, est responsable des errements et mécompréhension entre modélisations et observations.

2.3 Interactions de la subduction avec les plaques supérieures

La discussion précédente (section 2.2) suggère que les plaques supérieures interagissent significativement avec les zones de subductions. Les sections qui suivent montrent un exemple où la cinématique de subduction est modulée par les plaques adjacentes et un exemple ou la subduction elle même rétroagit sur les mécanismes de déformation de la plaque supérieure, en permettant l'exhumation de roches de hautes pression et leur insertion dans le prisme orogénique.

2.3.1 Modulation de la subduction par les plaques adjacentes

En collaboration avec P. Yamato et co-auteurs, nous avons construits un modèle tridimensionnel de subduction en portant une attention particulière au rôle des plaques adjacentes. En effet, l'essentiel des modélisations -numériques et analogiques- réalisées à l'échelle de la zone de subduction sont composées d'une plaque isolée en subduction dans le manteau. Nous optons ici pour la démarche inverse, où la zone de subduction est simplifiée au maximum, mais où l'existence seule des plaques adjacentes (supérieure et latérales) suffit à moduler les vitesses de subduction. Ce choix simpliste se justifie par la nécessité d'un contexte géodynamique simplifié permettant (i) une mise en place technique et (ii) d'examiner en détail la complexité (rhéologique essentiellement) du panneau plongeant et du prisme mantellique.

GEOPHYSICAL RESEARCH LETTERS, VOL. 36, L07303, doi:10.1029/2008GL036942, 2009

Click Here for Full Article

Influence of surrounding plates on 3D subduction dynamics

P. Yamato,[1] L. Husson,[1] J. Braun,[1] C. Loiselet,[1] and C. Thieulot[2]

Received 9 December 2008; revised 4 March 2009; accepted 6 March 2009; published 3 April 2009.

[1] Our 3D modelling study shows that the presence of lithospheric plates around a subducting plate has a significant influence on subduction dynamics, in particular on trench retreat rate, slab dip, and lateral shortening of the subducting plate. Neighbouring plates prevent unrealistic plate behaviour with no need for complex rheologies. Because, at the Earth's surface, plates form a continuous shell, they should not be neglected. **Citation:** Yamato, P., L. Husson, J. Braun, C. Loiselet, and C. Thieulot (2009), Influence of surrounding plates on 3D subduction dynamics, *Geophys. Res. Lett.*, *36*, L07303, doi:10.1029/2008GL036942.

1. Introduction

[2] At the Earth's surface, tectonic plates form a complete shell and, therefore, no plate can be considered in isolation. A "complete" subduction system is thus made of four plates: the subducting, overriding and lateral plates.

[3] A variety of models have been proposed, using physical [e.g., *Bellahsen et al.*, 2005; *Funiciello et al.*, 2003a, 2006, 2008; *Schellart*, 2008], semi-analytical [*Royden and Husson*, 2006] and numerical methods [e.g., *Stegman et al.*, 2006; *Clark et al.*, 2008] to study the dynamics of subduction zones in 3D. However most studies, with the exception of a few [e.g., *Zhong and Gurnis*, 1995; *Royden and Husson*, 2006; *Espurt et al.*, 2008; *Regard et al.*, 2008; *Clark et al.*, 2008; *Bonnardot et al.*, 2008], considered the subducting plate in isolation, by focusing on its interactions with the surrounding mantle. In cases where the overriding plate is not included, one commonly assumes that it has no effect on mantle flow since it passively accompanies the retreating trench [*Bellahsen et al.*, 2005; *Funiciello et al.*, 2003b].

[4] However, because plates are stiffer and denser than the upper mantle, the presence or absence of lithospheric material in the upper mantle influences the velocity field in and around a subducting plate, and the dynamics of subduction will depart from the "intrinsic" dynamics of an isolated subduction system. Both the poloidal (downdip, in a vertical plane) and toroidal (at the slab edges, in a plane parallel to the surface) components of the return flow induced by the motion of the slab in the viscous upper mantle is not limited to the deepest parts of the subduction system but also reaches the surface; this flow may affect the motion of other plates and conversely, be influenced by them.

[5] In most models where the subducting plate is considered in isolation, the plate is not prevented from flowing laterally by the presence of neighbouring plates, as it is in natural systems. The deformation of the edges of the plate naturally occurs in purely viscous models, a phenomena that seems to be fortuitously limited in physical models by the possible action of surface tension or by the elastic properties of the material used [e.g., *Schellart*, 2008]. To prevent this artificial lateral flow, several *ad hoc* parameterizations have been used, including using a very high viscosity contrast between the plate and surrounding mantle, incorporating plasticity through a yield strength that is sufficiently high to prevent the horizontal deformation but small enough to permit slab bending [e.g., *Moresi and Solomatov*, 1998; *Stegman et al.*, 2006], imposing an arbitrary cut-off for stress transmission [*Husson*, 2006], or adding elasticity [e.g., *Bonnardot et al.*, 2008].

[6] Herein we quantify the impact of surrounding plates on subduction dynamics through a series of simple experiments carried out using a 3D numerical model of linear viscous fluid flow. It is not our purpose here to explore the many parameters of the system (e.g., geometry of the lithosphere, boundary conditions, viscosity, or density ratios): we choose a given setup in all our experiments and focus on the influence of surrounding plates.

2. Model Setup

[7] We have used the 3D code *DOUAR* described in details by *Braun et al.* [2008], originally designed for thermo-mechanical modelling. In this study, we are interested in understanding the basic interactions of a subducting plate with the surrounding mantle and adjacent plates; we have thus used a linear viscous rheology for all components of the system, neglecting non-linear effects arising from the thermal and stress-dependence of rheology.

[8] The initial model and the material parameters (effective viscosity and density) are presented in Figure 1a. Since the YZ plan at X = 0 in our model is a plane of symmetry, we only model one half of the slab along the left-hand side (X = 0) of the 3D box, leaving enough space to its right (i.e., between X = 0.5 and X = 1.0) to prevent most boundary effects. In all experiments, the initial geometry corresponds to an ongoing, though immature, subduction zone. The size of the square unit model box corresponds to 3000 km. The upper/lower mantle boundary is characterized by a viscosity jump at 660 km. The crust and mantle lithosphere are respectively 30 and 120 km thick. We chose thick lithosphere and crust in order to preserve a high resolution (additional tests are performed with thicknesses that are twice thinner). The resolution of the model is ~25 km between the top of the model and the upper-lower mantle boundary, where most of the deformation occurs, and 50 km elsewhere. The resolution is further improved by the *divFEM* algorithm used in *DOUAR* that can be tailored to represent density variations at an even smaller scale (~6 km)

[1] Geosciences Rennes, UMR6118, Université de Rennes 1, CNRS, Rennes, France.
[2] Department of Earth Sciences, Bergen University, Bergen, Norway.

Copyright 2009 by the American Geophysical Union.
0094-8276/09/2008GL036942$05.00

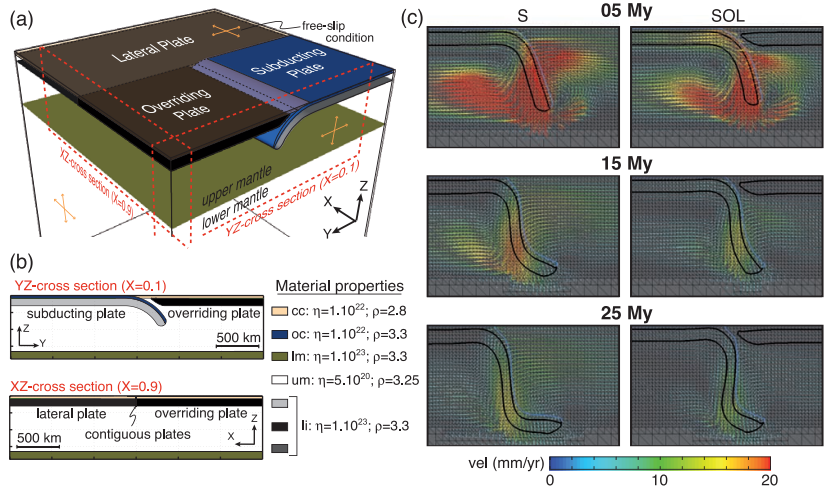

Figure 1. (a) 3D view of the model box at the beginning of the experiment. (b) Cross-sections showing plate stratification (crust and mantle) and material properties. *oc* and *cc*, oceanic and continental crust, *li*, *um* and *lm*: lithospheric, upper and lower mantle. Black, dark grey and light grey indicate overriding, lateral and subducting mantle lithosphere, respectively. (c) Subduction evolution during 25 My for the two models *S* and *SOL*. (YZ Cross-section taken at X = 0.1 corresponding to 300 km, see Figure 1a).

[*Braun et al.*, 2008]. Four configurations, that include respectively the Subducting plate only (S), the Subducting and Overriding plates only (SO), the Subducting and Lateral plates only (SL), and all plates together (SOL), were tested (Figure 1a). All models are nonetheless everywhere capped by a relatively buoyant, moderate viscosity crust, which in turns decreases the phenomena described below (e.g., trench retreat, lateral shortening and subduction).

[9] Material densities and viscosities are scaled to the upper mantle reference values (Figure 1b). In nature, the effective viscosity ratio between the subducting lithosphere and the upper mantle is thought to be in the range of 10 to 10^3 [e.g., *Hager*, 1984; *Davies and Richards*, 1992; *Mitrovica and Forte*, 2004]. We have thus used a viscosity ratio of 200, which also is a commonly used value that predicts realistic kinematics [e.g., *Funiciello et al.*, 2003a; *Schellart*, 2004, *Stegman et al.*, 2006, *Schellart*, 2008]. The lower mantle to lithosphere viscosity ratio is set to 1, high enough to limit slab penetration across the 660 km discontinuity. A crustal layer with a scaled viscosity of 20 caps the entire model; its scaled density is 1.015 over the subducting lithosphere and 0.8615 everywhere else (continental crust). All lithospheric mantle units are also contiguous, except for a rectangular gap between the subducting and the overriding lithosphere, where low viscosity material with upper mantle rheology facilitates the subduction process (Figure 1b). The crustal layer controls the kinematics [e.g., *Royden and Husson*, 2006] but the nature of this control is beyond our scope and we assign density and viscosity values that predict subduction velocities of a few mm.yr^{-1} (*v*-velocity component on Figure 2). Free-slip boundary conditions are imposed on all sides of the model and plate motion is resisted by the no-velocity conditions imposed at the plate boundaries (fixed plates, Figure 1a).

[10] This is an end-member situation in order to characterise the largest possible effect. Three-dimensional dynamic modelling of subduction zones is most relevant for small subduction zones. The behaviour of many small-sized subduction zones can thus be best approximated by the "fixed plate" setup we have used here, because their subduction rate is much faster than the plate convergence rate (e.g., Scotia, Hellenic, Tyrrhenian, Calabria…). We performed a few experiments with a free upper surface (no stress), but this required a much larger number of small time steps and did not lead to significantly different conclusions.

3. General Evolution of the Models

[11] In all experiments the subduction process evolves in three stages (Figure 1c) [see also *Bellahsen et al.*, 2005; *Stegman et al.*, 2006]: (1) the slab sinks in the upper mantle, (2) approaches the upper-lower mantle discontinuity and bends, (3) the slab tail (i.e., the bottom end of the slab) rests on the upper/lower mantle discontinuity and the system reaches a steady-state where further subduction is accompanied by trench retreat. The first sinking stage can be polluted by the initial geometry but can be assimilated to the transient stage existing between subduction initiation and

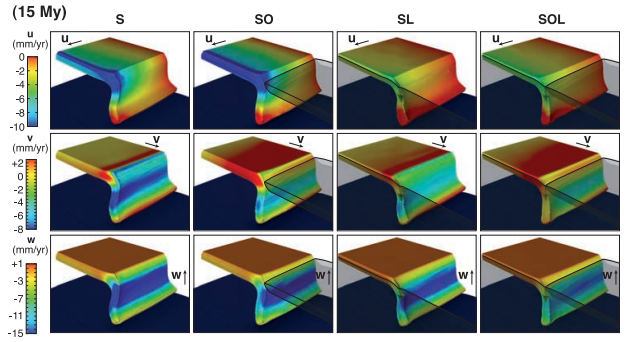

Figure 2. Velocity field components for the subducting plate for each experiment after 15 Myr. The shapes of the lateral and overriding lithospheres are presented as ghosts (the crust on the overriding and lateral plate is not shown).

'steady state' subduction. Trench retreat takes place when the slab approaches the 660 km discontinuity (stage 2), after an initial stage of advance (Figure 3a).

[12] In our models, the crust is advected in depth with the subducting lithosphere following the velocity field. The channel between the subducting and the overriding plates can thus evolve freely. The poloidal component of mantle flow is attenuated as the slab approaches the 660 km discontinuity (Figure 1c) because the upper mantle can no longer flow beneath the slab tail and the lower mantle.

[13] At intermediate depths (i.e., between 275 and 375 km), the slab dip is broadly similar in all experiments. During the first stage, slab dip increases from 60° to ~75–80°. In stage 2, it remains stable as the slab approaches the 660 km discontinuity, before increasing again during the bending of the slab tail along the 660 km discontinuity. In all experiments steady state is reached after ~20 Myr, with slab dips at intermediate depths ranging between 83° and 92°. The *SOL* and *SO* experiments display steeper slabs than in the *S* and *SL* experiments where slab dip is always lower than 90°.

4. Slab Rollback and Trench Retreat

[14] Subduction is accompanied by a faster rate of trench retreat in the experiments where the overriding plate is absent (y-component of the velocity field (*v*), mid. panel, Figure 2). This is illustrated in details in Figures 3a and 3b where the location (Figure 3a) and velocity (*v*-component, Figure 3b) of the trench are given as a function of time. Horizontal velocities, strain rates and deviatoric stresses along cross-sections from the models S and SOL are also given in the auxiliary material with description.[1]

[15] The poloidal flow induced by the sinking slab is made of two cylindrical cells, on either side of the slab. When the overriding plate is absent (Figure 1c), the cell in front of the slab extends from the slab tail to the surface. When the more viscous overriding plate is present, it does not extend to the surface but is limited to the base of the overriding plate. This difference influences subduction dynamics in two important ways. First, in the absence of overriding plate (*S* and *SL* experiments), the return flow amplifies trench retreat rates (Figure 2) by a factor of 2 to 5 (Figure 3b), as opposed to experiments with an overriding plate (*SO* and *SOL* experiments). Consequently, slab retreat rate will always be overestimated in experiments where the overriding plate is not accounted for. Secondly, the maximum velocity generated by the poloidal flow found at the top of the upper mantle, i.e. deeper with an overriding plate, explains the slightly higher slab dip values in *SO* and *SOL* than in *S* and *SL* (Figure 2).

5. Lateral Behaviour of the Subducting Plate

[16] Let's now consider the evolution of the slab in the third dimension (along the X axis, Figures 2, 3c, and S1). In both the *S* and *SO* experiments, the lateral edge of the subducting plate is not held by another plate alongside and is affected by trench parallel shortening (Figure 2, top). Significant shortening occurs for models with no lateral plate (Figure 3d) and is partly caused by subduction along the side of the subducting plate, driven by the negative buoyancy of the plate. The fact that the plate is fixed at the boundary induces additional extension on the plate, which stretches accordingly along the y-direction; this stretching has to be compensated by shortening along the x- and z-directions. Shortening is facilitated when the plate is not maintained laterally (*S* and *SO* experiments). After 20 Myr, total shortening values obtained are 3 times greater for the *S* and *SO* experiments (~15%) than for *SL* and *SOL* (~5%). As illustrated in Figure 3e where the maximum depth of the subducting plate measured along its edge is shown as a function of time for each of the four experiments, the presence of the neighbouring plate prevents shortening and thus the lateral subduction of the subducting plate.

[1] Auxiliary materials are available in the HTML. doi:10.1029/2008GL036942.

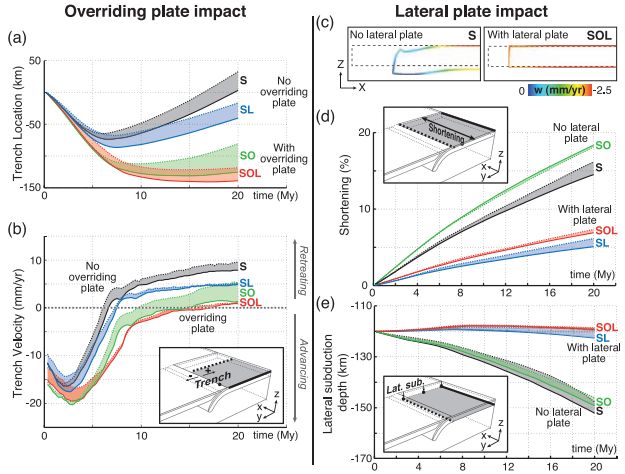

Figure 3. (a) Trench location and (b) velocity through time. Solid and dashed lines correspond to values calculated respectively at X = 0 and X = 0.35 (1050 km) from the right side of the model box (see inset). (c) Lateral behavior of the subducting lithosphere for the two models S and SOL after 20 Myr (XZ cross-section at Y = 0.1). Dashed and color lines correspond to the location of the subducting plate at t = 0 Myr and t = 20 Myr. (d) Lateral shortening of the subducting plate. (e) Maximum depth of lateral subduction (lat. sub.) reached by the lateral edge of the subducting plate. Solid and dashed lines correspond to the values at Y = 0 and Y = 0.4 (1200 km) from the backside of the model box (see inset).

Indeed, after 20 Myr, the plate edge has penetrated into the upper mantle to a depth of ~150 km for *S* and *SO* (Figure 3e), whereas it has remained at its initial depth when a lateral plate is included (*SL* and *SOL*, Figure 3c). Although the subducting lithosphere is equally gravitationally unstable in all four experiments and has thus the same tendency to subduct on all sides, the presence of a lateral plate reduces the negative buoyancy and thus prevents lateral subduction.

6. Conclusion and Discussion

[17] Surrounding plates in subduction systems affect the global dynamic of the subduction process in multiple ways. (1) The presence of an overriding plate modifies the poloidal flow generated by a subducting slab. Consequently, neglecting overriding plate leads to overestimating trench retreat velocities by a factor 2 to 5 and underestimating slab dips at depth. (2) The presence of a lateral plate prevents lateral shortening observed in many experiments where the subducting plate is considered in isolation; a phenomenon that leads to models including complex rheologies that prevent such undesirable effects [e.g., *Moresi and Solomatov*, 1998; *Stegman et al.*, 2006]. As previously shown [e.g., *King and Hager*, 1990; *Conrad and Hager*, 1999], 3D models composed of a single plate predict subduction velocities that have to be considered as upper bound values. However, in a purely viscous system, our experiments show that the absence of lateral plates leads to unrealistic lateral shortening and to the lateral subduction of the plate, which is not observed in natural subduction zones. Studies that do not account for the presence of surface plates may provide qualitative information that is only valid under the assumption that surrounding plates are weak (oceanic subduction in the presence of a well developed back-arc system, for instance). Our setup assumes that the plates are pinned to the sidewalls. When plates are ''free'', these effects are significantly reduced but still important. In real Earth, most small-scale subduction zones, for which our setup is relevant, are characterized by subduction rates that are much faster than the plate convergence rate (i.e., they are ''fixed''). In addition, the large model crustal and mantle lithosphere thicknesses seemingly enhance our results. However, because the model is Newtonian, assigning thinner lithosphere and crust leads to comparable results for a given amount of subduction (not for a given time), as confirmed by additional tests.

[18] Our results suggest that all plates must be included in modelling-based studies, where the effects of many parameters characterizing a subduction system (e.g., lithosphere thickness, viscosity and density ratios, friction between plates, velocity/stresses boundary conditions…) are explored.

[19] **Acknowledgments.** This work was supported by the ''Chair d'Excellence Senior de l'ANR'' (J.B.). Constructive reviews by L. Fleitout, D. Stegman and an anonymous reviewer are gratefully acknowledged.

References

Bellahsen, N., C. Faccenna, and F. Funiciello (2005), Dynamics of subduction and plate motion in laboratory experiments: Insights into the ''plate tectonics'' behavior of the Earth, *J. Geophys. Res.*, *110*, B01401, doi:10.1029/2004JB002999.

Bonnardot, M. A., R. Hassani, E. Tric, E. Ruellan, and M. Régnier (2008), Effect of margin curvature on plate deformation in a 3-D numerical model of subduction zones, *Geophys. J. Int.*, *173*, 1084–1094, doi:10.1111/j.1365-246X. 2008.03752.x.

Braun, J., C. Thieulot, P. Fullsack, M. DeKool, C. Beaumont, and R. Huismans (2008), DOUAR: A new three-dimensional creeping flow numerical model for the solution of geological problems, *Phys. Earth Planet. Inter.*, *171*, 76–91, doi:10.1016/j.pepi.2008.05.003.

Clark, S. R., D. Stegman, and R. D. Müller (2008), Episodicity in back-arc tectonic regimes, *Phys. Earth Planet. Inter.*, *171*, 265–279, doi:10.1016/j.pepi.2008.04.012.

Conrad, C. P., and B. H. Hager (1999), Effects of plate bending and fault strength at subduction zones on plate dynamics, *J. Geophys. Res.*, *104*, 17,551–17,571.

Davies, G. F., and G. F. Richards (1992), Mantle convection, *J. Geol.*, *100*, 151–206.

Espurt, N., F. Funiciello, J. Martinod, B. Guillaume, V. Regard, C. Faccenna, and S. Brusset (2008), Flat subduction dynamics and deformation of the South American plate: Insights from analog modeling, *Tectonics*, *27*, TC3011, doi:10.1029/2007TC002175.

Funiciello, F., C. Faccenna, D. Giardini, and K. Regenauer-Lieb (2003a), Dynamics of retreating slabs: 2. Insights from three-dimensional laboratory experiments, *J. Geophys. Res.*, *108*(B4), 2207, doi:10.1029/2001JB000896.

Funiciello, F., G. Morra, K. Regenauer-Lieb, and D. Giardini (2003b), Dynamics of retreating slabs: 1. Insights from two-dimensional numerical experiments, *J. Geophys. Res.*, *108*(B4), 2206, doi:10.1029/2001JB000898.

Funiciello, F., M. Moroni, C. Piromallo, C. Faccenna, A. Cenedese, and H. A. Bui (2006), Mapping mantle flow during retreating subduction: Laboratory models analyzed by feature tracking, *J. Geophys. Res.*, *111*, B03402, doi:10.1029/2005JB003792.

Funiciello, F., C. Faccenna, A. Heuret, S. Lallemand, E. Di Giuseppe, and T. W. Becker (2008), Trench migration, net rotation and slab-mantle coupling, *Earth Planet. Sci. Lett.*, *271*, 233–240, doi:10.1016/j.epsl.2008.04.006.

Hager, B. H. (1984), Subducted slab and the geoid: Constraints on mantle rheology and flow, *J. Geophys. Res.*, *89*, 6003–6015.

Husson, L. (2006), Dynamic topography above retreating subduction zones, *Geology*, *34*, 741–744.

King, S. D., and B. H. Hager (1990), The relationship between plate velocity and trench viscosity in Newtonian and power-law subduction calculations, *Geophys. Res. Lett.*, *17*, 2409–2412.

Mitrovica, J. X., and A. M. Forte (2004), A new inference of mantle viscosity based upon joint inversion of convection and glacial isostatic adjustment data, *Earth Planet. Sci. Lett.*, *225*, 177–189, doi:10.1016/j.epsl.2004.06.005.

Moresi, L., and V. Solomatov (1998), Mantle convection with a brittle lithosphere: Thoughts on the global tectonic styles of Earth and Venus, *Geophys. J. Int.*, *133*, 669–682.

Regard, V., C. Faccenna, O. Bellier, and J. Martinod (2008), Laboratory experiments of slab break-off and slab dip reversal: Insight into the Alpine Oligocene reorganization, *Terra Nova*, *20*, 267–273.

Royden, L. H., and L. Husson (2006), Trench motion, slab geometry and viscous stresses in subduction systems, *Geophys. J. Int.*, *167*, 881–905.

Schellart, W. P. (2004), Quantifying the net slab pull force as a driving mechanism for plate tectonics, *Geophys. Res. Lett.*, *31*, L07611, doi:10.1029/2004GL019528.

Schellart, W. P. (2008), Kinematics and flow patterns in deep mantle and upper mantle subduction models: Influence of the mantle depth and slab to mantle viscosity ratio, *Geochem. Geophys. Geosyst.*, *9*, Q03014, doi:10.1029/2007GC001656.

Stegman, D. R., J. Freeman, W. P. Schellart, L. Moresi, and D. May (2006), Influence of trench width on subduction hinge retreat rates in 3-D models of slab rollback, *Geochem. Geophys. Geosyst.*, *7*, Q03012, doi:10.1029/2005GC001056.

Zhong, S., and M. Gurnis (1995), Mantle convection with plates and mobile, faulted plate margins, *Science*, *267*, 838–843.

J. Braun, L. Husson, C. Loiselet, and P. Yamato, Geosciences Rennes, UMR6118, Université de Rennes 1, CNRS, Bat. 15, F-35042 Rennes CEDEX, France. (philippe.yamato.rennes1@gmail.com)

C. Thieulot, Department of Earth Sciences, Bergen University, Allegaten 41, N-5007 Bergen, Norway.

2.3.2 Exhumation des roches de hautes pressions

La dynamique propre des plaques supérieures affecte le régime de subduction. Cette interaction est bivalente. Un exemple probant est celui de la subduction indienne qui a ralentit lorsque la convergence a été empêchée par la collision continentale [Allègre et al., 1984, Patriat & Achache, 1984]. Cet évènement participe de la construction de l'édifice orogénique. En collaboration avec J-P. Brun, P. Yamato et C. Faccenna, nous explorons la possibilité que les comportements transitoires des zones de subduction puisse interagir avec la dynamique orogénique. Sur la base d'une chronologie des évènements géologiques en Méditerranée, les travaux récents des co-auteurs suggérent que l'entrée en subduction de lithosphères hétérogènes dans les fosses hellénique ou thyrrénienne créent un contexte favorable à l'exhumation des roches de hautes pressions (fig. 2.7).

L'oscillation géométrique du panneau plongeant et un régime cinématique transitoire associé [Royden & Husson, 2006] paraît propice à la remontée des roches de hautes pressions. L'article présenté ci-dessous quantifie la capacité de l'écoulement associé dans le prisme mantellique à faire remonter les roches de haute pression. Il ressort qu'un régime de subduction épisodique en *rollback* induit un flux ascendant, suffisant pour faire remonter les roches de haute pression, sans qu'il soit nécessaire d'invoquer d'autres mécanismes tels que l'érosion. Ce modèle respecte la cinématique en *rollback* du panneau plongeant, par opposition à la quasi-totalité des modèles existants ("channel flow" par exemple). Ce particularisme permet d'expliquer simplement l'exhumation des roches de haute pression.

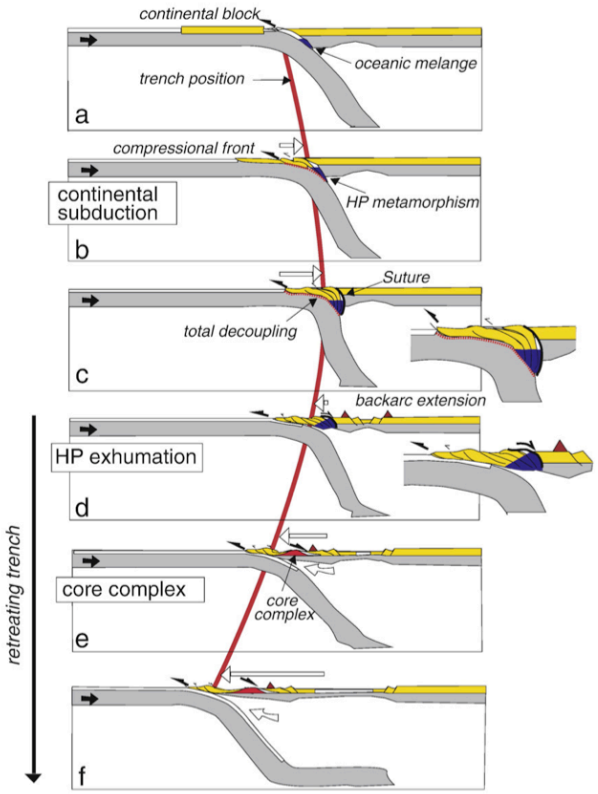

FIG. 2.7: Exhumation des roches de haute pression stimulée par l'évolution polyphasée de la subuction hellénique [Brun & Faccenna, 2008]. *Exhumation of HP rocks fostered by the polyphased evolution of the hellenic subduction [Brun & Faccenna, 2008].*

Geophys. J. Int. (2009) doi: 10.1111/j.1365-246X.2009.04372.x

Episodic slab rollback fosters exhumation of HP–UHP rocks

Laurent Husson,[1] Jean-Pierre Brun,[1] Philippe Yamato[1,2] and Claudio Faccenna[3]

[1]*Géosciences Rennes, CNRS* UMR6118*, Université Rennes* 1*,* 35042 *Rennes, France. E-mail: laurent.husson@univ-rennes1.fr*
[2]*ETH-Zürich, NO-E31 Sonneggstrasse* 5*,* CH-8092 *Zürich, Switzerland*
[3]*Dip. Scienze Geologiche, Università degli Studi "Roma TRE", Largo S.Leonardo Murialdo* 1*,* 00146 *Roma, Italy*

Accepted 2009 August 26. Received 2009 June 16; in original form 2009 March 25

SUMMARY

The burial–exhumation cycle of crustal material in subduction zones can either be driven by the buoyancy of the material, by the surrounding flow, or by both. High pressure and ultrahigh pressure rocks are chiefly exhumed where subduction zones display transient behaviours, which lead to contrasted flow regimes in the subduction mantle wedge. Subduction zones with stationary trenches (mode I) favour the burial of rock units, whereas slab rollback (mode II) moderately induces an upward flow that contributes to the exhumation, a regime that is reinforced when slab dip decreases (mode III). Episodic regimes of subduction that involve different lithospheric units successively activate all three modes and thus greatly favour the exhumation of rock units from mantle depth to the surface without need for fast and sustained erosion.

Key words: Subduction zone processes; Continental margins: convergent; Dynamics of lithosphere and mantle; High strain deformation zones.

1 INTRODUCTION

The burial and exhumation cycle of rocks that underwent high pressure and low temperatures with respect to a mean crustal geotherm (HP metamorphism) is related to the subduction process. Metamorphosed stacks of blueschists or eclogites are widely found in mountain belts (e.g. Maruyama *et al.* 1996; Ring *et al.* 1999; Chopin 2003). But the fact that not all orogenic systems display high pressure (HP) or ultra high pressure (UHP) rocks at the surface is remarkable: blueschists and eclogites are essentially found in convergence zones in which the lower subducting plate was anything but a uniform oceanic lithosphere during the burial cycle: the Alps (e.g. Handy *et al.* 1999; Rosenbaum & Lister 2005), Zagros (e.g. Agard *et al.* 2006), and the Himalayas (e.g. Allègre *et al.* 1984), but also smaller systems of the Mediterranean domain (e.g. Stampfli 2000; Jolivet *et al.* 2008), like the Hellenides and Tyrrhenian systems (e.g. Brun & Faccenna 2008) encompass most of Cenozoic HP rocks occurrences, as opposed for instance to the Andes that barely show HP rocks at surface level.

Downgoing lithospheric plates convey stacks of crustal rocks at depth. These rocks are either the crustal cover of the downgoing plate or scrapped off the upper plate crust. Their downward journey into subduction zones straightforwardly follows that of the subducting slab. Conversely, the exhumation of HP rocks that follows the burial episode is less intuitive. A plethora of models, both analogue (e.g. Chemenda *et al.* 1995, 1996; Boutelier *et al.* 2004) and numerical (e.g. Pfiffner *et al.* 2000; Burov *et al.* 2001; Gerya *et al.* 2002; Gerya & Stöckhert 2002; Yamato *et al.* 2007, 2008; Warren *et al.* 2008) have been proposed to explain the second part of the cycle, in which the rock aggregate goes towards the surface, paradoxically seemingly against the overall downward flow. In all models, HP rocks are either driven upward by their own buoyancy or advected by the surrounding flow. The following severe conditions are to be met to validate the models: comprehensive analysis of HP rocks (e.g. Ring *et al.* 1999; Agard *et al.* 2009) show that HP rock slices were assembled at depth and exhumed together. The residence time at depth lasts for ∼5–10 Myr; exhumation occurs within ∼10 Myr or less, that is, at rates that are in the same range as rates of plate boundary displacement (e.g. Rubatto & Hermann 2001). Such rates (up to 40–50 mm/yr) are therefore significantly higher than the highest sustained erosion rates that could be expected on the long term (much less than 10 mm/yr). In fact, two-stage exhumation is often identified, with a fast exhumation at depth, up to 10 kbar (10^9 Pa), followed by a slower event that can be attributed to erosion (e.g. de Sigoyer *et al.* 2000; Ernst 2001; Rubatto & Herman 2001; Parra *et al.* 2002; Walsh & Hacker 2004; Yamato *et al.* 2008), up to surface level.

Most previous models arbitrarily consider a stationary trench location (e.g. Chemenda *et al.* 1995; Ernst *et al.* 1997; Beaumont *et al.* 1999; Pfiffner *et al.* 2000; Gerya *et al.* 2002); such choice is very unfortunate; first, because it prevents any substantial extension in the upper plate that could favour the exhumation of rocks and, second, because the associated downward flow in the wedge tends to counter an upward motion of rocks at depth. Because these models ignore the dynamics of the mantle wedge itself that may vary depending on the subduction regime, and the potential advection of the rock within the wedge, they most often invoke more complex mechanisms like for instance the so-called subduction channel (e.g. England & Holland 1979; Cloos 1982; Shreve & Cloos 1986). In fact, stationary trenches are seldom observed, regardless of the

© 2009 The Authors
Journal compilation © 2009 RAS

reference frame (e.g. Lallemand *et al.* 2005), and slab rollback, that is, the motion of the entire subduction system (trench and subducting slabs) towards the foreland and relative to the lower mantle is the most natural behaviour of slabs (e.g. Funiciello *et al.* 2003). In addition, the subduction of a heterogeneous plate leads to transient subduction kinematics: subduction rate, trench migration rate and slab geometry very efficiently respond to heterogeneities in the plate rheology or buoyancy and are often unsteady (Martinod *et al.* 2005; Royden & Husson 2006). Thomson *et al.* (1998) or Brun & Faccenna (2008) noticed that such transient behaviour is observed in the Hellenides and in the Mediterranean domain in general (Royden 1993). Rollback-type settings favour the exhumation of HP rocks, chiefly because upper plate extension during rollback sets free space that can be filled up by rocks from underneath and therefore causes the exhumation of HP rocks (Gorczyk *et al.* 2007; Brun & Faccenna 2008; Faccenda *et al.* 2009).

The final exhumation of HP crustal slivers occurs inside the wedge. Field relationships and tectonic reconstructions show that their way back to the surface is often accompanied by 'syn-orogenic' extensional detachments positioned on the roof of the exhumed sliver (Platt 1986, 1993; Chemenda *et al.* 1995; Ring *et al.* 1999; Hacker *et al.* 2003; Jolivet *et al.* 2003, 2008). This deformation pattern suggests that during exhumation the overall backarc area was not under compression, although convergence and subduction were at work. This is typical of the Mediterranean realm, where exhumation was produced during the formation of the arc and often accompanied by backarc spreading (Jolivet *et al.* 2003; Brun & Faccenna 2008). In such tectonic context, most favourable to exhumation, the upper plate then plays a subordinate role, passively moving and deforming under the action of the return flow.

The aim of this work is to explore the advecting power of the sublithospheric wedge (simply referred to as 'wedge' in the following) and investigate how the poloidal flow in the wedge above the slab differently affects the upward journey of rock slices towards the surface. Our model can be pertinent to explore the movement of crustal buoyant sliver units detaching from the slab, penetrating into the mantle wedge and rising up at the boundary between the upper plate and subducting slab (i.e. the first stage of exhumation). With respect to previous work dealing with the interaction of a positively buoyant rock unit with the mantle flow excited by a purely downdip slab velocity (Hall & Kincaid 2001; Gerya & Yuen 2003; Manea *et al.* 2005; Castro & Gerya 2007), our study investigates the behaviour of units of variable buoyancies within a corner flow that is excited by different kinematical conditions, including slab rollback and oscillating slab dip.

In the following, because we consider the end-member situation where the upper plate has a negligible thickness, we do not consider the exhumation stage within the orogenic wedge but instead we explore the advecting power of the sublithospheric wedge (simply referred to as 'wedge' in the following) and investigate how the poloidal flow above the slab differently affects the upward journey of rock slices towards the surface. It is argued that slab rollback is more efficient than stationary trenches to exhume HP rocks, that slab shallowing does an even better job, and that the latter settings are commonly associated to HP rocks occurrences.

2 FORCES DRIVING EXHUMATION

In the wedge above the slab, a rock slice is primarily driven by two mechanisms: the buoyancy of the rock unit with respect to the surrounding material, and the flow of the material in the wedge that may advect it.

2.1 Intrinsic velocity of the HP rock units

Although there is no comprehensive description of HP rock units in terms of size and density, it seems that the vast majority is either neutrally or positively buoyant, that is, the mean density of the rock aggregate is equal or lower than that of the surrounding material and its natural velocity in a homogeneous viscous material is upward. A handful of units for which the density is higher than that of the surrounding material, like the Alpine eclogites (Zermatt–Saas, Monviso), is reported, but those units generally are embedded within serpentinite and/or continental crust rock units of lower density (e.g. Guillot *et al.* 2004; Agard *et al.* 2009) and it is unclear what the overall buoyancy is. Units of HP rocks are generally composed of stacks of rock slices that were assembled at depth. The observed characteristic size of the assemblage is tens to hundreds of kilometers. The vertical velocity of a unit scales with its size and, for a sphere in a viscous medium, its velocity v_0 is the Stokes velocity and increases like the squared radius of the sphere. It is therefore possible that HP rocks assemblages build up at depth until the intrinsic velocity of the assemblage is high enough to make it flow upwards. (Note, however, that the intrinsic velocity from the density of a rock stack in the wedge may depart from the Stokes velocity because the actual velocity of the particle also depends on many unknown parameters like the density contrast of course, but also the viscosity and the shape of the body of HP rocks itself).

This non-linear relationship in turn also implies that for a given density contrast between the rock stack at depth and surrounding material, there is a maximum size for the aggregate, after which rock units are removed faster than they are being aggregated: rocks stacks form at depth at a rate that is proportional to the subduction rate but the vertical velocity is not proportional to the volume of the body and therefore is not proportional to the rate at which rocks aggregate at depth. Removal of rock slices at depth is thus episodic and the period of removal is characterized by the balance between the 'productivity' of the subduction, that is, the rate at which rocks can be scrapped off the downgoing plate and accumulate at depth, and the rate at which the intrinsic velocity of the rock slice increases.

As emphasized in many studies (e.g. Chemenda *et al.* 1995; Ernst *et al.* 1997; Burov *et al.* 2001), the buoyancy of the aggregate is indeed a fundamental driving mechanism. But because the associated intrinsic velocity is generally too small (a few millimeters per year, Agard *et al.* 2009) and because the buoyancy of some units—eclogites for instance—is occasionally insufficient to achieve fast exhumation, other processes should be considered. Can the flow in which the aggregate moves be an additional contributor and efficiently advect it towards the surface?

2.2 Corner flow and subduction modes

Subduction zones have variable behaviours than can either be stationary, in which case the trench remains at the same location with respect to the lower mantle, or retreating (slab rollback) when the trench moves towards the foreland (and conversely, advancing). Because subducting lithospheres can be heterogeneous, subduction zones are often in transient regimes, and slab geometries varies accordingly (Garfunkel *et al.* 1986; Martinod *et al.* 2005; Royden & Husson 2006). For instance, the slab steepens when a

© 2009 The Authors, *GJI*
Journal compilation © 2009 RAS

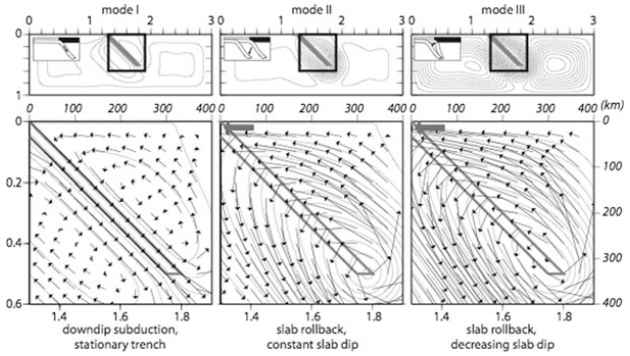

Figure 1. Flow field and streamlines in the mantle wedge for stationary trench (mode I); slab rollback (mode II); slab rollback accompanied by a decrease in slab dip (mode III). Top: cartoons and full models; bottom: zooms over the subduction wedges. Grey arrow denotes trench motion. Dimensionless and dimensional (italic) units.

unit of moderately negatively buoyant continent follows a highly negatively buoyant oceanic lithosphere. Examples can be found in the Banda and Tyrrhenian subduction zones (Royden & Husson 2009). Conversely, the subduction angle decreases when a negatively buoyant oceanic lithosphere follows the subduction of a less negatively buoyant unit like a continental island or an oceanic ridge embedded within a negatively buoyant lithosphere. The associated corner flow varies accordingly and can contribute to, or oppose, the exhumation of HP rocks. To compare the driving or resisting efficiency of the different subduction regimes, we solve for the poloidal flow of an isoviscous fluid within a two-dimensional domain (Fig. 1). It implies that return flow can always accommodate the displacement of the slab, although toroidal flow may also contribute and thus decreases the vigor of the poloidal flow (e.g. Piromallo *et al.* 2006; Stegman *et al.* 2006). The model can be naturally adimensionalized taking the subduction rate v_0, the upper mantle thickness H and the viscosity η_0 of the mantle (results are given in both dimensionless and dimensional values, computed for $v_0 = 40$ mm/yr, $H = 670$ km, and $\eta_0 = 10^{20}$ Pa s). The model represents a section of the upper mantle in which a subducting slab penetrates down to half the thickness of the upper mantle. The prescribed motion of a rigid panel that dips at 45° from the surface to a depth 0.5 (335 km) drives the flow. The fact that the slab only penetrates to half the upper mantle depth is designed to let the mantle flow freely in the poloidal field, because most small-scale slabs are dismantled at depth in the upper mantle, do not behave as consistent bodies all the way down to the top of the lower mantle, and therefore allow for poloidal flow originating at depth, around slab tails. This is opposed to many models of subduction zones (among many others, see Funiciello *et al.* 2003; Stegman *et al.* 2006; Royden & Husson 2006; Capitanio *et al.* 2007), but in fact more accurately reproduce the structure of the upper mantle as seen from geophysical observations (e.g. Faccenna *et al.* 2003 for the Mediterranean). We solve the stream function Ψ such that $\partial\Psi/\partial y = -u$; $\partial\Psi/\partial x = v$. For an incompressible fluid, Ψ verifies the biharmonic equation $\nabla^4\Psi = 0$. The stream function, and therefore the velocity, is prescribed at the boundaries and on the slab itself. The velocity at the boundaries is null and Ψ is defined on the slab such that the subduction rate v_0 is similar for all modes. The models are much simplified to allow for a comparison of the different subduction modes. To isolate the particular effect of variable corner flows, we assign the upper plate a null thickness, for it is supposed to play a passive role in the system. A thorough description of the flow in the wedge is beyond the scope of this work; we emphasize, however, that the comparison between simplified models is the most reliable way to quantify the relative contribution, in the exhumation process, of the corner flows within different modes of subduction.

The flow lines and velocity fields are shown on Fig. 1 for three different modes that highlight the contrasted, end-member flow patterns. For stationary trenches (mode I, Fig. 1a), where the slab does not change its dip or its location with respect to the mantle, slab motion is only downdip and two typical corner flow cells are well defined above and below the slab. The velocity field above the slab is downward and would not promote the exhumation of HP rocks. For purely retreating slabs (mode II, Fig. 1b), where the slab retreats with a velocity field that corresponds to a fixed foreland (the left hand side of the slab is fixed with respect to the bottom of the model), only one cell develops around the slab; above the slab the velocity field is essentially upward. The downdip velocity component along the slab is much smaller than the rollback component. Finally, for a decrease in slab dip (mode III, Fig. 1c), where the slab rotates around its tail that is anchored in the mantle, only one cell remains too, but the velocity field above the slab is strongly upward and higher than when the slab is only retreating without changing its dip. The downdip velocity component is neglected to more accurately represent the situation were only the shallowest part of the slab is dense enough to drive the subduction (see Section 4).

Amongst the three modes, two of them clearly show an upward velocity field above the slab: although a subduction zone with a stationary trench only drags the particles above the slab downward, a subduction zone with a retreating slab, and even more efficiently with a retreating slab whose dip decreases, induces an upward flow field that can only participates to the exhumation of high pressure rocks that are released from the slab at depth. Note that the velocities in the wedge are comparable in magnitude to that of the subducting slab. Other possible modes like slab steepening or trench advance are

© 2009 The Authors, *GJI*
Journal compilation © 2009 RAS

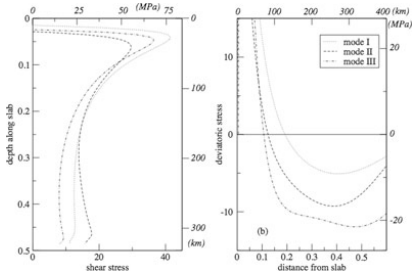

Figure 2. (a) Shear stresses along the surface of the slab and (b) deviatoric stresses at depth 0.1 (∼70 km) in front of the subducting slab. Dimensionless and dimensional (italic) units.

not considered here because they obviously oppose the exhumation of HP rocks.

In addition, the stress fields that are associated to the corner flows can also control the rate at which HP rocks make their way towards the surface. All three modes essentially display comparable positive shear stresses along the slab that favour the detachment of HP rock aggregates from the conveyor slab (Fig. 2a). Maximum shear stresses are found at depths lower than 0.1 (i.e. ∼70 km, typically the burial depth HP rocks reach before they are exhumed). Mode I, when the trench is stationary, favours the scrapping off rocks from the slab. Deviatoric stresses (measured in a horizontal plane) at a given depth (Fig. 2b, depth 0.1, ∼70 km) have comparable behaviours in all models, with localized strong compression (positive values) just above the slab and extension at larger distances. Horizontal extension is more than 2 times larger in mode III than in mode I, and ∼1.5 times larger than when in mode II. Extension favours the exhumation of HP aggregates throughout the wedge, rendering mode III more efficient than any other mode.

For all three modes, the very last episode of exhumation has to be driven either by extensional faulting or erosion, because the velocity field gradually becomes parallel to the surface, which of course reduces the advection capacity (Fig. 1).

3 KINEMATICS OF EXHUMATION

Once rocks are aggregated at depth and scrapped off the subducting slab, they may flow within the wedge and find their route to the surface. In the following, we test the relative influence of the buoyancy of a particle, which we characterize by its intrinsic velocity V_b, and of the wedge flow in the different modes.

3.1 Particle buoyancy and pathlines

The intrinsic velocity of the HP rock stack and the corner flow in which the aggregate is advected chiefly control the timing of exhumation. The corner flow can be driving (upward) or resisting (downward). We compare the kinematics of exhumation by tracking a particle released above the slab at a depth 0.15 (100 km) for the three modes. Unless otherwise specified, slab dip is 45° for modes I and II and the initial dip is 90° for mode III (slab dip varies in mode III and we start with the maximum dip to encompass the largest range of dip angles, from 90° to 0°).

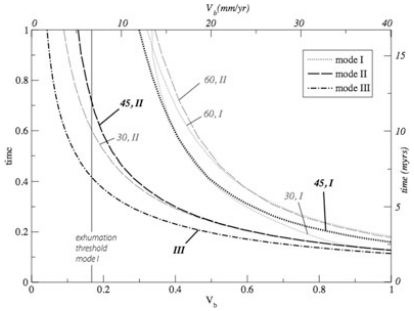

Figure 3. Delay for exhumation as a function of the intrinsic velocity of the rock unit V_b, subduction mode, and slab dip angle (labels give slab dip and mode). Vertical bar indicates the threshold under which exhumation is not achieved in mode I. Only one curve is displayed for mode III because its dip varies through time (initial dip is 90°). Dimensionless and dimensional (italic) units.

The total time necessary for the particle to reach the surface (Fig. 3) shows that mode III is much more efficient than mode I which on the contrary slows down the exhumation process. If the intrinsic particle velocity V_b is too small with respect to the corner flow velocities ($V_b < \sim 0.17 v_0$), mode I is unable to achieve the exhumation of the particle, as opposed to modes II and III that eventually drive the particle to the surface. In any mode, steep slabs are less prone to drive the particle upwards, but more drastically in mode II (Fig. 3). The differences in the timing of exhumation are related to the pathlines of the particles within the wedge velocity fields (Fig. 4). In mode I, the slab remains at its initial location.

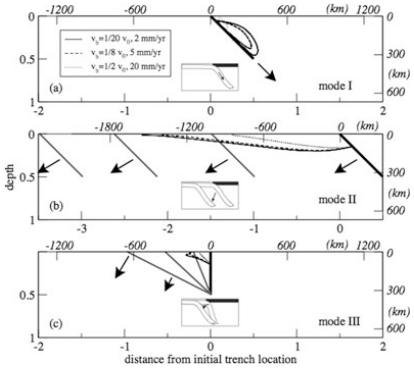

Figure 4. Flow lines for elementary rock units as a function of the ratio between intrinsic velocity of individual rock units V_b and subduction rate v_0 (1/20, solid curve; 1/8, dashed; 1/2, dotted. Dimensional values for $v_0 =$ 40 mm/yr). Arrows show slab motion. Bold black segment shows initial slab location, grey segments in modes II and III are the final locations. Overprinted path for $V_b = 1/20$ and $V_b = 1/8$ in mode I shows the multiple cycles. Dimensionless and dimensional (italic) units.

© 2009 The Authors, *GJI*
Journal compilation © 2009 RAS

During subduction, the particles remain at a short distance from the slab until they reach the surface. But low buoyancy particles are in a first stage driven to large depths before they reach the surface. Because this result is inconsistent with the vast majority of observed maximum burial depths of presently outcropping rocks, it suggests that essentially very positively buoyant units can be exhumed in mode I. This nevertheless is in agreement with the fact that deeper exhumed rocks are rather of continental origin (e.g. Chopin 2003; Liou *et al.* 2004). Note that, as opposed to modes II and III for which brittle extension is expected at the surface, mode I can only fully achieve the burial–exhumation cycle if erosion is efficient enough.

Very low buoyancy (or neutrally buoyant) particles are not exhumed in mode I and remain in the mantle wedge cell (Fig. 1a). In modes II and III, the particles are gradually exhumed, and even low-buoyancy particles eventually reach the surface. Pathlines are shorter in mode III than in modes I and II (Fig. 4).

3.2 Delay of exhumation

Dimensional units make it easier to compare model results to natural examples, and we keep dimensional values in the following. The total delay of exhumation (Fig. 5) essentially depends on the buoyancy of the particle and the flow in the wedge. In an inactive subduction ($v_0 = 0$), the delay is simply D times V_b, where D is the initial depth of the particle. In the following, D is set to 100 km; because the velocity field tends to parallel the surface near surface level, we consider a depth of 6.5 km as the final depth (for otherwise total time tends to infinity if the particle has no intrinsic velocity); it also means that this final exhumation process needs to be attributed to another mechanism such as erosion or crustal extension (e.g. Yamato *et al.* 2008). Depending on the location of the particle in the wedge, the flow advects the particle with a variable vigour. It can either help or resist the ascension of the particle towards the surface. The combination often produces complex behaviours.

Mode I is almost systematically resisting: the faster the subduction, the longer the total time before exhumation (Fig. 5). If the intrinsic velocity of the particle cannot overcome the downward wedge flow, the particle permanently remains in the mantle wedge cell. In mode I, exhumation does not occur, even at low subduction rates, unless the particle has an intrinsic velocity V_b higher than ∼5 mm/yr (Fig. 6). Under some circumstances in mode I, the particle benefits from the upwelling mantle, or return flow (Fig. 1), that balances the downwelling effect. This is for instance outlined by the total time before exhumation of a particle that has an intrinsic velocity of 5 mm/yr in mode I (Fig. 5): for subduction rates that range from ∼22 mm/yr to ∼28 mm/yr the particle follows a peculiar pathline because it takes advantage of the return flow; as a consequence, the total delay of exhumation becomes shorter than for subduction rates lower than 22 mm/yr.

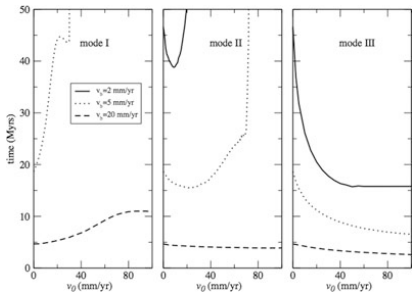

Figure 5. Total exhumation time for the three subduction modes, as a function of the intrinsic velocity of individual rock units V_b and subduction rate v_0. Dimensional units.

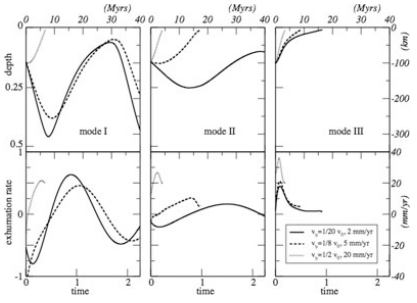

Figure 6. Burial depth (top) and exhumation rates (bot) of the rock units as a function of time and of the ratio between intrinsic velocity of individual rock units V_b and subduction rate v_0 (1/20, solid curve; 1/8, dashed; 1/2, dotted. Dimensional values for $v_0 = 40$ mm/yr). Dimensionless and dimensional (italic) units.

Mode II also shows a complex pattern (Fig. 5). Because at short distance from the slab the flow is downward, if subduction rates reach high values, the particle is dragged along with the slab and remains in the subduction cell. For instance, exhumation of a particle with an intrinsic velocity $V_b = 2$ mm/yr is fostered by subduction rates that are lower than ∼10 mm/yr, but higher rates increase the total exhumation delay. At rates higher than ∼28 mm/yr, the particle is never exhumed. Such scheme also holds for particles that have a higher intrinsic velocity: with $V_b = 5$ mm/yr, exhumation never occurs for subduction rates higher than ∼70 mm/yr.

Mode III is always helping exhumation. For a particle with $V_b =$ 2 mm/yr, the total delay of exhumation is divided by a factor 2 with a subduction rate of ∼10 mm/yr (from 50 to 25 m.yr between $v_0 =$ 0 mm/yr to $v_0 = 10$ mm/yr). A decrease in slab dip therefore very efficiently contributes to exhume HP rocks from depth.

3.3 Burial and exhumation

Because of these interactions between the vertical motion of a particle excited by its own intrinsic velocity and the wedge flow in which the particle is advected, the burial history is not monotonic (Figs 5 and 6). The most dramatic case is that of low buoyancy particles in mode I, that are stuck in the wedge cell. They are first driven to large depths before they are brought back to moderate depths and drown to large depths again, in a cyclic behaviour. The shape of the cell bounds the oscillation between depths of ∼300 and ∼50 km. The period of the cycle is controlled by the subduction rate v_0 (e.g. ∼30 m.yr for $v_0 = 40$ mm/yr). The vertical velocities are high (Fig. 6), comparable in magnitude to the tectonic velocities. In mode II, particles that have low intrinsic buoyancies are also caught in a comparable cyclic behaviour, although the vertical velocities are lower (<10 mm/yr) because the burial depths are

© 2009 The Authors, *GJI*
Journal compilation © 2009 RAS

constrained within a thinner domain (between depths of ∼60 and ∼160 km). Such behaviour can be relevant to real Earth in the description of the wedge flow, but it would prevent the exhumation of HP rocks; of course, no observation can likely report such a pattern yet. Only if the positive buoyancy of the particle makes it overcome the advection in the wedge the particle reaches the surface. In that case, exhumation rates increase as the particles move away from the downwelling (see Fig. 1). The ascension eventually slows down as the particles approach the surface. Note that this is true in any mode because at surface level the velocity vectors tend to be parallel to the surface. In mode III, the vertical motion is always directed towards the surface, the larger the intrinsic velocity of the particle the faster it reaches the surface. With $v_0 = 40$ mm/yr, the fastest exhumation rates range between 20 and 40 mm/yr for particles with 2 mm/yr $< V_b <$ 20 mm/yr and gradually slow down to lower values as the particles approach the surface.

4 DISCUSSION

These models outline the first order behaviour of three subduction modes during the exhumation process of HP rocks. When the trench is stationary with respect to the lower mantle (mode I), the subduction zone is characterized by a powerful downwelling that drags to depth the HP rock aggregate released on the Benioff zone. It is therefore more efficient than any other mode to bury crustal material that may even be positively buoyant at large depths, but is rather inefficient to drive rocks to the surface except in cases implying high buoyancy material. Conversely, when the trench retreats during subduction (modes II and III), the wedge flow tends to advect the rock aggregate towards the surface. The vertical velocities can reach values that are comparable to tectonic velocities, that is, the velocity at which the plate subducts in the mantle. This result solves the apparent paradox based on observations that states that blueschists metamorphic rocks are often exhumed at a rate that is comparable to the rate at which the subduction panel enters the upper mantle (e.g. Thomson *et al.* 1998; Rubatto & Hermann 2001).

When trench retreat is associated to a decrease in slab dip (mode III, as opposed to mode II, where the slab uniformly retreats during subduction), the exhumation process is even more efficient. The timing of exhumation can typically be divided by a factor of two if the subduction rate increases from $v_0 = 0$ mm/yr to $v_0 =$ 40 mm/yr when mode III is excited. We conclude that slab rollback accompanied by a decrease in slab dip is the most efficient yet simple mechanism for HP rock exhumation, simply because it pumps material upwards. The closer to the surface, the more efficient this process is.

Because our simple models only address a single aspect of the exhumation process and neglect the rheological complexity of subduction zones, we emphasize that the qualitative results as well as the comparison of the models relative to each other hold, but the quantitative results should be considered with care, that is, as orders of magnitude. For instance, toroidal flow may decrease the vigour of the upward, poloidal flow, by a factor of 2 (Piromallo *et al.* 2006). Similarly, radial and lateral viscosity variations, or the presence of erosion, may distort our quantitative conclusions, but would not discard the return flow as a significant contributor for HP rocks exhumation. In our models the boundary conditions are that of a fixed upper plate, that is, backarc extension occurs when the trench retreats; changing the 'upper plate' boundary conditions to either free slip or fixed velocity (set to trench velocity) modifies the flow field (e.g. Yamato *et al.* 2009), but in a way that do not alter our conclusions because the upward flow near the surface is also close to the subducting slab. Our results indeed suggest that only slab rollback can provide enough power to drive the exhumation of rock aggregates that have low or neutral positive buoyancies at rates that are comparable to tectonic velocities, as inferred from P–T–t paths (e.g. Duchêne *et al.* 1997; Gebauer *et al.* 1997; Rubatto & Hermann 2001; Agard *et al.* 2009) and from the dynamics of real Earth systems (Brun & Faccenna 2008).

Our analysis compares models at a given subduction rate. However, because the buoyancy and viscosity structures of subducting plates are heterogeneous, subduction dynamics may vary significantly. Alternatively, the power—literally, the rate of energy spent to move the surrounding mantle around the slab—could have been used as a reference. Equal-power comparison would give slightly different results: mode II and mode III are the least and the most energy consuming regimes, respectively, possibly making mode II more efficient than mode III to advect HP rock aggregates towards the surface within a short delay. However, equal-power comparisons are not very satisfying either, because of the association of the modes to subduction velocities. For instance, mode III is likely associated to increasing subduction rates, for instance when a dense unit of oceanic lithosphere enters the subduction (e.g. Royden & Husson 2006). Likewise, mode I requires specific conditions that may slow down subduction.

The three modes are currently found on Earth, but mode I should be considered as an oddity, in which coincidentally the lower plate is pushed towards the upper plate at a rate that is equal to the subduction rate. A steady subduction is unlikely to prevail during the 20–40 Myr long burial–exhumation cycle. In many cases, in particular where subduction zones are narrow, the behaviour of the trenches and slabs are transient. Modes II and III would thus naturally occur more often than mode I. For instance, the termination of the subduction of the African plate beneath Eurasia is characterized by the many small-scale Mediterranean subduction zones in which the incoming lithosphere is heterogeneous, which leads to a chaotic behaviour of subduction zones, that may subsequently retreat, advance or remain stationary (e.g. Royden & Husson 2009). The Mediterranean subduction zones are remarkable in that sense. One can also establish similar observations for the SE Asian subduction zones assemblage. Complex settings like those, where subduction zones are believed to occur in a succession of different stages, generally yield HP rocks. Well-documented examples include the Tyrrhenian and Hellenic subduction zones (e.g. Jolivet *et al.* 2003), Oman (e.g. Breton *et al.* 2004) or Papua New Guinea (e.g. Baldwin *et al.* 2004). Conversely, modern blueschists and eclogites metamorphic rocks are seldom found in subduction zones that undergo a steadier regime, like the long-lived, massive circum Pacific subduction zones. Many of these examples where HP rocks outcrop—particularly the Mediterranean ones—also correspond to case studies for slab rollback (e.g. Malinverno & Ryan 1986; Royden 1993). This support the idea that slab rollback promotes exhumation for two reasons. The first reason is that the overriding plate is thinner: modes II and III that prevail during rollback drive the rock unit up to shallow depths before it hits the base of the upper plate. Only mild erosion and extension suffice for the final stage of exhumation. Our simplified model considers an upper plate of negligible thickness; this assumption holds for subduction zones where significant phase of trench retreat occurred prior to the release of the rock unit at depth. Nevertheless, the thickness of the overriding plate is thought to be thinner than 100 km, and generally about 60 km (Currie & Hyndman 2006) because of the effects of enhanced corner flow and slab dehydration (e.g. Arcay *et al.* 2006)

© 2009 The Authors, *GJI*
Journal compilation © 2009 RAS

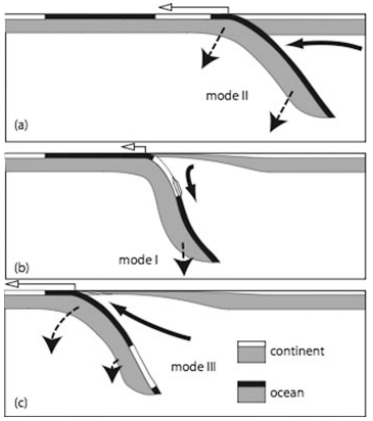

Figure 7. Sketch showing an episodic subduction triggering the burial–exhumation cycle of HP rocks. White arrow denotes trench migration rate, dashed arrows indicate slab motion and bold arrows show mantle flow.

and destabilization of the backarc lithosphere (Currie *et al.* 2008) and may tend to 0 km where backarc basins are active. Indeed, in the Mediterranean domain, overriding plates are thinned due to slab rollback (Royden 1993; Jolivet *et al.* 1994). Conversely there is, to our knowledge, no proven example where HP rocks are clearly associated with thick overriding lithospheres during the exhumation process: upper plates are thin in modern examples and older examples like the Alps or Himalayas are being debated. The second reason that we emphasize is that chaotic, or better-said episodic behaviour of subduction zones greatly promote the exhumation of HP rocks in a multi-stage story: following a subduction episode of dense oceanic lithosphere during which the trench retreats at a fast rate, in mode II (Fig. 7a); a fragment of less negatively buoyant continental lithosphere enters the subduction (Fig. 7b). The trench retreats slower and slab dip increases (although it seems counter intuitive, slab dip increases because negatively buoyant units at depth continue to sink, whereas the shallower, more buoyant units, resist subduction, Martinod *et al.* 2005; Royden & Husson 2006), entering mode I. The continental crust is buried and metamorphosed at high pressure and low temperatures. Because the wedge shears the Benioff zone and because the continental slices that are stacked in an aggregate of HP rocks have a constantly increasing upward force, the aggregate eventually detaches from the slab, at a depth at which shear stresses overcome the yield stress of the rock unit (e.g. Seno 2008). More negatively buoyant lithosphere enters the subduction and the slab rolls back again (Fig. 7c), and the dip of the slab decreases in mode III, inducing a wedge flow that triggers the exhumation of HP rocks from depth, with an upward velocity that is comparable to tectonic velocities and trench migration rate. The final exhumation stage is then promoted by the extensive strain in the upper plate. Throughout the entire cycle, the upper plate, therefore, never hampers the exhumation process. This cyclic episode can be followed by several other cycles that make it easy for HP rocks to be exhumed. More generally, any subduction zone that has a transient behaviour due to the presence of heterogeneities in the incoming lithosphere likely promotes the same mechanism.

© 2009 The Authors, *GJI*
Journal compilation © 2009 RAS

ACKNOWLEDGMENTS

We are grateful to C. Beaumont and T. Gerya for their reviews, and G. Ernst for his comments on an earlier version of the manuscript. LH is funded by CNRS/INSU program SEDIT; PY thanks J. Braun for financial support from the ANR in Computational Geology.

REFERENCES

Agard, P. *et al.*, 2006. Transient, synobduction exhumation of Zagros blueschists inferred from P-T, deformations, time, and kinematic constraints: implications for Neotethyan wedge dynamics, *J. geophys. Res.*, **111,** B11401, doi:10.1029/2005JB004103.

Agard, P., Yamato, P., Jolivet, L. & Burov, E., 2009. Exhumation of oceanic blueschists and eclogites in subduction zones: timing and mechanisms, *Earth Sci. Rev.,* doi:10.1016/j.earscirev.2008.11.002.

Allègre, C. *et al.*, 1984. Structure and evolution of the Himalaya–Tibet orogenic belt, *Nature,* **307,** 17–22, doi:10.1038/307017a0.

Arcay, D., Doin, M.P., Tric, E., Bousquet, R. & de Capitani, C., 2006. Overriding plate thinning in subduction zones: localized convection induced by slab dehydration, *Geochem. Geophys. Geosyst.,* **7,** doi:10.1029/2005GC001061.

Baldwin, S., Monteleone, B.D., Webb, L.E., Fitzgerald, P.G., Grove, M. & Hill, E.J., 2004. Pliocene eclogite exhumation at plate tectonics rates in eastern Papua New Guinea, *Nature,* **431,** 263–267.

Beaumont, C., Ellis, S. & Pfiffner, A., 1999. Dynamics of sediment subduction-accretion at convergent margins: short-term modes, long term deformation, and tectonic implications, *J. geophys. Res.,* **104,** 17573–17601.

Boutelier, D., Chemenda, A. & Jorand, C., 2004. Continental subduction and exhumation of high-pressure rocks: insights from thermo-mechanical laboratory modelling, *Earth planet. Sci. Lett.,* **222,** 209–216.

Breton, J.-P., Béchennec, F., Le Métour, J., Moen-Maurel, L. & Razin, P., 2004. Eoalpine (Cretaceous) evolution of the Oman Tethyan continental margin: insights from a structural field study in Jabal Akhdar (Oman Mountains), *GeoArabia,* **9,** 1–18.

Brun, J.-P. & Faccenna, C., 2008. Exhumation of high-pressure rocks driven by slab rollback, *Earth planet. Sci. Lett.,* **272,** doi:10.1016/j.epsl.2008.02.038.

Burov, E., Jolivet, L., Le Pourhiet, L. & Poliakov, A., 2001. A thermomechanical model of exhumation of HP and UHP metamorphic rocks in Alpine mountain belts, *Tectonophysics,* **342,** 113–136.

Capitanio, F.A., Morra, G. & Goes, S., 2007. Dynamic models of downgoing plate-buoyancy driven subduction: subduction motions and energy dissipation, *Earth planet. Sci. Lett.,* **262,** 284–297.

Castro, A. & Gerya, T.V., 2007. Magmatic implications of mantle wedge plumes: experimental study, *Lithos,* **103,** 138–148.

Chemenda, A.I., Mattauer, M. & Bokun, A.N., 1996. Continental subduction and a mechanism for exhumation of high-pressure metamorphic rocks: new modeling and field data from Oman, *Earth planet. Sci. Lett.,* **143,** 173–182.

Chemenda, A.I., Mattauer, M., Malavieille, J. & Bokun, A.N., 1995. A mechanism for syn-collisional deep rock exhumation and associated normal faulting: results from physical modelling, *Earth planet. Sci. Lett.,* **132,** 225–232.

Chopin, C., 2003. Ultrahigh-pressure metamorphism: tracing continental crust into the mantle, *Earth planet. Sci. Lett.,* **212,** 1–14.

Cloos, M., 1982. Flow melanges: numerical modelling and geologic constraints on 299 their origin in the Franscican subduction complex, California, *Bull. Geol. Soc. Am.,* **93,** 330–345.

Currie, C.A. & Hyndman, R.D, 2006. The thermal structure of subduction zone backarcs, *J. geophys. Res.,* **111,** B08404, doi:10.1029/2005JB004024.

Currie, C.A., Huismans, R.S. & Beaumont, C., 2008. Thinning of continental backarc lithosphere by flow-induced gravitational instability, *Earth planet. Sci. Lett.,* **269,** 436–447.

De Sigoyer, J., Chavagnac, V., Blichert-Toft, J., Villa, I., Luais, B., Guillot, S., Cosca, M. & Mascle, G., 2000. Dating the Indian continental subduction and collisional thickening in the northwest Himalaya: multichronology of the Tso Morari eclogites, *Geology,* **28,** 487–490.

Duchêne, S., Lardeaux, J.M. & Albarède, F., 1997. Exhumation of eclogites: insights from depth-time path analysis, *Tectonophysics,* **280,** 125–140.

England, P.C. & Holland, T.J.B., 1979. Archimedes and the Tauern eclogites: the role of buoyancy in the preservation of exotic eclogite blocks, *Earth planet. Sci. Lett.,* **44,** 287–294.

Ernst, W.G., 2001. Subduction, ultrahigh-pressure metamorphism, and regurgitation of bouyant crustal slices — implications for arcs and continental growth, *Phys. Earth planet. Interiors,* **127,** 253–275.

Ernst, W.G., Maruyama, S. & Wallis, S., 1997. Buoyancy-driven, rapid exhumation of ultrahigh-pressure metamorphosed continental crust, *Proc. Natl. Acad. Sci.,* **94,** 9532–9537.

Faccenda, M., Minelli, G. & Gerya, T.V., 2009. Coupled and decoupled regimes of continental collision: numerical modeling, *Earth planet. Sci. Lett.,* **278,** 337–349.

Faccenna, C., Jolivet, L., Piromallo, C. & Morelli, A., 2003. Subduction and the depth of convection in the Mediterranean mantle, *J. geophys. Res.,* **108**(B2), 2099, doi:10.1029/2001JB001690.

Funiciello, F., Faccenna, C., Giardini, D. & Regenauer-Lieb, K., 2003. Dynamics of retreating slabs: 2. Insights from three-dimensional laboratory experiments, *J. geophys. Res.,* **108**(B4), 2207, doi:10.1029/2001JB000896.

Garfunkel, Z., Anderson, C.A. & Schubert, G., 1986. Mantle circulation and the lateral migration of subducted slabs, *J. geophys. Res.,* **91,** 7205–7223.

Gebauer, D., Schertl, H.P., Brix, M. & Schreyer, W., 1997. 35 Ma old ultrahigh-pressure metamorphism and evident for very rapid exhumation in the Dora Maira Massif, Western Alps, *Lithos,* **41,** 5–24.

Gerya, T.V., Stöckert, B. & Perchuk, A.L., 2002. Exhumation of high-pressure metamorphic rocks in a subduction channel: a numerical simulation, *Tectonics,* **21**(6), 1056, doi:10.1029/2002TC001406.

Gerya, T.V. & Stoeckhert, B., 2002. Exhumation rates of high pressure metamorphic rocks in subduction channels: the effect of rheology, *Geophys. Res. Lett.,* **29**(8), 1261, doi:10.1029/2001GL014307.

Gerya, T.V. & Yuen, D.A., 2003. RayleighTaylor instabilities from hydration and melting propel ''cold plumes'' at subduction zones, *Earth planet. Sci. Lett.,* **212,** 47–62.

Gorczyk, W., Guillot, S., Gerya, T.V. & Hattori, K., 2007. Asthenospheric upwelling, oceanic slab retreat and exhumation of UHP mantle rocks: insights from Greater Antilles, *Geophys. Res. Lett.,* **34,** L21309, doi:10.1029/2007GL031059.

Guillot, S., Schwartz, S., Hattori, K., Auzende, A. & Lardeaux, J., 2004. The Monviso ophiolitic Massif (Western Alps), a section through a serpentinite subduction channel, *J. Virtual Explorer,* **16,** paper 3.

Hacker, B.R., Andersen, T.B., Root, D.B., Mehl, L., Mattinson, J.M. & Wooden, J.L., 2003. Exhumation of high-pressure rocks beneath the Solund Basin, Western Gneiss Region of Norway, *J. Metamorph. Geol.,* **21,** 613–629.

Hall, P.S. & Kincaid, C., 2001. Diapiric flow at subduction zones: a recipe for rapid transport, *Science,* **292,** 2472–2475.

Handy, M.R., Franz, L., Heller, F., Janott, B. & Zurbriggen, R., 1999. Multistage accretion and exhumation of the continental crust (Ivrea crustal section, Italy and Switzerland), *Tectonics,* **18,** 1154–1177.

Jolivet, L., Daniel, J.M., Truffert, C. & Goffé, B., 1994. Exhumation of deep crustal metamorphic rocks and crustal extension in back-arc regions. *Lithos,* **33,** 3–30.

Jolivet, J., Faccenna, C., Goffé, B., Burov, E. & Agard, P., 2003. Subduction tectonics and exhumation of high-pressure metamorphic rocks in the Mediterranean orogens, *Am. J. Sci.,* **303,** 353–409.

Jolivet, L. *et al.*, 2008. Subduction, convergence and the mode of backarc extension in the Mediterranean region. *Bull. Soc. Géol. France,* **179,** 525–550.

Lallemand, S., Heuret, A. & Boutelier, D., 2005. On the relationships between slab dip, back-arc stress, upper plate absolute motion, and crustal nature in subduction zones, *Geochem. Geophys. Geosyst.,* **6,** Q09006, doi:10.1029/2005GC000917.

Liou, J.G., Tsujimori, T., Zhang, R.Y., Katayama, I. & Maruyama, S., 2004. Global UHP metamorphism and continental subduction/collision: the Himalaya model. *Int. Geol. Rev.,* **46,** 1–27.

Malinverno, A. & Ryan, W.B.F., 1986. Extension of the Tyrrhenian Sea and shortening in the Apennines as result of a migration driven by sinking lithosphere, *Tectonics,* **5,** 227–245.

Manea, V.C., Manea, M., Kostoglodov, V. & Sewell, G., 2005. Thermomechanical model of the mantle wedge in Central Mexican subduction zone and a blob tracing approach for the magma transport, *Phys. Earth Planet. Inter.,* **149,** 165–186.

Martinod, J., Funiciello, F., Faccenna, C., Labanieh, S. & Regard, V., 2005. Dynamical effects of subducting ridges: insights from 3-D laboratory models, *Geophys. J. Int.,* **163,** 1137–1150, doi:10.1111/ j.1365-246X.2005.02797.x.

Maruyama, S., Liou, J.G. & Terabayashi, M., 1996. Blueschists and eclogites of the world, and their exhumation, *Int. Geol. Rev.,* **38,** 458–594.

Parra, T., Vidal, O. & Jolivet, L., 2002. Relation between the intensity of defor mation and retrogression in blueschist metapelites of Tinos Island (Greece) evidenced by chlorite–mica local equilibria, *Lithos,* **63,** 41–66.

Piromallo, C., Becker, T.W., Funiciello, F. & Faccenna, C., 2006. Three-dimensional instantaneous mantle flow induced by subduction, *Geophys. Res. Lett.,* **33,** L08304, doi:10.1029/2005GL025390.

Pfiffner, O.A., Ellis, S. & Beaumont, C., 2000. Collision tectonics in the Swiss Alps: insight from geodynamic modeling, *Tectonics,* **19,** 1065–1094.

Platt, J.P., 1986. Dynamics of orogenic wedges and the uplift of high-pressure metamorphic rocks, *Geol. Soc. Am. Bull.,* **97,** 1037–1053.

Platt, J.P., 1993. Exhumation of high-pressure rocks: a review of concept and processes, *Terra Nova,* **5,** 119–133.

Ring, U., Brandon, M.T., Willett, S. & Lister, G.S., 1999. Exhumation processes, in *Exhumation Processes: Normal faulting, ductile flow and erosion,* pp. 1–28, eds Ring, U., Brandon, M.T., Lister, G.S. & Willett, S., Special Publications Geological Soc., London.

Rosenbaum, G. & Lister, G.S., 2005. The Western Alps from the Jurassic to Oligocene: spatio-temporal constraints and evolutionary reconstructions, *Earth. Sci. Rev.,* **69,** 281–306.

Royden, L., 1993. Evolution of retreating subduction boundaries formed during continental collision, *Tectonics,* **12,** 629–638.

Royden, L. & Husson, L., 2006. Trench motion, slab geometry and viscous stresses in subduction systems, *Geophys. J. Int.,* **167,** 881–905, doi:10.1111/424 j.1365-246X.2006.03079.x.

Royden, L. & Husson, L. 2009. Subduction with variations in slab buoyancy: models and application to the Banda and Apennine systems, in *Subduction Zone Geodynamics, Frontiers in Earth Sciences,* Springer-Verlag, Berlin, doi:10.1007/978-3-540-87974-9.

Rubatto, D. & Hermann, J., 2001. Exhumation as fast as subduction? *Geology,* **29,** 3–6.

Seno, T., 2008. Conditions for a crustal block to be sheared off from the subducted continental lithosphere: what is an essential factor to cause features associated with collision?, *J. geophys. Res.,* **113,** B04414, doi:10.1029/2007JB005038.

Shreve, R.L. & Cloos, M., 1986. Dynamics of sediment subduction, melange formation, and prism accretion, *J. geophys. Res.,* **91,** 10229–10245.

Stampfli, G.M., 2000. Tethyan oceans, *Geol. Soc. London Spec. Publ.,* **173,** 1–23.

Stegman, D.R., Freeman, J., Schellart, W.P., Moresi, L. & May D., 2006. Influence of trench width on subduction hinge retreat rates in 3-D models of slab rollback, *Geochem. Geophys. Geosyst.,* **7,** Q03012, doi:10.1029/2005GC001056.

Thomson, S.N., Stockhert, B. & Brix, M.R., 1998. Thermochronology of the high-pressure metamorphic rocks of Crete, Greece: implications for the speed of tectonic processes, *Geology,* **26,** 259–262.

Warren, C., Beaumont, C. & Jamieson, R.A., 2008. Modelling tectonic styles and ultra-high pressure (UHP) rock exhumation during the transition from oceanic to continental collision, *Earth planet. Sci. Lett.,* **267,** 129–145.

Yamato, P., Agard, P., Burov, E., Le Pourhiet, L., Jolivet, L. & Tiberi, C., 2007. Burial and exhumation in a subduction wedge: mutual constraints from thermomechanical modeling and natural P-T-t data (Sch. Lustrés, W. Alps), *J. geophys. Res.,* **112,** B07410, doi:10.1029/2006JB004441.

Yamato, P., Burov, E., Agard, P., Le Pourhiet, L. & Jolivet, L., 2008. HP-UHP exhumation during slow continental subduction: self-consistent thermodynamically and thermomechanically coupled model with application to the Western Alps, *Earth planet. Sci. Lett.,* **271,** 63–74, doi:10.1016/j.epsl.2008.03.049.

Yamato, P., Husson, L., Braun, J., Loiselet, C. & Thieulot, C., 2009. Influence of surrounding plates on 3D subduction dynamics, *Geophys. Res. Lett.,* **36,** L07303, doi:10.1029/2008GL036942.

Walsh, E.O. & Hacker, B.R., 2004. The fate of subducted continental margins: two-stage exhumation of the high-pressure to ultrahigh-pressure Western Gneiss Region, Norway, *J. Metamorphic Geol.,* **22,** 671–687.

© 2009 The Authors, *GJI*
Journal compilation © 2009 RAS

© 2009 The Authors, *GJI*
Journal compilation © 2009 RAS

2.4 Rhéologie et déformation des panneaux plongeants

2.4.1 Rhéologie

Les techniques de modélisation permettent à présent de décrire la dynamique des interactions entre la lithosphère et le manteau de manière satisfaisante. Plus, la résolution qu'elles offrent est supérieure aux contraintes disponibles pour calibrer les modèles. Un des obstacles majeurs est en particulier la rhéologie. Le contraste de viscosité est un paramètre fondamental dans l'évolution des subductions. Or, les estimations disponibles sont basées sur des méthodes globales et l'incertitude atteint plusieurs ordres de grandeurs. Dans le cadre de la thèse de C. Loiselet, nous nous sommes proposés de quantifier la rhéologie de la lithosphère en subduction en examinant les géométries des panneaux plongeants vus par la tomographie sismique. Leur déformation longitudinale, c'est-à-dire le long du panneau, dans un plan situé à une profondeur uniforme, résulte de l'écoulement du manteau autour du panneau. Un modèle quantitatif semi-analytique, confronté aux observations, nous permet d'établir que le rapport de viscosité entre la lithosphère en subduction et le manteau supérieur est faible, de l'ordre de 50 et ne saurait excéder 100.

From longitudinal slab curvature to slab rheology

Christelle Loiselet*, Laurent Husson, and Jean Braun
Geosciences Rennes, UMR 6118 CNRS, Université de Rennes 1, Rennes Cedex CS 35042, France

ABSTRACT

The curvature of a subducting lithosphere is chiefly controlled by the viscosity ratio between the slab and the surrounding mantle. On the basis of a semi-analytical flow model, we explore the rheological dependence of the geometrical response of a viscous slab subjected to toroidal mantle flow. Mantle flow is excited by slab retreat at a prescribed mean velocity and is iteratively solved for by using a stream function approach, in turn providing the stresses that bend the slab. Comparison between model predictions and geophysical observations of slab curvature gives an average slab-to-mantle viscosity ratio of 45.

INTRODUCTION

Much effort has been recently devoted to improve our understanding of the dynamics of subduction zones; surprisingly, the viscosity of the subducting lithosphere remains a poorly known yet fundamental parameter. Modeling subduction dynamics (e.g., Billen and Hirth, 2007; Capitanio et al., 2007; Wu et al., 2008) or the geoid (e.g., Zhong and Davies, 1999) has led to a wide range of values. We take advantage of the dependence of slab curvature on the viscosity ratio between the slab and the mantle to determine this ratio by studying the response of a retreating slab in a longitudinal plane (i.e., perpendicular to the slab plane at a given depth) exciting a toroidal mantle flow. By means of a semi-analytical method, we quantify the mechanical behavior of the slab and compare our model results with observations from geophysical data on a selection of subduction zones.

GEOMETRY AND RHEOLOGY OF SLABS

The interaction between a subducting lithosphere and the surrounding mantle is strongly affected by their relative strengths. For example, whether slabs penetrate the lower mantle is controlled by the strength of the lithosphere in comparison with the viscosity structure of the mantle at the 660 km discontinuity (Goes et al., 2008). Commonly used values for the viscosity ratio between a slab and the surrounding mantle range between 10^2 and 10^5 (Christensen and Yuen, 1984; Zhong and Gurnis, 1994; Conrad and Hager, 1999; Funiciello et al., 2003; Schellart, 2004; Morra et al., 2006; Royden and Husson, 2006; Stegman et al., 2006; Billen and Hirth, 2007; Capitanio et al., 2007; Clark et al., 2008), but Kincaid and Griffiths (2004) modeled the flow around a rigid slab, while Husson (2006) reproduced observations of dynamic topography with an isoviscous rheology.

Most oceanic trenches have a convex arc shape, a feature that is not limited to surface level. Seismic tomography studies as well as earthquake occurrences provide information on the geometry of subducted slabs (Isacks and Molnar, 1971; Van der Hilst and Karason, 1999; Wortel and Spakman, 2000; Fukao et al., 2001). The shape of ocean trenches was first explained by the ping-pong ball analogy (Frank, 1968; Tovish and Schubert, 1978), which suggested that the curvature of the trenches is naturally imposed by the intersection of a slab and a spherical Earth. Alternatively, numerical and analogue simulations have shown that this curvature is more likely the response of the slab in a toroidal flow. This curvature seems to decrease when slab width increases (Dvorkin et al., 1993; Morra et al., 2006, 2009; Stegman et al., 2006; Schellart et al., 2007), as a response to the balance between the forces driving slab motion and the viscous resistance of the mantle (Schellart, 2004; Funiciello et al., 2006), although internal heterogeneities may have a strong impact (Morra et al., 2006).

Because the flow associated with a migrating slab is predominantly toroidal (e.g., Schellart, 2004; Funiciello et al., 2006; Piromallo et al., 2006), we assume that the time evolution of the shape of a vertical slab that retreats at a given rate can be directly compared to the depth evolution of the longitudinal shape of a slab; this operation can be performed via the conversion of depth along slab into a residence time into the mantle, calculated as the depth divided by the sinking velocity (assuming that retreat velocity, and therefore slab dip, is constant with depth).

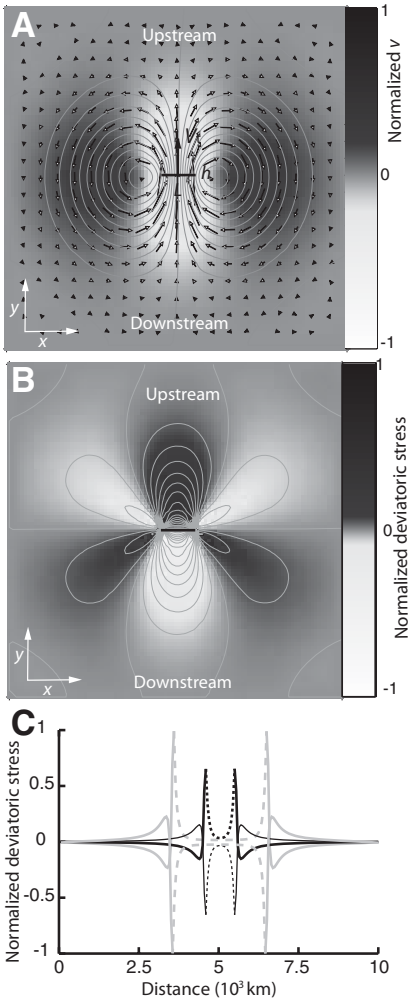

Figure 1. Map view of model. A: Normalized streamlines (gray curves), velocity field (arrows), and *v*, velocity field, parallel to *y* axis (background). V_t is translation velocity of slab. *L* and *h* are slab width and thickness. B: Normalized deviatoric stress, isocurves every 0.05. C: Deviatoric stress profile along line parallel to *x* axis and running on upstream (bold) and downstream (thin) side of 1000 km (black) and 3000 km (gray) plate across model. Dashed sections denote stresses along slab.

MODELING APPROACH

The retreating slab is approximated by a uniform infinite vertical viscous layer of variable width L and thickness h moving in a square domain of constant dimensions throughout (Fig. 1A). Our approach is based on a two-dimensional (2-D) numerical solution of the Stokes equation that requires the computation of (1) a stream function to describe the toroidal flow of a Newtonian, isoviscous, and incompressible mantle around a rigid retreating plate, infinite in the direction perpendicular to the model (2-D), and (2) from the resulting stress field, the deflection of a viscous slab of uniform yet different viscosity. The velocity of the fluid is obtained by solving the biharmonic equation for the stream function Ψ, $\nabla^4\Psi = 0$, with $u = -\frac{\partial\Psi}{\partial y}$ and $v = \frac{\partial\Psi}{\partial x}$, u and v being the x and y velocities, respectively. To simulate the presence of the retreating slab, we prescribe a velocity V_t (slab retreat rate) in

*E-mail: christelle.loiselet@univ-rennes1.fr.

© 2009 Geological Society of America. For permission to copy, contact Copyright Permissions, GSA, or editing@geosociety.org.

a rectangular region of width L and thickness h in the center of the model (Fig. 1A), while the velocities at the boundaries of the domain are set to zero. We then calculate Ψ at the nodes of a regular grid using a centered finite difference operator to approximate the spatial derivatives. In the first step of the model, we assume that the slab is rigid, and iteratively solve for the velocity field that minimizes work while satisfying the incompressibility condition.

The deflection of the slab is obtained in a second step by solving for the viscous bending of a half-plate embedded at its origin (and by symmetry, for the entire plate), of thickness h and length $L/2$, and subjected to a nonuniform load $q(x)$ (or spatially integrated deviatoric stress):

$$D\frac{\partial^5 w}{\partial x^4 \partial t} = q(x), \qquad (1)$$

where $D = \frac{\mu_s h^3}{3}$ is the viscous rigidity of the slab, μ_s the slab viscosity, and $q(x) = \mu_m \frac{\partial u}{\partial x}$ is the deviatoric stress induced by the mantle flow. The approximation is made that $\sigma_{yy} = 0$, which only holds when the slab viscosity is larger than the mantle viscosity μ_m. The deflection w of the half-plate as a function of time t and x is given by the integration of Equation 1. Standard boundary conditions are $w = 0$ and $\frac{dw}{dx} = 0$ at $x = 0$; $\frac{d^2w}{dx^2} = 0$ and $\frac{d^3w}{dx^3} = 0$ at $x = L/2$ (Turcotte and Schubert, 1982). The slab geometry is modified according to the computed final displacement after each time increment (small enough for the solution to become independent of its value). The coupled equations are iteratively solved through time in order to predict the evolving plate curvature.

We dimensionalized the model by assigning a mean slab retreat rate $V_s = 50$ mm/a in a 10,000-km-wide square box filled with a linear viscous fluid of viscosity 10^{20} Pa s. Note that in a Newtonian viscous fluid, the flow pattern does not depend on the absolute value of the viscosity, but rather on the viscosity ratios. Thus, if the imposed velocity is twice as large, we obtain the same velocity field but at twice the amplitude. Equation 1 breaks down when the viscosity ratio is too low; we must ensure that the slab rigidity is sufficiently large for the deflection to be inferior or equal to the slab displacement, which puts a minimum bound on the allowable viscosity ratio.

RESULTS

The resulting flow pattern (Fig. 1A) shows a pair of symmetrical toroidal cells, one on each side of the slab, focused close to the plate edges. Velocities are maximum just upstream and downstream of the plate (most positive values) and close to the slab edges (most negative values). On the sides of the slab, the negative y velocity is the return flow. Slab retreat results in compression along the upstream side of the slab and extension along the downstream side of the slab (Fig. 1B). The stress pattern also shows two opposite-sign ear-shape anomalies, on either side of the slab, of amplitudes proportional to the slab width. It is interesting that maximum stresses are found close to the slab edges (Fig. 1C); away from the slab edges, the stress field abruptly reverts and becomes extensional (negative) on the upstream side and compressive (positive) on the downstream side. Near the center of the slab, the deviatoric stresses diminish and tend toward zero (Fig. 1C). In all experiments, slab deformation is concentrated along its edges, where stresses are maximum. This surprising stress distribution (see also Morra et al., 2006) is responsible for slab curvature along their edges. As time progresses, the slab geometry evolves at a rate that is dictated by the slab to mantle viscosity ratio.

We performed a series of experiments in which the slab was alternatively 500, 1000, and 2000 km wide and 50, 100, and 200 km thick. For each experiment, the viscosity ratio between the slab and surrounding mantle was systematically changed to encompass the desired range. The system is bounded by the no-velocity conditions along the edges of the box, and the behavior of the slab depends on the box width to slab dimension ratio. This condition mimics real Earth conditions, where subduction zones are embedded in the finite terrestrial system.

We characterize slab curvature from a quadratic regression on the slab shape. After a mean retreat of 1000 km, the coefficient of curvature C of the slab (defined as the quadratic coefficient of a quadratic polynomial function fit) varies between 10^{-4} and 6 10^{-3} km^{-1} (Fig. 2). In all cases, curvature is inversely proportional to the viscosity ratio [$C \sim 1/(\mu_s/\mu_m)$], with the lowest ratio leading to the highest curvature, as imposed by the above equation for flexure. As slabs widen, the stresses in the fluid during slab retreat become high because free space around the slab decreases. Consequently, wide slabs get highly loaded and slab curvature increases accordingly. Slab rigidity varies as the cube of slab thickness, the thicker the slab the smaller the curvature, and our models accordingly yield $C \sim h^{-3}$.

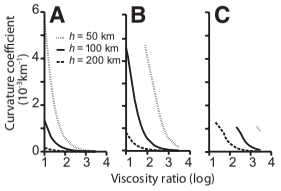

Figure 2. Slab coefficient of curvature (see text) as function of lithosphere to surrounding mantle viscosity ratio. Slab is alternatively 50 (dotted), 100 (solid), and 200 km (dashed) thick (*h*) and 500 (A), 1000 (B), and 2000 (C) km wide, respectively. Some curves are truncated when initial model assumptions no longer hold (see text).

COMPARISON TO REAL EARTH

The curvature of narrow slabs (e.g., Scotia, Calabria, Hellenic) is larger than that of wider slabs (e.g., Aleutian, South America, Java, Tonga). In order to determine the shape of slabs at depth, we use the results of P-wave seismic tomography (Li et al., 2008) and catalogues of earthquake locations (International Seismological Centre, 2008; Engdahl et al., 1998) for four subduction systems (Aleutians, Scotia, Hellenic, and Calabria) selected for the variety of width, thickness, and retreat velocity they present. We also compare our interpretation to the slab geometries derived from the RUM (regionalized upper mantle) model (Gudmundsson and Sambridge, 1998). In practice we mapped the tomographic model on a Cartesian grid, together with seismicity and the RUM slab geometry. We estimated slab curvature by contouring the fast seismic velocity anomalies. We measured the curvature between 50 and 700 km in the upper mantle, every 50 km. Because the depth along the subducted lithosphere correlates with a residence time in the mantle, i.e., the time during which the section of the slab entered the subduction zone and experienced the pressure field from the surrounding mantle, we expect the curvature of a viscous slab to increase with depth. One should, however, be careful in estimating slab curvature for very wide slabs, because other factors, such as the age of the lithosphere, the nature of the overriding plate, the presence of seamounts or oceanic plateaus in the subduction zone (Nur and Ben-Avraham, 1982), and possibly more important, the aspect ratio between upper mantle thickness and slab width, could affect the curvature of the slab near the surface.

We match observations to model results by computing the flow around the slab using kinematic and geometric characteristics of each natural system. Because trench velocity depends on the reference frame, we consider the Indo-Atlantic (O'Neill et al., 2005) and Pacific (Gripp and Gordon, 2002) hotspot reference frames, as well as the no-net-rotation frame (Kreemer et al., 2003). Trench migration rates are from Schellart et al. (2008) (Table 1). The slab-to-mantle viscosity ratio is therefore the remaining free parameter that we vary until

TABLE 1. KINEMATIC AND GEOMETRICAL CHARACTERISTICS OF THE SUBDUCTION SYSTEMS AND BEST-FIT SLAB-TO-MANTLE VISCOSITY RATIOS

	Velocity (mm a–1) Vs	Velocity (mm a–1) IA Vt	Velocity (mm a–1) HS3 Vt	Velocity (mm a–1) NNR Vt	Slab thickness (km)	Slab width (km)	μs/μm IA	μs/μm HS3	μs/μm NNR
Aleutian	71	12	–5	21	100	3000	40	*	80
Scotia	74	57	40	94	70	1000	60	50	100
Hellenic	44	23	51	10	100	1100	40	60	30
Calabria	68	68	52	10	100	600	10	5	1

Note: The trench–perpendicular trench migration rate (i.e., *Vt*, slab retreat rate) (trench retreat is taken as positive) and Vs, the velocity of the subducting plate in three global reference frames. IA—Indo-Atlantic hotspot reference frame (O'Neill et al., 2005); HS3—Pacific hotspot reference frame (Gripp and Gordon, 2002); NNR—no-net-rotation reference frame of Kreemer et al. (2003). μs/μm is the viscosity ratio between slab and surrounding mantle obtained by the best fit between model and natural data for each global reference frame. Kinematic values are from Schellart et al. (2007). Trench length is measured after Gudmundsson and Sambridge (1998).
*Observed slab curvature is incompatible with Aleutian trench advance in this reference frame.

the modeled and observed curvatures match (Fig. 3). In all cases the domain is 10,000 km wide, which may induce a systematic bias, because we do not know what the most appropriate dimension would be for Earth. This recurrent issue relates to the Stokes paradox (Lamb, 1932). Nonetheless, the slab to box edge distance (5000 km) is comparable to the characteristic distance that separates slabs from each other on Earth.

The estimated viscosity ratio varies between 1 and 100 (Table 1). We note that for narrow slabs (Scotia and Calabria slabs; Figs. 3B and 3D), slab curvature strongly increases with depth. For Calabria, the strong curvature is best fitted by using a slightly lower viscosity ratio, which may be consistent with local geodynamics (Faccenna et al., 2007). Wider slabs are characterized by a lower curvature (Figs. 3A and 3C) but the best-fit viscosity ratio is in the same range (40–80) as the narrower Scotia slab, also suggesting that the slab width-to-length ratio primarily controls slab curvature. In all cases, the RUM model leads to grossly overestimated slab curvature except for the wide Aleutian slab.

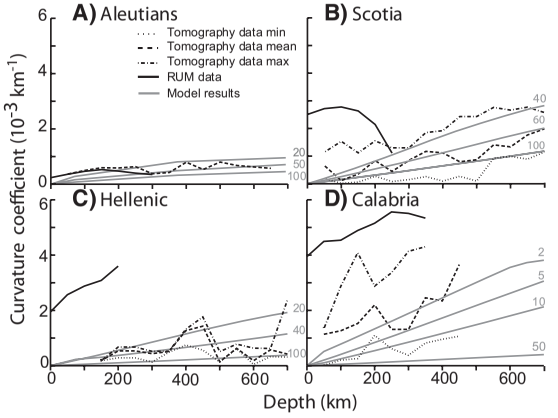

Figure 3. Evolution of predicted (gray curves) and observed (from geophysical data, black curves: minimum—dotted; mean—dashed; and maximum—dotted-dashed) coefficient of curvature of slab (see text) as function of depth for several viscosity ratios between slab and upper mantle, for Aleutian (A), Scotia (B), Hellenic (C), and Calabria (D) subduction zones (for Indo-Atlantic reference frame). Geophysical data used include global P-wave seismic tomography model (Li et al., 2008), location of seismic events from International Seismological Centre (2008) catalog, database published by Engdahl et al. (1998), and RUM (regionalized upper mantle) model for global slab geometry (Gudmundsson and Sambridge, 1998).

DISCUSSION AND CONCLUSION

Slab motion is primarily driven by the negative buoyancy of the slab with respect to the ambient mantle and is controlled to a large extent by slab width. The toroidal component of mantle circulation, unaccounted for in 2-D models, plays a key role in shaping the slab. Increasing slab width confines the toroidal flow into a constant size domain. It decreases trench velocity and the vigor of the mantle flow, and generates a higher stress field in the fluid, and ultimately a higher rate of viscous energy dissipation (Fig. 4B). Consequently, slab width also tends to inhibit trench retreat (Schellart, 2004; Stegman et al., 2006) (Fig. 4A), and, at a given stage in the temporal evolution of the slab, slab curvature will be lower for a wide slab than for a narrow one. Although the buoyancy of a slab is linearly proportional to its width, because the viscous dissipation increases as a power law of slab width in a mantle of finite dimension (Fig. 4B), the resisting force will ultimately dominate and large slabs will retreat at slower rates than small ones as an indirect consequence of the Stokes paradox (Lamb, 1932). Thus, these results in turn explain why narrow slabs (e.g., Calabria or Scotia) retreat faster (Fig. 4A) than wider ones. Our assumption that the surface is implicitly stress free (2-D approximation) affects our results (e.g., Jarvis and Lowman, 2005), as does the no-slip lateral boundary condition that will influence the flow pattern (e.g., Piromallo et al., 2006) and accentuate the Stokes paradox effect.

The comparison of theoretical computations with natural slab curvature independently delimits the viscosity ratio between the subducted lithosphere and the surrounding mantle to range from 1 to 100, with an average of ~45,

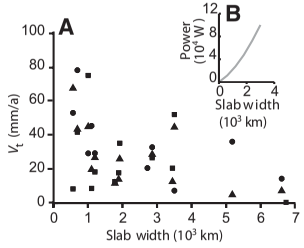

Figure 4. A: Average trench-perpendicular migration rate (V_t is slab retreat rate) as function of slab width in Pacific (circles, Gripp and Gordon, 2002) and Indo-Atlantic (triangles, O'Neill et al., 2005) hotspot reference frames, as well as in no-net-rotation model of Kreemer et al. (2003) (squares). Data are from Schellart et al. (2008). B: Predicted energy dissipation rate (power) as function of slab width.

smaller by a factor of 2 (Capitanio et al., 2007) to more than 10^4 (Billen and Hirth, 2007) compared to previous estimates. In other words, if the upper mantle viscosity is assumed to be 10^{20} Pa s, slab viscosity is in the range 10^{20}–10^{22} Pa s, with a mean value of 4.5×10^{21} Pa s. The choice of the reference frame may change the values of the viscosity ratio by a factor of 2 (Table 1; comparable to Funiciello et al., 2008). However, because the azimuthal distribution of trenches on Earth is approximately even, mean retreat rates, and therefore the mean viscosity ratios, should be independent of the reference frame.

ACKNOWLEDGMENTS

We thank W. Royden, F. Chambat, P. Yamato, and B. Huet for stimulating discussions. Loiselet and Braun acknowledge funding from the Agence National de la Recherche (ANR), and Husson from the Institut National des Sciences de l'Univers–Centre National de la Recherche Scientifique (INSU/CNRS) program "SEDIT." We thank editor S. Wyld, and F. Funiciello, W. Schellart, and an anonymous reviewer for constructive reviews.

REFERENCES CITED

Billen, M.I., and Hirth, G., 2007, Rheologic controls on slab dynamics: Geochemistry Geophysics Geosystems, v. 8, Q08012, doi: 10.1029/2007GC001597.

Capitanio, F.A., Morra, G., and Goes, S., 2007, Dynamic models of downgoing plate-buoyancy driven subduction: Subduction motions and energy dissipation: Earth and Planetary Science Letters, v. 262, p. 284–297, doi: 10.1016/j.epsl.2007.07.039.

Christensen, U., and Yuen, D., 1984, The interaction of a subducted lithosphere slab with a chemical or phase boundary: Journal of Geophysical Research, v. 89, p. 4389–4402, doi: 10.1029/JB089iB06p04389.

Clark, S.R., Stegman, D., and Muller, R.D., 2008, Episodicity in back-arc tectonic regimes: Physics of the Earth and Planetary Interiors, v. 171, p. 265–279, doi: 10.1016/j.pepi.2008.04.012.

Conrad, C.P., and Hager, B.H., 1999, Effect of plate bending and fault strength at subduction zones on plate dynamics: Journal of Geophysical Research, v. 104, p. 17,551–17,571, doi: 10.1029/1999JB900149.

Dvorkin, J., Nur, A., Mavko, G., and Ben-Avraham, Z., 1993, Narrow subducted slabs and the origin of backarc basins: Tectonophysics, v. 227, p. 63–79, doi: 10.1016/0040-1951(93)90087-Z.

Engdahl, E.R., van der Hilst, R., and Buland, R., 1998, Global teleseismic earthquake relocation with improved travel times and procedures for depth determination: Seismological Society of America Bulletin, v. 88, p. 722–743.

Faccenna, C., Civetta, L., Massimo, D.A., Moroni, M., and Piromallo, C., 2007, Slab disruption, mantle circulation, and the opening of the Tyrrhenian basins, *in* Beccaluva, L., et al., eds., Cenozoic volcanism in the Mediterranean area: Geological Society of America Special Paper 418, p. 153–169, doi: 10.1130/2007.2418(08).

Frank, F.C., 1968, Curvature of island arcs: Nature, v. 220, p. 363, doi: 10.1038/220363a0.

Fukao, Y., Widiyantoro, S., and Obayashi, M., 2001, Stagnant slabs in the upper and lower mantle transition region: Reviews of Geophysics, v. 39, p. 291–323, doi: 10.1029/1999RG000068.

Funiciello, F., Faccenna, C., Giardini, D., and Regenauer-Lieb, K., 2003, Dynamics of retreating slab: 2. Insights from three-dimensional laboratory experiments: Journal of Geophysical Research, v. 108, 2207, doi: 10.1029/2001JB000896.

Funiciello, F., Moroni, M., Piromallo, C., Faccenna, C., Cenedese, A., and Bui, H.A., 2006, Mapping mantle flow during retreating subduction: Laboratory models analyzed by feature tracking: Journal of Geophysical Research, v. 111, B03402, doi: 10.1029/2005JB003792.

Funiciello, F., Faccenna, C., Heuret, A., Lallemand, S., Di Giuseppe, E., and Becker, T.W., 2008, Trench migration, net rotation and slab-mantle coupling: Earth and Planetary Science Letters, v. 271, p. 233–240, doi: 10.1016/j.epsl.2008.04.006.

Goes, S., Capitanio, F., and Morra, G., 2008, Evidence of lower-mantle slab penetration phasesin plate motions: Nature, v. 451, p. 981–984, doi: 10.1038/nature06691.

Gripp, A.E., and Gordon, R.G., 2002, Young tracks of hotspots and current plate velocities: Geophysical Journal International, v. 150, p. 321–361, doi: 10.1046/j.1365-246X.2002.01627.x.

Gudmundsson, O., and Sambridge, M., 1998, A regionalized upper mantle (RUM) seismic model: Journal of Geophysical Research, v. 103, p. 7121–7136, doi: 10.1029/97JB02488.

Husson, L., 2006, Dynamic topography above retreating subduction zones: Geology, v. 34, p. 741–744, doi: 10.1130/G22436.1.

International Seismological Centre, 2008, Regional catalog of earthquakes: International Seismological Centre, http://www.isc.ac.uk/doc/products/catalogue.html.

Isacks, B., and Molnar, P., 1971, Distribution of stresses in the descending lithosphere from a global survey of focal mechanism solutions of mantle earthquakes: Reviews of Geophysics, v. 9, p. 103–174, doi: 10.1029/RG009i001p00103.

Jarvis, G.T., and Lowman, J.P., 2005, Sinking slabs below fossil subduction zones: Physics of the Earth and Planetary Interiors, v. 152, p. 103–115, doi: 10.1016/j.pepi.2005.05.002.

Kincaid, C., and Griffiths, R.W., 2004, Variability in flow and temperatures within mantle subduction zones: Geochemistry Geophysics Geosystems, v. 5, p. Q06002, doi: 10.1029/2003GC000666.

Kreemer, C., Holt, W.E., and Haines, A.J., 2003, An integrated global model of present-day plate motions and plate boundary deformation: Geophysical Journal International, v. 154, p. 8–34, doi: 10.1046/j.1365-246X.2003.01917.x.

Lamb, H., 1932, Hydrodynamics (sixth edition): Cambridge, Cambridge University Press, 768 p.

Li, C., van der Hilst, R.D., Engdahl, E.R., and Burdick, S., 2008, A new global model for P wave speed variations in Earth's mantle: Geochemistry Geophysics Geosystems, v. 9, p. 157–168, doi: 10.1016/j.epsl.2008.07.016.

Morra, G., Regenauer-Lieb, K., and Giardini, D., 2006, Curvature of oceanic arcs: Geology, v. 34, p. 877–880, doi: 10.1130/G22462.1.

Morra, G., Chatelain, P., Tackley, P., and Koumoutzakos, P., 2009, Earth curvature effects on subduction morphology: Modeling subduction in a spherical setting: Acta Geotechnica, doi: 10.1007/s11440-008-0060-5.

Nur, A., and Ben-Avraham, Z., 1982, Oceanic plateaus, the fragmentation of continents, and mountain building: Journal of Geophysical Research, v. 87, p. 3644–3661, doi: 10.1029/JB087iB05p03644.

O'Neill, C., Muller, D., and Steinberger, B., 2005, On the uncertainties in hot spot reconstructions and the significance of moving hot spot reference frames: Geochemistry Geophysics Geosystems, v. 6, Q04003, doi: 10.1029/2004GC000784.

Piromallo, C., Becker, T.W., Funiciello, F., and Faccenna, C., 2006, Three-dimensional instantaneous mantle flow induced by subduction: Geophysical Research Letters, v. 33, doi: 10.1029/2005GL025390.

Royden, L.H., and Husson, L., 2006, Trench motion, slab geometry and viscous stresses in subduction systems: Geophysical Journal International, v. 167, p. 881–905, doi: 10.1111/j.1365-246X.2006.03079.x.

Schellart, W.P., 2004, Kinematics of subduction and subduction-induced flow in the upper mantle: Journal of Geophysical Research, v. 109, B07401, doi: 10.1029/2004JB002970.

Schellart, W.P., Freeman, J., Stegman, D.R., Moresi, L., and May, D., 2007, Evolution and diversity of subduction zones controlled by slab width: Nature, v. 446, p. 308–311, doi: 10.1038/nature05615.

Schellart, W.P., Stegman, D.R., and Freeman, J., 2008, Global trench migration velocities and slab migration induced upper mantle volume fluxes: Constraints to find an Earth reference frame based on minimizing viscous dissipation: Earth-Science Reviews, v. 88, p. 118–144, doi: 10.1016/j.earscirev.2008.01.005.

Stegman, D.R., Freeman, J., Schellart, W.P., Moresi, L., and May, D., 2006, Influence of trench width on subduction hinge retreat rates in 3-D models of slab rollback: Geochemistry Geophysics Geosystems, v. 7, Q03012, doi: 10.1029/2005GC001056.

Tovish, A., and Schubert, G., 1978, Island arc curvature, velocity of convergence and angle of subduction: Geophysical Research Letters, v. 5, p. 329–332, doi: 10.1029/GL005i005p00329.

Turcotte, D.L., and Schubert, G., 1982, Geodynamics: Application of continuum physics to geological problem: New York, John Wiley and Sons, 450 p.

Van der Hilst, R., and Karason, H., 1999, Compositional heterogeneity in the bottom 1000 kilometers of Earths mantle: Toward a hybrid convection model: Science, v. 283, p. 1885–1888, doi: 10.1126/science.283.5409.1885.

Wortel, M.J.R., and Spakman, W., 2000, Subduction and slab detachment in the Mediterranean-Carpathian region: Science, v. 290, p. 1910–1917, doi: 10.1126/science.290.5498.1910.

Wu, B., Conrad, C.P., Heuret, A., Lithgow-Bertelloni, C., and Lallemand, S., 2008, Reconciling strong slab pull and weak plate bending: The plate motion constraint on the strength of mantle slabs: Earth and Planetary Science Letters, v. 272, p. 412–421, doi: 10.1016/j.epsl.2008.05.009.

Zhong, S., and Davies, G.F., 1999, Effects of plate and slab viscosities on the geoid: Earth and Planetary Science Letters, v. 170, p. 487–496, doi: 10.1016/S0012-821X(99)00124-7.

Zhong, S., and Gurnis, M., 1994, Controls on trench topography from dynamic models of subducted slabs: Journal of Geophysical Research, v. 99, p. 15,683–15,695, doi: 10.1029/94JB00809.

Manuscript received 21 January 2009
Revised manuscript received 24 March 2009
Manuscript accepted 1 April 2009

Printed in USA

2.4.2 Déformation des plaques en subduction

Il ressort de l'étude précédente que les plaques en subduction ont une viscosité effective faible aux regard des estimations précédentes (voir l'article). Les conséquences de ce résultat ne sont pas triviales pour l'interprétation des observations des panneaux plongeants en subduction. Leurs géométries, vues par la tomographie sismique, montrent des variations d'épaisseurs importantes [Fukao et al., 2001, Kárason & van der Hilst, 2001]. Dans l'hypothèse d'un rapport de viscosité fort entre la lithosphère et le manteau matriciel, une possible interpétation est celle de Ribe [Ribe et al., 2007] dans laquelle l'épaississement perçu au niveau de la zone de transition correspond à un empilement du panneau plongeant replié sur lui-même entre le manteau supérieur et le manteau inférieur, plus visqueux et plus dense. Dans l'hypothèse que nous défendons ici, où la viscosité du panneau plongeant est moins de deux ordres de grandeur plus visqueuse que celle du manteau, cette possibilité ne tient plus. Alternativement, nous montrons avec C. Loiselet et co-auteurs, que le comportement naturel d'un panneau visqueux en subduction est de former une sorte de panache inversé, une *méduse* composé d'une tête épaissie dont la forme s'optimise pour former une boule et minimiser le travail à mesure que le panneau plongeant pénètre dans le manteau. Cette tête est suivie d'une queue en extension qui connecte le panneau plongeant à la lithosphère non subductée en surface. Les observations géométriques et sismologiques soutiennent notre interprétation.

Subducting slabs: jellyfishes in the Earth mantle

Loiselet C.[1], Braun J.[1], Husson L.[1,2], Le Carlier de Veslud C.[1] , Thieulot C.[3],Yamato P. [1], and Grujic D.[4]

[1]Géosciences Rennes, Université de Rennes 1, UMR CNRS 6118, Rennes, France.

christelle.loiselet@univ-rennes1.fr

[2]Laboratoire de Planétologie et Géodynamique, Université de Nantes, UMR CNRS 6112, Nantes, France.

[3]Department of Earth Sciences, Bergen University, Norway.

[4]Department of Earth Sciences, Dalhousie University, Halifax, Canada.

- Submitted to G3 -

Abstract

The constantly improving resolution of geophysical data show that the lithosphere does not subduct as a slab of uniform thickness but is rather thinned in the upper mantle and thickened around the transition zone between the upper and lower mantle. This observation has been interpreted as an evidence for the buckling and piling of slabs having a viscosity many orders of magnitude higher than the surrounding mantle. Seismicity also revealed that slabs undergo vertical extension in the upper mantle and compression near the transition zone. In this paper, we show that during the subduction process, the shape of low viscosity slabs (1 to 100 times more viscous than the surrounding mantle) evolves toward a shape which minimizes viscous dissipation, i.e., that of an inverted plume that we coin *jellyfish*. Our 3D numerical models show that the leading tip of slabs deform toward a rounded head wrapped by lateral *tentacles* that

emerge from the sides of the *jellyfish* head. The head is linked to the body of the subducting slab by a thin tail. More accurately, our parametric study reveals a variety of shapes in good agreement with the diversity of natural slab shapes as seen from seismic tomography. It comes out that the slab to mantle viscosity ratio on Earth is most likely lower than 100. However, the sensitivity of slab shapes to upper and lower mantle viscosities and densities precludes any systematic deciphering of the observations.

Keywords: Subduction, mantle stratification, seismic tomography

Introduction

The wide range of shapes observed among subducting oceanic lithospheres [*Isacks and Barazangi*, 1977; *Isacks and Molnar*, 1971] suggests a complex dynamical behavior for the penetration of slabs into the mantle. The lack of earthquake activity below 700 km depth and the compressive nature of the focal mechanism of the deep earthquakes along the surface of the slabs have been interpreted to reflect the resistance of slabs in penetrating into the lower mantle [*Isacks and Molnar*, 1971]. Such observations are at least compatible with dynamic models of the long wavelength geoid anomalies associated with slabs requiring an increase in viscosity from the upper to the lower mantle by a factor 10-100 [*Hager and Richards*, 1989; *Lambeck and Johnston*, 1998; *Moresi and Gurnis*, 1996; *Peltier*, 1996; *Ricard and Y.*, 1993] or more [*Kido and Čadek*, 1997]. But travel time tomography has also revealed that positive seismic anomalies attributed to slabs often extend into the lower mantle [*Creager and Jordan*, 1984; *Grand*, 1994; *Jordan*, 1977; *Jordan and Lynn*, 1974]. In the last decade, images from seismic tomography have improved in resolution and accuracy, and have revealed that slabs tend to thicken during penetration into the lower mantle, i.e. from the transition zone to mid-mantle depths [*Bijwaard, et al.*, 1998; *Fukao, et al.*, 2001; *Grand, et al.*, 1997; *Ren, et al.*, 2007]. Examples thereof include the Central and South Americas [*Karason and Van der Hilst*, 2001], southern Asia [*Li, et al.*, 2008] or the Aegean slab [*Piromallo and Morelli*, 2003; *Wortel and Spakman*, 2000]. Slab thickening in the mid-lower mantle is often interpreted as evidence for periodic buckling of cold and stiff lithospheres as they penetrate into the mantle [*Gaherty and Hager*, 1994; *Guillou-Frottier, et al.*, 1995; *Gurnis and Hager*, 1988; *Loubet, et al.*, 2009; *Moresi and Gurnis*, 1996; *Ribe, et al.*, 2007; *Tao and O'Connell*, 1992; 1993]. However, the significant deformation of slabs going down to the mantle has also been interpreted as evidence that subducting plates could be very weak [*Bevis*, 1986; *Giardini and Woodhouse*, 1984]. In that sense, Tao and Gurnis [1993] showed that a weak slab model is consistent with seismic observation.

In this work, we explore the possibility that a plate sinking into the mantle deforms and naturally thickens at mid-depths, with no need for a stiff lithosphere nor a viscosity and density jump into the lower mantle. To demonstrate this point, we investigate the role of the viscosity ratios between the plate and the surrounding fluid and subsequently the role of a mantle stratification (in viscosity or density jump) in forming a wide range of shapes, ranging from that of the undeformed slab to the characteristic shape of a downwelling plume that we refer to as a *jellyfish*. In the latter part of this paper, we further discuss our results in light of observed slab geometries, which we extract from seismic tomography images.

Methodology

In order to explore the dynamic interactions between the subducting lithosphere and the surrounding viscous mantle, we evaluate the deformation pattern of a slab sinking into the mantle by means of a complex three-dimensional numerical model that is designed to track sharp, dynamically deforming interfaces. The 3D finite element code *DOUAR* [*Braun, et al.*, 2008]

solves the conservation equations for mass, momentum and energy in the Boussinesq approximation, assuming that the mantle is an incompressible viscous medium. *DOUAR* is an ALE Finite Element code based on an adaptive octree grid [*Thieulot, et al.*, 2008]. The computational domain is a unit cube whose elements are the leaves of the octree. A zero level octree only counts $(2^0)^3 = 1$ leaf. After one division, the octree has $(2^1)^3 = 8$ leaves and is of level L = 1. Consequently a 64 x 64 x 64 grid is a level 6 octree with $(2^6)^3 = 262{,}144$ leaves. The flow is driven by internal density difference $\Delta\rho$ between the subducting lithosphere and the surrounding mantle. We simplify our analysis by assuming an infinite Prandtl number in a fluid with very low Reynolds number and a linear rheology for all components of the system. The dimensionless *Navier-Stokes* and incompressibility equations are given by

$$\rho\frac{Du}{dt} = -\nabla P + \mu\Delta u + \rho g \qquad (1)$$

and

$$\nabla . u = 0 \qquad (2)$$

where ρ is the density, g, gravitational acceleration, P the pressure field, μ the dynamic viscosity and u the velocity, and t the time. Neglecting the local acceleration (i.e. the inertia in the system), equation (1) then reduces to the *Stokes* equation:

$$\mu\Delta u + \rho g = \nabla P \qquad (3)$$

Interfaces (between the slab, upper mantle and lower mantle) (they are advected by using the computed velocity field) are tracked by a dual method combining Lagrangian particles for accuracy and level set functions (see [*Braun, et al.*, 2008], for further details on this method).

The model setup is shown on Figure 1 A and parameters are given in Table 1. The computational numerical domain is a unit cube (i.e. 1 x 1 x 1 in x, y, z directions) representing a ~ 2750 km Cartesian box, corresponding to the earth mantle. The mantle is divided between a upper and lower mantle where discontinuity is localized to z_{660}=0.24 (~660 km). The grid counts $(64)^3$ (level 6 octree) regularly spaced elements everywhere but in and around the slab the resolution is increased to level 8. Free slip is assumed on all boundaries. The experiment is initiated by placing a vertical (unless otherwise specified) plate of length, l=0.066 (~ 182 km) and thickness h=0.03 (~ 83 km) in the mantle between depths of 0.03 to 0.096 (~ 83 km to 264 km, Fig. 1A). To ensure that the fall of the plate is solely controlled by the buoyancy forces arising from the density contrast and by the viscosity ratio between the plate and surrounding viscous fluid, the top boundary of the plate (located at a depth of 0.03 from the top of the model box) is artificially not advected by the computed velocity field. Otherwise, plate is attached to the top. In this way we discard any resistance to sinking that may arise in nature from the relative horizontal movement between the plate and the mantle. Our setup can also be regarded as that of an infinite lithospheric plate that is perfectly lubricated near the surface. We assign a constant density contrast between the slab and the surrounding mantle. All viscosities are Newtonian and uniform within the slab and the mantle; the upper mantle viscosity is taken as the reference viscosity (= 1). More complex rheologies may prevail in nature, especially taking into account the influence of temperature coupling with (e.g. [*Billen and Gurnis*, 2005]), but we choose to keep the model as simple as possible in order to quantify its behavior as a function of given effective slab to

mantle viscosity ratios that we vary from μ_s=0.01 to 100. Plate width, *w,* and slab dip, α, are also varied between 1/8, 1/4, and 1/2 of the box width and 90, 70, 60, 45 and 30 degrees respectively.

Results

We performed a series of 27 experiments to explore the dependence of the slab deformation on slab to lower mantle density contrast $\Delta\rho$, slab width, *w,* slab dip, α, slab to mantle viscosity ratio μ_s, lower to upper mantle viscosity ratio μ_{lm}. Some interesting features prevail regardless of the parameters that we review below. To illustrate this point, we first show the results of a simple experiment (reference model) in which the plate viscosity is 10 times that of the upper mantle. There is no viscosity or density contrast between upper and lower mantle. The initial plate width is 0.25 and the slab is vertical.

General evolution of the models

During the sinking of the plate into the mantle, its shape evolves in a way comparable to a large extent to a reverse or descending plume (Fig. 1A) [*Christensen and Yuen*, 1984]. Note, however, that, in most of our models, the viscosity ratio is inverted in comparison with a typical rising mantle plumes which have a lower viscosity than the surrounding mantle. The shape of the slab is characterized by a rounded head at its leading tip with two trailing "tentacles" along each narrow edge (Fig. 1B), connected to the surface by a long rectangular section tail. To a minor extent, the mantle also drags the longer edges and gently wraps them over the body of the slab (Fig. 1B). In the following, we refer to the deformed shape of the slab as that of a *jellyfish*, for both our model slabs and real jellyfishes are characterized by comparable shapes that minimize the viscous dissipation of energy while they penetrate/move into the fluid. The jellyfish shape can be characterized by the longitudinal radius of curvature R_w and the lateral radius of curvature R_h (see Fig. 1C). In practice, to calculate R_w and R_h, we compute the equation of the circle that circumscribes the triangle defined by the three vertices made by the leading tip (deepest point of the greatest *z*-value) and the two tips of the tentacles in the longitudinal direction (points of maximum and minimum *x*-value for R_w and *y*-value for R_h,). To further characterize the shape of the jellyfish and the flow it engenders in the mantle, we compute, for each of the numerical experiments: (a) the velocity of the jellyfish head (plate surface point at maximum *z*-direction and its curvature radius, (b) the maximum strain rate along the central vertical axis *z,* (c) the surface area of horizontal sections (distant by 0.03) of the plate as a function of depth and (d) the total viscous dissipation in the mantle.

During the first stages of subduction, the slab head becomes wider, thicker and curved in both plane (Fig. 1B). The sinking velocity (measured at the jellyfish head) increases with plate deformation (Fig. 2A). The radius of curvature R_w decreases rapidly (Fig. 2B) as the slab tip evolves from a straight horizontal edge into a curved body. During this phase both the strain rate (Fig. 3A) and the viscous dissipation in the mantle (Fig. 3B) increase rapidly. When the slab tip reaches depths of 0.2 to 0.4, the head of the jellyfish is fully developed and an optimal curvature has been reached as indicated by a constant minimal value for R_w (Fig. 2B).

As the slab further penetrates into the mantle, the ratio between the lateral and longitudinal radii increases (Fig. 2 B), suggesting that the jellyfish head evolves toward of the shape of a sphere. During this stage, the sinking velocity continues to increase towards a maximum value (Fig. 2A) yet the strain rate and mantle viscous dissipation remain constant (Fig. 3A and 3B). In fact, once the jellyfish is formed, only the "tentacles" continue to grow (Fig. 1B). A neck forms above the jellyfish head, along the tail connecting the head to the surface (Fig. 1B), its area remaining

constant. At this stage, the jellyfish head area is respectively 1.5 and 2 times larger than the maximum (which is at the surface) and minimum (at the neck) surface area of the tail (Fig. 3D). According to the distribution of vertical strain (Fig. 3C), the tail is stretched near the surface while the head is compressed (Fig. 3C). Consequently, the head perimeter is as enlarged as the tail is thinned with respect to the original dimension of the slab before subduction.

The final stage of evolution of the shape of the slab reflects the interaction of the jellyfish with the bottom of the box. The sinking velocity decreases to zero and the jellyfish head flattens.

This general scheme is modulated in order to understand the processes that control the behavior of the slab as it penetrated into the mantle.

Slab width

Plate width is known to influence the kinematics of subduction [*Di Giuseppe, et al.*, 2008; *Loiselet, et al.*, 2009; *Piromallo, et al.*, 2006; *Schellart, et al.*, 2007]. We evaluate its impact on the shape of the jellyfish by varying the plate width w between 0.125 and 0.5 (1/8 and 1/2 of the box width) while keeping the box size and plate thickness constant. In all cases, the radius of curvature R_w of the jellyfish head decreases through time and tends toward a minimal value (Fig. 4A). When normalized to slab width w and slab thickness h, R_w reaches a value comprised within a narrow range (~ 3/4) proportional to the width and thickness length sum, i.e jellyfish head evolves toward a uniform spherical shape with a diameter proportional to 1.5 times (w+h). This is better illustrated by the R_h/R_w ratio (Fig. 4B), which increases with slab penetration. Of course, the ratio between the initial slab width and thickness influences the curvature of the jellyfish head. If the plate has a square horizontal cross section diameter tends to 1 and R_w is always equal to R_h.

Slab dip

In most natural cases, subduction does not initiate vertically: slabs tend to dip at finite angle underneath the overriding plate. We explore the impact of the slab dip on the jellyfish evolution by varying its value between 30 and 90 degrees. In figure 5, we present results from two experiments, characterized by slab dip 60 and 30 degrees respectively. The radius of the jellyfish head decreases and tends toward a minimal R_w value, regardless of initial slab dip. However, the morphology gets highly asymmetrical for shallow dipping slabs and the jellyfish shape transforms into a spoon shape (Fig. 5A and 5B). Note that in our numerical setup, the point of subduction remains fixed with respect to the underlying mantle while, in nature, this may not be the case and slabs may gradually become vertical, thanks to the advance of the trench and/or retreat of the slab/head (Fig. 5C and 5D).

Slab to mantle viscosity ratio

We test different viscosity ratio (from 10^{-2} to 10^{2}) between the lithosphere and the surrounding mantle (Fig. 6A). Note that in the absence of any viscosity difference between the slab and mantle, the flow is that of a *Stokes* sinker.

Expanding the work of Olson and Singer [1985] on creeping, rising plumes, we identify three classes of jellyfishes based on the development of the jellyfish head: (i) Cavity jellyfishes, for which the plate viscosity is lower than that of the mantle; they feature well rounded heads connected to tails upon which tentacles are retracted (Fig. 6A, $\mu_s = 10^{-2}$). (ii) Diapiric jellyfishes develop when the system is isoviscous or close to it. They differ from cavity jellyfishes by their well-individualized tentacles and even better rounded head (Fig. 6A, $\mu_s = 1$). (iii) Anvil jellyfishes

develop when the viscosity ratio is much larger than 1. Slab grows into inverted anvil-shaped cap (i.e. jellyfish head) at its leading edge (Fig. 6A, $\mu_s = 10^1$-10^2). Anvil jellyfishes more likely applies to the Earth than the others and in the following we therefore focus on this class. The deformation highly depends on the viscosity ratio, as illustrated by the strain rates along the vertical *z*-axis of the jellyfish (Fig. 6B). The lower the viscosity ratio is, the higher strain rates are, extensive in the tail and compressive in the head. When $\mu_s >> 100$, the slab does not deform and the head and tail do not develop.

For high viscosity contrast, the radius of curvature R_w also decreases through time to reach a minimum value (Fig. 6C). This indicates that, in all cases and regardless of the viscosity ratio, the plate will tends toward an optimal shape (for an infinite domain in the vertical direction), although this might require a very long descent time for a very large viscosity ratio. In all cases, the velocity increases gradually during the early stages of evolution of the jellyfish at shallow depths; it reaches a maximum value, and eventually decreases when plate penetration is hindered by the undeformable bottom of the model experiment (Fig. 6D).

Interestingly, the viscosity ratio affects the sinking velocity. The slab penetrates faster into the mantle when μ_s is high (μ_s=100) and the velocity reaches its maximum value at greater depths than for less viscous slabs. When the viscosity ratio is low (μ_s=1), the velocity starts to decrease at rather shallow depths (~0.35). These results can be explained by the joint effects of the plate bulk mass (because the plate remained relatively undeformed, the flux boundary condition imposed near the surface results in a larger mass flux and thus larger negative buoyancy), of plate stretching in the tail (which for low viscosity slabs, favors viscous dissipation in the surrounding mantle and prevent efficient stress transmission) and the passive resistance of the bottom of the mantle. Both extensive and compressive strain rates respectively larger in the tails and in the heads of low viscosity jellyfishes than the high viscosity ones implies that the sinking velocity of low viscosity slabs will more easily tend to the *Stokes* velocity of the jellyfish head; this velocity yet remains lower than the sinking velocity of highly viscous slabs that are more negatively buoyant simply because of the plate volume.

Viscosity stratification between upper and lower mantle

Scaled analogue experiments of the subduction process [*Funiciello, et al.*, 2004; *Griffiths, et al.*, 1995; *Guillou-Frottier, et al.*, 1995; *Kincaid and Olson*, 1987] and numerical studies of subduction systems, [*Behounkova and Cizkova*, 2008; *Christensen*, 1996; *Cizkova, et al.*, 2007; *Davies*, 1995; *Enns, et al.*, 2005; *Gaherty and Hager*, 1994; *Goes, et al.*, 2008; *Houseman and Gubbins*, 1997; *Schellart, et al.*, 2007; *Tackley*, 1993; *Tao and O'Connell*, 1993; *Yoshioka and Wortel*, 1995; *Zhong and Gurnis*, 1995] have already illustrated the modes of deformation of a subducted slab reaching a fluid interface characterized by a viscosity and/or density increase. These studies have shown the importance of the density contrast [*Christensen and Yuen*, 1984] and viscosity ratio [*Kincaid and Olson*, 1987] in governing whether the slab will lie along the interface, sinks through it, or buckle and pile up at the interface [*Ribe*, 2003]. Here, we study the evolution of the jellyfish shape when the slab meets the 660 km boundary defining either with a viscosity or density contrast between the upper and lower mantle.

Figure 7 summarizes the behavior of the plate as it forms a jellyfish shape and/or penetrates into the lower mantle as function of μ_s, the viscosity ratio between the slab and the upper mantle, and μ_{lm}, the viscosity ratio between the lower and upper mantle.

A wide range of subducting plate and stratification boundary behavior is observed, an indication that several factors are involved in the style of slab deformation when a fluid interface is present. We can define four different cases:

(A) Jellyfishing and penetration ($\mu_s < 100$ and $\mu_{lm} < 100$). The plate has a sufficiently low viscosity to transform into a jellyfish shape. The jellyfish head radius of curvature R_w is low (Fig. 8A). The stratification is weak enough to permit the slab to sink into the lower mantle with minor deformation linked to mantle stratification. The plate continues to sink with a velocity decrease but without interruption (Fig. 8B). The interface deflects around the slab to form a blob and slowly collapses at the plate sinking velocity.

(B) Jellyfishing and no penetration ($\mu_s < 100$ and $\mu_{lm} > 100$). The plate transforms into jellyfish shape but does not penetrate the lower mantle. The plate stops close to the stratification boundary and the jellyfish head flattens. This case is also characterized by a rapid increase in R_w when the plate reaches the interface, followed by a phase of decreasing R_w (Fig. 8A).

(C) No jellyfishing and penetration ($\mu_s > 100$ and $\mu_{lm} < 100$). The plate is too viscous and cannot evolve toward a jellyfish shape before it reaches the upper/lower mantle boundary but crosses it because the viscosity ratio μ_{lm} is low enough. Consequently, the deflected interface collapses around rigid slab. The viscosity ratio between the plate and the fluid decreases in the lower mantle allowing plate thickening in the lower fluid.

(D) No jellyfishing and no penetration ($\mu_s > 100$ and $\mu_{lm} > 100$). The plate does not cross the stratification boundary and keeps a slab shape because the viscosity ratio with the surrounding mantle is too high. Furthermore the strong viscosity contrast with lower mantle does not permit slab deformation and slab penetration. The interface stays straight.

Our results therefore demonstrate that the penetration of the plate into the lower mantle depends mainly on mantle stratification while the slab tip widening and jellyfish formation depends mostly on the slab strength (i.e. viscosity ratio between the subducting plate and the surrounding mantle).

Density stratification between upper and lower mantle

To investigate the influence of the density contrasts between the sinking slab and the deep mantle, we used the critical dimensionless parameter r defined by Kincaid and Olson [1987] (Fig. 9) in which the slab/lower mantle density contrast is normalized by the slab/upper mantle density contrast: $r = (\rho_s - \rho_{lm}) / (\rho_s - \rho_{um})$. $r = 1$ corresponds to a homogeneous fluid (no density contrast between the upper and lower mantle), while negative values of r correspond to a denser lower mantle than the sinking slab. Results are given for $-0.2 < r < 1.0$ (Fig 8C and 9).

We identify four cases presented in figure 9:

(A) $r < -0.2$: strong stratification and no slab penetration. While the slab sinks through the upper mantle and reaches the discontinuity, its deformation is controlled by the viscosity ratio between the slab and the upper mantle. The leading edge thickens when it meets the underformable interface. It is accompanied by an increase in R_w and a decrease in the sinking velocity (Fig. 8 A and B).

(B) r~0 : partial slab penetration into the lower mantle. Sinking rates are lower than when $r < -0.2$ and R_w increases (Fig. 8A and B) when the slab reaches the mantle discotinuity. The leading edge of slab reclines onto the interface. Buoyancy forces in the lower mantle are not strong enough to stall subduction until the slab has penetrated below the discontinuity (around 1/10 penetration in the lower mantle). Within this range of densities the initial penetration is however always limited.

(C) $r \sim 0.5$: slab penetration. The slab sinks through the lower layer but only on a very long time scale because the sinking velocity decreases (Fig. 8 B). The deflected interface collapses around the slab into a blob. Both slab and deformed interface descend slowly .

(D) $r > 0.5$: weak stratification. The stratification is weak enough to permit the slab to sink into the lower mantle with only minor deformation of the interface. The slab acquires the jellyfish form as describe in the above section.

Whatever proprieties of boundary stratification, the leading edge of the low viscous plate to leading tip thickens (Fig. 8 C and D). The thickness is measured (Fig. 1C) at selected depths (440, 660, 850 and 1200 km) for simulations with, in one case, different lower to upper mantle viscosity ratio and, on the other case, different density contrast (r parameter). With mantle stratification, the slab slows down and thickens with increasing viscosity and density contrast.

With logarithm of viscosity contrast and *vs* r parameter, the measurements seem to lie approximately on a line, indicating a power-law relationship (Fig8. C and D). In the case of the viscosity layered mantle, the slab thickening is more important in depth, particularly for high viscous lower mantle. The effect of the density jump at the mantle stratification on the subducting plates occurs later (deeper slab) than viscosity stratification boundary. This could be explain by the fact that it exists a period of time before the system find the equilibrium more important in the density stratification case.

Comparison to real Earth

Several types of seismically derived data adress the problem of slab deformation within the mantle as reviewed by Lay [1994]. The quasi-planar geometry of subducting slabs was first defined from the distribution of large earthquakes along Wadati-Benioff zones [*Engdahl, et al.*, 1998; *Isacks and Barazangi*, 1977; *Jarrard*, 1986]. In addition, maps of earthquakes focal positions [*Engdahl, et al.*, 1998] provided high resolution three dimensional images of the seismogenic regions surrounding subduction zones that gave rise to general geometric and deformation models of mantle slabs, such as the RUM model [*Gudmundsson and Sambridge*, 1998].

Furthermore, global seismic tomography models [*Bijwaard, et al.*, 1998; *Ding and Grand*, 1994; *Fukao*, 1992; *Grand*, 1994; *van der Hilst*, 1995; *van der Hilst and Widiyantoro*, 1997; *Wortel and Spakman*, 2000] provide more insights into slab morphology, including those in models, characterized by a relatively low seismicity, as well as the distribution of velocity in the mantle surrounding the slabs. Most recently, seismic images have been interpreted in terms of the most probable density field yielding the observed seismic velocity anomalies, which, in turn, have been used to derive models of self-consistent mantle flow [*Conrad, et al.*, 2007; *Conrad and Husson*, 2009; *Forte and Mitrovica*, 1996; *Moucha, et al.*, 2007]

All above mentioned methods are complementary and show that subducting slabs are significant structures in the upper mantle, that the majority penetrates into the lower mantle and that they are characterized by a three-dimensional deformation pattern (rather than being planar slabs) [*Yamaoka, et al.*, 1986]. In many instances, which we will describe below, tomographic images suggest a characteristic shape for the slab, with a relatively narrow trace in the upper mantle and a wider anomaly in the mid–lower mantle [*Karason and Van der Hilst*, 2001]. Geophysical observations are therefore consistent with the idea that the subducted slabs deform as they penetrate into the mantle to take the shape of a jellyfish. The distribution of focal mechanisms shows that stresses within the subducted slab are characterized by down-dip extension in its upper part (between 100 and 300 km depth), which is also associated with the narrow section of

the slab, and by down-dip compression in the deeper part of the slab toward the 660 km boundary [*Apperson and Frohlich*, 1987; *Isacks and Molnar*, 1969; *Vassiliou, et al.*, 1984], which is associated with the thickest section of the slab. Such a distribution of stress, and thus strain rate, along the subducting plate is identical to that predicted in our models of a slab transforming into a jellyfish shape (Fig. 3C).

High resolution images of Wadati-Benioff zones derived from the accurate localization of seismicity [*Engdahl, et al.*, 1998] and tomographic images obtained from P-waves seismic travel time anomalies [*Li, et al.*, 2008] both strongly suggest that there are four mean classes of slabs (defined in Table 2) in the Earth mantle, varying in their shape and interaction at/with the 660 km discontinuity. To illustrate these categories, we show slab geometries derived from P-waves seismic tomography model [*Li, et al.*, 2008] in four well-studied, different subduction systems (Fig. 10). These categories are:

Type A: Penetration and thickening: the Hellenic slab (Fig. 10A). The subducted lithosphere crosses the 660 km boundary with a small perturbations of thickness, which increases in the mid-lower mantle. Below 660 km, a fast velocity anomaly appears in the subducting plate which widens to ~400 km in the mid-mantle (~1200 km depth). The penetration of the subducted slab through the 660 km discontinuity and slab thickening in the mid-mantle (~1200 km) are the two remarkable features that are observed in other tomographic studies of this region [*Piromallo and Morelli*, 2003; *Spakman, et al.*, 1993]. Other subduction zones where comparable features are observed include Central America, N-Kurile [*Ding and Grand*, 1994], Java [*Fukao*, 1992; *Puspito, et al.*, 1993; *Widiyantoro and van der Hilst*, 1996] and India-Tibet [*Bijwaard, et al.*, 1998; *Grand, et al.*, 1997].

Type B: Slab Deflection with little or no penetration: the Isu-Bonin slab. The second category slabs are significantly deflected above the 660 km discontinuity to form a sub-horizontal high seismic velocity zone. We show in figure 10B a vertical cross section in this area that clearly demonstrates that the slab has been strongly deflected at the 660 km discontinuity with only a slight hint that it may have penetrated in the lower mantle. The slabs in the Izu-Bonin [*Tajima and Grand*, 1998], in S-Kurile [*Tajima and Grand*, 1995] and Japan subduction systems are best examples of this second category.

Type C: Pure penetration: the Mariana slab. As shown in Fig. 10C and as seen in many tomographic studies (e.g. [*Fukao*, 1992; *van der Hilst and Seno*, 1993; *Zhou*, 1988]), the Mariana slab appears to penetrate the 660 km discontinuity to reach the mid-mantle without thickening. Another typical example of a slab belonging to this category is the Kermadec slab [*Zhao, et al.*, 2007].

Type D: No penetration and no thickening: the Scotia slab. The last category includes in the Calabria, Aleutian, Carribbean, Ryukyu and the Scotia slabs that do not penetrate into the lower mantle and do not seem to experience any thickening at their base. (Fig. 10D)

In order to better characterize the shape of the subducting slabs, we mapped data from the tomographic model of [*Li, et al.*, 2008] on a Cartesian grid with GMT [*Wessel and Smith*, 1991] to compute horizontal cross-sections of the seismic velocity anomalies from which we estimated the surface area of the slabs as they penetrate into the mantle at 100 km intervals, from 100 to 1400 km depths. At each depth, we considered three contours of the velocity anomaly contrast (minimum, mean and maximum relative velocities) to avoid artifacts arising from the inherent resolution of tomographic models. Note that no unique values for viscosity contrasts can be selected for they vary with depth, particularly because of the thermal relaxation of the slab; contouring is therefore arbitrary and to some extent, subjective. We normalized the surface areas

comprised inside each of the contours by the contour area at the surface to obtain dimensionless vertical profiles of the slab thickness. This procedure was also performed on some of our numerical model results. Profiles of areas obtained from the seismic tomography model and the numerical models are compared in figure 10.

For each of the four slab categories, we compared thickness profiles from the tomographic model to those obtained from numerical models in which we varied the viscosity ratio μ_s between 1 and 100, the viscosity ratio μ_{lm} between 1 and 1000 and the density parameter r between -0.2 and 1 (Fig. 10). To facilitate the comparison between data and models, we show model predicted surface area profiles for model times that correspond best to subduction/penetration level suggested by each of the four tomographic images.

We first notice that, in both the numerical models and the tomographic images, where the viscosity mantle stratification ($\mu_{lm} > 1$) or the density mantle stratification ($r < 1$) impacts on plate penetration and on its deformation, the corresponding thickening of the slab usually occurs deeper than the imposed viscosity/density jump at 660 km depth.

Considering the first two categories, slab thickening at (i.e., Izu Bonin slab, Fig. 10B) or below the 660 km discontinuity (i.e., Hellenic slab, Fig. 10A) is best explained either by a low increase in viscosity from upper to lower mantle ($\mu_{lm} \sim 10$), consistent with previous studies based on the interpretation of the geoid [*Moresi and Gurnis*, 1996] or by a weak jump in density between the upper and lower mantle ($r \sim 0.5$), as suggested by other model results [*Christensen and Yuen*, 1984]. In nature, it is not possible to determinate whether one parameter will dominate on the other and it is probably a combination of both that is responsible for slab thickening. The observed surface area vs. depth profiles are best explained with a relatively low slab viscosity (only ~10–100 times the mantle viscosity), as already suggested by Loiselet *et al.* [2009].

In the third category, the Mariana slab displays a rather different behavior suggesting that the slab may be stronger than slabs belonging to type A, and does not evolve into a jellyfish shape as it descends through the upper mantle. The slight thickening that appears in the slab cross-sectional area observed at depths between 1100 and 1650 km may be due to the relatively poor resolution of the tomographic images at those depths or to a mild density or viscosity stratification as suggested by [*Cizkova, et al.*, 1997; *Hager and Richards*, 1989; *Lambeck and Johnston*, 1998].

In the fourth category, thickening of the Scotia slab as it approaches the 660 km discontinuity could be explained by the formation of a jellyfish “head” which, in turns, implies a relatively low viscosity/strength subducting plate.

In order to evaluate the relationship between the geometries, densities and viscosities of subducted slabs, we alternatively use the parameter Φ, introduced by Wortel and Vlaar (1998), defined by $\Phi = age * V_s$ (*age* is the age of lithosphere at the time of subduction and V_s is the velocity of subduction (see Table 2). This parameter is therefore a proxy for the temperature in the slab, which affects both its viscosity and density of the slab. There is a clear distribution of slab types as a function of Φ (Fig. 11). It comes out that :

(i) slabs with small thermal parameters Φ deform more easily as jellyfishes (i.e type A) than those with larger values for Φ (i.e. type C); and (ii) slabs with large values of Φ tend to subduct

more easily for they are presumably stiffer and denser. For very small thermal parameters, thermal diffusion may have had enough time to heat up the slabs so that they do not show up in seismic tomography. Alternatively, heated slabs may have lost their initial negative buoyancy and are no longer able to continue to subduct at greater depths than the transition zone (type D Calabria, Scotia slabs). Last, type B slabs seem to be at odds with our previous analysis, for they appear to pond on the 660 km discontinuity, whereas in our models stiff slabs are predicted to penetrate into the lower mantle and not to deform. The departure between our models and the predictions given by the thermal parameter Φ may however reflect that the proxy do not apply for the slabs that are represented in type B (Izu-Bonin, S-Kurile, Japan and Tonga slabs).

In our numerical models, and thus in our interpretation of the various slab geometries suggested by tomographic models, we have assumed that slab motion is primarily driven by its buoyancy, i.e. the main force acting on the subducting oceanic lithosphere is the gravitational force arising from plate's high density with respect to the surrounding mantle. We interpret the observed thickening of slabs in the vicinity of the 660 km discontinuity as resulting from the formation of a jellyfish head in response to viscous drag between the slab and the mantle, potentially enhanced by the presence of a viscosity [*Gurnis and Hager*, 1998] and/or density [*Tackley*, 1993] contrast between the upper and lower mantle. The former process (jellyfish formation), in turn, implies that the viscosity ratio between the slab and the mantle is relatively small (order 10) and thus that slabs are relatively weak. The latter process (interaction with the 660 km discontinuity) is supported by the compressive nature of the focal mechanisms of deep earthquakes [*Isacks and Molnar*, 1969], which clearly indicates the presence of resisting forces deeper than the transition zone, resulting from an increase in viscosity or a decrease in the density contrast between the slab and the surrounding mantle and thus a decrease in the driving force.

Another explanation for the thickening of the slab along the 660 km discontinuity relies on the subduction (or penetration) velocity being imposed to the slab by external forces, either originating at the mid-ocean ridge (i.e. ridge push) or along other segments of the subducting lithosphere. If this is true and the trench migration velocity is significantly higher than the penetration velocity of the slab in the lower mantle (due to resistance force), slabs will have to deform on the 660 km discontinuity, to flatten and lie horizontally on it [*Christensen*, 1996; *Enns, et al.*, 2005; *Griffiths, et al.*, 1995; *Guillou-Frottier, et al.*, 1995; *Olbertz, et al.*, 1997; *Tagawa, et al.*, 2007; *van der Hilst and Seno*, 1993]. This is a possible scenario to explain why the Izu Bonin slab flattens on the 660 km discontinuity whereas the Mariana slab penetrates it; similarly, the change in the style of subduction from the northern to southern Kurile [*Ding and Grand*, 1994; *Fukao*, 1992] can illustrate this. Correspondingly, the Tonga trench is free to rollback because of its open northern end that allows for toroidal flow to occur, very significant trench migration has occurred at fast rates for the last 50 Ma [*Lithgow-Bertelloni and Richard*, 1998]. The Tonga slab consequently flattens on the 660 km discontinuity while the neighboring Kermadec slab, that cannot retreat freely, continues its route into the lower mantle.

Discussion and Conclusion

Images from seismic tomography provide evidence for a strong deformation of some sections of subducted lithosphere in the mid-mantle (such as Java, Hellenic, Central America, N-Kurile). Such slabs narrow in the upper mantle and anomalously thicken in the mid–lower mantle. Some authors explained this feature as resulting from buckling instability [*Griffiths and Turner*, 1988; *Ribe, et al.*, 2007]. Alternatively, our numerical models suggest that the deformation of the

subducting lithosphere results from the interaction of a relatively weak slab with the surrounding viscous mantle.

We have investigated the behavior of a subducting slab in the Earth mantle driven by negative buoyancy forces arising from its high density with respect to the mantle. This is based on the commonly accepted hypothesis that the negative buoyancy of slabs with respect to the mantle is the main driving force for plate tectonics [*Becker and O'Connell*, 2001; *Conrad and Lithgow-Bertelloni*, 2002; *Forsyth and Uyeda*, 1975; *Lithgow-Bertelloni and Richard*, 1998]. We have showed that a weak plate falling through a viscous fluid under its own weight will take a characteristic jellyfish shape. This is the optimum shape of a deformable object falling in a viscous fluid that will be reached regardless of its original shape, to minimize viscous dissipation in the fluid. The jellyfish shape consists of a wide head experiencing vertical shortening and a long tail experiencing vertical lengthening. This pattern of deformation, is consistent with observed distribution of down-dip extensional and compressional stresses along subducting slabs and with observed slab geometry at mid-mantle depths, derived from tomographic images.

We confirmed that slab and mantle rheologies are key parameters controling the slab deformation. We have used a linear viscosity for both the slab and the mantle which implies that strain rate and, subsequently, subduction velocity scale linearly with the imposed density contrast between the slab and the mantle. Modifying density parameter value does not impact the geometry of the solution at any stage of the subduction process. This implies that the depth range over which the jellyfish head forms does not depend on the density contrast between the plate and the slab, only on the viscosity ratio between the plate and the mantle. The final jellyfish shape also depends on the initial slab width, or more precisely, its aspect ratio (width to thickness ratio). In cases where the initial slab geometry is characterized by a finite dip, we have shown that the slab may turn into a non-symmetrical jellyfish shape. This "spoon" shape is consistent with many observed geometries derived from seismic tomographic images and with the distribution of earthquakes in Benioff-Wadati zones, the Hellenic slab being one of the most striking example of such spoon-shaped subducting slabs.

Current findings on lithosphere strength are based on various interpretations of the geological record as well as on geophysical observations and experimental data, and thus strongly depend on assumptions and extrapolations [*Brace and Kohlstedt*, 1980; *Burov and Watts*, 2006; *Jackson*, 2002; *Kohlstedt, et al.*, 1995]. Slab morphology and strain rates calculated from earthquake location and seismic moment released at intermediate depths appear to provide a limit to the viscosity ratio between slabs and the upper mantle [*Bevis*, 1986]. Indeed, any model predicting a significant thickening and/or deformation of subducting slabs (including the one we present in this paper) during its fall into the upper mantle, requires a weak subducted lithosphere, between 1 and 100 times more viscous that the upper mantle at most. Beyond that, slabs are too strong to deform at the scale of the upper mantle.

In the Earth's interior, we commonly observe that subducted slabs tend to be deflected to lie sub-horizontally on the upper to lower mantle transition region before, some of them, penetrating beneath the 660-km discontinuity in the mid-lower mantle (such as in N-Kurile, Hellenic, and the Philippines), or well into the lower mantle (beneath the Peruvian Andes, Java, Marianna and Kermadec). Other slabs simply flatten and reside above or within the 660-km discontinuity as beneath the Chilean Andes, the Aleutian, the S-Kurile, Japan, and Izu-Bonin.

By comparing model predictions with observations (seismic tomography images and seismic

focal mechanism locations) we provide additional constrains on the viscosity contrast between the subducting slab and the surrounding mantle. The apparent slab widening at depth suggests that the slab is indeed stronger than the mantle but an accurate estimate of the viscosity contrast cannot be obtained independently of any density variation that might exist across the 660 km discontinuity. For each of the four subduction systems considered here, comparison with model scenarios suggests a range of viscosity ratios between the slab and the upper mantle between 10 and 100 (as already suggested by Loiselet *et al.* [2009]). This is in accordance with Husson [2006] who showed that the topography above subducted slabs is a dynamic topography generated by linear viscous flow in the mantle driven by the fall of the slab. However, the slab strength contrast we obtain is lower than that suggested by laboratory and numerical modeling work [*Capitanio, et al.*, 2007; *Christensen and Yuen*, 1984; *Clark, et al.*, 2008; *Conrad and Hager*, 1999; *Funiciello, et al.*, 2003; *Morra, et al.*, ; *Royden and Husson*, 2006; *Schellart*, 2004; *Stegman, et al.*, 2006; *Zhong and Gurnis*, 1994] where the viscosity ratio between the subducted lithosphere and the surrounding mantle ranges between 10^2 and 10^5. Although rock strength experiments also predict stiffer slabs than suggested here [*Kohlstedt, et al.*, 1995], global models suggest that slabs should only be 100 times stiffer than the upper mantle in order to match the geoid [*Zhong and Davies*, 1999]. Furthermore, Cizkova et al. [2002] found (in a study similar to ours) that, in order to deflect strong slabs in the transition zone, slabs must be relatively weak.

One way to reconcile the observation that some slabs are characterized by a strong thickening around the 660 km discontinuity while, for others, this seems to take place at mid-lower mantle depths or deeper, is to consider that the subducted plate is, in general, sufficiently weak to undergo transformation into a jellyfish shape during its fall in the upper mantle and that it meets at the 660 km depth a low viscosity and/or high density jump. The particular case where slab flattens at the 660 km discontinuity can be explained by the retrograde motion of the subduction trench.

Acknowledgments

This work was supported by College doctoral de Bretagne (Université Européenne de Bretagne) (C. L.) and by the “Chair d’Excellence Senior de l’ANR” (J.B.). We thank P. Fullsack for stimulating discussion.

References

Apperson, K. D., and C. Frohlich (1987), Relationship between Wadati-Benioff zone geometry and P, T and B axes of intermediate and deep focus earthquakes, *J. Geophys. Res.*, *92*, 13821-13831.

Becker, T. W., and R. J. O’Connell (2001), Predicting plate velocities with mantle circulation models, *Geochemistry Geophysics Geosystems*, *2*.

Behounkova, M., and H. Cizkova (2008), Long-wavelength character of subducted slabs in the lower mantle, *Earth and Planet. Sci. Lett.*, *275*, 43-53.

Bevis, M. (1986), The curvature of Wadati-Benioff zones and the torsional rigidity of subducting plates. , *Nature*, *323*, 52-53.

Bijwaard, H., et al. (1998), Closing the gap between regional and global travel time tomography, *J. Geophys. Res.*, *103*.

Billen, M. I., and M. Gurnis (2005), Constraints on subducting plate strength within the Kermadec trench, *Journal of Geophysical Research*, *110*, B05407.

Brace, W. F., and D. L. Kohlstedt (1980), Limits on lithospheric stress imposed by laboratory experiments, *Journal of Geophysical Research*, *85*, 6248-6252.

Braun, J., et al. (2008), DOUAR: A new three-dimensional creeping flow numerical model for the solution of geological problems, *Physics of the Earth and Planetary Interiors*, *171*, 76-91.

Burov, E., and A. B. Watts (2006), The long-term strength of continental lithosphere: "jelly sandwich" or "creme brulee", *GSA Today*, 1052-5173.

Capitanio, F. A., et al. (2007), Dynamic models of downgoing plate-buoyancy driven subduction: Subduction motions and energy dissipation, *Earth and Planetary Science Letters*, *262*, 284-297.

Christensen, U., and D. Yuen (1984), The interaction of a subducting lithosphere slab with a chemical or phase boundary, *Journal of Geophysical Research*, *89*, 4389-4402.

Christensen, U. R. (1996), The influence of trench migration on slab penetration into the lower mantle, *Earth and Planetary Science Letters*, *140*, 27-39.

Cizkova, H., et al. (2007), Stress distribution within subducting slabs and their deformation in the transition zone, *Physics of The Earth and Planetary Interiors*, *161*, 202-214.

Cizkova, H., et al. (2002), The influence of rheological weakening and yield stress on the interaction of slabs with the 670 km discontinuity, *Earth and Planetary Science Letters*, *199*, 447-457.

Cizkova, H., et al. (1997), Slope of the geoid spectrum and contraints on mantle viscosity stratification, *Geophysical Research Letters*, *23*, 3063-3066.
Clark, S. R., et al. (2008), Episodicity in back-arc tectonic regimes, *Physics of the Earth and Planetary Interiors*, *171*, 265-279.
Conrad, C. P., et al. (2007), Global mantle flow and the development of seismic anisotropy: Differences between the oceanic and continental upper mantle, *Journal of Geophysical Research*, *112*, B07317.
Conrad, C. P., and B. H. Hager (1999), Effect of plate bending and fault strength at subduction zones on plate dynamics, *Journal of Geophysical Research*, *104*, 17551-17571.
Conrad, C. P., and L. Husson (2009), Influence of dynamic topography on sea level and its rate of change, *Lithosphere*, *1*, 110-120.
Conrad, C. P., and C. Lithgow-Bertelloni (2002), How mantle slabs drive plate tectonics, *Science*, 207-209.
Creager, K. C., and T. H. Jordan (1984), Slab Penetration Into the Lower Mantle, *Journal of Geophysical Research*, *91*, 3573-3589.
Davies, G. F. (1995), Penetration of plates and plumes through the mantle transition, *Earth and Planetary Science Letters*, 507-516.
Di Giuseppe, E., et al. (2008), Slab stiffness control of trench motion: Insights from numerical models, *Geochem. Geophys. Geosyst.*, *9*, Q02014.
Ding, X.-Y., and S. P. Grand (1994), Seismic structure of the deep Kurile subduction zone, *Journal of Geophysical Research*, *99*, 23767-23786.
Engdahl, E. R., et al. (1998), Global teleseismic earthquake relocation with improved travel times and procedures for depth determination, *Bulletin of the Seismological Society of America*, *88*, 722-743.
Enns, A., et al. (2005), The dynamics of subduction and trench migration for viscosity stratification, *Geophysical of Journal International*, *160*, 761-775.
Forsyth, D. W., and S. Uyeda (1975), On the relative importance of the driving forces of plate motion, *Geophys. J. R. Astron. Soc.*, *43*, 163-200.
Forte, A., and J. X. Mitrovica (1996), Newinferences of mantle viscosity from joint inversion of long-wavelength mantle convection and post-glacial rebound data., *Geophys. Res. Let.*, *23*, 1147–1150.
Fukao, Y. (1992), Seismic Tomogram of the Earth's Mantle: Geodynamic Implications, *Science*, *258*, 625-630.
Fukao, Y., et al. (2001), Stagnant Slabs in the Upper and Lower Mantle Transition Region, *Review of Geophysics*, *39*, 291-323.
Funiciello, F., et al. (2003), Dynamics of retreating slab: 2. Insights from three-dimensional laboratory experiments, *Journal of Geophysical Research*, *108*, 12.
Funiciello, F., et al. (2004), Role of lateral mantle flow in the evolution of subduction systems: insights from laboratory experiments, *Geophys. J. Int.*, *157*, 1393-1406.
Gaherty, J. B., and B. H. Hager (1994), Compositional vs. Thermal Buoyancy and the Evolution of Subducted Lithosphere, *Geophysical Research Letters*, *21*, 141-114.
Giardini, D., and J. H. Woodhouse (1984), Deep seismicity and modes of deformation in Tonga subduction zone, *Nature*, *307*, 505-509.
Goes, S., et al. (2008), Evidence of lower-mantle slab penetration phasesin plate motions., *nature*, *451*.
Grand, S. P. (1994), Mantle shear structure beneath the Americas and surrounding oceans, *Journal of Geophysical Research*, *99*, 11591-11621.
Grand, S. P., et al. (1997), Global seismic tomography: A snapshot of convection in the Earth, *GSA Today*, *7*, 1-7.
Griffiths, R. W., et al. (1995), A laboratory investigation of effects of trench migration on the descent of subducted slabs, *Earth and Planetary Science Letters*, *133*, 1-17.
Griffiths, R. W., and S. Turner (1988), Folding of viscous plimes impinging on a density or viscosity interface, *Geophysical Journal*, *95*, 397-419.
Gudmundsson, O., and M. Sambridge (1998), A regionalized upper mantle (RUM) seismic model, *Journal of Geophysical Research*.
Guillou-Frottier, L., et al. (1995), Laboratory experiments on the structure of subducted lithosphere, *Earth and Planetary Science Letters*, *133*, 19-34.
Gurnis, M., and B. H. Hager (1988), Controls of the structure of subducted slabs, *Nature*, *335*, 317-321.
Gurnis, M., and B. H. Hager (1998), Controls of the structure of subducted slabs, *Nature*, *335*, 317-332.
Hager, B. H., and M. A. Richards (1989), Long wavelength variation in earth's geoid: physical models and dynamical implications, *Philos. Trans. R. Soc. Lon.*, *328*, 309-327.
Heuret, A., and S. Lallemand (2005), Plate motions, slab dynamics and back arc deformation, *Physics of the Earth and Planetary Interiors*, *149*, 31-51.
Houseman, G. A., and D. Gubbins (1997), Deformation of subducted oceanic lithosphere, *Geophysical Journal International*, *131*, 535-551.
Husson, L. (2006), Dynamic topography above retreating subduction zones, *Geology*, *34*, 741-744.
Isacks, B., and M. Barazangi (1977), Geometry of Benioff zones: Lateral segmentation and downwards bending of the subducted lithosphere, in Island Arcs, Deep Sea Trenches and Back-arc Basins, *AGU, Washington*, 99-144.
Isacks, B., and P. Molnar (1969), Mantle earthquake mechanisms and the sinking of the lithosphere, *Nature*, *223*, 1121-1124.
Isacks, B., and P. Molnar (1971), Distribution of stresses in the descending lithosphere from a global survey of focal mechanism solutions of mantle earthquakes, *Review of Geophysics*, *9*, 103-174.
Jackson, J. (2002), Strength of the continental lithosphere: Time to abondon the jely sandwich?, *GSA today*.
Jarrard, R. D. (1986), Relations Among Subduction Parameters, *Reviews of Geophysics*, *24*, 217-284.
Jordan, T. H. (1977), Lithospheric slab penetration into the lower mantle beneatht he Sea of Okhots, *Journal of Geophysics*, *43*, 473-496.
Jordan, T. H., and W. S. Lynn (1974), A velocity anomaly in the lower mantle, *Journal of Geophysical Research*, *79*, 2679-2685.
Karason, H., and R. Van der Hilst (2001), Tomographic imaging of the lowermost mantle with differential times of refracted and diffracted core phases (PKP, Pdiff), *Journal of Geophysical Research*, *106*, 6569-6587.
Kido, M., and O. Čadek (1997), Inferences of viscosity from the oceanic geoid: indication of a low viscosity zone below the 660-km discontinuity., *Earth and Planet. Sci. Lett.*, *151*, 125-137.
Kincaid, C., and P. Olson (1987), An Experimental Study of Subduction and Slab Migration, *Journal of Geophysical Research*, *92*, 13832-13840.
Kohlstedt, D. L., et al. (1995), Strength of the lithosphere: contraints imposed by laboratory experiments, *Journal of Geophysical Research*, *100*, 17587-17602.

Lambeck, K., and P. Johnston (1998), *The viscosity of the mantle: evidence from analysis of glacial-rebound phenomena*, 461–502 pp., Cambridge University Press.

Lay, T. (1994), The fate of descending slabs, *Annual Review of Earth and Planetary Sciences*, *22*, 33-61.

Li, C., et al. (2008), A new global model for P wave speed variations in Earth's mantle, *Geochemistry Geophysics Geosystems*, *9*, Q05018.

Lithgow-Bertelloni, C., and G. Richard (1998), The dynamics of Cenozoic and Mesozoic plate motions, *Review of Geophysics*, *36*, 27-78.

Loiselet, C., et al. (2009), From longitudinal slab curvature to slab rheology, *Geology*, *37*, 747-750.

Loubet, N., et al. (2009), Deformation modes of subducted lithosphere at the core-mantle boundary: An experimental investigation, *Geochemistry Geophysics Geosystems*, *Q10004*, doi:10.1029/2009GC002492.

Moresi, L., and M. Gurnis (1996), Constraints on the lateral strength of slabs from three-dimentional dynamic flow models, *Earth and Planetary Science Letters*, *138*, 15-28.

Morra, G., et al. Earth curvature effects on subduction morphology: Modeling subduction in a spherical setting, *Acta Geotechnica*.

Moucha, R., et al. (2007), Lateral variations in mantle rheology: implications for convection related surface observables and inferred viscosity models, *Geophysical Journal International*, *169*, 113-135.

Muller, R., et al. (1997), Digital isochrons of the world's ocean floor, *Journal of Geophysical Research*, *104*, 3211-3214.

Olbertz, D., et al. (1997), Trench migration and subduction zone geometry, *Geophysical Research Letters*, *24*, 221-224.

Olson, P., and H. Singer (1985), Creeping plumes, *Journal of Fluid Mechanics Digital Archive*, *158*, 511-531.

Peltier, W. R. (1996), Mantle viscosity and ice-age ice sheet tomography, *Science*, *273*, 1359-1364.

Piromallo, C., et al. (2006), Three-dimensional instantaneous mantle flow induced by subduction, *Geophys. Res. Lett.*, *33*, L08304.

Piromallo, C., and A. Morelli (2003), P wave tomography of the mantle under the Alpine-Mediterranean area, *J. Geophys. Res.*, *108*, 2065.

Puspito, N. T., et al. (1993), Three-dimensional P-wave velocity structure beneath the Indonesian region, *Tectonophysics*, *220*, 175-192.

Ren, Y., et al. (2007), Understanding seismic heterogeneities in the lower mantle beneath the Americas from seismic tomography and plate tectonic history, *Journal of Geophysical Research*, *112*, B01302.

Ribe, N. M. (2003), Periodic folding of viscous sheets, *Physical Review Letters*, *E68*, DOI: 10.1103.

Ribe, N. M., et al. (2007), Buckling instabilities of subducted lithosphere beneath the transition zone, *Earth and Planetary Science Letters*, *254*, 173-179.

Ricard, Y., and L. S. Y. (1993), A Geodynamic Model of Mantle Density Heterogeneity, *Journal of Geophysical Research*, *98*, 21895-21909.

Royden, L. H., and L. Husson (2006), Trench motion, slab geometry and viscous stresses in subduction systems, *Geophysical Journal International*, *167*, 881-905.

Schellart, W. P. (2004), Kinematics of subduction and subduction-induced flow in the upper mantle, *Journal of Geophysical Research*, *109*, B07401.

Schellart, W. P., et al. (2007), Evolution and diversity of subduction zones controlled by slab width, *Nature*, *446*, 308-311.

Spakman, W., et al. (1993), Travel-time tomography of the European-Mediterranean mantle down to 1400 km, *Physics of The Earth and Planetary Interiors*, *79*, 3-74.

Stegman, D. R., et al. (2006), Influence of trench width on subduction hinge retreat rates in 3-D models of slab rollback, *Geochemistry Geophysics Geosystems*, *7*, Q03012.

Tackley, P. J. (1993), Effects of Strongly Temperature-Dependent Viscosity on Time-Dependent, Three-Dimensional Models of Mantle Convection, *Geophys. Res. Lett.*, *20*, 2187-2190.

Tagawa, M., et al. (2007), Dynamical modeling of trench retreat driven by the slab interaction with the mantle transition zone, *Earth Planets Space*, *59*, 65-74.

Tajima, F., and S. P. Grand (1995), Evidence of High Velocity Anomalies in the Transition Zone Associated with Southern Kurile Subduction Zone, *Geophysical Research Letters*, *22*, 3139-3142.

Tajima, F., and S. P. Grand (1998), Variation of transition zone high-velocity anomalies and depression of 660 km discontinuity associated with subduction zones from the southern Kuriles to Izu-Bonin and Ryukyu, *Journal of Geophysical Research*, *103*, 15015-15036.

Tao, W. C., and R. J. O'Connell (1992), Ablative Subduction: A Two-Sided Alternative to the Conventional Subduction Model, *J. Geophys. Res.*, *97*, 8877-8904.

Tao, W. C., and R. J. O'Connell (1993), Deformation of a weak subducted slab and variation of seismicity with depth, *Nature*, *361*, 626-628.

Thieulot, C., et al. (2008), Adaptive octree-based finite element analysis of two- and three-dimensional indentation problems, *Journal of Geophysical Research*, *113*, B12207.

van der Hilst, R. (1995), Complex morphology of subducted lithosphere in the mantle beneath the Tonga trench, *Nature*, *374*, 154-157.

van der Hilst, R., and T. Seno (1993), Effects of relative plate motion on the deep structure and penetration depth of slabs below the Izu-Bonin and Mariana island arcs, *Earth and Planetary Science Letters*, *120*, 395-407.

van der Hilst, R., and S. Widiyantoro (1997), Evidence for deep mantle circulation from global tomography, *Nature*, *386*, 578-584.

Vassiliou, M. S., et al. (1984), The distribution of earthquakes with depth and stress in subducting slabs, *Journal of Geodynamics*, *1*, 11-28.

Wessel, P., and W. H. F. Smith (1991), Free Software Helps Map and Display Data, *EOS Trans. AGU*, *72*, 445-446.

Widiyantoro, S., and R. van der Hilst (1996), Structure and Evolution of Lithospheric Slab Beneath the Sunda Arc, Indonesia, *Science*, *271*, 1566-1570.

Wortel, M. J. R., and W. Spakman (2000), Subduction and slab detachment in the Mediterranean-Carpathian region, *Science*, *290*, 1910-1917.

Wortel, M. J. R., and N. J. Vlaar (1988), Subduction zone seismicity and the thermo-mechanical evolution of downgoing lithosphere, *Pure and Applied Geophysics*, *128*, 625-659.

Yamaoka, K. Y., et al. (1986), Spherical shell tectonics: effects of sphericity and inextensibility on the geometry of the descending lithosphere, *Review of Geophysics*, *24*, 27-53.

Yoshioka, S., and M. J. R. Wortel (1995), Three-dimensional numerical modeling of detachment of subducted lithosphere, *J. Geophys. Res.*, *100*.

Zhao, D., et al. (1007), Depth extento f the Lau back-arcs preadingc enter and its relation to subductionp rocesses, *Science*, *278*, 254-257.

Zhong, S., and G. F. Davies (1999), Effects of plate and slab viscosities on the geoid, *Earth and Planetary Science Letters*, *170*, 487-496.

Zhong, S., and M. Gurnis (1994), Controls on trench topography from dynamic models of subducted slabs, *Journal of Geophysical Research*, *99*, 15683-15695.
Zhong, S., and M. Gurnis (1995), Mantle convection with plates and mobile, faulted plate margins, *Science*, *267*, 838-843.
Zhou, H.-w. (1988), How Well Can We Resolve the Deep Seismic Slab With Seismic Tomography?, *Geophysical Research Letters*, *15*.

Caption:

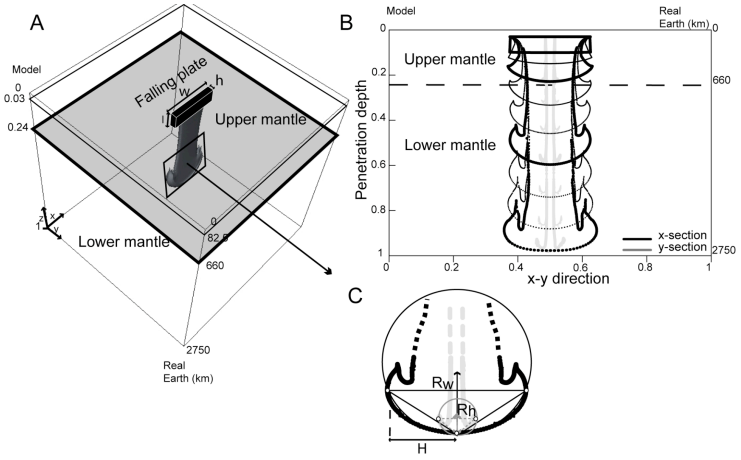

Figure 1: Reference model. A. Model setup and variables: h is plate thickness, w is plate width, l is initial plate penetration. μs and ρs are the slab to upper mantle viscosity and density ratios. The black parallelepiped is the initial state and the gray body is a typical slab shape after subduction to mid-depth. B. Vertical cross section along the y- (black) and x- (gray) sections of the leading edge of the subducting plate. R_w (black) (measured along the width w of the plate) and R_h (gray) (measured along its thickness h) give the radii of the circles that circumscribe the dotted triangles. H is the thickness of the plate head. C. y- (black) and x- (gray) cross-section series of the plate at different stages (uniform time steps). Bold profiles denote remarkable stages (see text).

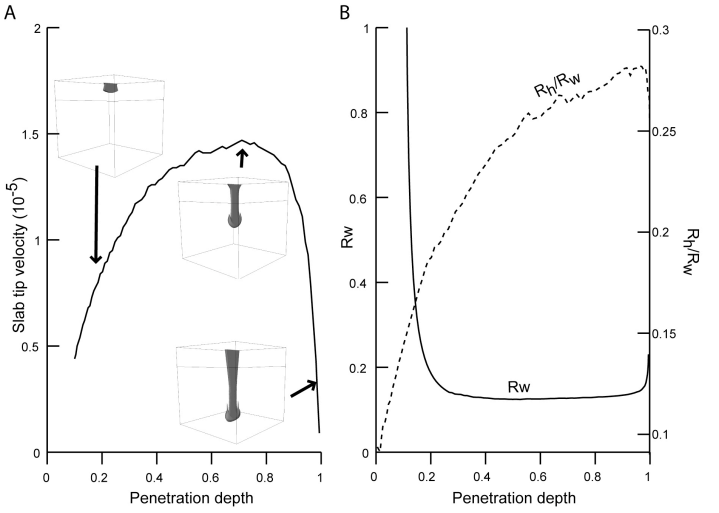

Figure 2: Reference model. A. Velocity of the slab head as a function of penetration depth. B. Radius of curvature R_w of the slab head across the y- profile (solid) and ratio between lateral (R_h) to longitudinal (R_w) radii of curvature of the jellyfish head (dashed).

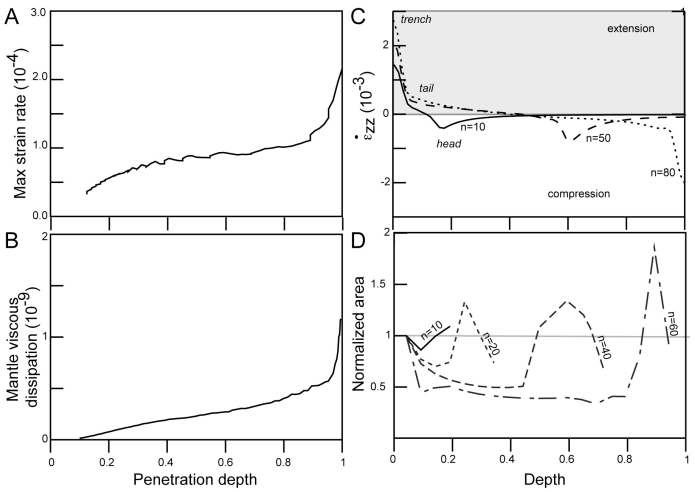

Figure 3: Reference model. A. Maximum strain rate as a function of plate penetration depth. B. Bulk viscous dissipation in the mantle as a function of plate penetration depth. C. Vertical strain rate ($\dot{\varepsilon}_{zz}$) profile along the central of the plate (x=0.5 and y=0.5) at different time steps. D. Normalized sectional area on horizontal sections as a function of depth, at different time steps n.

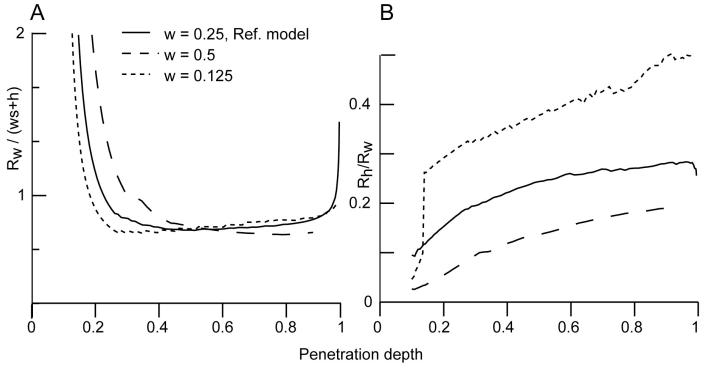

Figure 4: Reference model. A. Radius of curvature R_w of the jellyfish head as function plate penetration depth (normalized by the sum of slab width w and slab thickness h) for different slab width w, 0.25 (solid), 0.5 (dash) and 0.125 (dot). B. Same as (A) but for the ratio between lateral (R_h) to longitudinal (R_w) radii of curvature.

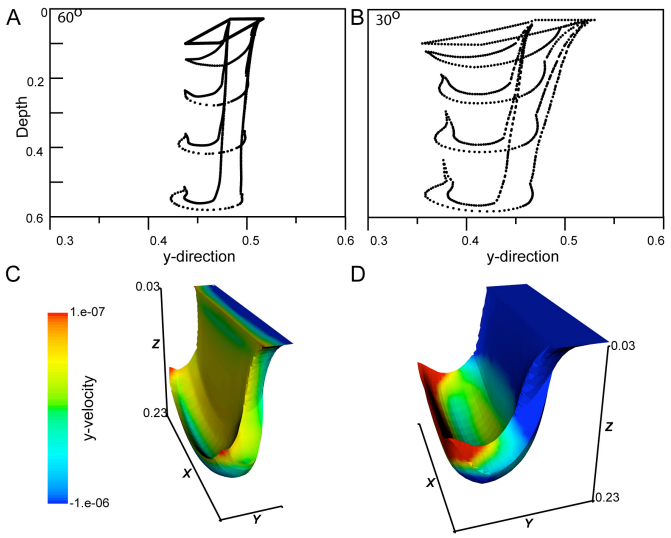

Figure 5: Geometry of the plate when subducted with an initial slab dip α (A and C, α=60°, and B and D, α =30°). A and B show across-strike profiles, regularly sampled in time (n=20), and C and D give a 3D view when the plate reaches ~660 km depth. The y-velocity on the surface of the plate is color-coded.

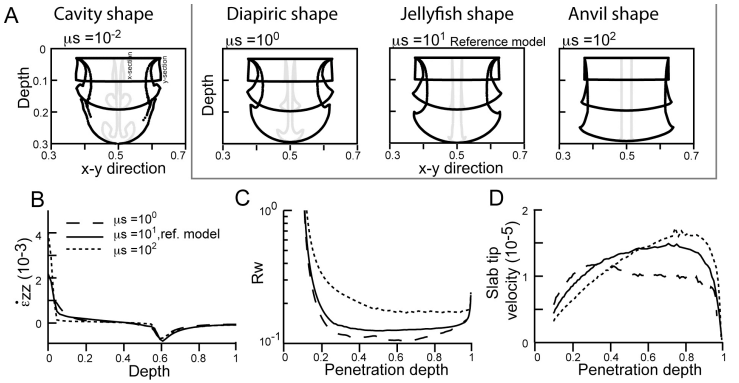

Figure 6: A. Cross sections at selected depths along-strike (black) and across-strike (grey) is as function of the plate to upper mantle viscosity ratio and model reference density contrast (see Table 1). Framed profiles are a selection of geologically plausible scenarii. B. Vertical strain rate ($\dot{\varepsilon}_{zz}$) profile along the central of the plate (x=0.5 and y=0.5). C. Radius of curvature of the jellyfish head R_w as a function of maximum penetration depth and μ_s. D. Velocity of the plate head as a function of plate depth.

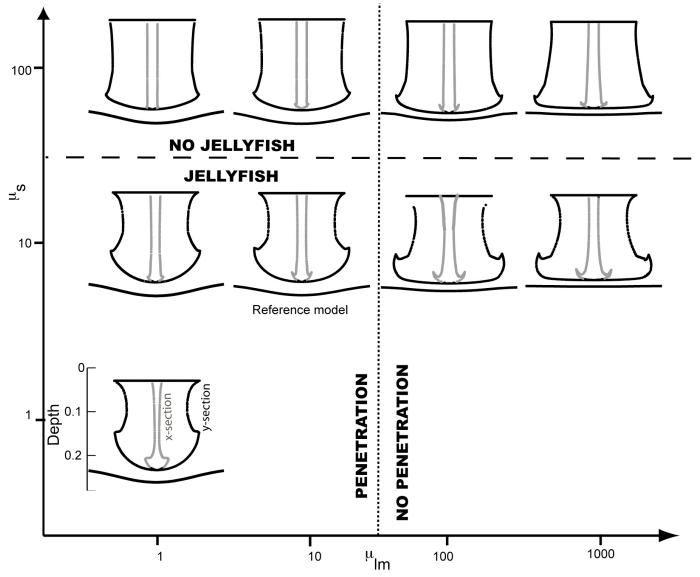

Figure 7: Different cases of slab geometry and slab penetration at the interface between the upper and lower mantle. Along-strike (black) and across-strike (gray) sections of the slab, as a function of the slab to upper mantle viscosity ratio μ_s and the lower mantle to upper mantle viscosity ratio μ_{lm}. Solid black lines show the upper/lower mantle boundary.

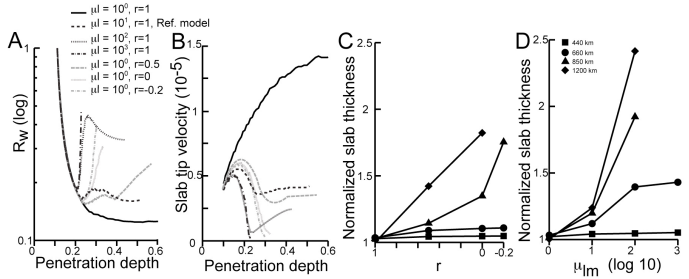

Figure 8: Radius of curvature (A) and velocity of slab tip (B) measured as a functions of the maximum plate penetration depth for different lower to upper mantle viscosity ratio μ_{lm} (black), and density indices *r* (see text). The slab to upper mantle viscosity ratio μs is set to 10.

Plot C and D shows the slab thickness *H* normalized to ½ slab width, *w*, when the slab tip reaches 440 km (square), 660 km (circle), 850 km (triangle) and 1200 km (lozenge) as function density parameter *r* (C) and lower to upper mantle viscosity ratio (D).

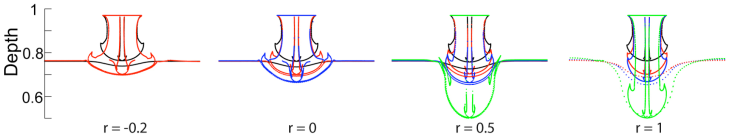

Figure 9: Across-strike and along-strike sections of the entire plate at four selected depths (0.24, black, 0.3 red, 0.34 blue and 0.5 green) for different values of the density parameter *r* (see text). The upper/lower mantle boundary is represented by horizontal lines. Note the selected depth miss when the plate do not cross the upper/lower mantle boundary.

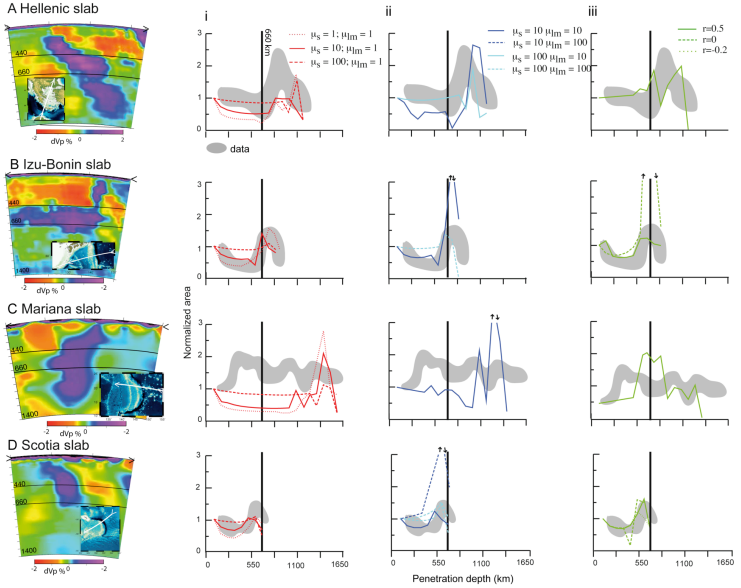

Figure 10: Tomographic profiles (left, derived from a global P-wave seismic tomography model [*Li, et al.*, 2008]) and right, evolution of the predicted (by numerical models) (color curves) and inferred (from geophysical data, gray areas) sectional area (on horizontal sections of the slab, see text) as a function of maximum penetration depth for ranges of: (i) slab to upper mantle viscosity ratio (red curves), (ii) lower to upper mantle viscosity ratio (blue curves) and (iii) density contrast between the slab and the lower mantle (green curves), for the Hellenic (A), Izu-Bonin (B), Mariana (C) and Scotia (D) subduction zones.

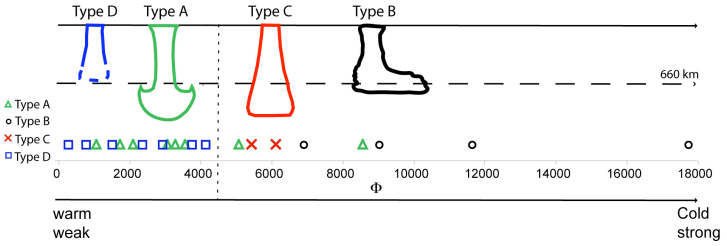

Figure 11: Geometrical classification of slabs (types A (green), B (black), C (red) and D (blue), see text) and correlation to the thermal parameter ϕ [*Wortel and Vlaar*, 1988]. **Φ** is the product of the age of lithosphere at the trench and of the subduction rate (age * Vs).

Table 1: Parameters used in the models

	Description	Parameter	Model	Nature
Slab	Thickness	h	0.03	~ 83 km
	Width	w	0.125 / 0.25* / 0.5	344 / 688 / 1375 km
	Dip angle	α	90* / 70 / 45 / 30	90* / 70 / 45 / 30

	Density	ρ_s	0.1024	~ 3328 kg. m^{-3}
	Viscosity ratio	μ_s	10^{-2} / 10^{0} / 10^{1*} / 10^{2}	10^{-2} / 10^{0} / 10^{1*} / 10^{2}
	Uniform octree level	L_s	8 (0.0039)	~ 10.72 km
Upper mantle	660 km boundary	z_{660}	0.24	660 km
	Density	ρ_{um}	0.1	~ 3250 km.m^{-3}
	Viscosity	μ_{um}	1	2.10^{-20}
	Uniform octree level	L_{um}	6 (0.0156)	~ 43 km
Lower mantle	Density	ρ_{lm}	0.1* / 0.1012/ 0.1024/ 0.1032	~ 3250 / 3289 / 3328/ 3434 kg.m^{-3}
	Viscosity ratio	μ_{lm}	10^{0} / 10^{1*} / 10^{2} / 10^{3}	10^{0} / 10^{1*} / 10^{2} / 10^{3}
	Uniform octree level	L_{lm}	6 (0.0156)	~ 43 km

* reference value

Table 2: Geometrical classification of slabs and subduction parameters

Name	Vs (mm/a) [(1)]	Age (My) [(2)]	Φ (Km) [(3)]
Type A	N-Kurile	77.99	110	8591
	Central America	62.27	17.6	1089.26
	Alaska W	59.4	52	3091.92
	Alaska E	50.2	41.8	2128.45
	Peru	61.1	28.8	1756.51
	Java	47.39	69.93	3356.64
	Hellenic	42	100	5100
	North-central Chile	68.13	52.12	3542.07
Type B	S-Kurile	75	120.4	9042.04
	Japan	89.75	129.5	11661.47
	Izu-Bonin	50	138.25	6943.23
	Tonga	157.25	107.25	17754.16
Type C	Mariana	40.11	151.61	6143.23
	Kermadec	55	99	5464.8
Type D	Scotia	40	38.16	1525.63
	Aleutian	53.21	56.23	2945.32
	Caribbean	8	96.66	788.23
	North America	31	9.4	292.90
	South Chile	70	33.8	2376.47
	Ryuku	85.8	44.2	3777,33
	Calabria	50	80	4160

[(1)] Vs = Vsub – Vt with Vsub velocity of the subducting plate and Vt trench migration velocity (from database compilation of [*Heuret and Lallemand*, 2005]). Classification of slab deformation is based on the shape of the Wadati-Benioff zone from deep seismicity [*Engdahl, et al.*, 1998] and the results of seismic tomography [*Li, et al.*, 2008]

[(2)] The age of the subducting lithosphere, estimated from [*Muller, et al.*, 1997]

902 [(3)] Φ : Slab thermal parameter (age * Vs)

903

904

905

906

907

908

Chapitre 3

Topographie dynamique

La notion de topographie dynamique appliquée à la Terre a été essentiellement développée lors des efforts déployés dans les années 80 pour comprendre les relations entre forme de la Terre, mesures gravimétriques et convection mantellique [e.g., Ricard et al., 1984]. Bien comprise sur le plan théorique, son existence réelle est restée élusive [Ricard et al., 1993, Čadek & Fleitout, 2003] à l'échelle globale.

3.1 Evidences régionales de la topographie dynamique

Une démarche inverse à celle des géodynamiciens globaux est d'aller explorer les observations locales dans les zones où la géodynamique est bien comprise. En particulier, les zones de subductions sont irrévoquablement les zones où les anomalies de densité en profondeur sont les plus fortes, du fait de la présence des panneaux plongeants, comme la gravimétrie l'atteste. Dans les articles qui suivent, j'examine des cas particuliers en les comparant avec un modèle théorique simple. Dans le premier travail, je me base sur un modèle où la rhéologie est isovisqueuse et j'utilse les observables géophysiques (tomographie sismique, gravimétrie et topographie) pour quantifier la topographie dynamique à l'aplomb des zones de subductions. Le deuxième volet, effectué dans le cadre de la thèse de B. Guillaume, utilise les variations temporelles de la topographie, mesurée sur le terrain à l'aide de la géomorphologie quaternaire, pour les comparer avec les résultats de modèles prédictifs comparables. Il ressort que sur les objets de petite dimension étudiés

(des subductions de taille bien inférieure au premier ordre spatial de la circulation mantellique), les déflections verticales dynamiques de la topographie atteignent plus de 1000 m. Il est probable que ce soit partiellement la dimension restreinte de ces objets isolés quipermette une représentation plus complète de la topographie dynamique en surface : pour des raisons géométriques, les ordres harmoniques supérieurs qui prennent naissance à faible profondeur dans la sphère terrestre, sont mieux représentés.

Ces résultats sont à rapprocher des conclusions contrastées obtenues à partir de la subsidence mesurée à l'aplomb des zones de subductions. Si les travaux de Gurnis en particulier expliquent les transgressions continentales qui sont à l'origine des bassins intracratoniques Permien en Eurasie et Crétacé en Amérique du Nord par l'effet de la topographie dynamique renforcé durant ces périodes de subduction très active [Gurnis, 1992, 1993, Mitrovica et al., 1989], des investigations sur des objets mieux détaillés conlcluent à un rôle mineur de la topographie dynamique [Wheeler & White, 2000] (notons que dans ce dernier travail, les auteurs établissent cependant des hypothèse fortes relatives au comportement mécanique de la lithosphère -subsidence thermique en particulier).

Dynamic topography above retreating subduction zones

Laurent Husson*
Department of Earth, Atmospheric and Planetary Sciences, Massachusetts Institute of Technology, Cambridge, Massachusetts 02139, USA

ABSTRACT

Dynamic topography provides a measure of stresses within the Earth's interior. Dense slabs induce an upper mantle flow that deflects the surface of the Earth downward above them. By combining a simple theoretical (Stokeslet) model of subduction, gravity modeling, and seismic tomography, I show that a significant fraction (as much as 2000 m) of the topographic variations observed above the Scotia, Mariana, and Hellenic subduction systems appears to be dynamically induced by stresses related to the underlying subduction.

Keywords: subduction, backarc basins, dynamic topography, Stokes flow.

INTRODUCTION

Dynamic topography provides fundamental information about the Earth for at least three reasons. First, it is a direct measurement of the stresses beneath the surface; above subducting slabs, it is critical in many respects, such as understanding seismic anisotropy. Second, as an observable, it informs us about the structure of the mantle. Third, it informs us about the nature of topography. Therefore, researchers have attempted to identify dynamic topography at a global scale (e.g., Hager, 1984; Cazenave et al., 1989; Colin and Fleitout, 1990; Ricard et al., 1993; Panasyuk and Hager, 2000), and have arrived at the controversial conclusion that the calculated magnitude of dynamic topography overestimates the magnitude that can be observed at the surface.

There are, however, some areas associated with retreating subduction systems where the bathymetry developed on the overriding plate near the subduction boundary is deeper than in adjacent regions. A retreating subduction system indicates subduction boundaries where the trench is retreating above the asthenosphere, moving away from the extending overriding plate. Because these systems are of limited lateral extent, the dynamic stresses and the associated dynamic topography should vary across the system in a systematic and predictable fashion. Most attempts to quantify the dynamic topography compare the mean topographies above deep density heterogeneities (e.g., Conrad et al., 2004; Wheeler and White, 2000); I examine the lateral variations in dynamic topography above a given structure. An analysis of the bathymetry developed above several retreating subduction boundaries (East Scotia, Mariana, and Aegean Seas; Fig. 1) allows me to quantify the extent to which the dynamic stresses related to subduction influence the shape of the Earth.

MODELING DYNAMIC TOPOGRAPHY

Stokeslets Approximation

Viscous flow associated with bodies of heterogeneous density and random shape embedded within a Newtonian viscous fluid can be conveniently assessed using a Stokeslet approximation (Morgan, 1965; Batchelor, 1967; Harper, 1984). In this approximation, the density field is discretized into point masses. Each point mass i induces a elementary spherical flow (Stokeslet) for which the Stokes stream function is known and can be written:

$$\Psi_i = \frac{\Delta\rho v_i g}{8\pi\eta} r_{ij} \sin^2\theta_{ij}, \quad (1)$$

where $\Delta\rho v_i$ is the mass anomaly associated with each point mass, g is gravitational acceleration, η is viscosity, r_{ij} is the distance from each point mass to the observation point j, and θ_{ij} is the angle between the vector ij and the direction of g. The normal stress on the upper free surface of a half-space can be calculated using the image technique (Morgan, 1965):

$$Fzz_{ij} = \frac{3\Delta\rho v_i g z_i^3}{\pi r_{ij}^5}, \quad (2)$$

where z_i is the depth of the point mass body beneath the surface. Because inertial terms are negligible, stress does not depend on viscosity. If the surface is stress free, then there will be a deflection of the surface by a distance h_{ij}, such that $(\rho_m - \rho^*)\, g h_{ij}$ is equal to Fzz_{ij}. The total Stokes flow is given by the sum of the Stokeslets; the total surface deflection H_j will be the sum of the deflections resulting from each point mass, hence

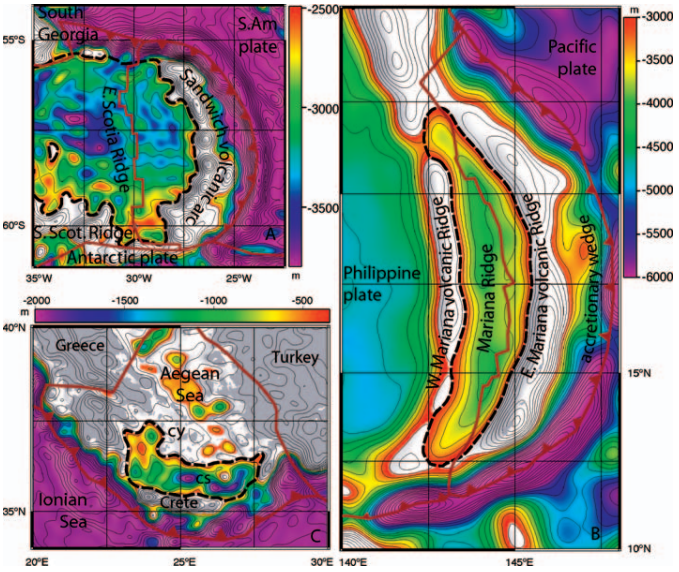

Figure 1. Topography of East Scotia (A), Mariana (B), and Aegean (C) seas (wavelengths <50 km are discarded). Deflection of topography toward center of basins can be pointed out by circumscribing (dashed lines) areas deeper than arbitrary reference depth in overriding plates (A, 2500 m; B, 3000 m; C, 350 m). Isocontours are every 250 m. S. Am.—South American Plate; S.Scot—South Scotia.

*E-mail: lhusson@mit.edu.

© 2006 Geological Society of America. For permission to copy, contact Copyright Permissions, GSA, or editing@geosociety.org.

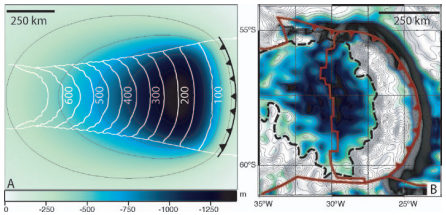

Figure 2. A: Map view of theoretical dynamic topography above slab. $\delta\rho$ = 40 *kg m*$^{-3}$, ρ^* = 1030 *kg m*$^{-3}$, η = 1.2 10^{21} *Pas*. White solid contours give shape of a slab (50 km isocontours). See text for details. B: Residual topography of East Scotia Sea after thermal subsidence, isostatic correction for sediment loading (sediment density ρ_s = 2500 *kg m*$^{-3}$), and −1800 m (depth of edges of ridge) have been removed. Only negative elevations are color-coded to emphasize similitude with theoretical predictions. Horizontal scales are different. Isocontours every 250 m.

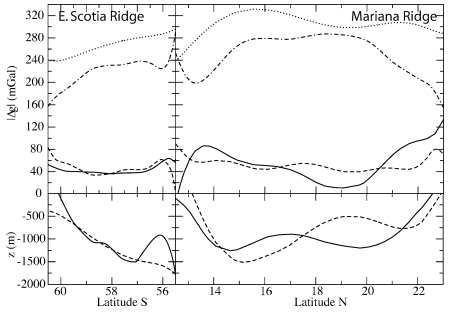

Figure 3. Observed (solid line) and modeled (from seismic tomography and bathymetry, dashed line) minimum residual topography (top) and gravity anomalies (bottom) along ridges of East Scotia (left) and Mariana (right) basins. Gravity anomalies from solid Earth only (dotted lines, top) and from seawater only (absolute value, dashed lines, top). Discrepancies between observed and modeled bathymetry are second-order chemical variations and uncertainties in tomographic data. z—dynamic topography; |Δg|—absolute value of the gravity anomaly.

$$H_j = \sum_i \frac{3\Delta\rho v_i z_i^3}{\pi r_{ij}^5(\rho_m - \rho_*)}, \quad (3)$$

where ρ_m denotes the density of the mantle and ρ^* either that of the air or of the seawater, depending on the geologic setting.

Theoretical Results

Subduction of a slab into the asthenosphere can be simulated by embedding a dense sheet of finite width within a viscous fluid of lower density. The Stokeslet approach requires that the fluid have uniform viscosity. The assumption that the slab has the same viscosity as the asthenosphere may limit our ability to fully understand the convective processes associated with subduction (Morra and Regenauer-Lieb, 2006). For example, with this model, trench retreat is the only way to have nonvertical slabs. However, the effective rheology of subducting slabs may be low (Moresi and Gurnis, 1996), and this simple choice gives a starting point to examine how subduction generates dynamic topography. There are few models of subduction that can provide for dynamically consistent trench motions (e.g., Enns et al., 2005; Royden and Husson, 2006), but a migrating trench can be mimicked in the Stokeslet approximation by specifying that the point masses that make up the dense sheet in the foreland have zero velocity until they become sufficiently close to the trench, at which point they are allowed to move in response to the Stokeslet flow. In this paper I assume that points in the foreland must be closer to the trench than a distance equal to half the width of the slab. This has the same effect as the somewhat ad hoc yield stress criterion found in other dynamic models (e.g., Moresi and Solomatov, 1998; Enns et al., 2005). This allows the trench to be freely distorted (the mantle flow controls trench shape) and to migrate toward the foreland.

In practice, an assemblage of point masses that collectively forms a slab of finite specified width ω describes the initial sine-shaped slab geometry. Each point mass induces a Stokeslet and these are summed to determine the flow (which includes the slab). For simplicity, the stream function for slab motion is computed in an infinite space (note that this approximation breaks down for the most shallow elements). The resulting flow is used to compute the evolving shape of the slab and the location of the trench until steady state is reached. Dense point masses are considered to drive the flow only within the upper mantle and are removed from the model when they reach the base of the upper mantle at 670 km depth. Figure 2 shows model slab geometry and dynamic topography for a slab in steady-state subduction; at the trench the slab is 100 km thick and 600 km wide. The trench migrates to the right at ~6.5 cm yr^{-1} for $\Delta\rho$ = 40 kg m^{-3} and η = 1.2 10^{21} Pa s. The surface trace of the trench is gently curved, concave toward the overriding plate, and the curvature of the slab increases with depth. This simple model reproduces most of the subduction features. Dynamic topography generated above the slab reaches its greatest value of ~1500 m at a distance of ~300 km from the trench. Note that H linearly scales with $\Delta\rho$ (equation 3). Dynamic topography decreases from its maximum value toward the sides of the subduction system, indicating that the pressure of fluid flow is more negative above the center of the slab than above the edges. The maximum gradient in dynamic topography is located ~100 km (~ω/6) inside the edges of the slab.

EVIDENCE OF NON-ISOSTATIC TOPOGRAPHY

The East Scotia, Mariana, and Aegean Seas are above three narrow subduction zones. Because their tectonics are comparable to the theoretical example described here, all three should exhibit topographic signals consistent with the model dynamic topography shown in Figure 2.

Observed Bathymetry

The East Scotia Sea (Fig. 1A) is a well-developed backarc basin that has opened since ca. 10 Ma (Barker, 2001). The trench is ~600 km wide and is migrating east at ~60–70 mm yr^{-1} (Lallemand and Heuret, 2005, and references therein). Figure 2B shows the residual topography computed by subtracting expected depth as a function of seafloor age (cooling model of Stein and Stein, 1992; ages from Vanneste and Larter, 2002; Reinecker et al., 2004). An isostatic correction has been applied to account for sediment loading (data from Laske and Masters, 1997). A datum at 1800 m given by the depth of the edges of the ridge after correction has subsequently been subtracted (Fig. 2B) in order to evaluate the minimum residual topography. In map view it is quite similar to the theoretical results shown in Figure 2A. In addition, the basin shows an overall ENE tilt (largely hidden by the arc) toward the center of the trench. The depth of the spreading ridge decreases by ~1500 m from the edges to the center of the basin, consistent with model dynamic topography (Fig. 3A). Without development of dynamic topography, or variations in chemical or thermal properties of the underlying mantle, the ridge axis is expected to exhibit an approximately uniform depth along its length. Lateral conduction of heat across the edge of the basin (at the ends of the spreading ridge), as well as the poloidal vs. toroidal flow, would be expected to create colder mantle and deeper seafloor near the edge of the basin (Kincaid and Griffiths, 2004), opposite to what is observed. In my interpretation, depth variations along the spreading ridge are a direct measure of the minimum dynamic topography due to subduction.

The Mariana subduction zone has developed largely since 3–4 Ma (Fig. 1B; Stern et al., 2003, and references therein), as the trench migrates eastward at rates of ~60–70 mm yr^{-1} (Lallemand and Heuret, 2005). The trench is 1000 km long and the backarc oceanic basin is narrow (<~300 km). Along the eastern side of the Mariana basin, a volcanic arc overlies a large portion of the basin, making it impossible to map a residual topography as in the Scotia Sea. However, the depth of the backarc spreading ridge still contains information about possible dynamic topography. As in the Scotia Sea, the ridge axis deepens away from the edges of the basin by more than 1000 m (Fig. 3B), similarly consistent with the basin center being dynamically deflected downward.

The Hellenic subduction zone (Fig. 1C) is an ~1000-km-wide segment of the African slab. The trench currently moves southwestward at ~35–40 mm yr^{-1} (McClusky et al., 2003). The Aegean upper plate consists of thinned continental crust, although arc-parallel extensional structures are no longer very active. In the southern part of the Aegean Sea, the Cretan trough forms an ~2000-m-deep depression. Measured crustal thicknesses are 20–26 km (Tirel et al., 2004, and references therein), which should correspond to an isostatically compensated bathymetry that is close to sea level. This suggests that a dynamic depression of the seafloor with a magnitude in excess of 1000–1500 m may be present in the Cretan trough region. However, unlike the oceanic backarc basins, where observed bathymetry can be readily referenced to oceanic depths of comparably aged lithosphere, continental basins have no obvious reference level with which to estimate dynamic topography. Nevertheless, the magnitude and distribution of apparent excess depth in the Aegean Sea region is comparable to that observed in the East Scotia and Mariana basins.

Seismic Tomography, Gravity Anomalies, and Dynamic Topography

The theoretical model presented here yields dynamic topography that is comparable to what is observed within the described systems. In order to account for density and thickness variations as well as idiosyncrasies in the geometry of the Scotia, Mariana, and Aegean slabs, I use seismic velocity anomalies to estimate the arrangement of the density anomalies within the upper mantle. To a first approximation, the difference ΔV, between the observed and the average seismic velocities at a given depth can be used as a proxy for the density anomalies at depth, where the density anomalies are linearly related to ΔV by a factor $\partial\rho/\partial\Delta V$. I use P-wave velocity anomalies computed from the three-dimensional grid of Van der Hilst (as updated from Kárason and van der Hilst, 2000) and assign mass anomalies,

$$\Delta\rho v = \Delta V_P \frac{\partial\rho}{\partial\Delta V_P} v, \quad (4)$$

to each Stokeslet cell, where v is the volume of each cell.

The conversion factor $\partial\rho/\partial\Delta V_r$ is deduced from free-air gravity anomalies (Sandwell and Smith, 1997). Free-air gravity anomalies are computed for each area using the entire set of point masses derived from the seismic velocity structure and the observed bathymetry. The conversion factors that provide the best fits are 24.5, 23, and 18 kg m^{-3}/% for the Scotia, Mariana, and Aegean seas, respectively, if no uniform background, long-wavelength value is added. These conversion factors yield excess densities of ~35–60 kg m^{-3} in the areas that might be occupied by subducted material, in the range of typical lithospheric density anomalies. Figure 3 shows the best-fit model free-air gravity, computed from V_P anomalies and bathymetry, and the observed free-air gravity anomalies, along profiles that follow the spreading-ridge axes in the Scotia and Mariana backarc regions.

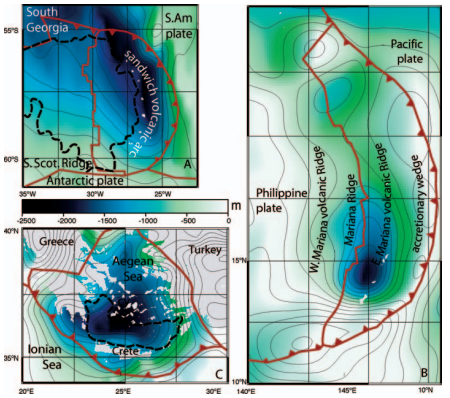

Figure 4. Dynamic topography induced by solid Earth density anomalies, in East Scotia (A), Mariana (B), and Aegean (C) seas. Relative densities are inferred from seismic tomography and conversion factor $\partial\rho/\partial\Delta V_*$ is deduced from gravity (see text). Isocontours every 250 m. Dashed lines outline inferred dynamic topography of Figure 1. S. Am.—South American Plate; S.Scot—South Scotia.

Dynamic topography is implicit in the model free-air anomalies because the observed bathymetry, which is used in the calculation of model values, has dynamic topography embedded within it. Both the observed and model free-air anomalies decrease toward the center of the backarc basins. This is consistent with a positive contribution to the gravity from a dense slab at depth partially counteracted by a negative contribution from dynamic topography at the surface. This can be scaled by noting that a point mass at depth z will generate a gravity anomaly that scales like $z/(z^2+d^2)^{3/2}$ while the dynamic topography generated by the same point mass scales as $z/(z^2+d^2)^{5/2}$ (d is the horizontal distance at surface level from above the point mass). This generates a longer-wavelength, lower-amplitude positive component and a shorter wavelength, larger amplitude negative component to the gravity. Maximum cancellation of the primary anomaly by the secondary therefore occurs above the point mass, i.e., in the center of the basin.

The density structure used to compute the model free-air gravity anomalies was also used to compute an explicit dynamic topography, using the same conversion factors for each area from equation 3. This is compared to the residual topography in the Scotia and Mariana basins and to the observed topography in the Aegean Sea (residual topography is difficult to compute for continental areas). A constant value corresponding to an unknown sum of background, large-scale mantle flow and relative position of the 0% V_p is implicitly added from the model values (600 m, 2000 m, and −2000 m for the Scotia Sea, Mariana Sea, and Aegean Sea, respectively).

In map view (Fig. 4), the maximum value of dynamic topography is located ~170 km, ~230 km, and ~280 km behind the Scotia, Aegean, and Mariana trenches, respectively, suggesting that the Scotia slab is the steepest slab and the Mariana is the flattest. In the East Scotia region the maximum dynamic topography is predicted to occur

beneath the volcanic arc that largely hides it. Because the ridge obliquely intersects the edge of the deflection, the profile mostly features a northward tilt. Beneath the Mariana basin, the dynamic topography can only be observed along the ridge axis due to the location of volcano-sedimentary edifices east and west of the ridge, but the fit between observed and model topography along the ridge is good. Within the Aegean region, the largest model dynamic topography occurs in the southern Aegean and beneath the Cretan Sea, reaching a magnitude of ~2 km. Thus, although it is not possible to compute a residual topography for the Aegean region, the model topography is in good agreement with total observed topography, suggesting that most of the deep bathymetry in the south Aegean could be dynamically maintained, and not due to an isostatic compensation of a thinned crust.

CONCLUSIONS

This study gives evidence for the signature of sinking slabs on the topography developed above them. A theoretical model of subduction, inversion of δV_P seismic data, and observations of gravity and bathymetry data above several subduction systems show that slab-induced mantle flow is a prominent control on the topographic signal in the vicinity of subduction boundary. This results in a curved shaped characteristic of retreating trenches and a depressed topography above the slab. Downward deflection of the surface topography for these retreating subduction zones is expected to be 1000–2000 m below that of the surrounding areas. The discrepancies between dynamic topography computed here and observed residual topography are primarily attributable to chemical anomalies (although significantly less than those suggested by Taylor and Martinez, 2003), to uncertainties in the seismic data and subsequent conversion to density anomalies, and to the approximation made on the viscosity. Elasticity of the upper plate plays a minor role because the wavelength of the deflection is much larger than the typical length scale for elastic flexure of the lithosphere.

Because of complications arising from large-scale mantle flow and mantle viscosity variations, the dynamic topography can only be clearly observed in particular areas, but any narrow retreating subduction system should yield its signature. For example, it can be inferred in the Lau, Manus, Caribbean, or Calabrian basins, but complex prerifting geodynamical events or multiple ridges make it difficult to isolate the dynamic signal.

Unlike other studies, I analyzed topographic variations within individual tectonic systems. Because they are small-scale tectonic systems, independent of large-scale mantle circulation and viscosity variations, a joint analysis of their bathymetry, tomography, and gravity shows that these subduction zones feature a dynamic component in the topography comparable to theoretical predictions. These results suggest that dynamic topography probably contributes to net topography in other locations where it is difficult to observe, and this raises the question of whether dynamic topography remains elusive only because isostatic processes hide it.

ACKNOWLEDGMENTS

This work originated from the enthusiasm of Wiki Royden. I thank Chang-Li and R. Van der Hilst for providing tomography data, and two anonymous reviewers. This work was funded by National Science Foundation grant EAR-0409373 (Medusa project).

REFERENCES CITED

Barker, P., 2001, Scotia Sea regional tectonic evolution: Implications for mantle flow and palaeocirculation: Earth Science Reviews, v. 55, p. 1–39, doi: 10.1016/S0012-8252(01)00055-1.

Batchelor, G., 1967, An introduction to fluid mechanics: Cambridge, UK, Cambridge University Press, 615 p.

Cazenave, A., Souriau, A., and Dominh, K., 1989, Global coupling of earth surface topography with hotspots, geoid and mantle heterogeneities: Nature, v. 340, p. 54–57, doi: 10.1038/340054a0.

Colin, P., and Fleitout, L., 1990, Topography of the ocean floor: Thermal evolution of the lithosphere and interaction of deep mantle heterogeneities with the lithosphere: Geophysical Research Letters, v. 17, p. 1961–1964.

Conrad, C., Lithgow-Bertelloni, C., and Louden, K., 2004, Iceland, the Farallon slab, and dynamic topography of the North Atlantic: Geology, v. 32, p. 177–180.

Enns, A., Becker, T.W., and Schmeling, H., 2005, The dynamics of subduction and trench migration for viscosity stratification: Geophysical Journal International, v. 160, p. 761–775, doi: 10.1111/j.1365-246X.2005.02519.x.

Hager, B.H., 1984, Subducted slabs and the geoid—Constraints on mantle rheology and flow: Journal of Geophysical Research, v. 89, p. 6003–6015.

Harper, J.F., 1984, Mantle flow due to internal vertical forces: Physics of the Earth and Planetary Interiors, v. 36, p. 285–290, doi: 10.1016/0031-9201(84)90052-9.

Kárason, H., and van der Hilst, R.D., 2000, Constraints on mantle convection from seismic tomography, *in* Richards, M., et al., eds., The history and dynamics of global plate motion: American Geophysical Union Geophysical Monograph 21, p. 277–289.

Kincaid, C., and Griffiths, R.W., 2004, Variability in flow and temperatures within mantle subduction zones: Geochemistry, Geophysics, Geosystems,v. 5, doi: 10.1029/2003GC000666.

Lallemand, S., and Heuret, A., 2005, On the relationships between slab dip, back-arc stress, upper plate absolute motion, and crustal nature in subduction zones: Geochemistry, Geophysics, Geosystems,v. 6, doi: 10.1029/2005GC000917.

Laske, G., and Masters, G., 1997, A global digital map of sediment thickness: Eos (Transactions, American Geophysical Union), v. 78, p. F483.

McClusky, S., Reilinger, R., Mahmoud, S., Ben Sari, D., and Tealeb, A., 2003, GPS constraints on Africa (Nubia) and Arabia plate motions: Geophysical Journal International, v. 155, p. 126–138, doi: 10.1046/j.1365-246X.2003.02023.x.

Moresi, L., and Gurnis, M., 1996, Constraints on the lateral strength of slabs from three-dimensional dynamic flow models: Earth and Planetary Science Letters, v. 138, p. 15–28.

Moresi, L., and Solomatov, V., 1998, Mantle convection with a brittle lithosphere: Thoughts on the global tectonic style of the Earth and Venus: Geophysical Journal International, v. 133, p. 669–682.

Morgan, W., 1965, Gravity anomalies and convection currents: Journal of Geophysical Research, v. 70, p. 6175–6187.

Morra, G., and Regenauer-Lieb, K., 2006, A coupled solid-fluid method for modeling subduction: Philosophical Magazine (in press).

Panasyuk, S., and Hager, B., 2000, Inversion for mantle viscosity profiles constrained by dynamic topography and the geoid, and their estimated errors: Geophysical Journal International, v. 143, p. 821–836, doi: 10.1046/j.0956-540X.2000.01286.x.

Reinecker, O., Heidbach, J., Tingay, M., Connolly, P., and Muller, B., 2004, The 2004 release of the world stress map: http://www. world-stress-map.org (October 2005).

Ricard, Y., Richards, M., Lithgow-Bertelloni, C., and Le Stunff, Y., 1993, A geodynamic model of mantle density heterogeneity: Journal of Geophysical Research, v. 98, p. 21,895–21,909.

Royden, L.H., and Husson, L., 2006, Trench motion: Slab geometry and viscous stresses in subduction systems: Geophysical Journal International (in press).

Sandwell, D.T., and Smith, W.H.F., 1997, Marine gravity anomaly from Geosat and ERS 1 satellite altimetry: Journal of Geophysical Research, v. 102, p. 10,039–10,054, doi: 10.1029/96JB03223.

Stein, C.A., and Stein, S., 1992, A model for the global variation in oceanic depth and heat flow with lithospheric age: Nature, v. 359, p. 123–129, doi: 10.1038/359123a0.

Stern, R., Fouch, M., and Klemperer, S., 2003, An overview of the Izu-Bonin-Mariana subduction factory, *in* Eiler, J.M., ed., Inside the subduction factory: Washington, D.C., American Geophysical Union Monograph 138, p. 175–222.

Taylor, B., and Martinez, F., 2003, Back-arc basin basalt systematics: Earth and Planetary Science Letters, v. 210, p. 481–497.

Tirel, C., Gueydan, F., Tiberi, C., and Brun, J.-P., 2004, Aegean crustal thickness inferred from gravity inversion. Geodynamical implications: Earth and Planetary Science Letters, v. 228, p. 267–280, doi: 10.1016/j.epsl.2004.10.023.

Vanneste, L.E., and Larter, R.D., 2002, Sediment subduction, subduction erosion, and strain regime in the northern South Sandwich forearc: Journal of Geophysical Research, v. 107, p. 2149, doi: 10.1029/2001JB000396.

Wheeler, P., and White, N., 2000, Quest for dynamic topography: Observations from Southeast Asia: Geology, v. 28, p. 963–966, doi: 10.1130/0091-7613(2000)28.

Manuscript received 12 December 2005
Revised manuscript received 19 April 2006
Manuscript accepted 25 April 2006

Printed in USA

Un effort particulier a été porté à la Patagonie. La migration vers le nord du point triple chilien du Miocène à l'actuel constitue un changement drastique du contexte géodynamique : la subduction rapide de la plaque Nazca sous la Patagonie est remplacée par la subduction très lente de la plaque Antarctique. La topographie dynamique devrait varier fortement en réponse et c'est ce qu'avec B. Guillaume et co-auteurs nous avons voulu tester par l'observations géologique.

TECTONICS, VOL. 28, TC2009, doi:10.1029/2008TC002324, 2009

Click Here for Full Article

Neogene uplift of central eastern Patagonia: Dynamic response to active spreading ridge subduction?

Benjamin Guillaume,[1,2,3,4] Joseph Martinod,[1,2,3] Laurent Husson,[5] Martin Roddaz,[1,2,3] and Rodrigo Riquelme[6]

Received 2 May 2008; revised 8 October 2008; accepted 23 December 2008; published 10 April 2009.

[1] The Chile Triple Junction (CTJ) episodically migrated northward during the past 14 Ma from 54°S to its present-day position at 46°30′S, as different almost trench-parallel spreading segments entered in subduction. This migration resulted in the opening of an asthenospheric window below Patagonia, inducing a disturbance in the regional mantle convection. On the overriding plate, the middle Miocene time corresponds to a major change in the central Patagonian basin dynamics, with a transition from subsidence to generalized uplift. The detailed mapping and the morphological study of post-middle Miocene terraces evidence regional-scale trench-parallel tilt histories that differ depending on latitude. South of 46°30′S, the slopes of the fluvial terraces indicate a change from northward to southward tilt during late Miocene. Terraces younger than the early Pliocene do not show any trench-parallel tilt. North of 46°30′S, in contrast, only northward tilt, active until the Pleistocene, is recorded. We use a semianalytical model of dynamic topography which suggests that the northward migration of the Chile Triple Junction should be accompanied by a dynamic uplift of the central Patagonian basin. Uplift would cause both north directed and south directed tilt, north and south of the triple junction, respectively, with values of ∼0.1–0.2% 500 km east of the trench. Tilt measured in the southeastern part of the central Patagonian basin (∼0.1%) is comparable to values predicted using the semianalytical model. The dynamic topography associated to the Chile ridge subduction may have exerted a major control on the Neogene dynamics of Patagonia. **Citation:** Guillaume, B., J. Martinod, L. Husson, M. Roddaz, and R. Riquelme (2009), Neogene uplift of central eastern Patagonia: Dynamic response to active spreading ridge subduction?, *Tectonics*, *28*, TC2009, doi:10.1029/2008TC002324.

[1]LMTG, Université de Toulouse, UPS (OMP), Toulouse, France.
[2]LMTG, CNRS, Toulouse, France.
[3]LMTG, IRD, Toulouse, France.
[4]Now at Dipartimento Scienze Geologiche, Università degli Studi Roma TRE, Rome, Italy.
[5]Géosciences Rennes, UMR 6118, Université Rennes-1, CNRS, Rennes, France.
[6]Departamento de Ciencias Geológicas, Universidad Católica del Norte, Antofagasta, Chile.

Copyright 2009 by the American Geophysical Union.
0278-7407/09/2008TC002324$12.00

1. Introduction

[2] Geologists often consider that the topography of the Earth essentially results from isostasy, topographic highs being balanced by crustal roots and/or hot lithospheric mantle [*Airy*, 1855; *Pratt*, 1859; *Froidevaux and Isacks*, 1984; *Molnar et al.*, 1993; *Garzione et al.*, 2006]. Mantle dynamics, however, also induce forces that deflect the Earth topography. Global numerical models predict associated vertical displacements of several hundreds of meters [*Hager and Clayton*, 1989; *Ricard et al.*, 1993; *Le Stunff and Ricard*, 1997; *Čadek and Fleitout*, 2003] and, therefore, that the direct contribution of mantle dynamics in the topography of the Earth is far from being negligible. Dynamic topography reaches its maximum amplitude above subduction zones, where mass anomalies are large at depth [e.g., *Mitrovica et al.*, 1989; *Gurnis*, 1993; *Zhong and Gurnis*, 1994; *Husson*, 2006].

[3] In continental domains, the dynamic component of topography is difficult to discriminate because the altitude is largely controlled by lithospheric loads and composition, which are highly variable. Active continental margins are nevertheless affected by long-wavelength surface deflections, and changes in the dynamics of subduction should be accompanied by vertical movements that can be recorded by the geological imprint [*Mitrovica et al.*, 1989; *Mitrovica et al.*, 1996; *Catuneanu et al.*, 1997; *Pysklywec and Mitrovica*, 2000; *Lock et al.*, 2006]. For instance, *Mitrovica et al.* [1989] showed that the process of subduction beneath western North America during the Cretaceous resulted in large-scale vertical deflection and tilting of the continental lithosphere that was followed by a Tertiary uplift of the area.

[4] In this paper, we study the Neogene evolution of central Patagonian, which was uplifted following the subduction of the Chile Ridge below the Andes since the middle Miocene. We focus our study on the mild deformed central Patagonian basin (Figure 1), which extends in the W-E direction from the eastern foothills of the Patagonian Andes to the Atlantic coast and in the N-S direction from the Sierra San Bernardo to the Deseado massif because this area is poorly affected by post-middle Miocene tectonics. Moreover, this region remained ice-free during glaciations. It shows a pristine morphology preserved from the erasure of glaciers that will be used to evidence its long-term Neogene uplift. The central Patagonian basin, which almost overlays the inland part of the San Jorge Gulf basin

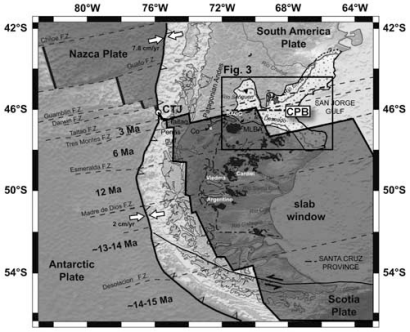

Figure 1. Geodynamic setting of southern South America displaying the different active segments and transform fault zones (FZ) of the Chile Ridge (modified from *Cande and Leslie* [1986]). Timing of ridge subduction is indicated by bold black numbers [from *Gorring et al.*, 1997] and relative present-day convergence velocities [from *De Mets et al.*, 1994]. The Chile Triple Junction (CTJ) is currently located west of the Taitao Peninsula. Neogene plateau basalts, including the Meseta del Lago Buenos Aires (MLBA), are displayed in black [from *Panza et al.*, 2003] and slab window current projection at the surface in gray [from *Breitsprecher and Thorkelson*, 2008]. The central Patagonian basin (CPB) and the Cosmelli basin (Co), south of the Buenos Aires–General Carrera Lake (BAGC), are displayed in white. The location of Figure 3 is indicated by the black box.

[*Bianchi*, 1981], is located at the latitude of the present-day Chile Triple Junction (CTJ), where the Chile active spreading ridge subducts beneath South America.

[5] During the past 14 Ma, the CTJ migrated northward, from the latitude of 54°S to its present-day position at about 46°30′S, west of the Taitao Peninsula, as different segments of the Chile spreading ridge successively entered the subduction zone [*Cande and Leslie*, 1986]. North of the CTJ, the convergence rate between Nazca and South American plates is 7.8 cm a^{-1}, whereas south of the CTJ, the convergence rate between South America and the Antarctic oceanic plate decreases to 2 cm a^{-1} [*De Mets et al.*, 1994], leading to the opening of an asthenospheric window [*Ramos and Kay*, 1992; *Kay et al.*, 1993; *Gorring et al.*, 1997, 2003; *D'Orazio et al.*, 2000, 2001, 2003, 2005; *Gorring and Kay*, 2001; *Guivel et al.*, 2003, 2006; *Lagabrielle et al.*, 2004, 2007; *Espinoza et al.*, 2005; *Breitsprecher and Thorkelson*, 2008] that disturbs mantle dynamics beneath the continent (Figure 1). In order to investigate the impact of the associated mantle flow on the vertical surface motion, we synthesize published data and analyze the evolution of sedimentation, erosion, and tectonic features as well as evidence of deformation during the Neogene. We produce a regional-scale map of the post-middle Miocene system of terraces, and measure the tilting affecting each of the terraces to characterize the uplift of the central Patagonian basin. Then, we compare its evolution with a semianalytical model of dynamic topography simulating the geodynamic context of Patagonia.

2. Geological Setting of Central Patagonia

2.1. Late Oligocene to Early Middle Miocene: Marine Transgression and Synorogenic Continental Molasse

[6] From late Oligocene to early Miocene, a widespread transgression occurred in the Patagonian basin. This transgression is marked by the deposition of nearshore marine Centinela Formation and lateral equivalents (Figure 2). The "Patagonian transgression" covered most of southern Patagonia [*Malumián*, 1999]. The epicontinental seaway was largely open to the south, south of the Deseado massif, and to the east, north of the Deseado massif [*Malumián*, 1999]. Close to the present-day Atlantic coast, the corresponding marine series are the Chenque (San Jorge Gulf) and Monte León formations. In Chile, marine series corresponding to the Centinela Formation are assigned to the Guadal Formation [*Suárez et al.*, 2000; *De la Cruz and Suárez*, 2006]. The marine transgression extended to the west above part of the present-day Cordillera, and Oligo-Miocene marine sediments are preserved in the Cosmelli syncline [*Flint et al.*, 1994; *De la Cruz and Suárez*, 2006], south of the Buenos Aires–General Carrera Lake. Although this locality is only 100 km east of the Miocene outcrops of the Penas Gulf area on the Pacific coast (Figure 1), the different macroinvertebrate fauna suggest that the marine transgression that invaded Patagonia from the Atlantic to the Guadal area was separated from the Pacific Ocean by the continuous geographic barrier of the Andean Cordillera [*Frassinetti and Covacevich*, 1999; *Flynn et al.*, 2002]. Marine series form an Oligocene to early Miocene eastward prograding sequence of coarse conglomerates, sandstones, and shales containing shells and microfossils [*Ramos*, 1989; *Barreda and Caccavari*, 1992; *Bellosi and Barreda*, 1993; *Frassinetti and Covacevich*, 1999; *Malumián*, 1999]. The thickness of the deposits reaches 500 m on the Atlantic coast [*Bellosi and Barreda*, 1993]. It generally varies between 225 and 375 m in the Cordillera foothills [*Ramos*, 1989], and in the Cosmelli syncline, measured thicknesses range between 110 m [*De la Cruz and Suárez*, 2006] and 650 m [*Flynn et al.*, 2002].

[7] South of the CTJ, marine series are followed by fluvial deposits of the Santa Cruz Formation and its lateral equivalent (Río Zeballos Group) [*Ramos*, 1989; *Suárez et al.*, 2000; *De la Cruz and Suárez*, 2006] (Figure 2). This synorogenic formation consists of sandstones and silts, interbedded with conglomerate lenses that deposited in a high-energy fluvial environment [*Ramos*, 1989; *De la Cruz and Suárez*, 2006]. The Santa Cruz Formation thickness locally reaches up to 1500 m, south of Buenos Aires–General Carrera Lake [*Ramos*, 1989] and exhibits minimum thicknesses of 900–1000 m in the Cosmelli basin [*De la Cruz and Suárez*, 2006]. These deposits have been dated using intercalated tuffs levels between 22 and 14 Ma [*Blisniuk et al.*, 2005]. North of the CTJ, the Río Frias Formation and lateral

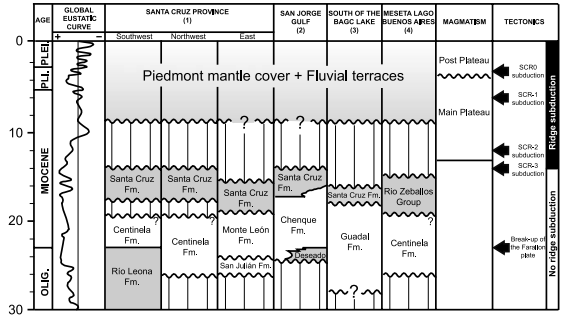

Figure 2. Chronological table displaying the stratigraphy of (1) the southwestern, northwestern and eastern sectors of the Santa Cruz province [*Parras et al.*, 2008], (2) the San Jorge Gulf [*Malumián*, 1999], (3) the south of the Buenos Aires–General Carrera (BAGC) Lake [*De la Cruz and Suárez*, 2006], and (4) the Meseta del Lago Buenos Aires [*Lagabrielle et al.*, 2007]. Continental formations are gray, and marine formations are white. The main magmatic and tectonic events along with the global eustatic curve [*Haq et al.*, 1987] are also indicated.

equivalents (Río Mayo and Pedregoso formations) also correspond to fluvial series that were deposited during the middle Miocene [*Marshall and Salinas*, 1990]. The maximum outcropping thickness of the Río Frias formation is about 250 m. Contractional tectonics during deposition of the continental series are evidenced by synsedimentary structures. Growth folds and intraformational thrusts have been reported in Chile in the Cosmelli syncline and south of the region of Río Las Horquetas and Meseta del Guenguel [*Flint et al.*, 1994; *Suárez and De la Cruz*, 2000; *Lagabrielle et al.*, 2004].

[8] The Patagonian transgression and the deposition of the overlying continental series are the result of a major change in the Andean geodynamic context. At around 26 Ma, the Farallon plate broke up [*Lonsdale*, 2005]. This period is also marked by a change to a more trench-perpendicular and faster convergence between the oceanic and South American plates [*Pardo-Casas and Molnar*, 1987; *Somoza*, 1998; *Lonsdale*, 2005]. Fission track analyses evidence an acceleration of the denudation at the western margin of the Cordillera during the late Oligocene [*Thomson et al.*, 2001], coeval with the deposition of the Oligo-Miocene series. Then, Oligocene and Miocene series were deposited during a major contractional period of the Andes at the latitude of the central Patagonian basin [*Ramos*, 1989; *Lagabrielle et al.*, 2004]. Between 47°30′S and 49°S, this shortening resulted in the formation of a complex fold-and-thrust belt in which the Tertiary molasse sequence (marine and continental) is involved [*Ramos*, 1989]. Shortening varies between 45 and 22 km from the north (47°40′S) to the south (49°S) of the fold-and-thrust belt [*Ramos*, 1989] and is at least of 35 km during the late Miocene in the fold belt at 50°S [*Kraemer*, 1998]. The segment of the Patagonian Andes located north of the present-day triple junction is characterized by a weaker Oligo-Miocene shortening, resulting in restricted areas of foreland sedimentation that only accumulated about 100 m of synorogenic deposits [*Ramos and Kay*, 1992].

2.2. Late Miocene to Holocene: Back-Arc Plateau Basalts and Widespread Detrital Cover

[9] The Patagonian back-arc region has been the locus of widespread volcanic activity during the entire Cenozoic. South of 46°S, a magmatic pulse started ~13 Ma ago during middle Miocene [*Ramos and Kay*, 1992; *Gorring et al.*, 1997; *Guivel et al.*, 2006]. The late Miocene to Pleistocene magmatism mainly consists of massive tholeiitic plateau lavas covered by less voluminous alkalic postplateau lavas [*Gorring et al.*, 1997]. The emplacement of main plateau lavas has been dated between 12.4 and 3.3 Ma at the Meseta del Lago Buenos Aires and between 8.2 and 4.4 Ma at the Meseta Chile Chico [*Guivel et al.*, 2006]. South of 46°30′S, the main plateau lavas range between 12 and 7 Ma in the western part of the back-arc region and between 5 to 2 Ma in the eastern part of the Deseado massif [*Gorring et al.*, 1997]. The Plio-Pleistocene postplateau basalts have ages from 3.4 to 0.125 Ma [*Gorring et al.*, 2003] at the Meseta del Lago Buenos Aires. Therefore, most of the plateau and postplateau basalts postdate the deposition of the early to middle Miocene continental molasses, and their emplacement helps in dating the subsequent evolution of the region. In the region of Buenos Aires–General Carrera Lake, plateau basalts are emplaced on a planar surface gently tilted toward the east, and seal the eastern thrust front of the Patagonian Andes [*Ramos*, 1989; *Lagabrielle et al.*, 2004]. This implies that the compressive tectonic activity in this part of the orogen essentially ceased before 13 Ma [*Lagabrielle et*

al., 2007]. The same observation has been done by *Coutand et al.* [1999] at the latitude of Viedma lake (49°S), where gently tilted early Pliocene basalts [*Mercer et al.*, 1975] unconformably overlie deformed Paleogene sediments.

[10] In northern Patagonia, in contrast, transpression is still active. Oblique thrusting predominates outside the magmatic arc, and dextral strike-slip shear zones develop within it [e.g., *Lavenu and Cembrano*, 1999; *Cembrano et al.*, 2002]. The transpressional dextral Liquiñe-Ofqui fault, whose present-day activity is demonstrated by seismic records [*Lange et al.*, 2008], is a more than 900-km-long structure that initiates close to the current Chile Triple Junction.

[11] In central Patagonia, following the deposition of the Santa Cruz Formation, the depositional environment drastically changes. The Santa Cruz Formation is overlain by late Cenozoic continental deposits, as the so-called "Rodados Patagonicos," which have formerly been accurately described by *Feruglio* [1950]. These series correspond to poorly consolidated conglomerates that are widespread from the Andean foothills to the Atlantic coast and which thickness often does not exceed 10 m. The pebbles generally have a roughly constant size from the Andes to the Atlantic Ocean. They form a piedmont mantle cover in which the activity of fluvial systems elaborated a succession of fluvial terraces (Río Senguerr, Río Deseado, Cañadon Salado, Cañadon del Carril, Río Mayo) (see *Panza* [2002] for a review).

3. Post-Middle Miocene Landscape Evolution

[12] We mapped the conglomeratic surfaces, (piedmont mantle cover and fluvial terraces), on the basis of the synthesis of *Panza* [2002], complemented by 1:250,000 scale geological maps of the Servicio Geológico Minero Argentino [*Dal Molin et al.*, 1998; *Giacosa*, 1998; *Sciutto et al.*, 2000; *Cobos and Panza*, 2001; *Servicio Geológico Minero Argentino*, 2001; *Ardolino et al.*, 2003; *Escosteguy et al.*, 2003; *Sciutto et al.*, 2004; *Panza and Genini*, 2005] and observation of Landsat images and SRTM digital elevation model, analyses being confirmed by field observations (Figure 3). We will use the different surfaces as geologic markers to infer the geomorphologic and tectonic evolution since middle Miocene.

3.1. Description of Piedmont Mantle Cover and Fluvial Terrace Systems

[13] We distinguish three sectors in which piedmont mantle cover deposits have been preserved (Río Guenguel and Arroyo Verde areas to the west, and Pampa del Castillo area to the east), extending from the Andes foothills to the Atlantic coast (Figure 3). Piedmont mantle cover gently dips eastward and results from the coalescence of alluvial cones [*Panza*, 2002], that generally lie more or less conformably on the Santa Cruz continental formation (early to middle Miocene) in the western region, and on the marine Patagonia and Chenque formations (late Oligocene to early Miocene) close to the Atlantic Ocean. The higher surface is ~850 m above sea level (asl) in the Río Guenguel area and is still remarkably high close to the Atlantic coast (~750 m asl in Pampa del Castillo, only 25 km NW of the coast). Seven younger levels of piedmont surfaces (T2Gu to T8Gu, see Figure 3) are preserved in the Río Guenguel area. The difference in elevation between the first and last level is roughly 200 m.

[14] Fluvial terrace levels correspond to more recent systems of terraces resulting from the activity of rivers flowing from the Andes into the Atlantic Ocean. We distinguish three main groups of terraces corresponding to different fluvial systems: (1) the Cañadon Salado-Cañadon del Carril, (2) the Río Senguerr, and (3) the Río Deseado. These fluvial terraces result from the action of rivers whose flow has been incomparably larger than that of the present-day rivers going to the Atlantic Ocean. The semiarid climate of the continent, east of the Cordillera, and the fact that the present-day drainage divide between rivers flowing toward the Atlantic Ocean versus rivers flowing toward the Pacific Ocean is essentially located on the eastern and drier side of the mountain belt explains the modest flow of these rivers at present-day. In fact, the drainage divide shifted eastward after Neogene glaciations remodeled the Andean landscape. Between 45°S and 47°30′S, several major glacial valleys crosscut the chain, the most striking example being the valley occupied by the Buenos Aires–General Carrera Lake and the Río Baker. Their formation resulted in the capture of Andean rivers flowing eastward by the Pacific side, subsequently starving rivers flowing into the Atlantic Ocean. During cold periods, however, the ice cap covers the Patagonian Andes, fills valleys in the Cordillera and the eastward flowing drainage is reactivated [*Feruglio*, 1950; *Mercer*, 1976; *Turner et al.*, 2005]. This evolution of the watershed system explains the presence of several major fluvial terrace systems that do not correspond to the flow of the present-day rivers.

[15] The Cañadon Salado–Cañadon del Carril fluvial system, located southwest and south of the Río Senguerr system, is the oldest preserved fluvial system of the study area. The Cañadon Salado and Cañadon del Carril are currently temporary rivers flowing into the Río Senguerr (Figure 3). The second level of this fluvial system (T2Cs) covers the Ruta 16 valley, indicating that the paleoriver flowed out east of its present-day course before being captured by the paleo-Río Senguerr, that was flowing at that time in the arc-shaped Hermoso valley (Figure 4). The capture of the Cañadon Salado occurred before the emplacement of the T3Cs deposits since the latter displays the same spatial organization than the present-day river (Figure 4).

[16] The Río Senguerr is currently 395 km long, flowing from Fontana Lake at an elevation of 925 m asl, into the Musters and Colhué-Huapi lakes at an elevation of 270 m asl. Its main tributaries are the Arroyo Verde and the Río Mayo. It produced a system of eight terraces, exposed from Nueva Lubecka to the north to the abandoned Hermoso valley. The presence of wide fluvial terraces north of 45°S (northern extent of the present-day course of the Río Senguerr) shows that during their formation, the major flow was coming from the north. In the region of Los Monos, the Río Senguerr abandoned the Hermoso valley during or after the deposition of the terrace T7Se (Figure 4), resulting in the present-day river flow toward the basin of the Musters and Colhué-Huapi lakes.

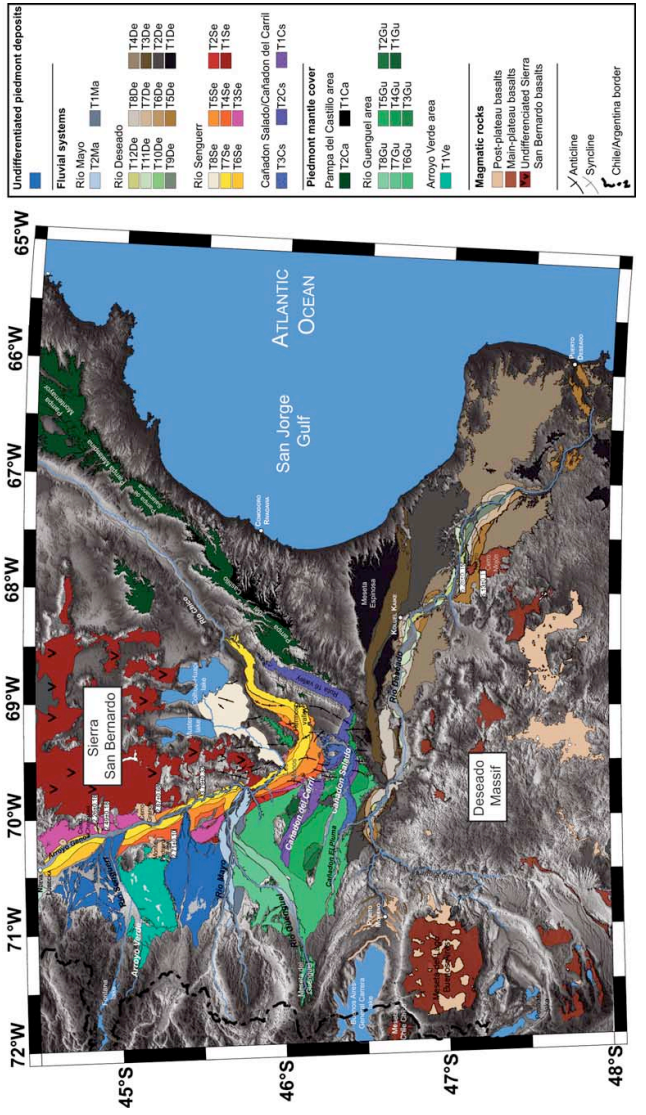

Figure 3. Map of the conglomerate surfaces covering central Patagonia. T1Ma and T2Ma, Río Mayo fluvial terraces; T1De to T12De, Río Deseado fluvial terraces; T1Se to T8Se, Río Senguerr fluvial terraces; T1Cs to T3Cs, Cañadon Saladon–Cañadon del Carril fluvial terraces; T1Ca and T2Ca, piedmont alluvial surfaces of the Pampa del Castillo area; T1Gu to T8Gu, piedmont alluvial surfaces of the Río Guenguel area; T1Ve, piedmont alluvial surface of the Arroyo Verde area.

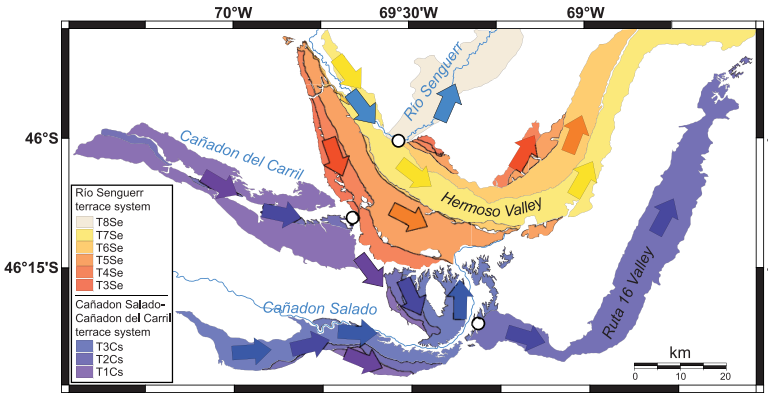

Figure 4. Stream directions during the deposition of the fluvial terraces of the Río Senguerr and Cañadon Salado–Cañadon del Carril systems. Captures are marked by white circles. Cañadon Salado and Cañadon del Carril have been captured by the paleo-Río Senguerr before the deposition of T3Cs, abandoning the Ruta 16 valley. Afterward, Río Senguerr has been captured by the Musters Lake during or just after the deposition of T7Se, abandoning the Hermoso valley.

[17] Río Deseado is a major fluvial system of the Patagonian foreland, located in the Santa Cruz province, in the southern part of the study area. Río Deseado currently originates from the region of Perito Moreno, east of the eastern edge of the Buenos Aires–General Carrera Lake, and flows on a length of 520 km to the Atlantic Ocean at Puerto Deseado. The river produced a system of twelve terraces (Figure 3). The course of the Río Deseado also changed through time, abandoning in the Meseta Espinosa, the T1De to T3De deposits tens of kilometers north of the present-day river course.

[18] In fact, all regional major river courses changed during the deposition of fluvial terrace systems. The courses of the northern rivers (Río Senguerr, Cañadon Salado) shifted northward, while the Río Deseado valley moved to the south, resulting in the present-day divergent hydrographic network. The Río Deseado now joins the Atlantic Ocean ~160 km south of the San Jorge Gulf, while the Río Senguerr flows through the Río Chico valley to the northeast and reaches the ocean ~300 km north of the San Jorge Gulf.

3.2. Age of Terraces

[19] Most of the ages proposed in the literature are relative ages based on stratigraphic relationships, which leads to discrepancy between authors. Only radiometric ages of basalt flows overlying some piedmont surfaces and fluvial terraces give some absolute constraints.

[20] All the terraces overlie the deposits of the Santa Cruz Formation and are consequently younger than ~14 Ma. Levels of piedmont mantle cover are older than the first level of each fluvial system (Río Senguerr, Cañadon Salado–Cañadon del Carril, Río Deseado). From their relative topographic position, we infer that T1Cs and T2Cs are older than T3Se, and T3Cs is at least older than T4Se and T1De.

[21] Five basalts crop out in the Río Senguerr valley. K/Ar radiometric ages have been obtained by *Bruni* [2007] in the basalts of Cerro Chenques (2.26 ± 0.11 Ma and 2.49 ± 0.18 Ma), Cerro Grande (2.87 ± 0.68 Ma) and Monte Pedrero (2.71 ± 0.10 Ma) (Figure 3). T3Se is covered by both the Cerro Chenques and Cerro Grande basalts, T4Se is covered by the Monte Pedrero basalts, and T5Se is covered by the Cerro Grande basalts. Thus, T5Se and older terraces of the Río Senguerr valley are older than 2.87 Ma and are at least middle Pliocene in age. T7Se bypasses the Cerro Grande basalts, suggesting that it formed following their emplacement and would therefore be younger than 2.87 Ma.

[22] Some absolute constraints on the age of the Río Deseado terrace system is also given by Ar/Ar radiometric ages on basalts emplaced above terraces. Ages of 5.13 ± 0.11 Ma and 5.28 ± 0.11 Ma have been obtained by *Gorring et al.* [1997] in the Cerro Monjón and Cerro Negro basalts, respectively. The Cerro Monjón basalts cover T5De, and the Cerro Negro basalts also cover younger terraces (T6De to T8De), indicating that the eight older terraces of the Río Deseado fluvial system are older than 5.28 Ma, i.e., that they are late Miocene. T9De, in contrast, is younger than 5.28 Ma and appeared during Pliocene.

[23] Figure 5 summarizes our knowledge of the age of the systems of terraces. Piedmont mantle terraces are middle to

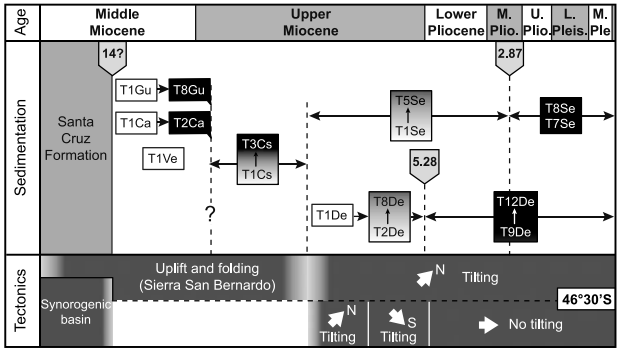

Figure 5. Age distribution of the piedmont mantle cover, fluvial terraces, and tectonic events north and south of the Chile Triple Junction. Absolute ages of basalts covering terraces are from *Gorring et al.* [1997] and *Bruni* [2007].

late Miocene in age, and the fluvial terrace system began its formation before Pliocene.

3.3. Local Tectonics

[24] As detailed above, the end of the deposition of the Santa Cruz Formation corresponds to the end of the major Oligo-Miocene shortening episode of the Cordillera. Farther east, at about 150 km from the Cordilleran thrust front, in the Sierra San Bernardo and farther south, mild deformation is attested by the presence of gentle folds and reverse faults that result from the reactivation of pre-Cretaceous extensional fault systems [*Barcat et al.*, 1989; *Homovc et al.*, 1995; *Peroni et al.*, 1995; *Chelotti*, 1997]. The San Bernardo fold belt, a 150-km-long and 50-km-wide NNW-SSE trending band, corresponds to the easternmost evidence of Andean shortening. *Rodriguez and Littke* [2001] present a detailed mapping of the folds affecting the top of the Lower Cretaceous Castillo Formation (Figure 6). Structures involve rocks of ages up to early middle Miocene, belonging to the Superpatagoniano succession, contemporaneous of the Santa Cruz Formation [*Peroni et al.*, 1995]. The San Bernardo fold belt is still today marked in the geomorphology of that part of Patagonia, locally reaching altitudes of 1500 m asl. The Río Senguerr deviates its course to the south to bypass the San Bernardo fold belt, approaching the Cañadon Salado and Río Deseado rivers.

[25] The San Bernardo folds do not deform the fluvial terraces of the Río Senguerr, showing that shortening in the Sierra San Bernardo is now inactive. However, older terrace systems are uplifted above the San Bernardo fold belt. The elevation of the piedmont cover terrace T4Gu and of the older fluvial terraces of the Cañadon Salado system (T1Cs and T2Cs) locally increases eastward approaching the western boundary of the fold belt (Figure 6). The elevation of T4Gu increases by ~90 m, and that of T1Cs of ~50 m over a distance of about 15 km. The ~E-W oriented Cañadon Salado valley is steep-sided within older piedmont terraces, evidencing that the local west directed slope of its oldest terraces does not result neither from lateral sediment supply nor from flows coming from the east (Sierra San Bernardo). Therefore, a modest-amplitude, large-wavelength uplift of the San Bernardo fold belt posterior to the formation of the Cañadon Salado–Cañadon del Carril terrace systems must have occurred, and this uplift is almost not accompanied by shortening.

3.4. Regional Tilt

[26] We studied the present-day slopes of terraces to investigate a possible long-wavelength regional uplift. If the initial downstream slope of terraces is difficult to constrain, it is reasonable to consider that terraces displayed horizontal profiles in the direction perpendicular to the paleovalleys. On the basis of this assumption, tilts would correspond to any deviation from this horizontality. Topographic profiles through terraces have been obtained using SRTM Digital Elevation Models.

3.4.1. South of the Current CTJ Position

[27] Figure 7 shows that at least the five older levels of the Río Deseado terrace system (south of 46°30′S) are inclined toward the south. The fact that steep scarps separate the different levels and that the southward slope of terrace levels is similar on both sides of the present-day Río Deseado valley shows that these slopes do not result from lateral sediment supply. In fact, southward tilt resulting from a larger regional uplift north of the terraces must have occurred to explain the observed slopes. In the N-S direction, however, T1De exhibits a slight slope toward the south (0.05 ± 0.01%) and appears locally subhorizontal. T2De and T3De, which can be followed on large distances, present a regional slope of 0.11 ± 0.01% and 0.10 ± 0.02% toward the

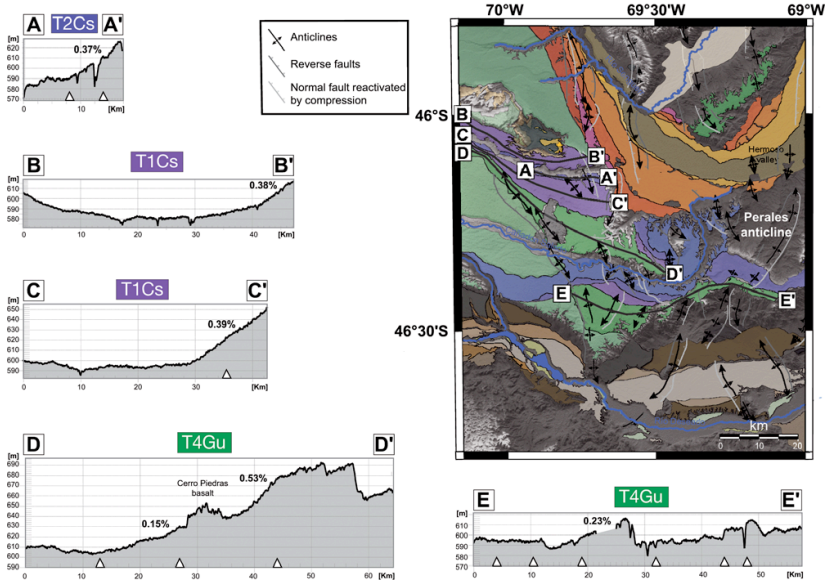

Figure 6. Topographic profiles of uplifted terraces (see map for location and Figure 3 for color legend). Vertical exaggeration is 180. T1Cs and T2Cs are for level 1 and level 2 of the Cañadon Salado–Cañadon del Carril terrace system, and T4Gu is for level 4 of the piedmont mantle cover of the Río Guenguel area. The white triangles below the topographic profiles indicate the position of the anticlines axis at the top of the Lower Cretaceous Castillo Formation [*Rodriguez and Littke*, 2001].

south, respectively, at the longitude of Koluel Kaike. The southward slope of T4De is smaller (0.07 ± 0.01% north of the Cerro Negro basalt and close to the mouth of the Río Deseado), and that of T5De, west of the Cerro Negro basalts, is even smaller (0.05 ± 0.01%). For comparison, these slopes are comparable to the longitudinal WNW-ESE trending slope of these terraces in the same area and to the present-day slope of the Río Deseado (0.08%). Terraces T6De and T7De are not extended enough to detect a potential tilt using SRTM data. The younger levels of the Río Deseado system (T8De to T12De) are not tilted. In fact, the present-day topography of the Río Deseado terrace system suggests that a gentle southward regional tilt occurred following the deposition of T3De and before T6De (or T8De). It would have been preceded by a northward regional tilt between the deposition of T1De and T2De, explaining why the present-day slope of T1De toward the south (0.05 ± 0.01%) is smaller than that of T2De (0.11 ± 0.01%). Figure 7 shows that the southward tilt that occurred between the formation of T2De and T8De resulted in the southward shift of the course of the Río Deseado, leaving abandoned the valley that resulted in the formation of T3De.

3.4.2. North of the Current CTJ Position

[28] In contrast, the analysis of the topography of terraces located just north of 46°30′S suggests that this region has essentially been tilted toward the north. East of the San Bernardo fold belt, T1Ca forms a wide planar surface that extends over 400 km from the Pampa del Castillo, west of Comodoro Rivadavia, to the Río Chico mouth to the north (Figure 8). The topography of this surface is tilted toward the northeast with a slope of 0.14 ± 0.05%. Clearly, part of the present-day slope of T1Ca results from its genesis and does not reflect subsequent tilt. However, paleocurrents observed using psephites orientations [*Beltramone and Meister*, 1992], although controversial [*Bellosi*, 1996], indicate an eastward flow direction in the Pampa del Castillo whereas the corresponding terrace is tilted toward the northeast. In addition, the present-day slope of this surface is more than three times larger than the longitudinal profile of Río Chico and larger than the longitudinal slope of other terraces that have been preserved in the eastern part of the study area (Hermoso valley, distal part of the Río Deseado terrace system). Thus, we propose that the present-day observed slope

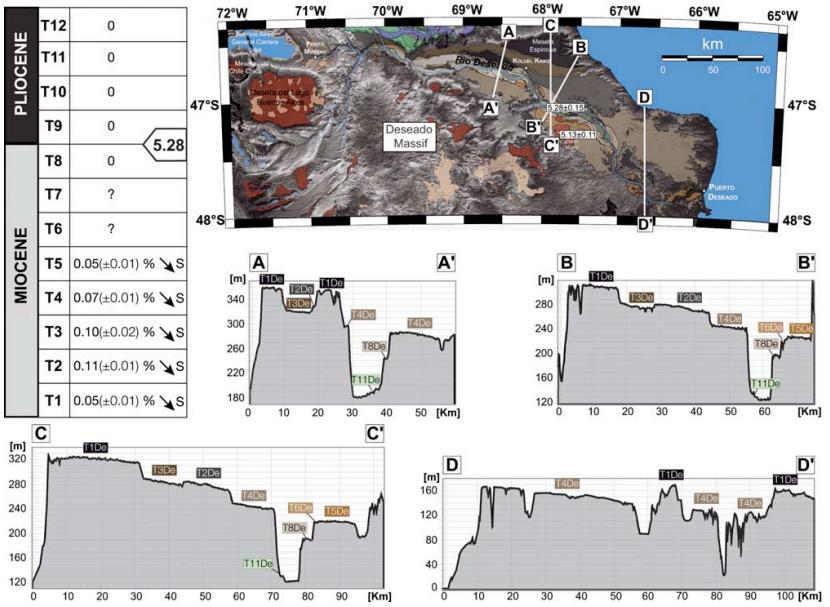

Figure 7. Topographic profiles of Río Deseado terraces (see map for location and Figure 3 for color legend) and values of N-S slope for each terrace. Numerical age of the Cerro Negro basalts is 5.28 Ma [*Gorring et al.*, 1997].

of T1Ca would partly result from a postdepositional tilt toward the north or northeast of that area.

[29] The northward tilt of the region located north of 46°30′S is also suggested by the longitudinal profile of the second terrace of the Cañadon Salado system in the Ruta 16 valley. This terrace corresponds to an abandoned valley incised within Oligo-Miocene sediments (Monte León and Santa Cruz formations). Its upstream portion is WNW-ESE oriented whereas the downstream part is directed toward the NE (Figure 8). The valley-parallel profile AA' in Figure 8 shows that the present-day longitudinal slope of that terrace is inverted toward the upstream direction in the upper WNW-ESE oriented part of the valley, whereas it goes down toward the NE in the lower part of the valley. In fact, again, this change in the slope of the terrace suggests that the area has been tilted northward. Tilting would have inverted the longitudinal slope of the part of the valley flowing toward the ESE and increased the slope of the lower part of the valley. Another possibility could be that the activity of the Sierra San Bernardo fold-and-thrust belt would have subsequently produced the uplift of the upper part of the valley and the observed counterslope for T2Cs. However, the nearest known tectonic structure along the course of T2Cs is the Perales anticline [*Homovc et al.*, 1995; *Rodriguez and Littke*, 2001] and its location at depth does not fit the change of slope observed in the Ruta 16 valley (Figure 8). Since T2Cs is not involved in any tectonic structure and since the change in its present-day slope coincides with the changing orientation of the valley, we suggest that a regional northward tilt may have caused this abnormal longitudinal profile.

[30] The longitudinal profiles of the seven terraces of the Río Senguerr system suggest that the northward tilt of the northern part of the study area pursued during their formation (Figure 9). The slope of each terrace is measured in the direction parallel to the current valley and obtained values are systematically smaller for the older terraces. For instance, T6Se lies 85 m above the present-day Río Senguerr bed just above the elbow of capture. Upstream, the difference in elevation decreases to 35 m, south of Cerro Chenques. Close to the capture, T2Se is 70 m above T6Se, while the two levels are close together 35 km NE of Cerro Chenques (Figure 9).

[31] Clearly, the higher longitudinal slope of the present-day Río Senguerr valley may also result from its capture by the Musters Lake basin. But in fact this capture may also

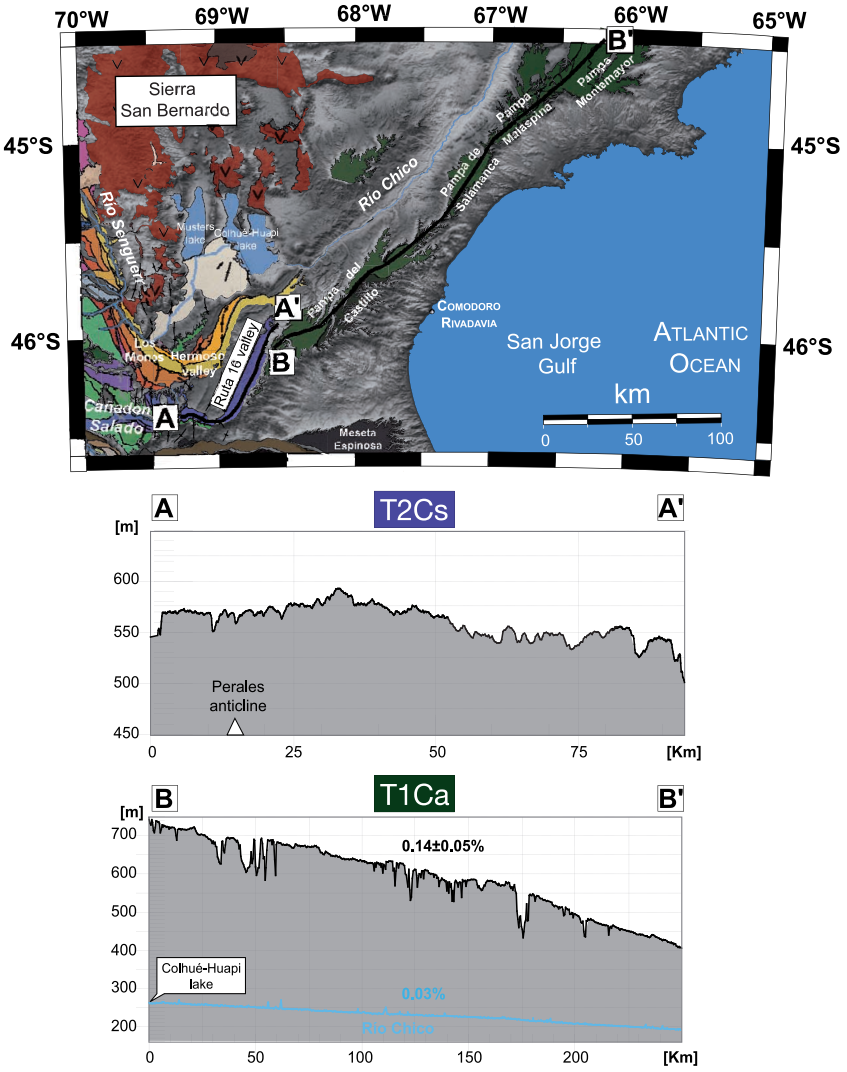

Figure 8

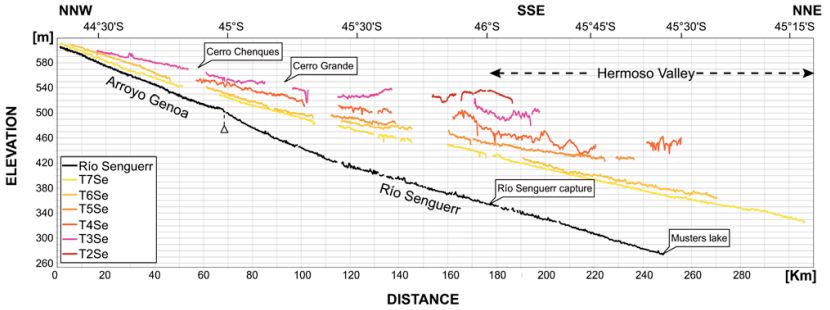

Figure 9. Topographic longitudinal profiles of the fluvial terraces of the Río Senguerr system.

have been triggered by the northward tilt of this region, as it has done for the capture of the Cañadon Salado by the Hermoso valley (Figure 4). Moreover, this capture having occurred following the formation of T7Se, it cannot explain the smaller longitudinal slopes of older terraces compared to that of T7Se. These captures would argue for a continuation of the northward tilt until recent times since the capture of the Río Senguerr postdates the deposition of the next to last terrace of the Río Senguerr fluvial system.

3.5. Synthesis of N-S Tilts Deduced From the Analysis of the Present-Day Slopes of Terraces

[32] Regions located north and south of the current CTJ position had different tilting histories from the late Miocene. In the northern area, the trench-parallel tilting is permanently northward directed and may have pursued until recent times. Absolute values of tilting are difficult to constrain since the course of the main valleys is almost parallel to the direction of tilting, the present-day slope of these terraces resulting both from tilting and from the process of terrace formation. Nevertheless, in the Río Senguerr fluvial system, if we consider that all terraces share a common upstream elevation at a latitude of 44°20′S (see Figure 9), the values of tilt can be approximated measuring the difference in elevation between the terraces at the latitude of the elbow of capture (46°S). We obtain values ranging between ~0.01 and 0.02% between successive terraces and the cumulative northward tilt between T2Se and T7Se would be ~0.06%. Present-day different slopes of the upstream and downstream segments of the older terrace T2Cs suggest a cumulative tilt of 0.12 ± 0.04% since its formation.

[33] In contrast, south of the CTJ, before 5.28 Ma, the area recorded a minimum northward tilt of 0.06 ± 0.02% (difference of N-S slope between T1De and T2De), that has been followed by a cumulative southward tilt of 0.11 ± 0.01% between T2De and T8De. Since the transition between the late Miocene and the Pliocene (T8De), southward tilting is not anymore recorded by the terraces of the Río Deseado.

[34] Both northward and southward tilts, north and south of the CTJ, resulted in captures that explain the present-day diverging pattern of the hydrographic network east of the Sierra San Bernardo and Deseado massif.

4. Possible Causes for the Post-Middle Miocene Uplift of Central Eastern Patagonia

[35] The analysis of the geological and morphological evolution of central Patagonia, east of the Andean front during the Neogene, shows a major shift from subsidence marked by the accumulation of the Santa Cruz Formation, followed by a regional uplift contemporaneous with the deposition of the piedmont mantle cover and fluvial terraces. The Oligo-Miocene transgression starts when the convergence between the Nazca and South American plates becomes more orthogonal to the margin, and is coeval to the major episode of shortening in central Patagonian Andes.

[36] Sedimentation of the Oligo-Miocene marine strata, followed by the deposition of the early to middle Miocene molasse east of the Andean front, could partly result from the flexural subsidence of the foreland induced by the growth of the chain at that time. Fission tracks data [*Thomson et al.*, 2001], indeed show that denudation accelerates in the western part of the mountain chain at that latitude in the Oligocene, which suggests that the Andes where uplifting close to the Pacific coast. We interpret the sedimentary record of the basin and especially the deposition of the Santa Cruz Formation and its equivalents, with a maximum depocenter

Figure 8. Topographic longitudinal profiles of Cañadon Salado–Cañadon del Carril terrace T2Cs (AA′) and Pampa del Castillo piedmont mantle cover level T1Ca (BB′). See map for location and Figure 3 for color legend. The present-day longitudinal slope of T2Cs depends on the orientation of the valley, suggesting that regional tilt occurred following the formation of T2Cs. The position of the Perales anticline axis is indicated by a white triangle on the profile AA′.

located close to the Cordillera foothills, as a result of the overfilling of a subsiding basin. Although the subsidence of this basin may result from the flexural response of the continental lithosphere to the growth of the Cordillera, it may also have been enhanced by the dynamic deflection of the lithosphere generated by the increasing velocity of the subduction of the Nazca slab [*Gurnis*, 1993] (see discussion below).

[37] The end of the deposition of the Santa Cruz continental series corresponds to drastic changes in the paleogeography of Patagonia. The end of early Miocene is marked by an increased aridity of the eastern side of southern Andes [*Bellosi*, 1999; *Blisniuk et al.*, 2005]. This climatic change essentially results from rain shadow phenomenon, the Cordillera being high enough to become a barrier to atmospheric circulation [*Blisniuk et al.*, 2005]. Blisniuk et al., in turn, suggest that the end of the deposition of the Santa Cruz Formation 14 Ma ago would also result from the increased aridity of the Patagonian foreland. Our data suggest that the main cause for the end of sedimentation is the uplift of the foreland. As a matter of fact, although Patagonia east of the Andes has been arid enough to preserve the fluvial terrace systems described in this paper since the late Miocene, the widespread occurrence of vast terraces covered by decimeter-scale pebbles covering the entire zone from the Andes to the Atlantic Ocean indicates that powerful streams episodically flowed from the Cordillera. These streams would certainly have brought sediments to the basin in case its subsidence would have pursued more recently than middle Miocene.

[38] Then, the question is to understand why the uplift of the Andes, controlling from the middle Miocene the semi-arid climate of eastern Patagonia, has been rapidly followed by the slow uplift of its foreland. Uplift of central eastern Patagonia correlates with a period of colder climate, culminating with the formation of an ice cap above the Andes. The long-term increasing ice load from the upper Miocene should have triggered subsidence of the Andean foreland, contrary to the observed uplift. In contrast, foreland uplift may have resulted from a decreasing load of the Cordillera, possibly enhanced by glacial erosion. We show below that flexural foreland rebound cannot explain the large dimension of the uplifted area. In contrast, dynamic topography resulting from the opening of the asthenospheric window may explain the continental-scale observed uplift.

4.1. Flexural Response of the Lithospheric Plate

[39] The growth of southern Andes in the Oligo-Miocene resulted from crustal shortening, which, in turn, triggered subsidence in the foreland and deposition of the Santa Cruz molasse [e.g., *Ramos*, 1989; *Alvarez-Marrón et al.*, 1993; *Thomson et al.*, 2001; *Kraemer et al.*, 2002; *Lagabrielle et al.*, 2004; *Ramos*, 2005]. Then, the subsequent uplift of the foreland may have resulted from the diminution of the Andean load above the continental plate. As a matter of fact, crustal shortening has been very small in the Patagonian Andes since middle Miocene [*Ramos*, 1989; *Coutand et al.*, 1999; *Lagabrielle et al.*, 2004, 2007]. Moreover, the very humid climatic conditions on the western side of the chain that has been enhanced by its uplift, and the development of Neogene glaciations may have increased the rapid erosion of the Pacific side of the continent and central part of the Cordillera. The flexural response of these accelerated erosion processes would favor uplift of the eastern foreland.

[40] The elastic thickness of the Patagonian continental lithosphere has been estimated between about 20 km and 30 km by *Tassara et al.* [2007] at the CTJ latitude using gravity data. Using standard elastic parameters [e.g., *Turcotte and Schubert*, 1982], the distance between the chain and the forebulge would range between 150 and 210 km. Flexural parameters of the continental plate are also evidenced by the distribution of the Santa Cruz continental deposits, which are restricted to the western part of the Patagonian foreland, less than 250 km from the Andes. In turn, the flexural uplift of the foreland resulting from the diminution of the Andean load should be restricted to a narrow area close to the chain, and should not affect the distal zones close to the Atlantic coast, ~500 km away from the present-day Cordillera.

4.2. Dynamic Topography

[41] Dynamic topography on Earth is the deflection of the surface in response to the viscous flow that occurs in the convecting underlying mantle. Over subduction zones, it may result in long-wavelength downward deflections of the overriding topographic surface exceeding 1000 m [*Mitrovica et al.*, 1989; *Gurnis*, 1993; *Zhong and Gurnis*, 1994; *Husson*, 2006]. The northward migration of the CTJ from middle Miocene lead to the opening of an asthenospheric window below southern Patagonia. South of 46°30′S, the Antarctic oceanic plate is now slowly subducting below the continent. The corresponding slab is short. A recent slab window reconstruction shows that the Antarctic slab should not have reached depths greater than 45 km [*Breitsprecher and Thorkelson*, 2008]. Thus, the dynamic effect of that subduction on the overriding continent is virtually absent. North of the CTJ, in contrast, the Nazca plate subducts rapidly, which in turn deflects the continental plate downward. We propose that this downward deflection has been progressively canceled in southern Patagonia as the CTJ was migrating northward, resulting in the uplift of that part of the continent. The free air anomaly is positive north of the CTJ (40 mGal) while it is neutral to slightly negative south of it; this observation outlines the departure of topography from an isostatic situation north of the CTJ and the fact that the dynamic deflection vanishes south of it.

[42] We computed the dynamic deflection induced by a slab subducting within the upper mantle with a dip angle of 37°, using a simple 3-D Newtonian model based on the Stokeslet approximation [*Morgan*, 1965; *Batchelor*, 1967; *Harper*, 1984; *Husson*, 2006]. A subducting slab of finite width is discretized into elementary spheres, or "Stokeslet," for which an analytical flow solution exists. Each point mass i induces an elementary spherical flow (Stokeslet) for which the Stokes stream function is known and can be written $\Psi_i = (\Delta\rho v_i g/8\pi\eta) r_{ij} \sin^2 \theta_{ij}$, where $\Delta\rho v_i$ is the mass anomaly associated with each point mass, g is the gravitational acceleration, η is the viscosity, r_{ij} is the distance from each point mass to the observation point j, and θ_{ij} is the angle between the vector ij and the direction of g. The normal

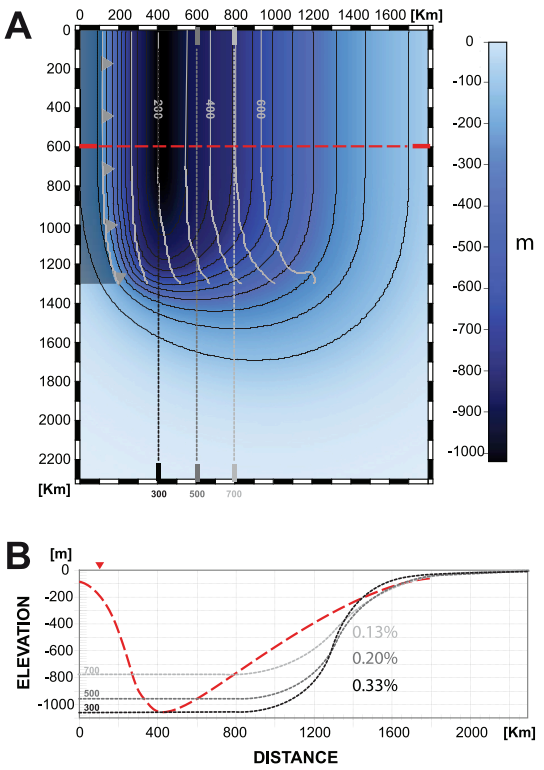

Figure 10. (a) Topographic deflections induced by the subduction of a semi-infinite, 50-km-thick negatively buoyant slab ($\Delta\rho = -80$ kg m^{-3}, steady state slab dip of 37°). Black solid lines are isodepth contours of topographic deflection and gray solid lines show the depth of the subducting slab (in km). The gray solid line with triangles indicates the position of the trench. (b) Topographic profiles of the dynamic topography, in the direction parallel to the trench, at a distance of 300 km (black dotted line), 500 km (dark gray dotted line), and 700 km (light gray dotted line) from the trench, and in the direction perpendicular to the trench (dashed line), with the corresponding trench-parallel slopes indicated on the right. Profiles are positioned on Figure 10a, and the location of the trench is indicated by a triangle.

stress on the upper free surface of a half-space can be calculated using the image technique [*Morgan*, 1965]. It writes $Fzz_{ij} = 3\Delta\rho v_i g z_i^3/\pi r_{ij}^5$, where z_i is the depth of the point mass body beneath the surface. Because inertial terms are negligible, stress does not depend on viscosity. If the surface is stress free, then there will instead be a deflection of the surface by a distance h_{ij}, such that $h_{ij} = Fzz_{ij}/\rho_m g$. The total Stokes flow is given by the sum of the Stokeslets; in aerial domains the total surface deflection H_j will be the sum of the deflections resulting from each point mass; hence,

$$H_j = \sum_i \frac{3\Delta\rho v_i z_i^3}{\pi r_{ij}^5 \rho_m}, \quad (1)$$

where ρ_m denotes the density of the mantle.

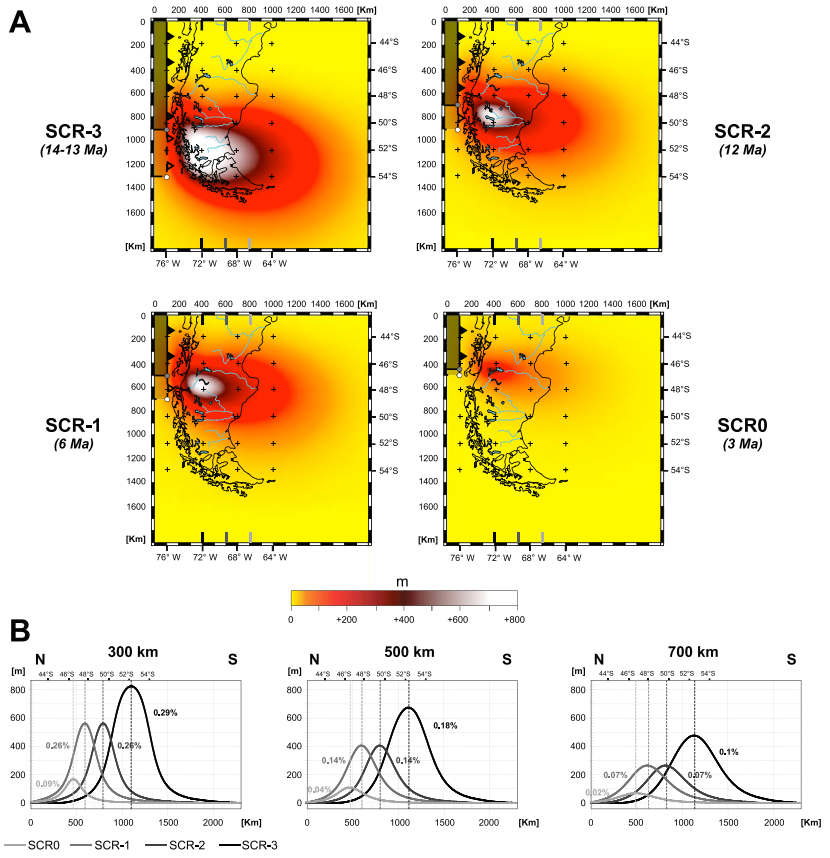

Figure 11. (a) Map of the uplift of the overriding plate resulting from the episodic subduction of 4 ridge segments below South America accompanying the northward migration of the CTJ. White and gray dots mark the position of the CTJ before and after the subduction of each ridge segment, respectively. (b) Topographic profiles parallel to the trench direction at 300 km, 500 km, and 700 km from the trench for each triple junction migration increment. The boundary between regions of northward and southward tilt for each longitudinal profile (dotted lines) shifts toward the north, delineating sectors with different tilt history.

[43] Deflections have been calculated for a 50-km-thick slab with a negative buoyancy of −80 kg m^{-3}. We assume that the deflection, south of the triple junction, is null. This is supported by the fact that the Antarctic slab currently reaches depths smaller than 45 km [*Breitsprecher and Thorkelson*, 2008]. Conversely, the dynamic effect of the trailing edge of the Nazca slab south of the CTJ should not be negligible but is difficult to quantify since it depends on many poorly constrained parameters like the slab geometry, the convergence velocity, the rheological stratification of the

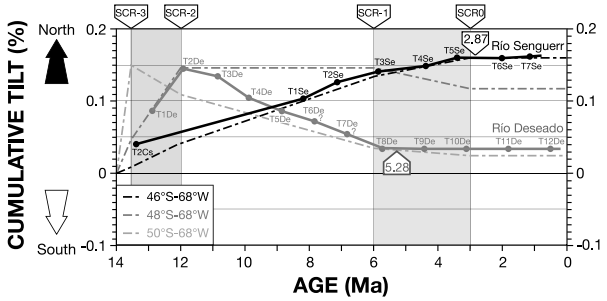

Figure 12. Modeled versus observed tilts in the central eastern Patagonia during the last 14 Ma. Dash-dotted lines indicate the predicted cumulative tilt at 46°S–68°W (black), 48°S–68°W (dark gray), and 50°S–68°W (light gray). The corresponding observed cumulative tilts observed in terraces south (Río Deseado), and north of the CTJ (Río Senguerr and Cañadon Salado) are indicated by light gray and black solid lines, respectively. Note that the ages of terraces are not known. We only know their stratigraphic position with respect to 5.28 Ma old basalts in the Río Deseado fluvial system [*Gorring et al.*, 1997], and 2.87 Ma old basalts in the Río Senguerr fluvial system [*Bruni*, 2007].

upper mantle, thermal erosion of the slab edge. Anyway, its effect would only introduce a delay between ridge subduction at trench, and dynamic uplift. A first-order approximation of this delay can be evaluated calculating the time necessary for the horizontal projection of the trailing edge of the slab to reach an horizontal distance greater than that of the central Patagonian basin (∼5 Ma).

[44] Analytical calculations predict that vertical deflections appear as far as 1600 km from the trench and reach a maximum value close to 1000 m at a distance of ∼325 km from the trench. The maximum N-S trending surface slope at a distance of 300, 500, and 700 km from the trench is ∼0.33%, 0.2%, and 0.13%, respectively (Figure 10). The amplitude of the deflection varies when parameters (thickness, buoyancy, and dip of the slab) are changed but the general observed pattern is maintained.

[45] The CTJ abruptly migrates northward when ridge segments enter the subduction zone. From middle Miocene, several ridge segments subducted below the southern Andes (Figure 1). We model the dynamic response of the subduction of four ridge segments with lengths of 400, 200, 200, and 50 km that correspond to the lengths of SCR-3, SCR-2, SCR-1, and SCR0 (South Chile Ridge segments), respectively. These segments subducted beneath South America 13.5, 12, 6, and 3 Ma ago, respectively [*Cande and Leslie*, 1986; *Gorring et al.*, 1997]. Figure 11a is a map view of surface uplift resulting from the subduction of each ridge segment, subsequent quasi cessation of the subduction and induced dynamic deflection. Figure 11b presents the corresponding uplift along three trench-parallel profiles located 300, 500, and 700 km from the trench. Uplift is maximum in front of each subducted ridge segment, resulting in northward tilt north of the segment and southward tilt south of it. Southern Patagonia can be divided into four domains. The first domain, located to the north, experienced a constant northward tilt during the whole migration of the triple junction. The three other domains first tilted northward and then southward as the CTJ was migrating to the north.

4.3. Discussion

[46] The calculations presented above show that dynamic topography resulting from subduction may result in significant long-wavelength deflections of the lithospheric plate, far enough from the trench to affect the entire width of Patagonia. At the end of Oligocene, the increase of trench-perpendicular convergence velocity between the Farallon-Nazca plate and South America may have resulted in a larger downward deflection of the continental plate, which would explain part of the Oligo-Miocene Patagonian transgression.

[47] Following the deposition of the Miocene continental molasse, the entire continental plate uplifted, resulting in the appearance of continental-scale terraces. Available ages on basalts covering terraces [*Gorring et al.*, 1997; *Bruni*, 2007] show that the older terraces are middle-late Miocene, and that only the lower terraces of the Río Senguerr and Río Deseado fluvial systems are Pliocene to Pleistocene. The present-day topography of these ancient terraces underlines periods of northward and southward tilt in the foreland of the Patagonian Andes. South of 46°30′S, terraces of the Río Deseado system evidence a former 0.06% northward tilt event (0.11% minus 0.05%) that occurred before the deposition of T2De, and partly following the deposition of T1De, followed by a 0.11% southward tilt that followed the deposition of T2De and ended before the deposition of T8De, i.e., before 5.28 Ma. Just to the north of 46°30′S (Cañadon Salado and Río Senguerr terrace systems), the oldest surfaces are tilted toward the north, and the northward tilt recorded by the youngest terraces of the Río Senguerr fluvial

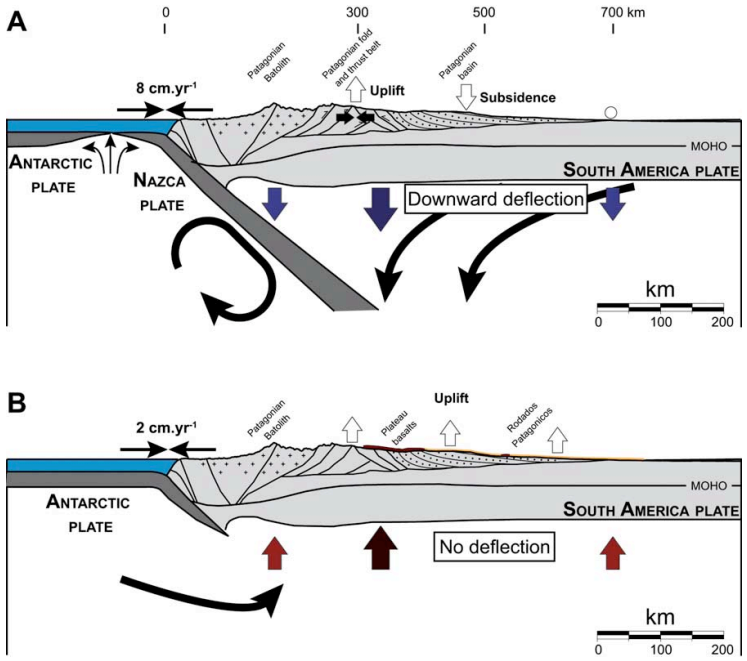

Figure 13. Cartoons illustrating the geodynamic setting south of the Chile Triple Junction. (a) Before the subduction of the Chile ridge, the Nazca slab subduction induces mantle flow that causes a downward deflection of the overlying Patagonian lithosphere. The rapid convergence rate is responsible for the emplacement of the eastern Patagonian fold and thrust belt and associated subsiding flexural basin. (b) After the subduction of the Chile ridge, the opening of the asthenospheric window cancels the downward mantle motion that deflected the South American plate, resulting in the uplift of the continent at that time.

system indicates that the tilt continued after the deposition of the Cerro Grande basalts, 2.87 Ma ago.

[48] This general pattern of tilt basically reproduces the predicted vertical movements from dynamic topography modeling (Figure 12) that accommodate the northward migration of the CTJ: south of the CTJ, our model predicts that the uplift is accommodated by northward tilt followed by southward tilt, and north of the CTJ, only northward tilt should occur. Moreover, observed tilt values are approximately 0.1% at the longitude of the Atlantic coast, which corresponds to the range of values predicted by the semi-analytical models.

[49] However, model results suggest that southward tilt of the region located between 46°30′S and 48°S would occur following the final step of migration of the CTJ that resulted from the subduction of the SCR0 ridge segment, 3 Ma ago. Moreover, as discussed above, our simple analytical model does not integrate the effect of the trailing edge of the Nazca slab at depth, south of the triple junction, which should introduce a delay between ridge subduction and the corresponding dynamic response. Ages of the Río Deseado fluvial system, in contrast, suggest that the southward tilt occurred in the Miocene, before the deposition of the 5.28 Ma old Cerro Negro basalts. This discrepancy outlines the limitation of our simple analytical analysis in explaining the timing and/or location of observed tilt. In the semianalytical model presented above, dynamic deflections are computed for a slab having an uniform buoyancy while the Nazca slab is in fact younger and therefore less negatively buoyant next to the CTJ. Thus, taking precisely into account the age structure of the subducting slab would subsequently shift the maximum deflection northward with respect to

model results (Figure 11) and southward tilt would occur earlier.

[50] Another possibility is that the migration of the CTJ has been preceded by a slab break-off, resulting in the opening of an asthenospheric window before the subduction of the last ridge segments, as already proposed by *Guivel et al.* [2006] to explain the occurrence of back-arc basalts older than the subduction of the ridge segments located at their latitude. Although the model could easily be adapted accordingly, such improvements would remain beyond the resolution of the model itself.

[51] *Ramos* [1989, 2005], *Ramos and Kay* [1992], and *Lagabrielle et al.* [2007] point out a striking difference in the elevation of the highest peaks of the Cordillera, they relate with the opening of the slab window beneath the continent. North of the CTJ, highest Cordillera peaks do not exceed 2500 m, whereas south of the CTJ, numerous peaks exceed 3000 m. Although larger amounts of uplift (>1000m) are indeed expected close to the Andes according to the analytical model, the signal is more difficult to decipher because of the tectonic activity, large erosion rates and the isostatic rebound related to episodic melting of late Miocene to Quaternary glaciers that make any attempt to extract a reference level dubious.

5. Conclusions

[52] The major Oligo-Miocene transgression that occurred in the southern Patagonia results both from shortening of the Cordillera and larger downward dynamic deflection of the continental plate resulting from the increase of the trench-perpendicular convergence velocity between the subducting and overriding plates (Figure 13). The Santa Cruz Formation deposited in the overfilled subsiding Patagonian basin. The middle Miocene time is characterized by a switch from subsidence to uplift of the Andean foreland. Terraces overlaid by coarse fluvial series are found across the entire continent, from the Andes to the Atlantic Ocean. They mark a generalized uplift of the continental plate that started in the middle-late Miocene when the overall subduction dynamics changed. Although part of this uplift, close from the Andes, could possibly result to some extent from the flexural response of the continental lithosphere to the erosion of the chain and subsequent unloading, dynamic topography resulting from mantle–lithosphere interaction is necessary to explain uplift occurring on larger wavelengths, from the Andes to the Atlantic coast. The episodic northward migration of the Chile Ridge Triple Junction, resulting in the opening of a slab window below southern Patagonia, cancels the dynamic downward deflection of the continental plate above the subduction zone and induces the uplift (or better said the cessation of the dynamic defection) of the overriding plate (Figure 13). The uplift resulting from the dynamic response of the continental lithosphere to subduction explains the diverging present-day pattern of the hydrographic network at the latitude of the CTJ, the region located north of the CTJ being tilted northward while the region located to the south tilts toward the south. The comparison between the model and the observations show that both the occurrence of the Patagonian basin and its evolution are of dynamic origin.

[53] **Acknowledgments.** This research was supported by the French CNRS-INSU "Reliefs de la Terre" program. The authors thank Serge Lallemand and two anonymous reviewers for a complete and detailed review of a previous version of this paper. They thank IRD (Institut de la Recherche pour le Développement) for help in organizing the field work and Silvia Espinach (Universidad de Buenos Aires) for field assistance. This work benefited from fruitful discussions with R. Giacosa (Universidad de Comodoro Rivadavia) and Ernesto Cristallini (Universidad de Buenos Aires).

References

Airy, G. B. (1855), On the computation of the effect of the attraction of mountain-masses as disturbing the apparent astronomical latitude of stations in geodetic surveys, *Philos. Trans. R. Soc. London, 145*, 101–104, doi:10.1098/rstl.1855.0003.

Alvarez-Marrón, J., K. R. McClay, S. Harambour, L. Rojas, and J. Skarmeta (1993), Geometry and evolution of the frontal part of the Magallanes foreland thrust and fold belt (Vicuña area), Tierra del Fuego, southern Chile, *AAPG Bull., 77*, 1904–1921.

Ardolino, A., J. L. Panza, and E. Yllañez (2003), Hoja Geológica 4566-I Garayalde, provincia del Chubut, scale , 1:250000, Serv. Geol. Minero Argent., Buenos Aires.

Batchelor, G. (1967), *An Introduction to Fluid Mechanisms*, 615 pp., Cambridge Univ. Press, Cambridge, U. K.

Barat, C., J. S. Cortiñas, V. A. Nevistic, and H. E. Zucchi (1989), Cuenca del Golfo San Jorge, in *Cuencas Sedimentarias Argentinas, Ser. Correl. Geol.*, vol. 6, edited by G. Chebli and L. Spaletti, pp. 319–345, Univ. Nac. de Tucumán, Tucumán, Argentina.

Barreda, D. V., and I. Caccavari (1992), Mimosoideae (Leguminosae) occurrences in the early Miocene of Patagonia (Argentina), *Palaeogeogr. Palaeoclimatol. Palaeoecol., 94*, 243–252, doi:10.1016/0031-0182(92)90121-K.

Bellosi, E. S. (1996), Fabrica de los "rodados patagónicos" y paleocorrientes: Comentario y replica, *Asoc. Geol. Argent. Rev., 51*(1), 87–89.

Bellosi, E. S. (1999), El Cambio climático-ambiental de la Patagonia en el Mioceno temprano-Medio, paper presented at 14th Congreso Geológico Argentino, Asoc. Geol. Argent., Salta, Argentina.

Bellosi, E. S., and D. V. Barreda (1993), Secuencias y Palinología del Terciario medio en la cuenca San Jorge, registro de oscilaciones eustáticas en Patagonia, paper presented at 12th Congreso Geológico Argentino and 2nd Congreso Exploración de Hidrocarburos, Asoc. Geol. Argent., Mendoza, Argentina.

Beltramone, C., and C. M. Meister (1992), Paleocorrientes de los Rodados Patagónicos, tramo Comodoro Rivadavia—Trelew, *Asoc. Geol. Argent. Rev., 47*(2), 147–152.

Bianchi, J. L. (1981), Cuenca del Golfo San Jorge. Su genesis e interconexiones, *Petrotecnia, Agosto 1981*, 27–35.

Blisniuk, P. M., L. B. Stern, C. P. Chamberlain, B. Idleman, and P. K. Zeitler (2005), Climatic and ecologic changes during Miocene surface uplift in the southern Patagonian Andes, *Earth Planet. Sci. Lett., 230*, 125–142, doi:10.1016/j.epsl.2004.11.015.

Breitsprecher, K., and D. J. Thorkelson (2008), Neogene kinematic history of Nazca-Antarctic-Phoenix slab windows beneath Patagonia and the Antarctic Peninsula, *Tectonophysics, 464*, 10–20, doi:10.1016/j.tecto.2008.02.013.

Bruni, S. (2007), The Cenozoic back-arc magmatism of central Patagonia (44°–46°S): Activation of different mantle domains in space and time, Ph.D. thesis, 159 pp., Univ. di Pisa, Pisa, Italy.

Čadek, O., and L. Fleitout (2003), Effect of lateral viscosity variations in the top 300 km on the geoid and dynamic topography, *Geophys. J. Int., 152*, 566–580, doi:10.1046/j.1365-246X.2003.01859.x.

Cande, S., and R. B. Leslie (1986), Late Cenozoic tectonics of the southern Chile Trench, *J. Geophys. Res., 91*, 471–496, doi:10.1029/JB091iB01p00471.

Catuneanu, O., C. Beaumont, and P. Waschbusch (1997), Interplay of static loads and subduction dynamics in foreland basins: Reciprocal stratigraphies and the "missing" peripheral bulge, *Geology, 25*(12), 1087–1090, doi:10.1130/0091-7613(1997025<1087:IOSLAS>2.3.CO;2.

Cembrano, J., A. Lavenu, P. Reynolds, G. Arancibia, G. López, and A. Sanhueza (2002), Late Cenozoic transpressional ductile deformation north of the Nazca-South America-Antarctica triple junction, *Tectonophysics, 354*, 289–314, doi:10.1016/S0040-1951(02)00388-8.

Chelotti, L. (1997), Evolución tectónica de la Cuenca del Golfo San Jorge en el Cretácico y Terciario: Algunas observaciones desde la interpretación sísmica, *Bol. Inf. Petrol., 49*, 62–82.

Cobos, J. C., and J. L. Panza (2001), Hoja Geológica 4769-III El Pluma, provincia de Santa Cruz, scale, 1:250000, Serv. Geol. Minero Argent., Buenos Aires.

Coutand, I., M. Diraison, P. R. Cobbold, D. Gapais, E. A. Rossello, and M. Miller (1999), Structure

and kinematics of a foothills transect, Lago Viedma, southern Andes (49°30S), *J. South Am. Earth Sci.*, *12*, 1–15, doi:10.1016/S0895-9811(99)00002-4.

Dal Molin, C., M. Márquez, and B. Maisonabe (1998), Hoja Geológica 4571-IV Alto Río Senguerr, provincia del Chubut, scale, 1:250000, Serv. Geol. Minero Argent., Buenos Aires.

De la Cruz, R., and M. Suárez (2006), Geología del área Puerto Guadal-Puerto Sánchez, Región Aisén del General Carlos Ibañez del Campo, in *Carta Geológica de Chile, Ser. Geol. Básica*, vol. 95, 58 pp., scale, 1:100000, Serv. Nac. de Geol. y Minería, Santiago, Chile.

De Mets, C., R. C. Gordon, D. F. Argus, and S. Stein (1994), Effect of recent revisions to the geomagnetic reversal time scale on estimates of current plate motions, *Geophys. Res. Lett.*, *21*, 2191–2194, doi:10.1029/94GL02118.

D'Orazio, M., S. Agostini, F. Mazzarini, F. Innocenti, P. Manetti, M. J. Haller, and A. Lahsen (2000), The Pali Aike Volcanic Field, Patagonia: Slab-window magmatism near the tip of South America, *Tectonophysics*, *321*, 407–427, doi:10.1016/S0040-1951(00)00082-2.

D'Orazio, M., S. Agostini, F. Innocenti, M. J. Haller, P. Manetti, and F. Mazzarini (2001), Slab window-related magmatism from southernmost South America: The late Miocene mafic volcanics from the Estancia Glencross area (~52°S, Argentina-Chile), *Lithos*, *57*, 67–89, doi:10.1016/S0024-4937(01)00040-8.

D'Orazio, M., F. Innocenti, P. Manetti, M. Tamponi, S. Tonarini, O. González-Ferrán, A. Lahsen, and R. Omarini (2003), The Quaternary calc-alkaline volcanism of the Patagonian Andes close to the triple junction: Geochemistry and petrogenesis of volcanic rocks from the Cay and Maca volcanoes (~45°S, Chile), *J. South Am. Earth Sci.*, *16*, 219–242, doi:10.1016/S0895-9811(03)00063-4.

D'Orazio, M., F. Innocenti, P. Manetti, M. J. Haller, G. Di Vicenzo, and S. Tonarini (2005), The late Pliocene mafic lavas from the Camusú Aike Volcanic Field (~50°S, Argentina): Evidences for geochemical variability in slab window magmatism, *J. South Am. Earth Sci.*, *18*, 107–124, doi:10.1016/j.jsames.2004.10.001.

Escosteguy, L., C. Dal Molin, M. Franchi, S. Geuna, and O. Lapido (2003), Hoja Geológica 4772-II Lago Buenos Aires, provincia de Santa Cruz, scale , 1:250000, Serv. Geol. Minero Argent., Buenos Aires.

Espinoza, F., et al. (2005), Petrogenesis of the Eocene and Mio-Pliocene alkaline basaltic magmatism in Meseta Chile Chico, southern Patagonia, Chile: Evidence for the participation of two slab windows, *Lithos*, *82*, 315–343, doi:10.1016/j.lithos.2004.09.024.

Feruglio, E. (1950), *Descripción Geológica de la Patagonia*, vol. III, Yacimientos Petrol. Fis., Buenos Aires, Argentina.

Flint, S. S., D. J. Prior, S. M. Agar, and P. Turner (1994), Stratigraphic and structural evolution of the Tertiary Cosmelli Basin and its relationship to the Chile Triple Junction, *J. Geol. Soc.*, *151*, 251–268, doi:10.1144/gsjgs.151.2.0251.

Flynn, J. J., M. J. Novacek, H. E. Dodson, D. Frassinetti, M. C. McKenna, M. A. Norell, K. E. Sears, C. C. Swisher, III, and A. R. Wyss (2002), A new fossil mammal assemblage from the southern Chilean Andes: Implications for geology, geochronology, and tectonics, *J. South Am. Earth Sci.*, *15*, 285–302, doi:10.1016/S0895-9811(02)00043-3.

Frassinetti, D., and V. Covacevich (1999), Fauna de invertebrados fósiles marinos de la Formación Guadal en Pampa Castillo, sur del Lago General Carrera, Aisén, Chile, *Bol. Serv. Nac. Geol. Minería*, *51*, 1–96.

Froidevaux, C., and B. L. Isacks (1984), The mechanical state of the lithosphere in the Altiplano-Puna segment of the Andes, *Earth Planet. Sci. Lett.*, *71*, 305–314, doi:10.1016/0012-821X(84)90095-5.

Garzione, C. M., P. Molnar, J. C. Libarkin, and B. J. Mac Fadden (2006), Rapid late Miocene rise of the Bolivian Altiplano: Evidence for removal of mantle lithosphere, *Earth Planet. Sci. Lett.*, *241*, 543–556, doi:10.1016/j.epsl.2005.11.026.

Giacosa, R. (1998), Hoja Geológica 4766-III/IV Puerto Deseado, Provincia de Santa Cruz, scale , 1:250000, Serv. Geol. Minero Argent., Buenos Aires.

Gorring, M. L., and S. M. Kay (2001), Mantle processes and sources of Neogene slab window magmas from southern Patagonia, Argentina, *J. Petrol.*, *42*(6), 1067–1094, doi:10.1093/petrology/42.6.1067.

Gorring, M. L., S. M. Kay, P. K. Zeitler, V. A. Ramos, D. Rubiolo, M. I. Fernandez, and J. L. Panza (1997), Neogene Patagonian plateau lavas: Continental magmas associated with ridge collision at the Chile Triple Junction, *Tectonics*, *16*, 1–17, doi:10.1029/96TC03368.

Gorring, M. L., B. Singer, J. Gowers, and S. M. Kay (2003), Plio-Pleistocene basalts from the Meseta del Lago Buenos Aires, Argentina: Evidence for asthenosphere-lithosphere interactions during slab window magmatism, *Chem. Geol.*, *193*, 215–235, doi:10.1016/S0009-2541(02)00249-8.

Guivel, C., Y. Lagabrielle, J. Bourgois, H. Martin, N. Arnaud, S. Fourcade, J. Cotten, and R. Maury (2003), Very shallow melting of oceanic crust during spreading ridge subduction: Origin of near-trench Quaternary volcanism at the Chile Triple Junction, *J. Geophys. Res.*, *108*(B7), 2345, doi:10.1029/2002JB002219.

Guivel, C., et al. (2006), Miocene to Late Quaternary Patagonian basalts (46–47°S): Geochronometric and geochemical evidence for slab tearing due to active spreading ridge subduction, *J. Volcanol. Geotherm. Res.*, *149*, 346–370, doi:10.1016/j.jvolgeores.2005.09.002.

Gurnis, M. (1993), Phanerozoic marine inundation of continents driven by dynamic topography above subducting slabs, *Nature*, *364*, 589–593, doi:10.1038/364589a0.

Hager, B. H., and R. W. Clayton (1989), Constraints on the structure of mantle convection using seismic observations, flow models and the geoid, in *Mantle Convection*, edited by W. R. Peltier, pp. 657–763, Gordon and Breach, New York.

Haq, B. U., J. Hardenbol, and P. R. Vail (1987), Chronology of fluctuating sea levels since the Triassic (250 millions years ago to present), *Science*, *235*, 1156–1167, doi:10.1126/science.235.4793.1156.

Harper, J. F. (1984), Mantle flow due to internal vertical forces, *Phys. Earth Planet. Inter.*, *36*, 285–290, doi:10.1016/0031-9201(84)90052-9.

Homovc, J. F., G. A. Conforto, P. A. Lafourcade, and L. A. Chelotti (1995), Fold belt in the San Jorge Basin, Argentina: An example of tectonic inversion, in *Basin Inversion*, edited by J. G. Buchanan and P. G. Buchanan, *Geol. Soc. Spec. Publ.*, vol. 88, pp. 235–248.

Husson, L. (2006), Dynamic topography above retreating subduction zones, *Geology*, *34*(9), 741–744, doi:10.1130/G22436.1.

Kay, S. M., V. A. Ramos, and M. Marquez (1993), Evidence in Cerro Pampa volcanic rocks for slab-melting prior to ridge-trench collision in southern South America, *J. Geol.*, *101*, 703–714.

Kraemer, P. E. (1998), Structure of the Patagonian Andes: Regional balanced cross section at 50°S, Argentina, *Int. Geol. Rev.*, *40*, 896–915.

Kraemer, P. E., J. V. Ploszkiewicz, and V. A. Ramos (2002), Estructura de la Cordillera Patagónica Austral entre los 46° y 52°S, provincia de Santa Cruz, Argentina, paper presented at the 15th Congreso Geológico Argentino, Asoc. Geol. Argent., El Calafate, Argentina.

Lagabrielle, Y., M. Suárez, E. A. Rossello, G. Hérail, J. Martinod, M. Régnier, and R. De la Cruz (2004), Neogene to Quaternary evolution of the Patagonian Andes at the latitude of the Chile Triple Junction, *Tectonophysics*, *385*, 211–241, doi:10.1016/j.tecto.2004.04.023.

Lagabrielle, Y., et al. (2007), Pliocene extensional tectonics in the eastern central Patagonian Cordillera: Geochronological constraints and new field evidence, *Terra Nova*, *19*, 413–424, doi:10.1111/j.1365-3121.2007.00766.x.

Lange, D., J. Cembrano, A. Rietbrock, C. Haberland, T. Dahm, and K. Bataille (2008), First seismic record for intra-arc strike-slip tectonics along the Liquiñe-Ofqui fault zone at the obliquely convergent plate margin of the southern Andes, *Tectonophysics*, *455*, 14–24, doi:10.1016/j.tecto.2008.04.014.

Lavenu, A., and J. Cembrano (1999), Compresional- and transpressional-stress pattern for Pliocene and Quaternary brittle deformation in fore arc and intra-arc zones (Andes of central and southern Chile), *J. Struct. Geol.*, *21*, 1669–1691, doi:10.1016/S0191-8141(99)00111-X.

Le Stunff, Y., and Y. Ricard (1997), Partial advection of equidensity surfaces: A solution for the dynamic topography problem?, *J. Geophys. Res.*, *102*, 24,655–24,667, doi:10.1029/97JB02346.

Lock, J., H. Kelsey, K. Furlong, and A. Woolace (2006), Late Neogene and Quaternary landscape evolution of the northern California Coast Ranges: Evidence for Mendocino triple junction tectonics, *Geol. Soc. Am. Bull.*, *118*(9–10), 1232–1246, doi:10.1130/B25885.1.

Lonsdale, P. (2005), Creation of the Cocos and Nazca plates by the fission of the Farallon plate, *Tectonophysics*, *404*, 237–264, doi:10.1016/j.tecto.2005.05.011.

Malumián, N. (1999), La sedimentación y el volcanismo terciarios en la Patagonia extraandina, in *Geología Argentina*, edited by R. Caminos, *Inst. Geol. Recursos Miner. An.*, vol. 29, pp. 557–612.

Marshall, L. G., and P. Salinas (1990), Stratigraphy of the Río Frías Formation (Miocene), along the Alto Río Cisnes, Aisén, Chile, *Rev. Geol. Chile*, *17*, 57–88.

Mercer, J. H. (1976), Glacial history of southernmost South America, *Quat. Res.*, *6*, 125–166, doi:10.1016/0033-5894(76)90047-8.

Mercer, J. H., R. J. Fleck, E. A. Mankinen, and W. Sander (1975), Southern Patagonia: Glacial events between 4 m.y. and 1 m.y. ago, in *Quaternary Studies*, edited by R. P. Guggatre and M. M. Cresswell, pp. 223–230, R. Soc. of N. Z., Wellington.

Mitrovica, J. X., C. Beaumont, and G. T. Jarvis (1989), Tilting of continental interiors by the dynamical effects of subduction, *Tectonics*, *8*, 1079–1094, doi:10.1029/TC008i005p01079.

Mitrovica, J. X., R. N. Pysklywec, C. Beaumont, and A. Rutty (1996), The Devonian to Permian sedimentation of the Russian platform: An example of subduction-controlled long-wavelength tilting of continents, *J. Geodyn.*, *22*(1–2), 79–96, doi:10.1016/0264-3707(96)00008-7.

Molnar, P., P. England, and J. Martinod (1993), Mantle dynamics, uplift of the Tibetan Plateau, and the Indian Monsoon, *Rev. Geophys.*, *31*, 357–396, doi:10.1029/93RG02030.

Morgan, W. (1965), Gravity anomalies and convection currents, *J. Geophys. Res.*, *70*, 6175–6187, doi:10.1029/JZ070i024p06175.

Panza, J. L. (2002), La cubierta detrítica del Cenozoico superior, paper presented at the 15th Congreso Geológico Argentino, Asoc. Geol. Argent., El Calafate, Argentina.

Panza, J. L., and A. Genini (2005), Hoja Geológica 4769-IV Monumento Natural Bosques Petrificados, provincia de Santa Cruz, scale, 1:250,000, Serv. Geol. Minero Argent., Buenos Aires.

Panza, J. L., L. E. Sacomani, and J. C. Cobos (2003), Mapa Geológico de la Provincia de Santa Cruz, República Argentina, scale, 1:750,000, Serv. Geol. Minero Argent., Buenos Aires.

Pardo-Casas, F., and P. Molnar (1987), Relative motion of the Nazca (Farallon) and South American plates since Late Cretaceous time, *Tectonics*, *6*, 233–248, doi:10.1029/TC006i003p00233.

Parras, A., M. Griffin, R. Feldmann, S. Casadío, C. Schweitzer, and S. Marenssi (2008), Correlation of marine beds based on Sr- and Ar-date determinations and faunal affinities across the Paleogene/Neogene boundary in southern Patagonia, Argentina, *J. South Am. Earth Sci.*, *26*, 204–216, doi:10.1016/j.jsames.2008.03.006.

Peroni, G. O., A. G. Hegedus, J. Cerdan, L. Legarreta, M. A. Uliana, and G. Laffitte (1995), Hydrocarbon accumulation in an inverted segment of the Andean Foreland: San Bernardo Belt, central Patagonia, in *Petroleum Basins of South America*, edited by A. J. Tankard, S. Suárez, and H. J. Welsink, *AAPG Mem.*, vol. 62, pp. 403–419.

Pratt, J. H. (1859), On the deflection of the plumb line in India caused by the attraction of the Himalaya Mountain and of the elevated regions beyond and its modification by the compensation effect of a deficiency of matter below the mountain mass, *Philos. Trans. R. Soc. London*, *149*, 745–778, doi:10.1098/rstl.1859.0029.

Pysklywec, R. N., and J. X. Mitrovica (2000), Mantle flow mechanisms of epeirogeny and their possible role in the evolution of the western Canada Sedimentary Basin, *Can. J. Earth Sci.*, *37*, 1535–1548, doi:10.1139/cjes-37-11-1535.

Ramos, V. A. (1989), Andean foothills structures in northern Magallanes Basin, Argentina, *AAPG Bull.*, *73*(7), 887–903.

Ramos, V. A. (2005), Seismic ridge subduction and topography: Foreland deformation in the Patagonian Andes, *Tectonophysics*, *399*, 73–86, doi:10.1016/j.tecto.2004.12.016.

Ramos, V. A., and S. M. Kay (1992), Southern Patagonian plateau basalts and deformation: Backarc testimony of ridge collisions, *Tectonophysics*, *205*, 261–282, doi:10.1016/0040-1951(92)90430-E.

Ricard, Y., M. Richards, C. Lithgow-Bertelloni, and Y. Le Stunff (1993), A geodynamic model of mantle density heterogeneity, *J. Geophys. Res.*, *98*, 21,895–21,909, doi:10.1029/93JB02216.

Rodriguez, J. F. R., and R. Littke (2001), Petroleum generation and accumulation in the Golfo San Jorge Basin, Argentina: A basin modeling study, *Mar. Pet. Geol.*, *18*, 995–1028, doi:10.1016/S0264-8172(01)00038-1.

Sciutto, J. C., O. César, V. Escribano, and H. Pezzuchi (2000), Hoja Geológica 4566-III Comodoro Rivadavia, provincia del Chubut, scale, 1:250,000, Serv. Geol. Minero Argent., Buenos Aires.

Sciutto, J. C., O. César, and N. Iantanos (2004), Hoja Geológica 4569-IV Escalante, provincia del Chubut, scale, 1:250,000, Serv. Geol. Minero Argent., Buenos Aires.

Servicio Geológico Minero Argentino (2001), Hoja Geológica 4569-III Samiento, provincia del Chubut, scale, 1:250,000, Buenos Aires.

Somoza, R. (1998), Updated Nazca (Farallon)–South America relative motions during the last 40 Ma: Implications for mountain building in the central Andean region, *J. South Am. Earth Sci.*, *11*, 211–215, doi:10.1016/S0895-9811(98)00012-1.

Suárez, M., and R. De la Cruz (2000), Tectonics in the eastern central Patagonian Cordillera plutons, Chile (45°30–47°30'S), *J. Geol. Soc.*, *157*, 995–1001.

Suárez, M., R. De la Cruz, and C. M. Bell (2000), Timing and origin of deformation along the Patagonian fold and thrust belt, *Geol. Mag.*, *137*, 345–353, doi:10.1017/S0016756800004192.

Tassara, A., C. Swain, R. Hackney, and J. Kirby (2007), Elastic thickness structure of South America estimated using wavelets and satellite-derived gravity data, *Earth Planet. Sci. Lett.*, *253*, 17–36, doi:10.1016/j.epsl.2006.10.008.

Thomson, S. N., F. Hervé, and B. Stöckhert (2001), Mesozoic-Cenozoic denudation history of the Patagonian Andes (southern Chile) and its correlation to different subduction processes, *Tectonics*, *20*, 693–711, doi:10.1029/2001TC900013.

Turcotte, D. L., and G. Schubert (1982), *Geodynamics Applications of Continuum Physics to Geological Problems*, John Wiley, New York.

Turner, K. J., C. J. Fogwill, R. D. McCulloch, and D. E. Sugden (2005), Deglaciation of the eastern flank of the North Patagonian Icefield and associated continental-scale lake diversions, *Geogr. Ann.*, *87*, 363–374, doi:10.1111/j.0435-3676.2005.00263.x.

Zhong, S., and M. Gumis (1994), Controls on trench topography from dynamic models of subducted slabs, *J. Geophys. Res.*, *99*, 15,683–15,695, doi:10.1029/94JB00809.

B. Guillaume, Dipartimento Scienze Geologiche, Università degli Studi Roma TRE, Largo San Leonardo Murialdo 1, I-00146 Roma, Italy. (benjamin.guillaume@uniroma3.it)

L. Husson, Géosciences Rennes, UMR 6118, Université Rennes-1, CNRS, Campus de Beaulieu, F-35042 Rennes CEDEX, France. (laurent.husson@univ-rennes1.fr)

J. Martinod and M. Roddaz, Université de Toulouse, UPS (OMP), LMTG 14, Avenue Édouard Belin, F-31400 Toulouse, France. (martinod@lmtg.obs-mip.fr; mroddaz@lmtg.obs-mip.fr)

R. Riquelme, Departamento de Ciencias Geológicas, Universidad Católica del Norte, Avenida Angamos 0610, Antofagasta, Chile. (rriquelme@ucn.cl)

TC2009 GUILLAUME ET AL.: DYNAMIC NEOGENE UPLIFT OF PATAGONIA TC2009

La morphologie Quaternaire, sur les terrasses fluviales permet d'enregistrer les variations subtiles de la topographie à grande longueur d'onde. Cependant, en mesurant des pentes locales, elle ne permet pas de déterminer les variations absolues de la topographie, idéalement les variations de la distance d'un point de la surface au centre de masse de la Terre. Une possibilité est d'examiner les variations par rapport au niveau marin. La longueur d'onde caractéristique d'une dépression topographique dynamique à l'aplomb d'une subduction est de plusieurs centaines de kilomètres. Si l'évolution morphologique de la côte atlantique patagone est conforme à cette hypothèse, le changement de régime de subduction devrait être enregistré par les terrasses marines, abondament répertoriées depuis Darwin [1846] (fig. 3.1 a). Pilotés par K. Pedoja, nous sommes allés évaluer sur le terrain les variations relatives du niveau marin à l'aide de l'aide de la géomorphologie cotière quaternaire, qui fait l'objet d'un article en préparation, résumé ci-après :

Quaternary uplift of Eastern Patagonia shorelines : Darwin revisited

Kevin Pedoja [a], *Vincent Regard* [b,c,d], *Laurent Husson* [e], *Joseph Martinod* [b,c,d], *Maximiliano Iglesias* [f], *Nicolas Robin* [a]

[a] Laboratoire de Morphodynamique Continentale et Côtière, CNRS, Université de Caen, 14000 Caen, France ;
[b] Université de Toulouse ; UPS (OMP) ; LMTG ; 14 Av Edouard Belin, F-31400 Toulouse, France ;
[c] IRD ; LMTG ; F-31400 Toulouse, France ;
[d] CNRS ; LMTG ; F-31400 Toulouse, France) ;
[e] CNRS, Géosciences Rennes, 35042 Rennes, France.

La description des morphologies côtière en Patagonie remonte à Darwin [1846], qui fut étonné de trouver des fossiles marins récents au dessus du niveau actuel de la mer. De nombreux sites ont été documentés, auquel nous ajoutons notre investigation (fig. 3.1a), en relevant systématiquement les profils topographiques moyens locaux (fig. 3.1 b). Les affleurements de bonne qualité ont pu être recensés auparavant à l'aide de photographies aériennes (fig. 3.2 a) et de modèles numériques de terrain locaux (SRTM). Les séquences sur le terrain apparaissent par une succession de paliers (fig. 3.2).

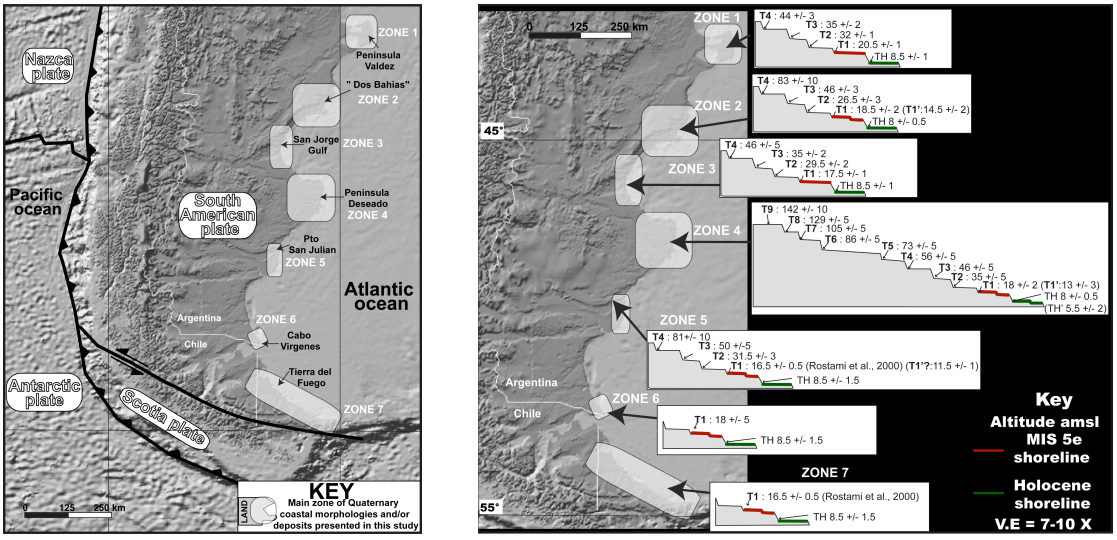

FIG. 3.1: Patagonie, zones principales d'échantillonnage (a) et profils topographiques moyens (b). *Patagonia, main sampling zones (a) and elevation profiles (b).*

Les données relevées sur le terrain sont venus compléter les travaux antérieurs, permettant d'obtenir une vue globale de la surrection le long de la côte atlantique (fig. 3.3). Au premier ordre, c'est l'ensemble de la côte qui est en surrection moyenne

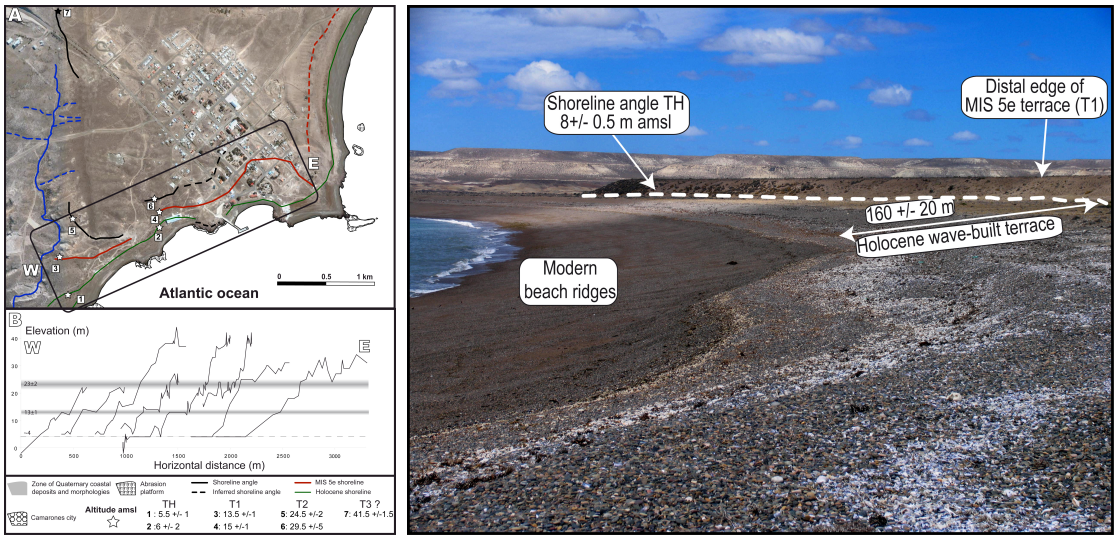

FIG. 3.2: Séquences de terrasses, vue aérienne à Bahia Camarones (a) et *in situ* à Puerto Mazerado (b). *Sequence of marine terraces, aerial view of Bahia Camarones (a) and field view in Puerto Mazerado (b).*

de ∼0.08 mm/an qui peut s'expliquer par une modification globale du contexte tectonique (voir chapitre 4). Dans le détail, la Patagonie se soulève plus fortement, à raison de ∼0.13 mm/an, et de très faibles surrections sont obtenus dans la zone de transition entre la Patagonie et le craton brésilien. Nous interprétons ce signal comme la signature de la cessation progressive dans le temps de la déflection dynamique de la Patagonie en réponse au changement de contexte géodynamique sur la marge Pacifique, conformémement aux résultats obtenus par la géomorphologie fluviatile obtenus par Guillaume et al. [2009].

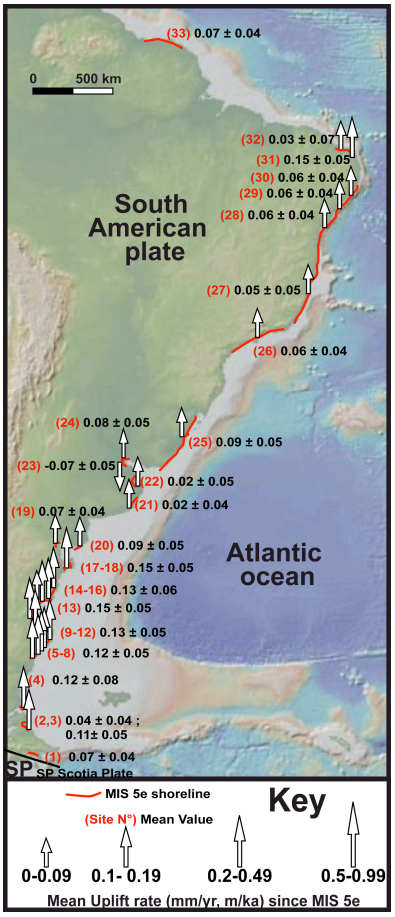

FIG. 3.3: Synthèse des taux de surrection relatifs mesurés sur la côte atlantique sud-américaine (comprenant les données de cet article complétés des travaux antérieurs). *Relative surrection rates along the coast of East Coast of South America (synthesis completed by data from previous studies).*

3.2 Topographie dynamique et niveau marin

Au premier ordre, les variations de l'âge moyen du plancher océanique sont identifiées de longue date [Cogné et al., 2006, Heller & Angevine, 1985] comme *proxy* pour les variations du niveau marin sur le temps caractéristique du cycle de Wilson. Cependant, cette assertion est à modérer. D'une part, les chartes eustatiques apparaîssent bien plus irrésolues qu'anticipé : les données qui servent de base aux synthèses classiques, comme celles de Haq et al. [1987] ou de Miller et al. [2005] sont échantillonées dans des endroits particuliers, considérés jusqu'à récemment comme stables. Or, comme le soulignent Moucha et al. [2008], la notion même de plate-forme stable est un non sens sur une Terre solide dont la figure évolue en permanence en réponse à la convection interne du manteau. En collaboration avec C. Conrad, nous avons construit un modèle de Terre sphérique afin de simuler l'écoulement du manteau et son impact sur les déflections dynamiques de la surface terrestre. D'une part, les variations temporelles de cet écoulement modifient la figure de la Terre et ainsi le niveau marin. D'autre part, les continents occultent une part du géoide. Leur circulation à la surface de la Terre rend cette occultation variable, et affecte en retour le niveau marin.

Downloaded from lithosphere.gsapubs.org on 5 May 2009

Influence of dynamic topography on sea level and its rate of change

Clinton P. Conrad[1]* and Laurent Husson[2]
[1]DEPARTMENT OF GEOLOGY AND GEOPHYSICS, SCHOOL OF OCEAN AND EARTH SCIENCE AND TECHNOLOGY (SOEST), UNIVERSITY OF HAWAII, HONOLULU, HAWAII 96822, USA
[2]GÉOSCIENCES RENNES, UNIVERSITÉ RENNES 1, CENTRE NATIONAL DE LA RECHERCHE SCIENTIFIQUE (CNRS), RENNES 35042, FRANCE

ABSTRACT

Mantle flow likely supports up to 2 km of long-wavelength topographic relief over Earth's surface. Although the average of this dynamic support must be zero, a net deflection of the ocean basins can change their volume and induce sea-level change. By calculating dynamic topography using a global mantle flow model, we find that continents preferentially conceal depressed topography associated with mantle downwelling, leading to net seafloor uplift and ~90 ± 20 m of positive sea-level offset. Upwelling mantle flow is currently amplifying positive dynamic topography and causing up to 1.0 m/Ma of sea-level rise, depending on mantle viscosity. Continental motions across dynamic topography gradients also affect sea level, but uncertainty over the plate motion reference frame permits sea-level rise or fall by ±0.3 m/Ma, depending on net lithosphere rotation. During a complete Wilson cycle, sea level should fall during supercontinent stability and rise during periods of dispersal as mantle flow pushes continents down dynamic topography gradients toward areas of mantle downwelling. We estimate that a maximum of ~1 m/Ma of sea-level rise may have occurred during the most recent continental dispersal. Because this rate is comparable in magnitude to other primary sea-level change mechanisms, dynamic offset of sea level by mantle flow should be considered a potentially significant contributor to long-term sea-level change.

LITHOSPHERE; v. 1; no. 2; p. 110–120. doi: 10.1130/L32.1

INTRODUCTION

During the mid-Cretaceous, several continents experienced oceanic transgressions that produced inland seas; the Western Interior Seaway of North America is a good example (e.g., Bond, 1976). These transgressions have been generally attributed to elevated eustatic sea level during the Cretaceous, which must have dropped by ~200 m to explain the observed continental inundations (e.g., Haq et al., 1987). Sea-level drops of this amplitude can be attributed to a major decrease in ridge volume, caused by a sustained shortening of the mid-ocean-ridge system or a slowdown in seafloor spreading rates (e.g., Pitman, 1978; Kominz, 1984; Xu et al., 2006; Cogné et al., 2006; Müller et al., 2008). However, recent sequence stratigraphy performed on the Atlantic seaboard of North America has cast doubt on the eustasy paradigm by suggesting a much smaller Cretaceous sea-level drop of only ~70 m or less (Miller et al., 2005), which could have been accomplished by climatic changes alone.

Recently, the discrepancy between these various observations of sea-level change has been attributed to vertical motion of continental margins caused by the dynamics of convection in Earth's mantle (Moucha et al., 2008; Müller et al., 2008). In particular, the east coast of North America lies above the subducted Farallon slab, which subducted beneath the U.S. west coast prior to 30 Ma, and it is observed today as a seismically fast anomaly in the lower mantle beneath the U.S. east coast (Bunge and Grand, 2000). The descent of this cold, dense feature is thought to be driving downwelling viscous flow that pulls the western half of the North Atlantic seafloor downward by ~0.5 km with respect to the eastern half (Conrad et al., 2004). In fact, nonisostatic topographic relief up to ~2 km or more has been attributed to dynamic support from viscous mantle flow in modeling studies (e.g., Hager et al., 1985), and numerous topographic features such as backarc basins (Husson, 2006), the Western Interior Seaway (e.g., Mitrovica et al., 1989), or the plateaus of southern Africa (Lithgow-Bertelloni and Silver, 1998; Gurnis et al., 2000) have been shown to be dynamically supported. On the U.S. east coast, the westward motion of North America over the Farallon slab should have produced dynamic subsidence since at least the Eocene (Liu et al., 2008; Spasojeviç et al., 2008). Combined with a global fall in sea level, this downward motion of the coastline may explain the anomalously small sea-level change that Miller et al. (2005) observed for the U.S. east coast. In fact, coastlines around the world are likely in constant motion as a result of the dynamics of the mantle interior, which significantly complicates the interpretation of relative sea-level measurements worldwide (Moucha et al., 2008).

While dynamic topography may dramatically affect observations of sea level made on coastlines, it is also possible that dynamically supported deflections of ocean basin seafloor can lead to a net change in global eustatic sea level. For example, Gurnis (1990) suggested, using a simple two-dimensional (2-D) model, that faster plate motions and fatter ridges should also produce growing slab anomalies that increase the negative dynamic topography near convergent margins, leading to continental inundation (Gurnis, 1993). The effect of this dynamic topography is to diminish the sea-level rise associated with the ridge volume change. Husson and Conrad (2006), however, used simple boundary layer theory to show that if plate acceleration is facilitated by a change in mantle viscosity, the effect of dynamic topography on basin volume, and thus sea level, is diminished. Furthermore, they showed that a sustained increase in plate motions leads to thinner mantle slabs, a positive change in dynamic topography, and elevated sea level. Thus, changes in plate motion should lead to a net change in eustatic sea level, but the amplitude, and even the sign, of the response depends on the time scales and causes of the plate motion change.

*Corresponding author e-mail: clintc@hawaii.edu.

 For permission to copy, contact editing@geosociety.org | © 2009 Geological Society of America

Downloaded from lithosphere.gsapubs.org on 5 May 2009

In practice, the mantle interior and surface plate motions are more complicated than suggested by either idealized 2-D modeling or boundary layer theory. Seismic tomography reveals complicated patterns of fast and slow velocity anomalies (e.g., Ritsema et al., 2004), some of which may be associated with slabs and upwelling flow, respectively. The dynamic topography produced by this flow should affect sea level (Fig. 1); for example, the depression of the western North Atlantic by the Farallon slab (Conrad et al., 2004) should increase the volume of the North Atlantic basin, and thus should lower sea level globally (Fig. 1, mode 1). Furthermore, continental regions move laterally over this time-varying dynamic topography field, variously exposing or concealing this deflected topography from the ocean basins, where it can affect sea level (Fig. 1, mode 2). To gain a full understanding of the ways in which mantle flow uplifts Earth's surface as a function of time, three-dimensional, time-dependent flow models are required in which dynamic topography is tracked temporally (e.g., Gurnis et al., 2000; Conrad and Gurnis, 2003). For example, Moucha et al. (2008) examined a full model for the past 30 Ma of global mantle flow and found that changes in dynamically supported seafloor topography caused eustatic sea level to rise ~100 m during this time period, or ~3 m/Ma.

In this study, we examine the ways in which the dynamics of viscous mantle flow affect average seafloor bathymetry and, thus, eustatic sea level. In particular, we consider the effects of mantle downwelling (driven by fast seismic anomalies, typically associated with slabs) and mantle upwelling (driven by slow seismic anomalies) separately. We also examine the relative importance of upper-mantle and lower-mantle flows, as well as the importance of mantle viscosity structure. Finally, we examine the relative contributions of time-varying dynamic topography (Fig. 1, mode 1) and continental motion (Fig. 1, mode 2) to the total net sea-level change. Because these two mechanisms are constantly operating together to affect sea-level change, it is difficult to extract their relative importance in a time-dependent dynamic model with plate motions (e.g., Moucha et al., 2008). However, we can constrain their relative importance by examining each effect separately and instantaneously. Therefore, we restrict our analysis to the present-day mantle flow field and its first time-derivative. Furthermore, the understanding gained from our analysis allows us to estimate the ways in which dynamic topography may affect sea level throughout a Wilson cycle (e.g., Wilson, 1966) of supercontinent aggregation and dispersal.

ESTIMATING DYNAMIC TOPOGRAPHY AND SEA-LEVEL OFFSET FROM GLOBAL MANTLE FLOW MODELS

To constrain the effect of dynamic topography on sea level, we first developed global mantle flow models that can be used to predict the time-dependent patterns of topography that are dynamically supported by the mantle's present-day flow field. To do this, we employed a spherical finite element code (CitComS [Zhong et al., 2000; Tan et al., 2006], accessed in January 2009 to obtain a version that includes recently added self-gravitation effects [Zhong et al., 2008]) to predict present-day mantle flow in a spherical Earth driven by the mantle's internal density heterogeneity. We used the S-wave seismic tomography model S20RTSb (Ritsema et al., 2004) to infer lateral variations of density within the mantle and employed a constant conversion factor of 0.15 g cm^{-3} km^{-1} s to convert seismic velocity anomaly to density anomaly. We chose this conversion factor because it is consistent with both laboratory data (e.g., Karato and Karki, 2001) and with previous studies (e.g., Conrad et al., 2007) (although this choice is accompanied by some uncertainty in both magnitude and potential depth-dependence). Also following previous work (e.g., Lithgow-Bertelloni and Silver, 1998; Conrad et al., 2007), we did not impose density anomalies above 300 km depth because seismically fast velocity anomalies associated with continental roots have been shown to correspond to neutrally buoyant "tectosphere" (e.g., Jordan, 1975), which implies that a straightforward conversion between seismic velocity and density is not appropriate for the continental lithosphere. Similarly, slow velocity anomalies detected near the surface beneath ridges (e.g., Ritsema et al., 2004) may be associated with decompression melting of passively upwelling mantle rocks. These near-surface anomalies require a very different treatment than we have applied below 300 km (e.g., Hernlund et al., 2008).

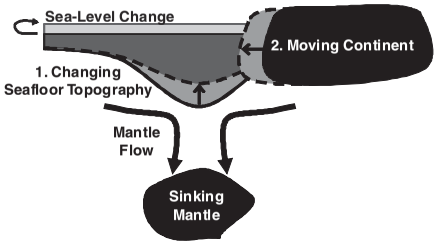

Figure 1. Two mechanisms by which dynamic topography can change sea level with time. Mode 1: Time-dependent mantle flow changes the pattern of seafloor dynamic topography. For the case shown, a mantle downwelling moves away from the surface, which causes the dynamic topography above the downwelling to become less depressed (e.g., Mitrovica et al., 1989), resulting in sea level rise. Mode 2: A continent moves laterally over a region of anomalously low topography. This moves the average dynamic deflection of the seafloor toward more positive values, which elevates sea level.

We assume a reference viscosity structure equivalent to the one that Conrad et al. (2007) used to successfully predict seismically anisotropic fabric beneath the ocean basins. This structure is entirely radial and ignores lateral viscosity variations; it includes a low-viscosity asthenosphere (between 300 and 100 km depth) that is a factor of 10 less viscous than the upper mantle, and higher-viscosity lower mantle (below 670 km) and lithospheric (above 100 km) layers that are 50 and 30 times more viscous than the upper mantle, respectively. This reference viscosity structure is similar to the one used by Lithgow-Bertelloni and Richards (1998) to predict the shape of the geoid and plate motions. Although the magnitude of dynamic topography is not sensitive to the absolute value of mantle viscosity, but only to its radial (e.g., Hager, 1984) and lateral (Cadek and Fleitout, 2003) variations, the rate of change of dynamic topography, which we examine next, is directly dependent on this absolute value. Therefore, we initially assume an upper-mantle viscosity of 0.5×10^{21} Pa s, which is consistent with estimates constrained from postglacial rebound (e.g., Mitrovica, 1996), and equal to the value that provides the best fit to anisotropy observations in Conrad et al.'s (2007) flow models.

In fact, the reference flow model that we develop here is the same as the highest-resolution model used by Conrad et al. (2007) (with 105 km horizontal and 17 km vertical resolution in the upper half of the upper mantle, and 100 km vertical resolution in the lower mantle; lower-resolution calculations produce similar results), with one exception. Conrad et al. (2007) combined flow driven by mantle density heterogeneity beneath a rigid surface boundary condition with flow driven by surface velocity boundary conditions consistent with observed plate motions. Neither condition is consistent with the free-slip surface condition of Earth, but they are consistent with observed plate motions. Here, we use free-slip surface boundary conditions to predict dynamic topography, as others have done (e.g., Zhong and Davies, 1999; Lithgow-Bertelloni and Richards, 1998), because Thoraval and Richards (1997) found that this boundary condition provides a better fit to the geoid than rigid or plate motion boundary conditions.

Downloaded from lithosphere.gsapubs.org on 5 May 2009

We calculated dynamic topography globally by computing the radial traction, σ_{rr}, that mantle flow exerts on the free-slip surface, perturbed to include self-gravitation effects using Zhong et al.'s (2008) implementation in CitcomS. For Earth's free surface, this perturbed radial stress is compensated by the mass anomaly associated with topographic deflection of the surface equal to $h = \sigma_{rr}/\Delta\rho g$, where g is the acceleration due to gravity and $\Delta\rho$ is the density contrast between seawater and mantle rocks, which we take to be 2310 kg/m^3. Note that continental areas feature a density contrast of 3340 kg/m^3 because subaerial topographic deflections are compensated by air rather than seawater. This reduces the amplitude of dynamically supported topography in continental areas, but it does not affect our estimates of seawater reservoir sizes unless topography crosses sea level during its deflection, which is a second-order effect that we will ignore here.

We measure the offset of average sea level caused by dynamic deflections of the seafloor relative to a (theoretical) static Earth with no dynamic topography. To do this, we considered that sea level is a geopotential surface known as the geoid, which we also computed using the self-gravitation implementation in CitcomS. Although Earth's internal density heterogeneity and dynamically deflected surfaces do produce geoid topography at a range of scales (e.g., Hager, 1984; Hager et al., 1985; Lithgow-Bertelloni and Richards, 1998), this sea-surface topography does not deflect average sea level because the geoid reference level is an arbitrary surface. A net deflection of the seafloor by dynamic topography, however, will cause a corresponding offset of sea level if the volume of seawater is constant (e.g., Moucha et al., 2008). To measure this offset, we express dynamic topography relative to a spherical surface centered on Earth's center of mass (e.g., Paulson et al., 2005). Thus, we remove the degree-one component of the geoid, which expresses offset of center of mass in the calculation coordinates, from the predicted dynamic topography. Note that the degree-one component of the resulting dynamic topography need not be zero if there is a net deflection of Earth's surface in one direction that is caused by degree-one density heterogeneity within Earth's interior. We ignore the degree-zero component of dynamic topography because its choice is arbitrary. The resulting dynamic topography (Fig. 2), which we compute as the sum of spectral degrees 1–20, is thus the net surface deflection that is dynamically supported by density heterogeneity in Earth's mantle. The associated geoid variations are generally anticorrelated to dynamic topography and are an order of magnitude smaller (e.g., Hager, 1984). As described already, geoid variations do not produce a net eustatic sea-level offset, but they may affect local measurements of sea level relative to the continents, which themselves may be experiencing time-dependent dynamic deflections (Moucha et al., 2008).

OFFSET OF SEA LEVEL BY DYNAMIC TOPOGRAPHY

Surface deflections associated with the previously described flow models show that Earth's surface presents positive dynamic topography above the two "superplumes" beneath southern Africa and the southern Pacific and negative dynamic topography near the major subduction zones of South America and Southeast Asia (Fig. 2A). Although some studies have suggested smaller magnitudes of topography than we estimate here (Colin and Fleitout, 1990; Le Stunff and Ricard, 1997), several recent studies have constrained similar or even larger amplitudes (e.g., Lithgow-Bertelloni and Gurnis, 1997; Moucha et al., 2008). Furthermore, our predictions are consistent with geologic observations of up to ~1 km uplift of southern Africa (Lithgow-Bertelloni and Silver, 1998; Gurnis et al., 2000) and up to ~0.5 km topography differential across the North Atlantic (Conrad et al., 2004).

If we integrate the mantle tractions that support dynamic topography over the entire surface of the globe, we find that the total of this dynamic support integrates to zero. This is an expected result of mantle circulation: every upwelling or downwelling that dynamically supports surface topography must be balanced by return flow (downwelling or upwelling, respectively) that supports opposing topography somewhere else on the globe. Thus, if oceans covered the entire globe, the net effect of dynamic topography on sea level would be zero. However, because continents cover nearly one third of the globe, a net deflection of continental areas by mantle flow will be balanced by an opposing net deflection of oceanic areas, leading to a net offset of sea level. This is exactly what we find: our model predicts an average dynamic uplift of the seafloor (Fig. 2A) by 132 m, while continental areas are depressed by an average of 295 m. Although compensation by air reduces continental dynamic topography by 70% compared to water-covered areas, the average continental deflection is larger than it is for ocean basins because continental area is 2.24 times smaller than ocean area. The continental deflection is negative because subduction tends to put slabs, and thus mantle downwelling, beneath continents (e.g., Asia, Australia, and South America in Fig. 2A). Because the changes to the water column above vertically deflected seafloor will be isostatically compensated, our estimate of 132 m of dynamic seafloor uplift actually elevates sea level by only 92 m (70%; Pitman, 1978; Husson and Conrad, 2006; Müller et al., 2008).

We performed a similar analysis to approximately constrain the mantle sources of the various features in the net dynamic topography field (Fig. 2A). To start, we calculated the dynamic topography produced by flow driven only by negative (Fig. 2B) and positive (Fig. 2C) density heterogeneities in the upper mantle, which generate active upwelling and downwelling, respectively. We find that these flow fields produce similar patterns of dynamic seafloor topography and offset sea level approximately equally (23 and 22 m, respectively), despite very different driving mechanisms. Active upwelling generates positive topography near Iceland, in the southern and northeast Pacific basin, and east of Africa, and passive return flow depresses Earth's surface elsewhere (Fig. 2B). Active downwelling is associated primarily with slabs in the western Pacific and South America, and it depresses the surface above them, while passive return flow uplifts the surface elsewhere (Fig. 2C). We observe similar patterns and amplitudes of topography supported by active upwelling and active downwelling in the lower mantle (Figs. 2D and 2E, which yield 25 and 23 m of sea-level offset, respectively). The lower-mantle response, however, is typically confined to longer wavelengths and features a stronger influence of the African superplume (Fig. 3D) and Farallon slab (Fig. 2E) than do the upper-mantle flows. The similar pattern observed for upwelling-driven (Figs. 2B and 2D) and downwelling-driven (Figs. 2C and 2E) flows indicates that areas of upwelling typically occur in the location of return flow from areas of downwelling, and vice versa. These four components of the flow field (Figs. 2B–2E) sum to the total topography (Fig. 2A) and contribute to positive sea-level offset approximately equally.

TIME-DEPENDENCE OF DYNAMIC TOPOGRAPHY AND SEA-LEVEL CHANGE

Because the patterns and amplitudes of dynamic topography change with time, the net offset of sea level by dynamic topography should change as well, resulting in a net sea-level rise or fall (Fig. 1, mode 1). To estimate the rate at which changing dynamic topography affects sea-level change, we used the previous flow model to advect the mantle's density heterogeneity field forward in time. As mantle density heterogeneity evolves with time, the mantle flow field does as well, which changes the dynamic topography field. We measured the rate of change of dynamic

Downloaded from lithosphere.gsapubs.org on 5 May 2009

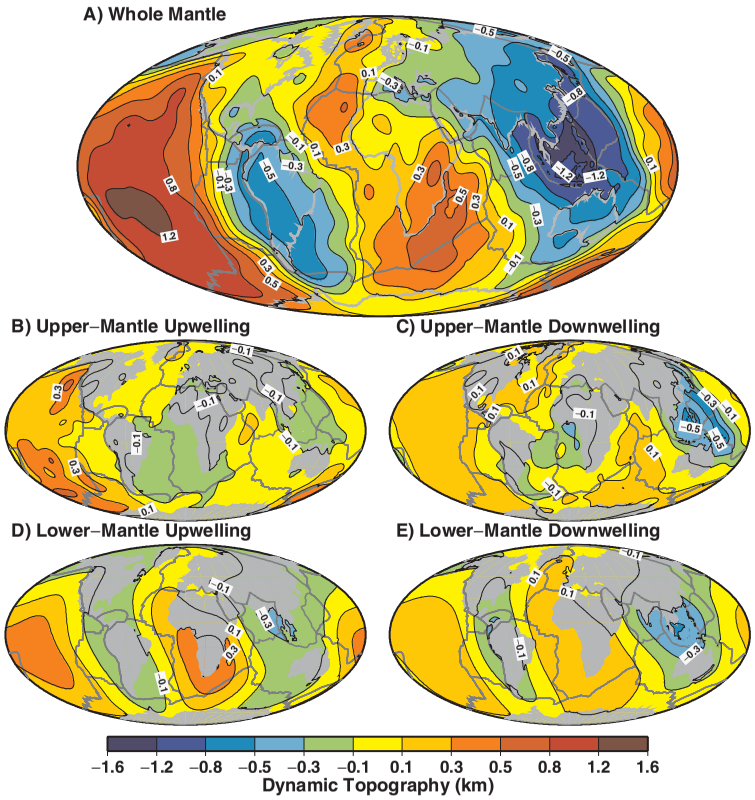

Figure 2. Dynamic topography determined by calculating mantle flow using density heterogeneity in (A) the whole mantle, and separated into portions driven by (B) negative density and (C) positive density anomalies in the upper mantle, and (D) negative density and (E) positive density anomalies in the lower mantle. Thus, parts B and D show topography associated with active upwelling flow, while C and E are driven by downwelling flow.

Downloaded from lithosphere.gsapubs.org on 5 May 2009

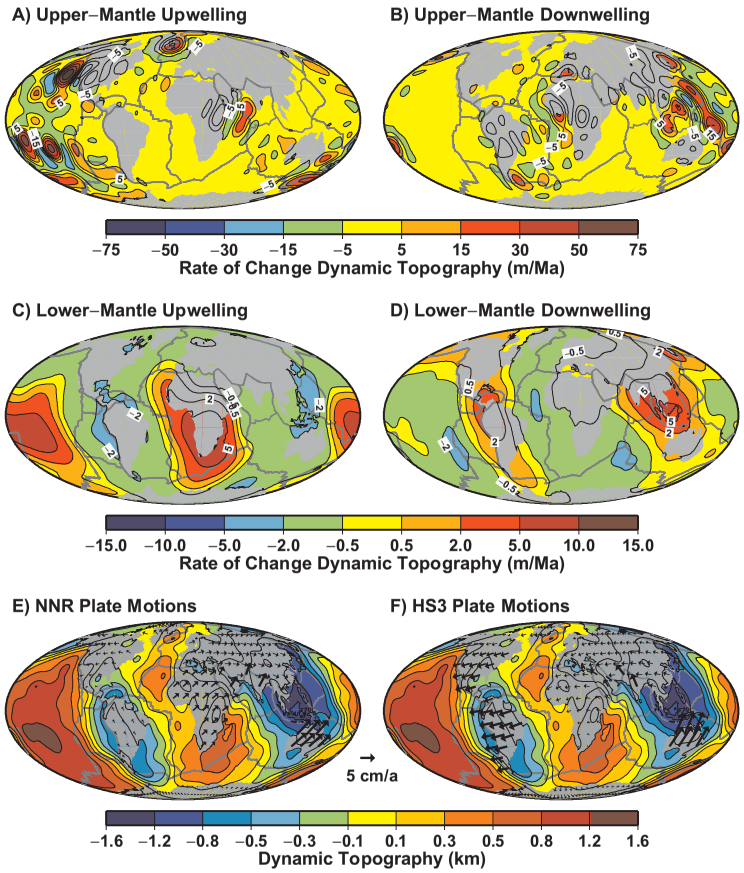

Figure 3. Rate of change of dynamic topography (e.g., Fig. 1, mode 1) determined from time-dependent flow models for (A–D) subsets of the flow field as broken down in Figures 2B–2E. Sea-level change is also caused by continental motions over the dynamic topography field (e.g., Fig. 1, mode 2), as shown here for global mantle flow (from Fig. 2A) and plate motions in the (E) no-net rotation (NNR) (De Mets et al., 1994) and (F) HS3 (Gripp and Gordon, 2002) reference frames.

Downloaded from lithosphere.gsapubs.org on 5 May 2009

topography for both upwelling- and downwelling-driven flows in both the upper and lower mantles (Figs. 3A–3D). For the upper-mantle flows, we compared the dynamic topography at the beginning of the calculation and again at 1.0 Ma, because this time interval was long enough for an observable change in dynamic topography to occur but short enough that the mantle's behavior is still approximately linear. From these two maps, we computed their time variation and obtained maps of the rate of change of dynamic topography driven by upper-mantle upwelling and downwelling (Figs. 3A and 3B). Because the higher viscosity of the lower mantle yields a slower evolution of the mantle flow field, we found that 2.0 Ma were necessary to resolve the time variation of dynamic topography induced by lower-mantle upwelling and downwelling (Figs. 3C and 3D).

By comparing maps of dynamic topography (Figs. 2B–2E) with its time variation (Figs. 3A–3D), we can infer the way in which dynamic topography is changing with time, as well as the implications for sea-level change. In general, we find that positive surface deflections above upwellings (Figs. 2B and 2D) tend to become reinforced (Figs. 3A and 3C), while negative deflections above areas of downwelling (Figs. 2C and 2E) tend to become diminished (Figs. 3B and 3D). For example, dynamic topography above the lower-mantle African and South Pacific superplumes (Fig. 2D) is growing (Fig. 3C). This is because the low-density mantle anomalies that support this elevated topography are moving closer to the surface, where they can produce additional surface uplift. By contrast, the negative topography above the western Pacific and South American slabs (Fig. 2E) is becoming less negative, as shown by the positive uplift in these regions (Fig. 3D). This occurs because these lower-mantle slabs are sinking away from the surface, which diminishes their ability to induce topography there. Upper-mantle flows show similar patterns of positive uplift above both active upwelling (e.g., the growing uplift in Iceland, and the northeastern and southern Pacific in Fig. 3A) and active downwelling regions (e.g., the upwelling above western Pacific slabs in Fig. 3B), although the shorter-wavelength nature of upper-mantle flows tends to locate return flow, and its associated depressing topography, closer to locations of growing topography.

Many of the lower-mantle patterns in Figures 3C and 3D are consistent with trends found in previous studies. For example, ongoing uplift of Africa was predicted by Gurnis et al. (2000), as was uplift of much of the Pacific by Moucha et al. (2008) during the past 30 Ma. We observe both trends here associated with the upward motion of lower-mantle upwelling (Fig. 3C). Liu et al. (2008) showed that the amplitude of subsidence of North America has been decreasing as the Farallon slab descends; this result was predicted by Mitrovica et al. (1989) and is observed here (Fig. 3D). However, our prediction of continuing uplift of South America and the western Pacific (Fig. 3D) is not supported by either time-dependent flow models or geologic evidence. Instead, these trends are caused by the descent of lower-mantle slabs away from the 670 km interface without the ongoing resupply of slab material that we would expect from continuous subduction at the surface. Unlike Farallon subduction beneath North America, both the western Pacific and South America have seen continuous subduction at least through the Cenozoic (Sdrolias and Müller, 2006), so surface upwelling in these areas (Fig. 3D) is probably not representative of the long-term dynamics of these areas. At best, uplift above these continuously subducting slabs may be representative of an end member case in which slabs have stalled at the 670 km discontinuity while their lower-mantle portions fall away, as may be occurring in Tonga (van der Hilst, 1995). However, because slabs do not appear to be stalling at 670 km depth everywhere, uplift above subduction zones shown in Figure 3D and the subsidence away from them associated with return flow are almost certainly overestimated. Similarly, uplift above upper-mantle slabs falling away from 300 km depth (Fig. 3B) is also probably overestimated.

In practice, the time-dependence of dynamic uplift or subsidence above active subduction zones is difficult to constrain because a full treatment of time-dependent subduction dynamics is required; this has not yet been fully realized for a global model. Because of this, we will only consider time-dependence associated with upwelling flow (Figs. 3A and 3C) in the subsequent analysis, but we anticipate that downwelling flow could also induce time-dependence with magnitudes up to those estimated here (Figs. 3B and 3D), but with potentially an opposite sign if the time-dependence of subduction is currently placing material into the shallow mantle faster than it is falling away. In principle, upwelling flow calculations have potentially the same problems as downwelling flows models, but in reverse: low-density upwelling material also cannot be removed from our model as it rises toward the surface, and thus will also always produce surface uplift. However, with the exception of Iceland (Fig. 3A), most of the uplifting areas (Figs. 3A and 3C) do not occur near ridges, so there is no obvious sink for upwelling material analogous to the sources of downwelling material (subduction zones). Note that the lack of accurate sources and sinks for mantle density heterogeneity in time-dependent flow models has been noted before (e.g., Conrad and Gurnis, 2003), and it should influence other studies that advect mantle density heterogeneity (e.g., Moucha et al., 2008).

With these caveats in mind, we measured the average rate of change of dynamic topography (Fig. 3) over the oceanic areas to see if the estimated 92 m of dynamically supported sea level is changing with time. We find that active upwelling in the upper and lower mantles increases the average seafloor dynamic topography at rates of 0.42 and 0.20 m/Ma, respectively, producing 0.30 and 0.14 m/Ma of sea-level rise when isostatically compensated. The positive sign in this case occurs because upwelling-induced uplift, which is amplifying as discussed already, preferentially occurs in oceanic areas. By contrast, downwelling-induced negative topography, which is uplifting in our model, tends to occur beneath continental areas, leading to net subsidence of oceanic areas. As a result, active downwelling in the upper and lower mantles leads to 0.21 and 0.22 m/Ma of sea-level drop in our models, respectively. Taking only the upwelling components for the reasons described already, we estimate that the time-dependence of dynamic topography may cause up to 0.44 m/Ma of sea-level rise. The uncertainty in this estimate, however, is large because we do not know even the sign of the influence of downwelling flow. Our models suggest that at most 0.22 m/Ma of sea-level drop is associated with areas of downwelling in the lower mantle, but only if lower-mantle slabs are not being replenished by subduction. Using this value for the maximum amplitude of uncertainty (and ignoring the contribution from upper-mantle slabs, since we can be sure that they are being replaced by subduction), we estimate that 0.44 ± 0.22 m/Ma of sea-level rise is currently associated with time-dependent mantle flow.

UNCERTAINTY IN ESTIMATES OF SEA-LEVEL OFFSET AND RATE OF CHANGE

The amplitude of dynamic topography (Fig. 2) scales linearly with the velocity to density scaling factor, which is assumed to be 0.15 g cm^{-3} km^{-1} s here (this approximately corresponds to $\partial \ln(\rho)/\partial \ln[v_s] \sim 0.2$ in the terminology of Karato and Karki [2001]). Because mantle flow velocities also scale linearly with this scaling factor, the rate of change of dynamic topography scales with its square. Karato and Karki (2001) suggested that the uncertainty in $\partial \ln(\rho)/\partial \ln(v_s)$ may be on the order of about ±50% and may vary with depth, although significant deviation from our choice will cause predictions of dynamic topography (Fig. 2) to violate geologic constraints on its magnitude (e.g., Africa—Lithgow-Bertelloni and Silver, 1998; North Atlantic—Conrad et al., 2004). This factor may also be affected by

Downloaded from lithosphere.gsapubs.org on 5 May 2009

chemical heterogeneity, especially for low-velocity anomalies in the lower mantle (e.g., Masters et al., 2000). Thus, we acknowledge the important influence of the velocity to density scaling factor on our results, but we will use uncertainty in our viscosity model, which is also large, to evaluate uncertainty in our estimates of dynamic offset of sea-level offset, and its rate of change.

As described herein, the rate of change of dynamic topography scales inversely with the absolute mantle viscosity; thus, rates of sea-level change may be higher than those reported here if upper-mantle viscosity is larger than the value of 0.5×10^{21} Pa s that is assumed here. Although this viscosity value falls within the range of upper-mantle viscosities constrained by Mitrovica (1996) using postglacial rebound ($0.3–0.6 \times 10^{21}$ Pa s), these data may not adequately constrain viscosities for oceanic areas (Paulson et al., 2005), where a significantly weaker upper mantle may be possible (Paulson et al., 2007). Thus, uncertainty in the absolute value of mantle viscosity may induce up to a factor of two uncertainty in the rate of sea-level rise (Fig. 4). Lateral viscosity variations may introduce another source of uncertainty; while such variations in the mantle interior probably only exert a small influence on dynamic topography (Moucha et al., 2007), the effect of lithospheric variations (e.g., plate boundary or slab rheology) can be large, particularly for slab-induced downwelling flow (Zhong and Davies, 1999).

Because both dynamic topography and the geoid are sensitive to the mantle's radial viscosity structure (e.g., Hager, 1984; Lithgow-Bertelloni and Richards, 1998), we vary the viscosity of the lower mantle relative to that of the upper mantle to determine the range of possible variations in the dynamically supported sea-level offset (Fig. 5A) and its rate of change (Fig. 5B). (We determined in tests that the lower-mantle viscosity generally has a larger influence on these parameters than does the viscosity of the asthenospheric or lithospheric layers.) We find that the sea-level offset decreases with increasing lower-mantle viscosity (Fig. 5A) because density heterogeneity is increasingly compensated at the core-mantle boundary, rather than by surface deflections (Hager, 1984). For a range of lower-mantle viscosities between 30 and 100 times that of the upper mantle, we find that the sea-level offset ranges from 69 to 109 m (Fig. 5A). The sea-level rate of change (Fig. 5B) similarly exhibits a dependence on viscosity structure, and rates of change typically increase as lower-mantle viscosity decreases because of larger amplitude offsets (Fig. 5A) and faster rates of flow. The contributions from upper- and lower-mantle upwellings, for example, may be as large as 0.32 and 0.26 m/Ma for a viscosity contrast of 30 between the upper and lower mantles (Fig. 5B). These rates may be even larger if accompanied by a smaller absolute mantle viscosity (Fig. 4), but they may be close to zero for a higher lower-mantle (Fig. 5B) or absolute mantle viscosity (Fig. 4).

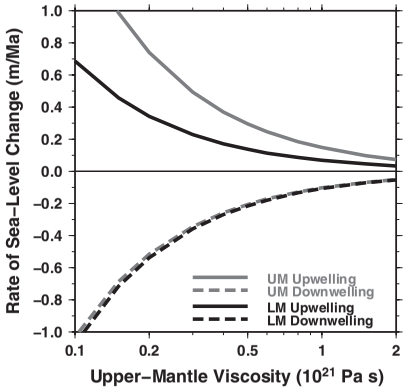

Figure 4. Rate of change of sea level caused by the time-dependence of dynamic topography as a function of the absolute value of upper-mantle viscosity. Calculations for dynamic topography driven by active upwelling and downwelling flow (solid and dashed lines), broken into upper-mantle (UM and lower-mantle (LM) components (gray and black lines), as in Figures 3A–3D, are shown separately.

Taking all of these uncertainties into account, and considering that poor constraints on the effects of downwelling introduce additional uncertainty, we infer that sea level is currently positively offset by ~90 ± 20 m, and that the rate of change of this offset is highly uncertain but probably positive at the present time. Considering (1) that the range of lower-mantle viscosities allow upwelling flow to induce sea-level rise at up to 0.5 m/Ma (Fig. 5B), (2) that the uncertainty in the absolute viscosity permits a factor of ~2 variation, and (3) that mantle downwelling may cause sea level to drop (Fig. 5B), we constrain the rate of sea-level rise to rates of ~0.5 ± 0.5 m/Ma.

CONTINENTAL MOTIONS AND SEA-LEVEL CHANGE

The horizontal motion of continents over dynamic topography can also lead to changes in sea level (Fig. 1, mode 2). To estimate the magnitude of this effect, we used observed present-day plate motions to advance the locations of the continents, as expressed on a 0.5 by 0.5 degree grid, forward in time by 5 Ma (significantly shorter time intervals do not allow for sufficient continental motion for differences in the continental masking of dynamic topography to be properly resolved) over the static dynamic topography field (Figs. 3E and 3F). Initially, we applied the NUVEL-1A model for present-day plate motions (DeMets et al., 1994) in the no-net rotation (NNR) reference frame. We find that the motion of continents over our reference model for dynamic topography (Fig. 3E) on average tends to cover up negative topography and expose positive topography, causing sea-level rise at a rate of 0.24 m/Ma. This trend is primarily caused by the motion of Asia and Australia toward the negative topography of the western Pacific (Fig. 3E). In this case, the predicted rate of sea-level change depends on rates of continental motion and not viscosity structure (at least not directly; rates of plate motion are ultimately dependent on mantle viscosity). Therefore, our constraints on the total sea-level offset (Fig. 5A) also apply to the continental motion over the dynamic topography that produces this offset. The resulting constraint (Fig. 5C) allows sea-level rise between 0.15 and 0.29 m/Ma.

Because patterns of dynamic topography are generated from depth, sea-level changes caused by motion of the continents over dynamic topography depend directly on the net rotation of the lithosphere relative to the deep mantle. Recently, the net lithosphere rotation has been a topic of some debate (e.g., Becker, 2006, 2008; Torsvik et al., 2008); most hotspot-based reference frames detect a present-day net westward motion of the lithosphere with poles of rotation clustered in the southern Indian Ocean (Becker, 2006). The amplitude of this net rotation, however, is much more variable and ranges from no-net rotation (NNR) (DeMets et al., 1994) to a maximum of 0.436°/Ma (for a maximum of 5 cm/a of westward motion) for the "HS3" Pacific hotspot model of Gripp and Gordon (2002); amplitudes for other studies fall somewhere between

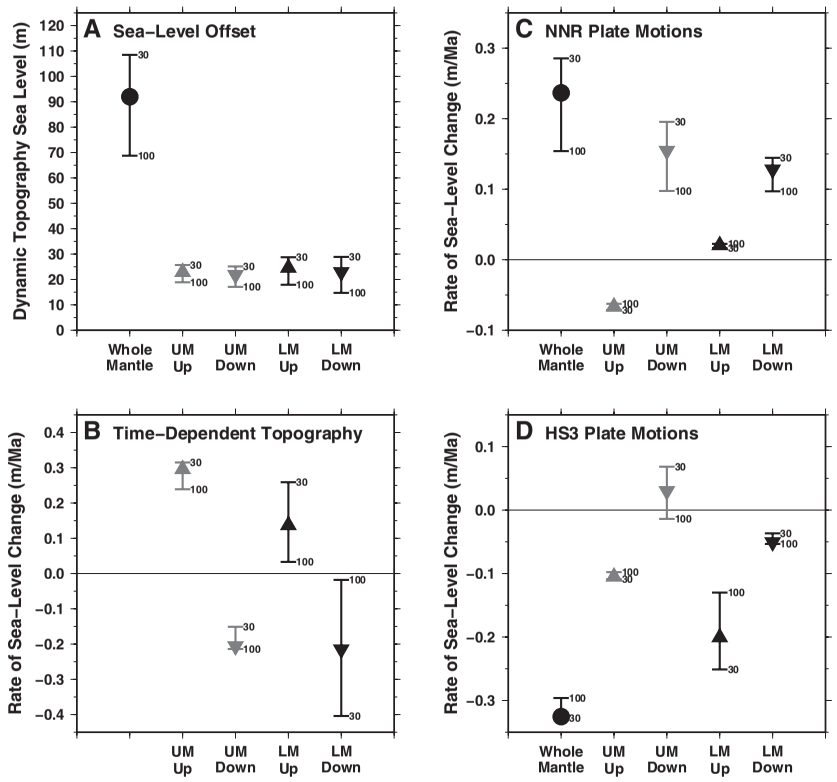

Figure 5. The effect of the lower-mantle viscosity on (A) the net present-day sea-level offset caused by dynamic topography, and the rate of change of this offset caused by either (B) the time-dependence of mantle flow (Fig. 1, mode 1) or continental motion (Fig. 1, mode 2) in the (C) no-net rotation (NNR) (De Mets et al., 1994) and (D) HS3 (Gripp and Gordon, 2002) reference frames. Flow is separated into four components as in Figures 2–4: upwelling (upward triangle) and downwelling (downward triangle) flows in the upper (gray) and lower (black) mantles. Solid dots show results for whole mantle flow, but the time-dependent component of this flow is not calculated in B because differing time scales control the upper-mantle (UM) and lower-mantle (LM) components (see text). Symbols show the results of calculations using lower-mantle viscosity that is 50 times that of the upper mantle (base model), while brackets show a range of this ratio varying from 30 to 100, as indicated.

these two extremes. Becker (2008) constrained a net rotation of ~50% of the amount implied by the HS3 model using anisotropy observations. To test the effect of net rotation on sea-level change rates, we added net rotation consistent with the end-member HS3 model (Gripp and Gordon, 2002) to the NNR plate motions. The introduction of this net rotation adds a westward drift to the continental motions (Fig. 3F), causes Eurasia to uncover negative dynamic topography in the western Pacific, and causes Africa and North America to cover positive dynamic topography in the Atlantic and Pacific basins, respectively. These changes are opposite to those produced by the NNR model, and they tend to lower sea level at a rate of 0.33 m/Ma with a small uncertainty (Fig. 5D).

Because dynamic topography caused by areas of upwelling and downwelling in the upper and lower mantles exhibits different spatial patterns (Figs. 2B–2E) than the dynamic topography of these fields combined (Fig. 2A), continental motion over these different topography fields produces a variety of effects on sea level. For example, sea-level rise produced by NNR motions is primarily associated with downwelling flow (Fig. 5C), while sea-level drop associated with HS3 motions is primarily associated

with upwelling flow (Fig. 5D). Altogether, we find that the net rotation of the lithosphere has a strong effect on sea-level change with time, and it can cause sea-level change ranging from sea-level rise at ~0.3 m/Ma for NNR to sea-level fall at ~0.3 m/Ma for HS3. As most constraints on net rotation fall somewhere between NNR and HS3 (e.g., Becker, 2006, 2008), sea-level change caused by continental motion should also fall between these extremes, and it should be nearly zero if Becker's (2008) estimate of 50% of the HS3 net rotation is correct. It is important to note that these results are for end member cases in which continents move over dynamic topography without regard to the mantle flow source of that topography. In fact, continental motions should be coupled to mantle flow, and thus should be correlated to dynamic topography, as we discuss next.

DISCUSSION: DYNAMIC OFFSET OF SEA LEVEL DURING A WILSON CYCLE

We can make inferences about the long-term effects of dynamic topography on sea level by interpreting the patterns predicted for the present day (e.g., Figs. 2–3) within the context of mantle evolution during a Wilson cycle of supercontinent aggregation and dispersal (e.g., Wilson, 1966; Phillips and Bunge, 2005; Zhong et al., 2007). We start by considering the lower-mantle flow field, which features basin-scale flow patterns that should evolve along with supercontinent aggregation and dispersal events (Collins, 2003). We have found that upwelling-dominated dynamic topography is currently amplifying at rates of 5–10 m/Ma (Fig. 3C). At these rates, the current ~500 m amplitude of the associated dynamic topography (Fig. 2D) could have grown entirely during the most recent continental dispersal event that began ~180 Ma ago with the opening of the Atlantic basin. Several authors that have studied the time-dependent evolution of lower-mantle structures (e.g., Conrad and Gurnis, 2003; Müller et al., 2008; Spasojević et al., 2008) have found that these structures develop over time scales on the order of 100 Ma because the high viscosity of the lower mantle produces sluggish flow. Therefore, it does not seem unreasonable that the lower-mantle component of our estimated sea-level change, up to ~0.25 m/Ma (Fig. 5B), should be maintained for a large fraction of the current continental dispersal event. Upper-mantle flow also produces long-wavelength topography (Figs. 2B–2C), but its time-dependence exhibits shorter wavelengths (Figs. 3A–3B). However, because the processes that control the evolution of upper-mantle density heterogeneity (e.g., superplume rise and seafloor aging) are also likely to develop on ~100 Ma time scales, we speculate that the upper-mantle contribution to dynamic offset of sea level may also evolve at time scales comparable to those of the lower mantle, and with similar magnitudes of up to ~0.3 m/Ma (Fig. 5B).

Since the long-wavelength patterns of dynamic topography are correlated with patterns of mantle flow, the motion of the continents should also be correlated with that flow, at least for long (plate-scale) wavelengths. For example, Bokelmann (2002) suggested that the North American plate has been decelerating as the cratonic root of North America becomes positioned above the center of the Farallon slab downwelling. Similarly, South America's motion may already be tied to the downwelling associated with the sinking Nazca slab (Fig. 2E). This motion of continents toward areas of downwelling occurs because upper-mantle flow, which typically moves from areas of upwelling toward downwelling, couples most strongly to the deep cratonic roots (Conrad and Lithgow-Bertelloni, 2006), pushing cratons away from areas of upwelling and toward areas of downwelling. In this view, cratons tend to move down gradients in dynamic topography; this process has been confirmed by evidence of net subsidence of continental interiors (Heine et al., 2008). This is the general pattern that is predicted for plate motions in the NNR reference frame (Fig. 3E), in which India, Eurasia, and Australia are moving toward the areas of downwelling in the western Pacific, Africa is moving away from the African upwelling, and North and South America are nearly stationary. Thus, the 0.25 m/Ma of sea-level rise associated with continental motion in the NNR frame (Fig. 5C) may apply for long-term sea-level change associated with continental motions during periods of continental dispersal, despite indications that a combination of the NNR and HS3 frames may be more appropriate for the present day (e.g., Becker, 2008). It is important to remember, however, that plates motions are controlled by a variety of factors, such as slab pull (e.g., Collins, 2003) or stress transfer across plates and upper mantle (e.g., Husson et al., 2008) that can generate continental motion up dynamic topography gradients (e.g., motion of South America or Eurasia in the HS3 model; Fig. 3F).

Because mantle upwelling is expected beneath a supercontinent during the dispersal phase of the Wilson cycle (e.g., Gurnis, 1988; Lowman and Jarvis, 1999), we expect that, on average, continents should be moving away from uplifted dynamic topography during dispersal, and later toward regions of low dynamic topography during reaggregation. Both phases involve continental motion down topography gradients, which should produce sea-level rise. We thus expect a corresponding sea-level drop during the supercontinent phase of the Wilson cycle, which can be ~150 Ma long (e.g., Hoffman, 1991). If supercontinent breakup occurs because of mantle upwelling (Gurnis, 1988; Lowman and Jarvis, 1999), then the downwelling that originally aggregated the supercontinent (note that subduction, and thus downwelling, is necessary for ocean basin closure) must develop into an upwelling. Considering that the net stress that the mantle exerts on the surface must always integrate to zero, a net uplift of the continental side of Earth during the lifetime of a supercontinent should accompany a net depression of the oceanic side of Earth, which would lower sea level. Note that supercontinents are likely to be surrounded by subduction zones during their lifetime, and a fully developed downwelling system within the oceanic side of Earth is not necessarily expected (Zhong et al., 2007). However, such a downwelling system is not necessarily required: we have inferred a net depression of the oceanic seafloor because net uplift must have occurred on the supercontinent. Therefore, uplifted seafloor on the oceanic side simply becomes less uplifted during the lifetime of a supercontinent, which would drop sea level.

This analysis suggests a cycle of net sea-level drop during the supercontinent phase of the Wilson cycle caused by a net decrease in dynamic topography in oceanic areas (e.g., Fig. 1, mode 1), followed by sea-level rise during the dispersal and reaggregation phases caused by net continental motion away from the uplifted center of a supercontinent (Fig. 1, mode 2). This pattern largely follows the gross pattern of sea-level trends: a period of sea-level fall (ca. 450 to ca. 250 Ma) (Cogné and Humler, 2008) occurred approximately during Pangean stability (ca. 400 and ca. 200 Ma) (Collins, 2003) followed by a period of sea-level rise during continental breakup (ca. 200 and ca. 100 Ma) (Cogné and Humler, 2008). Of course, dynamic topography is only one of several factors that affect sea level, so we do not expect a pure correlation between sea level and the Wilson cycle. For example, changes in the volume of the mid-ocean-ridge system are thought to be responsible for some of the most recent 100–200 m drop in sea level during the past ~100 Ma (e.g., Xu et al., 2006; Müller et al., 2008), which occurred during a period of continental dispersal. Furthermore, the complexity and time-dependence of mantle flow will produce aspects of flow that may not be directly associated with the Wilson cycle, such as the growing upwelling beneath the Pacific basin (Fig. 2A), which is currently responsible for much of the present-day predicted sea-level rise (Fig. 5B). Nevertheless, we anticipate that dynamic topography may be responsible for up to ~100 m of sea-level rise during times of supercontinent dispersal and reaggregation (as is presently observed) and a similar

amount of sea-level drop during times of supercontinent stability. Thus, the effect of dynamic topography on sea-level change should be comparable in magnitude to other major causes of sea-level rise or fall.

CONCLUSIONS

We have estimated that sea level is currently higher by ~90 ± 20 m due to the convective dynamics of the mantle interior. This time-dependent deflection of the seafloor by dynamic topography is presently causing sea level to rise at rates that may be as high as 1.0 m/Ma. Much of the associated uncertainty is due to the poorly constrained mantle viscosity structure, but it is also due to the difficulty of constraining the time-dependence of downwelling mantle flow. Because mantle downwelling causes dense slabs to fall away from Earth's surface, the dynamic topography they induce at that surface will get smaller with time. Unless global mantle flow models can accurately reinject slabs into the upper mantle at subduction zones, such models cannot reliably constrain the influence of mantle downwelling on sea-level change. At present, time-dependent treatment of subduction zones is more accurately realized in idealized (e.g., Gurnis, 1990) or analytic (Husson and Conrad, 2006) models, which should produce better constraints on downwelling-induced sea-level change compared to advection-dominated models of global mantle flow such as this study or Moucha et al. (2008).

The motion of the continents over Earth's dynamic topography can cause between 0.3 m/Ma of sea-level rise and 0.3 m/Ma of sea-level fall, depending on the net motion of the lithosphere relative to the deep mantle. Together with a net positive contribution of up to 1 m/Ma from growing mantle upwellings, our estimates suggest a wide range of sea-level rise contributions, but they do indicate that dynamic topography is probably currently producing net sea-level rise with a median value of ~0.5 m/Ma. This rate is significantly smaller than the rate implied by the 100 m of rise in 30 Ma (3.3 m/Ma) estimated by Moucha et al. (2008). We note, however, that Moucha et al.'s (2008) study included significant (~2 km) dynamic topography near mid-ocean ridges, which may be associated with low-velocity anomalies that have been imaged tomographically beneath ridges above 200 km depth (e.g., Ritsema et al., 2004). We do not include these features in our model because near-surface mantle anomalies will be strongly affected by both thermal diffusion and the details of the plate boundary implementation, both of which are difficult to implement in a time-dependent, backward-advection model (e.g., Conrad and Gurnis, 2003). Nevertheless, many of the dynamic topography trends predicted here (e.g., Fig. 3) are similar to those predicted by Moucha et al. (2008), who also showed large areas of the Pacific and circum-African ocean basins becoming shallower with time.

We have argued that a combination of continental motion and dynamic seafloor uplift should sustain as much as ~1 m/Ma of sea-level rise during the ongoing continental dispersal phase of the Wilson cycle. When included within a global tally of estimates for the various Cenozoic sea-level change mechanisms (Fig. 6), the dynamic topography contribution (~65 m rise) is comparable in magnitude to the net sea-level drop due to ice-sheet formation (~50 m; Harrison, 1990) or ocean area increase due to the India-Asia collision (~25 m; Harrison, 1990). It is also comparable to the uncertain rise that may be associated with the increased sedimentation and seafloor volcanism that are associated with increasing seafloor age (~60 and ~20 m, respectively; Müller et al., 2008; Harrison, 1990). Only ridge volume changes, estimated at 125–250 m by Xu et al. (2006) and ~200 m by Müller et al. (2008), are significantly more important as a Cenozoic source (Fig. 6). As a result, the introduction of a persistent dynamic topography–induced sea-level rise to the global tally (Fig. 6) produces a predicted Cenozoic sea-level change (140 m) that lies approximately midway between the curves presented in Haq et al. (1987) and Miller et al. (2005), which estimate sea-level drops of 240 m and 50 m, respectively. Previous studies (e.g., Müller et al., 2008; Spasojeviç et al., 2008) have inferred that some of the discrepancy between these curves is associated with subsidence of the U.S. east coast, where the measurements by Miller et al. (2005) were made. Our study suggests that as much as 1 m/Ma of eustatic sea-level rise is caused by the time-dependent nature of dynamic topography, and it should be included in attempts to match observations of long-term sea-level change to tallies of the various sources of that change.

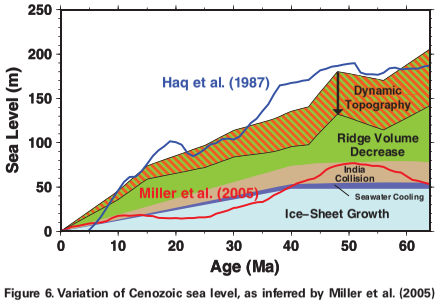

Figure 6. Variation of Cenozoic sea level, as inferred by Miller et al. (2005) (red line) and by Haq et al. (1987) (blue line), and the relative amplitudes of the different possible sources of this sea-level change. The effects of ice-sheet growth (light blue), seawater cooling (dark blue), and continental area shrinkage resulting from India-Asia collision (brown) are estimated from Harrison (1990). The effect of ridge volume decrease is estimated using the Hall (2002) case of Xu et al. (2006), and it is shown in green. Finally, the possible effect of dynamic topography is shown in red hatches, and produces sea-level rise of up to 1 m/Ma, based on the estimates determined here.

ACKNOWLEDGMENTS

This work was supported by National Science Foundation (NSF) grant EAR-0914712 (to Conrad). We thank S. Zhong and another anonymous referee for critical reviews that greatly improved the manuscript, and C. Lithgow-Bertelloni for helpful discussions and comments.

REFERENCES CITED

Becker, T.W., 2006, On the effect of temperature and strain-rate dependent viscosity on global mantle flow, net rotation, and plate-driving forces: Geophysical Journal International, v. 167, p. 943–957, doi: 10.1111/j.1365-246X.2006.03172.x.

Becker, T.W., 2008, Azimuthal seismic anisotropy constrains net rotation of the lithosphere: Geophysical Research Letters, v. 35, p. L05303, doi: 10.1029/2007GL032928.

Bokelmann, G.H.R., 2002, Which forces drive North America?: Geology, v. 30, p. 1027–1030, doi: 10.1130/0091-7613(2002)030<1027:WFDNA>2.0.CO;2.

Bond, G.C., 1976, Evidence for continental subsidence in North America during the Late Cretaceous global submergence: Geology, v. 4, p. 557–560, doi: 10.1130/0091-7613(1976)4<557:EFCSIN>2.0.CO;2.

Bunge, H.-P., and Grand, S.P., 2000, Mesozoic plate-motion history below the northeast Pacific Ocean from seismic images of the subducted Farallon slab: Nature, v. 405, p. 337–340, doi: 10.1038/35012586.

Cadek, O., and Fleitout, L., 2003, Effect of lateral viscosity variations in the top 300 km on the geoid and dynamic topography: Geophysical Journal International, v. 152, p. 566–580, doi: 10.1046/j.1365-246X.2003.01859.x.

Cogné, J.-P., and Humler, E., 2008, Global scale patterns of continental fragmentation: Wilson's cycles as a constraint for long-term sea-level changes: Earth and Planetary Science Letters, v. 273, p. 251–259, doi: 10.1016/j.epsl.2008.06.030.

Cogné, J.-P., Humler, E., and Courtillot, V., 2006, Mean age of oceanic lithosphere drives eustatic sea-level change since Pangea breakup: Earth and Planetary Science Letters, v. 245, p. 115–122, doi: 10.1016/j.epsl.2006.03.020.

Colin, P., and Fleitout, L., 1990, Topography of the ocean floor: Thermal evolution of the lithosphere and interaction of deep mantle heterogeneities with the lithosphere: Geophysical Research Letters, v. 17, p. 1961–1964, doi: 10.1029/GL017i011p01961.

Collins, W.J., 2003, Slab pull, mantle convection, and Pangaean assembly and dispersal: Earth and Planetary Science Letters, v. 205, p. 225–237, doi: 10.1016/S0012-821X(02)01043-9.

Conrad, C.P., and Gurnis, M., 2003, Mantle flow, seismic tomography and the breakup of Gondwanaland: Integrating mantle convection backwards in time: Geochemistry, Geophysics, Geosystems, v. 4, p. 1031, doi: 10.1029/2001GC000299.

Conrad, C.P., and Lithgow-Bertelloni, C., 2006, Influence of continental roots and asthenosphere on plate-mantle coupling: Geophysical Research Letters, v. 33, p. L05312, doi: 10.1029/2005GL025621.

Conrad, C.P., Lithgow-Bertelloni, C., and Louden, K.E., 2004, Iceland, the Farallon slab, and dynamic topography of the North Atlantic: Geology, v. 32, p. 177–180, doi: 10.1130/G20137.1.

Conrad, C.P., Behn, M.D., and Silver, P.G., 2007, Global mantle flow and the development of seismic anisotropy: Differences between the oceanic and continental upper mantle: Journal of Geophysical Research, v. 112, p. B07317, doi: 10.1029/2006JB004608.

DeMets, C., Gordon, R.G., Argus, D.F., and Stein, S., 1994, Effect of recent revisions to the geomagnetic reversal time scale on estimates of current plate motions: Geophysical Research Letters, v. 21, p. 2191–2194, doi: 10.1029/94GL02118.

Gripp, A.E., and Gordon, R.G., 2002, Young tracks of hotspots and current plate velocities: Geophysical Journal International, v. 150, p. 321–361, doi: 10.1046/j.1365-246X.2002.01627.x.

Gurnis, M., 1988, Large-scale mantle convection and the aggregation and dispersal of supercontinents: Nature, v. 332, p. 695–699, doi: 10.1038/332695a0.

Gurnis, M., 1990, Ridge spreading, subduction, and sea-level fluctuations: Science, v. 250, p. 970–972, doi: 10.1126/science.250.4983.970.

Gurnis, M., 1993, Phanerozoic marine inundation of continents driven by dynamic topography above subducting slabs: Nature, v. 364, p. 589–593, doi: 10.1038/364589a0.

Gurnis, M., Mitrovica, J.X., Ritsema, J.E., and van Heijst, H.-J., 2000, Constraining mantle density structure using geological evidence of surface uplift rates: The case of the African Superplume: Geochemistry, Geophysics, Geosystems, v. 1, 1999GC000035, doi: 10.1029/1999GC000035.

Hager, B.H., 1984, Subducted slabs and the geoid: Constraints on mantle rheology and flow: Journal of Geophysical Research, v. 89, p. 6003–6015, doi: 10.1029/JB089iB07p06003.

Hager, B.H., Clayton, R.W., Richards, M.A., Comer, R.P., and Dziewonski, A.M., 1985, Lower mantle heterogeneity, dynamic topography and the geoid: Nature, v. 313, p. 541–545, doi: 10.1038/313541a0.

Hall, R., and Spakman, W., 2002, Subducted slabs beneath the eastern Indonesia–Tonga region: insights from tomography: Earth and Planetary Science Letters, v. 201, p. 321–336, doi: 10.1016/S0012-821X(02)00705-7.

Harrison, C.G.A., 1990, Long-term eustasy and epeirogeny in continents, *in* Revelle, R.R., ed., Sea-Level Change: Washington, D.C., National Academy Press, p. 141–158.

Haq, B.U., Hardenbol, J., and Vail, P.R., 1987, Chronology of fluctuating sea levels since the Triassic: Science, v. 235, p. 1156–1167, doi: 10.1126/science.235.4793.1156.

Heine, C., Müller, R.D., Steinberger, B., and Torsvik, T.H., 2008, Subsidence in intracontinental basins due to dynamic topography: Physics of the Earth and Planetary Interiors, v. 171, p. 252–264, doi: 10.1016/j.pepi.2008.05.008.

Hernlund, J.W., Tackley, P.J., and Stevenson, D.J., 2008, Buoyant melting instabilities beneath extending lithosphere: 1. Numerical models: Journal of Geophysical Research, v. 113, B04405, doi: 10.1029/2006JB004862.

Hoffman, P.F., 1991, Did the breakout of Laurentia turn Gondwanaland inside-out?: Science, v. 252, p. 1409–1412, doi: 10.1126/science.252.5011.1409.

Husson, L., 2006, Dynamic topography above retreating subduction zones: Geology, v. 34, p. 741–744, doi: 10.1130/G22436.1.

Husson, L., and Conrad, C.P., 2006, Tectonic velocities, dynamic topography, and relative sea level: Geophysical Research Letters, v. 33, L18303, doi: 10.1029/2006GL026834.

Husson, L., Conrad, C.P., and Faccenna, C., 2008, Tethyan closure, Andean orogeny, and westward drift of the Pacific basin: Earth and Planetary Science Letters, v. 271, p. 303–310, doi: 10.1016/j.epsl.2008.04.022.

Jordan, T.H., 1975, The continental tectosphere: Reviews of Geophysics, v. 13, p. 1–12, doi: 10.1029/RG013i003p00001.

Karato, S.-I., and Karki, B.B., 2001, Origin of lateral variation of seismic wave velocities and density in the deep mantle: Journal of Geophysical Research, v. 106, p. 21,771–21,783, doi: 10.1029/2001JB000214.

Kominz, M.A., 1984, Oceanic ridge volumes and sea level change—An error analysis, *in* Schlee, J., ed., Interregional Unconformities and Hydrocarbon Accumulation: American Association of Petroleum Geologists Memoir 36, p. 109–127.

Le Stunff, Y., and Ricard, Y., 1997, Partial advection of equidensity surfaces: A solution for the dynamic topography problem?: Journal of Geophysical Research, v. 102, p. 24,655–24,667, doi: 10.1029/97JB02346.

Lithgow-Bertelloni, C., and Gurnis, M., 1997, Cenozoic subsidence and uplift of continents from time-varying dynamic topography: Geology, v. 25, p. 735–738, doi: 10.1130/0091-7613(1997)025<0735:CSAUOC>2.3.CO;2.

Lithgow-Bertelloni, C., and Richards, M.A., 1998, The dynamics of Cenozoic and Mesozoic plate motions: Reviews of Geophysics, v. 36, p. 27–78, doi: 10.1029/97RG02282.

Lithgow-Bertelloni, C., and Silver, P.G., 1998, Dynamic topography, plate-driving forces and the African superswell: Nature, v. 395, p. 269–272, doi: 10.1038/26212.

Liu, L., Spasojeviç, S., and Gurnis, M., 2008, Reconstructing Farallon plate subduction beneath North America back to the Cretaceous: Science, v. 322, p. 934–938, doi: 10.1126/science.1162921.

Lowman, J.P., and Jarvis, G.T., 1999, Effects of mantle heat source distribution on supercontinent stability: Journal of Geophysical Research, v. 104, p. 12,733–12,746, doi: 10.1029/1999JB900108.

Masters, G., Laske, G., Bolton, H., and Dziewonski, A., 2000, The relative behavior of shear velocity, bulk sound speed, and compressional velocity in the mantle: Implications for chemical and thermal structure, *in* Karato, S.-I., Forte, A.M., Liebermann, R.C., Masters, G., and Stixrude, L., eds., Earth's Deep Interior. Mineral Physics and Tomography from the Atomic to the Global Scale: American Geophysical Union (AGU) Monograph Series, Seismology and Mineral Physics, v. 117, p. 63–87.

Miller, K.G., Kominz, M.A., Browning, J.V., Wright, J.D., Mountain, G.S., Katz, M.E., Sugarman, P.J., Cramer, B.S., Christie-Blick, N., and Pekar, S.F., 2005, The Phanerozoic record of global sea-level change: Science, v. 310, p. 1293–1298, doi: 10.1126/science.1116412.

Mitrovica, J.X., 1996, Haskell (1935) revisited: Journal of Geophysical Research, v. 101, p. 555–569, doi: 10.1029/95JB03208.

Mitrovica, J.X., Beaumont, C., and Jarvis, G.T., 1989, Tilting of continental interiors by the dynamical effects of subduction: Tectonics, v. 8, p. 1079–1094, doi: 10.1029/TC008i005p01079.

Moucha, R., Forte, A.M., Mitrovica, J.X., and Daradich, A., 2007, Geodynamic implications of lateral variations in mantle rheology on convection related observables and inferred viscosity models: Geophysical Journal International, v. 169, p. 113–135, doi: 10.1111/j.1365-246X.2006.03225.x.

Moucha, R., Forte, A.M., Mitrovica, J.X., Rowley, D.B., Quere, S., Simons, N.A., and Grand, S.P., 2008, Dynamic topography and long-term sea-level variations: There is no such thing as a stable continental platform: Earth and Planetary Science Letters, v. 271, p. 101–108, doi: 10.1016/j.epsl.2008.03.056.

Müller, R.D., Sdrolias, M., Gaina, C., Steinberger, B., and Heine, C., 2008, Long-term sea-level fluctuations driven by ocean basin dynamics: Science, v. 319, p. 1357–1362, doi: 10.1126/science.1151540.

Paulson, A., Zhong, S., and Wahr, J., 2005, Modelling post-glacial rebound with lateral viscosity variations: Geophysical Journal International, v. 163, p. 357–371, doi: 10.1111/j.1365-246X.2005.02645.x.

Paulson, A., Zhong, S., and Wahr, J., 2007, Inference of mantle viscosity from GRACE and relative sea level data: Geophysical Journal International, v. 171, p. 497–508.

Phillips, B.R., and Bunge, H.P., 2005, Heterogeneity and time dependence in 3D spherical mantle convection models with continental drift: Earth and Planetary Science Letters, v. 233, p. 121–135, doi: 10.1016/j.epsl.2005.01.041.

Pitman, W.C., 1978, Relationship between eustasy and stratigraphic sequences of passive margins: Geological Society of America Bulletin, v. 89, p. 1389–1403, doi: 10.1130/0016-7606(1978)89<1389:RBEASS>2.0.CO;2.

Ritsema, J., van Heijst, H.J., and Woodhouse, J.H., 2004, Global transition zone tomography: Journal of Geophysical Research, v. 109, B02302, doi: 10.1029/2003JB002610.

Sdrolias, M., and Müller, R.D., 2006, Controls on back-arc basin formation: Geochemistry, Geophysics, Geosystems, v. 7, Q04016, doi: 10.1029/2005GC001090.

Spasojeviç, S., Liu, L., Gurnis, M., and Müller, R.D., 2008, The case for dynamic subsidence of the U.S. east coast, since the Eocene: Geophysical Research Letters, v. 35, L08305, doi: 10.1029/2008GL033611.

Tan, E., Choi, E., Thoutireddy, P., Gurnis, M., and Aivazis, M., 2006, GeoFramework: Coupling multiple models of mantle convection within a computational framework: Geochemistry, Geophysics, Geosystems, v. 7, Q06001, doi: 10.1029/2005GC001155.

Thoraval, C., and Richards, M.A., 1997, The geoid constraint in global geodynamics: Viscosity structure, mantle heterogeneity models and boundary conditions: Geophysical Journal International, v. 131, p. 1–8, doi: 10.1111/j.1365-246X.1997.tb00591.x.

Torsvik, T.H., Müller, R.D., Van der Voo, R., Steinberger, B., and Gaina, C., 2008, Global plate motion frames: Toward a unified model: Reviews of Geophysics, v. 46, RG3004, doi: 10.1029/2007RG000227.

van der Hilst, R., 1995, Complex morphology of subducted lithosphere in the mantle beneath the Tonga Trench: Nature, v. 374, p. 154–157, doi: 10.1038/374154a0.

Wilson, J.T., 1966, Did the Atlantic close and then re-open?: Nature, v. 211, p. 676–681, doi: 10.1038/211676a0.

Xu, X., Lithgow-Bertelloni, C., and Conrad, C.P., 2006, Global reconstructions of Cenozoic seafloor ages: Implications for bathymetry and sea level: Earth and Planetary Science Letters, v. 243, p. 552–564, doi: 10.1016/j.epsl.2006.01.010.

Zhong, S., and Davies, G.F., 1999, Effects of plate and slab viscosities on geoid: Earth and Planetary Science Letters, v. 170, p. 487–496, doi: 10.1016/S0012-821X(99)00124-7.

Zhong, S., Zuber, M.T., Moresi, L., and Gurnis, M., 2000, Role of temperature-dependent viscosity and surface plates in spherical shell models of mantle convection: Journal of Geophysical Research, v. 105, p. 11,063–11,082, doi: 10.1029/2000JB900003.

Zhong, S., Zhang, N., Li, Z.-X., and Roberts, J.H., 2007, Supercontinent cycles, true polar wander, and very long-wavelength mantle convection: Earth and Planetary Science Letters, v. 261, p. 551–564, doi: 10.1016/j.epsl.2007.07.049.

Zhong, S., McNamara, A., Tan, E., Moresi, L., and Gurnis, M., 2008, A benchmark study on mantle convection in a 3-D spherical shell using CitcomS: Geochemistry, Geophysics, Geosystems, v. 9, Q10017, doi: 10.1029/2008GC002048.

MANUSCRIPT RECEIVED 11 NOVEMBER 2008
REVISED MANUSCRIPT RECEIVED 23 FEBRUARY 2009
MANUSCRIPT ACCEPTED 27 FEBRUARY 2009

Printed in the USA

Sur des temps caractéristiques plus courts, les variations du niveau marin ont été corrélées à des périodes d'intensification de la productivité des dorsales, conduisant à un rajeunissement moyen du plancher océanique et une augmentation du niveau marin [Hays & Pitman, 1973]. Un pulse de production aux dorsales océaniques s'accompagne, par conservation de la surface de la Terre, d'un pulse de subduction, ce qui a conduit Gurnis à proposer que l'impact sur le niveau marin soit amplifié puisqu'une subduction plus dynamique s'accompagne d'une déflection dynamique également plus forte. Il s'agit alors d'une variation relative du niveau marin, qui est proposée comme mécanisme conduisant à une augmentation apparente du niveau marin pendant les transgressions, au Crétacé en particulier [Gurnis, 1992]. En créant un réservoir d'eau de mer local ou en augmentant sa dimension, un pulse tectonique affecte également le niveau marin absolu : les effets de la topographie dynamique sur le niveau marin pourraient alors compenser ceux de la dorsale. Dans l'article suivant, toujours en collaboration avec C. Conrad, nous ré-évaluons l'impact sur le niveau marin moyen sur la base de modèles analytiques couplés, isostatiques pour la bathymétrie océanique, et dynamique à l'aplomb des subductions. Nous montrons que c'est en général l'effet inverse qui se produit puisque le champ de densité dans le manteau se retrouve également modifié : de fortes vitesses tectoniques s'accompagnent d'une topographie dynamique plus faible à l'aplomb de panneaux plongeants plus jeunes et moins denses, conduisant à une diminution du niveau absolu des mers.

GEOPHYSICAL RESEARCH LETTERS, VOL. 33, L18303, doi:10.1029/2006GL026834, 2006

Click Here for Full Article

Tectonic velocities, dynamic topography, and relative sea level

Laurent Husson[1,2] and Clinton P. Conrad[3]

Received 8 May 2006; revised 10 July 2006; accepted 24 July 2006; published 19 September 2006.

[1] A simple dynamic model based on boundary layer theory shows that dynamic topography is unlikely to vary significantly in response to short term ($\leq$20 Myr) variations in the mean tectonic velocity. Tectonic velocities essentially mirror variations in mantle viscosity, but are not indicative of substantial modification of dynamic topography, which primarily reflects mass anomalies in the mantle. This implies that relative sea level is unlikely to be affected by "tectonic pulses" and also that observed tilting of cratonic margins cannot result from a pulse of increased tectonic velocities. Thus, relative sea level is primarily controlled by the seafloor age distribution, although long term ($\geq$100 Myrs) changes in tectonic velocity will produce dynamic topography that reinforces sea level changes associated with changing ridge volume. **Citation:** Husson, L., and C. P. Conrad (2006), Tectonic velocities, dynamic topography, and relative sea level, *Geophys. Res. Lett.*, *33*, L18303, doi:10.1029/2006GL026834.

1. Introduction

[2] Changes in ridge volume and the seafloor age distribution were the first obvious candidates to explain relative sea level change [e.g., *Hays and Pitman*, 1973; *Kominz*, 1984], which was seen as a eustatic process [e.g., *Vail et al.*, 1977]. Because sea level is observed via flooding of continental margins, subduction-related, epeirogenic processes have also been invoked [*Mitrovica et al.*, 1989]: observed transgressions could reflect the dynamic tilting of continents above sinking slabs, and may be enhanced by faster tectonic velocities [*Gurnis*, 1990, 1993]. This reasoning, which is valid for subduction onset or cessation, has also been applied to eustatic sea level: increased negative dynamic topography above more rapidly subducting slabs may compensate, and even overcome, the effect of increased ridge volume associated with faster spreading rates [*Hager*, 1980].

[3] In order to evaluate this competition, most studies are based on semi-dynamic models where tectonic velocity is an input. Therefore, it has been argued that fast subduction stuffs dense material into the upper mantle at high rates, causing it to accumulate and generate large dynamic topography [*Gurnis*, 1990]. Such interpretations, however, do not account for the dynamic equilibrium between mantle temperature and tectonic velocities. Because slabs are thought to drive plate motions [*Conrad and Lithgow-Bertelloni*, 2004], tectonic velocities must be regarded as the result of the density contrast within the mantle and not as its cause. Thus, plate and slab velocities must be consistent with (i) their intrinsic buoyancy and (ii) the density and viscosity of the mantle, as they are in several dynamically-consistent studies [e.g., *Mitrovica et al.*, 1989; *Ricard and Vigny*, 1989] (we discard dynamic fluctuations in upwellings as a control on plate dynamics below). These interactions can be captured by a simple, yet dynamically consistent, analysis based on steady-state boundary layer theory that evaluates the competition between seafloor age distribution and dynamic topography.

[1]Massachusetts Institute of Technology, Cambridge, Massachusetts, USA.

[2]Now at Géosciences Rennes, UMR CNRS 6118, Université de Rennes 1, Campus de Beaulieu, Rennes, France.

[3]Department of Earth and Planetary Sciences, Johns Hopkins University, Baltimore, Maryland, USA.

Copyright 2006 by the American Geophysical Union.
0094-8276/06/2006GL026834$05.00

2. Dynamic Topography in a Convective System

[4] Dynamic topography is the vertical component of the response of an interface, like the surface of the Earth, to the viscous flow of the underlying fluid. In a highly viscous system like the mantle, inertia is negligible and dynamic topography is independent of viscosity for a uniform Newtonian fluid [*Morgan*, 1965]. Therefore the dynamic volume of the deflected Earth surface can be reduced to an integral function of the mass heterogeneities in the Earth's mantle. Note that support of slabs by a high-viscosity lower mantle may decrease dynamic topography amplitudes at the surface [*Hager*, 1984]. Thus, our use of a mantle of uniform viscosity leads to upper bounds on dynamic volumes in the analysis below. In a chemically uniform convective system, density heterogeneities only depend on the thermal state of the mantle. In such a case, the key parameter affecting dynamic topography is the temperature of the mantle, which sets the magnitude of the density contrast and the volume of these density heterogeneities (i.e., the volume of the slab).

2.1. Plate Velocity and Boundary Layer Theory

[5] Boundary layer theory satisfactorily explains the structure and kinematics of a convecting Earth (see *Bercovici et al.* [2000] for a review). The buoyancy force F_B that drives the subduction is balanced by the drag forces F_{D_h} and F_{D_v} that act on the horizontal and vertical boundaries of the convection cell. Following the derivation of [*Turcotte and Schubert*, 2002], the forces per unit length are:

$$F_B = \rho_0 \alpha T_m g b \frac{\overline{u}}{\overline{v}} \left(\frac{\kappa\lambda}{\pi\overline{u}}\right)^{1/2}, \qquad F_{D_h} = 2\mu a\overline{u}; F_{D_v} = 2\frac{\mu}{a}\overline{v}. \tag{1}$$

$\rho_0\alpha T_m/2$ is the mean density contrast within the mantle, ρ_0 is the reference density for the mantle, α is the coefficient of thermal expansion, T_m the temperature increase in the mantle ($T_m/2$ is the temperature in the core of the convective mantle assuming a symmetric temperature profile), and κ is

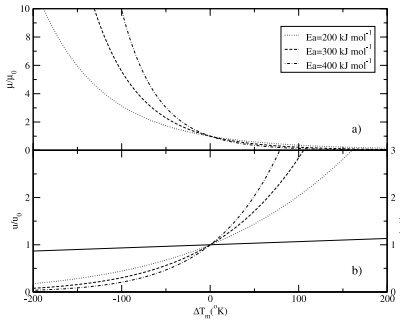

Figure 1. (a) Mantle viscosity variation as a function of changes in mantle temperature, ΔT_m; (b) Variations in the density contrast $\delta\rho$ through the mantle (right axis, solid line) and viscosity (left axis, broken lines) as a function of mean temperature variation in the mantle. Calculations are performed for different activation energies. Reference values are taken for present day ($T_{m0} = 3000K$, $u_0 = 3.1$ cm yr^{-1}, $b = 2800$ km, $\alpha = 3 \times 10^{-5}$ K^{-1}, $\rho_a = 3250$ kg m^{-3}), and an aspect ratio $a = 1$.

the thermal diffusivity. a is the mean aspect ratio of the convection cell, i.e. the ratio of its width λ over its thickness b, g is the acceleration of gravity, $\overline{u}$ is the average velocity of the upper and lower boundary layers, and $\overline{v}$ is the vertical velocity of these layers after foundering.

[6] A force balance leads to a relation between $\overline{u}$ and the Rayleigh number Ra:

$$\overline{u} = \frac{\kappa}{b}\frac{a^{7/3}}{(1+a^4)^{2/3}}\left(\frac{Ra}{2\sqrt{\pi}}\right)^{2/3} \quad (2)$$

where $Ra = \frac{\rho_0 \alpha T_m g b^3}{\mu \kappa}$. Note that this relation becomes flawed for stiff lithospheres ($\sim 10^{23}$ Pa s [*Conrad and Hager*, 1999]).

2.2. Average Mantle Temperature

[7] The temperature-dependent viscosity μ is given by

$$\mu = \mu_0 \exp\left[\frac{E_a}{RT_m/2} - \frac{E_a}{RT_{m0}/2}\right], \quad (3)$$

where E_a is the activation energy of olivine, R is the gas constant, and μ_0 is the viscosity at the reference average temperature $T_{m0}/2$. Although T_m is the only free parameter, μ is extremely sensitive to T_m due to the exponential nature of their relationship (Figure 1a). By combining equations 2 and 3 and setting $a = 1$, we write:

$$\overline{u} = \kappa^{1/3} b \left[\frac{\rho_0 \alpha T_m g}{4\sqrt{\pi}\mu_0 \exp\left(\frac{E_a}{RT_m/2} - \frac{E_a}{RT_{m0}/2}\right)}\right]^{2/3}. \quad (4)$$

Any variation in the vigor of the convection (as measured by Ra) should be mirrored by a variation in $\overline{u}$ (equation 2). Conversely, any observed variation in $\overline{u}$ implies a variation in T_m, which is the only free parameter in Ra. Equation 4 allows us to relate plate velocity variations to departures ΔT_m from the current mantle temperature (Figure 1b). Our choice of $\mu_0 = 6.1 \times 10^{22}$ Pa s is based on inferred present-day values for a whole mantle convection scheme (see reference values in Figure 1), and is in the range of independent estimates [*Lambeck and Chappell*, 2001; *Mitrovica and Forte*, 2004]. Possible values for E_a for diffusion creep of olivine range from ~200 to more than 400 kJ/mol [*Hirth and Kohlstedt*, 1995, 2003; *Korenaga and Jordan*, 2002], leading to a large uncertainty in μ due to its position in the exponential (Figure 1a). Because viscosity depends exponentially on E_a, it influences velocity significantly. An increase in T_m by ~45 K is needed to double the value of $\overline{u}$ with $E_a = 400$ kJ mol^{-1} whereas as much as ~100K is needed with $E_a = 200$ kJ mol^{-1} (Figure 1b).

[8] Because it depends exponentially on T_m, viscosity can vary by one to two orders of magnitude for reasonable changes in T_m (Figure 1a), while the density contrast increases by only ~6.5% per 100K temperature increase (Figure 1b). This implies that any changes to Ra are dominated by viscosity, not density, variations.

2.3. Dynamic Volume

[9] To first order, dynamic topography H is a linear function of the mass anomalies at depth. For a subduction zone, slab mass can be expressed as a function of slab volume and density contrast $\rho_0 \alpha T_m/2$. Both quantities may change with time due to changes in plate velocity (4) or the aspect ratio of the convective cell (2). According to (2) an increase in aspect ratio ($a > 1$) leads to a decrease in Ra, and thus a decrease in T_m for constant $\overline{u}$. However, the decrease in T_m is a maximum of 25K and modifies dynamic topography by only 3%. A decrease in aspect ratio, while leading to a larger T_m increase, is unphysical for the Earth.

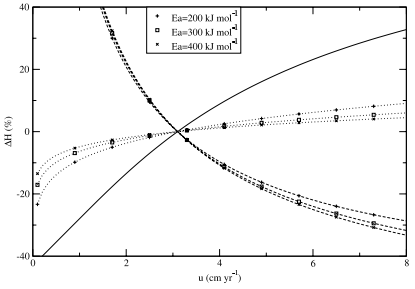

Figure 2. Relative variations of the dynamic volume as a function of mean plate velocity for an instantaneous (short-lived) departure from the 3.1 cm yr^{-1} reference tectonic velocity (dotted lines) and a change to a new steady state velocity (dashed lines). The variation in the volume of a half-ridge is shown for comparison (solid line). Note that changes in the absolute ridge volume are generally 1.5 to 6 times larger than instantaneous changes in the absolute dynamic volume. E_a is the activation energy, other parameters are as in Figure 1.

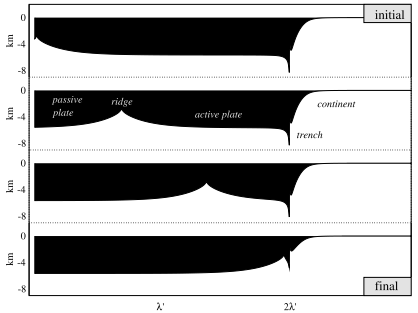

Figure 3. Evolution of the modeled morphologies (here calculated for $\overline{u}$ = 3.1 cm/yr). Trench morphology is dynamic, see text for details.

[10] Instantaneous variations in tectonic velocity do not affect the volume of subducted material, and thus cause only small (5–7%) changes in dynamic topography associated with the inferred change in T_m (Figure 2, dotted lines). Long-term variations in velocity may arise, for instance because of the blanketing effect of continents [e.g., *Trubitsyn et al.*, 2003], and should lead to thinner slabs because plates are younger when they subduct. In steady state [see *Turcotte and Schubert*, 2002], the thickness of the boundary layer δ varies as

$$\delta = 1.7\frac{b}{Ra^{1/3}}. \quad (5)$$

The volume of the slab is its length times its thickness. Thus assuming similarity between the thickness of the conductive and the mechanical layers, the volume also varies as $Ra^{-1/3}$. Dynamic topography is expected to vary linearly with the volume of the slab, and therefore with its thickness δ. We evaluate δ as a function of $\overline{u}$ (or T_m) from equation 2 and 5 and get

$$\delta = \frac{1.7}{(2\sqrt{\pi})^{1/3}}\left(\frac{b\kappa}{\overline{u}}\right)^{1/2}, \quad (6)$$

which shows that δ varies as $u^{-1/2}$. Figure 2 (dashed lines) shows the relative variation of dynamic topography accounting for both density and plate thickness variations consistent with a long-term change in average plate velocity. The effect of plate thickness variations opposes and overcomes that of density variations; it can modify the dynamic volume by ±25% for a reasonable range of velocities.

[11] Long-term thermal disturbances are expected to accompany the Wilson cycle and should obey (6). Unfortunately, we do not have access to plate velocities over an entire cycle to verify this correlation. However, if the above relationship is correct, the dynamic volume would be smaller during periods of a warmer mantle characteristic of a supercontinental setting compared to times after continental breakup, when temperatures (and presumably tectonic velocities) are lower.

3. Examples

3.1. The Model

[12] Following the formulation of section 2, we constructed an idealized system that incorporates a spreading ridge moving toward a subduction zone (somewhat akin to the Mesozoic-Cenozoic disappearance of the Farallon plate). The modeled section is one period of an idealized periodic Earth-like system. In order to keep a surface balance for the model, plate formation is balanced by plate destruction. This implies that subduction rates and trench migration rates are linear functions of spreading rates. The basin volume above the ridge is calculated from the age-depth relationship of cooling seafloor [after *Stein and Stein*, 1992]. The dynamic volume above the subducting slab is calculated for a sine-shaped thin sheet slab sinking to a depth of 670 km with a half-wavelength of 500 km (slabs in the lower mantle are neglected). The slab is discretized into horizontal mass lines (or linear *Stokeslets*) sinking vertically; the total Stokes flow is given by the sum of the elementary *Stokeslets* [*Morgan*, 1965; *Batchelor*, 1967; *Davies*, 1981; *Harper*, 1984; *Husson*, 2006]. Stresses normal to the surface are calculated using the "image" technique [*Morgan*, 1965], which accounts for the presence of the surface interface. The buoyancy of the subducting material is computed from the age of the oceanic lithosphere at the time it subducts, and compared to the density of the asthenosphere, as calculated in section 2.

[13] Although not readily applicable to Earth's history, the following examples encompass most possible scenarii. The reference tectonic velocity is set to $\overline{u}$ = 3.1 cm yr^{-1} (mean present-day half-spreading rates, *Cogné and Humler* [2004]), from which T_{m0}, μ_0 and δ are calculated. The initial state (Figure 3, top) is set to an end-member situation, where the entire ocean consists of a plate of length $2\lambda'$ subducting beneath a continent of length λ'. The length

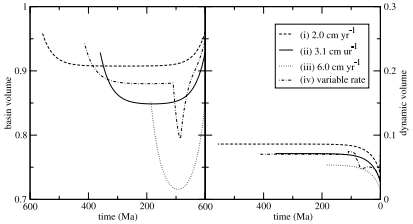

Figure 4. Changes in ridge volume associated with (a) the evolving age distribution of the seafloor and (b) changes in the dynamic volume associated with changes in subduction-induced dynamic topography. In each case, the volume is given as a fraction of the total volume of the ocean basin relative to the initial volume (basin volume + dynamic volume) of the reference case (Figure 3, top). Here 0 Ma (present-day) is the final state.

scale λ' is the plate length produced in 180 myrs at u_0 = 3.1 cm yr^{-1} (5580 km). The ridge spreads and migrates toward the subduction zone, causing the subducting plate to shrink at the expense of a passive oceanic plate, which grows with time (Figure 3). In the final state (Figure 3, bottom), the ridge meets the trench, leaving only a single oceanic plate spanning the expanse of the ocean.

3.2. Ridge Volume Versus Dynamic Volume

[14] Let us first consider changes in the volume of the ocean basin due to age-related changes in bathymetry. For steady tectonic velocities (Figure 4, $\bar{u}$ = 2.0 cm/yr (i), $\bar{u}$ = 3.1 cm/yr (ii, reference) and $\bar{u}$ = 6.0 cm/yr (iii)), we modify plate thickness according to (6) and measure changes in basin volume by calculating changes in ridge volume (Figure 4a). In each case, basin volume initially decreases due to the replacement of old subducting lithosphere with young seafloor created at the ridge. As the calculation nears the present-day (0 Ma), basin volume increases again as destruction of young seafloor increases the average seafloor age. The total variation in basin volume for a given spreading rate ranges between 6% and 19% depending on the rate (Figure 4a). Lower rates show larger basin volumes and smaller variations in basin volume because the average seafloor age is older and therefore less variable. The minima in basin volume vary by 8–15% compared to the reference case.

[15] The dynamic volume associated with deflection of the seafloor by subduction-induced downwelling also varies with time as the ridge moves toward the trench (Figure 4b). However, most of the variation occurs only within the last ~50 Myr as the ridge nears the trench. This process causes increasingly younger material to be subducted, which decreases mantle densities associated with subduction and thus the dynamic topography as well (although not completely to zero because some slab is still present when the ridge meets the trench). The total variation in volume is always less than 10% of the total volume, significantly smaller than the volume changes associated with changes in the seafloor age distribution. Expected variations in plate rates produce at most only a 3% variation in total volume at any given time (Figure 4b).

3.3. Variable Plate Rates

[16] The impact of a tectonic pulse on dynamic volume can be addressed by considering the controversial [*Heller et al.*, 1996; *Cogné and Humler*, 2004] end-member situation proposed by *Hays and Pitman* [1973] for changes in Cretaceous tectonic velocities: we assign 2.5 cm yr^{-1} before 110 Ma, 6.5 cm yr^{-1} between 110 and 85 Ma, 2.24 cm yr^{-1} between 85 and 10 Ma, and 3.1 cm yr^{-1} for the last 10 Ma. Again, the mean seafloor age controls the first-order basin volume and increased spreading rates generate a significant eustatic perturbation of about 10% of basin volume after only a few *myrs* (Figure 4a). However, because the pulse is relatively short lived, the volume of subducted material remains nearly constant through time and only the mantle density contrast varies. As a result, changes in dynamic topography are minor (Figure 4b): dynamic topography increases slightly (about 1% of total basin volume) during the tectonic pulse due to the more rapid placement of oceanic lithosphere into the mantle. The larger decrease in dynamic volume that follows (70 to 50 Ma) represents subduction of the more buoyant lithosphere generated during the pulse.

4. Discussion

[17] Instantaneous (short-lived) variations in plate velocity only increase the dynamic volume by at most ±5–7% because fluctuations in plate velocity are primarily due to changes in viscosity rather than density. In terms of volumes, the dynamic topography that we evaluate from the Stokeslets approximation [e.g., *Harper*, 1984; *Husson*, 2006] above a subducting slab is typically ~2.4 × 10^9 m^3 per m of subduction zone. This yields a maximum variation of 0.17 × 10^9 m^3 per unit length associated with a change in tectonic velocity. If all upper plates flooded simultaneously, such a variation, integrated over the 43500 km of present-day trench length and distributed over the surface of the ocean, would induce a 22 m variation in relative sea level. Such amplitudes are unlikely to be recorded by the geological record. We conclude that short-term variations in relative sea level are most reflective of changes to the seafloor age distribution, as emphasized by *Heller and Angevine* [1985] and *Heller et al.* [1996] and constrained by *Xu et al.* [2006].

[18] Long-lived increases in tectonic velocities decrease the volume of subducted material, and thus lead to larger fluctuations in dynamic topography than can be expected from short-term variations. Variations of up to ±25% of the dynamic volume (but only about 3% of the basin volume) can be expected. Following the above calculation, 25% variations of the dynamic volume indicate volume changes of 0.61 × 10^9 m^3 per m of trench, and would generate a 78 m high variation in relative sea level. Note that this process reinforces the accompanying variations of ridge volume with plate velocity (Figure 4a) and in no case does it compensate them. By comparison, the volume of a half-ridge with a half-spreading rate of 3.1 cm yr^{-1} is about 3 × 10^9 m^3 per m of ridge length [following *Stein and Stein*, 1992]. This volume varies efficiently with plate velocities and it can bulge up by 25% while doubling the plate velocity (Figure 2, solid line), inducing volume variations of about 0.75 × 10^9 m^3 per unit length. For long-term tectonic changes, dynamic topography reinforces trends associated with seafloor rejuvenation caused by continental breakup or increased tectonic velocities. Both processes are comparable in magnitude and can certainly be recorded in the Earth's long term history.

[19] Another consequence of dynamic topography is the tilt of continental margins. *Gurnis* [1990, 1993] suggested that increased dynamic topography and epeirogenic processes on the margin of continents would accompany a tectonic pulse; the present model suggests that this effect is minor because tectonic velocity reflects mantle temperature more strongly than the buoyancy contrast between the slab and the mantle. The tilt of a margin can be modified only when the buoyancy of the slab is modified, typically during subduction initiation or cessation, or in the event of slab detachment [*Buiter et al.*, 2002; *Mitrovica et al.*, 1989].

[20] **Acknowledgments.** We thank Wiki Royden, Henri Samuel, Adam Maloof, and two anonymous reviewers for helpful discussions and comments. This work is part of the MEDUSA project, NSF grant EAR-0409373.

References

Batchelor, G. (1967), *An Introduction to Fluid Mechanics*, Cambridge Univ. Press, New York.

Bercovici, D., Y. Ricard, and M. Richards (2000), The relation between mantle dynamics and plate tectonics: A primer, in *The History and Dynamics of Global Plate Motions*, *Geophys. Monogr. Ser.*, vol. 121, edited by R. G. M. A. Richards and R. van der Hilst, pp. 5–46, AGU, Washington, D. C.

Buiter, S. J. H., R. Govers, and M. J. R. Wortel (2002), Two-dimensional simulations of surface deformation caused by slab detachment, *Tectonophysics*, *394*, 195–210.

Cogné, J. P., and E. Humler (2004), Temporal variation of oceanic spreading and crustal production rates during the last 180 my, *Earth Planet. Sci. Lett.*, *227*, 427–439.

Conrad, C. P., and B. H. Hager (1999), The thermal evolution of an Earth with strong subduction zones, *Geophys. Res. Lett.*, *26*, 3041–3044.

Conrad, C. P., and C. Lithgow-Bertelloni (2004), The temporal evolution of plate driving forces: Importance of "slab suction" versus "slab pull" during the Cenozoic, *J. Geophys. Res.*, *109*, B10407, doi:10.1029/2004JB002991.

Davies, G. F. (1981), Regional compensation of subducted lithosphere: Effects on geoid, gravity and topography from a preliminary model, *Earth Planet. Sci. Lett.*, *54*, 431–441.

Gurnis, M. (1990), Ridge spreading, subduction, and sea-level fluctuations, *Science*, *250*, 970–972.

Gurnis, M. (1993), Phanerozoic marine inundation of continents driven by dynamic topography above subducting slabs, *Nature*, *364*, 589–593.

Hager, B. (1980), Eustatic sea level and spreading rate are not simply related, *Eos Trans. AGU*, *61*, 374.

Hager, B. H. (1984), Subducted slabs and the geoid: Constraints on mantle rheology and flow, *J. Geophys. Res.*, *89*, 6003–6015.

Harper, J. F. (1984), Mantle flow due to internal vertical forces, *Phys. Earth Planet. Inter.*, *36*, 285–290.

Hays, J., and W. Pitman (1973), Lithospheric plate motion, sea level changes and climatic and ecological consequences, *Nature*, *246*, 18–22.

Heller, P. L., and C. L. Angevine (1985), Sea-level cycles during the growth of Atlantic-type oceans, *Earth Planet. Sci. Lett.*, *75*, 417–426.

Heller, P. L., D. L. Anderson, and C. L. Angevine (1996), Is the middle Cretaceous pulse of rapid sea-floor spreading real or necessary?, *Geology*, *24*, 491–494.

Hirth, G., and D. Kohlstedt (1995), Experimental constraints on the dynamics of the partially molten upper-mantle: Deformation in the diffusion creep regime, *J. Geophys. Res.*, *100*, 1981–2001.

Hirth, G., and D. Kohlstedt (2003), Rheology of the upper mantle wedge: A view from the experimentalists, in *Inside the Subduction Factory*, *Geophys. Monogr. Ser.*, vol. 138, edited by J. Eiler and M. Hirschmann, pp. 83–104, AGU, Washington, D. C.

Husson, L. (2006), Dynamic topography above retreating subduction zones, *Geology*, *34*(9), 741–744, doi:10.1130/G22436.

Kominz, M. (1984), Oceanic ridge volume and sea-level change—An error analysis, in *Interregional Unconformities and Hydrocarbon Accumulation*, *Mem. Ser.*, vol. 36, edited by J. Schlee, pp. 109–127, Am. Assoc. of Petrol. Geol., Tulsa, Okla.

Korenaga, J., and T. H. Jordan (2002), On "steady-state" heat flow and the rheology of oceanic mantle, *Geophys. Res. Lett.*, *29*(22), 2056, doi:10.1029/2002GL016085.

Lambeck, K., and J. Chappell (2001), Sea level change through the last glacial cycle, *Science*, *292*, 679–686.

Mitrovica, J. X., and A. M. Forte (2004), A new inference of mantle viscosity based upon joint inversion of convection and glacial isostatic adjustment data, *Earth Planet. Sci. Lett.*, *225*, 177–189.

Mitrovica, J., C. Beaumont, and G. Jarvis (1989), Tilting of continental interiors by the dynamical effects of subduction, *Tectonics*, *8*, 1079–1094.

Morgan, W. (1965), Gravity anomalies and convection currents, *J. Geophys. Res.*, *70*, 6175–6187.

Ricard, Y., and C. Vigny (1989), Mantle dynamics with induced plate tectonics, *J. Geophys. Res.*, *94*, 17,543–17,559.

Stein, C. A., and S. Stein (1992), A model for the global variation in oceanic depth and heat flow with lithospheric age, *Nature*, *359*, 123–129.

Trubitsyn, V. P., W. D. Mooney, and D. H. Abbott (2003), Cold cratonic roots and thermal blankets: How continents affect mantle convection, *Int. Geol. Rev.*, *45*, 479–496.

Turcotte, D., and G. Schubert (2002), *Geodynamics*, Cambridge Univ. Press, New York.

Vail, P., R. Mitchum, R. Todd, J. Widmier, S. Thompson, J. Sangree, J. Bubb, and W. Hatelid (1977), *Seismic Stratigraphy and Global Changes of Sea Level: Seismic Stratigraphy—Applications to Hydrocarbon Exploration*, pp. 49–212, Am. Assoc. of Petrol. Geol., Tulsa, Okla.

Xu, X. Q., C. Lithgow-Bertelloni, and C. P. Conrad (2006), Global reconstructions of cenozoic seafloor ages: Implications for bathymetry and sea level, *Earth Planet. Sci. Lett.*, *243*, 552–564.

C. P. Conrad, Department of Earth and Planetary Sciences, Johns Hopkins University, Baltimore, MD 21218, USA. (conrad@jhu.edu)

L. Husson, Géosciences Rennes, UMR CNRS 6118, Université de Rennes 1, Campus de Beaulieu, F-35042 Rennes, France. (lhusson@mit.edu)

Chapitre 4

Tectonique des plaques

L'ensemble du travail que je discute dans ce chapitre est basé sur l'impact de l'aggrégation en courante de la majorité des continents -Eurasie, Afrique, Arabie, Inde et Australie- au cours du Tertiaire en un supercontinent que nous proposons avec C. Conrad comme *Hapagea* (fig. 4.1). La vitesse de convergence entre chacun de ces continents a diminué sensiblement à mesure que les subductions qui conduisaient la convergence vers l'Eurasie de chacun de ces continents est remplacée par des collisions.

Dans le chapitre 1 j'abonde sur le rôle majeur des chaînes de montagnes dans l'équilibre des forces tectoniques. Il apparaît que ces forces sont d'une magnitude comparable, mais opposée, aux forces principales motrices de la tectonique des plaques. Le remplacement progressif des subductions par des collisions lors de la formation de *Hapagea* correspond à un remplacement de forces motrices par des forces résistantes. Il est possible d'évaluer approximativement les variations des forces en présence (table 4.1). La traction des panneaux plongeants est estimée pour une force moyenne par unité de longueur de $15\,10^{12} N\,m^{-1}$ (calculée d'après la synthèse de Lallemand et al. [2005]) et une longueur des fosses changeant avant et après l'aggrégation de *Hapagea*. Après la disparition presque complète de la subduction téthysienne, cette traction totale diminue de $\sim 120\,10^{18} N$, soit 16%. Parallèlement les orogènes se développent. La force résistante globale qu'elles exercent peut être quantifiée en suivant l'approche développée dans le chapitre 1 par intégration sur l'ensemble de la Terre des forces de flottabilité orogéniques (fig. 4.2). Restreintes essentiellement à la Cordillière nord-américaine avant l'aggrégation

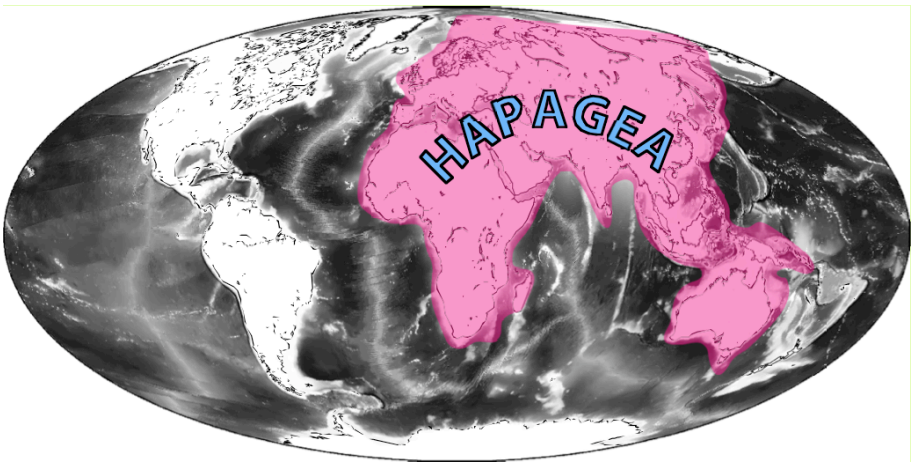

FIG. 4.1: Aggrégation actuelle des continents en un supercontinent : Hapagea.
Present-day continental aggrégation towards a supercontinent : Hapagea.

	pré-*Hapagea*	*Hapagea*	variation
traction des panneaux plongeants	750 10^{18} N	630 10^{18} N	-16%
poussée orogénique	40 10^{18} N	160 10^{18} N	+300%

TAB. 4.1: Traction des panneaux plongeants et poussée orogénique (pour des forces moyennes par unité de longueur de $15\,10^{12} N\,m^{-1}$ et $5\,10^{12} N\,m^{-1}$, respectivement) avant et après l'aggrégation de *Hapagea*.
Slab pull and orogenic push (computed assuming mean forces per unit length of $15\,10^{12} N\,m^{-1}$ *and* $5\,10^{12} N\,m^{-1}$*, respectively) before and after the aggregation of Hapagea.*

de *Hapagea*, la résistance augmente de $\sim 120\,10^{18} N$, soit 300%, avec le développement des chaînes alpines *sensu lato*.

L'impact sur la tectonique des plaques se traduit par (i) une diminution du rapport entre forces motrices et forces résistantes. La dissipation visqueuse dans le manteau diminue en consequence dans le manteau, ce qui s'exprime par une diminution de la vigueur de la convection. Ce changement est manifeste par la baisse de productivité aux dorsales océaniques (fig. 4.3), (ii) un changement des conditions à la surface du manteau ; *Hapagea* est un supercontinent qui est un forçage sur la convection mantellique [Grigné et al., 2007, Gurnis & Zhong, 1991, Zhong & Gurnis, 1993] et (iii) à l'échelle d'une plaque individuelle, les conditions dynamiques aux limites latérales sont modifiées et la cinématique est perturbée.

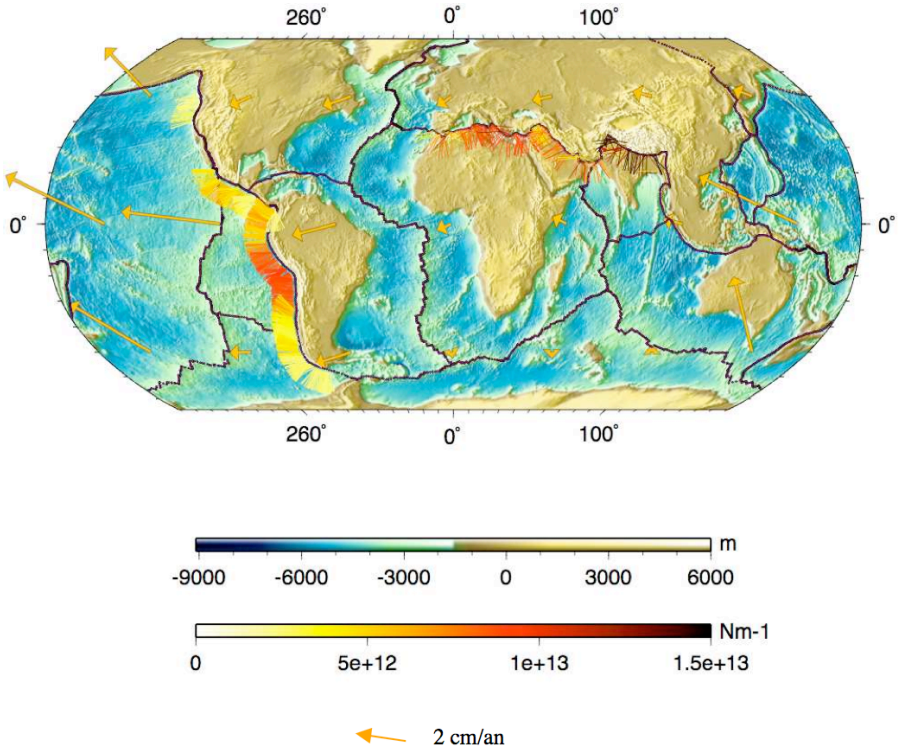

FIG. 4.2: Forces de flottabilité orogéniques (figure Mélanie Gérault). *Orogenic buoyancy forces (fig. Mélanie Gérault)*

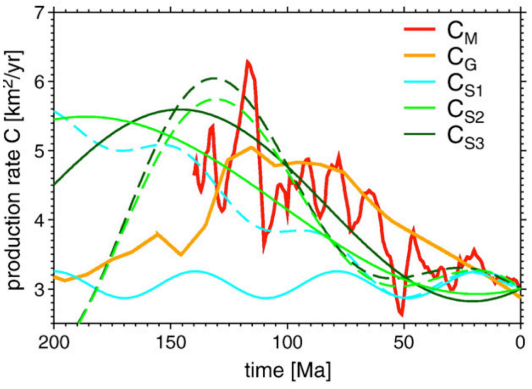

FIG. 4.3: Diminution de la productivité océanique depuis 100 Ma, estimée à partir des reconstructions des âges océaniques de Müller et al. [2008] (en rouge), [Becker et al., 2009]. *Decrease in oceanic productivity since 100 Ma, based on the reconstructions of Müller et al. [2008] (in red), [Becker et al., 2009].*

4.1 Restructuration tectonique suivant l'aggrégation de Hapagea

Sous l'angle de la tectonique des plaques, ce changement de conditions aux limites des plaques correspond à la cessation progressive de la convergence des continents Afrique, Arabie, Inde et Australie vers l'Eurasie. L'exemple le plus marquant est bien sûr la convergence de l'Inde et de l'Eurasie [Allègre et al., 1984, Patriat & Achache, 1984], mais des observations similaires valent pour les autres assemblages de plaques. Il s'ensuit une redistribution de la déformation. Les forces motrices qui animent l'ouverture des océans ont -*a priori*- pas ou peu varié durant le Cenozoique. Puisque la convergence devient de plus en plus empêchée par la disparition des panneaux plongeants tethysiens et la croissance des orogènes aux limites des plaques, ces forces doivent être équilibrées par d'autres mécanismes, en particulier la déformation sur les marges ouest américaines. Ce changement de régime tectonique a été proposé par Russo & Silver [1996] et Silver et al. [1998]. C'est sur cette base que sont construits les deux articles suivant, écrits en collaboration avec C. Conrad et C. Faccenna. Il est d'abord mis en évidence que la circulation actuelle des plaques, liée à la distribution problématique, *triangulaire* des âges océaniques (la probabilité de repésentation d'un âge diminue linéairement avec le temps entre 0 et 180 Ma, [Parsons, 1982, Rowley, 2002]) est une conséquence de la distribution actuelle des continents. Puis je montre que forçage par les continents apparaît suffisament puissant pour modifier complètement le régime de tectonique des plaques et induire par exemple un mouvement net vers l'ouest de la coquille lithosphérique par rapport au manteau.

Impact of the *Hapagea* supercontinental aggregation on American Cordilleras and the seafloor age distribution

Laurent Husson (1,2), Clinton P. Conrad (3)

[1]CNRS UMR 6118, Géosciences Rennes, Université Rennes 1, France (laurent.husson@univ-rennes1.fr)

[2]CNRS UMR 6112, Laboratoire de Planétologie et Géodynamique de Nantes, France

[3]Department of Geology and Geophysics, SOEST, University of Hawaii, Honolulu, HI 96822, USA (clintc@hawaii.edu)

Abstract :

The ongoing aggregation of Africa, Arabia, India and Australia onto Eurasia is forming a supercontinent that we refer to as *Hapagea*. Although not as large as the older Pangea and Rodinia, *Hapagea* is nevertheless large enough to profoundly modify Cenozoic plate kinematics as it gradually becomes a hub apart from which American continents spread. The continuation of Atlantic spreading is carried out at the expense of the Pacific Ocean, forcing the Farallon / Nazca plates down into eastern Pacific subduction zones, despite the fact that this seafloor is theoretically too young and too buoyant to subduct efficiently. This process occurred later for South America, where the subduction of the Tethys buffered the impact of the Atlantic expansion, and earlier for North America where this configuration was never met. The implications of the current plate tectonics are multiple and include (i) increased compression on the western coasts of the Americas, leading to Cordillera formation in North America (Sevier and Laramide) and later in South America (Andean), (ii) the transition from a *rectangular* distribution of seafloor ages to a *triangular* distribution as westward progress of the Americas engulfs young Farallon/Nazca seafloor, and

(iii) a decrease in the convective efficiency of mantle flow that results in decreased rates of lithospheric production at ridges, a situation that is cyclically met during the Wilson cycle and diminishes both mantle heat flow and sea level. These results imply that mantle drag causes the Atlantic spread and dominates the force balance of the Earth's lithospheric shell.

Keywords : seafloor age, plate tectonics, orogenesis, supercontinent, Wilson cycle, sea level

1) Introduction

Cordilleran mountain belts grow from continental shortening associated with convergence between an oceanic plate and a continental plate. However, despite a global abundance of subduction zones, actual thickening of an overriding continent is far from being the rule, and aside from the American Cordilleras, examples are sparse. Indeed, even the Andes and the North American Cordillera can be regarded as oddities: although the Farallon-Nazca plate subducted at least for the entire Mesozoic and Cenozoic (e.g. Atwater, 1970; Engebretson et al., 1985), the modern Andes only developed during the Tertiary. In North America, the continent underwent various phases of compression but the present-day continental margin essentially displays extension, towards the restoration of a more uniform crustal thickness (e.g. Atwater, 1970; Wernicke et al., 1988; Sonder and Jones, 1999). By contrast, most modern examples of ocean/continent convergence essentially display extension (Western Pacific subduction zones, Sumatra-Java-Banda, and the smaller Mediterranean subduction zones) (Heuret and Lallemand, 2005).

The collision between continents that naturally follows plate convergence and basin closure eventually leads to the cessation of convergence that impacts plate kinematics. A well-known illustration is offered by the decrease in the convergence rate between the Indian and Eurasian plates after the Indian continent collided with the continental buttress of Eurasia (Patriat and Achache, 1984, Conrad and Lithgow-Bertelloni, 2007). In another plate-to-plate example, the development of the Andean Cordillera correlated with a decrease in the convergence rate between the Nazca and South American plates (Pardo-Casas and Molnar, 1987), as a consequence of feedback interaction between mountain building and plate convergence (Iaffaldano et al., 2006; Meade and Conrad, 2008). Evidence for disruption of the plate circuit at a global scale following continental collision also exists. The closure of the Tethys gradually impeded the northeastward migration of the African plate towards Eurasia. The ongoing spreading of the Atlantic Ocean thus could only continue at the expense of the Pacific Ocean. This additional forcing not only led to the growth of the Andes (Russo and Silver, 1996; Silver et al., 1998) but also to the westward shear of the entire Pacific system down to the base of the upper mantle; this process in turn provides an explanation for the observed westward drift of the lithosphere (Husson et al., 2008) and the asymmetry of Pacific basin trench motions (Nagel et al., 2008).

Indeed, one can anticipate a variety of changes in plate kinematics to be induced by the closure of the Tethys, which is continuing to aggregate the African, Arabian, Indian and Australian plates onto Eurasia, forming what could be referred to as the soon-to-be formed *Hapagea* (from Hawaiian *hapa* "mixed parts", and Ancient Greek *gaia,* "Earth") supercontinent. In the light of Cenozoic plate kinematics, we explore the possibility that this non-trivial episode in the current Wilson cycle (Wilson, 1966) variably impacted the spreading of the Atlantic Ocean and consequently the westward motion of American plates away from *Hapagea*. Such a disruption may explain the timing of American cordillera growth as well as a variety of modern geodynamic features, including the surprising *triangular* distribution of seafloor ages (Parsons, 1982; Rowley, 2002, Xu et al., 2006) and its evolution through time (Becker et al., 2009), with consequences for sea level, mantle heat flow, and the efficiency of mantle convection.

2) Atlantic growth and Pacific shrinkage

The end of the Cretaceous corresponds to the onset of the re-aggregation of various plates after a time of maximum dispersal around 100 Ma (e.g. Cogné and Humler, 2008). In the North Atlantic, spreading can only happen at the expense of the

Pacific Ocean (e.g. Garfunkel et al., 1986), in association with the subduction and disappearance of the Farallon plate beneath North America. By contrast, the expansion of the South Atlantic Ocean can be accommodated by two subduction zones: seafloor space can be gained not only from Farallon / Nazca subduction beneath South America, but also from the Tethys subduction beneath Eurasia. The latter subduction allows for the convergence of the African plate towards Eurasia, and therefore facilitates South Atlantic opening, as opposed to the North Atlantic where this convergence is not available (Fig. 1a). Because of its intermediate location, the expansion of the Central Atlantic domain can only partly benefit from Tethyan subduction.

Reappraisals of the absolute reference frame from hotspot independent techniques (Becker, 2008; Schellart et al., 2008) and from tectonic reconstructions (Collins, 2003) indicate that Eurasia is amongst the slowest plates. From recent plate motion reconstructions (fig. 1, Müller et al., 2008), we extracted the location of continents along characteristic small circles around the present-day Euler poles (NUVEL-1A, DeMets et al., 1994) of North America with respect to Eurasia, and of South America with respect to Africa (fig. 2). In both cases, in Müller et al.'s reconstructions, the margin of Eurasia remains steady while the Americas spread apart from it. In the North (Figs. 2a, 2c), the mid-Atlantic ridge has no choice but to migrate westward, along with North America but half as fast as the total spreading rate (respectively 30 mm/yr and 15 mm/yr on average). Note that the mid Atlantic ridge *sensu stricto* actually has a slower motion (~11 mm/yr) because the opening of the Labrador Sea, which can be considered part of the North Atlantic ridge system, also contributes to the expulsion of North America away from Eurasia. In the South Atlantic (Figs. 2b, 2d, 2e), the expansion of the ocean is accommodated by both the westward migration of South America (~28 mm/yr) and the northeastward migration of Africa (~11 mm/yr), leaving a slow westward motion of the South Atlantic ridge (8.5 mm/yr, or 22% of the total spreading rate).

The timing of plate tectonic evolution relative to orogenic events suggests a causal mechanism. The coevality of Eurasian orogenies (from the Western Alps to the Himalayas) and of the Andean orogeny (Fig. 3a) suggests that the formation of the *Hapagea* supercontinent gradually impeded further migration of Africa towards Eurasia. During the closure of the Tethys, the reconstructions of Müller et al. (2008) (fig. 2d) indicate that the migration of the Atlantic margin of Africa decreased by 40%, from ~17 mm/yr (from 50 to 30 Ma) to ~11 mm/yr (from 30 to 0 Ma). There is no obvious alternative reason for Atlantic spreading not to remain constant. In fact, the growth of *Hapagea* made it easier to shear the mantle beneath the smaller South American plate than under the entire *Hapagea*. The resulting South American motion subsequently increased compression on the Benioff zone of the Nazca plate and eventually led to the formation of the Andes (Russo and Silver, 1996; Silver et al., 1998). Conversely, North America had no subduction zone separating it from the massive Eurasia. Without Tethyan closure to accommodate some of the Atlantic opening, North American Cordilleras (Sevier and Laramide orogenies) were forced to form prior to the Andean orogeny.

3) Dynamic feedback of plate tectonics onto mantle convection

Correlations between plate kinematics and orogenesis can be more clearly and globally understood by considering the relationships between the lithospheric force balance and mantle flow, which ultimately drives the plates. Among the resisting forces, mountain belts are the surface manifestation of resisting forces that result from collisional interactions between plates. Since Argand (1924), it is understood that the gravitational potential energy stored during the formation of Cenozoic mountain belts converts into a collisional torque (e.g. Richardson, 1979) that is comparable in magnitude but resists the driving torques of plate tectonics (Ghosh et al., 2003; Husson and Ricard, 2004). Most modern mountain belts formed during the Tertiary as a consequence of the ongoing aggregation of the African, Arabian, Indian, Australian, and Eurasian plates onto the *Hapagea* supercontinent. This episode of the current Wilson cycle globally redistributes the stresses in the Earth's lithospheric shell.

Records of Atlantic spreading rates can be used to examine changes in the force balance that result from *Hapagea* formation. Although somewhat chaotic between 65 to 45 Ma, spreading in the North, Central and South Atlantic basins globally

decreased (Fig. 3b) when American orogenies formed (Fig. 3a). Half-spreading rates decreased first in the Central and North Atlantic, from ~20 to ~12 mm/yr between 90 and 0 Ma (Central) and between 56 and 0 Ma (North). This slowdown resulted from the growing resistance on the eastern side from the massive Eurasian continent and on the western side from the subduction of the Farallon plate beneath North America. Only later did spreading clearly slow in the South Atlantic basin for the same reason: beginning at ~30 Ma the post-Tethys formation of *Hapagea* introduced resistance to spreading on the east, while the Nazca/Farallon subduction and Andean growth generated resistance to the west. The peculiar decrease in spreading rates in the South Atlantic between 65 and 45 Ma is coeval with the faster spreading in the West Indian basins before India collided with Eurasia; after the collision, this spreading was slowly given back to the South Atlantic (Conrad and Lithgow-Bertelloni, 2007).

Finally, to explain the timing of Cordillera orogenesis in the Americas, we must add another ingredient to our spreading analysis of the Atlantic. The most natural mode of trench movement is slab rollback (e.g. Garfunkel et al., 1986, Funiciello et al., 2003), in which trenches migrate towards their forelands (the unsubducted portion of the subducting lithosphere). However, the rate at which rollback may occur depends on the intrinsic properties of ea ch subduction zone, i.e. it is essentially controlled by the slab and its surrounding mantle densities and rheologies (e.g., Funiciello et al., 2003; Billen et al., 2008; Royden and Husson, 2006; Stegman et al., 2006; Di Giuseppe et al., 2009). Departure from this intrinsic regime may occur when overriding plates do not accompany trench migration at a consistent rate (Schellart, 2008; Yamato et al., 2009). If the overriding plate motion is slower than trench migration, back-arc extension occurs, as it is the case in most of the western Pacific. Contrarily, if the upper plate moves faster towards the foreland, compression occurs and mountain belts develop. Mountain belts and back-arc basins can exert an additional forcing on subduction zones, and rollback can either be sped up or delayed.

The development of the Sevier and Laramide orogenies in North America is coeval to the opening of the North Atlantic (see review by DeCelles, 2004), and the Andes began to grow after the collision of Africa onto Eurasia mostly precluded further northeastward migration of Africa. In essence, the two Cordilleras formed in the same pattern, occurring when only the western side of the Atlantic ridge could accommodate the spreading of the Atlantic basin. The modification of the force balance at the Western American subduction zones is expressed by the very existence of the Cordilleras: it caused trenches to retreat westward more quickly than the retreat rate inherent to these subduction zones. The forcing exerted by the opening of the Atlantic can be quantified by the kinematics of deformation at the plate boundary (Husson et al., 2008), and plate motion reconstructions (Müller et al., 2008) indicate that it is large enough to make the American plates override the young oceanic lithospheres of the eastern Pacific. Observable consequences are the shallow dipping slabs beneath South America (Cahill and Isacks, 1992) and the present-day location of the Farallon slab some 2000 km east of the west coast of North America (Bunge and Grand, 2000). The slab beneath North America is deeper and farther east because the process began earlier in North America than in South America. In North America, the Farallon plate was forced down into the mantle until the overriding plate eventually reached the mid-Pacific rise. A similar scenario in South America is expected, but has not yet been achieved due to the delayed formation of southern *Hapagea*.

Because slab buoyancy varies with slab age, young oceanic lithosphere is theoretically not easily subducted. Thus, the subduction force balance should evolve with time while an always-younger lithosphere is entering a subduction zone. This evolution is recorded by the deformation kinematics of the American plate boundaries, which correlate with the mean seafloor age of the lithosphere that enters the subuction zone (fig. 3). In North America, the Sevier and Laramide orogenies formed while the mean seafloor age at the trench decreased by ~50 Myr over a 50 Myr time period. Compression was eventually released when the continental margin began to reach the Pacific ridge at ~40 Ma. The orogen subsequently collapsed and the Basin and Range developed (Atwater, 1970; Wernicke et al., 1988; Sonder and Jones, 1999). Similarly, the Andes essentially started to grow when the age of the Farallon/Nazca plate decreased to less than 40 Myr at ~20 Ma.

Indeed, the timing of Andean building is relatively well documented. A variety of techniques including the analysis of fossil leaf morphology (Gregory-Wodzicki, 2000), stable isotopes (e.g. Ghosh et al., 2006, Quade et al., 2007), and phylochronology (Picard et al., 2008) indicate that the Andes acquired most of their present-day elevation during the last 10 Myr. Crude estimates based on the above

studies indicate that elevation grew at rates less than 200 m/Myr before 10 Ma, when mean seafloor was older than 40 Myr old, which accelerated to rates between 300 and 1200 m/Myr between 10 and 7 Ma, when seafloor age abruptly decreased to less than 30 Myr. Maximum elevation was probably reached at ~7 Ma, after which the Cordillera expanded laterally, towards a high plateau (the latter episode can be explained by a non-linear relationship between elevation and force balance, but also by the evolution of crustal rheology during crustal thickening). These correlations show that Cordilleran growth is not only controlled by the motion of overriding plates but also by the age-buoyancy of the subducting plate. Because the load of mountain belts must balance the tectonic forces exerted at plate boundaries (e.g. Husson and Ricard, 2004), the American Cordilleras developed in response to spreading forces arising from the opening Atlantic Ocean in addition to increased resistance to subduction of the Farallon plate.

The westward migration of the Americas provides a plate tectonic explanation for the much-debated *triangular* distribution of present-day seafloor ages (e.g. Sclater, 1981; Parsons, 1982; Rowley, 2002). Boundary layer convection theory suggests (e.g. Turcotte and Schubert, 1982) that there is a critical age at which the lithosphere subducts. In that case, the distribution of seafloor age is *rectangular*, i.e. no subduction occurs prior to the critical age and no seafloor older than this age remains. Assuming equilibrium between total ridge length, mean spreading rates and the capacity of the Earth to evacuate its internal heat, the present-day kinematics and geometry of the seafloor yield a critical cooling age of about 100 Myr for the oceanic lithosphere (mean ridge to continent length / mean half-spreading rate). Instead, at present the areal coverage of the seafloor decreases almost linearly from a maximum near ridges to zero for a 180 Myr seafloor, with a median age of 55 Myr (fig. 4). The destruction of the seafloor at subduction zones is therefore seemingly independent of seafloor age, at odds with the theory that relates a slab's age to its buoyancy, and hence to its capacity to subduct.

But boundary layer theory does not account for continents. Regardless of their location within subducting or overriding plates, continents can be viewed as positively buoyant units that drift over the underlying convecting mantle. They are only moderately involved in mantle convection, and evidence for Phanerozoic recycling of continents into the mantle is sparse. A continent embedded within a subducting plate will subduct down to a few hundred kilometers before it can stop convergence, as is the case for the Mediterranean or Banda subduction zones (Royden and Husson, 2009). In addition, as the continent moves faster towards the foreland, it forces subduction at a rate that is faster than the intrinsic rate. This forced subduction started in North America when the Central Atlantic opened, and has more recently moved to South America. In both cases, the Farallon/Nazca plate was forced down into the mantle thanks to the additional forces arising from the opening of the Atlantic, and from the increasing resistance exerted by subduction of lithosphere that is younger than the theoretically critical age (and possibly positively buoyant). During this process, which began with North America at ~100 Ma, the American plates gradually overrode the oceanic lithosphere and consequently removed young ages from the rectangular seafloor age distribution, skewing them towards the present-day more triangular distribution (fig. 4). Thus, because the triangular distribution only results from the present-day configuration of plate tectonics, it should not be interpreted as a general feature of the Earth. Instead, we expect the shape of the seafloor age distribution to evolve between rectangular shapes characteristic of dispersed continents (e.g., Fig. 4d) and triangular shapes characteristic of continental aggregation (e.g., Fig. 4a), which forces premature subduction of young lithosphere at the expense of old.

4) Discussion and Conclusions

The geodynamic aftermath of the *Hapagea* aggregation, which consists of (i) the peri-Tethys orogenesis and American Cordillera formation, (ii) changes in absolute plate motion combined with Atlantic spreading and Pacific shrinking, and (iii) the evolution of the seafloor age distribution, seems to indicate that these Neogene events are indirect consequences of the supercontinental aggregation. Of course, the driving mechanism is ultimately mantle convection, but we emphasize that most geodynamic events reflect the interplay of convection with the stiff and buoyant continental lithospheres at the surface. Mechanically, the aggregation of *Hapagea*, or of any supercontinental unit, results from the segregation of some less dense, more viscous,

and chemically differentiated material that almost never enters the convecting system but instead resists its flow. *Hapagea* itself represents two thirds of the continental surface and about a fifth of the Earth surface. Prior to the aggregation, Eurasia was the largest continental unit and covered only a tenth of the Earth's surface. It is therefore not surprising that this drastic -though seldom mentioned- disruption in the plate tectonic regime has generated a series of perturbations. Given the loss of the Tethys to *Hapagea*, the Atlantic had no choice but to spread at the expense of the Pacific. This process naturally started earlier in the North Atlantic, where there was no subduction to the east to buffer the spreading, than in the South were the subduction of the Tethys could accommodate some spreading until the Tethys closed. Consequently, the North American Cordillera also developed earlier than its southern Andean equivalent. For the same reason, the northern subduction of the Farallon plate was forced earlier than in the South, making a too-young-to be-subducted lithosphere disappear until the Pacific ridge reached the margin of North America, a situation that has not yet been achieved in the South.

This reasoning attributes a prominent role to *Hapagea*. In fact, *Hapagea* is largely circumbscribed by ridges and the observed plate kinematics simply indicates that *Hapagean*-American spreading forces are large enough to make the drift occur. Straightforward analysis indicates that slab pull is the largest driver of plate motions while ridge push only plays a minor role (e.g. Turcotte and Schubert, 1982). This seemingly contradicts our results, which implicitly suggest that oceanic spreading is the prominent driver of plate tectonics. In particular, slab pull cannot explain a variety of observations such as the existence of 4000 m high mountain belts that balance the spreading force of the Atlantic (Husson et al., 2008), or the absolute motion of plates away from *Hapagea*. Active drag of the lithosphere by the convecting mantle remains difficult to quantify and as such is neglected in many studies. Convective drag, however, is very likely the missing component of the force balance. North American seismic anisotropy observations have been shown to be more consistent with a mantle flow, rather than ridge push, as a driver of North America (Bokelmann, 2002). Active upwelling beneath Africa or return flow associated to circum-Pacific subduction downwelling (Steiner and Conrad, 2007) could thus drive the associated Atlantic spreading. In order to produce sufficient spreading, basal tractions must be large enough to balance the fat American Cordilleras and force the Farallon plate into the mantle. Cordilleran kinematics indicates that spreading must exert up to 10^{13} N per unit length of trench (Husson and Ricard, 2004, Iaffaldano et al., 2006). Because ridge push only typically amounts to ~10^{12} N m^{-1} (e.g. Turcotte and Schubert, 1982) basal drag must be much larger, as already suggested for the India/Eurasia convergence (Ghosh et al., 2003). Recent global flow models (Conrad and Lithgow-Bertelloni, 2006) suggest that basal tractions beneath the Atlantic are of order ~2 MPa, and are oriented to produce spreading. Integrated over the ~5000 km width of the Atlantic easily produces the required cross-Atlantic spreading force of ~10^{13} N m^{-1}. Tractions beneath the American and *Hapagean* cratons would add to this total, and may be amplified by enhanced coupling of thicker lithosphere to mantle flow (Conrad and Lithgow-Bertelloni, 2006).

The *Hapagean* accumulation and its associated tectonic consequences for the Americas and the global seafloor may exemplify an important control that supercontinents exert on mantle convection. During the dispersal phases of the Wilson cycle, continents are smaller than the wavelength of convection cells and passively ride the convecting mantle. But during the convergence phase, supercontinents develop with a characteristic size that is comparable to -if not larger than- that of convection. Such supercontinents thus can no longer passively drift over the mantle but instead their presence resists convective flow. The growth of the American Cordilleran belts and the premature subduction of Nazca/Farallon seafloor attest that supercontinental resistance is comparable in magnitude to the convective driving forces associated with slab pull and mantle drag. Thus, convergent phases in the Wilson cycle may ultimately slow down mantle convection. Although controversial (e.g. Cogné and Humler, 2006), seafloor production rates probably decreased during Neogene by about 20% (Conrad and Lithgow-Bertelloni, 2007), and by 25-50% during the last 140 Myr (Becker et al., 2009) (Fig 4 shows a decrease in ridge production rate from more than 4 km^2/yr at 90 Ma to less than 3 km^2/yr today). We interpret this observation as the evidence that the aggregating *Hapagea* has resisted oceanic accretion. Because the aggregation of *Hapagea* is not yet fully completed, the convective slowdown may continue into the future. Similarly, the resisting effect of larger supercontinents like Proterozoic Rodinia or Phanerozoic Pangea would have been even greater.

Indirect consequences of the plate reorganization during *Hapagean* formation are variations in sea level and heat flow (Korenaga, 2007), which occur for two reasons. First, because bathymetry increases with lithospheric age, the forced destruction of the young Farallon lithosphere, which skews the seafloor age distribution and increases its mean age, implies a eustatic fall (Xu et al., 2006; Müller et al., 2008). Similarly, because heat flow also decreases with seafloor age, the present-day mean heat flow also decreases in the aftermath of the aggregation (Loyd et al., 2007). Second, this heat flow slowdown (Becker et al., 2009) may represent an important impact of supercontinental growth on the efficiency of convective heat transport in the mantle. If continental aggregation slows down lithospheric production rates by 20% or more (Conrad and Lithgow-Bertelloni, 2007; Becker et al., 2009; Fig. 4), then the average seafloor will grow older because it is not being replaced by younger material. Thus, a gradual increase in the mean oceanic age should follow supercontinetal formation, causing heat flow and sea level to decrease. Indeed, Wilson cycle episodes are correlated with sea level oscillations, in which the timing of eustatic maxima matches phases of maximum continental dispersion, and conversely (Nikishin, 2006; Korenaga, 2007, Cogné and Humler, 2008). Supercontinental slowdown of convection, however, is ultimately unstable because it prevents the mantle from evacuating enough heat; the subcontinental mantle where hot plumes concentrate subsequently warms up (Grigné et al., 2005; Zhong et al., 2007), which may eventually induce continental breakup and dispersal (Gurnis, 1988). If the aggregation phase lasts long enough, the impact of supercontinents on the convective vigor of the mantle could thus easily exert a first order control on sea level. The present formation of the *Hapagean* supercontinent, and the accompanying impact on seafloor ages and the American Cordillleras exemplify the first phase of this type of convective slowdown.

Figures :

Figure 1 – Seafloor age maps at present-day (A) and at 90 Ma (B). Coastlines in panel B show their location at present-day. Green and blue curves show the small circles around Euler poles (green and blue circles) for North America / Eurasia and South America / Africa used in figure 2 and red arrows indicate present-day plate motion with respect to fixed Eurasia (NUVEL-1A, DeMets et al., 1994).

Figure 2 – Localisation of continents and plate boundaries along W-E small circles that cross the North (a) and South (b) Atlantic (localization figure 1), as a function of time. Panels (c, d, e) are zooms in. 0 distance corresponds to the intersection of the 2 profiles at 68 E. *na*: North Atlantic; *sa*: South Atlantic; *ar*: Arabia; *te*: Tethys. Magenta and cyan curves show ridge and subduction locations, respectively.

Figure 3 – Timing of the (a) main orogenic events and (b, right axis) half spreading rates, as a function of time in the South (solid), Central (dashed) and North (dotted-dashed) Atlantic. Mean age (b, left axis) of the subducting Farallon-Nazca plate along the South American (solid bold) and North American (dashed bold) plates as a function of time (calculated by averaging the along-trench ages from Müller et al., 2008, although age distribution along the margin may vary by up to 70 myrs).

Figure 4 – Seafloor age surface distribution through time, from the *rectangular* distribution at 90 Ma to the present-day *triangular* distribution (data from Müller et al., 2008). The lithospheric production rate at each of the four times can be inferred from x-intercept at age=0 Myr.

References

Argand, E., 1924. La tectonique de l'Asie. Comptes-rendus du XIIIeme Congrès Géologique International, Liège, 202, p. 195.

Atwater, T., 1970. Implications of plate tectonics for the Cenozoic tectonic evolution of western North America. Bull. Geol. Soc. Amer. 81, 3513-3536.

Becker, T. W., Conrad, C. P., Buffett, B., Müller, R. D., 2009. Past and present seafloor age distributions and the temporal evolution of plate tectonic heat transport.

Earth Planet. Sci. Lett. 278, 233-242.

Becker, T. W., 2008. Azimuthal seismic anisotropy constrains net rotation of the lithosphere. Geophys. Res. Lett. 35, doi:10.1029/2007GL032928.

Billen, M.I., 2008. Modeling the dynamics of subducting slabs. Annual Review of Earth and Planetary Sciences 36, 325-356.

Bokelmann, G.H.R., 2002. Convection-driven motion of the North American craton: Evidence from P-wave anisotropy. Geophys. J. Int. 248, 278-287.

Bunge, H.P., Grand, S.P., 2000. Mesozoic plate-motion history below the northeast Pacific Ocean from seismic images of the subducted Farallon slab. Nature. 405, 337 - 340.

Cahill, T., Isacks, B.L., 1992. Seismicity and Shape of the Subducted Nazca Plate. Journal of Geophysical Research-Solid Earth 97, 17503-17529.

Cogné, J.P., Humler, E., 2008. Global scale patterns of continental fragmentation, Wilson's cycles as a constraint for long-term sea level changes. Earth Planet. Sci. Lett. 273, 251-259.

Collins, W.J., 2003. Slab pull, mantle convection, and Pangaean assembly and dispersal. Earth. Planet. Sci. Lett. 205, 225-237, 2003.

Conrad, C.P., Lithgow-Bertelloni, C., 2006. Influence of continental roots and asthenosphere on plate-mantle coupling. Geophys. Res. Lett. 33, L05312, doi:10.1029/2005GL025621.

Conrad, C.P., Lithgow-Bertelloni, C., 2007. Faster seafloor spreading and lithosphere production during the mid-Cenozoic, Geology. 35, 39-32.

DeCelles, P.G., 2004. Late Jurassic to Eocene evolution of the Cordilleran thrust belt and foreland basin system, western U.S.A., American Journal of Science. 304, 105-168, doi:10.2475/ajs.304.2.105.

DeMets, C., Gordon, R.G. Argus, D.F. Stein, S., 1994. Effect of recent revisions to the geomagnetic reversal time scale on estimates of current plate motions, Geophys. Res. Lett. 21, 2191-2194.

Di Giuseppe, E., Faccenna, C. Funiciello, F., van Hunen, J., Giardini, D., 2009. On the relation between trench migration, seafloor age, and the strength of the subducting lithosphere. Lithosphere 1, 121-128.

Engebretson, D.C., Cox, A., Gordon, R.G., 1985. Relative motions between oceanic plates of the Pacific basin. Journal of Geophysical Research 89, 10291-10310.

Garfunkel, Z., Anderson, D.L., Schubert, G., 1986, Mantle curculation and lateral migration of subducting slabs, J. Geophys. Res., 91, 7205–7223.

Ghosh, A., Holt, W.E., Flesch, L.M., Haines, A.J., 2006. Gravitational potential energy of the Tibetan Plateau and the forces driving the Indian plate. Geology 34, 321-324.

Ghosh, P., Garzione, C.N., Eiler, J.M., 2006. Rapid uplift of the Altiplano revealed in 13C–18O bonds in paleosol carbonates. Science 311, 511–515.

Gregory-Wodzicki, K.M., 2000. Uplift history of the Central and Northern Andes: a review. Geol. Soc. Amer. Bull. 112, 1091–1105.

Grigné, C., Labrosse, S., Tackley, P.J., 2005. Convective heat transfer as a function of wavelength. Implications for the cooling of the Earth. J. Geophys. Res. 110, B03409, doi:10.1029/2004JB003376.

Gurnis, M., 1988. Large-scale mantle convection and the aggregation and dispersal of supercontinents. Nature 332, 695-699.

Heuret, A., Lallemand, S., 2005. Plate motions, slab dynamics, and back-arc deformation. Phys. Earth Planet. Int. 149, 31-51.

Husson, L., Conrad, C.P., Faccenna, C., 2008. Tethyan closure, Andean orogeny, and westward drift of the Pacific basin. Earth and Planetary Science Letters, 271, 303-3 249.

Husson, L., Ricard, Y., 2004. Stress balance above subduction zones - application to the Andes. Earth Planet Sc. Lett. 222, 1037-1050.

Iaffaldano, G., Bunge, H.P., Dixon, T.H., 2006. Feedback between mountain belt growth and plate convergence. Geology 34, 893-896.

Korenaga, J., 2007. Eustasy, supercontinental insulation, and the temporal variability of terrestrial heat flux. Earth Planet. Sci. Lett. 257, 350-358.

Loyd, S. J., Becker, T. W., Conrad, C. P., Lithgow-Bertelloni, C., and Corsetti, F.A., 2007. Time-variability in Cenozoic reconstructions of mantle heat flow: plate tectonic cycles and implications for Earth's thermal evolution. Proceed. Nat. Acad. Sci. 104, 14266-14271.

Meade, B.J., Conrad, C.P., 2008. Andean growth and the deceleration of South American subduction: Time evolution of a coupled orogen-subduction system. Earth and Planetary Science Letters 275, 93-101.

Müller, R.D., Sdrolias, M., Gaina, C. Steinberger, B. Heine, C., 2008. Long-term sea-level fluctuations driven by ocean basin dynamics. Science 319, 1357-1362, doi:10.1126/science.115154.

Nagel, T.J., Ryan, W.B.F., Malinverno, A., Buck, W. R., 2008. Pacific trench motions controlled by the asymmetric plate configuration. Tectonics 27, TC3005, doi:10.1029/2007TC002183.

Nikishin, A.M., 2006. Supercontinental cycles and eustatic variations in the world ocean level. Doklady Earth Sciences 409, doi:10.1134/S1028334X06050011.

Pardo-Casas, F., Molnar, P., 1987. Relative motion of the Nazca (Farallon) and South American plates since Late Cretaceous time. Tectonics 6, 233-248, 1987.

Parsons, B., 1982. Causes and consequences of the relation between area and age of the ocean floor, J. Geophys. Res. 87, 289-302.

Patriat, P., Achache, J., 1984. India–Eurasia collision chronology has implications for crustal shortening and driving mechanism of plates. Nature 311, 615-621.

Picard, D., Sempere, T., Plantard, O., 2008. Direction and timing of uplift propagation in the Peruvian Andes deduced from molecular phylogenetics of highland biotaxa. Earth and Planetary Science Letters 271, 326-336, doi:10.1016/j.epsl.2008.04.024.

Quade, J., Garzione C.N., Eiler, J., 2007. Paleoelevation reconstructions using paleosol carbonates. Rev. Mineral. Geochem. 66, 53–87.

Royden, L., Husson, L., 2006. Trench motion, slab geometry and viscous stresses in subduction systems. Geophysical Journal International 167, doi:10.1111/j.1365-246X.2006.03079.x.

Royden, L., Husson, L., 2009. Subduction with variations in slab buoyancy: models and application to the Banda and Apennine systems, in: Funiciello, F. and Lallemand, S. (Eds), Subduction Zone Geodynamics, Frontiers in Earth Sciences, Springer Berlin Heidelberg, doi:10.1007/978-3-540-87974-9.

Rowley, D.B., 2002. History of plate creation 180 Ma to Present. Geological Society of America Bulletin 114, 927-933.

Russo, R., Silver, P.G., 1996. Cordillera formation, mantle dynamics, and the Wilson Cycle. Geology 24, 511-514.

Sclater, J. G., Parsons B., Jaupart, C., 1981. Oceans and continents: Similarities and differences in mechanisms of heat loss. J. Geophys. Res. 86, 11535-11552.

Schellart, W.P., Stegman, D.R., Freeman, J., 2008. Global trench migration velocities and slab migration induced upper mantle volume fluxes: Constraints to find an Earth reference frame based on minimizing viscous dissipation. Earth-Science Reviews 88, 118-144, doi:10.1016/j.earscirev.2008.01.005.

Schellart, W.P., 2008. Subduction zone trench migration: slab driven or overriding-plate-driven? Physics of the Earth and Planetary Interiors 170, 73-88, doi:10.1016/j.pepi.2008.07.040.

Silver P.G., Russo R.M., Lithgow-Bertelloni, C., 1998. The coupling of plate motion and plate deformation. Science, 279, 60-63.

Sonder, L.J., Jones, C.H., 1999. Western United States extension: How the West was widened. Ann. Rev. Earth Planet. Sci. 27, 417-462.

Steiner, S.A., Conrad, C.P., 2007. Does active mantle upwelling help drive plate motions? Phys. Earth Planet. Int. 161, 103-114.

Stegman, D.R., Freeman, J., Schellart, W.P., Moresi, L., May, D., 2006. Influence of trench width on subduction hinge retreat rates in 3-D models of slab rollback. Geochemistry Geophysics Geosystems 7, doi:10.1029/2005GC001056.

Turcotte, D.L., Schubert, G., 1982. Geodynamics: Applications of continuum physics to geological problems, John Wiley and Sons, New York.

Xu, X., Lithgow-Bertelloni, C., Conrad, C.P., 2006. Global reconstructions of Cenozoic seafloor ages: Implications for bathymetry and sea level. Earth and Planetary Science Letters 243, 552-564.

Wernicke, B., Axen, G.J., Snow, J.K., 1988. Basin and Range extensional tectonics at the latitude of Las Vegas, Nevada. Geological Society of America Bulletin 100, 1738-1757.

Wilson, J.T., 1966. Did the Atlantic Close and then Re-Open? Nature 211, 676-681.

Yamato P., Husson L., Braun J., Loiselet C., Thieulot C., 2009. Influence of surrounding plates on 3D subduction dynamics, Geophysical Research Letters 36, doi:10.1029/2008GL036942.

Zhong, S., Zhang, N., Li, Z.X., Roberts, J.H., 2007. Supercontinent cycles, true polar wander, and very long-wavelength mantle convection. Earth and Planetary Science Letters 261, 551-564.

Figure 1
Click here to download Figure: fig1_husson.pdf

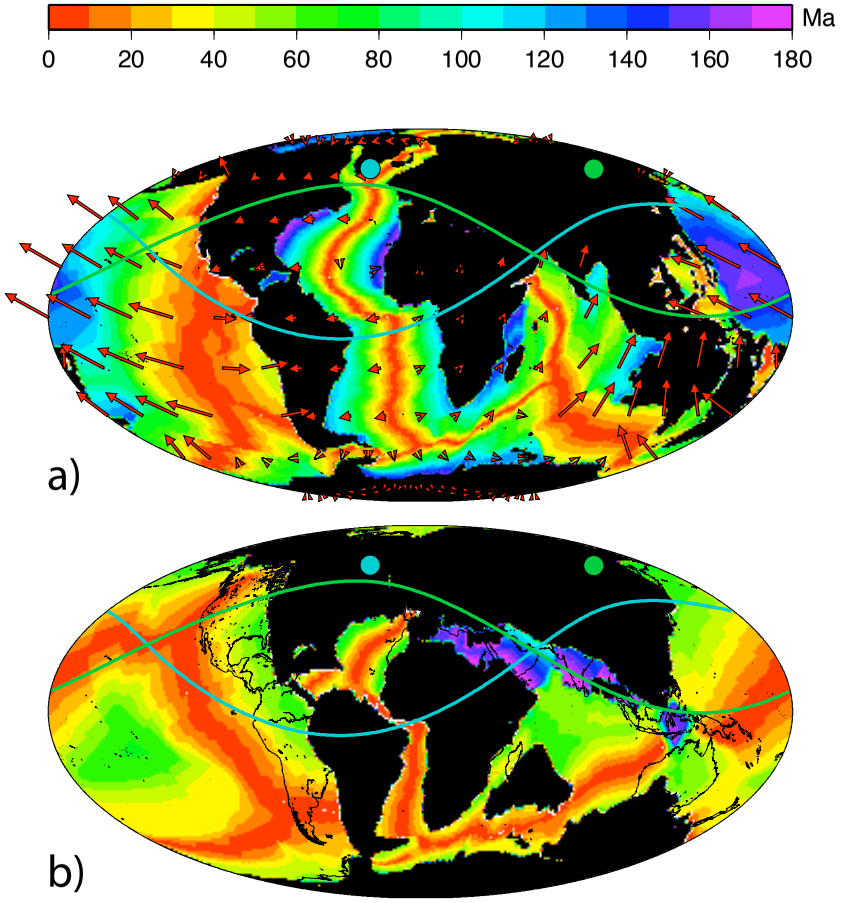

oad Figure: fig2_husson.pdf

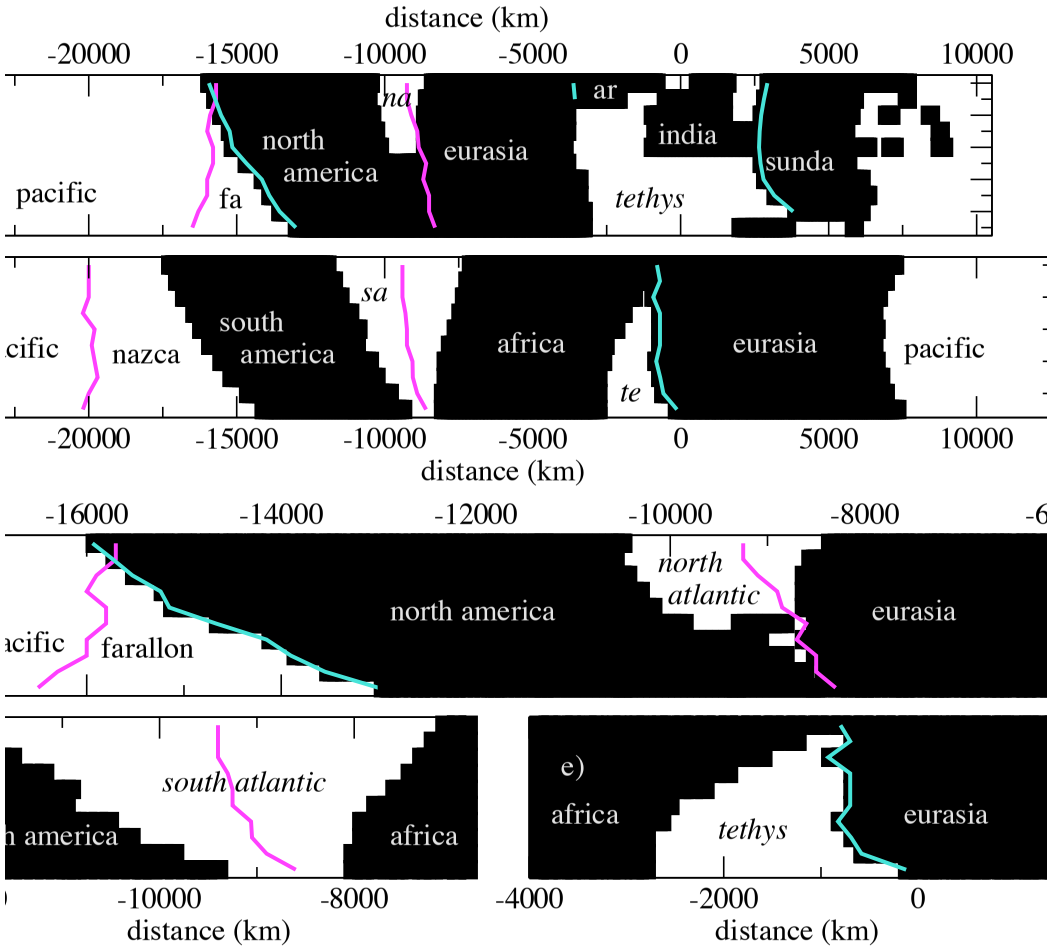

oad Figure: fig3_husson.pdf

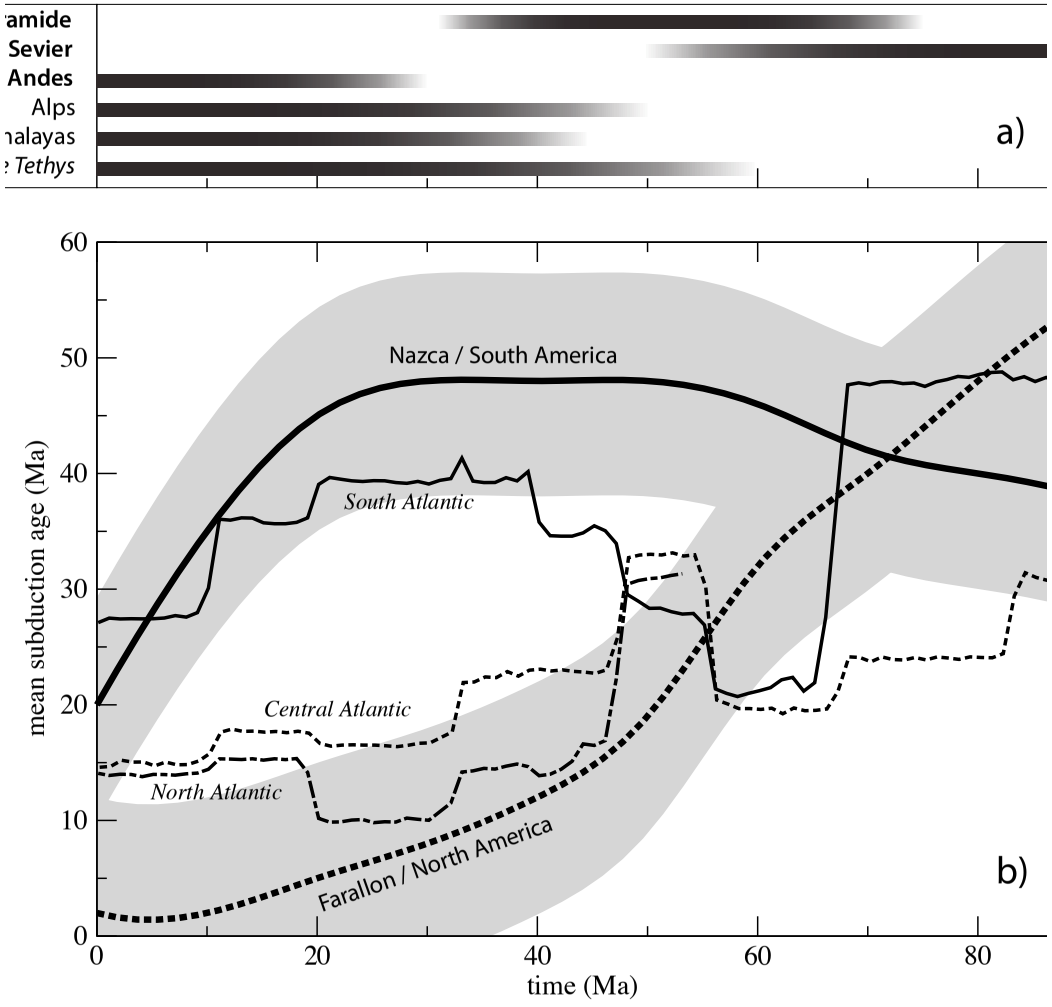

Figure 4
Click here to download Figure: fig4_husson.pdf

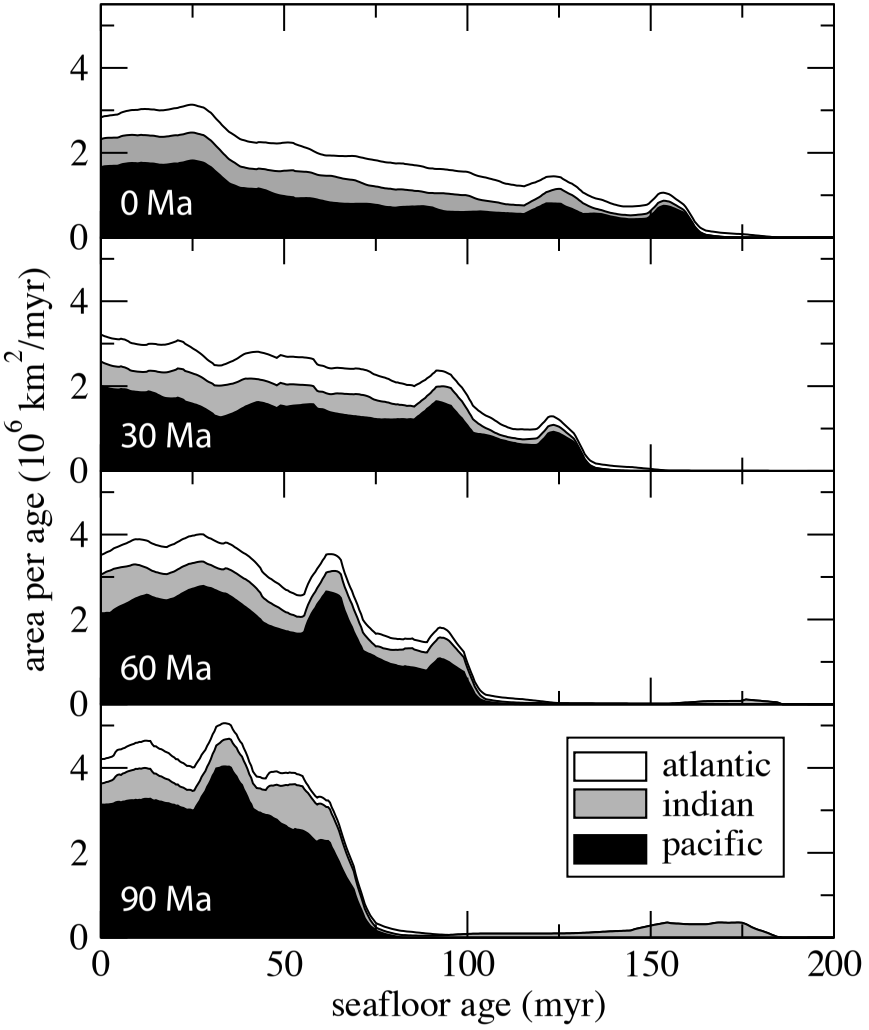

Author's personal copy

Earth and Planetary Science Letters 271 (2008) 303–310

Contents lists available at ScienceDirect

Earth and Planetary Science Letters

journal homepage: www.elsevier.com/locate/epsl

Tethyan closure, Andean orogeny, and westward drift of the Pacific Basin

Laurent Husson [a,*], Clinton P. Conrad [b], Claudio Faccenna [c]

[a] Géosciences Rennes, Université Rennes 1, Université Rennes 1, Rennes, France
[b] Department of Earth and Planetary Science, Johns Hopkins University, Baltimore, Maryland, USA
[c] Dipartimento di Scienze Geologiche, Universita Roma Tre, Rome, Italy

ARTICLE INFO

Article history:
Received 22 June 2007
Received in revised form 12 October 2007
Accepted 11 April 2008
Available online 26 April 2008

Editor: C.P. Jaupart

Keywords:
mantle flow
subduction
net rotation
trench motion
Pacific

ABSTRACT

The deep-sea trenches that circumscribe the Pacific basin are moving westward relative to the deep mantle by a few cm/yr, together with the Pacific seafloor. While the westward drift of the Pacific basin dominates the observed net westward rotation of Earth's tectonic plates relative to the deep mantle source of the Pacific hotspots, its cause remains uncertain. We demonstrate that the source of this westward drift is tectonic in origin: the westward push of the high Andean topography along the eastern Pacific margin is large enough to shear the entire Pacific upper mantle with a surface velocity of ~30 mm/yr. In addition, because the Pacific upper mantle is confined between vertically coherent slabs of subducted lithosphere on both sides of the Pacific, slabs in the western Pacific are forced to advance toward upper plates because the eastern Pacific slabs are pushed westward. This cross-Pacific interaction provides an explanation for trench advance, which is observed in the western Pacific and is not easily explained by the local dynamics of subduction in which dense sinking slabs essentially tend to retreat from overriding plates. Thus, the basic asymmetry of the Pacific system, which has been noted for almost all tectonic features including slab dips, trench motions, and upper plate tectonics, is the result of one-sided Andean forcing on the volume of Pacific upper mantle. The net rotation of the lithosphere is then the result of surface tectonics: westward motion is an accident resulting from the current distribution of tectonic plates, and was triggered by the mid-Cenozoic closure of the Tethys Ocean, via a westward expansion of the Atlantic and Andean cordilleran building.

© 2008 Elsevier B.V. All rights reserved.

1. Introduction

The tectonic plates that cover the surface of the Earth are, on average, drifting westward relative to the locations of hotspots that are tied to the deep mantle (Bostrom, 1971; Uyeda and Kanamori, 1979; Doglioni, 1990). This westward drift, a consistent feature of kinematic reconstructions (Minster and Jordan, 1978; Gordon and Jurdy, 1986), is reported to be occurring at rates as large as 48 mm/yr in the HS3 (Pacific hotspot) reference frame (Gripp and Gordon, 2002)] and is dominated by the rapid westward motion of the large Pacific plate (Fig. 1a). Although other hotspot reference frames exhibit smaller magnitudes of net lithosphere rotation, all choices require a net westward motion of the lithosphere relative to the deep mantle (see Becker, 2006 for a review).

The net rotation is a puzzling feature of Earth's surface tectonics because convective mantle flow, which drives plate motions, cannot induce a net surface rotation unless some plates are more tightly coupled to this flow than others. While net rotation of the lithosphere can be induced in numerical models that include thick roots beneath continental cratons (Ricard et al., 1991) and temperature and strain-rate dependent viscosities (Becker, 2006), these models predict amplitudes of net rotation that are generally smaller than amplitudes constraints supplied by hotspot reference frames (Zhong, 2001; Becker, 2006). Furthermore, these models do not explain basic differences between the tectonics of the western Pacific, where subducting slabs are steeper and associated with extensional upper plate settings ("Marianas" type of Uyeda and Kanamori, 1979) compared to the eastern Pacific with shallower slabs ("Chilean" type of Uyeda and Kanamori, 1979) and compression that forms Andean-style mountain belts.

It has nevertheless been proposed that the westward motion of the Pacific system could be correlated to the cross-Pacific tectonic dichotomy (Ricard et al., 1991; Doglioni et al., 1999). The net rotation of the lithosphere and westward motion of the Pacific plate have also been related to the contrasted migration behavior of trenches, with predominantly advancing trenches along the western margin of the Pacific and retreating trenches along its eastern margin (Carlson and Melia, 1984; Heuret and Lallemand, 2005; Faccenna et al., 2007). The correlation between subduction kinematics and local intrinsic subduction properties such as slab age-buoyancy is not straightforward (Jarrard, 1986; Doglioni et al., 1999; Lallemand et al., 2005). However, a positive correlation between slab dip and the dynamics of the upper plate (Lallemand et al., 2005) suggests consideration of the possibility that upper plates may exert an external forcing not only on cross-Pacific subduction dynamics, but on the entire Pacific system.

* Corresponding author.
E-mail address: laurent.husson@univ-rennes1.fr (L. Husson).

0012-821X/$ – see front matter © 2008 Elsevier B.V. All rights reserved.
doi:10.1016/j.epsl.2008.04.022

Author's personal copy

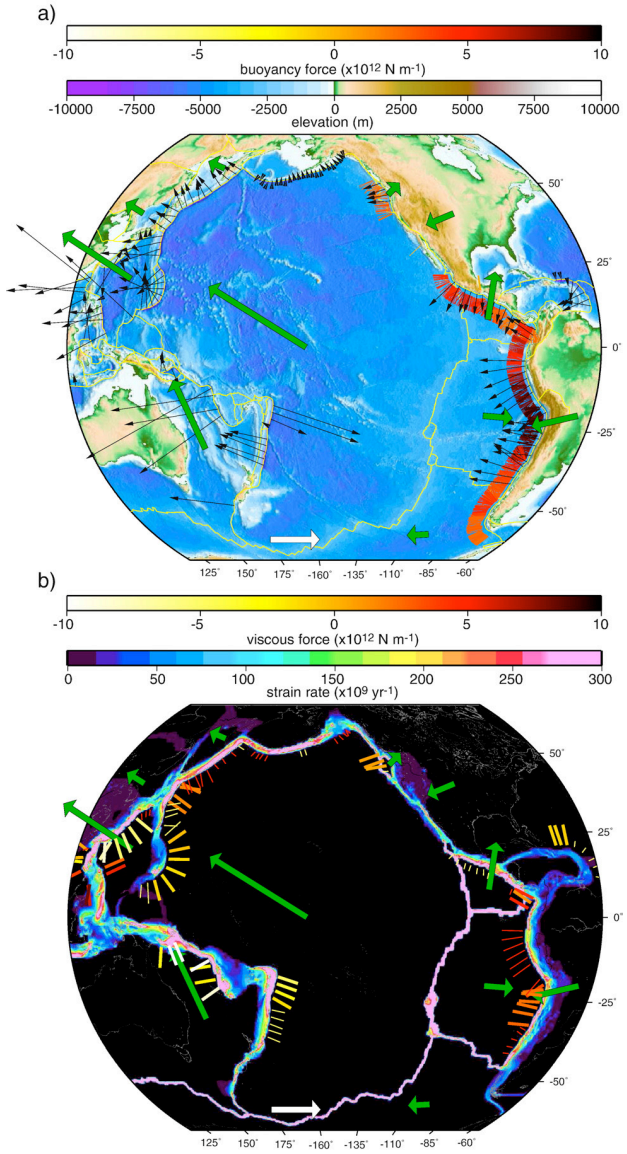

We therefore present an original view of tectonic forcing on the Pacific upper mantle that explains both the net rotation of the lithosphere and cross-Pacific differences in subduction kinematics. In this view, subduction zones are explored within a global framework that separates the upper mantle, slabs and lithosphere into two prominant and interacting, convection cells: the Pacific, or Panthalassan, and the Indo-Atlantic, or Pangean, domains (Collins, 2003; Davaille et al., 2005).

2. Net rotation of the Pacific system

A tectonic explanation for westward drift is suggested by the absolute motions of trenches, which are found where plates bend and enter the subduction system. Subduction in its most basic form involves a plate following itself into the mantle. Trenches can easily retreat toward the subducting plate; by contrast, trench advance (toward the overriding plate) is gravitationally unfavorable because it requires mantle to fill in the space beneath the slab, and requires specific boundary (Bellahsen et al., 2005) and rheologic (Billen and Hirth, 2007; Faccenna et al., 2007) conditions. A recent global survey of trench migration rates (Lallemand et al., 2005), however, shows that a plethora of trenches in the western Pacific advance at fast rates (Fig. 1a) in the Pacific hot spot reference frame (model HS3-NUVEL 1A, Gripp and Gordon, 2002). Along-strike averages of trench migration rates from Lallemand et al. (2005) indicate trench advance at ~ −23 mm/yr and retreat at ~37 mm/yr on the western and eastern Pacific sides, respectively. The fact that westward advance of the western Pacific trenches is accompanied by westward retreat of trenches in the eastern Pacific (at rates up to 40 mm/yr, Fig. 1a) suggests that the entire Pacific basin is migrating westward at ~30± 7 mm/yr, together with other known bimodal features of the Pacific (Table 1), (Jarrard, 1986; Doglioni et al., 1999; Lallemand et al., 2005). For example, west-subducting and east-subducting plates are moving at rates of 110 mm/yr and 50 mm/yr respectively (Gripp and Gordon, 2002), i.e 30 mm/yr faster and slower than the half-spreading rate of the intermediate East Pacific ridge. This indicates a ~30 mm/yr general westward drift of the entire Pacific system, including both overriding and subducting plates and the trenches between them. This pattern suggests that trench advance in the western Pacific and overall westward drift of the lithosphere are related issues.

Although global mantle flow models based on seismic tomography (Zhong, 2001; Becker, 2006) can reproduce the westward direction of the observed HS3 (Gripp and Gordon, 2002) net rotation, they generally do not reproduce the 48 mm/yr amplitude of this rotation. Instead, the maximum amplitude of the predicted net rotation matches the minimum net rotation estimated using Indo-Atlantic and Pacific hotspots (Gordon and Jurdy, 1986) and even remains lower than the amplitude estimated using the Indo-Pacific hot-spot tracks (Steinberger et al., 2004). Although the magnitude of the westward drift incorporated by the HS3 model is controversial and might be an end-member, we consider it to be more appropriate for our analysis of Pacific subduction zone kinematics because it is based on Pacific hot spots. In addition, note that the overall pattern of trench motion (advancing versus retreating) is a persistent feature because a large portion western Pacific trenches are advancing regardless of the reference frame (Funiciello et al., 2007).

The bimodal setting of the Pacific basin allows for a two-dimensional approximation; total trench lengths are comparable on both eastern and western sides (~12,000 km from Tierra del Fuego to northern British Columbia and from the south of New Zealand to Kamchatka, respectively, Table 1) and the subducting lithosphere forms a N–S cylindrically folded sheet that wraps the Pacific upper mantle (Fig. 2). This volume is also bounded on its underside at 670 km by the high viscosity of the lower mantle, which is thought to be up to two orders of magnitude greater than that of the upper mantle (Lambeck and Chappell, 2001). The slabs that bound the Pacific upper mantle are slightly discontinuous: upper mantle "leaks", where the mantle can escape from the Pacific zone via toroidal flow, are mostly restricted to the ~6000 km wide southern boundary, which is orthogonal to the slabs, and the ~1700 km long transform boundary of North America, which together account for only ~20% of the total circum Pacific length (within the ~N–S oriented slabs bounding the eastern and western sides of the Pacific upper mantle, openings only amount to less than ~10% of the total trench length). Therefore the length and continuity of slabs not only moderate the rate of Pacific shrinkage but also prevent toroidal flow almost everywhere; hence if some slabs retreat, the trapped upper mantle must accompany the journey of the slabs. This in turn implies that any slab retreat on one side also has to be accompanied by slab advance on the other side. Thus, a westward-directed net force on the oceanic plates of the Pacific basin will cause the entire system of Pacific upper mantle, trenches, and plates to drift westward. This will tilt upper mantle slabs increasingly toward the east (Fig. 2).

Table 1
Mean geometric/kinematic characteristics of W. Pacific and E. Pacific subduction zones (after Lallemand et al., 2005), in the hot spot reference frame (HS3-Nuvel1A Gripp and Gordon, 2002)

	Slab dip	Length	UP	Trench velocity	UP velocity	LP velocity
East	50° E	12000 km	Continental	37 mm/yr	42 mm/yr	30 mm/yr
West	70° W	11000 km	Oceanic	-23 mm/yr	-40 mm/yr	100 mm/yr

Positive velocities are trenchward. UP: upper plate, LP: lower plate. See details in text (neglecting the ~E–W trending Aleutian trench).

3. Driving mechanism

What is the driving force that causes this westward drift of the Pacific? Forces that arise from upper plates may have a significant impact on subduction dynamics (Royden and Husson, 2006), and for the Pacific, significant differences between the eastern- and western-bounding upper plates are evident (Table 1). Most notable among these differences is the presence of a mountain range on the east (the Andes) and its absence on the west (Uyeda and Kanamori, 1979). Silver et al. (1998) demonstrated that the faster westward motion of South America triggered by the mid-Cenozoic closure of the Tethys sea (collision of Africa and India with Eurasia), is responsible for the Andean cordilleran orogeny. Here we consider the possibility that this forcing is also transferred through South America and on to the subducting plates of the Pacific, thus driving their westward motion. Thus, instead of regarding upper plate deformation as a by-product of subduction dynamics, we consider it as an external forcing on the Pacific system. In this respect, we develop a semi-analytical approach that avoids the technical difficulties and associated modeling uncertainties that are currently an inherent part of efforts to embed detailed subduction dynamics within numerical models of mantle flow (Conrad and Hager, 2001; Becker, 2006).

3.1. Force balance

Because it is challenging to model the dynamics of the upper plate, we alternatively use upper plate kinematics to infer its dynamics (England and Molnar, 1997). In this case, viscous stresses result from

Fig. 1. Kinematic and dynamic descriptions of Pacific tectonics. Black and green arrows indicate trench and plate velocities in the hot spot reference frame (Gripp and Gordon, 2002), respectively (white arrow is 50 mm/yr). Colours represent (a) topography and (b) strain rates (after Kreemer et al., 2000). Thick ticks show (a) the maximum buoyancy force per unit trench length in the upper plates (with ρ_c=2800 kg m^{-3} and ρ_m=3300 kg m^{-3}) and (b) the maximum viscous force per unit trench length in the upper plates. Thin ticks in (b) show compressive (red) and extensive (yellow) viscous forces (length is qualitative magnitude from Lallemand et al., 2005). Positive values denote trenchward forces.

Author's personal copy

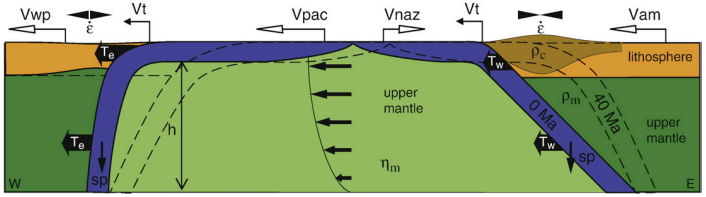

Fig. 2. Conceptual model for the Pacific upper mantle and plate circulation. Vt: trench velocity, Vnaz, Vpac, Vam, Vwp: Nazca, Pacific, American (North/South), West Pacific (Australia/Eurasia) velocities. $\dot{\varepsilon}$: viscous deformation; sp: slab pull. Thin black arrows indicate Poiseuille flow in the upper mantle.

the disequilibrium between boundary stresses and buoyancy stresses. In a continuous media, gradients of stress are balanced by the force of gravity per unit volume,

$$\partial \sigma_{ij}/\partial x_j = -\rho g_i, \tag{1}$$

where σ_{ij} is the ij^{th} component of the stress tensor ($\sigma_{ij}=\tau_{ij}-P\,\delta_{ij}$, where τ_{ij} is the deviatoric stress tensor and P is pressure), x_j is the j^{th} coordinate direction, ρ is the density, g_i the i^{th} component of the gravitational acceleration. In 2D, i and j only stand for the x (horizontal) and z (vertical) directions. The lithosphere can be conveniently approximated as a thin viscous sheet; this approximation has been extensively applied (England and McKenzie, 1982; Houseman and England, 1993) and here we only briefly develop the governing equations that are based on the vertical integration of the Navier–Stokes equation over the lithosphere thickness. Such models assume that the vertical variations of the horizontal velocity can be neglected within the lithosphere, and that deformation occurs at wavelengths larger than lithosphere thickness. The total vertical stress induced by a column of rock in the lithosphere is (neglecting 2nd order terms),

$$\sigma_{zz}(z) = g\int_0^z \rho(z')dz'. \tag{2}$$

Upper plate deformation is controlled by the distribution of basal shear stresses, either between the plates or at the asthenosphere/lithosphere boundary (Husson and Ricard, 2004). By vertically integrating the horizontal equilibrium over the lithosphere thickness L, we obtain,

$$\frac{\partial}{\partial x}\int_0^L \sigma_{xx}dz + \sigma_{xz} = 0, \tag{3}$$

which relates the horizontal gradient of the mean horizontal stress over the lithosphere to the basal shear stress σ_{xz}. Balancing horizontal and vertical stress terms via the pressure P, we write $\sigma_{xx}=\tau_{xx}-\tau_{zz}+\sigma_{zz}$. For a Newtonian fluid, $\tau_{ij}=\eta\left(\frac{\partial u_i}{\partial x_j}+\frac{\partial u_j}{\partial x_i}\right)$, where η is the viscosity, and u_i and u_j are the components of the velocity vector. Plugging Eq. (2) into Eq. (3), the horizontal equilibrium becomes (again, neglecting 2nd order terms, Husson and Ricard, 2004)

$$4L\frac{\partial}{\partial x}\eta\frac{\partial u_x}{\partial x} + \sigma_{xz} = \frac{\partial M}{\partial x}, \tag{4}$$

where η is now the average viscosity of the lithosphere, and $M=\int_0^{-\infty}\delta\rho g z dz$ is the moment of the lithospheric mass anomalies (Artyushkov, 1973; Fleitout and Froidevaux, 1982). Restricting density variations in the lithosphere to crustal thickness variations (i.e. neglecting the density contrast between continental lithosphere and asthenosphere), we calculate the isostatic crustal thickness $S=h\rho_m/(\rho_m-\rho_c)$. Assuming isostasy, elevation h can therefore be used as a proxy for the moment because $M=\frac{1}{2}g\frac{\rho_c\rho_m}{\rho_m-\rho_c}h^2$, where ρ_c and ρ_m are the crust and mantle densities. Eq. (4) can thus be conveniently written

$$\sigma_{xz} = \frac{1}{2}\frac{\rho_c\rho_m}{\rho_m-\rho_c}\frac{\partial h^2}{\partial x} - 4L\frac{\partial}{\partial x}\eta\frac{\partial u_x}{\partial x}, \tag{5}$$

where σ_{xz} is the traction at the base of the plate, and the first and second terms on the right hand side of the equation are the buoyancy and viscous components of stresses, respectively. When applied to plate margins, positive values of σ_{xz} indicate compression due to interplate traction and negative values quantify the resistance of the asthenosphere to the displacement of the lithosphere (Husson and Ricard, 2004).

3.2. Net westward force

The total force T transmitted from one plate to the other is the sum of buoyancy and viscous forces. It can be approximated by the horizontal integration of the shear stresses between the two plates given by Eq. (5), i.e. by the sum of the moment and the deviatoric stresses integrated over the lithosphere thickness. Along the eastern margin of the Pacific, buoyancy forces that build up as a result of compression (primarily the Andean mountain belt) are large and locally reach more than 10^{13} N m^{-1} (Fig. 1a), with an average of 4.8×10^{12} N m^{-1}. To obtain these estimates, we Fourier-filtered the topography in order to discard wavelengths smaller than 75 km (and thus the extreme peaks) and used the normal distance between the trench and the location of the maximum moment (i.e. the location of the maximum elevation) to approximate the integration distance Δ that corresponds to interplate traction (which in essence is given by the sum of positive values of σ_{xz}). From Eq. (5),

$$T = \int_{\Delta}\sigma_{xz}dx. \tag{6}$$

On the western margin of the Pacific, the buoyancy forces are negligible (beyond our approximation) and we discarded them. Viscous forces can be evaluated from deviatoric stresses inferred from strain rates in the upper plates (deduced from Lallemand et al., 2005). Of course they are highly dependent on the viscosity of the lithosphere which has an uncertainty of an order of magnitude. Choosing a low effective viscosity of the lithosphere of $3\times10^{21}\pm2\,10^{21}$ Pa s (England, 1986; Husson and Ricard, 2004), a characteristic width of deformation of 100 km and plate thicknesses of 100 km and 50 km for the continental and oceanic lithospheres, respectively (10 km for active back-arc systems), we find minimum mean viscous forces of 1.2×10^{12} N m$^{-1}\pm2.5\times10^{12}$ N m^{-1} and -3.7×10^{12} N m$^{-1}\pm2.5\times10^{12}$ N m^{-1} along the eastern and western margins, respectively (Fig. 1b and Table 2). Along the eastern margin, they are significantly lower than buoyancy forces, indicating that buoyancy -or body-forces balance boundary -or tectonic-forces, and that tectonic equilibrium is almost achieved in mountain belts (Husson and Ricard, 2004). The mean total force transmitted from the upper plates to the lower ones are thus $T_e=6.0\times10^{12}$ N m^{-1} and $T_w=-3.7\times10^{12}$ N m^{-1}, along the eastern and western margins, respectively.

Table 2
Mean dynamic characteristics of W. Pacific and E. Pacific subduction zones, in the hot spot reference frame (HS3-Nuvel1A, Gripp and Gordon, 2002)

	Mean elevation, UP	Buoyancy force	Strain rate	Viscous force	Total force
East	2270 m	4.8×10^{12} N m^{-1}	-2×10^{-15} s^{-1}	1.2×10^{12} N m^{-1}	$T_e=6.0\times10^{12}$ N m^{-1}
West	/	/	12×10^{-15} s^{-1}	-3.7×10^{12} N m^{-1}	$T_w=-3.7\times10^{12}$ N m^{-1}

Positive forces denote compression. UP: upper plate. See details in text.

Author's personal copy

3.3. Upper mantle shear

This result suggests that upper plates are pushing the lower plates westward along the eastern margin and pulling them westward along the western margin. A comparison between the kinematics (Table 1) and dynamics (Table 2) of the eastern and western margins of the Pacific makes this long recognized dichotomy (Uyeda and Kanamori, 1979; Jarrard, 1986) even more striking. In fact, when the Pacific domain is considered in 2D, it seems that the only difference between eastern and western sides of the Pacific arises from this additional forcing from upper plates. Slab pull is generally considered as the main driving force, and as such is presumed responsible for trench retreat. But because the Pacific upper mantle is bounded almost everywhere – laterally by slabs, beneath it by a lower mantle where the viscosity increases by two orders of magnitude – it essentially has to remain within the domain of the Pacific basin. There is no obvious contrast between eastern and western slab pull forces, which drive the relative motions of the Pacific and Nazca plates but are mutually annihilated in a net sense. This leaves the Pacific domain in a *status quo* of antagonistic forces that, by itself, precludes systematic trench retreat. In fact, Lallemand (1998) already suggested that "sub-Pacific mantle resistance to contraction may induce a delay in retrograde slab migration".

The forces that are transmitted from the upper plates are directed westward on both sides of the Pacific, i.e toward the subducting plate along the eastern margin, and toward the overriding plate along the western side. The sum of the westward components of the forces, $|T_e|+|T_w|\simeq10\times10^{12}$ N m^{-1} (Table 2) is comparable in magnitude to the main plate-driving forces such as slab pull (Conrad and Lithgow-Bertelloni, 2002). This total traction is distributed over the Pacific width, shears the upper mantle, and induces westward drift of the entire Pacific system, including oceanic lithospheres, upper mantle, slabs, and trenches. The validity of this hypothesis is tested in Appendix A, in which the Pacific system is simplified into two vertical slabs of width W, facing each other and separated by a distance W. When one slab moves steadily toward the other, the Stokes flow between these two slabs shows that the open ends between the slabs do not permit enough mantle leakage to significantly diminish the transmission of compressive stresses between the converging slabs. This implies that only mantle that is close to Tonga and the San Andreas can escape the Pacific system, and that the presence of these openings does not significantly diminish the stress transmission required to shear the Pacific upper mantle.

The velocity at which the system drifts is controlled by the viscosity of the upper mantle, which deforms in response to surface plate motions. To estimate the viscosity, η_{lum}, that produces the observed surface drift, we consider 2D Poiseuille flow of the upper mantle with a free surface slip, where slabs transmit surface stresses to the upper mantle because they are stiffer than the asthenosphere and anchored in the lower mantle. The velocity at the surface is:

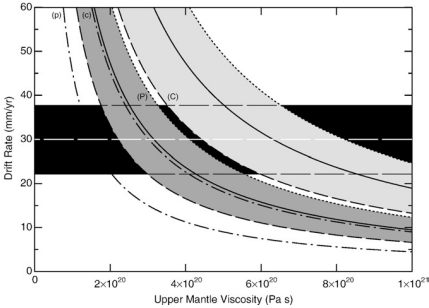

Fig. 3. Upper mantle flow in the Pacific described by Poiseuille (P, dark shaded) and Couette (C, light shaded) flows for a total force of 7×10^{12} N m^{-1} (dashed lines), 10×10^{12} N m^{-1} (solid lines) and 13×10^{12} N m^{-1} (dotted lines), and 4.8×10^{12} N m^{-1} (dotted-dashed line, (d) and (c), only considering buoyancy forces), $W=10{,}000$ km, $h=600$ km (removing a 70 km thick lithosphere thickness). Dotted line and grey box bounds the westward drifting rate of the Pacific domain (30 ± 7 mm/yr).

$$u_0 = -\frac{h}{2\overline{\eta}_{um}}\frac{|T_e|+|T_w|}{W}, \tag{7}$$

where W is the average width of the Pacific ocean and h is the thickness of the upper mantle. For the estimated total force, a surface velocity $u_0=30\pm7$ mm/yr requires a mean upper mantle viscosity $\overline{\eta}_{um}=3.1\times10^{20}\pm10^{20}$ Pa s (Fig. 3). The fact that this value is consistent with independent estimates (Lambeck and Chappell, 2001; Steinberger et al., 2004; Mitrovica and Forte, 2004) supports our model. If we neglect viscous forces in the overriding lithospheres, the required viscosity is smaller ($\overline{\eta}_{lum}=1.5\ 10^{20}\pm10^{20}$ Pa s). If slabs are not strong enough to transmit surface stresses down to the upper mantle, but the stresses are exerted directly on the subducting plates, then the drift of those plates will instead induce laminar (Couette) shear flow in the upper mantle. In this case, the force balance on the lithosphere yields a drift rate that is twice that of Eq. (7), which implies estimates for the upper mantle viscosity that are twice as large as those for Poiseuille flow for the same driving force and drift rate (Fig. 3), but still in the range of independent estimates (Lambeck and Chappell, 2001; Steinberger et al., 2004; Mitrovica and Forte, 2004). It may be argued that the convecting, heterogeneous mantle may prevent stresses from being transmitted across the system. In particular, in the strict case of Couette shear flow, the stresses on the system must be transmitted across the East Pacific ridge, which could be thought problematic because of the supposed weakness of ridge systems. However, there is no reason for ridges to be stress free. Because stresses are continuous and add up linearly, only deformation may vary rapidly as a result of spatial variations in viscosity, not stresses. Moreover, in a continuous media stresses can be transmitted laterally beneath the ridge via the upper mantle. The divergence that is observed at ridges only mirrors stresses arising from the underlying convecting mantle. Far field compressive stresses associated with the shrinking of the Pacific are exerted on top of the diverging convective stresses; it would be an extraordinary coincidence if these two sets of stresses cancel. We conclude that the drift rate of the Pacific is consistent with both the tectonic forces that drive drift and the viscous deformation that resists it.

For Poiseuille flow, the mean upper mantle velocity is $\overline{u}_{lum}=\frac{2}{3}u_0$, which implies that plates and trenches drift at faster rates ($\overline{u}_0\simeq30$ mm/yr) than the upper mantle on average ($\overline{u}\simeq20$ mm/yr).

Author's personal copy

Also notice that that lower estimates for the Pacific drift rate derived in different reference frames (Gordon and Jurdy, 1986; Steinberger et al., 2004) imply higher viscosities. Because deeper layers move more slowly, western slabs dip more steeply than eastern ones (Fig. 2), as noted by observations (Jarrard, 1986; Doglioni et al., 1999; Lallemand et al., 2005). A regional expression of the general westward drift of the upper mantle is (paradoxically) the rapid eastward retreat of the Tonga trench associated with the opening of the Lau basin (Fig. 1): the discontinuous northern edge of the Tonga slab is an uncommon setting in which toroidal flow around the edge that permits slab retreat. Significant unbounded edges are absent elsewhere in the western Pacific; as a result these trenches only advance. The presence of such "leaks" also explains the faster westward motion of eastern trenches than that of western ones: part of the upper mantle volume that is trapped under the Pacific manages to flow outside of the Pacific domain, which is shrinking in response to the growth of the Atlantic and Indian spreading systems.

4. Discussion

Implications are twofold. First, trench advance can be explained by an additional forcing from upper plates: heterogeneities in the vigour of subduction roll-back, boosted or not by stresses arising from upper plates at places that depend on the given distribution of tectonic plates, impose an overall shear of the upper mantle that causes trench advance at other locations. This mechanism is thus alternative to models where trench motion is driven purely by slab parameters (Bellahsen et al., 2005; Faccenna et al., 2007; Capitanio et al., 2007). In this regard, the change in trench migration behavior during Mid-Miocene (e.g. Sdrolias and Muller, 2006) toward more advancing and retreating regimes for western and eastern slabs, respectively, could be correlated to the onset of Andean building, which can be regarded as the triggering mechanism. It follows that subduction kinematics – in the Pacific in particular – can be considered as dependent on the dynamics of the broader Pacific system (the Panthalassan framework of Collins (2003), and not solely a result of the local subduction properties.

Second, the long-recognized net rotation of the lithosphere in general (Bostrom, 1971; Uyeda and Kanamori, 1979; Doglioni, 1990; Ricard et al., 1991), and of the Pacific in particular, is governed by the motion of the upper plates, in the sense that they form boundary layers that transmit stresses from one convecting unit to another. The current force exerted by the South American plate plays a major role; it accounts for about half of the total force that shears the Pacific upper mantle. This effect may be somewhat surprising, but it is in fact not unexpected since such large transmission of stresses across the interplate contact has been evidenced by other means: Andean growth may be responsible for the decrease in convergence rates between Nazca and South American plates (Iaffaldano et al., 2006). In Tibet, the very large gravitational potential energy compresses and buckles the Indian lithosphere (Chamot-Rooke et al., 1993; Martinod and Molnar, 1995): the long-wavelength undulations of the Indian plate are viscous folds resulting from the increased compression between the Indian plate and Tibet.

This situation connects the Pacific system to the current understanding of the Atlantic system and global plate circuit (Fig. 4): the mid-Cenozoic closure of the Tethys and subsequent aggregation of Africa to Eurasia led to the formation of a massive continent,

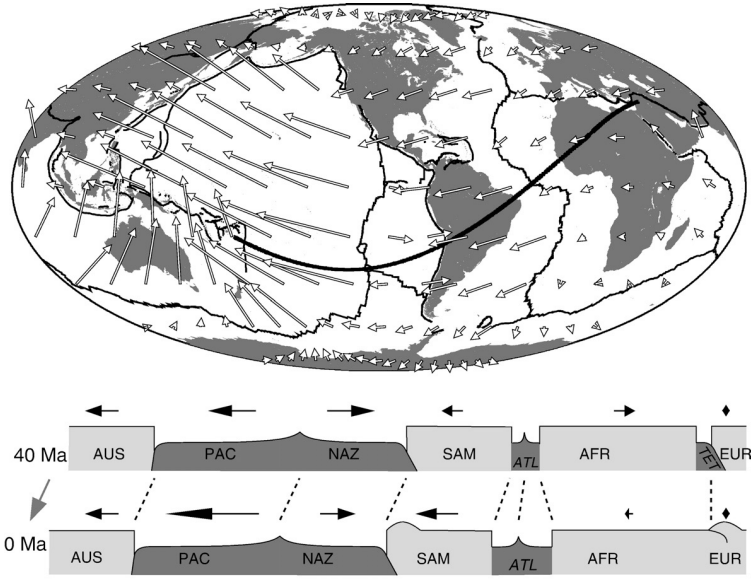

Fig. 4. Top) Map view of the present day plate motion in the hot spot reference frame (Gripp and Gordon, 2002; bottom) section along a great circle crosscutting the Pacific/Atlantic plate circuit (location on map) before (40 Ma) and after (0 Ma) the closure of the Tethys. Note that spreading of both Atlantic and Pacific oceans changed from symmetric to asymmetric. Dark (light) shaded areas are oceanic (continental) units. AUS: Australia; PAC: Pacific; NAZ: Nazca; SAM: South America; AFR: Africa; EUR: Eurasia; ATL: Atlantic; TET: Tethys. Black arrows indicate plate velocities in the hotspot reference frame. Dashed lines indicate the moving location (in the hotspot reference frame) of characteristic locations.

Author's personal copy

profoundly anchored into the mantle by its highly viscous lithospheric keel. The surrounding plates are thinner and easily move apart from it. This abrupt change disrupted the global plate circuit and in particular triggered a westward drift of the Atlantic ridge and a faster westward motion of the South American plate, subsequently increasing stresses along the South American margin sufficient to develop the Andean belt (Silver et al., 1998; Sobolev and Babeyko, 2005). Those large stresses are in turn transmitted to the subducting plates and the Pacific upper mantle. In the theoretical situation where the closure of the Tethys and subsequent western expansion of the Atlantic started abruptly, the total force was transmitted to the Pacific system instantaneously: it was transmitted via viscous stresses in the upper plate before the Andes formed and via buoyancy stresses associated with the presence of a mature Andean orogenic belt afterwards (Eq. (5)). The net transmitted force T would then be constant through time. This implies that the net rotation of the Pacific and Andean growth are coeval, unless interplate coupling evolved through time (Iaffaldano et al., 2006).

A small amount of upper mantle material leaks out of the Pacific domain, which explains why western subduction zones are moving westward more slowly than eastern ones by ~14 mm/yr, which causes the area of the Pacific basin to shrink by ~0.1% per Myr, while the Atlantic basin expands. We estimate that $\sim 0.1 \times 10^9$ km^3/Myr of upper mantle material flows from the Pacific reservoir into the Atlantic reservoir (from the Panthalassan domain to the Pangean domain, (Collins, 2003; Davaille et al., 2005) through the 1700 km long North American transform margin, which can be considered the only significant outlet. This volume transfer is independent of the reference frame. Thus, even if the HS3 reference frame (Gripp and Gordon, 2002) overestimates the magnitude of the westward drift of trenches, other reference frames (see Becker, 2006 for a review) tend to accommodate Pacific shrinkage by holding western trenches steady while eastern trenches retreat. The cross-Pacific dichotomy is therefore persistent and we conclude in any case that the mid-Cenozoic plate circuit reorganization at least led to the onset of Pacific shrinking with the same mechanism of stress transmission.

Therefore, eastern Pacific mountain belts – the Andes in particular – transmit stresses from the Atlantic domain to the Pacific domain; note that these stresses will last as long as the spreading of the Atlantic prevails at such rate. Eventually, the entire Pacific upper mantle system is sheared, as multiple geometric and kinematic features suggest (Table 1). Similarly, the Laramide and Sevier orogenies, which formed during the Cretaceous when the Andean belt was rather small, may also have caused westward drift, this time imposed by the North American plate; the present-day location of the Farallon slab beneath eastern North America (Bunge and Grand, 2000) seems to testify for this drift. In spite of its early timing, the Hawaii–Emperor seamount bend at 50–42 Ma (Sharp and Clague, 2006) could potentially be interpreted as a record of the onset of this mechanism.

The westward drift of the lithosphere is thus the consequence of a particular setting of tectonic plates on their global course and is not an intrinsic property of the Earth, as has already been suggested by others (Ricard et al., 1991; Ranalli, 2000). In fact, net rotation, which requires degree one toroidal flow, may only exist if lateral viscosity variations exist in the upper mantle (Hager and O'Connell, 1979; Ricard et al., 1991). In this particular case, the African and Eurasian lithospheric keels form a very thick and stiff unit that is anchored into the mantle, allowing for a westward expansion of the Atlantic ocean and subsequently a net westward motion of the lithosphere. This result emphasizes that while plate motions are ultimately the result of forces that arise from mantle flow (Zhong, 2001; Becker, 2006), the dynamical deformation of these plates both at the surface (e.g., Andean tectonics) and at depth (e.g., the slabs as barriers to flow) modifies the interaction of mantle flow and plates in ways that cannot yet be predicted by numerical models of mantle convection.

Acknowledgments

Comments by two anonymous reviewers and Claude Jaupart greatly helped to improve the paper. Contribution from CPC was supported by NSF grant EAR-0609590.

Appendix A. A Stokes flow between 2 slabs

In order to validate the approximation to 2 dimensions, we evaluate how stresses can be transmitted between the slabs. We solve the biharmonic stream function Ψ for incompressible Stokes flow in a square domain of width $5W$ (Fig. A.1). A vertical slab of width W retreats at a prescribed velocity toward a steady parallel slab of width W. The biharmonic function is:

$$\nabla^4 \psi = 0, \tag{A.1}$$

with $u = -\frac{\partial \psi}{\partial y}$ and $v = -\frac{\partial \psi}{\partial x}$, u and v being the velocities along the x and y cartesian directions. Compressive stresses (positive) induced by the retreat of the eastern slab are transmitted across the entire width to the western slab, even close to the edges of the slabs (note the compressive singularities at the edges of the rigid slabs). This result suggests efficient stress transmission in the Pacific domain, where the situation is even more favorable for stress transmission because the width of the openings at the N and S ends of the domain are much narrower than at center. The uniformity of this stress transmission verifies that our 2D approximation is valid for this problem.

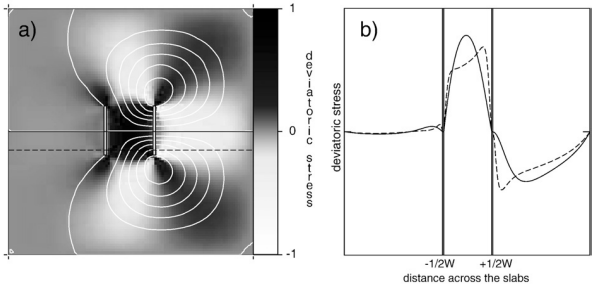

Fig. A.1 a) Map view of deviatoric stress for the Stokes flow between two vertical slabs of the W separated by a distance W; deviatoric stress (color coded) and stream lines (white curves). b) Profile of the deviatoric stresses on a section across the slabs, at the center (solid curve) and at the edges (dashed).

Author's personal copy

References

Artyushkov, E.V., 1973. Stresses in the lithosphere caused by crustal thickness inhomogeneities. Journal of Geophysical Research 78, 7675–7708.

Becker, T.W., 2006. On the effect of temperature and strain-rate dependent viscosity on global mantle flow, net rotation, and plate-driving forces. Geophysical Journal International 167 (2), 943–957.

Bellahsen, N., Faccenna, C., Funiciello, F., 2005. Dynamics of subduction and plate motion in laboratory experiments: Insights into the "plate tectonics" behavior of the earth. Journal of Geophysical Research 110 (B1), B01401.

Billen, M.I., Hirth, G., 2007. Rheologic controls on slab dynamics. Geochemistry Geophysics Geosystems 8, Q08012.

Bostrom, R.C., 1971. Westward displacement of the lithosphere. Nature 234, 536–538.

Bunge, H.P., Grand, S.P., 2000. Mesozoic plate-motion history below the northeast pacific ocean from seismic images of the subducted farallon slab. Nature 405, 337–340.

Capitanio, F., Morra, G., Goes, S., 2007. Dynamic controls on subduction kinematics: the role of the downgoing lithosphere and passive mantle flow. Earth and Planetary Science Letters 262, 284–297.

Carlson, R.L., Melia, P.J., 1984. Subduction hinge migration. Tectonophysics 102, 399–411.

Chamot-Rooke, N., Jestin, F., de Voogd, B., 1993. The PHEDRE working group, intraplate shortening in the central Indian ocean determined from a 2100 km long north-south deep seismic reflection profile. Geology 21, 1043–1046.

Collins, W.J., 2003. Slab pull, mantle convection, and Pangaean assembly and dispersal. Earth and Planetary Science Letters 205, 225–237.

Conrad, C., Hager, B.H., 2001. Mantle convection with strong subduction zones. Geophysical Journal International 144, 271–288.

Conrad, C., Lithgow-Bertelloni, C., 2002. How mantle slabs drive plate tectonics. Science 298, 207–209.

Davaille, A., Stutzmann, E., Silveira, G., Besse, J., Courtillot, V., 2005. Convective patterns under the indo-atlantic "box". Earth and Planetary Science Letters 239 (3–4), 233–252.

Doglioni, C., 1990. The global tectonic pattern. Journal of Geodynamics 12, 21–38.

Doglioni, C., Harabaglia, P., Merlini, S., Mongelli, F., Peccerillo, A., Piromallo, C., 1999. Orogens and slabs vs. their direction of subduction. Earth-Science Reviews 45, 167–208.

England, P.C., 1986. Brittle failure in the upper mantle during extension of continental lithosphere — comment. Journal of Geophysical Research 91 (B10), 487–490.

England, P.C., McKenzie, D.P., 1982. A thin viscous sheet model for continental deformation. Geophysical Journal Royal Astronomical Society 70 (2), 295–321.

England, P.C., Molnar, P., 1997. Active deformation of Asia: from kinematics to dynamics. Science 278, 647–650.

Faccenna, C., Heuret, A., Funiciello, F., Lallemand, S., Becker, T.W., 2007. Predicting trench and plate motion from the dynamics of a strong slab. Earth and Planetary Science Letters 257, 29–36.

Fleitout, L., Froidevaux, C., 1982. Tectonics and topography for lithosphere containing density heterogeneities. Tectonics 1, 21–57.

Funiciello, F., Heuret, A., Faccenna, C., Lallemand, S., Di Giuseppe, E., 2007. How does mantle viscosity influence the subduction process? Insights from laboratory models, General Assembly 7 of the European Geosciences Union, Wien.

Gordon, R.G., Jurdy, D.M., 1986. Cenozoic global plate motion. Journal of Geophysical Research 91 (B12), 2389–2406.

Gripp, A.E., Gordon, R.G., 2002. Young tracks of hotspots and current plate velocities young tracks of hotspots and current plate velocities. Geophysical Journal International 150, 321–361.

Hager, B.H., O'Connell, R.J., 1979. Kinematic models of large scale flow in the earth's mantle. Journal of Geophysical Research 84 (NB3), 1031–1048.

Heuret, A., Lallemand, S., 2005. Plate motions, slab dynamics and back-arc deformation. Physics of the Earth and Planteray Interior 149, 31–51.

Houseman, G., England, P.C., 1993. Crustal thickening versus lateral expulsion in the Indian–Asian continental collision. Journal of Geophysical Research 98 (B7), 12233–12249.

Husson, L., Ricard, Y., 2004. Stress balance above subductions: application to the Andes. Earth and Planetary Science Letters 222, 1037–1050.

Iaffaldano, G., Bunge, H.P., Dixon, T.H., 2006. Feedback between mountain belt growth and plate convergence. Geology 34 (10), 893–896.

Jarrard, R.D., 1986. Relations among subduction parameters. Reviews of Geophysics 24, 217–284.

Kreemer, C., Haines, J., Holt, W.E., Blewitt, G., Lavallée, D., 2000. On the determination of a global strain rate model. Earth Planets Space 52, 765–770.

Lallemand, S., 1998. Possible interaction between mantle dynamics and high rates of arc consumption by subduction processes in circum-pacific area. In: Flower, C.-H.L.M.F. J., Chung, Sun, Lee, T.-Y. (Eds.), Mantle dynamics and plate interactions in East Asia. AGU Geophysical Monograph, vol. 27, pp. 1–10.

Lallemand, S., Heuret, A., Boutelier, D., 2005. On the relationships between slab dip, back-arc stress, upper plate absolute motion, and crustal nature in subduction zones. Geochemistry Geophysics Geosystems 6. doi:10.1029/2005GC000917.

Lambeck, K., Chappell, J., 2001. Sea level change through the last glacial cycle. Science 292 (5517), 679–686.

Martinod, J., Molnar, P., 1995. Lithospheric folding in the Indian ocean and the rheology of the oceanic plate. Bulletin de la Soci'et'e G'eologique de France 166 (6), 813–821.

Minster, J.B., Jordan, T.H., 1978. Present-day plate motion. Journal of Geophysical Research 83 (NB11), 5331–5354.

Mitrovica, J.X., Forte, A.M., 2004. A new inference of mantle viscosity based upon joint inversion of convection and glacial isostatic adjustment data. Earth and Planetary Science Letters 225 (1–2), 177–189.

Ranalli, G., 2000. Westward drift of the lithosphere: not a result of rotational drag. Geophysical Journal International 141, 535–537.

Ricard, Y., Doglioni, C., Sabadini, R., 1991. Differential rotation between lithosphere and mantle — a consequence of lateral viscosity variations. Journal of Geophysical Research 96 (B5), 8407–8415.

Royden, L.H., Husson, L., 2006. Trench motion, slab geometry and viscous stresses in subduction systems. Geophysical Journal International 167 (2), 881–905.

Sdrolias, M., Muller, R.D., 2006. Controls on back-arc basin formation. Geochemistry Geophysics Geosystems 7, Q04016.

Sharp, W.D., Clague, D.A., 2006. 50-ma initiation of Hawaiian–Emperor bend records major change in pacific plate motion. Science 313, 1281–1284.

Silver, P.G., Russo, R.M., Lithgow-Bertelloni, C., 1998. Coupling of south American and African plate motion and plate deformation. Science 279, 60–63.

Sobolev, S.V., Babeyko, A.Y., 2005. What drives orogeny in the Andes? Geology 33 (8), 617–620.

Steinberger, B., Sutherland, R., O'Connell, R.J., 2004. Prediction of Emperor–Hawaii seamount locations from a revised model of global plate motion and mantle flow. Nature 430 (6996), 167–173.

Uyeda, S., Kanamori, H., 1979. Back-arc opening and the mode of subduction. Journal of Geophysical Research 84, 2017–2037.

Zhong, S.J., 2001. Role of ocean-continent contrast and continental keels on plate motion, net rotation of lithosphere, and the geoid. Journal of Geophysical Research 106 (B1), 703–712.

4.2 Un nouveau référentiel absolu pour le mouvement des plaques

Le remplacement graduel des subductions téthysiennes par des orogènes se traduit probablement par une augmentation de la compression moyenne dans la lithosphère. Il ressort de l'étude précédente que le mouvement des plaques s'effectue probablement de manière centrifuge à partir du centre de masse de *Hapagea*. Sur cette base, il est raisonnable de suggérer que la lithosphère en compression doit enregistrer cette compression centrifuge. C'est ce que nous avons voulu tester dans l'article en préparation suivant, réalisé en collaboration avec C. Kreemer.

On the correlation between the intraplate stress field and absolute plate motions

Corné Kreemer [a], *Laurent Husson* [b]

[a] Nevada Bureau of Mines and Geology and Seismologic Lab, University of Nevada, Reno ;
[b] CNRS, Géosciences Rennes, 35042 Rennes, France.

Kreemer [2009] a proposé en 2009 un référentiel absolu pour le mouvement des plaques indépendant de l'hypothèse de fixité des points chauds. Son idée était d'utiliser les orientations d'anisotropie sismique des ondes *SKS*, supposées refléter le cisaillement du manteau sub-lithosphérique. En minimisant l'écart entre les observations (près de 500 points de contrôle retenus) et le mouvement des plaques, son modèle *GSRM-APM* permet d'ajouter une composante de rotation nette de la lithosphère à un modèle de référence comme GSRM-NNR2 [Kreemer et al., 2006] ou NUVEL1 [DeMets et al., 1994], qui donne le mouvement relatif des plaques sans rotation nette. Le modèle prédit une rotation nette de 0.2065°/Ma de la coquille lithosphérique autour d'un pôle situé à 57.6°S et 63.2° E. Cette valeur est sans surprise : le pôle de rotation est très proche des modèles antérieurs [e.g., Becker, 2006, Kreemer, 2009] et la magnitude de la rotation est également attendue (moins forte que *NUVEL1-HS3* [Gripp & Gordon, 2002] et comparable aux estimations de Becker [2008]).

D'une manière comparable, les orientations de contraintes compilées par le World Stress Map (fig. 4.4, [Heidbach et al., 2007]) réflètent en réalité le champ de déformation de la lithosphère en déplacement au dessus du manteau. La relation entre ces orientations et le mouvement absolu des plaques a été envisagé auparavant [Richardson, 1992, Zoback et al., 1989] et utilisé pour débattre de l'origine des forces motrices de la tectonique des plaques, en particulier l'entraînement par le manteau, par opposition à la poussée par la dorsale [Bird, 1998, Richardson, 1992]. Cependant, ces études sont basées sur un modèle de mouvement absolu des plaques ancien [Minster & Jordan, 1978], qui diffère largement des modèles plus récents [Becker, 2006, 2008, Kreemer, 2009]. Il apparaît maintenant que le flux mantellique entraîne -ou en tout cas est aligné- avec le mouvement des plaques [Lithgow-Bertelloni & Guynn, 2004, Steinberger et al., 2001]. Si les orientations de contraintes reflètent le flux mantellique, une inversion comparable à celle de Kreemer [2009] peut être réalisée à partir des données du *WSM*.

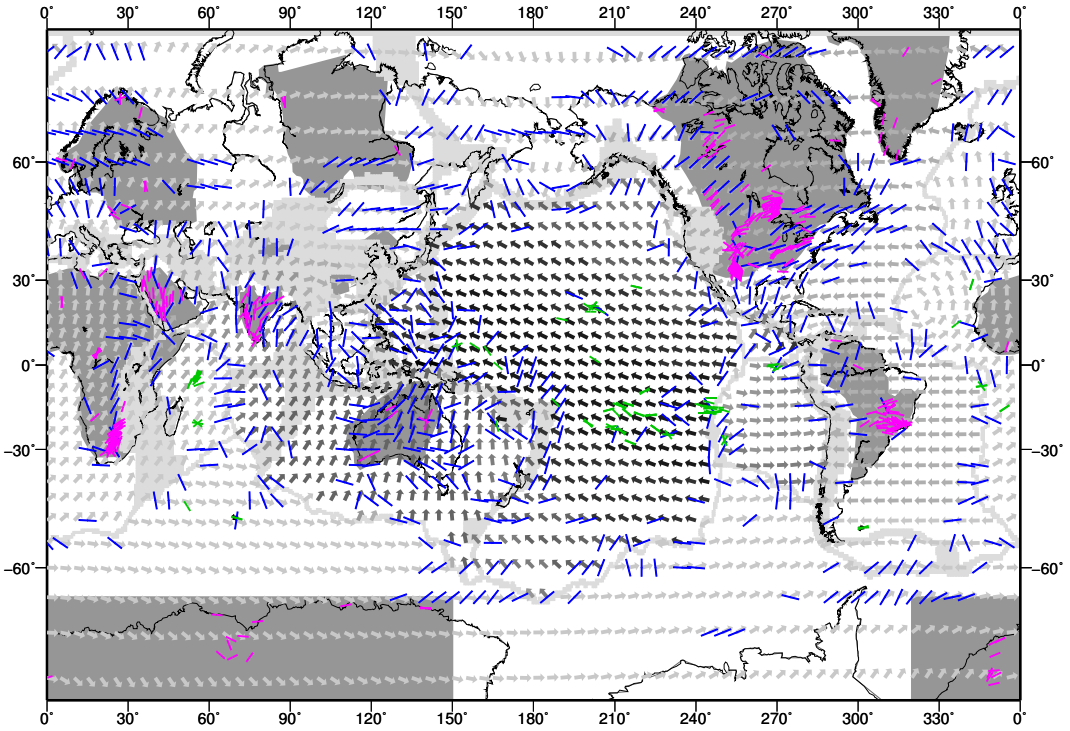

FIG. 4.4: Mesures d'orientation de l'anisotropie sismique des ondes *SKS* (en vert, domaine océanique, en rose, cratonique) retenus par Kreemer [2009] pour l'inversion qui prédit un mouvement des plaques donné par les flèches grises. Les barres bleues donnent l'orientation des contraintes horizontales compressives maximales, moyennées sur une grille régulière d'après le World Stress Map [Heidbach et al., 2007]. *Orientation measurements of SKS wave anisotropy (green : oceans, pink : cratons) selected by Kreemer [2009] for an inversion that predicts the absolute plate motion represented by gray arrows. Blue bars indicate the orientation of the maximum horizontal compression axis, interpolated on a regular grid (data from the World Stress Map [Heidbach et al., 2007].)*

Techniquement, l'inversion est très semblable à celle décrite dans Kreemer [2009]. Les données ont été sélectionnées de manière à éliminer les données trop proches des dorsales, où le champ de contraintes est perturbé par des processus locaux. Les données correspondant aux limites de plaques (*sensu WSM*) n'ont pas été retenues. Le mouvement net obtenu (fig. 4.5) est proche de celui obtenu par inversion des orientations d'anisotropie sismique (fig. 4.4). La rotation nette est de 0.2216°/Ma.

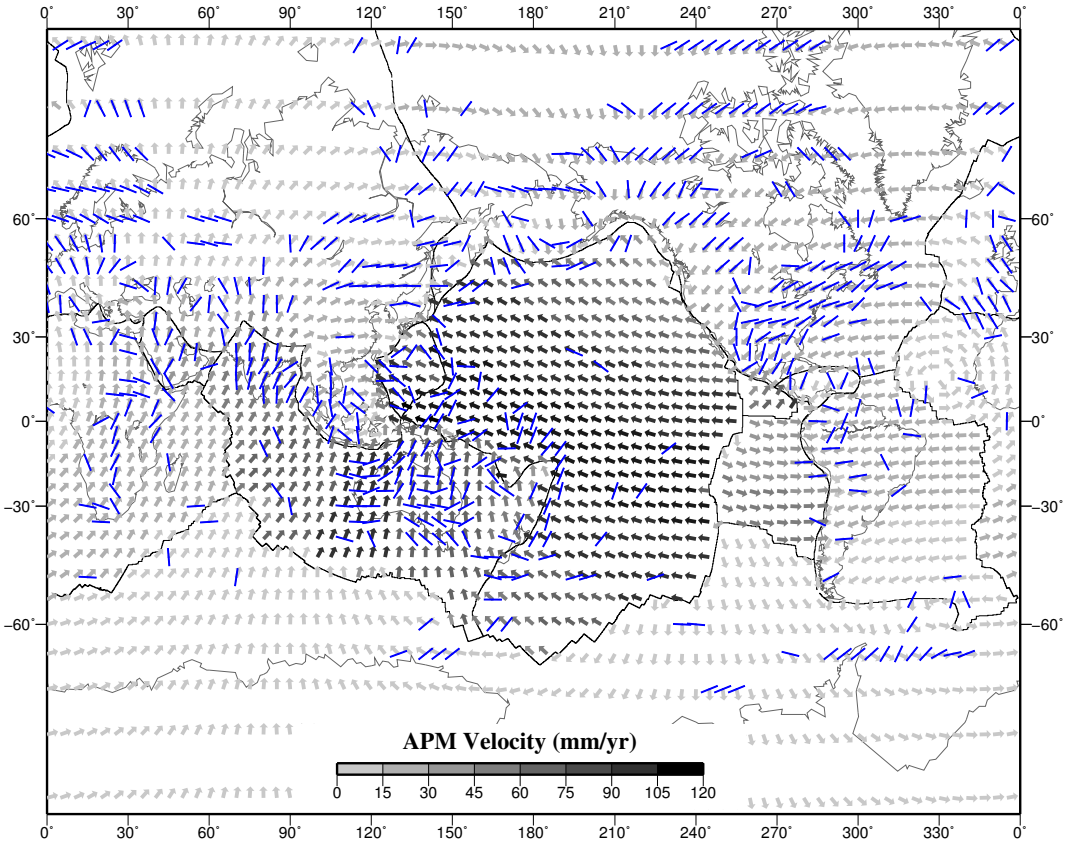

FIG. 4.5: Mouvement absolu des plaques prédit par l'inversion d'une selection de données d'orientation de contraintes (en bleu, voir texte). *Absolute plate motion predicted from the inversion of the orientation of the horizontal maximum compression axis (blue bars).*

4.3 Surrection généralisée des marges continentales

L'augmentation de la compression moyenne de la lithosphère, qui résulte de la diminution du rapport des forces motrices sur résistantes redistribue les contraintes dans la lithosphère. En conséquence, les marges passives sont soumises à une dynamique différente. En collaboration avec K. Pedoja et co-auteurs, nous avons compilé les mouvements apparents relatifs du niveau marin sur l'ensemble des côtes depuis le dernier maximum interglaciaire (∼125000 ans). Il ressort que l'ensemble des marges, passives et actives, sont en surrection relative. Nous attribuons cette surrection à l'augmentation de la compression résultant de l'aggrégation de *Hapagea*.

Click here to download Manuscript: Pedoja et al ESR.doc Click here to view linked References

Relative sea-level fall since the Last Interglacial Maximum : Why are coasts uplifting worldwide?

Kevin Pedoja[1], Laurent Husson[2], Peter Cobbold[2], Vincent Regard[3, 4, 5], Emilie Ostanciaux[2], Markes E. Johnson[6], Stephen Kershaw[7], Joseph Martinod[3, 4, 5], Lucille Furgerot[1], Pierre Weill[1], Bernard Delcaillau[1]

1 *Laboratoire de Morphodynamique Continentale et Côtière, CNRS, Université de Caen, 14000 Caen, France;* ***2*** *CNRS, Géosciences Rennes, 35042 Rennes, France;* ***3*** *Université de Toulouse ; UPS (OMP) ; LMTG ; 14 Av Edouard Belin, F-31400 Toulouse, France;* ***4*** *IRD ; LMTG ; F-31400 Toulouse, France;* ***5*** *CNRS ; LMTG ; F-31400 Toulouse, France).****6*** *Williams College, Massachusetts 01267 USA;* ***7*** *Institute for the Environment, Halsbury Building Brunel University, Uxbridge UB8 3PH, UK.*

Abstract

Paleo-coastal studies received a boost some 40 years ago with the application of versatile numerical and correlative dating techniques. Simultaneously the emergence and refinement of plate tectonic theory refocused attention on paleo-shorelines as tectonic indicators. Although there have been many local studies of the Quaternary vertical motions of coastlines during this interval, we know of no comprehensive worldwide synthesis. Here we release a compilation of 890 records of shorelines from the Last Interglacial Maximum that we use as a datum to evaluate uplift rates during the Quaternary. We find that most coastal segments have risen relative to sea level. The mean rate of uplift is ~0.20 mm/yr, which is about four times faster than the estimated eustatic drop in sea level. The uplift rate is faster for active margins than for passive margins. We suggest that long-term continental accretion, in the current Wilson cycle, has led to compression of continental plates and uplift of their margins, as recorded by paleo-shoreline sequences. In addition, our study suggests that plate tectonics impacts all margins and that the notion of stable platform is

unrealistic; this challenges accuracy in the evaluation of past sea level from the fossil shoreline record.

Keywords: paleo-shoreline; Last Interglacial Maximum; sea-level change; Quaternary sequence; plate tectonics; Wilson cycle

1 Introduction

Emerged Quaternary sequences of paleo-shorelines form remarkable stepped coastal landscapes that have been a long-standing geological curiosity. As early as 1830, Lyell wondered whether the sequences were of tectonic or eustatic origin (Lyell, 1830). Pleistocene paleo-coasts have proven to be combinations of both (e.g. Lajoie, 1986) and therefore can be used as tools to quantify vertical displacements, or past sea levels.

Positive or negative vertical deformation displacements are responsible for emerged and submerged sequences of paleo-shorelines. Classic examples are Indonesia (e.g. Sumba Island, Pirazzoli et al., 1993) or Chile (Paskoff, 1977), and New Caledonia (Frank et al., 2006) or Hawaii (Szabo and Moore, 1986; Ludwig et al., 1991). Emerged sequences have been more abundantly described than submerged sequences because they are much easier to study and to sample.

In terms of tectonics, some syntheses have been done both on regional scales (e.g. Japan, Italy, Australia, see further) and continental scales (Hoyt, 1967; Wythe Cooke, 1971) but we know of no comprehensive worldwide synthesis.

Because the Last Interglacial Maximum (LIM) has been very well documented worldwide (e.g. Johnson and Libbey, 1997), we use it as a datum to evaluate the vertical motions of the Quaternary sequences of paleo-shorelines.

Therefore, the main objectives of this study are to compile as much information as possible about LIM paleo-shorelines, especially their altitudes and to calculate homogeneous rates of vertical displacement, in order to establish LIM paleo-shorelines as a tectonic benchmark and to interpret the inferred worldwide displacement field from a geodynamical standpoint during the Quaternary.

2 Paleo-shorelines of the Last Interglacial Maximum

Paleo-shorelines tend to exhibit characteristically stepped landforms. Series (also referred as sequence of flights) of terraces (Fig.1) or to a lesser extent series of notches, running parallel to the present-day shoreline, shape many coastlines and define past sea level positions during the total duration of uplift. Sedimentary deposits may be laid on eroded terrace surfaces, thus it is important to distinguish between an eroded and a deposited terrace form. In this section of the paper, we survey the characteristics of erosional and depositional forms associated with the last Interglacial highstand, and draw attention to the critical relevant literature. This survey is important because it provides the essential background to the methodology and data presented later in the paper.

It is now widely accepted that coastal sequences form during separate highstands of interglacial stages (Zeuner, 1952), which correlate with Marine Oxygen Isotopic Stages (MIS) (e.g. James et al., 1971; Chappell, 1974; Bull, 1985; Lajoie, 1986; Ota, 1986). Although the timing and duration of the LIM is now rather well known (see below), there is less information concerning the timing and duration of other interglacial periods, in particular MIS 7, 9 and 11 (e.g. Dutton et al., 2009; Winograd et al., 1997). MIS 11 is generally considered to be the best analogue for the Holocene period and has been the subject of two regional syntheses: one in Japan (Masuda, 2007) and one in Chile (Ortlieb et al., 1996).

For the last 40 years, a variety of numerical and correlative dating techniques have been applied to paleo-coasts (Veeh, 1966), making them available as tools in order to characterize change in sea-level reconstruction (e.g. Antonioli et al., 2006a), tectonics and geodynamics (e.g. Merrits and Bull, 1989; Pedoja et al., 2006a, b,c; 2008a) paleo-environments (e.g. Aguirre et al., 2003), pedology (e.g. Muhs, 2001), archeology (e.g. Shackleton et al., 1984), diamond deposits (Jacob et al., 2006; Spaggiari et al., 2006), sedimentology (Crook and Felton, 2008), glacial and periglacial evolution (e.g. Bates et al., 2003), patterns of drainage (Personius, 1995) and paleontology (e.g.Pandolfi, 2001) or even to refine plate tectonic models (Pedoja et al., 2006c). Numerical modeling also has been applied to paleo-shoreline (i.e. marine terrace) development (Scheidegger, 1962; Veldkamp, 1994; Trenhaile, 2002). However, we know of no examples of analogue modeling for the formation of coastal sequences.

Some zones have been heavily documented on a global sacle, either for the long-standing sequences, like in the classic sites of coastal Quaternary sequences on the Huon Peninsula in New Guinea (more than 20 articles, see supplementary data) or Barbados islands (approximately 14 articles, see supplementary data). Other regions have been intensively investigated with respect to a particular datum, either Holocene (e.g. Woodroffe and Horton, 2005; Pirazzoli, 1991) or MIS 5e paleo-shoreline, for instance in Italy (Bordoni & Valensise, 1998; Ferranti et al., 2006), Australia (Murray-Wallace and Belperio, 1991), Japan (Koike and Machida, 2001), and the West coast of North America (Muhs et al., 2002). But for the most part, each documented zone is described in only one or two articles, as for the Philippines (Omura et al., 2004), China (Pedoja et al., 2008a), Cuba (Peñalver Hernadez et al., 2001, 2003) or Haiti (Dodge et al., 1983; Dumas et al., 2006), or Jamaica (Mitchell et al., 2001, 2000).

2. 1 Marine Isotopic Substage 5e (MIS 5e)

In its broadest sense, the last interglacial complex (MIS 5) is all of what is recorded as stage 5 in the marine oxygen isotope record (Martinson et al., 1987) and covers the period from 130 to 85 ka (e.g. Chappell and Shackleton, 1986). This interglacial is characterized by three second-order highstands ranked from the oldest MIS 5e (or MIS 5.5 see below for timing and duration) through MIS 5c (or MIS 5.3, ~ 105 ka) to the youngest MIS 5a (MIS 5.1, ~ 85 ka). MIS 5e is the prominent and best-recorded sub-stage of the MIS 5, and in the following the LIM is referred to as MIS 5e for simplicity. The Last Interglacial Maximum (MIS 5e) represents the last time that mean sea level was at or near modern levels, and by inference, the last time that ice volumes and global climatic conditions were similar to those of the present day (e.g. Siddall, 2006). Considerable effort has been made to determine the timing, duration and paleo-temperature regime of the maximum (or peak) of the last interglacial period, (e.g. Hearty and Neumann, 2001; Muhs et al., 2002a & b, Rohling et al., 2008).

Interpretation of the MIS 5e has evolved since pioneering studies of the 1970s (e.g. Stearns 1976; Chappell and Veeh 1978). Whether or not sea level fluctuated within MIS 5e is unclear (Kaufman, 1986). In some places two to three highstands in the Last Interglacial Maximum are inferred from dating and local morpho-stratigraphy. For example, two highstands during MIS 5e are deduced either from morphological analysis or deposits in Tunisia (Jedoui et al., 2003), Italy (Antonioli et al., 2006); the Balearic Islands (Bardaji et al., 2009), Bermuda (latest reference, Hearty et al., 2007), or the Red Sea coast of Egypt (latest reference, Choukri et al., 2007). Three highstands are observed in Qatar (Williams and Walkden, 2002), Erythrea (Bruggemann et al., 2004) and Barbados (Johnson, 2001).

Our aim is not to discuss the timing, duration or number of highstands of MIS 5e, but rather to establish the paleo-shorelines attributed to this time range as tectonical benchmarks. Therefore, we take into account the ages and eustatic sea levels from the latest review on the subject (Siddall et al., 2006), which points out that the estimates of several authors converge on a highstand lasting from 128 ± 1 ka BP to 116 ± 1 ka BP (e.g. Stirling et al. 1998) with sea levels

around + 2 to + 4 m (e.g. Schellmann and Radtke 2004; Stirling et al. 1998; Hearty and Kindler 1995). Consequently we use an age of 122 +/- 6 ka and discuss the impact of a possible sea level higher by 3+/- 1 m. We take advantage of our compilation to discuss further the significance of the concept of eustasy.

The Last Interglacial Maximum corresponds to the vernacular nomenclatures of Eemian (in Western Europe, for a review see Shackleton et al., 2003), Ipswitchian (England, Bates et al., 1997), Eutyrrhenian (Mediterranean, e.g. Kindler et al., 1997), Rocky Bay Fm (Bermuda, e.g. Harmon et al., 1978), Grotto Beach Formation (Bahamas, e.g. Hearty and Kindler, 1995), Sangamonian or Sangamon (North America, e.g. Sainsbury et al., 1965; Dupré, 1984), Waimanalo Formation (Hawaiian Islands, e.g. Jones, 1993), Ouljian (West Morocco e.g. Weisrock et al., 1999), Mikulinian (Northern Russia, e.g. Mangerud et al., 1999), Kharagatian (Black Sea, Zubakov, 1988), and Pelukian (Alaska, Brigham-Grette and Hopkins, 1995). In the following, we simply make use of the more generic term LIM (paleo) shorelines.

2.2 Paleo-shorelines

Various geomorphic features, erosional or depositional, develop near sea level and form what is the generic shoreline. Quaternary, and particularly LIM, fossil shorelines reflect the diversity of modern coasts, because the shorelines are frequently preserved after a change in sea level. In other words, depending on various parameters (e.g. hydrodynamics, latitude or sediments supplies) LIM fossil shorelines, like modern ones, are expressed through a large range of morphologies and deposits (e.g. van de Plassche, 1986). In order to avoid the uncertainty issue relative to the initial elevation of a paleo-shoreline (a few meters above or below the current sea level), it is desirable to measure the

elevation of a fossil shoreline with respect to the current shoreline, not the current sea level (Pirazzoli, 1996). Unfortunately, this practice is seldom applied, chiefly because dual observations of comparable past and present-day shorelines are commonly difficult to make.

Erosional indicators are represented by “abraded” marine terraces, benches (e.g. Lyell, 1830, Chambers, 1848), *trottoirs* (Dalongeville et al., 2000), notches (e.g. Nunn et al., 2002), or sea-caves (for example the discussed Mt Carmel cave, Zviely et al., 2009; Ronen et al., 2007; Vita-Finzi and Stringer, 2007). Common depositional indicators include wave-built terraces (e.g. in Argentina, Rutter et al., 1989), beach deposits (e.g. Cotentin, Coutard et al., 2006), beachrocks (e.g. Israel, Galili et al, 2007), beach ridges (Darwin, 1846), reef flats (Darwin, 1842), tidal flats and other coastal deposits (e.g. Canary islands, Meco et al., 2007). In practice, indicators are often misleading and differences are not so easy to establish. For example, uplifted coral reefs (depositional features) are frequently “terraced“ (erosional) by sea-level highstands. Marine terraces frequently include nearshore deposits and some notches may preserve some fixed biological indicators. Thus erosional paleo-shorelines are most commonly representated by paleo-rocky shores whereas depositional ones are represented by paleo-sedimentary deposits (normally clastic) or paleo-constructed shores (principally algal *trottoirs* and coral reefs). It must be emphasized here that on the modern shore as for the LIM palaeoshorelines, lateral change in facies can be extremely rapid from one morphology (or deposit) to another (for example, in Eastern Patagonia, Pedoja et al., 2008b).

Although the geometrical description of fossil shores and their associated deposits provides critical information for interpreting sea level histories, dating is also required. A variety of techniques have been used, depending on the time of origin and nature of the relict shoreline. These include ^{14}C (for Holocene paleo-shorelines but may give indications of older paleo-shorelines if the maximum age of c.30 ka is obtained(e.g. Navas et al., 2006), U/Th series applied to

corals (e.g. Stirling and Andersen, 2009), molluscs (McLaren and Rowe, 1996) or cement (Ramsay and Cooper, 2002), Be 10 and 16 Al (e.g. Saillard et al., 2009; Melnick et al., 2009), Ne 21 (Quezada et al., 2007), Uranium-Helium (Bender et al., 1973), Pa/U (Giresse, 1989), 226Ra/238U (Ota and Omura, 1992), Electron Spin Resonance (ESR, e.g. Schellmann and Radtke, 1997), amino-acid racemization (e.g. Goodfriend et al., 1996), thermo-luminescence (e.g. Balescu et al., 1997a&b), optically stimulated luminescence (e.g. Mauz et al., 2009; Wood, 1994), paleontologic studies such as malacology (e.g. Sanlaville, 1974) or diatom stratigraphy (e.g. Miettinen et al., 2005), archeological artifacts (e.g. flints artifacts, Galili et al., 2007, tephro-chronology (e.g. Okumura, 1996), palynology (Korotky et al., 1997) and morpho-stratigraphy (for example the occurrence of periglacial deposits on marine terraces, e.g. Orme, 1966). Some pilot studies were performed to compare different techniques of dating. For example, cross-comparison dates of marine terrace sediments by ESR, thermo-luminescence and optically stimulated luminescence in Japan (Tanaka et al., 2007).

Erosional features generally are inadequate to date former sea levels, whereas marine deposits may include guide fossils or organic material liable to be dated radiometrically. However, depositional features (with the exception of paleo-reefs flats and crests) generally are inadequate to estimate accurately the heights of former sea level due to the uncertainties on sediment compaction, precise position of the deposits above or below sea level and tidal changes. Ideally, altitudes should be measured on erosional geomorphic indicators, whereas materials for dating should be sampled on adjacent depositional geomorphic indicators. In the following, we review the variety of landforms that allow for the characterization of fossil shorelines.

2.2.1 Erosional paleo-shores

The reliability of erosional coastal benches, platforms and terraces as sea-level indicators depends on the identification and understanding of the processes by which these features were produced.

- **Marine terrace,**

On steadily uplifting coasts, marine terrace sequences are represented by flights of terraces up to hundreds of meters in altitude above mean sea level. Each terrace corresponds to a gently seaward-dipping erosional platform backed by a relict sea cliff. The shoreline angle or inner edge of the terrace (i.e. intersection of the relict platform and the relict sea cliff) provides a good approximation to the location and elevation of a former shoreline and, hence, a marker for relative sea level (e.g. Bull, 1985).

- **Notches**

Uplift can also be registered through sequences of notches that are visible as horizontal incisions in cliffs. Their widths and excavation depths may reach up to a few meters. Notches are often portrayed as forming at sea level; however notch types actually reflect a continuum from wave notches formed under quiet conditions at sea-level to surf notches formed under more turbulent conditions and as much as 2 m above sea level (Pirazzoli et al., 1996). Notches are particularly well documented for the Holocene (e.g. Cooper et al., 2007) but few data are also known from the Pleistocene (e.g. Maeda et al., 2004). Marine and coral terraces are often backed up by abrasion notches. Notches are problematic if there is a rocky platform seaward of the notch, because this can store debris used by waves to erode the rock and produce an abrasion notch. Therefore notches are reliable as sea-level indicators only when they form on steep rock walls without platforms; also notches occur most commonly in limestones, hence their extensive use in the Mediterranean region.

- **Sea caves**

Sea caves are excavated by erosion into a cliff in the range of wave action. They generally develop into weaker parts of the rock formation or are often of karstic origin. A sea cave opened on both sides of a promontory is called a sea arch. Sea caves and arches are generally inaccurate sea-level indicators; however, in limestone formations, their floor, if regular and flat, may be related to a former low-tide position (e.g. Pirazzoli, 2005).

2.2.2 Depositional paleo-shores

Depositional traces of paleo-shores are frequently used in sea level or tectonic reconstructions. The most striking example to document Quaternary sea-level oscillations arises from uplifted coral reefs (e.g. Barbados and Huon peninsula, New Guinea). In this section we include the beach deposits (often called raised beaches) that can often be considered as cropping out and deposited on marine terraces.

- **Coastal and tidal deposits**

The main difficulties in reconstructing former sea-level histories from coastal and tidal deposits are complicated by the estimate of sediment compaction and tidal changes.

Tidal flats are marshy or muddy land areas that are periodically covered by the tide (e.g in Brazil, Martin et al., 1996). Sand deposits are common where wave energy is moderate and are found on beaches and intertidal shores near the inlets of lagoons (e.g. Brazil Martin et al., 1996). Pebbles are generally found only in high-energy shores, usually on exposed beaches (e.g. Argentinian Patagonia, Rutter et al., 1989).

In more sheltered areas, such as indented bays and estuaries, chenier ridges

are useful indicators of the former shorelines. Cheniers are transgressive beach ridges that become isolated from the shore by a band of prograding mudflat (Otvos and Price, 1979). They result from a balance between fine-grained sediment source, derived from fluvial or tidal dynamics (mudflat progradation), and coarse-grained sediment supplied and piled up by wave action. Mainly composed of shell debris, cheniers provide material for accurate dating, which can be used to determine the lateral continuity between other depositional (gravel beach ridges) or erosional morphologies. These features are common in Holocene coastal plains (Augustinus, 1989), but have rarely been described in older Quaternary deposits. Meldahl (1995) describes chenier ridges in the northern gulf of California, which formed during Pleistocene highstands, and more especially during MIS 5e. Other Pleistocene cheniers are suspected to be present in Bahía San Sebastián (Argentina), or in the northeastern part of the Gulf of Mexico. The lack of description of cheniers in pre-Holocene deposits is probably due to confusion with beach-ridge sequences, and a lack of sub-surface and stratigraphic information (Hoyt, 1969).

- **Beach deposits, raised beaches, beach rocks**

Raised or submerged beaches are sometimes used as sea-level indicators even where there are large uncertainties in determining a clear relationship between a beach sample and the ancient mean sea level. Among the first descriptions of paleo-shores were raised beaches (e.g. Bravais, 1845; Chambers, 1848; Prestwich, 1865, 1892; Dunlop, 1893; Strahan, 1897; Evans, 1907). The term originally refers to some beach deposits observable above an erosion surface. In fact, most of the raised beaches in England, Ireland or Northern France correspond to marine terraces on which the shoreline angle is barely noticeable due to the influence of “glacial” continental deposits (e.g. heads, loess). Thus, such beach deposits are often the depositional component of a terrace sequence, so that an erosional terrace is overlain by deposited sediments.

Beachrocks are hard coastal sedimentary formations consisting of various beach sediments, lithified through the precipitation of carbonate cements (for a review on formation and modern occurrence see Vousdoukas et al., 2007). Beachrocks are generally limited to areas of warm or temperate waters. A beachrock is generally a good indicator of sea level, its vertical uncertainty depending on the local tidal range (Pirazzoli, 2005).

- **Wave-built terrace, depositional shore platform and beach ridges**

Wave-built terraces develop near sea level and are accumulations of marine materials removed by shore erosion. Examples of depositional shore platforms produced by the supply of marine sediments (sand, shingles, or shells) to the shore are: the Crescent city coastal plain, USA (Polenz and Kelsey, 1999) and the coastal plains where many shelly ridges run roughly parallel to the shore, in the northeast Gulf of Mexico (Otvos, 1981).

A variety of views on the mode of formation and conditions for preservation of beach ridges has been expressed regarding modes of beach-ridge construction (during high or low wave energy, during bar welding, by swash action, by sea-level change, or by eolian processes; e.g. Sanjaume and Tolgensbakk, 2009). The lack of abundant sediment supply is an obstacle to the formation of beach-ridge plains. Arguments supporting the formation of beach ridges during high wave-energy appear convincing where coarse clastic beaches enhance percolation rates leading to promote deposition at the limit of wave run-up (e.g. Otvos, 2000). The spacing between beach ridges is reported to indicate the recurrence of the triggering processes (storm, sea-level variations, sediment availability; Isla and Bujalesky, 2000). The most common interval for constructing a single swash-built sand beach is 30-60 years (Tanner, 1995a, 1995b).

- **Coral terrace**

Corals and other reef-building organisms such as algae live within the photic zone, rarely deeper than 100 m, and are limited upwards by intertidal exposure. A coral terrace can be considered as a reef flat, or reef platform. Reef flats are stony expanses of reef rock with a flat surface (Pirazzoli, 2005). This surface is limited toward the sea by a frontal crest and an external slope and toward the continent by a break in slope sometimes underlined by a notch (Darwin, 1842). Of all the above-mentioned morphologies, the notch and the landward break of slope are the best geomorphic indicators for Quaternary sea level and/or tectonics. But sometimes, only the altitude of the reef platform is determinable and therefore used (e.g. Mangaia Island, Ward et al., 1971). Well-preserved reefs, up to hundreds of meters above modern sea level are found in many parts of the world (e.g. SE Asia, Red Sea, Caribbean Sea).

All types of reefs are found in an emergent condition, but the most common are fringing reefs occurring as terraces built over volcanic or other non-carbonate foundations. Uplifted atolls also are known (e.g. Daito Islands, Ota and Omura, 1992). Emerged barrier reefs appear to be rare, even in Indonesia which has both extensive, modern barrier reefs and numerous emerged fringing reefs (Hantoro, 1992).

3 Methods

From a geodynamical standpoint, we have compiled a large number of dispersed studies into a worldwide synthesis of sea- level changes related to the highstands of the Last Interglacial Maximum (LIM, isotopic stage MIS5e, 122±6 ka,). We collected printed materials from articles, conference proceedings, book chapters, thesis, field trip reports etc.

3.1. Data base

Out of 807 published references, we uniformly reappraised the mean vertical velocities for 890 sites, organized into 24 major provinces. The compilation is fully available online at http://www.elsevier.com and summarized in Table 1. The data is compiled in a table that includes the location and elevation of MIS 5e paleo-shorelines around the world. The table includes 22 columns listing the location (province, continent, ocean, country), the morphologies (marine terraces, notches etc) or deposits (beach ridge, beach rock, coastal deposits, etc), their maximum elevation, the implied average vertical rate since MIS 5e, the duration of uplift, the references and the degree of confidence in the data.

In this compilation, we systematically attributed a minimum error range of 1 meter to the measurements on altitude (E) published without a margin of error. Where authors provide altitude range, we took the mean value of the range. For example, with a shoreline angle between 20 -30 m, E = 25 +/- 5 m. Where authors only correlate the paleo-coast to MIS 5 undifferentiated, we made the assumption that it is correlated to MIS 5e, which gives the minimum uplift rate. Where data are extremely abundant (e.g. Italy, California, Baja California), we sometimes derived means for the primary tectonic zones. We adopt the age, A = 122 +/- 6 ka , which corresponds to the peak of Last Interglacial Maximum. The degree of confidence is noted on a scale of 5 points. The higher the value, the better the data. The score is primarily based on the nature of the geomorphic indicator, the quality of dating, precision in measurements of altitudes, geographical descriptions, etc.

We rejected some outlets, 21 sites where MIS 5e paleo-shorelines are described (e.g. Gonave Island, Haiti, Thornton-Horsfield, 1975) or inferred (e.g. Sao Tomé, Tristan da Cunha, Nunn, 1984) but where no altitude are proposed. We rejected only one site where a MIS 5e paleo-shoreline altitude is known (i.e.

on the South Island of New Zealand) because the anomalously high altitude (991 +/- 5 m) of MIS 5e marine terrace (Bull & Cooper, 1986) has been strongly debated (Ward, 1988; Bull & Cooper, 1988) but was not re-appraised.

Authors disagree on altitude of MIS 5e shoreline at three sites . This is the case in 1) San Juan de Marcona (Peru) where Hsu et al., (1989) and Hsu, (1992, 1988) described it at 65 +/- 1 m whereas Macharé & Ortlieb (1992), Ortlieb et al., (1991) and Ortlieb & Macharé, (1990a & b) describe it at 105 +/- 1 m. 2) Agadir (West Morocco) where Meghraoui et al., (1998) describe it at 28 m whereas other authors describe it at 8 +/- 1 (e.g. Weisrock et al., 1999), 3) Santa Cruz (California, USA) where MIS 5e palaeoshoreline was described at 39 +/- 1 by several authors (White et al., 2009, 2008; Anderson et al., 1999; Anderson & Menking, 1994; Rosenbloom & Anderson, 1994; Lajoie et al., 1991; Lajoie, 1986; Dupré, 1984; Wehmiller, 1982, Bradley & Griggs, 1976) but were 10 Be dating led Perg et al., (2001) to identify MIS 5e marine terrace at 175 +/- 25m. The dating itself has been discussed by Brown and Bourlès (2001).

In this case we “accomodate” two sites for the same place, given the fact that without knowing the places we can not decide which authors are right.

3.2. Uplift rates

In order to assemble results on the vertical motions of the Earth’s crust, it is necessary to calculate mean vertical deformation rates. The normal method of calculating uplift is sometimes referred to as the classic method (e.g. Lajoie, 1986). In the present study we calculate the mean displacement rate since MIS 5e using both the classical method and a new more simpler method.

The classic equation for calculating vertical motion rate (V) is **V = (E-e)/A** where E is the current elevation of the paleo-shoreline relative to current local sea level, A is the age of the Last Interglacial maximum, and (e) is the correction for eustasy (i.e. the altitude of the paleo-sea-level stand relatively to the modern one).

But the quantification of eustasy is far from straightforward. First, because uncertainty remains large and second because the very notion of stability of passive margins, upon which many studies on eustasy rely, is challenged in many respects (see for instance Moucha et al., 2008). In first instance, we therefore decided not to use the classic equation and did not take into account any eustatic correction (e).

We, therefore, calculated **V = E/A**. In fact, estimates on sea- level variations during MIS 5e (with respect to today's datum) are principally based on coastal indicators found on platforms formerly considered stable, but that we show in the following to be undergoing uplift. Because a major result of this study concerns the challenge of estimating passed sea level, we decided not to make any eustatic correction.

As the worldwide mean elevation of MIS 5e shorelines ranges between 26 and 27 m (this study), eustasy is supposed to have been influenced only by 10 % of the actual MIS-5e-shoreline elevation and, therefore, is dismissed.

4 Results

Based on data from the 890 sites classified into 24 major provinces (table 1). These provinces include from 1 (Aleutian) to 165 sites (Mediterranean N). The compilation is fully available online and summarized in Table 1. We first briefly present the different provinces of coastal deformation since LIM and then propose a geodynamical interpretation of the observed uplift.

The province of *Africa S* includes 25 sites and encompasses the coasts of Kenya, Madagascar, Mauritius, Mozambique, Seychelles, South Africa, Tanzania, Saint Helena Island. *Africa W* includes 31 sites and encompasses the coasts western Morocco, Canary Islands (Spain) Mauritania, Senegal, Cape Verde, Ghana, Sierra Leone, Angola. *Aleutian* has only 1 site along the coast of Amichtka. *Antarctica* includes 4 sites and encompasses the coasts of Shetlands islands and Cape Ross. *Australia SE* includes 14 sites along the coasts of south eastern Australia and Tasmania. *Australia W* includes 9 sites along the coasts of western Australia. *California and Baja* includes 71 sites and encompasses the coasts of northwestern Mexico in Baja California and southwestern USA. *Caribbean* includes 28 sites from the island coasts of Bahamas, Bermuda, Barbados, Haiti, Providencia (Colombia), Jamaica, Cuba, Leewards Puerto Rico and the coasts of Yucatan (Mexico), Belize, Eastern Costa Rica and Venezuela. *Cocos* includes 4 sites and encompasses the coasts of western Costa Rica and Southwestern Mexico. *Europe W* includes 103 sites and encompasses the coasts of Denmark, Estonia, Norway, Ireland, northwestern France, England, Portugal, West Russia. *Indian* includes 4 sites from the coasts of Peninsular India. *Indo-Pacific* refers to the 93 sites along the offshore coasts of archipelago of Indonesia, Hawaii, Vanuatu, New Caledonia, Kiribati, Papua New Guinea. *Juan de Fuca* includes 21 sites at the subducting margin of California, Oregon, Washington and British Columbia. *Mediterranean N* province includes 165 sites and encompasses the coasts of north and west Mediterranean and Black Sea (Spain, Italy, Greece, Turkey, Lebanon, Syria, Israel, Russia, Ukraine). *Mediterranean S* includes 37 sites from the coasts of northern Morocco, Algeria, Tunisia and Lybia. *New Zealand* includes 18 sites over the coasts of the northern and southern islands of New Zealand. *North America E* includes 21 sites from Florida to Newfoundland. The *Persian Gulf* province includes 11 sites and encompasses the coasts of Iran, Oman, Qatar, and United Arab Emirates. The *Philippines* province includes 4 sites along the coasts of the islands of Pangla, Palawan, and Sabang. *Red Sea* includes 19 sites from the coasts of Egypt, Jordania, Sudan, Djibouti, Saudi Arabia, and Erythrea. *Continental Asia SE* includes 19 sites and encompasses the coasts of China, Korea, Cambodia,

Vietnam. *South America E* includes 36 sites from the coasts of French Guyana, Brazil, Argentina and southeast Chile. *South America W* includes 40 sites along the coasts of Ecuador, Chile and Peru. Finally the *W Pacific* province includes 110 sites and encompasses the coasts of Japan and Eastern Russia.

The current elevations of the well-preserved (e.g. Johnson and Libbey, 1997) LIM palaeocoasts convert into an apparent vertical velocity of the continental margins. The most striking feature of the data is the almost ubiquitous apparent uplift of continental margins (Fig. 2 This apparent) condition is due to a long-standing process because in many instances the LIM marker is embedded in a sequence of palaeoshorelines that span Holocene, Pleistocene, and sometimes Pliocene structures. The mean elevation of LIM terraces is 28 m, indicating a mean rate of uplift of 0.23 mm/yr. Not only do some 93% of the observations give positive values, but also they are widespread and cover almost all coastlines. For obvious reasons, submerged domains are poorly documented, but from visual inspection they encompass many fewer coastlines than uplifted ones (Fig. 2). This eliminates the possibility that the dataset is significantly biased by the difficulty of examining submerged palaeoshorelines. In fact, most of the shorelines for which data are lacking lie at high latitudes or close to major deltas. Along the Arctic margins and coasts of Antarctica, Holocene icecaps have eroded most of the LIM shorelines. Around major deltas, such as the Mississippi, Indus, Bengal, Amazon and Orinoco, sediment-induced subsidence is extreme. Besides these regions, the only undocumented margin is the south-western margin of Sundaland, where there is no reported evidence of vertical motion. Last, subsidence only locally occurs, in particular on the overriding plates of small subduction zones like the Aegean Sea.

Active margins are uplifted at faster rates on average (0.36 mm/yr) than passive margins (0.13 mm/yr). But given the fact that the vast majority of passive margins undergo persistent loading from sedimentation, they may not be so different. Except for deltas, long-term sedimentation rates at passive margins

typically range from 2 10^{-2} to 4 10^{-1} mm/yr (Einsele, 2000). Isostatic corrections of the ID type (writen $v_{sub} = v_{sed}(\rho_s - \rho_w)/(\rho_m - \rho_w)$, where v_{sub} and v_{sed} are the subsidence and sedimentation rates, ρ_s, ρ_w and $\rho_m$are the densities of the sediments, seawater and mantle, respectively), yield subsidence rates as high as 2 10^{-1} mm/yr and, therefore, a corrected value for the mean uplift rate at passive margins as high as 0.3 mm/yr. It may of course be argued that 1D isostasy is limited by the flexural response of the lithosphere, by comparison to the effects of denudation on passive margins (e.g. Gunnell and Fleitout, 1998). Although we keep the raw values in the following, we suggest that this upper bound is a reasonable approximation to explain the discrepancy between passive and active margins for several reasons. First, because the radius of curvature is actually so large (or the deflection so small with respect to the wavelength), the classic solution based of the flexure equation of a purely elastic loaded beam probably is inappropriate. This can be pictured by the considerable amounts of sediments that pile up at passive margins: if the elastic lithosphere were opposing subsidence, the conditions for piling up several kilometers of sediments at passive margins, as seen worldwide, would never be met. Second, if viscous flexure is invoked instead, it may slow down subsidence by a very small amount, for loading is rather small (compared to that of a mountain belt for instance) and the characteristic rate at which it is loaded is also too small. This can be shown by solving for the flexure of a viscous beam (e.g. Turcotte and Schubert, 1982) embedded at one end, which means that, for typical rates and parameters, the velocity at which the lithosphere is deflected is many times higher than typical sedimentation rates. Last, if a more appropriate visco-elastic (Maxwell) rheology is considered, given the characteristic rates, it can be shown following the same procedure that the viscous behaviour would dominate over the elastic one and that the lithosphere relaxes faster than it is loaded. It implies that the lithosphere at passive margins most likely offers no resistance to subsidence and that, corrected for subsidence, the mean uplift rate at passive margins thus reaches a maximum of 0.3 mm/yr, more comparable to that of active margins (as opposed to the minimum rate of 0.13 mm/yr).

Additional evidence of passive-margin uplift comes from longer time scales: low-temperature thermochronometers and palaeostress indicators suggest, for example, that the passive coasts of Brazil, Africa, Great Britain and Australia have been uplifting on a time-scale of millions of years in response to horizontal compression (Brown et al., 2002; Cobbold et al., 2001; Hillis et al., 2008a & b). Additional evidence also based on low-temperature thermochronometers and palaeostress indicators, suggests that some passive margins have been uplifting for millions of years in response to horizontal compression. Good examples are the margins of Norway (Blystad et al., 1995; Lundin and Doré, 2002; Stoker et al., 2005), Great Britain (Boldreel and Anderson, 1998; Hillis et al., 2008a; Holford et al., 2009), Brazil (Cobbold et al., 2001) and Australia (Hillis et al., 2008b).

5 Discussion

What processes might be responsible for the apparent uplift of continental margins worldwide? The most obvious candidate is eustasy, but a variety of other mechanisms can be invoked.

- **Eustasy**

Eustasy is the uniform variation of sea level, either due to the change in the volume of seawater (variations in the storage capacity of ice caps), or to changes in the geometry of the oceanic basins. In particular, the bulk volume of small and young oceanic basins is smaller than that of old and wide oceanic basins. Heller and Angevine (1985) formerly proposed this mechanism to explain the long-term (> 100 Myrs) variations in sea level. According to a non-uniform and not necessarily representative compilation of data from a variety of palaeo-sea level records and oxygen isotope data, mean sea level has dropped by 2 to 4 m since the LIM (122 +/- 6 ka), at an average rate of less than 2 10^{-2} mm/yr (see Siddall et al., 2006, and references therein), which only slightly modifies the observed rates (see supplementary data and Fig. 2). We note, however, that a variety of studies base on oxygene isotopes, also referred to by

Siddal et al. (2006) suggest a larger uncertainty for they give sea- level highstands approximately ranging from -10 m to +15 m. On average, reports of eustatic sea level changes are about an order of magnitude lower than the mean apparent uplift rate. But an even more convincing argument that discards eustasy as the cause of this generalized vertical movement of coastlines comes form the sequences of palaeoshoreline into which the LIM is embedded. Palaeoshoreline sequences of Plio-Pleistocene age (see supplementary data) indicate continuous uplift that cannot be reconciled with eustatic variations for older isotopic stages: isotopic studies indicate that Quaternary highstands MIS 7, MIS 9 and MIS 11 never exceeded +10 m, leaving MIS 5 the last highest sea level stand. Margins so far considered as stable actually feature time series of uplift therefore discarding any passive (or eustatic) cause for the observed uplift long-standing uplift. For instance, the East Coast of North America has been uplifting since at least Early Pleistocene, Western Europe since at least MIS 11, the West coast of Africa since at least Mid Pliocene, the Eastern coast of South America since at least MIS 9 or MIS 11. The LIM therefore should be regarded as the prominent marker of a sequence that reveals a generalized uplift of continental margins rather than an isolated datum that bounds the period of surrection. Again, a long-standing uplift can also be inferred from other, longer term evidence of uplift, indicated by the Tertiary to present-day tectonic activity at both active and passive margins. This discards eustasy as an explanation for the generalized deformation of continental margins.

- **Glacio-hydro-isostasy**

Another candidate is glacio-hydro-isostasy, whereby melting of icecaps causes changes in the shape of the solid Earth and of the body of seawater above it. The feedback interactions between the two bodies and consequences on relative sea level are given by the sea- level equation (e.g. Farrell and Clark, 1976; Spada et al., 2006; Peltier, 2001). There is evidence for this mechanism in the Holocene and late Pleistocene (e.g. Peltier, 1998; Lambeck and Chappell, 2001). The characteristic time scale for glacio-hydro-isostasy chiefly depends on the viscosity of the mantle, for which a large uncertainty remains,

but observations and models suggest that the relaxation occurs within a few thousand years, even at low harmonic degrees (e.g. Peltier, 2004). Therefore even the effects of the most recent glacio-hydro-isostatic event, that followed the mid-Holocene deglaciation at ~6 ka, are decreasing. It indeed modified the elevation of the Holocene shorelines and similarly the older markers of the sequence by comparable amounts. Assuming no other process is involved, the maximum impact of the last glacio-hydro-isostatic event can be inferred from the widespread Holocene palaeoshorelines. Except at high latitudes, these generally lie a couple of meters above sea level on average (for an example in the Indo-Pacific realm, Woodroffe and Horton, 2005), ~25 m lower than the mean elevation of MIS 5e palaeoshorelines, and only very seldom are raised higher than 6 meters. Averaged over the entire period since the LIM, the rate of uplift is at most 3×10^{-2} mm/yr, so that glacio-hydro-isostasy is unlikely to be a mechanism for our global observations of sea-level change since the LIM. At this stage, the time- integrated impact on relative sea level is unclear and the corrections that we could apply would be very small and comparable to the uncertainty. Thus, we prefer not to show any corrected map, that in any case would critically resemble the map of raw rates.

- **Dynamic topography**

Dynamic topography is the response of the surface of the Earth to mantle flow. Convective viscous stresses may deflect the surface of the Earth by several hundred meters (Hager et al., 1985; Le Stunff and Ricard, 1997; Conrad et al., 2004; Spasojeviç et al., 2008) although the magnitude may be significantly hampered by lateral viscosity variations (Cadek and Fleitout, 2003). Dynamic topography makes the shape of the Earth depart from the geoid and therefore controls absolute sea level (e.g. Gurnis, 1993; Husson and Conrad, 2006). Dynamic topography changes as the heterogeneous mantle flows, which modifies relative sea level (Lithgow-Bertelloni and Gurnis, 1997; Gurnis et al., 2000) at typical rates of $\pm 10^{-3}$ to $\pm 10^{-2}$ mm/yr (Moucha et al., 2008; Conrad and Husson, 2009). The impact of dynamic topography on relative sea- level

variations is therefore too small to explain the apparent sea- level change at continental margins. In addition, because the volume of the Earth remains constant, the surface- integrated deflection of the Earth sums up to zero, implying that relative sea- level variations can be both positive and negative. Integrated over the surface of the Earth, because dynamic topography is unevenly distributed with respect to continents, it converts into absolute sea-level rise of $5\ 10^{-4}$ to $3\ 10^{-3}$ mm/yr (Husson and Conrad, 2006; Conrad and Husson, 2009; Moucha et al., 2008), small in magnitude and above all, opposed to the apparent sea level fall. Measured rates could be corrected from the effects of dynamic topography variations on relative and absolute sea level change, but the rates are so small that the corrected and uncorrected maps would look almost similar. Dynamic topography can therefore be discarded as a mechanism to explain the generalized apparent coastal uplift.

- **Plate tectonics**

The previous analysis suggests that none of the commonly invoked processes that impact both relative and absolute sea level satisfactorily explains the observations. Instead, we suggest that generalized uplift of continental margins could result from the current accretion of Africa, Australia, and India to the Eurasian plate following a period of dispersal that peaked during the Late Cretaceous. A prominent consequence of such a mechanism is the gradual disappearance of subduction zones - the Tethys in particular - whereas the total ridge length approximately remains approximately constant. Because subduction zones are the only means by which the compression from the spreading ridges and mantle flow can be released, the average magnitude of compressive stress most likely increased in the lithosphere during the gradual disappearance of subduction zones. The aggregation of many continents onto Eurasia has resulted in a robust continental unit, deeply anchored into the mantle. A variety of observations illustrate the long-term consequences of this mechanism, including the decrease in the mean production rate at ridges by

about 20% during Neogene (Conrad and Lithgow-Bertelloni, 2007), and by 25-50% during the last 140 Myr (Becker et al., 2009). This decrease can be related to the increasing resistance to plate tectonics that accompanies the gradual replacement of subduction zones by mountain belts around Eurasia. Other lines of evidence, indicating that compression is centrifugally transmitted from the massive continental unit on geological time scales, include compression of the Indian oceanic plate (Bull and Scrutton, 1990; Chamot-Rooke et al., 1993; Martinod and Molnar, 1995), formation of the Andes (Russo and Silver, 1996) and westward drift of the Pacific basin (Husson et al., 2008).

The observed uplift of continental margins identified worldwide by the elevation of the MIS 5e paleo-shorelines may reflect the same process at a shorter time scale. Once again, we use the LIM as a worldwide datum, but the mechanism applies on longer time-scales as indicated by the sequences of marine terraces that often span the Quaternary, but also by geological evidence for tectonic activity and exhumation on continental margins, including passive margins (see above). Higher magnitudes of compressive stress in the lithosphere, following the accretion of the supercontinent, induce deformation at passive margins and favor crustal thickening and uplift (Leroy et al., 2004) (Fig. 3). This mechanism may explain the post- break-up deformation of passive margins during the Tertiary, for which there is good evidence in Norway (Blystad et al., 1995; Lundin and Doré, 2002; Stoker et al., 2005), Great Britain (Boldreel and Anderson, 1998; Hillis et al., 2008a; Holford et al., 2009), Brazil (Cobbold et al., 2001) and Australia (Hillis et al., 2008b). Continuous uplift and exhumation are required to explain this deformation and the presence of high grade metamorphism along these margins. Southwest England, where previously deeply buried Variscan rocks are found, is in that sense a very good illustration (see for instance Floyd et al., 1993).

Similarly, along subduction zones, higher compression should favour crustal thickening. In addition, by forcing subduction (*i.e.* making trench retreat faster

than its intrinsic rate, that we refer to as driven by slab buoyancy) the continent overrides the subducting plate faster than the trench retreats, and its elevation increases (Fig. 3). Indeed, in physical models (Espurt et al., 2008), faster convergence rates between overriding and subducting plates make the slab dip less steeply and induce higher strain rates and mountain building in the overriding plate.

Conclusion : continental margins in the current plate circuit

In our opinion, the rate of convergence of India, Africa and Australia decreases because the Tethyan subduction zones gradually vanish, and also because the weights of the Alpine, Himalayan, and Banda continental collision zones oppose the driving forces of plate tectonics (Argand, 1924). Because subduction can no longer accommodate their migration toward Eurasia, Africa, India and Australia became compressed between the ridges on their trailing edges and Eurasia on their leading sides, possibly causing uplift of their leading margins, in the Banda and Mediterranean seas for Australia and Africa. The external margins of the aggregating supercontinent would in turn undergo compression. The ridges that circumscribe the supercontinent repel the peripheral continental plates, namely South and North America and Antarctica. The spreading of the Atlantic Ocean is resisted on the Pacific Ocean side along its Aleutian, Juan de Fuca, Cocos and Nazca subduction zones, as highlighted by the very existence of the American Cordilleras. This process was re-inforced after Africa collided with Eurasia, fostering compression of the South American pate and leading to Cordillera building (Russo and Silver, 1996). The intrinsic properties of subduction zones control rates of trench retreat (Funiciello et al., 2003; Royden and Husson, 2006). Departure from this balance occurs when overriding plates are driven at different rates from trench rates, either causing back-arc extension or orogenies. American upper plates force slab rollback at fast rates, as exemplified by the Andes forcing the subduction of the Nazca plate after the Tethys closed (Silver et al., 1998). Slab rollback is resisted by sub-slab mantle flow, which in turn puts the entire Pacific system under compression (Husson et

al., 2008). Horizontal forces necessarily transmit across ridges, albeit at depth.Therefore, compression follows its circuit to reach circum-Pacific margins (Fig. 4). Similarly, because ridges surround Antarctica, it remains constricted.

The accretion of the African, Indian and Australian plates to Eurasia should make compression consistently propagate in a centrifugal mode (along small circles) from Eurasia across surrounding plates, following plate motion and causes the uplift of continental margins. This can be seen by comparing (Fig. 4) the absolute plate motion (from Kreemer, 2009) to the orientation of the axis of maximum horizontal compression (Heidbach et al., 1997). It is on this basis that we attempt to extrapolate stress-regime indicators and conclude that circum-Arctic and peri-Antarctic coastlines, where icecaps could not possibly have spared the LIM coastal morphology, are also uplifting. In fact, almost no continental margin seems to avoid this new stress regime and the uplift of all margins appear to fit into this scenario. After it was dragged into the Banda subduction zone, the Australian continent became trapped between the Southeast Indian Ridge and its northern margin that can no longer be subducted; India became squeezed between the Carlsberg ridge and Eurasia while the Himalayas rose; Africa became compressed after it collided with Eurasia, between the South Atlantic ridge and the Alps, from Western Europe to Zagros. On the subduction side, both the North and South Americas became squeezed between the Atlantic ridges and the circum-Pacific subduction zones. The margins of all those continental units feature uplifting coasts.

Besides subsiding deltas, only the long SW margins of Sundaland are not documented and aerial views reveal no uplifted palao-shorelines. This suggests that they may be either steady or subsiding. Indeed, lines of evidence indicate that subsidence dominates in the western part of Sundaland (see Bird et al., 2006, and references therein). We interpret this atypical behaviour in terms of their peculiar geodynamic setting, which currently spares them from the compression that follows supercontinental accretion. This can be seen on the current plate circuit (Fig. 4). The subduction of the Indian plate towards

Sundaland, underneath the southwestern margin of Sundaland (Sumatra and Java trenches), does not operate along a small circle that would go towards the massive Eurasia. This almost unique setting leaves the convergence regime unchanged and there is no reason for increased compression along this margin following the aggregation of the many continents onto Eurasia. In fact, this situation can be compared to that of the Aegean Sea where local subsidence accompanies slab rollback. Because nothing makes subduction in these areas depart from their intrinsic rates (see above), no additional compression on the upper plate occurs and there is no reason for uplift of the overriding margin. Conversely, the subduction occurs freely, extension takes place in the upper plate and subsidence most likely results. Therefore, we emphasize that, because their odd behavior with respect to the general tendency uplifted margins can be explained by their almost unique situation in the current plate circuit, the peculiar margins of SW Sundaland and of Aegea are at least compatible, if not supporting, the plate tectonic explanation for global uplift of continental margins. We conclude that the accretion of plates towards the end of the latest Wilson cycle (Wilson, 1966) led to a redistribution of stresses responsible for the overall short-term uplift of continental margins, as recorded by sequences of Quaternary paleo-shorelines.

Rephrasing Moucha et al. (2008), our study reveals that there is no such thing as a stable continental platform. Their argument was based on the long-term (~100 Myrs) comprehension of the figure of the Earth. Our data confirm this idea by observations on much shorter time scales. Because the notion of eustasy is based on the hypothesis of time stability of passive continental margins that would give a datum around which absolute sea level oscillates, this once more challenges accuracy in the evaluation of past sea level from the fossil- shoreline record and challenges the significance of eustasy.

Figure Caption

Figure 1: Examples of sequences of Quaternary paleoshorelines. A) Africa Mount, central coast of eastern Kamchatka, sequence of five marine terraces reaching an altitude of 850 m. The sequence is bordered seaward by a succession of Holocene marine and wave- built terraces that reach ~ 35 m in altitude. The T1 terrace is correlated to MIS 5e on the basis of tephrochronology and morphostratigraphy (unpublished data). A') E-W transect of the area. B) Bahia Laura, Patagonia, Argentina, sequence of beach-ridges. The photograph only shows the distal part of the sequence which reaches at least 70 m. Correlation of some beach ridges to MIS 5e comes from morpho-stratigraphy of the site by comparison with other places where U/Th, ESR and 14C are available. B') Altitudinal transect of the area. All altitudes are in meters above sea level.

Figure 2: Apparent rates of vertical motion on coastlines as inferred from heights of paleo-shorelines, which formed during the Last Interglacial Maximum. Arrow size indicates degree of confidence. Numbers in italics indicate rates corrected for eustasy + 3 m (see text).

Figure 3: Cartoon showing uplift of passive margins (a) and active margins (b), due to intensification of compression in lithosphere. Black arrows point at uplifting shorelines.

Figure 4: World map (top) showing apparent uplift rates of continental margins (yellow values) in the framework of plate kinematics. Arrows along small circles indicate relative plate motion for diverging plates (pink) and converging plates (green), interpreted as indicators of stress increments from one plate to another. Global plate velocities (red arrows, Kreemer, 2009) follow directions of maximal horizontal compression on continents (blue bars, averaged from Heidbach et al., 2008). Schematic cross-section (bottom) along global E-W plate-circuit (white great circle). Focal mechanisms (beach balls) indicate compression; yellow arrowheads indicate uplift and mean uplift rates.

Table 1: Mean apparent rates of uplift for various provinces and geodynamic settings. Quality refers to confidence in measurements (see supplementary data).

Acknowledgement

We acknowledge the pioneering work of all authors that made this compilation possible and we kindly thank all the people (too many to cite individually) that sent us articles or gave us details about the places where they have worked.

Author information Correspondence and requests for materials should be addressed to K.P. (e-mail: kevin.pedoja@unicaen.fr).

References

Aguirre, M. L., 2003, Late Pleistocene and Holocene palaeoenvironments in Golfo San Jorge, Patagonia: molluscan evidence: Marine Geology, v. 194, p. 3-30.

Anderson, R. S., A. L. Densmore, and M. A. Ellis, 1999, The generation and degradation of marine terraces: Basin Research, v. 11, p. 7-19.

Anderson, R. S., and K. M. Menking, 1994, The Quaternary marine terraces of Santa Cruz, California : evidence for coseismic uplift of two faults: Geological Society of America Bulletin, v. 106, p. 649-664.

Antonioli, F., S. Kershaw, D. Rust, and V. Verubbi, 2003, Holocene sea-level change in Sicily, and its implications for tectonic models: new data from the Taormina area, northeast Sicily: Marine Geology, v. 196, p. 53-71.

Antonioli, F., L. Ferranti, and S. Kershaw, 2006, A glacial isostatic adjustment origin for double MIS 5.5 and Holocene marine notches in the coastline of Italy: Quaternary International Quaternary sea-level changes: contributions from the 32nd IGC, v. 145-146, p. 19-29.

Argand, E., 1924, *La tectonique de l'Asie*, comptes-rendus du XIIIeme Congrès Géologique

International, Liege, 202 p.

Augustinus, P., 1989, Cheniers and chenier plains : a general introduction: Marine Geology, v. 90, p. 219-229.

Balescu, S., B. Dumas, P. Guérémy, M. Lamothe, R. Lhénaff, and J. Raffy, 1997, Thermoluminescence dating tests of Pleistocene sediments from uplifted marine shorelines along the southwest coastline of the Calabrian Peninsula (southern Italy): Palaeogeography, Palaeoclimatology, Palaeoecology, v. 130, p. 25-41.

Balescu, S., B. Dumas, P. Guérémy, M. Lamothe, R. Lhénaff, and J. Raffy, 1997, Erratum to "Thermoluminescence dating tests of Pleistocene sediments from uplifted marine shorelines along the southwest coastline of the Calabrian Peninsula (southern Italy)" [Palaeogeogr., Palaeoclimatol., Palaeoecol. 130 (1997) 25-41]: Palaeogeography, Palaeoclimatology, Palaeoecology, v. 136, p. 375-376.

Bardají, T., J. L. Goy, C. Zazo, C. Hillaire-Marcel, C. J. Dabrio, A. Cabero, B. Ghaleb, P. G. Silva, and J. Lario, 2009, Sea level and climate changes during OIS 5e in the Western Mediterranean: Geomorphology Coastal Geomorphology, v. 104, p. 22-37.

Bates, M. R., D. H. Keen, and J. P. Lautridou, 2003, Pleistocene marine and periglacial deposits of the English Channel: Journal of Quaternary Science, v. 18, p. 319-337.

Bender, M. L., F. T. Taylor, and R. K. Matthews, 1973, Helium-uranium dating of corals from Middle Pleistocene Barbados reef tracts: Quaternary Research, v. 3, p. 142-146.

Becker, T. W., C.P. Conrad, B. Buffett, and R.D. Müller. 2009, Past and present seafloor age distributions and the temporal evolution of plate tectonic heat transport. Earth Planet. Sci. Lett., v. 278, p.233-242.

Bird, M. I., W. C. Pang, and K. Lambeck, 2006, The age and origin of the straits of Singapore: Palaeogeography, Palaeoclimatology, Palaeoecology, v. 241, p. 531-538.

Boldreel, L.O. and M.S. Andersen, 1998, Tertiary compressional structures on the Faroe Rockall Plateau in relation to northeast Atlantic ridge-push and Alpine foreland stresses: Tectonophysics, v. 300, p. 13–28.

Blystad, P.L., H. Brekke, R.B. Faerseth, B.T. Larsen, J. Skogseid and B. Torudbakken, 1995, Structural elements of the Norwegian continental shelf. II. The Norwegian Sea Region: Norwegian Petroleum Directorate Bulletin, v. 8, p. 1-44.

Bordoni, P., and G. Valensise, 1998, Deformation of the 125 ka marine terrace in Italy: tectonic implications: Geological Society, London, Special Publications, v. 146, p. 71-110.

Bradley, W. C., and G. B. Griggs, 1976, Form, genesis, and deformation of central California wave-cut platforms: Geological Society of America Bulletin, v. 87, p. 433-449.

Bravais, M. A., 1845, On the lines of ancient level of the sea in Finmark: Quarterly Journal of the Geological Society, v. 1, p. 534-549.

Brigham-Grette, J., and D. M. Hopkins, 1995, Emergent Marine Record and Paleoclimate of the Last Interglaciation along the Northwest Alaskan Coast: Quaternary Research, v. 43, p. 159-173.

Brown, E. T., and D. L. Bourlès, 2002, Use of a new 10 Be and 26 Al inventory method to date marine terraces, Santa Cruz, USA : comment and reply : comment: Geology, v. 30, p. 1147-1148.

Bruggemann, J. H., R. T. Buffler, M. M. M. Guillaume, R. C. Walter, R. von Cosel, B. N. Ghebretensae, and S. M. Berhe, 2004, Stratigraphy, palaeoenvironments and model for the deposition of the Abdur Reef Limestone: context for an important archaeological site from the last interglacial on the Red Sea coast of Eritrea: Palaeogeography, Palaeoclimatology, Palaeoecology, v. 203, p. 179-206.

Bull, J.M. and Scrutton, R.A., 1990, Fault reactivation in the central Indian Ocean and the rheology of oceanic lithosphere. Nature, v.344, p. 855-858.

Bull, W. B., 1985, Correlation of flights of global marine terraces: 15th Annual Geomorphology Symposium, p. 129-152.

Bull, W. B., and A. F. Cooper, 1986, Uplifted Marine Terraces Along the Alpine Fault, New Zealand: Science, v. 234, p. 1125-1228.

Bull, W. B., and A. F. Cooper, 1988, Response:New Zealand Marine Terraces: Uplift Rates: Science, v. 240, p. 804-805.

Cadek, O., and L. Fleitout, 2003, Effect of lateral viscosity variations in the top 300 km on the geoid and dynamic topography. Geophysical Journal International, 152, 566-580.

Chambers, R., 1848, Ancient Sea-margins, as memorial of changes in the relative level of sea and land: Edinburgh, W & R Chambers, 332 p.

Chamot-Rooke, N., F. Jestin, and B. deVoogd, 1993, Intraplate shortening in the central Indian Ocean determined from a 2100 km long north-south deep seismic reflection profile, Geology, 21, 1043-1046.

Chappell, J., 1974, Geology of Coral Terraces, Huon Peninsula, New Guinea; A Study of Quaternary Tectonic Movements and Sea-Level Changes: Geol Soc Am Bull, v. 85, p. 553-570.

Chappell, J., and N. J. Shackleton, 1986, Oxygen isotopes and sea level: Nature, v. 324, p. 137-140.

Chappell, J., and H. H. Veeh, 1978, Late Quaternary tectonic movements and sea-level changes at Timor and Atauro Island: Geological Society of America Bulletin, v. 89, p. 356-367.

Choukri, A., O. K. Hakam, J. L. Reyss, and J. C. Plaziat, 2007, Radiochemical data obtained by [alpha] spectrometry on unrecrystallized fossil coral samples from the Egyptian shoreline of the north-western Red Sea: Radiation Measurements, v. 42, p. 271-280.

Cobbold, P.R., Meisling, K. and Mount, V. S, 2001. Reactivation of an obliquely rifted margin, Campos and Santos basins, southeastern Brazil. American Association of Petroleum Geologists Bulletin, v. 85, p. 1925-1944.

Conrad, C.P., C. Lithgow-Bertelloni, and K.E. Louden, 2004, Iceland, the Farallon slab, and dynamic topography of the North Atlantic, Geology, *32,* 177-180.

Conrad, and C. Lithgow-Bertelloni, 2007, Faster seafloor spreading and lithosphere production during the Mid-Cenozoic, Geology, v. 35, p. 29–32; doi:10.1130/G22759A.1

Conrad, C.P., and L. Husson, 2009, Influence of dynamic topography on sea level and its rate of change, Lithosphere, v.1, p. 110-120.

Cooper, F. J., G. P. Roberts, and C. J. Underwood, 2007, A comparison of 10^3–10^5 year uplift rates on the South Alkyonides Fault, central Greece: Holocene climate stability and the

formation of coastal notches: Geophysical Research Letters, v. 34, p. 1-6.

Coutard, S., J.-P. Lautridou, E. Rhodes, and M. Clet, 2006, Tectonic, eustatic and climatic significance of raised beaches of Val de Saire, Cotentin, Normandy, France: Quaternary Science Reviews, v. 25, p. 595-611.

Crook, K. A. W., and E. A. Felton, 2008, Sedimentology of rocky shorelines 5: The marine samples at + 326m from Stearns swale (Lanai, Hawaii) and their paleo-environmental and sedimentary process implications: Sedimentary Geology, v. 206, p. 33-41.

Dalongeville, R., B. Keraudren, P. Bernier, and J. R. Renault-Miskovsky, 2000, Stepped corrosion benches of Tyrrhenian age (stade 5.1) in Malia, Crete: Géomorphologie: relief, processus, environnement, v. 1, p. 21-24.

Darwin, C. R., 1842, The structure and distribution of coral reefs. Being the first part of the geology of the voyage of the Beagle, under the command of Capt. Fitzroy, R.N. during the years 1832 to 1836: London, Smith Elder and Co., 214 p.

Darwin, C. R., 1846, Geological observations on South America. Being the third part of the geology of the voyage of the Beagle, under the command of Capt. Fitzroy, R.N. during the years 1832 to 1836: London, Smith Elder and Co., 279 p.

Dodge, R. E., R. G. Fairbanks, L. K. Benninger, and F. Maurrasse, 1983, Pleistocene Sea Levels from Raised Coral Reefs of Haiti: Science, v. 219, p. 1423-1425.

Dumas, B., C. T. Hoang, and J. Raffy, 2006, Record of MIS 5 sea-level highstands based on U/Th dated coral terraces of Haiti: Quaternary International Quaternary sea-level changes: contributions from the 32nd IGC, v. 145-146, p. 106-118.

Dunlop, A., 1893, On Raised Beaches and Rolled Stones at High Levels in Jersey: Quarterly Journal of the Geological Society, v. 49, p. 523-530.

Dupré, W. R., 1984, Reconstruction of paleo-wave conditions during the Late Pleistocene from marine terrace deposits, Monterey Bay, California: Marine Geology Hydrodynamics and Sedimentation in Wave-Dominated Coastal Environments, v. 60, p. 435-454.

Dutton, A., E. Bard, F. Antonioli, T. M. Esat, K. Lambeck, and M. T. McCulloch, 2009, Phasing and amplitude of sea-level and climate change during the penultimate interglacial, v. 2, p. 355-359.

Einsele, G., 2000, Sedimentary basins; evolution, facies, and sediment budget 2nd edition, Springer, Berlin, 792 p.

Espurt, N., F. Funiciello, J. Martinod, B. Guillaume, V. Regard, C. Faccenna, and S. Brusset, 2008, *Flat subduction dynamics and deformation of the South American plate: Insights from analog modeling*, Tectonics, 27, doi:10.1029/2007TC002175.

Evans, O. H., 1907, Notes on the Raised Beaches of Taltal (Northern Chile): Quarterly Journal of the Geological Society, v. 63, p. 64-68.

Farrell W.E., and J.A. Clark, 1976, On postglacial sea level. Geophysical Journal, **v. 46** p. 79–116.

Ferranti, L., F. Antonioli, B. Mauz, A. Amorosi, G. Dai Pra, G. Mastronuzzi, C. Monaco, P. Orrù, M. Pappalardo, U. Radtke, P. Renda, P. Romano, P. Sansò, and V. Verrubbi, 2006, Markers of the last interglacial sea-level high stand along the coast of Italy: Tectonic implications: Quaternary International Quaternary sea-level changes: contributions from the 32nd IGC, v. 145-146, p. 30-54.

Floyd, P.A., C.S. Exley, and M.T. Styles, 1993, Igneous rocks of South-West England, Chapman & Hall, London, 256 p.

Frank, N., L. Turpin, G. Cabioch, D. Blamart, M. Tressens-Fedou, C. Colin, and P. Jean-Baptiste, 2006, Open system U-series ages of corals from a subsiding reef in New Caledonia: Implications for sea level changes, and subsidence rate: Earth and Planetary Science Letters, v. 249, p. 274-289.

Funiciello, F., C. Faccenna, D. Giardini, and K. Regenauer-Lieb, 2003, Dynamics of retreating slabs: 2. Insights from three-dimensional laboratory experiments, Journal of Geophysical Research, 108, 2207, doi:10.1029/2001JB000896.

Galili, E., D. Zviely, A. Ronen, and H. K. Mienis, 2007, Beach deposits of MIS 5e high sea stand as indicators for tectonic stability of the Carmel coastal plain, Israel: Quaternary Science Reviews, v. 26, p. 2544-2557.

Giresse, P., 1989, Quaternary sea-level changes on the Atlantic coast of Africa, *in* M. J. Tooley, and I. Shennan, eds., Sea-level changes: London, Basil Blackwell, p. 249-275.

Goodfriend, G. A., J. Brigham-Grette, and G. H. Miller, 1996, Enhanced Age Resolution of the Marine Quaternary Record in the Arctic Using Aspartic Acid Racemization Dating of Bivalve Shells: Quaternary Research, v. 45, p. 176-187.

Gunnell, Y. and L. Fleitout, 1998, Morphotectonic evolution of the Western Ghats, India. In: M. Summerfield, Editor, Geomorphology and Global Tectonics, John Wiley and Sons Ltd, Chichester pp. 321–338.

Gurnis, M., 1993, Phanerozoic marine inundation of continents driven by dynamic topography above subducting slabs, Nature, v. 364, p. 589-593.

Gurnis, M., J.X. Mitrovica, J. Ritsema, and H.J. van Heijst, 2000, Constraining mantle density structure using geological evidence of surface uplift rates: The case of the African Superplume, Geochem. Geophys. Geosys., 1, 1999GC000035.

Hager, B.H., R.W. Clayton, M.A. Richards, R.P. Comer, and A.M. Dziewonski 1985, Lower mantle heterogeneity, dynamic topography and the geoid, Nature, v. 313, p. 541-545.

Hantoro, W. S., 1992, Etudes des terrasses récifales Quaternaires soulevées entre le détroit de la Sonde et lîle de Timor, Indonésie : Mouvements verticaux de la croute terrestre et variations du niveau de la mer: Ph.D thesis, Aix Marseille II, Aix Marseille, 743 p.

Harmon, R. S., H. P. Schwarcz, and D. C. Ford, 1978, Late Pleistocene sea level history of Bermuda: Quaternary Research, v. 9, p. 205-218.

Hearty, P., and P. Kindler, 1995, Sea-level highstand chronology from stable carbonate platforms (Bermuda and The Bahamas): Journal of Coastal Research, v. 11, p. 675-689.

Hearty, P. J., J. T. Hollin, A. C. Neumann, M. J. O'Leary, and M. McCulloch, 2007, Global sea-level fluctuations during the Last Interglaciation (MIS 5e): Quaternary Science Reviews, v. 26, p. 2090-2112.

Hearty, P. J., and A. C. Neumann, 2001, Rapid sea level and climate change at the close of the Last Interglaciation (MIS 5e): evidence from the Bahama Islands: Quaternary Science Reviews, v. 20, p. 1881-1895.

Heidbach, O., Tingay, M., Barth, A., Reinecker, J., Kurfeß, D., and Müller, B., 2008, The 2008

release of the World Stress Map (available online at www.world-stress-map.org).

Heller, P.L., Angevine, C.L., 1985, Sea-level cycles during the growth of Atlantic-type oceans. Earth and Planetary Science Letter, v. 75, p. 417–426.

Hillis, R.R., Holford, S.P., Green, P.F., Doré, A.G., Gatliff, R.W., Stoker, M.S., Thomson, K., Turner, J.P., Underhill, J.R. and Williams, G.A., 2008, Cenozoic exhumation of the southern British Isles. Geology, 36, p. 371-374, doi: 10.1130/G24699A.

Hillis, R.R., Sandiford, M., Reynolds, S.D. and Quigley, M.C., 2008 Present-day stresses, seismicity and Neogene-to-Recent tectonics of Australia's 'passive' margins: intraplate deformation controlled by plate boundary forces, Geological Society, London, Special Publications; 306, p. 71-90, doi:10.1144/SP306.3.

Holford, S.P., J.P. Turner, P.F. Green and R.R. Hillis, 2009, Signature of cryptic sedimentary basin inversion revealed by shale compaction data in the Irish Sea, western British Isles: Tectonics, v. 28, TC4011, doi:10.1029/2008TC002359.

Hoyt, J. H., 1967, Intercontinental Correlation of Late Pleistocene Sea Levels: Nature, v. 215, p. 612-614.

Hoyt, J. H., 1969, Chenier versus barrier, genetic and stratigraphic distinction: American Association of Petroleum Geologist Bulletin, v. 53, p. 299-306.

Hsu, J. T., 1992, Quaternary uplift of the Peruvian coast related to the subduction of the Nazca Ridge: 13.5 to 15.6 degrees south latitude: Quaternary International, v. 15-16, p. 87-97.

Hsu, J. T., E. M. Leonard, and J. F. Wehmiller, 1989, Aminostratigraphy of Peruvian and Chilean Quaternary marine terraces: Quaternary Science Reviews, v. 8, p. 255-262.

Hsu, J. T.-J., 1988, Emerged Quaternary marine terraces in southern Peru: sea-level changes and continental margin tectonics over the Subducting Nazca ridge: Ph.D thesis, University of Cornell, Cornell, 456 p.

Husson, L.,2006, Dynamic topography above retreating subduction zones, Geology, v. 34, p. 741-744.

Husson, L., and C.P. Conrad, 2006, Tectonic velocities, dynamic topography, and relative sea level, Geophysical Research Letters, 33, L18303, doi:10.1029/2006GL026834.

Husson, L., C.P. Conrad, and C. Faccenna, 2008, Tethyan closure, Andean orogeny, and westward drift of the Pacific basin, Earth and Planetary Science Letters, v. 271, p. 303-310.

Isla, F. I., and G. G. Bujalesky, 2000, Cannibalisation of Holocene gravel beach-ridge plains,northern Tierra del Fuego, Argentina: Marine Geology, v. 170, p. 105-122.

Jacob, J., J. D. Ward, B. J. Bluck, R. A. Scholz, and H. E. Frimmel, 2006, Some observations on diamondiferous bedrock gully trapsites on Late Cainozoic, marine-cut platforms of the Sperrgebiet, Namibia: Ore Geology Reviews Special Issue on Placer Formation and Placer Minerals - Selected Papers presented at the 26th International Sedimentological Congress, Rand Afrikaans University, South Africa, 8 -- 12 July, 2002, v. 28, p. 493-506.

James, N. P., E. W. Mountjoy, and A. Omura, 1971, An early Wisconsin reef terrace at Barbados, West Indies, and its climatic implications: Geological Society of America Bulletin, v. 82, p. 2011-2017.

Jedoui, Y., J.-L. Reyss, N. Kallel, M. Montacer, H. B. Ismaïl, and E. Davaud, 2003, U-series evidence for two high Last Interglacial sea levels in southeastern Tunisia: Quaternary Science Reviews, v. 22, p. 343-351.

Johnson, M. E., and L. K. Libbey, 1997, Global review of upper Pleistocene (substage 5e) rocky shores : Tectonic segregation, substrate variation, and biological diversity: Journal of Coastal Research, v. 13, p. 297-307.

Johnson, R. G., 2001, Last interglacial sea stands on Barbados and an early anomalous deglaciation timed by differential uplift: Journal of Geophysical Research, v. 106, p. 11 543-11 551.

Jones, A. T., 1993, Review of the chronology of marine terraces in the Hawaiian archipelago: Quaternary Science Reviews, v. 12, p. 811-823.

Kaufman, A., 1986, The distribution of 230Th/234U ages in corals and the number of Last Interglacial High Sea Stands: Quaternary Research, v. 25, p. 55-62.

Kindler, P., E. Davaud, and A. Strasser, 1997, Tyrrhenian coastal deposits from Sardinia (Italy): a petrographic record of high sea levels and shifting climate belts during the last interglacial (isotopic substage 5e): Palaeogeography, Palaeoclimatology, Palaeoecology, v. 133, p. 1-25.

Koike, K., and H. Machida, 2001, Atlas of Quaternary marine terraces in the Japanese Islands: Tokyo, University of Tokyo press, 105 p.

Korotky, A., T. Grebennikova, N. Razjigaeva, V. Volkov, L. Mokhova, L. Ganzey, and V. Bazarova, 1997, Marine terraces of Western Sakhalin Island: CATENA, v. 30, p. 61-81.

Kreemer, C., Absolute plate motions constrained by shear wave splitting orientations with implications for hotspot motions and mantle flow, Journal of Geophysical Research, 2009, in press.

Lajoie, K. R., 1986, Coastal Tectonics, *in* N. A. Press, ed., Active tectonic: Washington D,C, National Academic Press, p. 95-124.

Lajoie, K. R., D. J. Ponti, C. L. Powell, A. M. Mathieson, and S.-. Wojcicki, 1991, Emergent marine strandlines and associated sediments, coastal California: a record of Quaternary sea-level fluctuations, vertical tectonic movements, climatic changes, and coastal processes, *in* Morrison, ed., Quaternary Nonglacial Geology: Conterminous U.S.: The Geology of North America, v. K-2: Boulder, Colorado, Geological Society of America, p. 190-214.

Lambeck, K., and J. Chappell, 2001, Sea level change through the last glacial cycle, Science, v. 292, p. p. 679-686.

Leroy, M., O. Dauteuil, and P.R. Cobbold, 2004, Incipient shortening of a passive margin : the mechanical roles of continental and oceanic lithospheres. Geophysical Journal International. 159 (40-41).

Le Stunff, Y., and Y. Ricard,1997, Partial advection of equidensity surfaces: A solution for the dynamic topography problem?, Journal of Geophysical. Research, v. 102, p. 24655-24667.

Lithgow-Bertelloni, C., and M. Gurnis, 1997, Cenozoic subsidence and uplift of continents from time-varying dynamic topography, Geology, v. *25*, p. 735-738.

Ludwig, K. R., B. J. Szabo, J. G. Moore, and K. R. Simmons, 1991, Crustal subsidence rate off

Hawaii determined from 234 U/ 238 U ages of drowned coral reefs: Geology, v. 19, p. 171-174.

Lundin, E. and A.G. Doré, 2002, Mid-Cenozoic post-breakup deformation in the 'passive' margins bordering the Norwegian-Greenland Sea: Marine and Petroleum Geology, v. 19, p. 79-93.

Lyell, C., 1830, Principles of geology, being an attempt to explain the former changes of the earth's surface, by reference to causes now in operation: London, John Murray, 481 p.

Macharé, J., and L. Ortlieb, 1992, Plio-Quaternary vertical motions and the subduction of the Nazca Ridge, central coast of Peru: Tectonophysics Andean geodynamics, v. 205, p. 97-108.

Maeda, Y., F. Siringan, A. Omura, R. Berdin, Y. Hosono, S. Atsumi, and T. Nakamura, 2004, Higher-than-present Holocene mean sea levels in Ilocos, Palawan and Samar, Philippines: Quaternary International, v. 115-116, p. 15-26.

Mangerud, J., J. I. Svendsen, and V. Astakhov, 1999, Age and extent of the Barents and Kara ice sheets in Northern Russia: Boreas, v. 28, p. 46-80.

Martin, L., K. Suguio, J. M. Flexor, J. M. L. Dominguez, and A. C. S. P. Bittencourt, 1996, Quaternary sea-level history along the central Part of the Brazilian Coast. Variations in coastal dynamics and their consequences on coastal plain construction: Anais da Academia Brasileira de Ciencias, v. 68, p. 304-354.

Martinod, J., and P. Molnar, 1995, Lithospheric folding in the Indian Ocean and the rheology of the oceanic plate, Bulletin de la Society Géologique de France, 1995.v. 166, p. 813-821.

Masuda, F., 2007, Paleoclimate of Interglacial Marine Isotope stage 11 (MIS 11) from strata in the japanese Islands: The Quaternary Research, v. 46, p. 235-240.

Mauz, B., 1999, Late Pleistocene records of littoral processes at the Tyrrhenian Coast (Central Italy): depositional environments and luminescence chronology: Quaternary Science Reviews, v. 18, p. 1173-1184.

McLaren, S. J., and P. J. Rowe, 1996, The reliability of uranium-series mollusc dates from the western mediterranean basin: Quaternary Science Reviews, v. 15, p. 709-717.

Meco, J., S. Scaillet, H. Guillou, A. Lomoschitz, J. Carlos Carracedo, J. Ballester, J.-F. Betancort, and A. Cilleros, 2007, Evidence for long-term uplift on the Canary Islands from emergent Mio-Pliocene littoral deposits: Global and Planetary Change, v. 57, p. 222-234.

Meghraoui, M., F. Outtani, A. Choukri, and D. F. De Lamotte, 1998, Coastal Tectonics across the South Atlas Thrust Front and the Agadir Active Zone, Morocco, *in* I. S. Stewart, and C. Vita-Finzi, eds., Coastal tectonics, v. 146: London, Geological Society Special Publications, p. 239-253.

Meldahl, K. H., 1995, Pleistocene shoreline ridges from tide-dominated and wave-dominated coasts: northern Gulf of California and western Baja California, Mexico: Marine Geology, v. 123, p. 61-72.

Melnick, D., B. Bookhagen, M. R. Strecker, and H. Echtler, 2009, Segmentation of megathrust rupture zones from forearc deformation patterns over hundreds to millions of years, Arauco Peninsula, Chile: Journal of Geophysical Research, v. 114.

Merritts, D. J., and W. B. Bull, 1989, Interpreting Quaternary uplift rates at the Mendocino triple junction, northern California, from uplifted marine terraces: Geology, v. 17, p. 1020-1024.

Miettinen, A., H. Haila, H. Hyvärinen, K. Rinne, and M. Eronen, 2005, Eemian crustal deformation in the eastern Baltic area in the light of the new sites at Peski, Russia and Põhja-Uhtju, Estonia: Quaternary International Baltic Sea Science Congress 2001, v. 130, p. 31-42.

Mitchell, S. F., R. K. Pickerill, B. A. B. Blackwell, and A. R. Skinner, 2000, The age of the Port Morant formation, south-eastern Jamaica: Carribean Journal of Earth Science, v. 34, p. 1-4.

Mitchell, S. F., R. K. Pickerill, and T. A. Stemann, 2001, The Port Morant Formation (Upper Pleistocene, Jamaica): high resolution sedimentology and paleoenvironmental analysis of a mixed carbonate clastic lagoonal succession: Sedimentary Geology, v. 144, p. 291-306.

Moucha, R., A.M. Forte, J.X. Mitrovica, D.B. Rowley, S. Quere, N.A. Simons, and S.P. Grand, 2008, Dynamic topography and long-term sea-level variations: There is no such thing as a stable continental platform, Earth Planetary Science Letters, v. 271, p. 101-108.

Muhs, D. R., 2001, Evolution of soils on Quaternary reef terraces of Barbados, West Indies: Quaternary Research, v. 56, p. 66-78.

Muhs, D. R., K. R. Simmons, G. L. Kennedy, and T. K. Rockwell, 2002, The last interglacial period on the Pacific Coast of North America: Timing and paleoclimate: Geological Society America Bulletin, v. 114, p. 569-592.

Muhs, D. R., K. R. Simmons, G. L. Kennedy, and T. K. Rockwell, 2002, The last interglacial period on the Pacific Coast of North America: Timing and paleoclimate: Geological Society America Bulletin, v. 114, p. 569-592.

Muhs, D. R., K. R. Simmons, and B. Steinke, 2002, Timing and warmth of the Last Interglacial period: new U-series evidence from Hawaii and Bermuda and a new fossil compilation for North America: Quaternary Science Reviews, v. 21, p. 1355-1383.

Murray-Wallace, C. V., and A. P. Belperio, 1991, The last interglacial shoreline in Australia -- A review: Quaternary Science Reviews, v. 10, p. 441-461.

Navas, A., J. Lopez-Martinez, C. J., J. Machin, J. J. Duran, E. Serrano, and J.-A. Cuchi, 2006, Marine Surfaces on Byers Peninsula, Livingston Island, South Shetland Islands, *in* D. D. Dieter Karl Fütterer, Georg Kleinschmidt, Hubert Miller and Franz Tessensohn, ed., Antarctica: Berlin, Springer Berlin Heidelberg, p. 467-473.

Nunn, P. D., 1984, Review of evidence for late Tertiary shorelines occurring on South Atlantic coasts: Earth Science Reviews, v. 20, p. 185-210.

Nunn, P. D., C. Ollier, G. Hope, P. Rodda, A. Omura, and W. R. Peltier, 2002, Late Quaternary sea-level and tectonic changes in northeast Fiji: Marine Geology, v. 187, p. 299-311.

Okumura, 1996, Tephrochronology, correlation, and deformation of marine terraces in eastern Hokkaido, Japan: Geographical Report of Tokyo Metropolitan University, v. 31, p. 19-26.

Omura, A., Y. Maeda, T. Kawana, F. P. Siringan, and R. D. Berdin, 2004, U-series dates of Pleistocene corals and their implications to the paleo-sea levels and the vertical displacement in the Central Philippines: Quaternary International, v. 115-116, p. 3-13.

Orme, A. R., 1966, Quaternary Changes of Sea-Level in Ireland: Transactions of the Institute of British Geographers, p. 127-140.

Ortlieb, L., A. Diaz, and N. Guzman, 1996, A warm interglacial episode during oxygen isotope stage 11 in northern Chile: Quaternary Science Reviews, v. 15, p. 857-871.

Ortlieb, L., B. Ghaleb, C. Hillaire Marcel, J. Macharé, and P. Pichet, 1991, Geocronologia de terrazas marinas en la costa sur-peruana: enfoque metodologico: VII Congreso Peruano de Geologia.

Ortlieb, L., and J. Macharé, 1990, Quaternary marine terraces on the Peruvian coast and recent vertical motion: Géodynamique Andine, p. 95-98.

Ortlieb, L., and J. Macharé, 1990, Geocronologia y morfoestratigrafia de terrazas marinas del Pleistoceno superior: el caso de San Juan-Marcona, Peru: Bol.Soc.Geologica del Peru, v. 81, p. 87-106.

Ota, Y., 1986, Marine terraces as reference surfaces in late Quaternary tectonics studies: examples from the Pacific Rim: New Zealand Journal of Geology and Geophysics, v. 24, p. 357-375.

Ota, Y., and A. Omura, 1992, Contrasting styles and rates of tectonic uplift of coral reef terraces in the Ryukyu and Daito Islands, Southwestern Japan: Quaternary International, v. 15/16, p. 17-29.

Otvos, E. G., 1981, Tectonic lineaments of Pliocene and Quaternary shorelines, northeast Gulf Coast: Geology, v. 9, p. 398-404.

Otvos, E. G., and W. Price, 1979, Problems of chenier genesis and terminology - An overview: Marine Geology, v. 31, p. 251-263.

Pandolfi, J. M., 2001, Numerical and taxonomic scale of analysis in paleoecological data sets: Examples from neo-tropical Pleistocene reef coral communities: Journal of Paleontology, v. 75, p. 546-563.

Paskoff, R., 1977, Quaternary of Chile : The State of research: Quaternary Research, v. 8, p. 2-31.

Pedoja, K., J. Bourgeois, T. Pinegina, and B. Higman, 2006, Does Kamchatka belong to North America? An extruding Okhotsk block suggested by coastal neotectonics of the Ozernoi Peninsula, Kamchatka, Russia: Geology, v. 34, p. 353-356.

Pedoja, K., J. F. Dumont, M. Lamothe, L. Ortlieb, J.-Y. Collot, B. Ghaleb, M. Auclair, V. Alvarez, and B. Labrousse, 2006, Plio-Quaternary uplift of the Manta Peninsula and La Plata Island and the subduction of the Carnegie Ridge, central coast of Ecuador: Journal of South American Earth Sciences, v. 22, p. 1-21.

Pedoja, K., L. Ortlieb, J. F. Dumont, M. Lamothe, B. Ghaleb, M. Auclair, and B. Labrousse, 2006, Quaternary coastal uplift along the Talara Arc (Ecuador, Northern Peru) from new marine terrace data: Marine Geology, v. 228, p. 73-91.

Pedoja, K., V. Regard, L. Husson, J. Martinod, and M. Iglesias, 2008, Why is the passive margin of Argentinean Patagonia uplifting?: An insight by marine terrace and tidal notches sequences: Seventh International Symposium on Andean Geodynamics (ISAG).

Pedoja, K., J. W. Shen, S. Kershaw, and C. Tang, 2008, Coastal Quaternary morphologies on the northern coast of the South China Sea, China, and their implications for current

tectonic models; a review and preliminary study: Marine Geology, v. 255, p. 103-117.

Peltier W.R, 1998, Postglacial Variations in the Level of the Sea: Implications for Climate Dynamics and Solid-Earth Geophysics. Reviews of Geophysics. 36(4),603-689. (1998).

Peltier, W.R., 2001, Global Glacial Isostatic Adjustment and Modern Instrumental Records of Relative Sea Level History, in Sea Level Rise: History and Consequences, B.C. Douglas, M.S. Kearney and S.R. Leatherman eds. pp. 65-95. Acad. Press, San Diego.

Peltier, W.R., 2004, Global Glacial Isostasy and the Surface of the Ice-Age Earth: The ICE-5G (VM2) Model and GRACE, Annual Review of Earth and Planetary Science, v. 32, p. 111-149.

Peñalver Hernadez, L. L., M. Cabrera, H. Trujillo, H. Morales, M. Fundora, J. Perez Lazo, L. Molerio, M. Guerra, and I. Pedroso, 2001, Evolucion paleoclimatica y paleogeografica de Cuba durante el Cuaternario: IV Congreso de Geologia y Mineria.

Peñalver Hernadez, L. L., E. Castellanos Abella, R. O. Perez Aragon, and R. Rivada Suarez, 2003, Las terrazas marinas de Cuba y su correlacion con algunas del area circumcaribe: V Congreso de Geologia y Mineria.

Personius, S. F., 1995, Late Quaternary stream incision and uplift in the forearc of the Cascadia subduction zone, western Oregon: Journal of Geophysical Research, v. 100, p. 20193-20210.

Pirazzoli, P. A., 1991, World Atlas of Holocene Sea-Level Changes: Amsterdam, Elsevier, 300 p.

Pirazzoli, P. A., 1996, Sea-Level Changes: The Last 20,000 Years, Wiley, 224 p.

Pirazzoli, P. A., 2005, Sea-level indicators, geomorphic, *in* M. L. Schwartz, ed., Encyclopia of coastal science: Dordrecht, The Netherlands, Springer, p. 836-838.

Pirazzoli, P. A., U. Radtke, W. S. Hantoro, C. Jouannic, C. T. Hoang, C. Causse, and M. B. Best, 1993, A one million-year-long sequence of marine terraces on Sumba Island, Indonesia: Marine Geology, v. 109, p. 221-236.

Polenz, M., and H. M. Kelsey, 1999, Development of a Late Quaternary Marine Terraced Landscape during On-Going Tectonic Contraction, Crescent City Coastal Plain, California: Quaternary Research, v. 52, p. 217-228.

Prestwich, J., 1865, Additional Observations on the Raised Beach of Sangatte with reference to the Date of the English Channel, and the Presence of Loess in the Cliff Section: Quarterly Journal of the Geological Society, v. 21, p. 440-442.

Prestwich, J., 1892, The Raised Beaches, and 'Head' or Rubble-drift, of the South of England: their Relation to the Valley Drifts and to the Glacial Period; and on a late post-Glacial Submergence : Quarterly Journal of the Geological Society, v. 48, p. 263-343.

Quezada, J., G. Gonzalez, T. Dunai, A. Jensen, and J. Juez-Larré, 2007, Alzamiento litoral Pleistoceno del norte de Chile: edades 21Ne de la terraza costera más alta del área deCaldera-Bahía Inglesa: Revista Geológica de Chile, v. 34, p. 81-96.

Ramsay, P. J., and J. A. G. Cooper, 2002, Late Quaternary Sea-Level Change in South Africa: Quaternary Research, v. 57, p. 82-90.

Rohling, E. J., K. Grant, C. Hemleben, M. Siddall, B. A. A. Hoogakker, M. Bolshaw, and M. Kucera, 2008, High rates of sea-level rise during the last interglacial period, v. 1, p. 38-

42.

Ronen, A., D. Zviely, and E. Galili, 2007, Did the Last Interglacial sea penetrate Mount Carmel caves? Comments on "The setting of the Mt.Carmel cavzes reassessed " by C.Vita-Finzi and C.Stringer: Quaternary Science Reviews, v. 26, p. 2684-2691.

Rosenbloom, N. A., and R. S. Anderson, 1994, Hillslope and channel evolution in a marine terraced landscape, Santa Cruz, California: Journal of Geophysical Research, v. 99, p. 14013-14029.

Royden, L.H., and L. Husson, 2006, Trench motion, slab geometry and viscous stresses in subduction systems, Geophysical Journal.International, v. 167, p. 881–905.

Russo, R.M., and P.G. Silver, 1996, Cordillera formation, mantle dynamics, and the Wilson cycle, Geology, v. 24, p. 511-514.

Rutter, N., E. J. Schnack, J. d. Rio, J. L. Fasano, F. I. Isla, and U. Radtke, 1989, Correlation and dating of Quaternary littoral zones along the Patagonian coast, Argentina: Quaternary Science Reviews, v. 8, p. 213-234.

Saillard, M., S. R. Hall, L. Audin, D. L. Farber, G. Hérail, J. Martinod, V. Regard, R. C. Finkel, and F. Bondoux, 2009, Non-steady long-term uplift rates and Pleistocene marine terrace development along the Andean margin of Chile (31°S) inferred from 10Be dating: Earth and Planetary Science Letters, v. 277, p. 50-63.

Sainsbury, C. L., R. Kachadoorian, R. H. Campbell, and D. W. Scholl, 1965, Marine platform of probable Sangamon age, and associated terrace. deposits, Cape Thompson area, northwestern Alaska: Arctic, v. 18, p. 231-245.

Sanjaume, E., and J. Tolgensbakk, 2009, Beach ridges from the Varanger Peninsula (Arctic Norwegian coast): Characteristics and significance: Geomorphology, Coastal Geomorphology, v. 104, p. 82-92.

Sanlaville, P., 1974, Le rôle de la mer dans les aplanissements côtiers du Liban: Revue de géographie de Lyon, v. 49, p. 295-310.

Scheidegger, A. E., 1962, Marine terraces: Pure and Applied Geophysics, v. 52, p. 69-82.

Schellmann, G., and U. Radtke, 1997, Electron spin resonance (ESR) techniques applied to mollusc shells from South America (Chile, Argentina) and implications for palaeo sea-level curve: Quaternary Science Reviews, v. 16, p. 465-475.

Schellmann, G., and U. Radtke, 2004, A revised morpho- and chronostratigraphy of the Late and Middle Pleistocene coral reef terraces on Southern Barbados (West Indies): Earth-Science Reviews, v. 64, p. 157-187.

Shackleton, J. C., T. H. v. Andel, and C. N. Runnels, 1984, Coastal Paleogeography of the Central and Western Mediterranean during the Last 125,000 Years and Its Archaeological Implications: Journal of Field Archaeology, v. 11, p. 307-314.

Shackleton, N. J., M. F. Sánchez-Goñi, D. Pailler, and Y. Lancelot, 2003, Marine Isotope Substage 5e and the Eemian Interglacial: Global and Planetary Change, THE EEMIAN INTERGLACIAL: A GLOBAL PERSPECTIVE, v. 36, p. 151-155.

Siddal, M., J. Chappell, and E.-K. Potter, 2006, Eustatic sea level during past interglacials, *in* F. Sirocko, M. Claussen, M. F. Sanchez Goñi, and T. Litt, eds., The Climate of Past Interglacials: Amsterdam, Elsevier, p. 75-92.

Silver, P.G., Russo, R.M., and Lithogw-Bertelloni, C., 1998, Coupling of South American and African Plate Motion and Plate Deformation, Science, 279, p. 60-63.

Spada, G., Antonioli, A., Cianetti, S., Giunchi, C., 2006, Glacial isostatic adjustment and relative sea-level changes: the role of lithospheric and upper mantle heterogeneities in a 3-D spherical Earth. Geophysical Journal International, 165, 692-702. doi: 10.1111/j.1365-246X.2006.02969.x.

Spaggiari, R. I., B. J. Bluck, and J. D. Ward, 2006, Characteristics of diamondiferous Plio-Pleistocene littoral deposits within the palaeo-Orange River mouth, Namibia: Ore Geology Reviews, Special Issue on Placer Formation and Placer Minerals - Selected Papers presented at the 26th International Sedimentological Congress, Rand Afrikaans University, South Africa, 8 -- 12 July, 2002, v. 28, p. 475-492.

Spasojeviç, S., L. Liu, M. Gurnis, and R.D. Müller , 2008, The case for dynamic subsidence of the U.S. east coast, since the Eocene, Geophysical Research Letter, 35, L08305, doi:10.1029/2008GL033511.

Stearns, C. E., 1976, Estimates of the position of seal level between 140, 000 and 75,000 years ago: Quaternary Research, v. 6, p. 445-449.

Stirling, C. H., and M. B. Andersen, 2009, Uranium-series dating of fossil coral reefs: Extending the sea-level record beyond the last glacial cycle: Earth and Planetary Science Letters, v. 284, p. 269-283.

Stirling, C. H., T. M. Esat, K. Lambeck, and M. T. McCulloch, 1998, Timing and duration of the Last Interglacial: evidence for a restricted interval of widespread coral reef growth: Earth and Planetary Science Letters, v. 160, p. 745-762.

Stoker, M.S., R.J. Hoult, T. Nielsen, B.O. Hjelstuen, J.S. Laberg, P.M. Shannon, D. Praeg, A. Mathiesen, T.C.E. van Weering and A. McDonnell, 2005, Sedimentary and oceanographic responses to early Neogene compression on the NW European margin: Marine and Petroleum Geology, v. 22, p.1031–1044.

Strahan, A., 1897, The Raised Beaches and Glacial Deposits of the Varanger Fiord: Quarterly Journal of the Geological Society, v. 53, p. 147-156.

Szabo, B. J., and J. G. Moore, 1986, Age of -360-m reef terrace, Hawaii, and the rate of late Pleistocene subsidence of the island: Geology, v. 14, p. 967-968.

Tanaka, K., R. Hataya, N. A. Spooner, D. G. Questiaux, Y. Saito, and T. Hashimoto, 1997, Dating of marine terrace sediments by ESR, TL and OSL methods and their applicabilities: Quaternary Science Reviews, v. 16, p. 257-264.

Thornton Horsfield, W., 1975, Quaternary vertical movements in the greater Antilles: Geological Society of America Bulletin, v. 86, p. 933-938.

Turcotte, D.L., and Schubert, G., 1982, Geodynamics, 2nd edition, John Wiley and Sons, 450 p.

van de Plassche, O., 1986, Sea-level research : a manual for the collection and evaluation of data: Norwich, UK, Geo Books, 618 p.

Veeh, H. H., 1966, Th230/U238 and U234/U238 ages of pleistocene high sea level stand: Journal of Geophysical Research, v. 71, p. 3379-3386.

Veldkamp, A., 1994, Evaluating Quaternary erosional dynamics at uplifting coastal areas by modelling marine terrace formation: Zeitschrift für Geomorphologie, v. 38, p. 223-237.

Vita-Finzi, C., and C. Stringer, 2007, The setting of Mt.Carmel caves reassessed: Quaternary Science Reviews, v. 26, p. 439-440.

Vousdoukas, M. I., A. F. Velegrakis, and T. A. Plomaritis, 2007, Beachrock occurrence, characteristics, formation mechanisms and impacts: Earth-Science Reviews, v. 85, p. 23-46.

Ward, C. M., 1998, New Zealand Marine Terraces: Uplift Rates: Science, v. 240.

Ward, W. T., P. J. Ross, and D. J. Colquhoun, 1971, Interglacial high sea levels--an absolute chronology derived from shoreline elevations: Palaeogeography, Palaeoclimatology, Palaeoecology, v. 9, p. 77-99.

Wehmiller, J. F., 1982, A review of amino acid racemization studies in Quaternary mollusks: Stratigraphic and chronologic applications in coastal and interglacial sites, pacific and Atlantic coasts, United States, United Kingdom, Baffin Island, and tropical islands: Quaternary Science Reviews, v. 1, p. 83-120.

Weisrock, A., S. Occhietti, C. T. Hoang, A. Lauriat - Rage, P. Brebion, and P. Pichet, 1999, Pleistocene littoral sequences of the Atlantic Atlas between Agadir and Cape Rhir, Morocco: Quaternaire, v. 10, p. 227-244.

White, A. F., M. S. Schulz, D. A. Stonestrom, D. V. Vivit, J. Fitzpatrick, T. D. Bullen, K. Maher, and A. E. Blum, 2009, Chemical weathering of a marine terrace chronosequence, Santa Cruz, California. Part II: Solute profiles, gradients and the comparisons of contemporary and long-term weathering rates: Geochimica et Cosmochimica Acta, v. 73, p. 2769-2803.

White, A. F., M. S. Schulz, D. V. Vivit, A. E. Blum, D. A. Stonestrom, and S. P. Anderson, 2008, Chemical weathering of a marine terrace chronosequence, Santa Cruz, California I: Interpreting rates and controls based on soil concentration-depth profiles: Geochimica et Cosmochimica Acta, v. 72, p. 36-68.

Williams, A. H., and G. M. Walkden, 2002, Late Quaternary highstand deposits of the southern Arabian Gulf: a record of sea-level and climate change, *in* P. D. Clift, D. Kroon, C. Gaedicke, and J. Craig, eds., The Tectonic and Climatic evolution of the Arabian sea region, v. 195: London, Geological Society Special Communication, p. 371-386.

Wilson, J.T., 1966, Did the Atlantic Close and then Re-Open? Nature, v. 211: p. 676-681.

Winograd, I. J., J. M. Landwehr, K. R. Ludwig, T. B. Coplen, and A. C. Riggs, 1997, Duration and Structure of the Past Four Interglaciations: Quaternary Research, v. 48, p. 141-154.

Wood, P. B., 1994, Optically stimulated luminescence dating of a late quaternary shoreline deposit, Tunisia: Quaternary Science Reviews, v. 13, p. 513-516.

Woodroffe, C. D., and B. P. Horton, 2005, Holocene sea-level changes in the Indo-Pacific: Journal of Asian Earth Sciences, v. 25, p. 29-43.

Wythe Cooke, C., 1971, American emerged shorelines compared with levels of Australian marine terraces: Geological Society of America Bulletin, v. 82 (11) p. 3231-3234.

Zeuner, F. E., 1952, Pleistocene Shore-lines: International Journal of Earth Sciences, v. 40, p. 39-50.

Zubakov, V. A., 1988, Climatostratigraphic scheme of the Black Sea Pleistocene and its correlation with the oxygen - isotope scale and glacial event: Quaternary Research, v. 29, p. 1-24.

Zviely, D., E. Galili, A. Ronen, A. Salamon, and Z. Ben-Avraham, 2009, Reevaluating the tectonic uplift of western Mount Carmel, Israel, since the middle Pleistocene: Quaternary Research, v. 71, p. 239-245.

Figure 1
Click here to download high resolution image

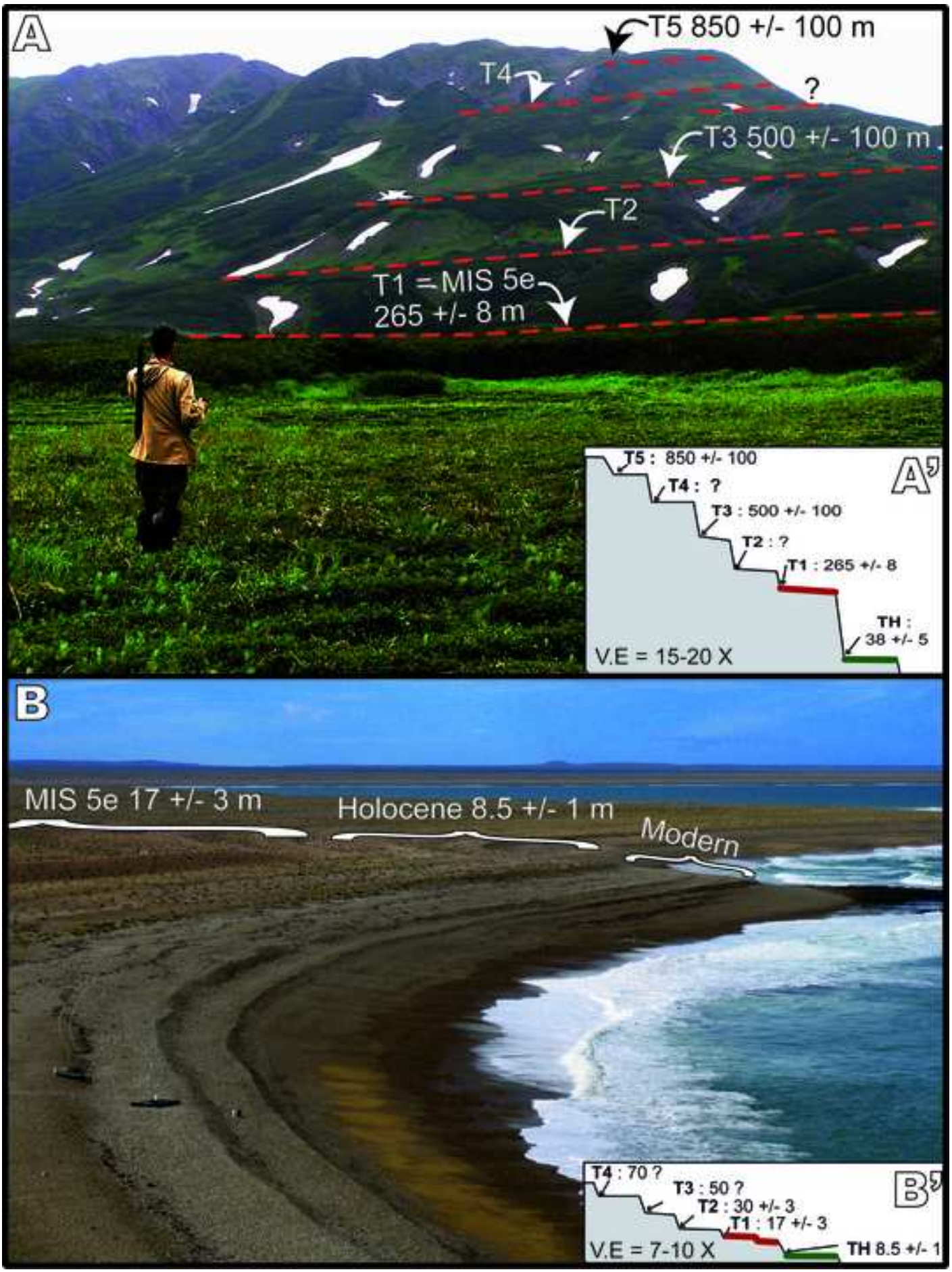

Figure 2
Click here to download high resolution image

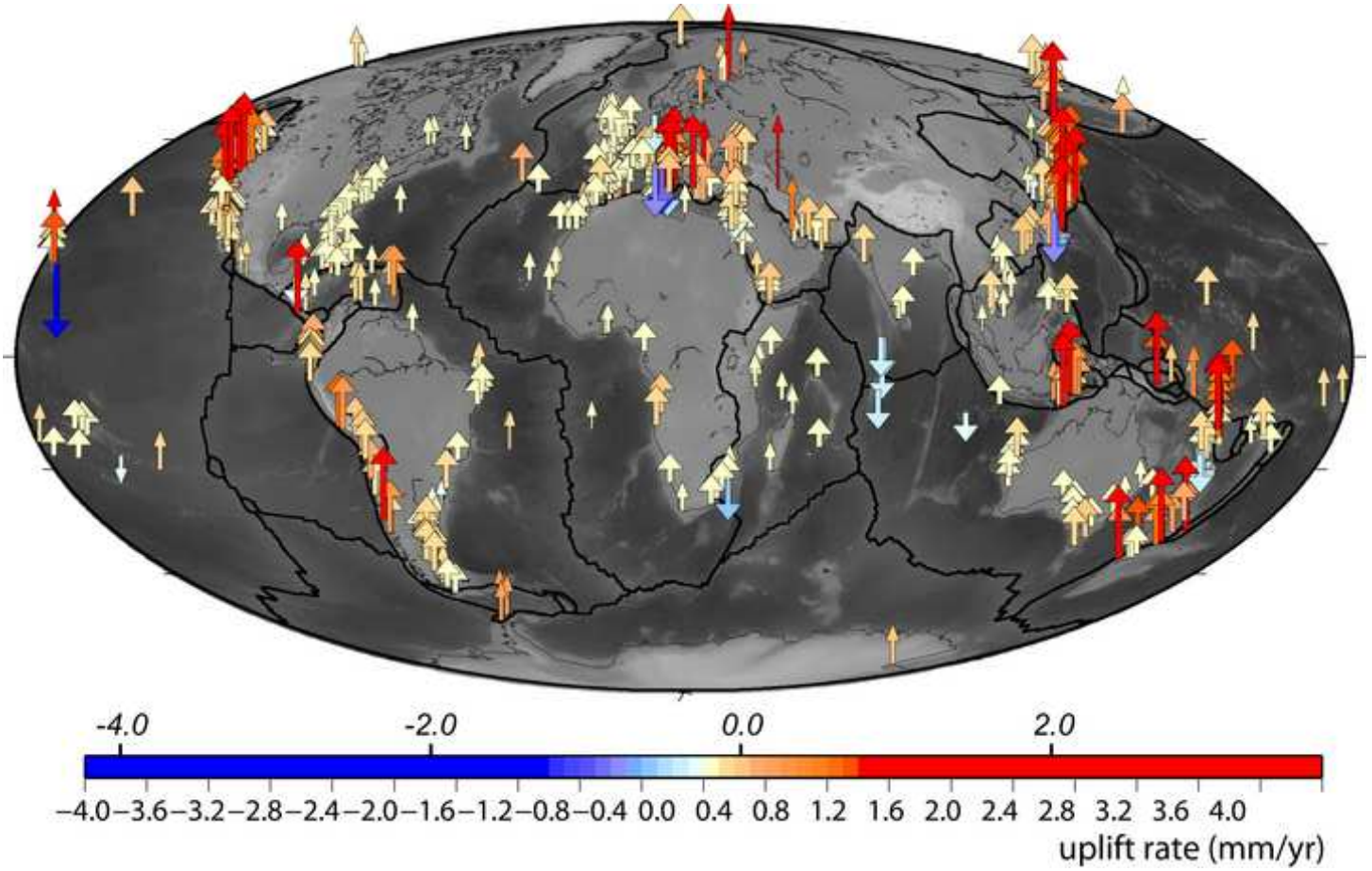

Figure 3
Click here to download high resolution image

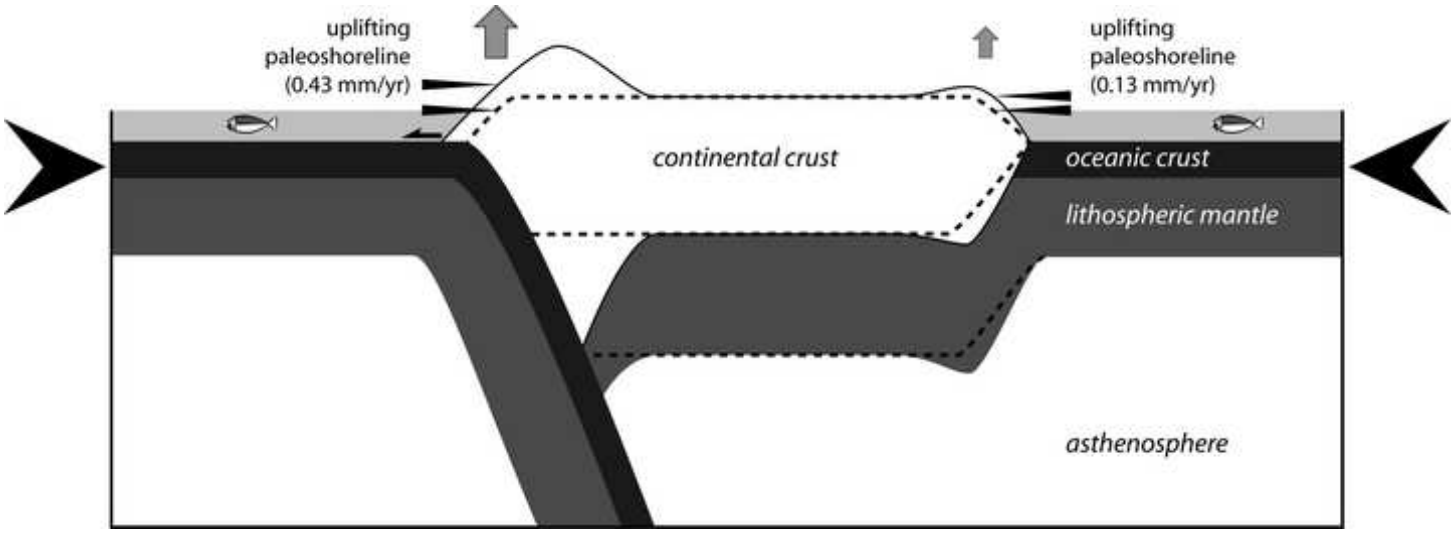

Figure 4
Click here to download high resolution image

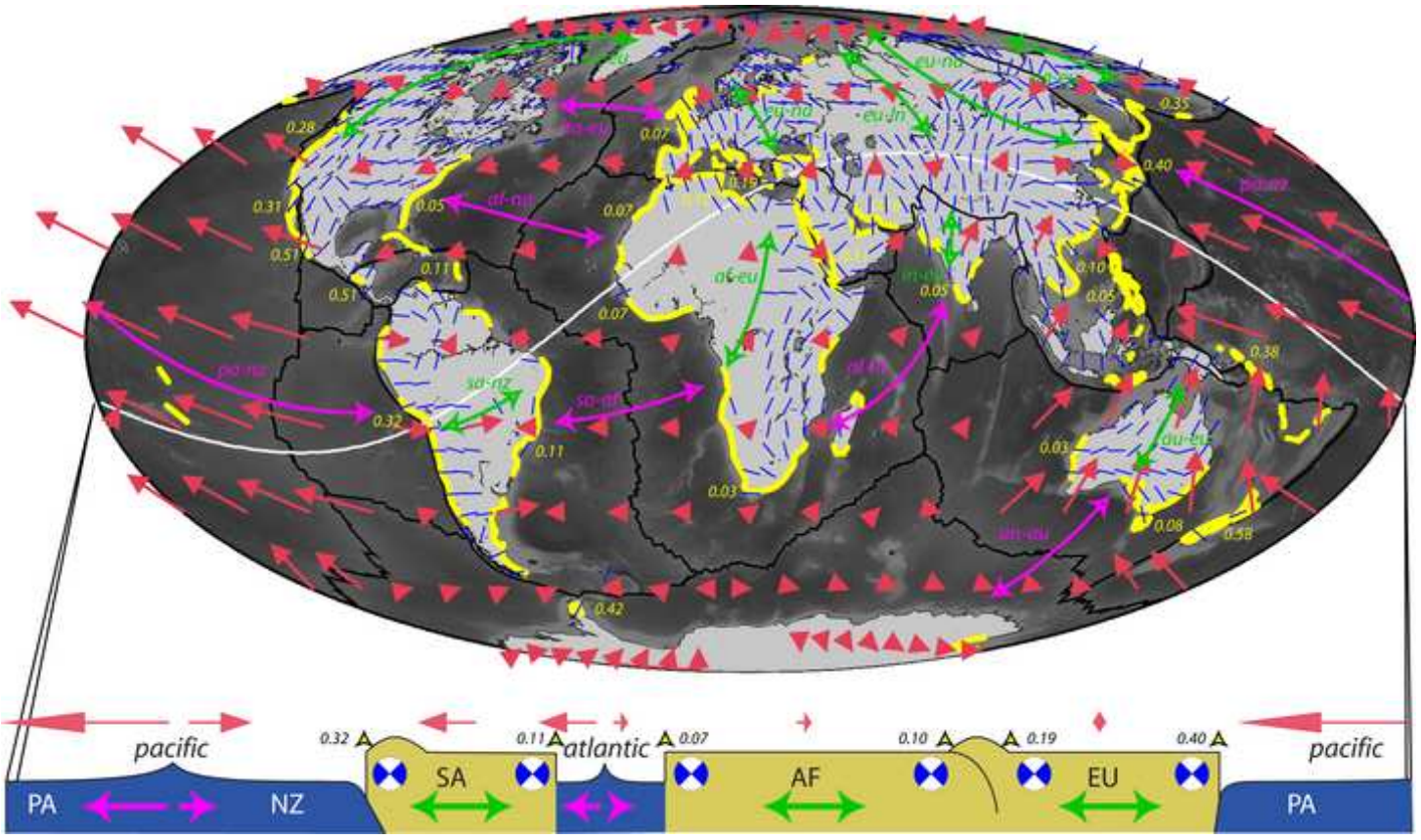

Table
Click here to download Table: table1.xls

Province	geodynamic setting	apparent vertical rate V (mm/yr)	MoE	eustasy-corrected vertical rate Vc (mm/yr)	MoE	standard deviation	number of sites	mean quality	Means (V)
Indo-Pacific	*	0.38	0.04	0.35	0.05	0.75	93	4	0.38
Persian Gulf	*	0.16	0.02	0.14	0.03	0.2	11	4	0.16
Aleutian	active	0.35	0.07	0.33	0.07	/	1	5	
Carribbean	active	0.11	0.02	0.09	0.03	0.14	28	4	
Cocos	active	0.51	0.05	0.49	0.05	0.66	4	2	
Juan de Fuca	active	0.28	0.04	0.26	0.04	0.33	21	4	
Mediterranean N	active	0.19	0.03	0.16	0.04	0.35	165	4	0.31
New Zealand	active	0.58	0.06	0.56	0.07	1.82	18	4	
Pacific W	active	0.40	0.05	0.38	0.06	0.42	110	4	
Philippines	active	0.05	0.01	0.03	0.01	0.04	4	4	
South America W	active	0.32	0.03	0.30	0.04	0.30	40	4	
Africa S	passive	0.03	0.01	0.01	0.02	0.08	25	3	
Africa W	passive	0.07	0.01	0.04	0.02	0.05	31	3	
Antarctica	passive	0.42	0.08	0.40	0.09	0.15	4	2	
Australia SE	passive	0.08	0.02	0.05	0.02	0.07	14	5	
Australia W	passive	0.03	0.01	0.00	0.01	0.06	9	9	
California & Baja	passive	0.31	0.04	0.28	0.04	0.34	71	5	
SE Continental Asia	passive	0.10	0.02	0.08	0.03	0.08	19	3	0.12
Europe W	passive	0.07	0.02	0.05	0.03	0.12	103	3	
India	passive	0.05	0.01	0.02	0.02	0.03	6	4	
Mediterranean S	passive	0.10	0.01	0.07	0.02	0.09	37	3	
North America E	passive	0.05	0.01	0.03	0.02	0.02	21	4	
South America E	passive	0.11	0.02	0.08	0.03	0.05	36	4	
Red Sea	rift	0.11	0.02	0.11	0.02	0.08	19	5	0.11
Means or sum		0.20	0.03	0.18	0.04	0.27	890	3.93	

Chapitre 5

La chaleur dans la lithosphère

Dans les chapitres précédents de ce mémoire, j'ai peu abordé, voire éludé, un aspect fondamental de la dynamique de la lithosphère : l'incidence du régime thermique. C'est évidement un paramètre clef pour la rhéologie et la géodynamique au sens large, puisque c'est par exemple à partir des géothermes suppposés que sont définis les profils rhéologiques de la lithosphère et de la croûte [Goetze & Evans, 1979], sur lesquels le débat ne tarit pas [Maggi et al., 2000, McKenzie & Jackson, 2002, Schmalholz et al., 2009, Watts & Burov, 2003].

Le champ thermique dans la lithosphère est d'autant plus complexe que les processus transitoires s'y cumulent. Dans les cratons, le régime thermique stationnaire permet d'obtenir une résolution raisonnable Jaupart & Mareschal [2003], comme dans le bouclier canadien [Mareschal & Jaupart, 2004]. En revanche, les propriétés pétrophysiques dans la lithosphère soumise à des processus transitoires, comme la sédimentation, l'érosion et la circulation de fluides sont mal connues et l'incertitude devient par conséquent très forte. Dans les exemples qui suivent, le champ thermique est inferé à partir de mesures *in situ* de la température en profondeur d'origine industrielle. Il est possible de reconstruire l'histoire tectonique et sédimentaire à partir de l'enregistrement géologique. Des modèles directs permettent de prendre en compte l'impact thermique de chaque évènement dans le temps, et les mesures actuelles fournissent des points de calibration. Des enregistrements du régime thermique passé peuvent être déduits par d'autres techniques qui renseignent en général sur la température maximale rencontrée par un échantillon (traces de fission, maturation du kérogène, réflectance de la vitrinite).

Ces don´ees fournissent des points de calibration sur l'histoire thermique passée. Lorsque l'ensemble des processus qui affecte le champ thermique est connu, les inconnues sont essentiellement le flux de chaleur à la base de la croûte et la production radiogénique, et une évaluation argumentée par la reconstruction de l'histoire géologique permet de déterminer ces grandeurs. Au vu des incertitudes qui en découlent, il est évident que c'est la valeur statistique des résultats qui a un sens dans des études régionales, un point de contrôle unique n'offrant que peu de fiabilité puisque dans la réalité, d'une part les propriétés pétrophysiques transitoires sont mal connues et que d'autre part les informations sur les mesures industrielles sont souvent incomplètes sur la mise en oeuvre de la mesure (l'état de relaxation thermique au moment de l'acquisition, en particulier, est peu renseigné).

5.1 Les fronts de chaînes de montagnes : le cas des Andes

Dans les front des chaînes de montagnes, les processus thermiques transitoires sont en nombre restreints. Par opposition aux zones internes des chaînes de montagnes, les règles cinématiques et géométriques qui caractérisent l'évolution tectonique des avant-pays sont bien connues et permettent théoriquement de prédire l'impact de chacun des processus (érosion, sédimentation, circulation de fluides, etc...). C'est le cas du front subandin, présenté dans l'article suivant.

ELSEVIER

Tectonophysics 345 (2002) 253–280

TECTONOPHYSICS

www.elsevier.com/locate/tecto

Thermal regime of fold and thrust belts—an application to the Bolivian sub Andean zone

Laurent Husson [a,b,*], Isabelle Moretti [a]

[a] *Institut Français du Pétrole, RB 10, 1-4 Avenue de Bois-Préau, 92852 Rueil-Malmaison, France*
[b] *Ecole Normale Supérieure de Lyon, 46 allée d'Italie, 69364, Lyon cédex, 07, France*

Received 8 April 2000; received in revised form 11 March 2001; accepted 15 March 2001

Abstract

A quantitative analysis of the various parameters influencing the thermal regime in orogenic belts and related foredeeps shows that (i) the increasing heat flow in internal zones is mainly due to the thickening of radiogenic layers, although there is no simple proportionality between crustal thickness and heat flow signal at large scale; (ii) in external zones, where the horizontal strain rate is large (such as in the Bolivian Andes), surface processes can be of first order within the first kilometers of the crust. Hence, they induce a large scatter in the thermal data which are acquired at shallow depths. The deep thermal regime can be restored only by a quantitative assessment of these parameters. Active erosion (respectively sedimentation) can increase (resp. reduce) the heat flow by a factor of 2 in the uppermost kilometers. The effects of fluid circulation percolating at depth can also generate significant local disturbances. Other processes such as heat advection during thrusting, surface morphology and climate change have a minor influence in most settings, compared to the aforesaid effects. In the Bolivian Sub Andean Zone, between 18°S and 22°S, the very active deformation enhances the surface thermal perturbations (particularly erosion and sedimentation) and disturb the thermal field. The analysis of these data accounting for the kinematics of the belt allows the lateral variations of the thermal regime at various scales to be assessed. A slight eastward increase in the thermal regime towards the Chaco plain is evidenced as well as towards the Boomerang area, as the Mesozoic and Cenozoic sedimentary cover gets thinner. © 2002 Elsevier Science B.V. All rights reserved.

Keywords: Thermal regime; Bolivian Andes; Erosion; Sedimentation; Fluid flow; Topography

1. Introduction

At large scale, the thermal field in the crust is mainly influenced by the geodynamic setting, the mantle heat flow (called "reduced heat flow"), the crustal thickness and its radiogenic content. In extensional zones, such as rift systems, the heat flow data (HFD) usually have typical patterns that correlate well to the crustal and lithospheric thinning (Turcotte and Schubert, 1982). On the contrary in collision settings, the thermal profiles are highly variable (Figs. 1 and 2). Depending on the geological history of the orogen, a geomorphological unit can show strong HFD differences with regards to the HFD of a similar unit in another mountain belt. A striking example is the contrast between the

* Corresponding author. Ecole Normale supérieure de Lyon, 46 allée d'Italie, 69364, Lyon cédex, 07, France. Fax: +33-4-72-72-86-77.

E-mail address: laurent.husson@ens-lyon.fr (L. Husson).

0040-1951/02/$ - see front matter © 2002 Elsevier Science B.V. All rights reserved.
PII: S0040-1951(01)00216-5

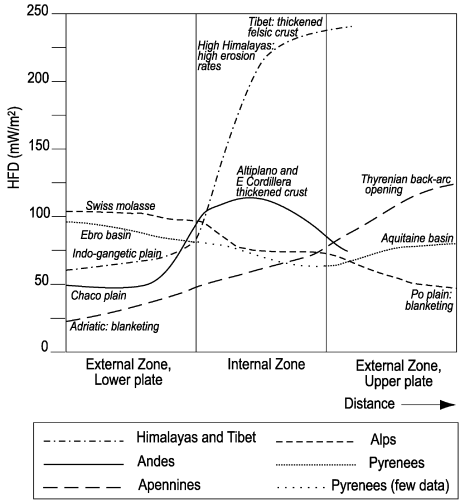

Fig. 1. Thermal profiles through various mountain belts (data source: Pollack et al., 1993).

Swiss molassic zone of the Alps and the Apenninic foredeep, where differences in their average HFD achieve more than 70 mW/m^2 (Fig. 1) and, in mountain belts, lateral variations of the HFD over a few tenths of kilometers commonly reach 40 mW/m^2 (Pollack et al., 1993). As heat diffuses in space, short wavelength HFD anomalies have shallow origin. Hence, a significant part of the thermal anomalies is due to the transient effects of superficial phenomena, which become in some places higher than the deep phenomena (mainly crustal heat generation and mantle heat flow). The effects of fast sedimentation or erosion (e.g. Lucazeau and Le Douaran, 1985), thrusting, topographically driven fluid flows (e.g. Deming, 1994) and surface morphology (e.g. Lachenbruch, 1970) have been mentioned to explain such thermal anomalies. These processes are controlled by the kinematics and are therefore dependent on the geological history of the area; in addition they can interact, being then either enhanced or reduced. In the present paper, we investigate the various surface processes affecting the thermal field in mountain belts and quantify their influences in time, space and magnitudes. This numerical approach lead to quantitative conclusions often in contradiction with the qualitative hypotheses proposed previously to explain local anomalies. Since thermal data come from the upper kilometers of the crust, well temperatures, measurements in lake sediments, mines and caves, they are influenced by surface processes. One of the key issues of these calculations is to make precise the depth below which a potential disturbance can be neglected.

In the second part, we analyze the thermal regime of the Bolivian Sub Andean Zone in the light of our

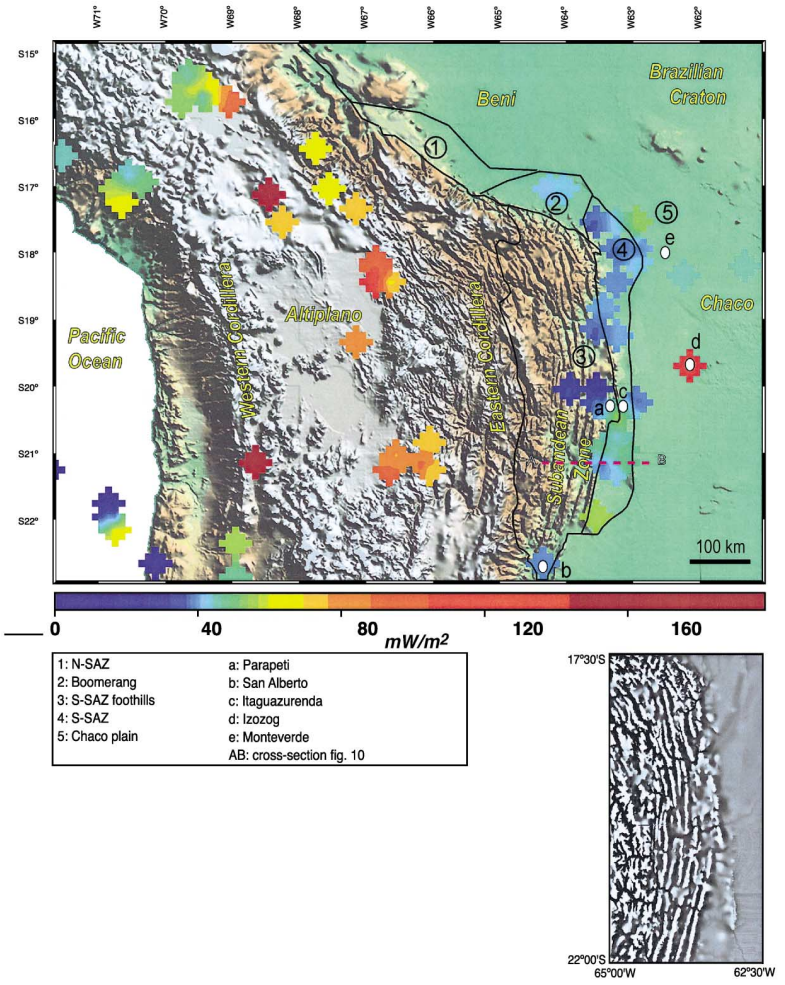

Fig. 2. Thermal data (diamonds) in the Andes between 15°S and 23°S (modified after Sclater et al., 1970, Uyeda and Watanabe, 1982, Henry and Pollack, 1988; Springer and Forster 1998) overlain on a digital elevation map. Box: periodic setting evidenced by filtering of topographical high frequencies. Solid black lines are the limits between the domains numbered from 1 to 5.

theoretical models. Since the data are affected by the aforesaid processes, we accounted for the tectonic history of the fold and thrust belt in order to avoid misleading from the large scatter in the data and to determine the deeper thermal signal.

2. Surface thermal controls in external zones of orogenic belts

Thickening of collision belts is due to the deformation and stacking of mostly crustal units at different scales. In internal zones, thick crustal units are affected; elevation subsequently increases at large scale, inducing widespread erosion. Due to the isostatic response, erosion induces relative uplift and denudation of the initially deeply buried material. On the contrary, in external zones, collision belts are mostly characterized by a thin-skinned deformation pattern involving only the sedimentary cover, and no major crustal thickening occurs. Subsequently, horizontal strain dominates in the foreland whereas vertical strain is prominent in internal parts. For instance, in the Bolivian Andes, the current denudation rate of the intrusive bodies near La Paz is about 10 km in the last 10 Ma with a drastic acceleration in the most recent period (Benjamin et al., 1987; Masek et al., 1994), and evidence of current horizontal shortening in the Eastern Cordillera is very scarce or localized at the border. On the contrary, in the Sub Andean Zone (SAZ), horizontal shortening is about 10 km/Ma (Kley, 1996; Baby et al., 1997) or even faster during the last 10 Ma. Erosion is localized over anticlines with sedimentation in piggy-back basins.

The different tectonic regimes in internal and external zones influence the surface heat flow signal. In internal zones, crustal thickening increases the thermal radiogenic production since it thickens the radiogenic layers. Increase in the HFD in the vicinity of fault zones due to friction along fault planes is still debated (Lachenbruch and Sass, 1980; England and Molnar, 1993; Leloup et al., 1999) although many data suggest that friction is very low (Evans, 1992; Blanpied et al., 1992); no significant thermal anomaly is thus expected. Deeper processes can also significantly disturb the thermal regime. Burial of crustal material may induce metamorphism and phase changes. These reactions are either endo- or exothermic and therefore affect the deep heat flow signal (Giunchi and Ricard, 1999). Lithospheric thinning, either due to back-arc activity as in the Western Apennines, delamination (e.g. Davies and von Blanckenburg, 1995) or convective removal of mantle lithosphere (e.g. Platt and England, 1994), can significantly enhance the HFD of mountain belts. Additionally, heat advection by intense magmatism potentially increases the HFD (e.g. Arndt et al., 1997).

In this paper, we focus our quantitative analysis on external causes and do not discuss any further the deep phenomena affecting internal zones as intrusion of hot material or change in the crustal thickness. Horizontal shortening in folded belts induces a series of ramp-folds prograding towards the foreland. Subsequently, the geometry can usually be regarded as a periodic system of synclines and anticlines/monoclines striking parallel to the orogen as the south SAZ (Fig. 2). Numerous superficial processes are controlled by the structural pattern of the fold and thrust belt. Among these, many exert transient perturbations on the near-surface thermal regime (Fig. 3), i.e. erosion, sedimentation, fluid circulation and terrain effects (surface morphology and geographically dependent perturbations). An integrative assessment of the impact of these processes is required in order to interpret the temperature data, to evaluate the steady state thermal signal and restore the deep signal. For each process, we first review the previous works on their thermal effects and then we quantify them versus time and depth using numerical modeling.

2.1. Thrust propagation

The impact of thrusting results from the competition between the advection and the conduction: the thrust sheet has its own thermal stage and it will be re-equilibrated, by conduction, in the overall crust after (and during) thrusting. The key parameter is the 1D Péclet number (Carslaw and Jaeger, 1959; Endignoux and Wolf, 1990) given by the V_{diff}/V_{adv} ratio, where V_{diff} and V_{adv} are the diffusion and advection velocities. When the ratio equals 1, no distortion of the thermal field is expected. The range of parameters (thickness of the thrust sheet, rate of horizontal shortening, thermal conductivity) for which thrusting may definitely be discarded as a thermal control is presented on Fig. 4a. Thrusting has commonly been

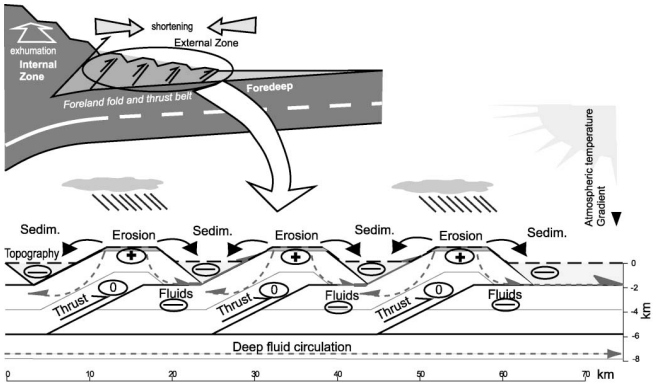

Fig. 3. Schematic cross-section through an ideal frontal thrust system. Influence of the various processes on the near-surface thermal field. The signs indicate the associated potential anomalies.

invoked in the past as a main transient control on the thermal regime, potentially responsible for inverted thermal gradients. However, using realistic crustal properties, it has also been suggested that thrusting could not be responsible for inverted gradient beneath thrusts (e.g. Jaupart and Provost, 1985; Ruppel and Hodges, 1994; Huerta et al., 1996, 1998) but only induces low thermal perturbations (Shi and Wang, 1987; Endignoux and Wolf, 1990).

In order to decipher and estimate the potential anomaly on the thermal field induced by thrusting, 2D numerical modeling (THRUSTPACK finite element program, Appendix A) was used. The thermal field was calculated for various sheet thicknesses and thrust velocities (Fig. 4b). Basal heat flow is 50 mW/m^2. Surface temperature is 0 °C. Only very thick slices and thrusting at unrealistic rates induce inverted thermal fields at depth. Most thrusts displace at a velocity slower than 20 mm/year. If the thrust sheet is more than 20-km thick and faster than 10 mm/year, minor distortion of the thermal field may appear (Fig. 4b). For instance, in the Bolivian foothills, active structures have velocities lower than 7 mm/year and the sheet thicknesses are less than 7 km (after reconstructions by Roeder and Chamberlain, 1995 and Moretti et al., 1996). From a general knowledge over several fold and thrust belts, we assume that usual values of sheet thicknesses are lower than 10 km and velocities are lower than 20 mm/year. Fig. 4b shows that that ramp folds can thus only generate minor anomalies. Therefore in most cases, thrusting is very unlikely to disturb significantly the thermal fields in fold and thrust belts.

2.2. Changes in the sedimentary regime: erosion and sedimentation

The blanketing effect is the cooling impact of high sedimentation rate and relevant examples are numerous, such as the Viking graben in the North sea and the Golfe du Lion between France and Corsica (Lucazeau and Le Douaran, 1985). In the Apennines foreland, the sedimentation rate is very high (up to 7 km in 4 Ma) and the HFD is lower than 30 mW/m^2 whereas it is twice as high in the frontal thrusts. On the contrary, erosion significantly increases the apparent thermal regime.

The thermal effects of erosion and sedimentation were quantified using the GENEX program (see Appendix A). Boundary conditions are given in Appendix A and figure captions. The thermal effects of erosion can be described in 1D as a simple advection

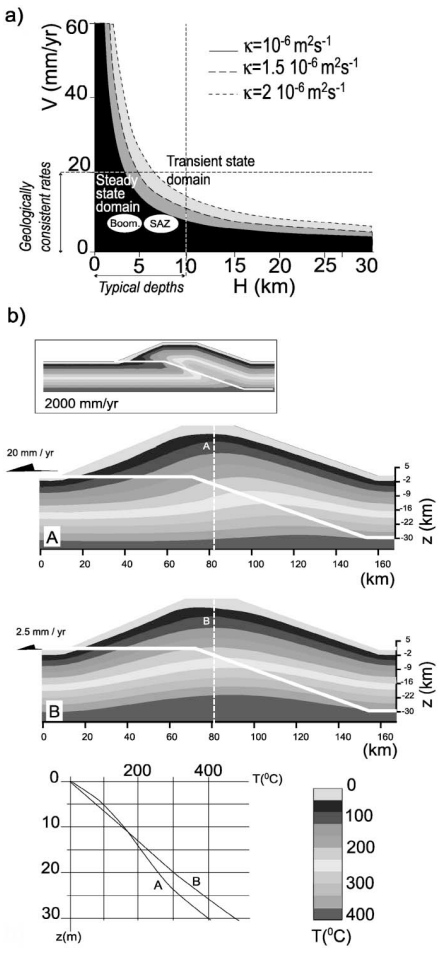

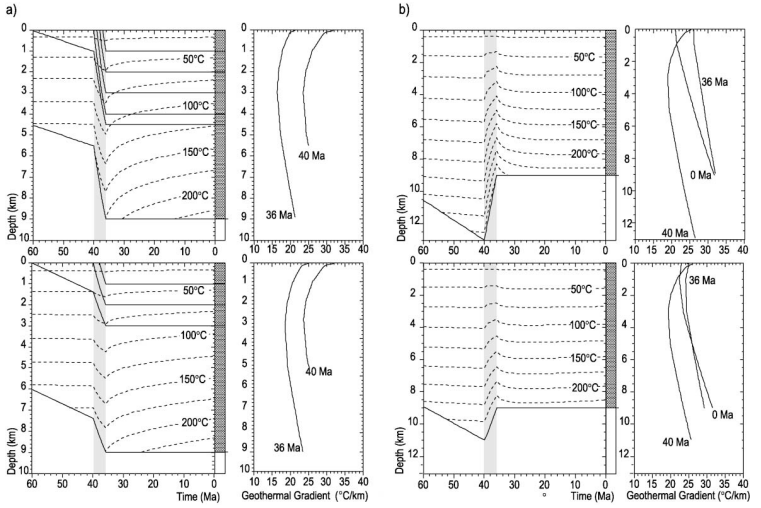

Fig. 5. Impact of different erosion and sedimentation rates on the thermal field through time: 1000 and 500 m/Ma sedimentation (a) and erosion (b) rates for 4 Ma. Dashed lines are isothermal lines. Solid lines in (a) are burial curves. Shaded domains between 40 and 36 Ma indicate the fast sedimentary/erosional event. Thermal conductivity is compaction- and temperature-dependent. The basal heat flow (50 mW/m^2) and the surface temperature (0 °C) are constant.

of heat from warm rocks towards the surface and sedimentation as a downward advection of colder material. 2D approximations should account for the local slope and use diffusion laws for instance (e.g. Beaumont et al., 1992; Avouac and Burov, 1996). For given petrophysical parameters, the amplitude of the resulting thermal anomaly is mainly a function of sedimentation/erosion rates and thickness of the sedimented/eroded layer. Fig. 5 shows the temperature as a function of time and depth for various erosive and sedimentary events, and the associated thermal gradient. Realistic sedimentary rates (Fig. 5a: 4000- and 2000-m thick sedimentary pile deposited in 4 Ma) induce drastic changes in the thermal field due to blanketing effects. The thermal gradient during the depositional event decreases from 24 to 17 °C/km at 2000-m depth in the first case and to 20 °C/km where the sedimentary pile is only 2000-m thick. Similar disturbances occur in the case of erosion (Fig. 5b: 4000 and 2000 m of erosion in 4 Ma), where the

Fig. 4. Thermal influence of thrusting. (a) Steady and transient state domains as a function of sheet thickness H, slip rate on the fault V, and diffusivity κ. Dotted and dashed lines correspond to Pe = 1 for the different diffusivities. SAZ is the Sub Andean Zone domain; Boom. is the Boomerang Zone. (b) Influence of thrust propagation on the thermal field at 20 (A) and 2.5 mm/year (B). White lines are thrusts, gray scale is temperature. Box: unrealistic case of inverted thermal field. Thrust is sub-instantaneous (2000 m/year). Graph: Geotherms for A and B. Boundary conditions are constant basal heat flow (50 mW/m^2), constant surface temperature (0 °C), diffusivity $\kappa = 10^{-6}$ m^2 s^{-1} and adiabatic lateral gradient.

thermal gradient drops from 20 to 26 °C/km in the former case, and to 24 °C/km when the erosion rate is lower.

The transient state was assessed as a function of sedimentation/erosion rates and sedimented/eroded thicknesses. The ratio $Q/Q0$ is given in Fig. 6 (top),

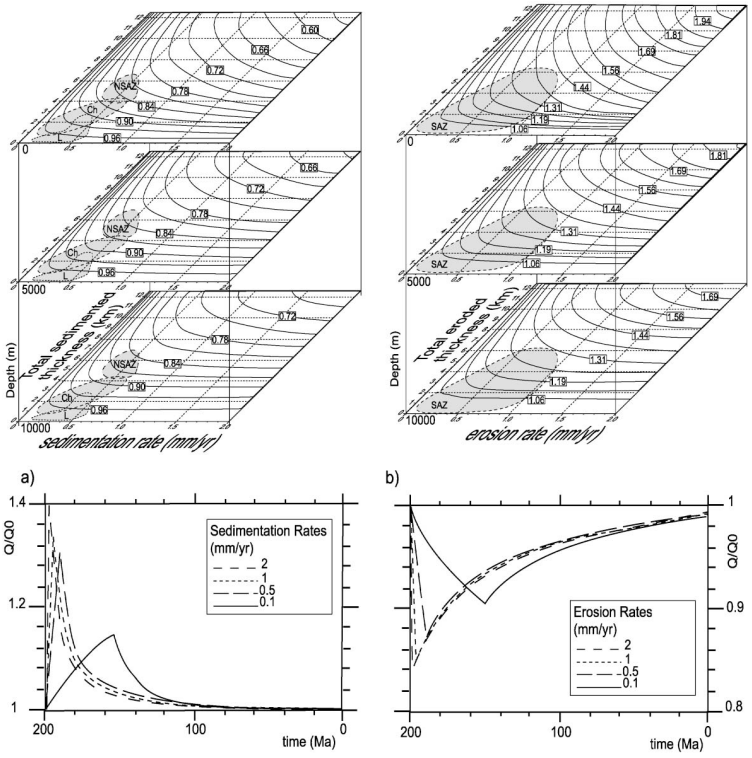

Fig. 6. Top: impact of active erosion and sedimentation on the thermal regime as a function of erosion/sedimentation rates and eroded/sedimented thickness, at 0-, 5-, and 10-km depth below surface. The impact is given by the ratio $Q/Q0$ where Q is the actual heat flow and $Q0$ is the steady state heat flow. Boundary conditions are the same as in Fig. 5. Shaded domains indicate the rates at which the sedimentary/erosive processes act in selected areas of Bolivia. NSAZ is the North Sub Andean Zone (after Baby et al., 1995b); Ch is Chaco plain; SAZ is Sub Andean Zone (N and S); L is the Sub Andean Zone Llanura (Fig. 9a).Bottom: quantitative assessment of the transient state at 10-km depth for various erosion/sedimentation rates during and after a 5-km erosion/sedimentation event. Q is the actual heat flow and $Q0$ is the steady state heat flow. Boundary conditions are the same as in Fig. 5.

where Q is the actual heat flow and $Q0$ is the steady state heat flow. The heat flow can be divided by 2 (sedimentation) or doubled (erosion) for fast rates and large thicknesses, even at several kilometers of depth. For a geologically consistent rate of erosion (1 mm/year) and an eroded thickness of 5 km, the heat flow is increased by more than 20% at 10 km; 5 km of sedimentation at a mean rate of 1 mm/year would decrease the heat flow by 10–20%.

Although the influences of sedimentation and erosion on the thermal field show similarities, the amplitude of their effects slightly differs. The change in petrophysical properties during the burial/exhumation history of the rocks affects the thermal properties of rocks. Erosion leads to the exhumation of compacted rocks, for which diffusivity is higher than for low-compaction sediments. Diffusivity results from the balance between temperature dependence of conductivity, increasing conductivity due to water extraction and decreasing calorific capacity with burial. It subsequently decreases the time span required for thermal relaxation after the erosive event, and also results in a lower steady state thermal gradient than the initial one at shallow depths (< 1000 m) and a higher gradient at larger depths (see geothermal gradients, Fig. 5b).

After surface disturbances from sedimentation and erosion stopped, a thermal relaxation is observed (Fig. 6, bottom). The relaxation time depends on the total amount of eroded/sedimented material and the erosion/sedimentation rates. For a 50 mW/m^2 steady state heat flow, the remaining anomaly after 10 Ma at 10-km depth rarely exceeded 10 mW/m^2. Such a value explains the observation that relatively ancient foredeeps (e.g. the Ebro and Aquitaine basins) do not display low HFD values compared to the active ones such as the Pô (Pasquale and Verdoya, 1990) or Chaco plains (Fig. 2).

In internal zones, mountains are eroded until isostatic equilibrium is reached. Mountain belts have a crustal root of about seven times their average elevation (e.g. Turcotte and Schubert, 1982). For instance, the Bolivian Andes has a crustal root of 35 km below the Eastern Cordillera (Beck et al., 1996). At regional scale, denudation induces uplift and the root is gradually exhumed, involving very large thicknesses for long periods. On the contrary, relief in external zones is mainly supported by folds, which are distributed with a short wavelength across-strike. Topography is sustained by regional isostasy (flexure of the subducted lithosphere) and only the highs, made of thrusting units, are eroded. In the absence of internal strain, the eroded thickness should not exceed the thickness of the thrust sheet whatever the time span over which erosion is active. To summarize, erosion in internal zones has a long wavelength and acts during long periods of time whereas, in folded belts, erosion is controlled by tectonics and preferably denudes anticlinal highs while synclinal valleys can be the locus of sedimentation (e.g. Baby et al., 1995b; Mugnier et al., 1999).

The thermal effects of erosion and sedimentation are antagonistic. 2D effects may have to be accounted for when the variations in erosion and sedimentation rates between anticlines and synclines are strong. Depending on the wavelengths of the phenomena, their effects would not penetrate deeply due to lateral diffusion and compensation at depth between positive, erosion-induced and negative, sedimentation-induced anomalies. Most fold and thrust belts display wavelengths ranging from 10 to 30 km (among these, we can mention the Sub Andean Zone illustrated in Fig. 2, or Mugnier et al., 1999 for the Himalayan foothills). Therefore, 1D estimates are an upper approximation of the thermal anomalies associated to erosion and sedimentation and the values given in Fig. 6 should be lowered for very short wavelengths.

2.3. Fluid circulation

Topographically driven fluids circulation can also induce thermal perturbations. Highs constituted by hinterland elevated zones and sometimes anticlinal hinges in the foreland constitute recharge areas for meteoric water percolation. Depending on the hydrodynamic gradients, discharge areas are likely to be located either in the deformed part of the foreland or in the foredeep.

Evidence for fluid circulation suggests that water circulation may occur at large depths (down to 10 km; Torgensen, 1991; Larroque et al., 1993). Meteoric water can act as a convective mechanism of heat transfer as high hydrostatic pressure related to the amplitude of the topographical high leads to fast circulation beneath the topographic slopes. Fluids percolate and the hydraulic charge induced by the

relief leads to fluid circulation. This water can also progressively mix with formation fluids inherited from sedimentation and/or mineralogical phase changes.

Thrusting of old, already compacted material over younger, less compacted sediments in continental areas induces under-pressure in the low-compaction foreland, due to the deficit of water charge from strata insulation (Belitz and Bredehoeft, 1988; Villegas et al., 1994; Moretti, in press). We model the thermal effects of this process using TEMISPACK program (see Appendix A). Basal heat flow is 50 mW/m^2. Surface temperature is 20 °C. Our model mimics the fluid flow during a thrusting event. Heavy fluid flow from the elevated recharge areas to the lower external zones is initiated. Lateral fluid circulation may affect hundreds of kilometers as previously mentioned by many authors (e.g. Banner et al., 1989; Deming, 1994) and the meteoric water below recharge areas can reach more than 10-km depth in accordance with previous works in the Canadian Rockies (Deming, 1994; Nesbitt and Muehlenbachs, 1989, 1991).

Depending on the permeability paths within the percolated rock, the flowing water may remain in a thermal disequilibrium with the surrounding rocks and generate thermal anomalies if Darcy velocities are high enough. Regarding the flow down, short wavelength thermal anomalies are well known by tunnelers when approaching and passing through faults or karsts.

Fig. 7a and b shows the results when permeability is homogeneous and when the thrust sheet has a lower permeability. Our analysis suggests that rocks at depth can be cooled below the recharge area and that a temperature decrease of 10 to 15 °C at 3000-m depth can be expected. Intuitively, the lateral flow through the distal foreland should induce a positive thermal anomaly. However, we found that whatever the hinterland fluid flow (within the range of known fluid flows), fluid velocity severely decreases when the water invades the foreland basin and only a minor positive thermal anomaly can be generated. These results are dependent of the permeability of the layers

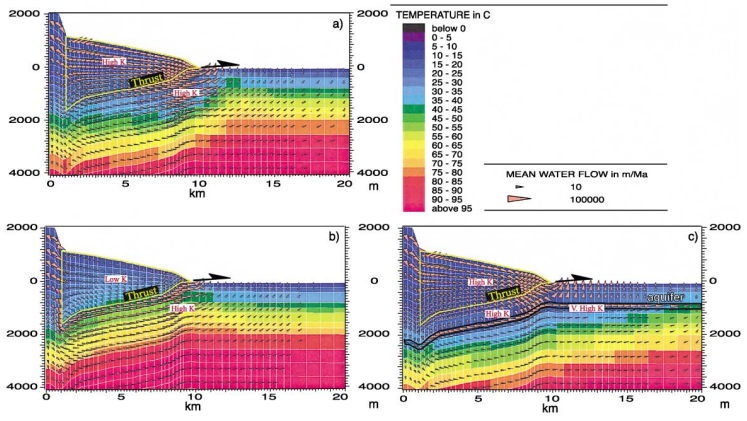

Fig. 7. Thermal impact of fluid circulation during a thrusting event. (a) Reference case: permeability only depends on compaction, i.e. depth; (b) thrusting of compacted rocks (low permeability) over low-compacted (high permeability) foreland sediments; (c) permeability only depends on compaction excepted for an aquifer layer (very high permeability). Arrows are calculated water flow vectors. Thermal boundary conditions are constant basal heat flow (50 mW/m^2), adiabatic lateral gradient and constant surface temperature (20 °C). Permeability is compaction (depth)-dependent in all cases.

and indeed, introducing a fast drain induce drastic changes on the thermal field (Fig. 7c), as in that case, it significantly cools the distal parts of the foreland. Previous authors documented this cooling on organic thermometers in few basin including the Mahakam delta (Burrus et al., 1992). Due to the decreasing velocities towards the foreland, the magnitude of the disturbance decreases as the distance from the belt increases. Within mountains belts, warm sources connect into very localized streams area also usual. Their influences on the thermal field are restricted to thin levels surrounding the water flow (Moretti et al., in press).

2.4. Surface morphology

The atmospheric thermal properties give boundary conditions to the near-surface thermal field. The contrast between atmospheric and rock conductivities induces a distortion of the thermal field lines in uneven areas. These converge towards the valleys, enhancing the apparent thermal regime and diverge beneath the highs, lowering it (Lachenbruch, 1970; Blackwell et al., 1980; Turcotte and Schubert, 1982; Safanda, 1994; Stüwe et al., 1994; Mancktelow and Grasemann, 1997). At depth, the anomaly vanishes due to lateral heat conduction. The affected depth and the magnitude of the anomaly are a function of the amplitude and wavelength of the topography.

In order to quantify the thermal divergence between hills and valleys, finite element thermal modeling (TEMISPACK program, see Appendix A) beneath various topographies characterized by their amplitudes and wavelengths has been used. Boundary conditions are described Fig. 8. In all cases, the basal heat flow is 50 mW/m^2. The angular shape of ridges is assumed to be realistic as tests featuring sine-shaped topographies show similar results. Results are presented here for topographies with amplitudes ranging between 0 and 2000 m, which are typical of folded belts. In order to quantify the specific effect of topography, we assume that dynamic equilibrium constrains the topography of ramp-folds, which implies that topography is maintained for several Ma in fold and thrust belts.

The simplest topographies are single ridges. Fig. 8a shows the ratio $Q(z)/Q0$ as a function of wavelength (ridge width) and depth. For ridges larger than 20 km, the thermal anomaly is very small. However, as soon as the width of the ridge is lower than 15 km, the HFD does not exceed 0.7 times the basal heat flow. Below the reference level, the heat flow anomaly tends to be very low; $Q(z)/Q0$ ratios are higher than 0.85. The temperature difference between a flat ground geotherm and a geotherm below a ridge reaches its maximum value at the reference level and then equals $A \times G$, where A is the amplitude of the topography and G the thermal gradient. In the present case, the gradient is about 25 °C/km; the negative anomaly is thus about 50 °C (2000-m ridges). Isotherms have to flatten at some depth. At that level, $Q(z)/Q0$ tends to 1. This balance level increases from 6 to 8 km below the reference level for ridge widths between 5 and 25 km.

Due to the spatial diffusion of heat, interactions between adjacent topographical structures have to be accounted for. Since foreland fold and thrust belts show broad cylindrical patterns, we assume that two-dimensional geometry is appropriate for modeling. The main consequences are lower thermal anomalies at depth and shallower balance levels, as cooling below anticlines is counteracted by warming below synclines. Another feature which is linked to topography is the atmospheric thermal gradient. An average value is 6.5 °C/km. Again, it lowers the topography-induced anomaly as the contrast between the crustal and atmospheric temperatures decreases at higher elevations. Fig. 8b outlines the effects on the heat flow at depth beneath 2000-m-high ridges in periodic systems, as a function of wavelength. The surface HFD is 0.75 times the basal heat flow for wavelengths longer than 10 km and the anomaly becomes negligible for wavelengths longer than 20 km. It is also negligible below the reference level, i.e. syncline topography. The depth of balance, where the temperature equals the temperature below flat areas increases from 1- to 5-km depth for wavelengths ranging from 5 to 30 km (Fig. 8b), and below 100 m for smaller amplitudes (Fig. 8c).

Hence, thermal data coming from a well few hundreds meters deeper than the topographic elevation could be consider as almost free of topographic disturbances. On the contrary, data from tunnels have to be carefully corrected before being incorporated in a geodynamical model. Topography has been mentioned as a prominent contributor to thermal distur-

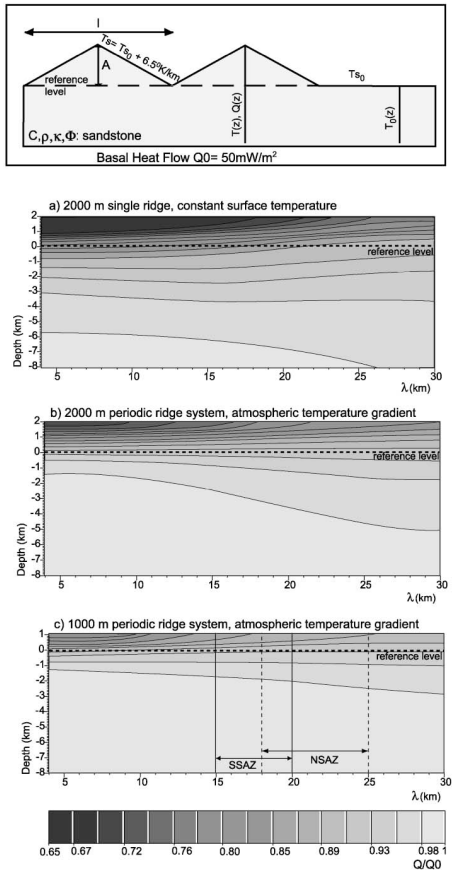

Fig. 8. Top: topographic effect on the thermal field, conceptual model. C is the heat capacity, ρ the density, κ the thermal conductivity, φ the porosity. A is the amplitude (elevation above the reference level) and λ the wavelength of the topography. Ts_0 is the surface temperature at the reference level. Bottom: thermal disturbances below a single ridge of 2000-m elevation with a constant surface temperature (a), below a periodic relief of 2000- (b), and 1000-m (c) amplitude, in the presence of an atmospheric temperature gradient, as a function of wavelength λ and depth. $Q(z)/Q0$ is the actual heat flow $Q(z)$ over basal heat flow $Q0$ ratio. In all cases, boundary conditions include constant basal heat flow (50 mW/m^2), adiabatic lateral gradient.

bances by many authors (e.g. Stüwe et al., 1994; Mancktelow and Grasemann, 1997) who calculated the thermal anomalies for end-members topographies, unlikely to be found in most settings. Furthermore, the atmospheric gradient significantly lowers the thermal anomaly.

2.5. Terrain effects

Other effects related to the surface morphology are the so-called terrain effects (Blackwell et al., 1980). These include slope dip and orientation relative to solar radiation and vegetation cover. Variations of about 5 °C are documented (Blackwell et al., 1980) for very different slope attitudes at very shallow levels. In any case, the effect is entirely annihilated in the first 500 to 1000 m. Ground surface temperature (GST) is a boundary condition for the near-surface thermal field. GST oscillations induce transient effects on the thermal field. The amplitude of the anomaly deadens as it progrades downward with time. Following the equations of Turcotte and Schubert (1982), we find on average that temperature variations are less than 5% at 1 cm for diurnal/nocturnal changes, about 1 m for seasonal variations and 1000 m for glaciations. For a 20 °C ground surface temperature variation over 100,000 years, the temperature anomaly at 1500-m depth does not exceed 5 °C.

Hence, microclimatic influences and climate change are of minor impact on the thermal regime, and most of the time do not need to be accounted for while inverting thermal data such as well temperatures, which are generally acquired at depths larger than 1000 m. However, shallow thermal measurements, from mines or shallow sediments for instance, may suffer from the last major cooling event (16th century). The permanent average GST related to the geographical setting influences the thermal regime as a boundary condition.

2.6. Discussion

This systematic quantification of the processes allows us to conclude that:

(1) The main surface processes disturbing the thermal field are erosion and sedimentation, and occasionally heat transfer from fluid circulation.

(2) In regular conditions in the external zones where thrust slices are not too thick, thrusting does not affect the thermal field.

(3) Rough terrains induce near surface perturbations, up to 1000–2000-m depth, from both topography and terrain effects; they do not have any influence on source rock maturation at 3 or 4 km but it means that near surface data in rough areas cannot be extrapolated for deeper processes. Before using mine or tunnel data for geodynamical or thermal maturation models, an integrative 2D study should be carried out in order to characterize the near surface thermal field; 1D thermal inversions should only be performed in flat or tectonically simple areas.

(4) The local incidence of fluid circulation is difficult to model because the permeability field is generally unknown; few data may be assessed from field measurements (such as isotopic studies of waters, Banner et al., 1989; or composition of mineralized veins, Larroque et al., 1993; Larroque et al., 1996) but correspond to particularly fast migration pathway near faults. Numerous authors in similar geological settings (e.g. Majorowicz and Jessop, 1993; Majorowicz et al., 1985; Bodri and Rybach, 1998) have interpreted large-scale anomalies as the result of fluid circulation. However, as far as we know, regional temperature decrease (-5°C) has been documented only in the Mahakam delta (not in a specific drain but at a regional scale in the shaly basin, Burrus et al., 1992). Our modeling suggests that due to the pressure field and velocity of migration, high amplitude thermal anomalies from fluid circulation can only be local.

3. The Bolivian sub Andean zone

3.1. Geological setting

The Sub Andean Zone is the eastern border of the Andes in Bolivia and constitutes a foreland above the westward continental subduction of the Brazilian shield. The thrusts are composed by an almost complete sequence starting with the Paleozoic. Ordovician to Devonian rocks were deposited in a broad NW–SE retroarc foreland basin along the western and central part of the country, which included the Madre de Dios, Sub Andean Zone, and Chaco basins (Fig. 9a; Sem-

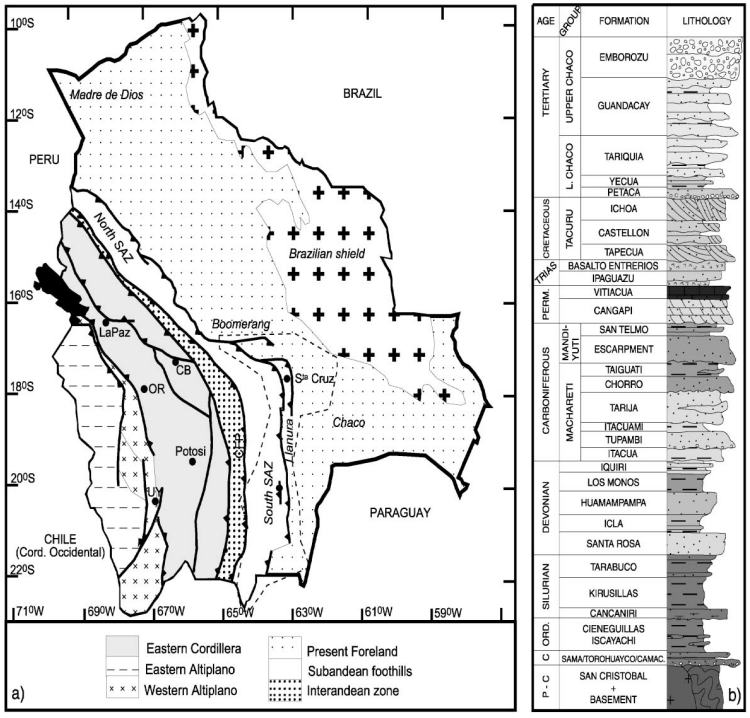

Fig. 9. (a) Structural map of the Bolivian Andes (modified from Baby et al., 1995a). (b) Stratigraphic column of the southern Sub Andean Zone (from Moretti et al., 1996).

pere, 1995; Sempere et al., 1990; Montemurro, 1992; Isaacson and Diaz Martinez, 1995). This basin was bounded to the SW by an active margin with abundant clastic supply and to the NE by a relatively stable cratonic margin with less sediment input. The South Sub Andean Zone (18°S to 23°S, Fig. 9a) presents the most complete Phanerozoic sequence in Bolivia, from Late Proterozoic to Cenozoic (Fig. 9b). Proterozoic and Lower Palaeozoic rocks crop out in the southern Eastern Cordillera and along the north-eastern border of the Chaco basin. The Silurian and Devonian sequences in this area are very thick (over 4000 m), with a considerable thickness of shales (especially in the Kirusillas, Icla and Los Monos Fms) alternating with more sandy units (Tarabuco, Santa Rosa, Huamapampa and Iquiri Fms). The Carboniferous is characterized by a glacial marine environment and shows strong lateral facies variations. Regarding the thermal history, none of the geodynamic activity related to these periods is thought to have a large influence on the current heat flow, and therefore, constant heat flow is used in the thermal models.

Permian units, both sandy (Cangapi Fm.) and calcareous (Copacabana and Vitiacua Fms.), recorded successive marine transgressions and regressions. A basalt flow can be found locally, which dates the end of this sequence as mid-Triassic (233 Ma, Soler and Sempere, 1993). This unit is interpreted as a result of a rifting process, which caused the Pre-Jurassic erosion that can be observed throughout the Sub Andean Zone. Mesozoic deposition is continental and mainly sandy (Tapecua, Castellón and Ichoa Fms). This Mid-Triassic to Cretaceous unit, known as the Tacuru Group, may be up to 1500-m thick. The crustal thinning and therefore the heat flow increase due to this rifting phase is not well known, since the amount of normal faults remains extremely small even if the magmatic activity is described at a large regional scale (Sempere et al., 1999). The intrusion of sills or the volcanic activity has a short wavelength and was short-lived (this can be shown after Turcotte and Schubert, 1982); in the models, we therefore consider that the eventual Triassic/Jurassic rifting thermal anomaly deadens before the Miocene. In the northern part of Southern Sub Andean Zone and Chaco plain (Fig. 9a), the Late Cretaceous sandstones and lacustrine limestones of the Cajones Fm (Maestrichtian) are observed. The Paleogene is reduced and often consists of a few meters of paleosoils.

In the northern areas, most of the Cenozoic deposition took place during the Neogene (Late Oligocene to recent), with up to 4000 m of continental deposits (Petaca, Yecua, Tariquia, Guandacay and Emborozu Fms). The Petaca Fm usually starts with a conglomeratic unit followed by sandstones. When present, the Yecua Fm shows lacustrine facies. Then the sequence is a classical foreland sequence starting from a distal facies showing anastomosed channels (Lower Chaco Fm) to a more proximal affinity characterized by conglomeratic beds (Upper Chaco Fm). Locally, the upper part of the sequence has been preserved; it is a massive conglomerate, which reveals the eastward progradation of the relief. In the southern part of Bolivia the full sequence is present: the Petaca is 35-m thick, the Lower Chaco 4000-m thick, the Upper Chaco 900-m thick and the final conglomerate (Jujuy conglomerate) more than 50 m.

The Bolivian Sub Andean Zone (SAZ) is a foreland fold and thrust belt, which constitutes the eastern border of the Andes (Roeder, 1988; Baby et al., 1989; Sheffels, 1990). The northern branch (15° to 18°S) is relatively narrow (50 to 100 km; Fig. 2) and shortening reaches 74 km (Baby et al., 1997). The southern branch (18° to 22°S) is rather wide (150 km) and shortening decreases from 140 km at 20°S to 86 km at 22°S (Baby et al., 1997). The development of the Neogene foreland started at least during Late Oligocene times (27 Ma ago) when the deformation front migrated eastward from the current position of the Altiplano (Marshall and Sempere, 1991). Later, since late Miocene, the current SAZ has been affected by compression (Gubbels et al., 1993). However, in the Eastern Cordillera, deformation may have started before Late Oligocene, as suggested by Sempere (personal communication) and Butler et al. (1995). In the external zone, where oil exploration is currently carried out, deformations are very recent and mainly occurred between 6 Ma and present (Fig. 10). Dates derive from tuff absolute ages and apatite fission-tracks analysis from sandstones outcropping on the anticlinal hinges, which indicate very recent erosion of the anticlines (Moretti et al., 1996). The maximum burial is indicated by kerogen maturity data.

The structural style of the foothills is well documented by many authors (e.g. Dunn et al., 1995; Moretti et al., 1996; Baby et al., 1997; Kley et al., 1999; Colletta et al., 1999). To summarize, the SAZ is deformed by thin-skinned tectonics, with lateral variations being due to shortening amount, variable involved décollement levels and stratigraphic thickness. In the Interandean Zone, the basement is involved in the deformation (Kley, 1996). In the north SAZ, the sedimentary pile involved in the thrusts is thick and the décollement level is on the Silurian shales. In the southern branch, the main décollement level remains the Silurian, but additional décollements are also active in the Middle Devonian (Los Monos Fm) and locally in the Carboniferous diamictites. Transfer zones help to accommodate the different throws over the various décollement levels (Guillier et al., 1992), even if the structures are largely cylindrical. The average distance between the structures is between 15 and 20 km in the southern SAZ and between 17 and 25 km in the northern SAZ. Displace-

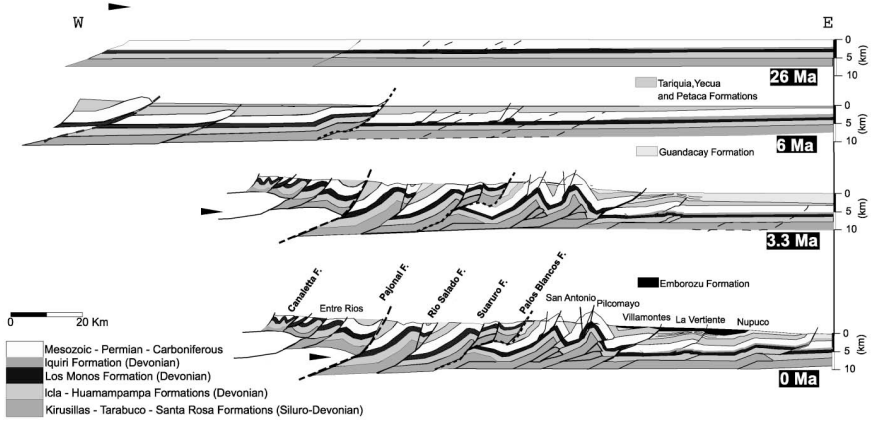

Fig. 10. Structural evolution of the South Sub Andean Zone (modified and extended from Moretti, in press). The kinematics are constrained from apatite fission tracks analysis and kerogen maturity data.

ment along a single thrust, connected to the Silurian décollement level, may be up to 20 km. Some smaller reverse faults may affect anticlinal hinges, branching on the Middle Devonian or even the Carboniferous detachment levels. Eastward in the foredeep, shortening is weak and the structures are blind thrusts detached on the Silurian décollement level, close to the foothills. However, only Quaternary levels crop out and we had no access to core samples in order to study the deformation in this province.

3.2. Data set

In order to characterize the thermal field in the SAZ of Bolivia, a large data set of well temperatures has been acquired from the various oil companies present in Bolivia. About 1400 temperature data were compiled; the geographic distribution of well data is closely related to the occurrence of exploration. We distinguish: the North SAZ, the Boomerang, the South SAZ foothills, the southern SAZ Llanura (blind structures below Tertiary deposit), the Chaco plain and the Alto de Izozog (Figs. 2 and 9a). Although not in the external zone, we also present temperature data for the Altiplano as a comparison.

A source of error in the data, which has to be corrected, is the fact that some temperature data are acquired before thermal equilibrium is reached in the well during geophysical analysis of exploratory well-logging. The disequilibrium induced by the circulation of drilling mud decreases logarithmically as a function of circulation time of the mud and shut-in-time (time span after mud circulation ceased). Data correction was processed following the previous work of Springer and Forster (1998). When possible, the Horner-plot correction technique was performed (Bullard, 1947; Horner, 1951; Lachenbruch and Brewer, 1959; Deming, 1989). Whenever information was missing (mostly circulation times and shut-in-times), the statistical correction approach from Deming and Chapman (1988) and Springer and Forster (1998) in Bolivia was applied. Circulation times were assumed to be 5 h, which is a correct average estimate according to Deming (1989), and shut-in-times, 7 h. According to the previous analysis of the authors and to Luhesi (1983), the use of an average circulation time leads to only a little uncertainty with regards to the temperature value; 70% of the data lie in a shut-in-time range of 5 to 15 h, which leads to a gradient uncertainty of ±1.5 °C/km (Springer and Forster, 1998).

3.3. General overview of the thermal field over the studied area

In order to avoid excessive near-surface disturbances, only temperature values acquired below 1000 m are investigated. The linear regression of the global data set features an average gradient of 23 °C/km for the whole studied area, which is in agreement with the value given by Springer (1997) and Springer and Forster (1998). The intercept value gives a mean surface temperature of 22 °C, which in turn corresponds to the mean Ground Surface Temperature. The scatter is up to ±15 °C and the correlation coefficient is 0.92. Some provinces are distinguished in order to separate the various thermal influences (Fig. 11); they are located in Fig. 2.

1D and 2D modeling, using the GENEX and THRUSTPACK programs (see Appendix A), allow us to predict past and present thermal regimes for the last 25 Ma; these models are calibrated by well temperatures and kerogen maturity data (Maximum temperature, Tmax and Hydrogen index, HI). The GENEX models are shown by: (i) the burial curves, which indicate the total sedimentary/erosive history; (ii) the temperature windows overlain on the burial curves for the last 25 Ma; (iii) the present geothermal gradient; (iv) the calculated temperature versus depth, calibrated with the measured well temperatures; (v) the calculated Hydrogen Index calibrated with the measured Rock–Eval values; and (vi) the calculated maximum temperature, calibrated with the Rock–Eval measured temperature.

3.3.1. The north-SAZ

The N-SAZ is less documented than the south since the number of well is still poor. Nevertheless, few structures have been drilled: internal thrusts as Liquimumi, Tacuaral, blind thrust in the south as Villa Tunari, and Isiboro wells and even the last emerging thrust, looking for a sub-trap structure (Yaryapo). The thermal gradient is fairly cold and varies from 16 to 23 °C/km in this area (Fig. 11a). The variations in magnitude of surface processes are extremely high in this area and can easily be explain by the sed-

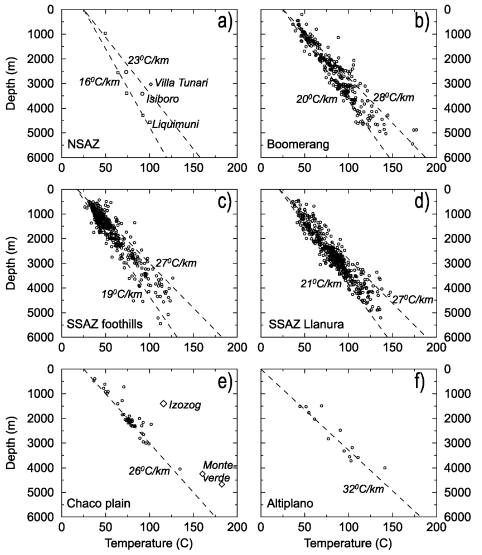

Fig. 11. Thermal profiles within the various units of the external zone of the Bolivian Andes and within the Altiplano for comparison. (a) North Sub Andean Zone, (b) Boomerang, (c) South Sub Andean Zone foothills, (d) South Sub Andean Zone Llanura, (e) Chaco plain, (f) Altiplano.

imentation/erosion processes. Along strike, erosion can be up to 5000 m in the anticlinal hinges, and syntectonic sedimentation up to 7000 m in the synclines (Baby et al., 1994), which explains the large scatter in this unit. In the foreland, the upper tertiary sequence reaches 6 km and more than 3 km are younger than 5Ma, at least in the Secure area. Due to this deep and young foredeep, the average gradient in the first 5 km is less than 20 °C/km, resulting in an oil window deeper than 5 km and in a gas window at 6 km with a basal heat flow of 55 mW/m^2 (Isoboro area) (Colletta and Moretti, 1999—Confidential report for REPSOL).

3.3.2. The Boomerang

This area is located on the wedge of the Palaeozoic basin, at the level of the Santa Cruz bend. The thickness of the sedimentary sequences decreases from the SW towards the NE. Blind thrusts beneath Tertiary strata are present over most of the area (Baby et al., 1994). The mean gradient (Fig. 11b) is between 20 and 28 °C/km, the best value being 24 °C/km. Due to the short wavelength of these variations, this scatter has to be explained by active surface processes and/or fluid circulation. Tertiary sedimentation has an impact on the thermal regime, while some blind structures like San Juan are already undergoing erosion. All the models have not been represented here but data are all compatible with a basal heat flow of 52 mW/m^2 (±3 mW/m^2) when taking into account the kinetic of the structures. In the Boomerang area, regional fluid flow has been documented by chemical data from the various oil and gas fields, which show a systematic water (and gas) flushing

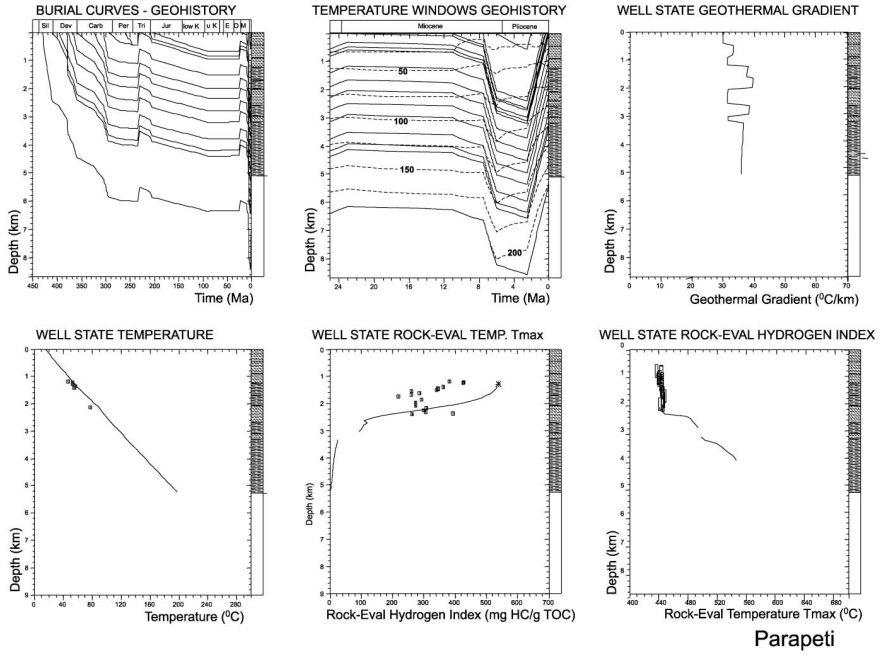

Fig. 12. Heat flow increase due to erosion in the Sub Andean Zone: thermal modeling (GENEX) of the Parapeti field. (i) Burial curves, which indicate the total sedimentary/erosive history, (ii) temperature windows overlain on the burial curves for the last 25 Ma (solid lines are burial curves and dashed lines are isothermal lines), (iii) present geothermal gradient, (iv) calculated temperature versus depth, calibrated with the measured well temperatures (dots), (v) calculated Hydrogen Index calibrated with the measured Rock–Eval values (dots), and (vi) calculated maximum temperature, calibrated with the Rock–Eval measured temperature (dots). Conductivity is temperature-dependent. Basal heat flow is 50 mW/m^2. Surface temperature is 18 °C.

from the internal part (south-west) to the external part. Nevertheless, while the existence of this long distance migration is proven by the geochemistry analyses (especially gas isotopes), there is no evidence of a thermal anomaly related to this migration (Moretti et al., in press).

3.3.3. The south-SAZ foothills

This range alternatively displays eroded anticlines and synclines. For obvious structural reasons, only anticlines are drilled, and few data are available below synclines. Nevertheless, some anticlines are still blind even in the western part of the south SAZ (e.g. Monteagudo) and erosion does not uniformly affect the structures. As a result, the scatter is large and the thermal gradient varies from 19 to 27 °C/km with a 23 °C/km mean value (Fig. 11c). The warmer values correspond to the measurements of eroded anticlines near the surface. Modeling has been done for the Parapeti structure (Fig. 2). This anticline is eroded down to Carboniferous horizons. About 3.5 km have been removed in less than 3.5 Ma and erosion is still active. As the kinematics are not too complicated and because the topography is not too rough, 1D modeling is assumed to be reasonably correct. Fig. 12 shows the sedimentary/erosive evolution, the thermal state and the calibration from various data: current temperatures in the well, palaeo-thermometers (kerogen maturity data based on the Rock–Eval pyrolysis). The warming effects of erosion are obvious as the current gradient is 30 to 35 °C/km in the first upper kilometers, whereas it was only 25 °C/km after the Miocene sedimentation, and 30 °C/km before the Late Miocene erosive event.

In the hinges of some anticlines, the Los Monos Fm has been shortened in a disharmonic way and now achieves an apparent thickness of up to 2000 m whereas the stratigraphic thickness is no more than 700 m. This is the case of the San Alberto anticline (Figs. 2 and 9a). This structure was shortened fairly rapidly, involving thick units (up to 8000–9000 m). In order to account for the complex disharmonic kinematics and the very steep relief, 2D modeling was performed. Fig. 13 shows the modeling performed with THRUSTPACK on this structure. The computed gradient is 20 °C/km, which is lower than the value calculated to the north (Parapeti field). It fits with a basal heat flow (at the bottom of the Silurian) of about 40 mW/m^2 whereas the data was compatible with a basal heat flow of 50 mW/m^2 in almost all other wells in the north of the south SAZ foothills.

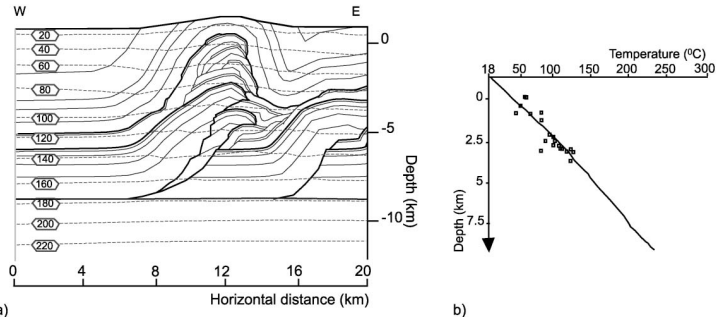

Fig. 13. Integrative study of the various controls on the thermal field: thermal modeling (THRUSTPACK) of the San Alberto field. The structure and kinematics is from Colletta et al. (1999), and personal communication. Dashed labeled lines on (a) are calculated isothermal lines. (b) Calibration using well data, where the solid line is the calculated geotherm and the dots are the measured temperatures. Basal heat flow is 40 mW/ m^2. Surface temperature is 24–6.5 °C/km a.s.l.

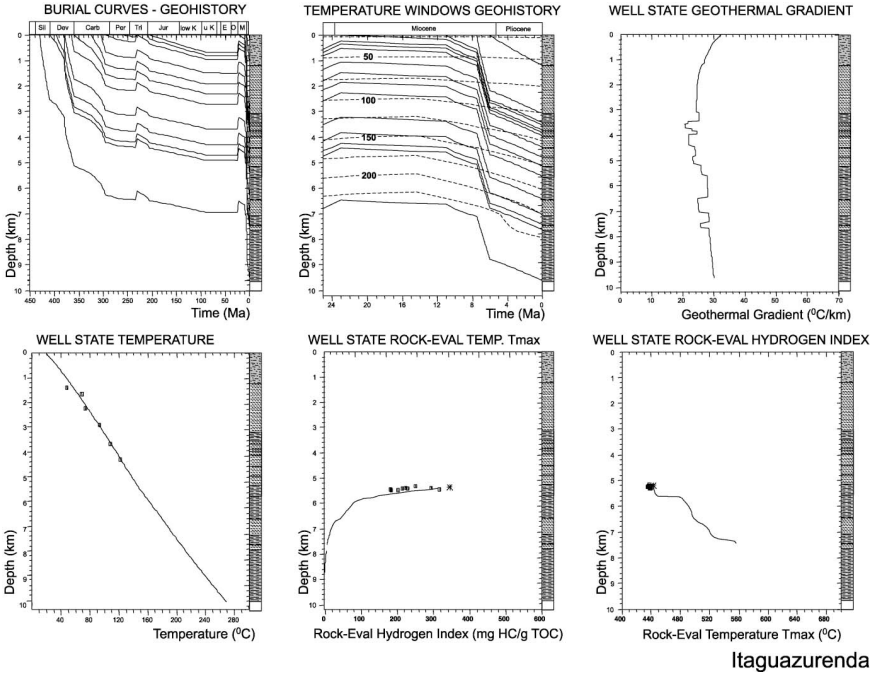

Fig. 14. Blanketing effect in the Sub Andean Zone: thermal modeling (GENEX) of the Itaguazurenda field. Legend of the figures is the same as Fig. 12. Basal heat flow is 55 mW/m^2. Surface temperature is 21 °C.

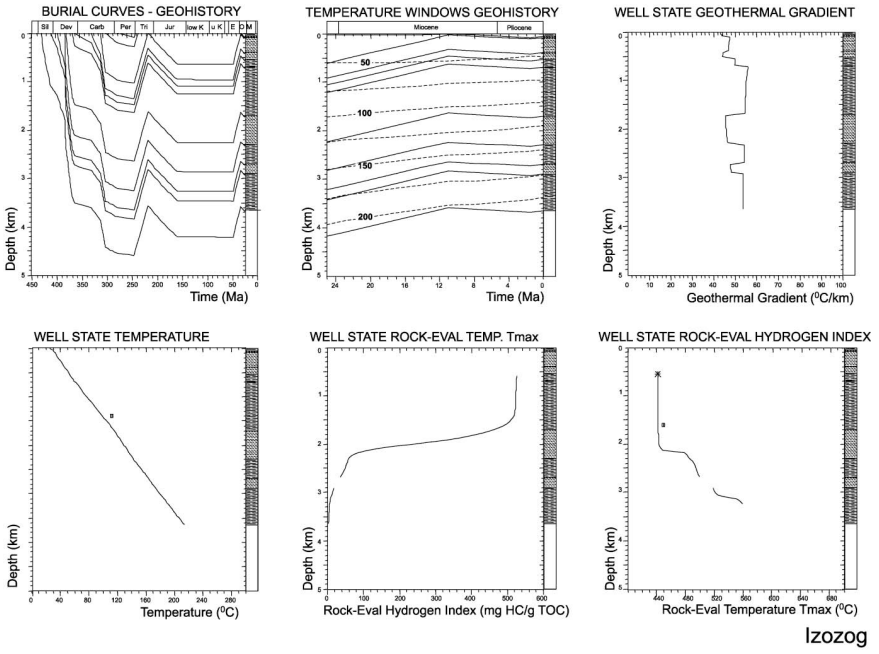

Fig. 15. Thermal modeling (GENEX) of the Alto de Alto de Izozog structural high. Legend of the figures is the same as Fig. 12. Basal heat flow is 100 mW/m^2. Surface temperature is 23 °C.

3.3.4. The south-SAZ Llanura plains

Fig. 11d shows the value below the Tertiary deposits in the foreland basin. The mean values for the gradient range from 21 to 27 °C/km (average is 25 °C/km). As in the other provinces, the gradients are rather variable but the analysis of specific structures outlines the influence at shallow depth of the fast Late Tertiary sedimentation rate (up to 3000 m in less than 8 Ma). Fig. 14 shows the modeling for the Itaguazurenda field (Fig. 2), where the Miocene to Recent sequence is thick (more than 3000 m). The current gradient is around 24 °C/km at a depth of about 3000–4000 m due to the blanketing, whereas it was more than 30 °C/km before the sedimentation event. The best fit is found with a basal heat flow of 55 mW/m^2.

3.3.5. The Chaco plain

The values from the eastern wells indicate a gradient around 26 °C/km (Fig. 11e), which is slightly more than the gradient in the other areas. This apparently higher gradient is due to the lack of Late Tertiary sedimentation in this area (decreasing eastwards); it also remains compatible with a basal heat flow around 52 mW/m^2. On the other hand, the Alto de Izozog is incompatible with this thermal regime (Fig. 2). It corresponds to a persistent structurally elevated zone onto which all the series pinch out since the Carboniferous (Coudert et al., 1995; Montemurro and Del Rosario Mercardo, 1996). The gradient there is extremely high (up to 50 °C/km). Fig. 15 shows a model based on the few data available. A heat flow of more than 100 mW/m^2 at the base of the sedimentary layer is needed. Based on its structural position, the Alto de Izozog has been interpreted as the forebulge of the subduction of the Brazilian shield (Coudert et al., 1995) but it can also be related to a warm zone induced by deep processes (mantle or crust). There is no particular reason for a forebulge to be warm but a permanent continental warm zone is also difficult to explain. The Monteverde field, North of the Alto de Izozog, also presents abnormally high heat flow values (Fig. 11e); because of the scarce data (no paleothermometers), we cannot discuss if it is due to a lateral heat flow increase in the vicinity of the hot Alto de Izozog or if the two high temperatures are uneven data.

3.3.6. The Altiplano

Even if the Altiplano area does not belong to the Sub Andean zone, we present the data in order to give a comparison between external and internal provinces. The average ground surface temperature is currently no more than 0 °C and the mean gradient is more than 32 °C/km (Fig. 11f). This value is consistent with the mean heat flow (80–100 mW/m^2) suggested by Pollack et al. (1993). Although poorly documented, the Cordillera seems warmer with values up to 150 mW/m^2. The Altiplano is an endoreic basin where the current sedimentation rates are minor after having been very high during the Miocene (Rochat et al., 1999). No major erosion occurs either in the Altiplano but there is very fast erosion in the surrounding Cordilleras (about 10 km in 10 Ma). Surface processes have therefore major influences in the Cordillera where the surface heat flow is enhanced by the erosion and almost no influence over the Altiplano. Like Tibet, the Altiplano/Cordillera area is a good illustration of the effects of deep thermal processes. The very thick crust and, although controversial, thinned lithospheric mantle, help to explain this high heat flow which in some places, is responsible for partial melting at relatively shallow depths (Schmitz et al., 1997; Chmielowski et al., 1999). Nevertheless, a careful study of the surface processes on the data has to be carried out before interpreting the difference of heat flow between the Altiplano and the Eastern Cordillera as the reflection of any deep process. One have also to keep in mind that in the Cordillera most data were collected from mines.

4. Discussion

In the Bolivian SAZ, the foothills are very recent—most of the drilled structures are younger than 6 Ma. It has been shown by the specific modeling of various fields that a global consistency can be restored when the transient effects of surface processes are accounted for. Temperature data are generally compatible with a basal heat flow of 50 to 55 mW/m^2 and all the scattering in the data is due to superficial phenomena. However, lateral variations at regional scale have been individualized by time-dependent thermal modeling and reconstruction of

the 3D thermal field. There is an increase in the thermal gradient towards the NE (towards the Boomerang transfer zone) as the thickness of the Mesozoic and Cenozoic sedimentary cover decreases and as the recent sedimentation rates become lower. From the foothills towards the Chaco plain, there is also a slight eastward increase in the thermal regime, although erosion of the foothills induces a transient heating effect, and sedimentation in the Llanura induces cooling. All these data point to the fact that the basal HFD under the foredeep is slightly warmer than below the foothills in the Sub Andean Zone. The topography at regional scale increases towards the West. Now, considering the thermal effects of topography at a regional scale also helps to explain this slight eastward increase in the thermal gradient, which mainly occurs in the uppermost kilometers (within the part of the crust which is above sea level).

Seismic experiments (Beck et al., 1996) revealed that the crust is thinner than predicted by an Airy type isostatic model. The relatively elevated topography of the Chaco plain ($\approx$300–400 m), relative to its crustal thickness, requires either support by the flexural rigidity of a strong lithosphere (Lyon-Caen et al., 1985; Watts et al., 1995) or a warmer, lighter, and therefore thinner crust. The relatively high thermal gradients and heat flows measured in the Chaco support the second hypothesis since elastic flexuration does not explain the relatively high heat flow beneath the sedimentary basin.

In the first part of this paper, systematic modeling of the various phenomena has allowed us to define sedimentation and erosion as first order processes on the near-surface thermal regime in recent external zones, through space and also through time. Other surface parameters, which have occasionally been mentioned as significant controls on the thermal regime, have been quantified and it has been shown that they do not penetrate deeply enough or have only a minor impact, often because of the lateral conduction of the thermal anomalies. Many of these effects may be neglected when studying the hydrocarbon maturity and the crustal process if, and only if, data are available from deeper zones. Surface processes are time-dependent and controlled by the tectonic activity: erosion, sedimentation and terrain effects all depend on the kinematics of the belt. Predictions concerning past and present thermal regimes, can only be made when the kinematics is well constrained. It is the case in Bolivia where, based on previous structural studies, we have been able to isolate a deep signal.

Acknowledgements

We are grateful to Chaco, Andina, Repsol, Petrobras, Maxus, and particularly to Genaro Montemurro, for the thermal data which allowed us to perform this study. We acknowledge Jean Chéry, Teresa Jordan, Jean-Pierre Burg and Etienne Jaillard for their constructive reviews.

Appendix A.

A.1. THRUSTPACK

THRUSTPACK is a 2D finite-element forward program developed by IFP for modeling of fold and fault relationships (e.g. Sassi et al., 1998). Thrust evolution is based on pre-defined fault geometries and kinematics. The model allows for displacements and remeshing through time. Active sedimentation and erosion can be integrated into the model during deformation. A mechanical compaction module is also available. Thermal evolution is computed either in transient or steady sate, accounting for conductive heat transfer. Although not used, hydrocarbon maturation and migration are also computed, based on thermal evolution and overpressure calculation during the deformation events.

In the theoretical part, the basal heat flow is 50 mW//m^2 and the surface temperature is fixed to 0 °C.

The San Alberto anticline shows major disharmonic stacking within the anticline core. As THRUSTPACK only allows for isopach deformation, the Los Monos ductile shale formation has been divided into very short slices stacked on top of each other.

A.2. GENEX

The GENEX program is a one-dimensional basin modeling tool developed by IFP/BEICIP. It accounts for backstripping compaction to compute final petrophysical properties, conductive thermal evolution, and hydrocarbon maturation and migration through time. Thermal evolution is recorded through time and a final module quantifies the kerogen maturation in order to constrain the models with Rock–Eval pyrolysis measurements. These include the Hydrogen Index (HI) and the maximum temperature (Tmax) used for calibration during the modeling.

A.3. TEMISPACK

TEMISPACK is a 2D finite-elements software developed by IFP/BEICIP for basin modeling. It is composed of several modules which include: (i) backstripping; (ii) a mechanical compaction module to compute the water flow, the overpressure and the final porosity for each layer; (iii) a thermal module, which allows computation to be done either in steady state or transient state, in conductive or conductive and convective modes. This module records the thermal histories at depth. In addition, although not mentioned in the paper, TEMISPACK also allows the assessment of kerogen maturity, based on kinetic reactions (Tissot and Espitalié, 1975). Hydrocarbon migration, based on a two-phase (HC+water) Darcy equation, is also computed in response to driving forces (buoyancy, gradients of hydraulic head and capillary forces). Additional information and details can be found in Doligez et al. (1987), Ungerer (1990) and Burrus et al. (1992).

TEMISPACK does not allow lateral motions and only vertical phenomena are accounted for (sedimentation, compaction, uplift and erosion). In the paper, we modeled the progradation of a thrust to assess the transient effects linked to the associated fluid flow. Lateral displacement and thrusting were modeled as the sedimentation of layers thinning towards the foreland on top of each other. Moreover, acting on compaction and topography allows the fluid circulation during the thrusting event to be mimicked for the convective and thermal processes.

References

Arndt, J., Bartel, T., Scheuber, E., Schilling, F., 1997. Thermal and rheological properties of granodioritic rocks from the Central Andes, North Chile. Tectonophysics 271, 75–88.

Avouac, J.P., Burov, E.B., 1996. Erosion as a driving mechanism of intracontinental mountain growth. J. Geophys. Res. 101, 17747–17770.

Baby, P., Lopez, J.M., Lopez, O., Oller, J., Pareja, J., Sempere, T., Tufiño, D., 1989. Structure de la Zone Subandine: influence de la géométrie des séries sédimentaires antéorogéniques sur la propagation des chevauchements. C.R. Acad. Sci. Paris 309, 1717–1722.

Baby, P., Specht, M., Oller, J., Montemurro, G., Colletta, B., Letouzey, J., 1994. The Boomerang–Chapare transfer zone: Structural interpretation and experimental approach. In: Roure, F., Ellouz, N., Shein, V.S., Skvortsov, I. (Eds.), Geodynamic Evolution of Sedimentary Basins, International Symposium, Moskow. Technip, Paris, pp. 203–218.

Baby, P., Moretti, I., Guillier, B., Limachi, R., Mendez, E., Oller, J., Specht, M., 1995a. Petroleum maturation versus thrust emplacement on the bolivian foothills. In: Tankard, R., Suarez, S., Welsink, H.J. (Eds.), Petroleum of South America. AAPG Memoir, vol. 62, pp. 445–458.

Baby, P., Colletta, B., Zubieta, D., 1995b. Etude géométrique et expérimentale d'un bassin transporté: exemple du synclinorium de l'Alto Beni (Andes Centrales). Bull. Soc. Geol. Fr. 166, 797–811.

Baby, P., Rochat, P., Mascle, G., Hérail, G., 1997. Neogene contribution to crustal thickening in the back-arc of the Central Andes. Geology 25, 883–886.

Banner, J.L., Wasserburg, G.J., Donson, P.F., Carpenter, A.B., Moore, C.H., 1989. Isotopic and trace element constraints on the origin and evolution of saline groundwaters from central Missouri. Geochim. Cosmochim. Acta 53, 383–398.

Beaumont, C., Fullsack, P., Hamilton, J., 1992. Erosional control of active compressional orogens. In: McClay, K. (Ed.), Thrust Tectonics. Allen Unwin, London, pp. 1–18.

Beck, S.L., Zandt, G., Maers, S.C., Wallace, T.C., Silver, P.G., Drake, L., 1996. Crustal scale variations in the Central Andes. Geology 24, 407–410.

Belitz, K., Bredehoeft, J., 1988. Hydrodynamics of Denver basin: explanation of subnormal fluid pressure. AAPG Bull. 72, 1334–1359.

Benjamin, M.T., Johnson, N.M., Naeser, C.W., 1987. Recent rapid uplift in the Bolivian Andes: evidence from fission-track dating. Geology 15, 680–683.

Blackwell, D.D., Steele, J.L., Brott, C.A., 1980. The terrain effect on terrestrial heat flow. J. Geophys. Res. 85, 4757–4772.

Blanpied, M., Lockner, D., Byerlee, J., 1992. An earthquake mechanism based on rapid sealing of faults. Nature 358, 574–576.

Bodri, B., Rybach, L., 1998. Influence of topographically driven convection on heat flow in the Swiss Alps: a model study. Tectonophysics 291, 19–27.

Bullard, E.C., 1947. The time necessary for a borehole to attain temperature equilibrium. Mon. Not. R. Astron. Soc. 5, 127–130.

Burrus, J., Brosse, E., Choppin de Janvry, G., Grosjean, Y., Oudin, J.L., 1992. Basin modeling in the Mahakam delta based on the integrated model Temispack. Proc. Indon. Petr. Ass., 31 Annual Convention, 25–43.

Butler, R., Richards, D., Sempere, T., Marshall, L., 1995. Paleomagnetic determinations of vertical-axis tectonic rotations from

Late Cretaceous and Paleocene strata of Bolivia. Geology 23, 799–802.
Carslaw, H.S., Jaeger, J.C., 1959. Conduction of Heat in Solids. Clarendon Press, Oxford.
Chmielowski, J., Zandt, G., Haberland, C., 1999. The Central Altiplano–Puna magma body. Geophys. Res. Lett. 26, 783–786.
Colletta, B., Letouzey, J., Soares, J., Specht, M., 1999. Detachment versus fault propagation folding: insights from the Sub Andean ranges of Southern Bolivia. Thrust Tectonics 99 Abstr., 106–109, London.
Coudert, MacClay, L., Frappa, M., Viguier, C., Arias, R., 1995. Tectonic subsidence and crustal flexure in the Neogene Chaco basin of Bolivia. Tectonophysics 243, 277–292.
Davies, J.H., von Blanckenburg, F., 1995. Slab breakoff: a model of lithosphere detachment and its test in the magmatism and deformation of collisional orogens. Earth Planet. Sci. Lett. 129, 85–102.
Deming, D., 1989. Application of bottom-hole temperature corrections in geothermal studies. Geothermics 18, 775–786.
Deming, D., Chapman, D.S., 1988. Inversion of bottom-hole temperature data: the Pineview field, Utah–Wyoming thrust belt. Geophysics 53, 707–720.
Deming, D., 1994. Fluid flow and heat transport in the upper continental crust. In: Parnell, J. (Ed.), Geofluids: Origin, Migration and Evolution of Fluids in Sedimentary Basins. Geol. Soc. Spec. Publ., vol. 78, pp. 27–42, London.
Doligez, B., Ungerer, P., Chenet, P., Burrus, J., Bessis, F., Besserau, G., 1987. Numerical modeling of sedimentation, heat transfer, hydrocarbon formation and fluids migration in the Viking graben, North Sea. In: England, W.A., Flett, A.J. (Eds.), Petroleum Geology of Northwest Europe. Heyden, London, pp. 1039–1048.
Dunn, J., Hartshorn, K.G., Hartshorn, P.W., 1995. Structural styles and hydrocarbon potential of the Sub Andean thrust belt of Southern Bolivia. In: Tankard, R., Suarez, S., Welsink, H.J. (Eds.), Petroleum Basins of South America. AAPG Memoir, vol. 62, pp. 523–543.
Endignoux, L., Wolf, S., 1990. Thermal and kinematic evolution of thrust basins: a 2D numerical view. In: Letouzey, J. (Ed.), Petroleum and Tectonics in Mobile Belts. Technip, Paris, pp. 181–192.
England, P., Molnar, P., 1993. The interpretation of inverted metamorphic isograds using simple physical calculations. Tectonics 12 (1), 145–157.
Evans, B., 1992. Greasing the faults. Nature 358, 544–545.
Giunchi, C., Ricard, Y., 1999. High pressure–low temperature metamorphism and the dynamics of an accretionary wedge. Geophys. J. Int. 136, 620–628.
Gubbels, T.L., Isacks, B.L., Farrar, E., 1993. High levels surfaces, plateau uplift and foreland development, Bolivian Central Andes. Geology 21, 695–698.
Guillier, B., Baby, P., Mendez, E., Oller, J., Marquez, H., 1992. Modificaciones del mapa estructural del subandino sur de Bolivia por compabilitad cinemática de cortes balanceados. X Congreso Geologico Boliviano, Resumenes extendidos. Bol. Soc. Geol. Boliviana, vol. 27, pp. 74–76.
Henry, S.G., Pollack, H.N., 1988. Terrestrial heat flow above the Andean subduction zone in Bolivia and Peru. J. Geophys. Res. 93, 15153–15162.
Horner, D.R., 1951. Pressure build-up in wells. Proc Third World Petroleum Congress. The Hague, pp. 503–519.
Huerta, A.D., Royden, L.H., Hodges, K.V., 1996. The interdependence of deformational and thermal processes in mountain belts. Science 273, 637–639.
Huerta, A.D., Royden, L.H., Hodges, K.V., 1998. The thermal structure of collisional orogens as a response to accretion, erosion and radiogenic heating. J. Geophys. Res. 103, 15287–15302.
Isaacson, P.E., Diaz Martinez, E., 1995. Evidence for a middle–late Palaeozoic foreland basin and significant latitudinal shift, Central Andes. In: Tankard, R., Suarez, S., Welsink, H.J. (Eds.), Petroleum Basins of South America. AAPG Memoir, vol. 62, pp. 231–249.
Jaupart, C., Provost, A., 1985. Heat focussing, granite genesis and inverted metamorphic gradients in continental collision zones. Earth Planet. Sci. Lett. 73, 385–397.
Kley, J., 1996. Transition from basement-involved to thin-skinned tectonics in the Cordillera Oriental of Southern Bolivia. Tectonics 15, 163–186.
Kley, J., Monaldi, C.R., Salfity, J.A., 1999. Along-strike segmentation of the Andean foreland: causes and consequences. Tectonophysics 301, 75–94.
Lachenbruch, A.H., Brewer, M.C., 1959. Dissipation of the temperature effect of drilling a well in arctic Alaska. U. S. Geol. Surv. Bull. 1083, 73–109.
Lachenbruch, A.H., 1970. Rapid estimation of the topographic disturbance to superficial thermal gradients. Rev. Phys. 6, 365–380.
Lachenbruch, A.H., Sass, J.H., 1980. Heat flow and energetics of the San Andreas fault zone. J. Geophys. Res. 85, 6185–6222.
Larroque, C., Guilhaumou, N., Nicot, E., 1993. Caractérisation de paléo-circulations de fluides dans le niveau de décollement du prisme d'accrétion néogène de Sicile. C. R. Acad. Sci. 317, 1485–1492.
Larroque, C., Guilhaumou, N., Stéphan, J.-F., Roure, F., 1996. Advections of fluids at the front of the Sicilian Neogene subduction complex. Tectonophysics 254, 41–55.
Leloup, P.H., Ricard, Y., Battaglia, J., Lacassin, R., 1999. Shear heating in continental strike-slip shear zones: model and field examples. Geophys. J. Int. 136, 19–40.
Lucazeau, F., Le Douaran, S.L., 1985. The blanketing effect of sediments in basins formed by extension: a numerical model. Application to the Gulf of Lion and Viking graben. Earth Planet. Sci. Lett. 74, 92–102.
Luhesi, M.N., 1983. Estimation of formation temperatures from borehole measurements. Geophys. J. R. Astron. Soc. 74, 747–776.
Lyon-Caen, H., Molnar, P., Suarez, G., 1985. Gravity anomalies and flexure of the Brazilian shield beneath the Bolivian Andes. Earth Planet. Sci. Lett. 75, 81–92.
Majorowicz, J.A., Jones, F.W., Lam, H.L., Jessop, A.M., 1985. Terrestrial heat flow and geothermal gradients in relation to

hydrodynamics in the Alberta basin, Canada. J. Geodyn. 4, 265–287.
Majorowicz, J.A., Jessop, A.M., 1993. Relation between heat flow and thermal state of the sedimentary succession of the Alberta Plains. Bull. Can. Pet. Geol. 41, 358–368.
Mancktelow, N.S., Grasemann, B., 1997. Time-dependent effects of heat advection and topography on cooling histories during erosion. Tectonophysics 270, 167–195.
Marshall, L.G. and Sempere, T., 1991. The Eocene to Pleistocene vertebrates of Bolivia and their stratigraphic context: a review. Fósiles y facies de Bolivia (1), Revista técnica de YPFB, Santa Cruz: 631–652.
Masek, J.G., Isacks, B.L., Gubbels, T.L., Fielding, E.J., 1994. Erosion and tectonics at the margin of continental plateaus. J. Geophys. Res. 99, 13941–13956.
Montemurro, G., 1992. Desarollo de facies sedimentarias del Silurico-Devonico en el sector Boomerang-Subandino Centro, Bolivia. Conferencias Internacional Cuencas Fanerozoicas del Gondwana Suroccidental, Santa Cruz (Bolivie).
Montemurro, G., Del Rosario Mercardo, M., 1996. Evolución del Alto de Alto de Izozog en el foreland Boliviano. Memorias del XII Congreso Geologico de Bolivia, Tarija, Bolivia, 29–33.
Moretti, I., Baby, P., Mendez, E., Zubieta, D., 1996. Hydrocarbon generation in relation to thrusting in the Sub Andean Zone from 18 to 22°S, Bolivia. Pet. Geosci. 2, 17–28.
Moretti, I., 2001. Thrust emplacement and fluid circulation in a foreland. Pet. Geosci., in press.
Moretti, I., Labaume, P., Sheppard, S., Boulègue, J., 2001. Compartimentalization of the migration pathways in the Sub-Andean Zone, Bolivia. Tectonophysics, in press.
Mugnier, J.L., Leturmy, P., Mascle, G., Huyghe, P., Chalaron, E., Vidal, G., Husson, L., Delcaillau, B., 1999. The Siwaliks of Western Nepal: I — Geometry and kinematics. J. Asian Earth Sci. 17, 629–642.
Nesbitt, B.E., Muehlenbachs, K., 1989. Origins and movements of fluids during deformation and metamorphism in the Canadian Cordillera. Science 245, 733–736.
Nesbitt, B.E., Muehlenbachs, K., 1991. Stable isotopic constraints on the nature of the syntectonic fluid regime of the Canadian Cordillera. Geophys. Res. Lett. 18, 963–966.
Pasquale, V., Verdoya, M., 1990. Geothermal regime of the Po basin, Italy. Bull. Soc. Geol. Fr. 156, 135–143.
Platt, J.P., England, P.C., 1994. Convective removal of lithosphere beneath mountain belts: thermal and mechanical consequences. Am. J. Sci. 294, 307–336.
Pollack, H.N., Hurter, S.J., Johnson, J.R., 1993. Heat flow from the Earth's interior: analysis of the global data set. Rev. Geophys. 31, 267–280.
Rochat, P., Hérail, G., Baby, P., Mascle, G., 1999. Bilan crustal et controle de la dynamique érosive et sédimentaire sur les mécanismes de formation de l'Altiplano. C. R. Acad. Sci. 328, 189–195.
Roeder, D., 1988. Andean-age structure of Eastern Cordillera (province of La Paz, Bolivia). Tectonics 5, 23–39.
Roeder, D., Chamberlain, R.L., 1995. Structural geology of Sub Andean fold and thrust belt in northwestern Bolivia. In: Tankard, A.J., Suarez, S., Welsink, H.J. (Eds.), Petroleum Basins of South America. AAPG Memoir, vol. 62, pp. 459–479.
Ruppel, C., Hodges, K.V., 1994. Role of horizontal thermal conduction and finite time thrust emplacement in simulation of $P-T-t$ paths. Earth Planet. Sci. Lett. 123, 49–60.
Safanda, J., 1994. Effects of topography and climatic changes on the temperature in borehole GFU-1, Prague. Tectonophysics 239, 187–197.
Sassi, W., Rudkiewicz, J.L., Divies, R., 1998. New methods for integrated modeling of deformation and petroleum generation in fold and thrust belts. AAPG Annual Meeting, Salt Lake City.
Schmitz, M., Heinsohn, W.D., 1997. Seismic, gravity and petrological evidence for partial melt beneath the Central Andean crust (21–23S). Tectonophysics 270, 313–326.
Sclater, J.G., Vacquier, V., Rohrhirsch, J.H., 1970. Terrestrial heat flow measurements on Lake Titicaca, Peru. Earth Planet. Sci. Lett. 8, 45–54.
Sempere, T., Hérail, G., Oller, J., Bonhomme, M.G., 1990. Late Oligocene–Early Eocene major tectonic crisis and related basins in Bolivia. Geology 18, 812–815.
Sempere, T., 1995. Phanerozoic evolution of Bolivia and adjacent regions. In: Tankard, R., Suarez, S., Welsink, H.J. (Eds.), Petroleum Basins of South America. AAPG Memoir, vol. 62, pp. 207–230.
Sempere, T., Carlier, G., Carlotto, V., Jacay, J., Jimenez, N., Rosas, S., Soler, P., Cardenas, J. and Boudesseul, N., 1999. Late Permian-early Tertiary mesozoic rifts in Peru and Bolivia, and their bearing on Andean-age teconics: 4th I.S.AG. ext. abstr., Gottingen, Germany.
Shi, Y., Wang, C.H., 1987. Two-dimensional modeling of the $P-T-t$ paths of regional metamorphism in simple overthrust terrains. Geology 15, 1048–1051.
Sheffels, B.M., 1990. Lower bound on the amount of crustal shortening in the Central Bolivian Andes. Geology 18, 812–815.
Soler, P., Sempere, T., 1993. Stratigraphie, géochimie et signification paléotectonique des roches volcaniques basiques mésozoïques des Andes Boliviennes. C. R. Acad. Sci. 316 (II), 777–784.
Springer, M., 1997. Die regionale Oberflächenwärmeflussdichte-Verteilung in den zentralen Anden und daraus abgeleite Temperaturmodelle der Lithosphäre; PhD thesis; Scientific Technical Report STR97/05, GeoForschungsZentrum, Potsdam.
Springer, M., Forster, A., 1998. Heat Flow density across the Central Andean subduction zone. Tectonophysics 291, 123–139.
Stüwe, K., White, L., Brown, R., 1994. The influence on eroding topography on steady state isotherms: applications to fission track analysis. Earth Planet. Sci. Lett. 124, 63–74.
Tissot, B., Espitalié, J., 1975. L'évolution de la matière organique des sédiments: application d'une simulation numérique. Rev. Inst. Fr. Pet. 30, 743–777.
Torgensen, T., 1991. Crustal-scale fluid transport: magnitude and mechanisms. Geophys. Res. Lett. 18, 917–918.
Turcotte, D.L., Schubert, G., 1982. Geodynamics. Applications of Continuum Physics to Geological Problems. Wiley, New York, pp. 135–197.

Ungerer, P., 1990. State of art of research in kinetic modeling of oil formation and expulsion. Org. Geochem. 16, 1–25.
Uyeda, S., Watanabe, T., 1982. Terrestrial heat flow in Western South America. Tectonophysics 83, 63–70.
Villegas, M., Bachu, S., Ramon, J., Underschultz, J., 1994. Flow of formation waters in the Cretaceous–Miocene succession of the Llanos Basin, Colombia. AAPG Bull. 78, 1843–1862.
Watts, A.B., Lamb, S.H., Fairhead, J.D., Dewey, J.F., 1995. Lithospheric flexure and bending of the Central Andes. Earth Planet. Sci. Lett. 134, 9–21.

5.2 Le Golfe du Mexique

Les zones où l'histoire géologique est compliquée par une succession d'évènements géodynamiques majeurs, comme le Golfe du Mexique (*c.f* chapitre 1) sont, par opposition aux fronts de chaînes et *a forti ori* aux cratons, plus difficiles à évaluer du point de vue thermique. Les processus tectoniques et l'évolution cinématique y sont mal connus et il est difficile de contraindre *a priori* les différents contrôles thermiques. L'interprétation de mesures isolées est rendue malaisée. Alternativement, il est possible d'interpéter une population de mesures thermiques de manière statistique. C'est l'approche retenue dans l'étude du Golfe du Mexique présentée ci-après sous forme d'un couple d'articles. Des anomalies thermiques récurrentes par rapport à un modèle de référence montrent une anomalie thermique persistente, qui peut ensuite être mise en corrélation avec l'évolution tectonique régionale à l'échelle de la lithosphère. Dans le cas du Golfe du Mexique, les résultats obtenus par l'interprétation des données thermiques peuvent en retour être utilisée de manière spéculative pour préciser la magnitude et la chronologie des évènements tectoniques.

Bull. Soc. géol. Fr., 2008, t. 179, n° 2, pp. 129-137

Thermal regime of the NW shelf of the Gulf of Mexico. Part A: Thermal and pressure fields

LAURENT HUSSON [1,2], PIERRE HENRY [1] and XAVIER LE PICHON[1]

Keywords. – Gulf of Mexico, Geotherm, Pressure.

Abstract. – The thermal field of the Gulf of Mexico (GoM) is analyzed from a comprehensive temperature-depth database of about 8500 bottom hole temperatures and reservoir temperatures. Our stochastic analysis reveals a widespread, systematic sharp thermal gradient increase between 2500 and 4000 m. The analysis of the pressure regime indicates a systematic correlation between the pressure and temperature fields.

Régime thermique de la marge nord-ouest du golfe du Mexique. Partie A: Champs de température et de pression

Mots-clés. – Golfe du Mexique, Géotherme, Pression.

Résumé. – Le régime thermique du golfe du Mexique (GoM – Gulf of Mexico) est examiné à partir d'une base de 8 500 données de températures de fond de puit et de températures de réservoir. Notre analyse stochastique révèle une augmentation brutale systématique et régionale du gradient de température entre 2 500 et 4 000 m. L'analyse du régime de pression montre une corrélation entre les champs de température et de pression.

INTRODUCTION

Although the NW margin of the Gulf of Mexico (GoM) has been the locus of myriads of geological studies, both its thermal and tectonic structures remain unclear. Even the geometry of the thermal field is still controversial due to the high complexity of the tectonic and sedimentary processes but also due to the lack of a coherent analysis at the scale of the entire shelf, as most studies have industrial aims and focus on reservoir scales. As a first step toward understanding the thermal regime of the NW shelf of the GoM, we performed a joint analysis of the thermal and pressure fields of the Louisiana and Texas shelf basins to characterize the general thermal structure, examine its possible relationship with the tectonic structure, and discuss the processes that may be responsible for such a complexity. Thermal modeling is a complementary analysis that is given in a companion paper [Husson *et al.,* 2008].

Geological setting

The NW margin of the GoM is characterized by a large Oligo-Miocene detachment on which a series of NE-SW to E-W trending normal faults branch (fig. 1). Among them, the Wilcox and Corsair fault zones (WFZ and CFZ) display offsets of more than 20 km and run across the whole width of Texas. Extension on these fault systems is generally attributed to gravitational collapse toward the gulf on a Cenozoic detachment [Pindell and Dewey, 1982; Diegel *et al*., 1995; Hall, 2002]. The bulk strain is assumed to have been transmitted at the base of the slope where it is accommodated by the Perdido and Mississippi fan fold belts. The structural style of the deep shelf drastically differs as it is mostly characterized by the abundance of salt canopies; only small quantities of salt remain in the proximal shelf. The Rio Bravo marks the location of a left-lateral Tertiary fault which separates the Texan and Mexican units [Russell et Snelson, 1994 ; Flotté *et al.*, 2008]. We identified six tectono-stratigraphic provinces (fig.1) that we will consider in order to explore their relationships with the thermal field, namely the CFZ and its onshore analogue the WFZ, the intermediate zone in between (Intermediate Texas Zone ITZ), the north-west of the WFZ (North West Wilcox, NWW), Louisiana (LA), and the N. Mexican Burgos basin (BUR), subdivided in East and West Mexican Burgos basins (EBUR and WBUR, respectively). Additional support for this division is given by their thermal state (see § Inversion of the local thermal fields).

Temperature data sets

A compilation of ~2000 offshore reservoir temperature data (RT) and ~6500 both offshore and onshore bottom hole

1. Collège de France, Chaire de Géodynamique, Europôle de l'Arbois, 13545 Aix-en-Provence, France. henry@cdf.u-3mrs.fr (P. Henry); lepichon@cdf.u-3mrs.fr (X. Le Pichon)
2. Géosciences Rennes, UMR CNRS 6118, Université de Rennes 1, Campus de Beaulieu, 35042 Rennes cedex, France. laurent.husson@univ-rennes1.fr (L. Husson)
Manuscrit déposé le 27 novembre 2006 ; accepté après révision le 9 juin 2007

FIG. 1. – Structural sketch map of the NW Gulf of Mexico (normal faults in red). Green crosses: bottom hole temperatures; black triangles: reservoir temperatures; blue: location of the morphotectonic zones. LA: Louisiana, CFZ: Corsair fault zone, ITZ: Intermediate Texan zone, WFZ: Wilcox fault zone, NWW: North West Wilcox, EBUR: East Burgos, WBUR: West Burgos.
FIG. 1. – *Carte structurale du Nord-Ouest du golfe du Mexique (failles normales en rouge). Croix vertes : températures de fond de puit* (BHT) *; triangles noirs : températures de réservoir* (RT). *Enveloppes bleues : localisation des unités morpho tectoniques.*

temperature data (BHT) of industrial origin have been used to characterize the thermal regime (fig.1). The complete databases are provided as electronic supplements http://www.sgfr.org/publier/editions/BSGF/Resumes-2008/Res08B2-3.php (tables E1 and E2). RT provide direct measures of the temperature at depth and are fairly reliable. On the contrary, many BHT data were acquired before thermal equilibrium was reached. Empirical [e.g., Bullard, 1947; Horner, 1951]) and statistical [e.g., Deming and Chapman, 1988] correction techniques exist, but they require information unavailable to us like circulation time and shut-in-time; we therefore simply increase the BHT by 10% ΔT ($\Delta T=T_b-T_s$, where T_s is the surface temperature and T_b the temperature at depth). Due to the general lack of data, this is a routine technique for hydrocarbon exploration purpose. After correction, the BHT and RT show consistent tendencies (fig.2). The BHT database shows a stronger scattering (standard deviation from the mean linear temperature-depth regression is 21.2°C) than the RT database (standard deviation is 7.2°C). This reflects both the uncertainty induced by the measurement process and the dispersion due to the larger spatial coverage of the BHT. Unfortunately, we did not have access to the RT onshore at the time of our study.

TABLE I. – Mean surface temperatures T_s and surface temperature gradients deduced from the shallow (< 3000 m) temperature measurements. z_s is ground depth below sea level, σ is standard deviation.
TABL. I. – *Température moyenne de surface T_s et gradients de température de surface déduits des données de températures superficielles (<3000 m). z_s et la profondeur sous le niveau de la mer, σ est l'écart-type.*

zone	T_s (°C)	Grad (°C/km)	Z_s (mbsl)	σ(m)
NWW	/	/	62	34
WFZ	/	/	30	28
ITZ	30	20	13	14
CFZ	28	23	58	88
BUR	27	28	72	56
LA	26	21	42	101

TEMPERATURE AND GRADIENT FIELDS

Surface temperature

Before carrying any further this investigation, we need to determine the surface temperature, which is a boundary condition. Considering only the shallow measurements (< 3000 m), linear regressions give near-surface thermal gradients of 20 to 23°C/km, and up to 28°C/km in the Burgos basin. Data are synthesized in table I. This operation could not be performed for the two onshore units (NWW and WFZ) due to data scarcity at shallow depths. The average surface temperature is given by the intercept of the regression curves with the surface. A bias is induced by the variations in elevation within a single unit, shown by the standard deviations in depths. These estimates are consistent on average with the results of the NOAA for the GoM [after Antonov *et al.*, 1998], and we write accordingly a depth-dependent seafloor temperature $Ts = 4 + 26\exp^{-z_s/300}$, where z_s is the depth below sea level. Onshore ground temperature is set to 30°C.

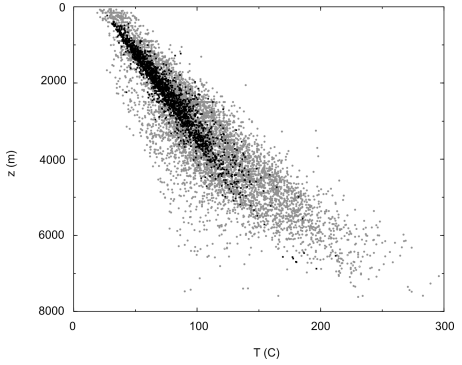

FIG. 2. – Raw temperature-depth data sets. Gray: BHT (corrected by 10% of $\Delta T=T_b-T_s$, where T_s is the surface temperature -here set to 30°C- and T_b the temperature at depth); black: RT.
FIG. 2. – *Données brutes de températures-profondeur. Gris :* BHT *(corrigées de 10 % de $\Delta T=T_b-T_s$, où T_s est la température de surface -ici fixée à 30°C- et T_b la température en profondeur); noir :* RT.

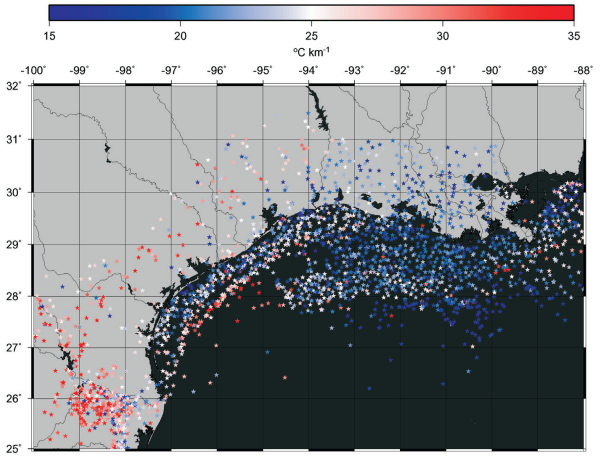

FIG. 3. – Gradient computed by a linear regression of the BHT and RT data.
FIG. 3. – *Gradient donné par régression linéaire des données BHT et RT.*

Inversion of the local thermal fields

One could consider a linear regression of the temperature *vs.* depth (fig. 3) as a convenient first-order approximation of the thermal gradient. This approximation allows us to delineate several thermal units that match the structural pattern. At a large scale, a warm Texas contrasts with a cool Louisiana. Several shorter wavelength warm zones matching the CFZ, WFZ and BUR are superimposed, while the ITZ and NWW are colder. We used these rough spatial subdivisions to explore the more detailed features of the thermal field. In most places, the temperature-depth data sets are well fit by two constant gradients (fig. 4), the surface temperature being set according to precedent section. In Texas, a sharp break in the thermal gradient at 2500 m to 3000 m has previously been documented [e.g. Jones, 1975]. We discuss the significance of this break in following section. For each zone, we determine three parameters from a stochastic analysis (table II): the upper gradient a_1 (*i.e.* the thermal gradient at shallow depths), the lower gradient a_2 (*i.e.* the thermal gradient at large depths), and the rupture depth z_0 (transition depth between upper and lower gradient). We introduce here the ratio between the lower and upper gradients.

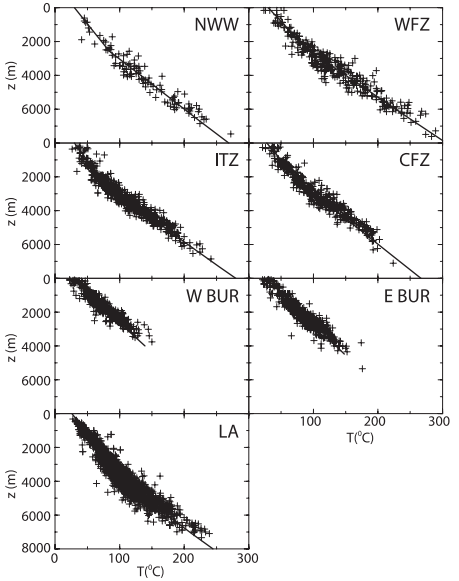

FIG. 4. – Temperature-depth data subsets. Data are pooled by structural/thermal provinces. Regressions are calculated with fixed surface temperature. EBUR and WBUR are the eastern and western zones of the Burgos basin. Depths are burial depths.
FIG. 4. – *Echantillonnage des données températures / profondeurs. Les données sont groupées selon les provinces thermales / structurales. Les régressions sont calculées avec une température de surface fixée.* EBUR *et* WBUR *sont les zones orientales et occidentales du bassin de Burgos. Les profondeurs sont les profondeurs d'enfouissement.*

TABLE II. – Computed parameters for the 2 gradients fits of spatial data sets. z_0 is the rupture depth from gradient a_1 to a_2. Surface temperature T_s is set according to section "Surface temperature"
TABL. II. – *Paramètres calculés pour l'interpolation par 2 gradients linéaires des groupes de données. z_0 est la profondeur de rupture entre les gradients a_1 et a_2. La température de surface T_s est définie selon la section « Température de surface ».*

Zone	T_s (°C)	a_1 (°C/km)	a_2 (°C/km)	z_0 (m)	a_2/a_1
NWW	30	20.2	34.1	2450	1.69
WFZ	30	24.4	38.8	2450	1.59
ITZ	30	18.9	36.1	2300	1.92
CFZ	28	22.3	34.0	2250	1.51
W.BUR	27	29	no data	no data	/
E.BUR	27	27	no data	no data	/
LA	26	20.8	36.3	4350	1.75

For WFZ, ITZ, CFZ and LA, a composite two-gradients fit has a considerably better fit than that given by a single linear regression (or even a quadratic regression). Error minimization has been performed using both L1 (sum of errors) and L2 (mean square of errors) norms. We eliminated outliers until norms L1 and L2 gave consistent results. Only 20 outlying values had to be withdrawn. We also compared regressions obtained using RT and BHT data separately. Once the rupture depth in the temperature profile is fixed, the upper gradients from RT and BHT are in good agreement. We conclude that the sharp downward increase in the temperature profiles is a real feature.

The rupture depth in the thermal gradient occurs at about 2500 m for WFZ, ITZ, and CFZ. In NWW, the rupture depth of the gradient is poorly constrained. As the geological setting does not differ much from that of the neighboring WFZ, we adopt the same break in gradient depth in NWW as in the WFZ. In LA, the gradient rupture exists too, but at a greater depth than in the other zones (4250 m). For LA, because the rupture depth is large, the high gradient is deep and the temperature is low at all depths. In BUR, not enough data are available at large depths and only a single regression can be performed. Maximum and minimum upper section gradients are found respectively in BUR (29°C/km for WBUR and 27°C/km for WBUR), and ITZ (18.9°C/km), respectively, making the upper gradient cold everywhere except in BUR.

Three-dimensional mapping of the thermal field with depth

We use the results of the previous analysis to assess the 3D temperature field of the GoM from all available BHT and RT data. The previous analysis gives the mean tendency of the subsurface thermal gradient, where the geotherm $T(z)$ writes

$$T(z)=T_s+a_1 z, \quad (z<z_0)$$
$$T(z)=T_s+a_1 z+a_2(z-z_0), \quad (z>z_0) \qquad (1)$$

Assuming that the previously calculated values for z_0 hold anywhere within a given zone, we then extrapolate the general laws to individual data i. We keep a constant ratio a_2/a_1 and calculate for each data a new coefficient b_i so that the temperature evolves with depth like

$$T(z)_i=T_s+b_i a_1 z, \quad (z>z_0)$$
$$T(z)_i=T_s+b_i a_1 z+b_i a_2(z-z_0), \quad (z>z_0) \qquad (2)$$

We then filtered (see appendix A1) and mapped the upper and lower thermal gradients by interpolating $b_i a_1$ and $b_i a_2$, respectively. The upper gradient (fig. 5a) peaks in the WFZ and CFZ (up to 28-30°C/km) but remains fairly homogeneous (≃ 19 to 25°C/km). BUR remains the warmest zone at a large scale (≃ 30°C/km). At depth (fig. 5b), the gradient increases everywhere between ≃ 34 and 39°C/km (we do not extrapolate the results to the deep gradient south of 26° latitude because of the lack of data). Such gradient increase is an unexpected feature since the thermal regimes of sedimentary basins are above all controlled by the conductivity, which increases with compaction. Notice the strong discrepancy between the gradient obtained from a linear fit of the data (fig. 3) and the gradients obtained with the two-gradient fit. A striking consequence is that the Texas/Louisiana dichotomy vanishes almost entirely on the gradient maps.

Another view of the thermal field is given by temperature slices at various depths levels (fig. 6). Temperatures are computed and mapped using the local upper and deep gradients $b_i a_1$ and $b_i a_2$, and the rupture depths z_0. Because z_0 is deeper in Louisiana than in Texas, a dichotomy becomes prominent at depth. Although the WFZ and CFZ remain warmer than the ITZ and NWW, the whole Texan shelf is warm at depth. The temperature field strikingly matches the distribution of oil and gas shows in the NW GoM, oil shows being mainly found in the Louisiana shelf whereas the Texan shelf essentially features dry gas occurrences. However, one should be aware that although it is true that the temperature field controls the maturation of hydrocarbons, the kinetics of kerogen maturation, which can vary with the nature of the source rocks, also plays a significant role. The striking apparent opposition between the temperature and gradient maps (fig. 5 and 6) only reflects the spatially

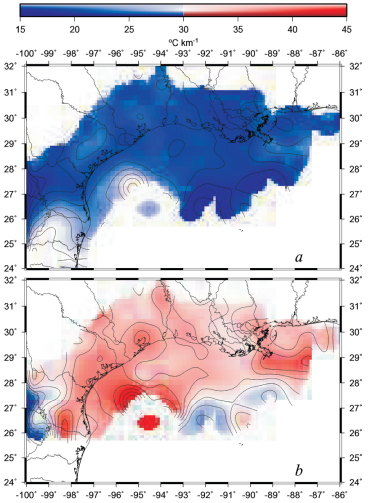

FIG. 5. – Shallow (a) and deep (b) thermal gradient. Wavelengths shorter than 30 km were Gaussian filtered (see appendix for details). Isolines every 5°C km^{-1}.
FIG. 5. – *Gradient superficiel* (a) *et profond* (b). *Les longueurs d'ondes inférieures à 30 km ont été filtrées (voir appendice). Courbes d'isovaleurs chaque 5°C km^{-1}.*

variable rupture depth, which implies that Louisiana is colder than Texas. In southeast Louisiana, the apparent cooling (in temperature as well as gradient) actually reflects the sharp deepening of the bathymetry beyond the shelf break (we extrapolated z_0 from the adjacent LA zone). Although only shallow data are available in BUR, its very high upper thermal gradient suggests that it is a warm zone.

We conclude that in terms of temperature (but not in gradients) LA is cold, WFZ, CFZ, and BUR are warm, and ITZ and NWW are intermediate. The sharp gradient increase with depth, rather than a smooth gradient decrease as observed in many other basins is generally attributed to a progressive increase of thermal conductivity with depth. Blanketing effect

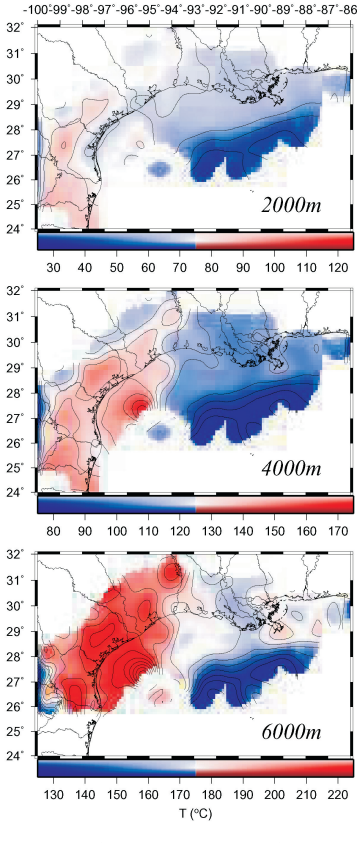

FIG. 6. – Temperature slices at 2000 m, 4000 m, and 6000 m below sea level (°C). Wavelengths shorter than 30 km were Gaussian filtered (see appendix for details). Isolines every 10°C.
FIG. 6. – *Cartes de température à 2000 m, 4000 m, et 6000 m sous le niveau de la mer (°C). Les longueurs d'ondes inférieures à 30 km ont été filtrées (voir appendice). Courbes d'isovaleurs chaque 10°C.*

with high sedimentation rates (> 300 m/Myr) is a process that could cause an increase in the thermal gradient with depth [Carslaw and Jaeger, 1959; Lucazeau and Le Douaran, 1985; Husson and Moretti, 2002]. Although fast sedimentation rates on the GoM shelf must affect the thermal regime, blanketing is a diffusive processus and induces a progressive increase of gradient with depth, rather than a sharp transition as observed (see following sections).

LINKING THE PRESSURE AND TEMPERATURE FIELDS

Pressure fields

We compiled information on the pressure state within the sediments of the Texan margin from an industry database [14]; they are available as supplementary electronic material (table E3). Available data are local isobaric depths of *in situ* leakoff tests pressures (LOT), which is the pressure at which fracturation occurs, and mud weights (MW), which control the pressure in a well bore and prevents unwanted flow into the well. Therefore the MW pressure (P_{MW}) gives an upper bound of the fluid pressure in a formation at a given depth. We interpolated isobaric depths to obtain pressure slice maps at fixed depths (2000, 3000, 4000, 5000 m, fig. 7). Wavelengths shorter than 30 km are FFT cut. P_{MW} slices form an E-W trending saddle, the pressure decreasing to the South at a given level because of the increasing bathymetry but also to the North, beneath the Mississippi delta. The MW pressure is also imprinted by the recent sedimentation of the CFZ too, particularly at 3000 m depth. This indicates that the near hydrostatic pressure field extends deeper in fast sedimentation areas such as the CFZ and the Mississippi delta than in other areas.

Overpressure

MW pressure P_{MW} is necessarily between lithostatic P_{lit} and hydrostatic P_{hyd} pressures. The overpressure state is quantified by the ratio $R=(P_{MW}-P_{hyd})/(P_{lit}-P_{hyd})$. Details are given in appendix A2. Figure 8 shows interpolated overpressure slice maps. Wavelengths shorter than 30 km are FFT cut. Within the NW GoM margin, the transition from low pressures ($R < 0.5$) toward high pressures ($R > 0.5$) occurs between 2500 m and 3200 m in the Texan zone and at ~4500 m in Louisiana. The zones of highest recent sedimentation rates (Mississippi delta and CFZ) match the zones of lower fluid pressure. This is explained if these recent sediments have a high enough permeability and compact normally. A spatial analysis confirms these observations.

The curves of figure 9 give the evolution of P_{MW}, P_{lit}, and P_{hyd} with depth. We arbitrarily define a mean curve, which runs through the mean depths at each reference pressure. The transition from almost hydrostatic to high pressures occurs at lower depths in CFZ and ITZ (~3000 m) than in LA (~4200 m). The lithostatic pressure is never reached in our interpolation and the measurements indicate that the actual geopressure curve is asymptotic to the lithostatic gradient curves. This can be due to a choice of too high a density for recent sediments. In that case, the transition depth should be slightly shallower (~2500 in Texas and ~4000 in Louisiana).

On a general point of view, one should expect a thick recent sedimentary pile to be overpressured. The fact that in the GoM shelf overpressure only appears at large depths suggests that the upper section is highly permeable allowing

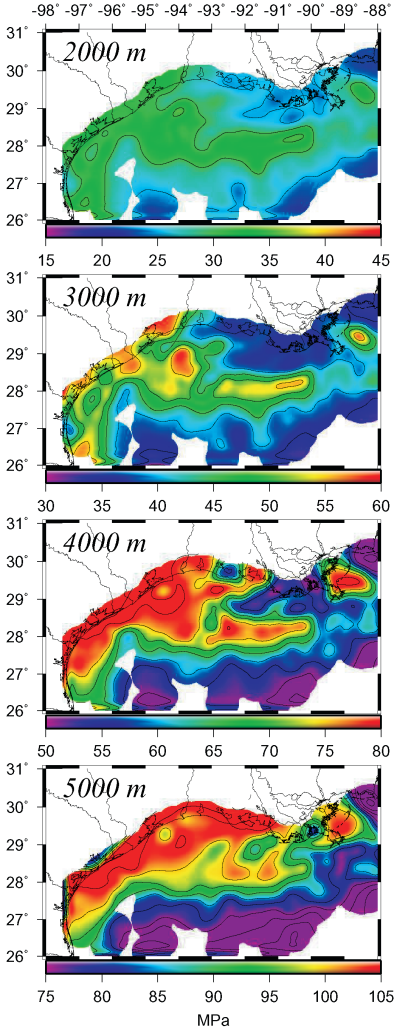

FIG. 7. – Interpolated mud weights pressures at variable depths.
FIG. 7. – *Pression de boue (mud weight) interpolée à différentes profondeurs.*

for the water to be expelled at fast rates. The LOT pressures P_{LOT} give the pressure at which fracturing occurs in an open formation, *i.e.* the measured pressure is comparable to the magnitude of the σ3 component of the local stress tensor. Here we just want to mention that in the NW of the GoM margin, P_{LOT} (data in table E3) is rather close to the hydrostatic pressure at shallow depths where the sedimentary pile is dominated by recent sediments. This implies that fracturation in these areas occurs at shallow depth, and in turn indicates that fracture permeability is high in the recent sediments of the GoM margin. The transition depth from nearly hydrostatically-pressured to high-P is correlated with the thickness of Plio-Pleistocene sediments [Husson *et al.*, 2008; Galloway *et al.*, 2000].

Pressure, fluid flow, and temperature

The pressure field matches the thermal field described in § "Three-dimensional mapping", since the thermal gradient shows a sharp increase where the downward transition towards high pressures occurs. Indeed, this sharp transition toward near-lithostatic pressure has been previously acknowledged onshore Texas [e.g. Jones, 1975; Pfeiffer and Sharp, 1989; McKenna and Sharp, 1998; McKenna, 1997; Sharp *et al.*, 2001]. The thermal field also match the thickness of the sedimentary cover, as previously acknowledged [for instance in the NE GoM, Nagihara and Jones, 2005]. Our analysis shows that this setting is widespread over the whole NW GoM margin.

The most obvious processes which can be invoked to explain the temperature gradient increase with depth is the blanketing effect [Carslaw and Jaeger, 1959; Lucazeau and Le Douaran, 1985; Husson and Moretti, 2002]. The downward advection of heat while sedimentation occurs cools the sediments close to surface level. In the absence of compaction and with constant petrophysical properties, the heat equation writes

$$\frac{\partial T}{\partial t} = \frac{\partial^2}{\partial z^2}\frac{kT}{\rho c_p} + \frac{A}{\rho C_p} - U\frac{\partial T}{\partial z}, \qquad (3)$$

where $U\frac{\partial T}{\partial z}$ is the advective term, $\frac{\partial^2}{\partial z^2}\frac{kT}{\rho C_p}$ the diffusive term. Because of this diffusion, sedimentation will affect the thermal field in a smooth fashion that is incompatible with the observed abrupt gradient increase, and this process can already be discarded. This is also graphically highlighted in figure 10, which shows the temperature profiles calculated from equation (3), after 25 m.y. of sedimentation at 0, 0.2, and 0.46 mm/yr. The profiles are smooth, and the anomaly is penetrative, *i.e.* sedimentation has an impact at much larger depths than that of the observed bend in the GoM margin. Hence, although it significantly cools the sediments of the GoM, sedimentation can be discarded as responsible for the two-gradients shape of the temperature profiles.

A variety of alternative processes have already been invoked to explain the sharp rupture. The most acknowledged is that the pressure contrast affects the conductivity (higher in the high-P domain than in the low-P domain), and because the pressure transition is rather sharp, there would be a sharp break in the thermal gradient [Jessop, 1990]. A transition toward more shaly facies of lower thermal

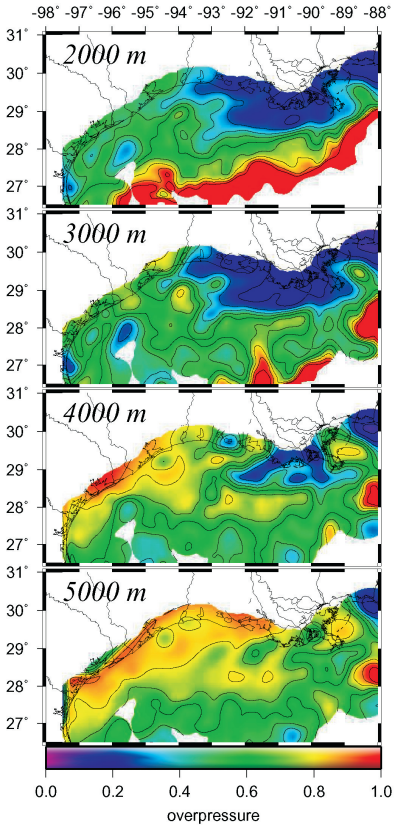

FIG. 8. – Overpressure state (0 is 100% hydrostatic and 1 is 100% lithostatic) at variable depths. Seawater density: 1030 kg m^{-3}; sediment density: 2670 kg m^{-3}.
FIG. 8. – *Etat de surpression (0 correspond à 100 % hydrostatique et 1 à 100 % lithostatique) à différentes profondeurs. Densité de l'eau de mer : 1030 kg m^{-3}; densité des sédiments : 2670 kg m^{-3}.*

conductivities has been proposed but it is incompatible with the stratigraphy of the GoM [Coelho *et al.*, 1996]. Revil [2000] extrapolated his analysis of the thermal conductivities in a reservoir of the GoM to suggest that gas capillary sealing could explain both the pressure and thermal fields. Using the equation and parameters of Revil [after Somerton, 1992], to decrease the conductivity by a factor 0.67 in the lower section (which is equivalent in steady state conditions, in a homogeneous medium, to increase the gradient by 1.5), the pore space should be gas-saturated by 65% in the lower section, and 0% in the upper section, implying that the entire sedimentary basin of the GoM margin below ~2500 m should be considered as a giant gas reservoir, which is of course incorrect. Warm fluid advection in the high-P strata has also been suggested [Pfeiffer and Sharp, 1989; McKenna, 1997; Bodner and Sharp, 1988], but Blackwell and Steele [1989] discard this hypothesis showing that the maintenance of high temperature gradients through the upper overpressured section cannot be attributed to fluid flow.

In the Gulf coast, that fluid circulates is agreed upon [Sharp *et al.*, 2001] but how fluid circulation occurs remains debated. The observed thermal field shows that the heat flow in the upper section is 1.5 to 1.9 times lower than in the lower section (see table II). If free convection were responsible for heat extraction in the upper section, 1.5 would be a minimum for the ration a_2/a_1. That would require

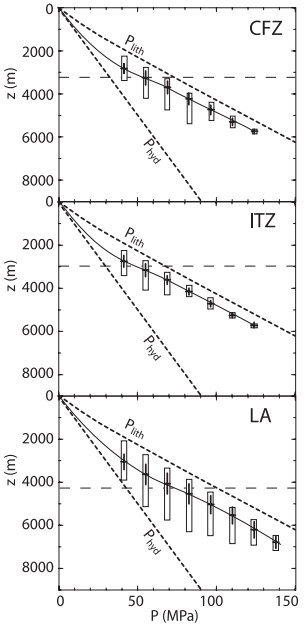

FIG. 9. – Mud weights data subsets. Data are pooled by location (ITZ, CFZ and LA). Dotted lines: estimated hydrostatic and lithostatic pressures. Seawater and sediment density is the same as in figure 8. Black crosses: mean depths and standard deviations at given mud weights/pressures, white boxes give the envelope of the data. Dashed lines show the transition from the mostly hydrostatic domain to the mostly lithostatic domain (R=0.5).
FIG. 9. – *Echantillonnage des pressions de boues. Les données sont groupées par localisation (ITZ, CFZ et LA). Pointillés : estimation des pressions lithostatiques et hydrostatiques. Les densités de l'eau et des sédiments sont les mêmes que pour le figure 8. Croix noires : profondeurs moyennes et écart-types des données de pression de boues / profondeurs ; les boîtes blanches donnent l'enveloppe des données. Les lignes tiretées indiquent la transition entre les domaines hydrostatiques et lithostatiques (R = 0.5).*

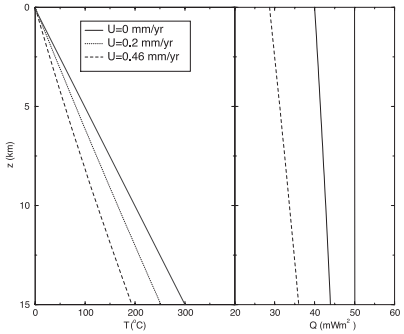

FIG. 10. – Theoretical blanketing effect. Basal heat flow: 50 mW m^{-2}. U: sedimentation rate. C_P=1123 J kg^{-1}K^{-1}, ρ_S=2670 kg m^{-3}, k=2.5 W m^{-1} K^{-1}. No compaction. No radiogenic production.
FIG. 10. – *Effet théorique de blanketing. Flux de chaleur basal : 50 mW m^{-2}. U : taux de sédimentation. C_P = 1123 J kg^{-1}K^{-1}, ρ_S= 2670 kg m^{-3}, k = 2.5 W m^{-1} K^{-1}. Pas de compaction. Pas de production radiogénique.*

a rather low permeability. However, permeability is scale-dependent [Neuman and Federico, 2003] and the effective conductivity can be significantly raised with respect to the laboratory sample scale. In addition, the *LOT* pressures are almost hydrostatic in the upper sections [data in table E3], indicative of a higher fracture permeability in the recent, shallow sediments than in the older, deeper ones. Furthermore, localized high permeability conduits allow free convection to occur and disturb the thermal field in a heterogeneous medium of low average permeability [Sharp *et al*., 2001; Simmons *et al.,* 2001; Sharp *et al.,* 2003; Simms and Garven, 2004]. Because the rupture in the thermal gradient has a regional extent over the Gulf of Mexico and because it is correlated to the low-P/high-P transition, we suggest that widespread free convection could be regarded as a potential mechanism.

CONCLUSIONS

Analyzing the thermal field in the NW shelf of the GoM is not easy because of its atypical configuration and fast processes. We have shown that the gradient increases with depth within the sedimentary pile while it decreases in most sedimentary basins. The main characters of the thermal and pressure fields are summarized below:

1) in terms of temperatures, Louisiana is cool and Texas is warm. This pattern is not reflected by the thermal gradient, because of the combined transient effects of erosion, sedimentation and pressure;

2) a widespread (in Texas and Louisiana, but not in the Burgos basin of Mexico) two-layer distribution of the thermal field: an upper section with a relatively low thermal gradient (19 to 25°C/km everywhere except in the Burgos basin) and a lower one with a higher one (34 to 39°C/km);

3) the transition depth from the upper section to the lower one varies laterally from 2250-2500 m in the Texan zones to more than 4000 m depth in Louisiana. This depth is not only correlated with the thickness of the Plio-Pleistocene sedimentary pile but also with the overpressure field. The upper section constitutes a low pressure domain while the lower one is highly pressured;

4) the pressure field suggests that the permeability of the upper section is high. This is surprising because thick recent sedimentary piles are generally overpressured as sedimentation is faster than fluid expulsion. However, we found that in the NW shelf of the GoM, the pressure is almost hydrostatic in the first kilometers, which implies that fluids are expelled at fast rates in the upper section of the sedimentary pile.

This stochastic analysis allowed us to extract the main processes that control the thermal regime of the NW shelf of the GoM. It provides the tools and simplification required to model the physical processes and characterize the deep thermal regime. This is the scope of a companion paper [Husson *et al.,* 2008], where we show that, when transient effects are removed, the heat flow is very high in this area.

APPENDIX

A1: *Gaussian filter*: For mapping, we use a Gaussian filter to remove short wavelengths. We set $\nabla T_{m,n} = \frac{\sum_i w_i \nabla T_i}{\sum_i w_i}$, where $w_i = \exp\frac{-D_i^2}{2\sigma^2}$ is the weight of any data *i* and D_i its distance to the sliding origin of coordinates *(m,n)*. σ gives the wavelength of the filter, that we set to 30 km.

A2: *Overpressure*: The overpressure state is quantified by he ratio $R=(P_{ww}- P_{hyd})/(P_{lit} - P_{hyd})$. The end members P_{lit} *and* P_{hyd} are calculated using a seawater density ρ_{sw}=1030 kg m^{-3} and a sediment grain density ρ_s=2670 kg m^{-3}. We use a homogeneous compaction law ($\phi=\phi_1 + \phi_0\, e^{-\alpha z}$, with ϕ_0=0.46, ϕ_1=0.05, and $a=0.64\ 10^{-3}$ m^{-1}, (after McKenna and Sharp [1998] for the GoM) to calculate the lithostatic pressure ($P_{lit} = \rho_s g z(1-\phi_m) + \rho_{sw} g z \phi_m$, where $\phi_m = \phi_1 + \frac{\phi_0}{az}(1 - e^{-az})$ is the average porosity above depth *z*).

References

ANTONOV J., LEVITUS S., BOYER T., CONKRIGHT M., BRIEN T.O. & STEPHENS C. (1998). – World Ocean Atlas 1998, vol.1: Temperature of the Atlantic Ocean. – NOAA Atlas NESDIS 27.

BLACKWELL D. & STEELE S. (1989). – Thermal conductivity of sedimentary rock–measurement and significance. *In*: N. NAESER and N. MCCULLOH, Eds., Thermal history of sedimentary basins-methods and case histories. – Springer-Verlag, Heidelberg, 13–36.

BODNER D. & SHARP J. (1988). – Temperature variations in south temperature variations in south Texas subsurface. – *AAPG Bull*., **72**, 21-32.

BULLARD E. (1947). – The time necessary for a borehole to attain temperature equilibrium. – *Mon. Not. R. Astron. Soc.* **5**, 127–130.

CARSLAW H. & JAEGER J. (1959). – Conduction of heat in solids. – Clarendon Press, Oxford.

COELHO D., ERENDI A. & CATHLES L. (1996). – Temperature, pressure and fluid flow modeling in block 330, south Eugene island using 2D and 3D finite element algorithms. *In*: AAPG-SEPM, Annual Meeting Abstracts, 28.

DEMING D. & CHAPMAN D. (1988). – Inversion of bottom-hole temperature inversion of bottom-hole temperature data: the Pineview field, Utah-Wyoming thrust belt. – *Geophysics,* **53**, 707–720.

DIEGEL F., KARLO J., SCHUSTER D., SHOUP R. & TAUVERS P. (1995). – Cenozoic structural evolution and tectonostratigraphic framework of the northern Gulf coast continental margin. *In*: M. JACKSON, D. ROBERTS & S. SNELSON, Eds., Salt tectonics: a global perspective. – *AAPG Mem.* **65**, 109-151.

FLOTTÉ N., MARTINEZ-REYES J., RANGIN C., HUSSON L., TARDY M. & LE PICHON X. – The Rio Bravo fault, a major late Eocene-Oligocene left-lateral shear zone. – *Bull. Soc. géol. Fr.,* **179**, 2, 147-160.

GALLOWAY W., GANEY-CURRY P., LI X. & BUFFLER R. (2000). – Cenozoic depositional history of the Gulf of Mexico basin. – *AAPG Bull.,* **84**, 1743-1774.

HALL S.H. (2002). – The role of autochthonous salt inflation and deflation in the northern Gulf of Mexico. – *Mar. Petrol. Geol.*, **19**, 649–682.

HORNER D. (1951). – Pressure build-up in wells. *In*: Proc. of the Third world petroleum congress, The Hague, 503-519.

HUSSON L. & MORETTI I. (2002). – Thermal regime of fold and thrustbelts. An application to the Bolivian Sub-Andean zone. – *Tectonophysics*, **345**, 253–280.

HUSSON L., LE PICHON X., HENRY P., FLOTTE N. & RANGIN C. (2008). – Thermal regime of the NW shelf of the Gulf of Mexico. Part 2: Heat flow density. – *Bull. Soc. géol. Fr.*, **179**, 2, 139-145.

JESSOP A.M. (1990). – Thermal geophysics. – Elsevier, Amsterdam, 316 p.

JONES P. (1975). – Geothermal and hydrocarbon regimes, northern Gulf of Mexico basin. *In*: M.H. DORFMAN & R.W. DELLER, Eds., *First Geopressured geothermal energy conference Proceedings.* – Univ. Texas at Austin, Center for Energy Studies, 15-89.

LUCAZEAU F. & LE DOUARAN S. (1985). – The blanketing effect of sediments in basins formed by extension: a numerical model. Application to the Gulf of Lion and Viking graben. – *Earth Planet. Sci. Lett.*, **74**, 92-102.

MCKENNA T. (1997). – Fluid flow and heat transfer in overpressured sediments of the Rio Grande embayment, Gulf of Mexico basin. – *Gulf Coast Ass. Geol. Soc. Trans.,* **47**.

MCKENNA T. & SHARP J. (1998). – Radiogenic heat production of the Gulf of Mexico basin, south Texas. – *AAPG Bull.,* **82**, 484-496.

NAGIHARA S. & JONES K.O. (2005). – Geothermal heat flow in the northeast margin of the Gulf of Mexico. – *AAPG Bull.*, **89**, 821-831.

NEUMAN S. & FEDERICO V.D. (2003). – Multifaceted nature of hydrogeologic scaling and its interpretation. – *Rev. Geophys.*, **4**, doi: 10.1029/2003RG000130.

PFEIFFER D. & SHARP J. (1989). – Subsurface temperature distributions in south Texas. – *Gulf Coast Ass. Geol. Soc. Trans.*, **31**, 231–245.

PINDELL J. & DEWEY J. (1982). – Permo-Triassic reconstruction of western Pangea and the evolution of the Gulf of Mexico/Caribbean region. – *Tectonics* **1**, 179-211.

REVIL A. (2000). – Thermal conductivity of unconsolidated sediments with geophysical applications. – *J. Geophys. Res.,* **105**, 16749-16768.

RUSSELL L.R. & SNELSON S. (1994). – Structure and tectonics of the Albuquerque basin segment of the Rio Grande rift. *In*: G.R. KELLER and S.M. CATHER, Eds., Basins of the Rio Grande rift: structure, stratigraphy, and tectonic setting: insights from reflection seismic data. – *Geol. Soc. Amer. Spec. Paper*, **291**, 83-112.

SHARP J., FENSTEMAKER T., SIMMONS C., MCKENNA T. & DICKINSON J. (2001). – Potential salinity-driven free convection in a shale-rich sedimentary basin: Example from the Gulf of Mexico basin in south Texas. – *AAPG Bull.*, **85**, 245–275.

SHARP J., SHI M. & GALLOWAY W. (2003). – Heterogeneity of fluvial systems – control on density driven flow and transport. – *Env. Eng. Geos.*, **9**, 5-17.

SOMERTON W. (1992). – Thermal properties and temperature-related behavior of rock/fluid systems. – Elsevier, Amsterdam.

SIMMONS C., FENSTEMAKER T. & SHARP J. (2001). – Variable density groundwater flow and solute transport in heterogeneous porous media: approaches, resolutions, and future challenges. – *J. Contamin. Hydrol.*, **52**, 245-275.

SIMMS M. & GARVEN G. (2004). – Thermal convection in faulted extensional sedimentary basins: theoretical results from finite element modeling. – *Geofluids*, **4**, 109-130.

Bull. Soc. géol. Fr., 2008, t. 179, n° 2, pp. 139-145

Thermal regime of the NW shelf of the Gulf of Mexico Part B : Heat flow

LAURENT HUSSON [1,2], XAVIER LE PICHON [1], PIERRE HENRY [1], NICOLAS FLOTTE [1,3] and CLAUDE RANGIN [1]

Key words. – Heat flow, Gulf of Mexico, Blanketing effect, Erosion, Lithospheric thinning

Abstract. – We restore the steady state heat flow of the NW shelf of the GoM by removing the transient effects of sedimentation, erosion and compaction. We estimate sedimentation and erosion rates for the NW margin of the GoM from stratigraphic data and vitrinite reflectance data, respectively, and show that they both affect significantly the thermal field. We perform a thermal modeling for 166 wells within the Texan shelf. We conclude that there is a general southeastward increase in the heat flow. This increase also correlates with major tectonic features of the NW shelf of the GoM. We propose that the main zones of extension, of fast recent sedimentation, and crustal thinning are due to geologically recent lithospheric thinning responsible for the higher heat flow.

Régime thermique de la marge nord-ouest du golfe du Mexique. Partie B : Flux de chaleur

Mots-clés. – Flux de chaleur, Golfe du Mexique, Blanketing, Erosion, Lithosphère

Résumé**. –** Nous restaurons le flux de chaleur en régime permanent de la marge nord-ouest du golfe du Mexique (GoM–Gulf of Mexico) en éliminant les effets transitoires de la sédimentation, de l'érosion et de la compaction. Nous évaluons les taux de sédimentation et d'érosion pour la marge nord-ouest du golfe du Mexique à partir de données stratigraphiques et de réflexion de la vitrinite, respectivement. Nous montrons que ces processus affectent significativement le régime thermique que nous modélisons pour 166 puits sur la marge du golfe du Mexique. Nous concluons qu'il y a une augmentation générale du flux de chaleur vers le NW du GoM. Cet accroissement coïncide avec les structures tectoniques majeures de la marge. Nous suggérons que les zones principales d'extension, sédimentation récente et d'amincissement crustal sont dues au même amincissement de la lithosphère que celui qui est responsable du fort flux de chaleur.

INTRODUCTION

In the NW shelf of the Gulf of Mexico (GoM), the superposition of numerous transient thermal effects of strong magnitudes due to sedimentation, erosion and fluid flow makes it difficult to assess the deep thermal regime that we wish to characterize by the steady state surface heat flow Q_{ss}, *i.e.* the heat that would flow in the absence of transient thermal processes. Although the GoM is the focus of intensive industrial studies, no basin-wide synthesis has been published on this aspect to our knowledge. In the following, we first analyze the thermal effects of erosion, sedimentation from a general point of view. Second, we restore Q_{ss} for 166 wells on the offshore Texan shelf, accounting for these transient effects. We then relate Q_{ss} to the structural evolution of the GoM margin. All data (stratigraphic, thermal, fluid pressures and vitrinite reflectance) are of industrial source and available as supplementary electronic data, on http://www.sgfr.org/publier/editions/BSGF/Resumes-2008/Res08B2-4.php.

EVALUATING THE TRANSIENT THERMAL EFFECTS

The thermal regime of near-surface rocks is affected by numerous transient effects due in particular to erosion and sedimentation. The large majority of the temperature data available in the NW GoM margin were acquired within the depth range of the hydrocarbon resources (i.e. up to ~7000 m). Since the basin is almost flat on the shelf of the GoM, terrain effects can be ignored, but the effects of fast sedimentation, erosion need to be assessed. Blanketing due to sedimentation [e.g. Lucazeau and Le Douaran, 1985; Husson and Moretti, 2002] induces cooling [Carslaw and Jaeger, 1959]. Erosion has the opposite effect. For both processes, the heat equation writes

$$\left(\rho C_p\right)_b \frac{\partial T}{\partial t} \nabla(k\nabla T) + A - [(1-\phi)\left(\rho C_p\right)_m U(t)_m + \phi\left(\rho C_p\right)_w U(t)_w] \bullet \nabla T \quad (1)$$

where $\mathbf{U}(t)_*$ is the time dependent velocity of rock matrix $\mathbf{U}(t)_m$ and pore water $\mathbf{U}(t)_w$ with respect to the seafloor (*m*

1. Collège de France, Chaire de Géodynamique, Europôle de l'Arbois, 13545 Aix-en-Provence, France.
2. Geosciences Rennes, UMR CNRS 6118, Univ. Rennes 1, Campus de Beaulieu, 35042 Rennes cedex, France. laurent.husson@univ-rennes1.fr
3. AREVA T&D, Tour Areva, 1 place de la Coupole, 92084 Paris la Défense, France
Manuscrit déposé le 27 novembre 2006; accepté après révision le 9 juin 2007

denotes the matrix, *w* the water and *b* the bulk rock), k, ρ, C_p and A the depth dependent thermal conductivity, density, heat capacity and radioactive heat generation, respectively. In a steady state compaction of a semi-infinite space, $\mathbf{U}_w=0$ and $(1-\phi)\mathbf{U}_m$ is a constant, where Φ is the porosity, and $\mathbf{U}_m=\mathbf{U}_s$ at surface level, where $\mathbf{U}_s$ is the sedimentation (or erosion) rate. Equation (1) then writes, in one dimension

$$\left(\rho C_p\right)_b \frac{\partial T}{\partial t} = \frac{\partial}{\partial z} k \frac{\partial T}{\partial z} + A - (1-\phi)\left(\rho C_p\right)_m U_m \frac{\partial T}{\partial z} \qquad (2)$$

$U_m \frac{\partial T}{\partial z}$ is the advective term, $\frac{\partial}{\partial z} k \frac{\partial T}{\partial z}$ the diffusive term.

The vertical integration of the steady state solution of equation (2) through the conductive lithosphere gives an expression of the heat advection $Q_s(U_s)$, which can be regarded as the heat flowing dynamically with respect to the surface. This heat is transported upward as the eroding sediments get closer to the surface in the case of erosion, downward in the case of sedimentation. For uniform petrophysical parameters (conductivity and heat capacity of sedimentary grains) and neglecting the radiogenic production, it writes

$$Q_s(U_s) = U_s T_m \rho C_p, \qquad (3)$$

where T_m is the temperature increase through the lithosphere. In the case of erosion for example, with C_p=1123 J kg^{-1}K^{-1}, ρ=2670 kg m^{-3}, and T_m=1300°C, equation (3) gives $Q_s(0.46\ mm/yr)$=57 $mW\ m^{-2}$ and $Q_s(0.2\ mm/yr)$=25 $mW\ m^{-2}$. The advected heat is then higher in magnitude than the heat flowing at the base of the conductive lithosphere (often called reduced heat flow). The solution for sedimentation is similar but opposite in magnitude because sedimentation corresponds to a downward advection of heat. Both processes can thus be first order phenomena. For instance, in the GoM margin, sedimentation rates are commonly up to 0.5 mm/yr and the Neogene pile is up to 25 km thick.

We numerically solved the heat equation (2) in transient state in order to estimate the impact of such conditions. Figure 1 shows the disturbance on the heat flow and thermal regime in the case of sedimentation and erosion, for two different basal heat flow conditions. Different sets of parameters can result in the same near surface heat flow. For instance, after a period of 25 m.y., a surface heat flow of 38 $mW\ m^{-2}$ can either be produced by low basal heat flow and sedimentation rate (50 $mW\ m^{-2}$, 0.1 mm/yr) or by high basal heat flow (75 $mW\ m^{-2}$) and sedimentation rate (0.25 mm/yr). These values are in the range observed on the GoM margin. Comparable results can be obtained for erosion: a 75 $mW\ m^{-2}$ heat flow at 5000 m can either result from a low basal heat flow (50 $mW\ m^{-2}$) combined to fast erosion rates (-0.25 mm/yr) or from a high basal heat flow (75 $mW\ m^{-2}$) in the absence of erosion.

In the following, we address the potential impact of erosion and sedimentation in the GoM on the thermal field.

Blanketing effect in the NW GoM margin

On the GoM margin, Neogene sedimentation is fast [*e.g.* Galloway *et al.,* 2000]. We compiled more than 11,000 stratigraphic Tertiary biomarkers from well logs (table E1, electronic supplementary data) with ages from a biochronological scale. When the time span separating two markers is short enough (*i.e.*< 5 m.y.), the stratigraphic intervals were interpolated to generate a 1 m.y. regular array. About 7500 markers were selected (mean of intervals is 1.1 m.y., standard deviation is 0.9 m.y.) and 7800 final synthetic markers computed at regular time steps of 1 m.y. over the entire area.

Neogene sedimentation is terrigenous and variations in lithology are modeled as variations of the average sand/shale ratio as a function of age (table I). Back-stripping was performed assuming a standard compaction law ($\Phi=\Phi_1+\Phi_0 e^{-a/z}$, with $\Phi_0=0.46$, $\Phi_1=0.05$, and $a=0.64\ 10^{-3}$ m^{-1} [after McKenna and Sharp, 1998].

We identified 5 major Neogene deposition episodes from the spatial distribution of sedimentation rates (fig. 2). From 20.5 to 18.5 Ma, the general sedimentation rate was lower than 0.4 mm/yr apart from a trend running parallel to the coastline, next to the Corsair fault zone (CFZ, see location fig. 5). From 18.5 to 14.5 Ma, a fast sedimentation rate (~1 mm/yr) wide trend became prominent forming the CFZ fan. From 14.5 to 9.5, this trend became confined to the CFZ; the overall sedimentation rate was lower (~0.2 mm/yr) but ranged between 0.5 and 0.8 mm/yr within the CFZ. The depocenter remained in the CFZ but gently migrated southward from 20 Ma to 10 Ma. From 9.5 Ma to 4.5 Ma, the depocenter jumped northward, retaining a 0.4 mm/yr sedimentation rate while the mean rate around the CFZ was about 0.1 mm/yr. The sedimentation rate increased close to Louisiana as the Mississippi delta developed. According to figure 1, for this range of sedimentation rates, the expected surface heat flow anomaly is between -25% to -33%. This sedimentation pattern indicates that strong thermal blanketing effects should be present particularly in the CFZ and Louisiana, where sedimentation is fast.

Erosion in the NW GoM marginal plain

During the Neogene, while most of the shelf of the GoM was heavily sedimented offshore, its onshore part was eroded. We used a compilation of 282 vitrinite reflectance data R_0 (electronic supplementary data, table E2) on 34 wells in S. Texas to assess the impact of erosion on the thermal regime. We calculated for each point the maximum temperature T_{max} met by a sample using standard conversion law [Barker and Pawlewicz, 1994]. Details on the calculation are given in appendix A1. We then estimate the difference ΔT between T_{max} and the present-day temperatures at the same depth, from our companion paper [Husson *et al.*, 2008]. Data were

TABLE I. – Synthetic stratigraphic log for the NW GoM [pers. com. from industrial partners]
TABL. I. – *Log stratigraphique synthétique pour le Nord-Ouest du golfe du Mexique.*

Period (Ma)	% shale	% sand
0-3	70	30
3-6.15	86	14
6.15-9.1	90	10
9.1-10.85	84	16
10.85-10.95	69	31
10.95-12	93	7
12-12.8	58	42
12.8-12.85	92	8
12.85-13.55	86	14
13.55-15.47	97	3
15.47-24	80	20
24-36	90	10

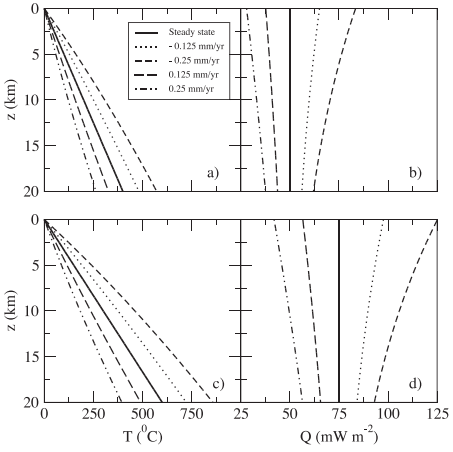

FIG. 1. – Transient effects of erosion and sedimentation on the temperature (left) and heat flow (right) as a function of depth after 25 m.y. a) & b) Q_0 = 50 $mW\ m^{-2}$, c) & d) $Q0$ = 75 $mW\ m^{-2}$. Cp = 1123 $J\ kg^{-1}K^{-1}$, ρ = 2670 kg m^{-3}, k = 2.5 $W\ m^{-1}\ K^{-1}$. No compaction, no radiogenic production. Negative (positive) values indicate erosion (sedimentation) rates. Initial thickness of the conductive layer is 100 km.
FIG. 1. – *Effets thermiques transitoires dus à l'érosion et de la sédimentation sur la température (gauche) et le flux de chaleur (droite) en fonction de la profondeur après 25 m.y.* a) *et* b) Q_0 = 50 $mW\ m^{-2}$, c) *et* d) $Q0$ = 75 $mW\ m^{-2}$. Cp = 1123 $J\ kg^{-1}K^{-1}$, ρ = 2670 $kg\ m^{-3}$, k = 2.5 $W\ m^{-1}\ K^{-1}$. *Pas de compaction ni de production radiogénique. Les valeurs négatives (positives) indiquent les taux d'érosion (sédimentation). L'épaisseur initiale de la couche conductive est de 100 km.*

then averaged for each well. Any departure from the present-day thermal regime (fig. 3a) either indicates an erosive event Δh if the gradient remained constant through time (fig. 3b), a lower present day gradient if the burial depth remained constant (fig. 3c), or a combination of both. The structure of the basin in SW Texas is interpreted from seismic reflection (fig. 4). Oligocene to Early Miocene sediments outcrop on the western edge of the basin. Their high R_0 indicate that they had previously experienced higher temperatures (fig. 3a). The fact that the upper strata do not onlap on the shelf (fig. 4) indicates that they have been eroded and that erosion is at least partly responsible for the discrepancy between present-day temperatures and T_{max}. These higher temperatures correspond to an erosion of more than 3000 m if the gradients are the same as today. Westward in the Maastritchian coals, high reflectance vitrinites (0.58%) are reported at ground level [San Filipo, 1999] and high rank coal (in the bituminous domain) confirm this erosion.

The structural section (fig. 4) indicates that the erosive event postdates the deposition of Eocene to Early Miocene layers. If recent, erosion increases the near-surface gradient with respect to the steady state (fig. 1). Using the abaqus of figure 1, it comes out that if these 3000 m of erosion occurred during the last 25 m.y. at 0.125 mm/yr, the heat flow at surface level is increased by +25% to +35% at 5000 m depth for a basal heat flow ranging between 50 and 75 $mW\ m^{-2}$.

HEAT FLOW MODELLING

Modelling setup

In order to characterize the steady state heat flow Q_{ss}, *i.e.* the total amount of heat flowing out of the Earth surface per unit area in steady state conditions, we need to solve the heat equation (2) through time accounting for the effects of sedimentation, erosion and compaction. Sedimentation and erosion have large spatial extents and can in a first approximation be considered as 1D processes. This approximation does not hold in the deep shelf where many salt domes drastically affect the thermal field.

A sharp thermal gradient increase with depth is systematically observed on the northern shelf of the GoM [Husson *et al.*, 2008]. This thermal gradient increase correlates with a fluid pressure increase, from an upper "near-hydrostatic" (low-P) domain to a lower "near-lithostatic" (high-P) domain at depth. The depth of the transition increases eastward from ~2500 meters below seafloor in the western GoM, to 4000-4500 meters offshore Louisiana and correlates with the thickness of the sedimentary layers. The most acknowledged explanation is a variation in conductivity controlled by the pressure field [Jessop, 1990], but we consider that free convection could also be a mechanism [Husson *et al.,* 2008], which also has the effect to modify the apparent conductivity between an upper, low-P sedimentary unit and a lower, overpressured unit. This sharp transition in conductivity is given by the ratio between the lower and upper gradients and is set to its minimum value of 1.5 in the following models. Because the pressure field within the GoM margin appears in a first approximation to correlate with the age of the sediments, this increased effective conductivity is attributed to Plio-Quaternary sediments rather than being attributed to a time-invariant layer of constant thickness.

Thermal and stratigraphic data were compiled for 166 significant wells. We used a selection of stratigraphic data and reservoir temperatures (RT) from industrial databases, made available as electronic supplementary material (tables E1 and E3). We solve the heat equation in 1D on each well, accounting for variable lithologies (blends of sandstones and shales), and compaction. We used a common synthetic lithostratigraphic column for all the models (table I). Sediments are shale-dominated [Galloway *et al.,* 2000; Galloway, 2001], which suggests that lithological variations have only a minor influence on the modeling results. As no paleo-indicators such as kerogen maturation are available to us offshore to calibrate the past heat flow, we assume a constant basal (beneath the sedimentary pile) heat flow through time. Details on the modelling parameters, petrophysical properties and back-stripping techniques are given in the appendix A2.

The present-day reduced heat flow (at the base of the radiogenic-rich layer) is determined by minimizing the misfit between the predicted and observed geotherms. This reduction has only been carried out for the RT data, as they are more reliable than bottom hole temperatures (BHT). The steady state heat flow is the sum of the reduced heat

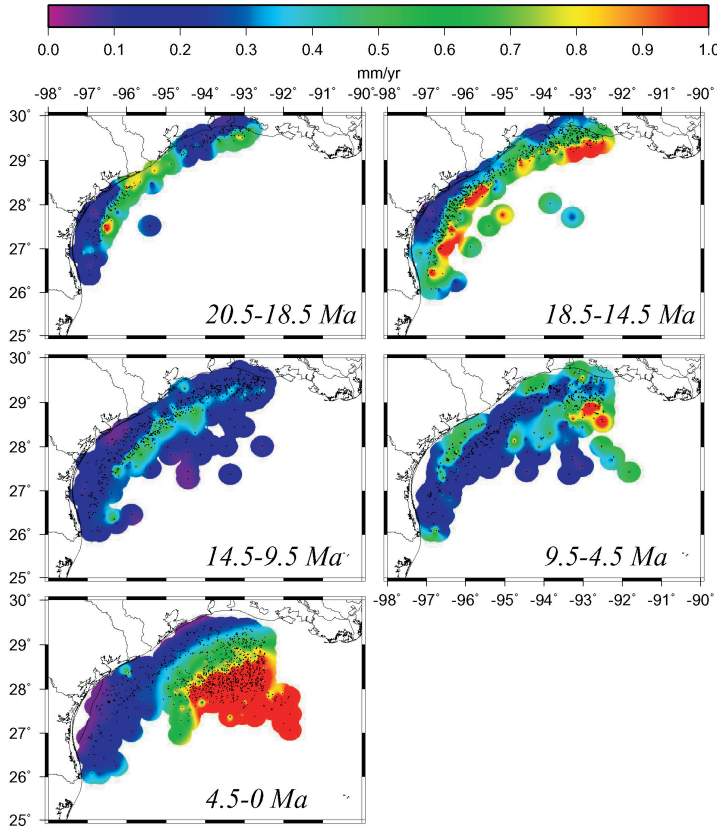

FIG. 2. – Mean sedimentation rates from mid-Miocene, on-shore Texas. Black dots indicate data location for the corresponding time period.
FIG. 2. – *Taux de sédimentation au Miocène moyen, en offshore Texas. Les points noirs indiquent la localisation des données à chaque période.*

flow and the total radiogenic production within the basement and the sedimentary pile.

Results and discussion

The numerical values of the results are given as electronic supplementary data (table E4). Maximum Q_{ss} values are greater than 90 $mW\,m^{-2}$ in the CFZ and minimum values are about 45 $mW\,m^{-2}$. Q_{ss} (fig. 5a) outlines the trend of the CFZ, where the mean value is ~80 $mW\,m^{-2}$ while lower values are found shoreward in the ITZ (~60 $mW\,m^{-2}$). This high basal heat flow area extends to the NE at least to the western zone of Louisiana. Q_{ss} is controlled by long-term deep-seated processes. Therefore the CFZ thermal high is the result of a lithospheric-scale process. The excess heat flow results from heat advection from the asthenosphere to the thinned lithosphere. Using Sclater and Christie [1980] after McKenzie [1978], a Q_{ss} increase by 30-40% in the CFZ with respect to the ITZ indicates the existence of a recent significant stretching event (< 25 m.y.), the stretching factor β being between 2 and 4. In other terms, the lithosphere beneath the CFZ has to be as thin as 30 to 60 km if the regional lithospheric thickness is ~120 km thick. The fact that the CFZ is the main fault zone is compatible with this conclusion. We thus interpret the CFZ, where the Neogene sedimentary pile can be thicker than 8000 m, as a Neogene rift area. Of course, because the lithospheric rifting is now deeply buried, its surface heat flow expression is smoothed. Its wavelength cannot be defined because we lack control on the SE side. However, since the increase of Q_{ss} can be measured at surface level, the wavelength at depth is greater than 100 km, if the lithosphere is 30-60 km thick [Jaupart

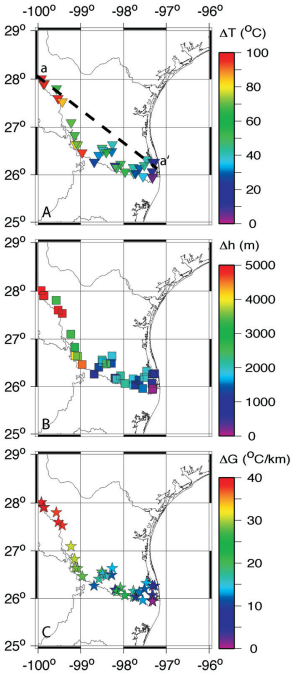

FIG. 3. – a) Difference between the current temperature and the maximum temperature recorded by the vitrinite in the sediments (ΔT , triangles); b) Equivalent maximum erosion Δh (squares); c) Equivalent maximum gradient change ΔG (stars). Sampling depth ranges from 1500 m to 5000 m. aa': location of the cross-section. Δh is calculated assuming a constant gradient through time, identical to the present one; ΔG is calculated assuming that the present burial depth is the maximum depth met by the sample.
FIG. 3. – a) *Différence entre températures actuelles et les températures maximales enregistrées par la vitrinite dans les sédiments (ΔT , triangles); b) Equivalent en érosion maximale Δh (carrés); c) Equivalent en changement de gradient ΔG (étoiles). La profondeur d'échantillonnage varie de 1500 m to 5000 m.* aa': *localisation de la coupe sur la figure 4. Δh est calculé en supposant un gradient constant dans le temps; DG est calculé en supposant que la profondeur d'enfouissement actuelle est la profondeur maximale connue par l'échantillon.*

and Mareschal, 1999]. In contrast with the steady state heat flow Q_{ss}, the transient state heat flow Q_{ts} that is affected by transient effects shows a much lower variation (~55 $mW\,m^{-2}$ and ~45 $mW\,m^{-2}$ in the CFZ and ITZ, respectively, fig. 5b). This smoothing of the heat flow anomaly is due to the competition between the sedimentation blanketing effect and the lithospheric thinning: the maximum reduced heat flow occurs where maximum lithospheric thinning is. But this deep-seated process is counteracted by a shallow blanketing effect since maximum sedimentation occurs where maximum thinning is. This is illustrated by the overall positive correlation between Q_{ss} and mean Neogene sedimentation rates *Vs* (correlation coefficient = 0.57) while the correlation is irrelevant between Q_{ts} and *Vs* (correlation coefficient = 0.22) (fig. 6).

One might wonder how this heat flow structure connects to the neighboring areas. In Louisiana, the high sedimentation from the Mississipi delta has a strong effect on the surface heat flow. For such amount of sedimentation (~0.2 mm/yr for 25 m.y.), the measured heat flow and thermal gradient underestimates Q_{ss} and the steady state gradient by about 35% at 5000 m depth (see abaqus fig. 1). Therefore the measured gradient ~32°*C/km* [Husson *et al.*, 2008] hides a ~50°*C/km* steady state gradient and the thermal blanketing effect of sedimentation appears to hide the prolongation of the warm CFZ thermal high. To the NW of the ITZ, because sedimentation rates are low, the deep thermal gradient reflects a steady thermal state and is proportional to Q_{ss}. Further to the NW onshore Texas, we showed in previous section that the total recent erosion is high (> 0.12 mm/yr for 25 m.y.). Therefore, the surface thermal gradient and heat flow are increased by erosion and higher than the steady state gradient and Q_{ss}. For such amount of erosion, the transient heat flow and gradient overestimate Q_{ss} and steady state gradient by 20% at 5000 m depth. Therefore, we conclude that the measured transient ~30°*C/km* gradient [Husson *et al.*, 2008] hides a ~25°*C/km* steady state gradient onshore Texas.

CONCLUSIONS

This study shows that significant so-called steady-state Q_{ss} variations occur in the NW GoM margin. We computed 166 such heat flow estimates corrected for the transient effects of sedimentation, radiogenic production, and compaction. Thermal processes in the NW GoM are extremely active and opposite processes tend to cancel their effects. The

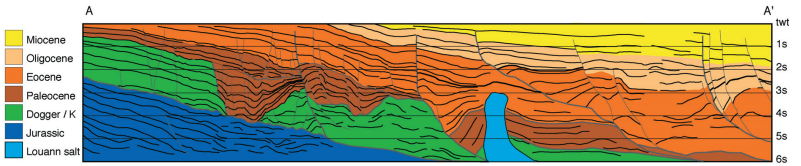

FIG. 4. – Cross-section in S. Texas (form unpublished seismic data). Location figure 3a.
FIG. 4. – *Coupe du Sud Texas (données sismiques non publiées). Localisation figure 3a.*

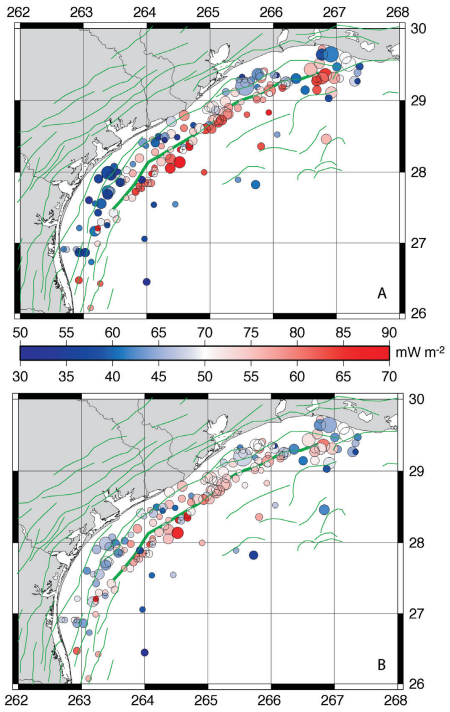

FIG. 5. – Steady state heat flow Q_{ss} (a), transient state heat flow Q_{ts} (b), i.e. including the thermal effects of transient processes. Symbol size increases with the number of calibration temperature values.
FIG. 5. – *Flux de chaleur en régime permanent Q_{ss} (a), flux de chaleur en régime transitoire Q_{ts} (b), c'est-à-dire en corrigeant des effets thermiques transitoires. La taille des symboles dépend du nombre de données.*

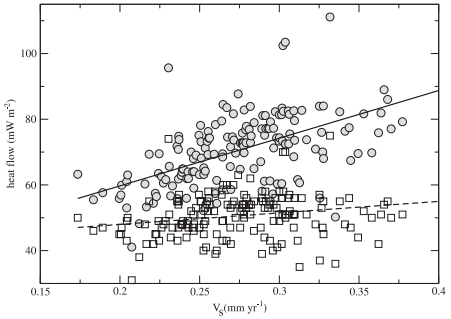

FIG. 6. – Heat flow vs mean sedimentation rate (over the last 25 m.y.). Circles: steady state heat flow Q_{ss}; regression: Q_{ss}=*30.7+145Vs* (correlation coef.: 0.57); squares: transient state heat flow Q_{ts}. Q_{ts}=*40.1+35Vs*, (correlation coef.: 0.22).
FIG. 6. – *Flux de chaleur et taux de sédimentation (sur les derniers 25 m.y.). Cercles: régime permanent Q_{ss}; régression: Q_{ss}=30.7+145Vs (coefficient de corrélation: 0.57); carrés : régime transitoire Q_{ts}. Q_{ts} = 40.1+35 Vs, (coefficient de corrélation: 0.22).*

surprising correlation between Q_{ss} and mean Neogene sedimentation rate (fig. 6) summarizes this behavior: removing the transient thermal processes to restore Q_{ss} allows us to reveal significant variations (> 20 *mW m*$^{-2}$) of the deep thermal field, while the transient state thermal regime appears more homogeneous.

The main thermal feature evidenced by this study is the CFZ thermal high. This major fault system is accompanied by a thinning of the Mesozoic layers. Because it is also correlated with the thermal high, we propose that the CFZ corresponds to a zone of Neogene lithospheric-scale thinning. Since high Q_{ss} continue toward the NE of the CFZ, this lithospheric thinning may continue on the shelf of Louisiana. On the other hand, to the NW, onshore, Q_{ss} is low, but the transient effects of erosion increase its apparent magnitude.

Appendices

A1) Vitrinite reflectance

We use the equation of Barker and Pawlewicz [1994, comparable to that of Burnham and Sweeney, 1989], and write T_{max} = $(In(Ro) + (1.68) / 0.0124$, where T_{max} is the maximum temperature met by the sample.

A2) Thermal modelling

The temperature variation through time is in one dimension

$$(\rho C_p)_b \frac{\partial T}{\partial t} = \frac{\partial}{\partial z}\left(k \frac{\partial T}{\partial z}\right) + A - [(1-\phi)(\rho C_p)_m U(t)_m + \phi(\rho C_p)_w U(t)_w] \frac{\partial T}{\partial z},$$

where U(t) denotes the velocity of the matrix *m*, water *w* or bulk rock *b* in 3D at time *t*, *z* is depth, *k*, *Cp* and ρ are the lithology – and depth – dependent conductivity, heat capacity and density, A is the radiogenic heat generation. The previous equation is solved in the vertical dimension using

Genex finite difference program, where *U(t)* is the sedimentation rates. Heat production is always set to 1 µW m^{-3}, which is generally found in this area [McKenna and Sharp, 1998]. The thermal conductivity is given by

$k = km\ (1 - \phi)kw\ \phi$

where k_w is the water thermal conductivity (0.61 W m^{-1} K^{-1}) and k_m is the sediment matrix thermal conductivity.

The porosity ϕ of a mixed lithology is given by

$$\frac{1}{1-\phi(z)} = \sum_i \frac{C_i}{1-\phi_i(z)},$$

where C_i is the volume of the lithologic component *i*, on a fully compacted basis, and $\phi_i(z)$ is the porosity of a component at a given depth *z*. (table A1)

The temperature dependence of conductivity is given by

$$k = k_{273}\left(\frac{1}{1+\alpha(T-273)}\right),$$

where k_{273} is the conductivity at 273 K and α the temperature dependence of conductivity factor. In order to account for the convective component in the upper unit of the sediments, we multiply the conductivity by a factor *Nu* = 1.5 in the upper section (see text). This value is given by the ratio between the upper unit gradient and the lower one (low-P and high-P sections, see companion paper [Husson *et al.*, 2008]). Offshore Texas, we fix the rupture depth between the sections to ~2500 m and we take a minimum value of *Nu* = 1.5.

The heat capacity is given by

$$Cp = \frac{1}{\rho}[\rho_w C_w \phi + \rho_m C_m (1-\phi)],$$

where C_w is the water heat capacity (4.185 10^6 J kg^{-1} K^{-1}), ρ_w is the water density (1.030 kg m^{-3}), ρ_m the matrix conductivity, and C_m the matrix heat capacity. For a blend of lithologies, the average matrix conductivity is the arithmetic mean of the independent lithologies heat capacities. Surface temperature is always set to 25°C.

The basement is defined as a 20 km thick conductive layer (with A = 1 µW m^{-3}), acting as a buffer below which a constant reduced heat flow is applied.

Thermal parameters are synthetized in table A2.

TABLE A1. – Porosity depths arrays (%) used for 1D thermal modelling.
TABL. A1. – *Porosité (en %) utilisée pour la modélisation 1D.*

z (m)	% sandstone	% shale
0	42	70
100	36	50
200	34	42
500	30	32
1000	24	23
1500	20	18
2000	16	14
3000	11	10
5000	7	6
8000	6	5.2
20000	2	2

TABLE A2. – Thermal parameters used for thermal modelling.
TABL. A2. – *Paramètres thermiques utilisés pour la modélisation.*

parameter	sandstone	shale
α (K^{-1})	3 10^{-3}	5 10^{-4}
k_m (W m^{-1} K^{-1})	3.50 (N u = 1) 5.25 (N u = 1.5)	1.90 (N u = 1) 2.85 (N u = 1.5)
ρ (kg m^{-3})	2653	2800
C_m (J kg^{-1} K^{-1})	2.9 10^6	2.3 10^6

References

BARKER C. & PAWLEWICZ M. (1994). – Calculation of vitrinite reflectance from thermal histories and peak temperatures. a comparison of methods. *In*: P. MUKHOPADHAYAY and W. DOW, Eds., Vitrinite reflectance as a maturity parameter: applications and limitations. – *ACS Symposium Series*, 216-229.

BURNHAM A. & SWEENEY J. (1989). – A chemical kinetic model of vitrinite reflectance maturation, – *Geochim. Cosmochim. Acta*, **53**, 2649-2657.

CARSLAW H. & JAEGER J. (1959). – Conduction of heat in solids. – Clarendon Press, Oxford.

GALLOWAY W. (2001). – Cenozoic evolution of sediment accumulation in deltaic and shore-zone depositional systems, northern Gulf of Mexico basin. – *Mar. Petrol. Geol.*, **18**, 1031-1040.

GALLOWAY W., GANEY-CURRY P., LI X. & BUFFLER R. (2000). – Cenozoic depositional history of the Gulf of Mexico basin. – *AAPG Bull.*, **84**, 1743-1774.

HUSSON L., HENRY P. & LE PICHON X. (2008). – Thermal regime of the NW shelf of the Gulf of Mexico. Part A) Thermal and pressure fields. – *Bull. Soc. géol. Fr.*, **179**, 2, 129-137.

HUSSON L. & MORETTI I. (2002). – Thermal regime of fold and thrustbelts. An application to the Bolivian Sub-Andean zone. – *Tectonophysics*, **345**, 253-280.

JAUPART C. & MARESCHAL J.C. (1999). – The thermal structure and thickness of continental roots. – *Lithos*, **48**, 93-114.

JESSOP A.M. (1990). – Thermal geophysics. – Elsevier, Amsterdam, 316 p.

LUCAZEAU F. & LE DOUARAN S. (1985). – The blanketing effect of sediments in basins formed by extension: a numerical model. Application to the Gulf of Lion and Viking graben. – *Earth Planet. Sci. Lett.*, **74**, 92-102.

MCKENNA T. & SHARP J. (1998). – Radiogenic heat production of the Gulf of Mexico basin, south Texas. – *AAPG Bull.*, **82**, 484-496.

MCKENZIE D. (1978). – Some remarks on the development of sedimentary basins. – *Earth Planet. Sci. Lett.*, **40**, 25-32.

SANFILIPO J. (1999). – Some speculations on coal-rank anomalies of the south Texas Gulf province and adjacent areas of Mexico and their impact on coal-bed methane and source rock potential. *In*: P. WARWICK, C. AUBOURG & J. WILLETT, Eds, Tertiary coals in South Texas; anomalous cannel-like coals of Webb County (Claiborne Group, Eocene) and lignites of Atascosa County (Jackson Group, Eocene); geologic setting, character, source-rock and coal-bed methane potential. – USGS Open File Report, **99-301**.

SCLATER J. & CHRISTIE P. (1980). – Continental stretching: an explanation of the post-mid-Cretaceous subsidence of the central North Sea basin. – *J. Geophys. Res.*, **85**, 3711–3739.

Bibliographie

Allègre, C. J., Courtillot, V., Tapponnier, P., Hirn, A., Mattauer, M., Coulon, C., Jaeger, J. J., Achache, J., Schärer, U., Marcoux, J., Burg, J. P., Girardeau, J., Armijo, R., Gariépy, C., Göpel, C., Tindong, L., Xuchang, X., Chenfa, C., Guangqin, L., Baoyu, L., Jiwen, T., Naiwen, W., Guoming, C., Tonglin, H., Xibin, W., Wanming, D., Huaibin, S., Yougong, C., Ji, Z., Hongrong, Q., Peisheng, B., Songchan, W., Bixiang, W., Yaoxiu, Z., & Xu, R., 1984. Structure and evolution of the Himalaya-Tibet orogenic belt, *Nature* , **307**, 17–22.

Argand, E., 1924. La tectonique de lAsie, *XIII Intern. Geol. Congr.*, pp. 171–372.

Atwater, T., 1970. Implications of plate tectonics for the Cenozoic tectonic evolution of western North America, *Bull. Geol. Soc. Amer.*, **81**, 3513–3536.

Avouac, J. & Burov, E., 1996. Erosion as a driving mechanism of intracontinental mountain growth, *Journal of Geophysical Research*, **101**(B8), 17747–17769.

Baumont, D., Paul, A., Zandt, G., Beck, S., & Pedersen, H., 2002. Lithospheric structure of the central Andes based on surface wave dispersion, *Journal of Geophysical Research*, **107**.

Beaumont, C., Jamieson, R., Nguyen, M., & Lee, B., 2001. Himalayan tectonics explained by extrusion of a low-viscosity crustal channel coupled to focused surface denudation, *Nature*, **414**(6865), 738–742.

Becker, T. W., 2006. On the effect of temperature and strain-rate dependent viscosity on global mantle flow, net rotation, and plate-driving forces, *Geophysical Journal International*, **167**, 943–957.

Becker, T. W., 2008. Azimuthal seismic anisotropy constrains net rotation of the lithosphere, *Geophysical Research Letters*, **35**, 5303–+.

Becker, T. W., Conrad, C. P., Buffett, B., & Müller, R. D., 2009. Past and present seafloor age distributions and the temporal evolution of plate tectonic heat transport, *Earth and Planetary Science Letters*, **278**, 233–242.

Bellahsen, N., Faccenna, C., & Funiciello, F., 2005. Dynamics of subduction and plate motion in laboratory experiments : Insights into the "plate tectonics" behavior of the Earth, *Journal of Geophysical Research*, **110**, 1401–+.

Bellahsen, N., Fournier, M., d'Acremont, E., Leroy, S., & Daniel, J. M., 2006. Fault reactivation and rift localization : Northeastern Gulf of Aden margin, *Tectonics*, **25**, C1007+.

Bird, P., 1991. Lateral extrusion of lower crust from under high topography, in the isostatic limit, *Journal of Geophysical Research*, **96**, 10275–+.

Bird, P., 1998. Testing hypotheses on plate-driving mechanisms with global lithosphere models including topography, thermal structure, and faults, *Journal of Geophysical Research*, **103**, 10115–10130.

Brun, J.-P. & Faccenna, C., 2008. Exhumation of high-pressure rocks driven by slab rollback, *Earth and Planetary Science Letters*, **272**, 1–2.

Capitanio, F. A., Morra, G., & Goes, S., 2007. Dynamic models of downgoing plate-buoyancy driven subduction : Subduction motions and energy dissipation, *Earth and Planetary Science Letters*, **262**, 284–297.

Christensen, U. & YuenN, D., 1984. The interaction of a subducting lithosphere slab with a chemical or phase boundary, *Journal of Geophysical Research*, **89**(NB6), 4389–4402.

Clark, M. & Royden, L., 2000. Topographic ooze : Building the eastern margin of Tibet by lower crustal flow, *Geology*, **28**(8), 703–706.

Cogné, J.-P., Humler, E., & Courtillot, V., 2006. Mean age of oceanic lithosphere drives eustatic sea-level change since Pangea breakup, *Earth and Planetary Science Letters*, **245**, 115–122.

Conrad, C. P. & Molnar, P., 1999. Convective instability of a boundary layer with temperature-and strain-rate-dependent viscosity in terms of 'available buoyancy', *Geophysical Journal International*, **139**, 51–68.

d'Acremont, E., Leroy, S., Beslier, M.-O., Bellahsen, N., Fournier, M., Robin, C., Maia, M., & Gente, P., 2005. Structure and evolution of the eastern Gulf of Aden conjugate margins from seismic reflection data, *Geophysical Journal International*, **160**, 869–890.

Dahlen, F. A., 1990. Critical Taper Model of Fold-and-Thrust Belts and Accretionary Wedges, *Annual Review of Earth and Planetary Sciences*, **18**, 55–+.

Dahlen, F. A., Suppe, J., & Davis, D., 1984. Mechanics of fold-and-thrust belts and accretionary wedges Cohesive Coulomb theory, *Journal of Geophysical Research*, **89**, 10087–10101.

Darwin, C., 1846. *Geological observations on South America. Being the third part of the geology of the voyage of the Beagle, under the command of Capt. Fitzroy, R.N. during the years 1832 to 1836. London*, Smith Elder and Co.

Davis, D., Suppe, J., & Dahlen, F. A., 1983. Mechanics of fold-and-thrust belts and accretionary wedges, *Journal of Geophysical Research*, **88**, 1153–1172.

DeMets, C., Gordon, R., Argus, D., & Stein, S., 1994. Effect of recent revisions to the geomagnetic reversal timescale on estimates of current plate motions, *Geophysical Research Letters*, **21**(20), 2191–2194.

Di Giuseppe, E., van Hunen, J., Funiciello, F., Faccenna, C., & Giardini, D., 2008. Slab stiffness control of trench motion : Insights from numerical models, *Geochemistry, Geophysics, Geosystems*, **9**, 2014–+.

England, P. & Houseman, G., 1985. Role of lithospheric strength heterogeneities in the tectonics of Tibet and neighbouring regions, *Nature* , **315**, 297–301.

England, P. & McKenzie, D., 1982. A thin viscous sheet model for continental deformation, *Geophysical Journal International*, **70**, 295–321.

England, P. & McKenzie, D., 1983. Correction to : a thin viscous sheet model for continental deformation, *Geophysical Journal International*, **73**, 523–532.

Faccenna, C., Davy, P., Brun, J., Funiciello, R., Giardini, D., Mattei, M., & Nalpas, T., 1996. The dynamics of back-arc extension : An experimental approach to the opening of the Tyrrhenian Sea, *Geophysical Journal International*, **126**(3), 781–795.

Faccenna, C., Becker, T., Lucente, F., Jolivet, L., & Rossetti, F., 2001. History of subduction and back-arc extension in the Central Mediterranean, *Geophysical Journal International*, **145**(3), 809–820.

Foley, B. J. & Becker, T. W., 2009. Generation of plate-like behavior and mantle heterogeneity from a spherical, viscoplastic convection model, *Geochemistry, Geophysics, Geosystems*, **10**, 8001–+.

Fournier, M., Bellahsen, N., Fabbri, O., & Gunnell, Y., 2004. Oblique rifting and segmentation of the NE Gulf of Aden passive margin, *Geochemistry, Geophysics, Geosystems*, **5**, 11005–+.

Fukao, Y., Widiyantoro, S., & Obayashi, M., 2001. Stagnant slabs in the upper and lower mantle transition region, *Reviews of Geophysics*, **39**, 291–324.

Funiciello, F., Faccenna, C., Giardini, D., & Regenauer-Lieb, K., 2003. Dynamics of retreating slabs : 2. Insights from three-dimensional laboratory experiments, *Journal of Geophysical Research*, **108**, 2207–+.

Garzione, C. N., Hoke, G. D., Libarkin, J. C., Withers, S., MacFadden, B., Eiler, J., Ghosh, P., & Mulch, A., 2008. Rise of the Andes, *Science*, **320**(5881), 1304–1307.

Gerbault, M., Martinod, J., & Hérail, G., 2005. Possible orogeny-parallel lower crustal flow and thickening in the Central Andes, *Tectonophysics*, **399**, 59–72.

Goetze, C., 1978. The Mechanisms of Creep in Olivine, *Royal Society of London Philosophical Transactions Series A*, **288**, 99–119.

Goetze, C. & Evans, B., 1979. Stress and temperature in the bending lithosphere as constrained by experimental rock mechanics, *Geophysical Journal International*, **59**, 463–478.

Grigné, C., Labrosse, S., & Tackley, P. J., 2007. Convection under a lid of finite conductivity in wide aspect ratio models : Effect of continents on the wavelength of mantle flow, *Journal of Geophysical Research (Solid Earth)*, **112**, 8403–+.

Griot, D.-A., Montagner, J.-P., & Tapponnier, P., 1998. Phase velocity structure from Rayleigh and Love waves in Tibet and its neighboring regions, *Journal of Geophysical Research*, **103**, 21215–21232.

Gripp, A. E. & Gordon, R. G., 2002. Young tracks of hotspots and current plate velocities, *Geophysical Journal International*, **150**, 321–361.

Gudmundsson, O. & Sambridge, M., 1998. A regionalized upper mantle (RUM) seismic model, *Journal of Geophysical Research*, **103**(B4), 7121–7136.

Guillaume, B., Martinod, J., Husson, L., Roddaz, M., & Riquelme, R., 2009. Neogene uplift of central eastern Patagonia : Dynamic response to active spreading ridge subduction ?, *Tectonics*, **28**, C2009+.

Gurnis, M., 1992. Rapid Continental Subsidence Following the Initiation and Evolution of Subduction, *Science*, **255**, 1556–1558.

Gurnis, M., 1993. Phanerozoic marine inundation of continents driven by dynamic topography above subducting slabs, *Nature* , **364**, 589–593.

Gurnis, M. & Zhong, S., 1991. Generation of long wavelength heterogeneity in the mantle by the dynamic interaction between plates and convection, *Geophysical Research Letters*, **18**, 581–584.

Haq, B. U., Hardenbol, J., & Vail, P. R., 1987. Chronology of Fluctuating Sea Levels since the Triassic, *Science*, **235**, 1156–1167.

Hays, J. D. & Pitman, W. C., 1973. Lithospheric Plate Motion, Sea Level Changes and Climatic and Ecological Consequences, *Nature* , **246**, 18–22.

Heidbach, O., Müller, B., Fuchs, K., Wenzel, F., Reinecker, J., Tingay, M., Sperner, B., Cadet, J.-P., & Rossi, P., 2007. World Stress Map Published, *EOS Transactions*, **88**, 504–504.

Heller, P. L. & Angevine, C. L., 1985. Sea-level cycles during the growth of Atlantic-type oceans, *Earth and Planetary Science Letters*, **75**, 417–426.

Heuret, A. & Lallemand, S., 2005. Plate motions, slab dynamics and back-arc deformation, *Physics of the Earth and Planetary Interiors*, **149**(1-2), 31–51.

Hirth, G. & Kohlstedt, D. L., 1995a. Experimental constraints on the dynamics of the partially molten upper mantle : Deformation in the diffusion creep regime, *Journal of Geophysical Research*, **100**, 1981–2001.

Hirth, G. & Kohlstedt, D. L., 1995b. Experimental constraints on the dynamics of the partially molten upper mantle 2. Deformation in the dislocation creep regime, *Journal of Geophysical Research*, **100**, 15441–15450.

Houseman, G. A., McKenzie, D. P., & Molnar, P., 1981. Convective instability of a thickened boundary layer and its relevance for the thermal evolution of continental convergent belts, *Journal of Geophysical Research*, **86**, 6115–6132.

Huismans, R., Podladchikov, Y., & Cloetingh, S., 2001. Dynamic modeling of the transition from passive to active rifting, application to the Pannonian basin, *Tectonics*, **20**(6), 1021–1039.

Iaffaldano, G., Bunge, H.-P., & Dixon, T. H., 2006. Feedback between mountain belt growth and plate convergence, *Geology*, **34**, 893–+.

Jarrard, R. D., 1986. Relations Among Subduction Parameters (Paper 5R0903), *Reviews of Geophysics*, **24**, 217–+.

Jaupart, C. & Mareschal, J.-C., 2003. Constraints on Crustal Heat Production from Heat Flow Data, *Treatise on Geochemistry*, **3**, 65–84.

Jaupart, C., Molnar, P., & Cottrell, E., 2007. Instability of a chemically dense layer heated from below and overlain by a deep less viscous fluid, *Journal of Fluid Mechanics*, **572**, 433–469.

Jolivet, L. & Faccenna, C., 2000. Mediterranean extension and the Africa-Eurasia collision, *Tectonics*, **19**(6), 1095–1106.

Kárason, H. & van der Hilst, R. D., 2001. Tomographic imaging of the lowermost mantle with differential times of refracted and diffracted core phases, *Journal of Geophysical Research*, **106**, 6569–6588.

Kirby, S. H., 1983. Rheology of the Lithosphere, *Reviews of Geophysics*, **21**, 1458–1487.

Kirby, S. H. & Kronenberg, A. K., 1987. Rheology of the Lithosphere : Selected Topics (Paper 7R0302), *Reviews of Geophysics*, **25**, 1219–+.

Kreemer, C., 2009. Absolute plate motions constrained by shear wave splitting orientations with implications for hotspot motions and mantle flow, *Journal of Geophysical Research*, **114**.

Kreemer, C., Lavallée, D. A., Blewitt, G., & Holt, W. E., 2006. On the stability of a geodetic no-net-rotation frame and its implication for the International Terrestrial Reference Frame, *Geophysical Research Letters*, **33**, 17306–+.

Lallemand, S., Heuret, A., & Boutelier, D., 2005. On the relationships between slab dip, back-arc stress, upper plate absolute motion, and crustal nature in subduction zones, *Geochemistry, Geophysics, Geosystems*, **6**, 9006–+.

Le Pichon, X., 1968. Sea-Floor Spreading and Continental Drift, *Journal of Geophysical Research*, **73**, 3661–+.

Lee, C.-T. A., 2003. Compositional variation of density and seismic velocities in natural peridotites at STP conditions : Implications for seismic imaging of compositional heterogeneities in the upper mantle, *Journal of Geophysical Research*, **108**, 2441–+.

Lithgow-Bertelloni, C. & Guynn, J., 2004. Origin of the lithospheric stress field, *Journal of Geophysical Research*, **109**(B1).

Loiselet, C., Husson, L., & Braun, J., 2009. From longitudinal slab curvature to slab rheology, *Geology*, **37**(8), 747–750.

Long, M. D. & Silver, P. G., 2008. The Subduction Zone Flow Field from Seismic Anisotropy : A Global View, *Science*, **319**, 315–.

Maggi, A., Jackson, J. A., McKenzie, D., & Priestley, K., 2000. Earthquake focal depths, effective elastic thickness, and the strength of the continental lithosphere, *Geology*, **28**, 495–+.

Mareschal, J. C. & Jaupart, C., 2004. Variations of surface heat flow and lithospheric thermal structure beneath the North American craton, *Earth and Planetary Science Letters*, **223**, 65–77.

Martinod, J., Funiciello, F., Faccenna, C., Labanieh, S., & Regard, V., 2005. Dynamical effects of subducting ridges : insights from 3-D laboratory models, *GEOPHYSICAL JOURNAL INTERNATIONAL*, **163**(3), 1137–1150.

McKenzie, D. & Jackson, J., 2002. Conditions for flow in the continental crust, *Tectonics*, **21**(6), 060000–1.

McKenzie, D. P. & Parker, R. L., 1967. The North Pacific : an Example of Tectonics on a Sphere, *Nature* , **216**, 1276–1280.

Meade, B. J. & Conrad, C. P., 2008. Andean growth and the deceleration of South American subduction : Time evolution of a coupled orogen-subduction system, *Earth and Planetary Science Letters*, **275**, 93–101.

Miller, K. G., Kominz, M. A., Browning, J. V., Wright, J. D., Mountain, G. S., Katz, M. E., Sugarman, P. J., Cramer, B. S., Christie-Blick, N., & Pekar, S. F., 2005. The Phanerozoic Record of Global Sea-Level Change, *Science*, **310**, 1293–1298.

Minster, J. B. & Jordan, T. H., 1978. Present-day plate motions, *Journal of Geophysical Research*, **83**, 5331–5354.

Mitrovica, J. X., Beaumont, C., & Jarvis, G. T., 1989. Tilting of continental interiors by the dynamical effects of subduction, *Tectonics*, **8**, 1079–1094.

Molnar, P. & Houseman, G. A., 2004. The effects of buoyant crust on the gravitational instability of thickened mantle lithosphere at zones of intracontinental convergence, *Geophysical Journal International*, **158**, 1134–1150.

Molnar, P., Houseman, G. A., & Conrad, C. P., 1998. Rayleigh-Taylor instability and convective thinning of mechanically thickened lithosphere : effects of non-linear viscosity decreasing exponentially with depth and of horizontal shortening of the layer, *Geophysical Journal International*, **133**, 568–584.

Morgan, W. J., 1968. Rises, Trenches, Great Faults, and Crustal Blocks, *Journal of Geophysical Research*, **73**, 1959–+.

Moucha, R., Forte, A. M., Mitrovica, J. X., Rowley, D. B., Quéré, S., Simmons, N. A., & Grand, S. P., 2008. Dynamic topography and long-term sea-level variations : There is no such thing as a stable continental platform, *Earth and Planetary Science Letters*, **271**, 101–108.

Müller, R. D., Sdrolias, M., Gaina, C., & Roest, W. R., 2008. Age, spreading rates, and spreading asymmetry of the world's ocean crust, *Geochemistry, Geophysics, Geosystems*, **9**, 4006–+.

Parsons, B., 1982. Causes and consequences of the relation between area and age of the ocean floor, *Journal of Geophysical Research*, **87**, 289–302.

Patriat, P. & Achache, J., 1984. India-Eurasia collision chronology has implications for crustal shortening and driving mechanism of plates, *Nature*, **311**, 615–621.

Pearce, J. A., Leat, P. T., Barker, P. F., & Millar, I. L., 2001. Geochemical tracing of Pacific-to-Atlantic upper-mantle flow through the Drake passage, *Nature* , **410**, 457–461.

Pindell, J., Cande, S., Pitmaniii, W., Rowley, D., Dewey, J., Labrecque, J., & Haxby, W., 1988. A plate-kinematic framework for models of Caribbean evolution, *Tectonophysics*, **155**, 121–138.

Rangin, C., Le Pichon, X., Martinez-Reyes, J., & Aranda-Garcia, M., 2008. Gravity tectonics and plate motions - The western margin of the Gulf of Mexico - Introduction, *Bull. Soc. Géol. Fr.*, **179**(2), 107–116.

Rey, P. F. & Houseman, G., 2006. The impact of body forces on Archaean orogenic processes, *Geochimica et Cosmochimica Acta Supplement*, **70**, 527–+.

Ribe, N. M., Stutzmann, E., Ren, Y., & van der Hilst, R., 2007. Buckling instabilities of subducted lithosphere beneath the transition zone, *Earth and Planetary Science Letters*, **254**, 173–179.

Ricard, Y., Fleitout, L., & Froidevaux, C., 1984. Geoid heights and lithospheric stresses for a dynamic earth, *Annales Geophysicae*, **2**, 267–285.

Ricard, Y., Richards, M., Lithgow-Bertelloni, C., & Le Stunff, Y., 1993. A geodynamic model of mantle density heterogeneity, *Journal of Geophysical Research*, **98**, 21895–21909.

Richardson, R. M., 1992. Ridge forces, absolute plate motions, and the intraplate stress field, *Journal of Geophysical Research*, **97**, 11739–+.

Rowley, D., 2002. Rate of plate creation and destruction : 180 Ma to present, *Geol. Soc. Am. Bull.*, **114**(8), 927–933.

Royden, L., Burchfiel, B., King, R., Wang, E., Chen, Z., Shen, F., & Liu, Y., 1997. Surface deformation and lower crustal flow in eastern Tibet, *Science*, **276**(5313), 788–790.

Royden, L. H., 1993. Evolution of retreating subduction boundaries formed during continental collision, *Tectonics*, **12**, 629–638.

Royden, L. H. & Husson, L., 2006. Trench motion, slab geometry and viscous stresses in subduction systems, *Geophysical Journal International*, **167**, 881–905.

Royden, L. H., Burchfiel, B. C., & van der Hilst, R. D., 2008. The geological evolution of the Tibetan plateau, *Science*, **321**(5892), 1054–1058.

Russo, R. M. & Silver, P. G., 1996. Cordillera formation, mantle dynamics, and the Wilson cycle, *Geology*, **24**, 511–+.

Schellart, W. P., 2004. Kinematics of subduction and subduction-induced flow in the upper mantle, *Journal of Geophysical Research*, **109**, 7401–+.

Schellart, W. P., Freeman, J., Stegman, D. R., Moresi, L., & May, D., 2007. Evolution and diversity of subduction zones controlled by slab width, *Nature* , **446**, 308–311.

Schmalholz, S. M., Kaus, B. J., & Burg, J.-P., 2009. Stress-strength relationship in the lithosphere during continental collision, *Geology*, **37**(9), 775–778.

Sdrolias, M. & Müller, R. D., 2006. Controls on back-arc basin formation, *Geochemistry, Geophysics, Geosystems*, **7**, 4016–+.

Sempere, T., Hartley, A., & Roperch, P., 2006. Comment on "Rapid uplift of the altiplano revealed through C-13-O-18 bonds in paleosol carbonates", *Science*, **314**(5800).

Silver, P. G., Russo, R. M., & Lithgow-Bertelloni, C., 1998. Coupling of South American and African Plate Motion and Plate Deformation, *Science*, **279**, 60–+.

Sonder, L. J. & Jones, C. H., 1999. Western United States Extension : How the West was Widened, *Annual Review of Earth and Planetary Sciences*, **27**, 417–462.

Stegman, D. R., Freeman, J., Schellart, W. P., Moresi, L., & May, D., 2006. Influence of trench width on subduction hinge retreat rates in 3-D models of slab rollback, *Geochemistry, Geophysics, Geosystems*, **7**, 3012–+.

Steinberger, B., Schmeling, H., & Marquart, G., 2001. Large-scale lithospheric stress field and topography induced by global mantle circulation, *Earth and Planetary Science Letters*, **186**, 75–91.

Suppe, J., 1983. Geometry and kinematics of fault-bend folding, *American Journal of Science*, **283**(7), 684–721.

Suppe, J. & Medwedeff, D., 1990. Geometry and kinematics of fault-propagation folding, *Eclogae Geologicae Helevtiae*, **83**(3), 409–454.

Tapponnier, P., Xu, Z., Roger, F., Meyer, B., Arnaud, N., Wittlinger, G., & Yang, J., 2001. Geology - Oblique stepwise rise and growth of the Tibet plateau, *Science*, **294**(5547), 1671–1677.

Turcotte, D. L. & Schubert, G., 2002. *Geodynamics*, Wiley and sons.

Čadek, O. & Fleitout, L., 2003. Effect of lateral viscosity variations in the top 300 km on the geoid and dynamic topography, *Geophysical Journal International*, **152**, 566–580.

Watts, A. B. & Burov, E. B., 2003. Lithospheric strength and its relationship to the elastic and seismogenic layer thickness, *Earth and Planetary Science Letters*, **213**, 113–131.

Wernicke, B., Spencer, J. E., Burchfiel, B. C., & Guth, P. L., 1982. Magnitude of crustal extension in the southern Great Basin, *Geology*, **10**(10), 499–502.

Wheeler, P. & White, N., 2000. Quest for dynamic topography : Observations from Southeast Asia, *Geology*, **28**, 963–+.

Willett, S. D., 1999. Orogeny and orography : The effects of erosion on the structure of mountain belts, *Journal of Geophysical Research*, **104**, 28957–28982.

Yang, Y., Liu, M., & Stein, S., 2003. A 3-D geodynamic model of lateral crustal flow during Andean mountain building, *Geophysical Research Letters*, **30**(21), 210000–1.

Zhong, S. & Gurnis, M., 1993. Dynamic feedback between a continentlike raft and thermal convection, *Journal of Geophysical Research*, **98**, 12219–+.

Zoback, M. L., Zoback, M. D., Adams, J., Assumpcao, M., & Bell, S., 1989. Global patterns of tectonic stress, *Nature* , **341**, 291–298.